COOL 07

Workshop on Beam Cooling and Related Topics

September 9-14, 2007
Bad Kreuznach, Germany
(organized by GSI, Darmstadt, Germany)

The workshop will highlight the state of the art in electron cooling, stochastic cooling, muon cooling, and storage of particles in antiproton and heavy ion traps. Presentations of new developments and techniques as well as of the status of existing and future facilities are invited.

The workshop will be held at the Parkhotel in Bad Kreuznach, a health resort in the center of Germany's Nahe wine growing area.

Local Organizers at GSI
Brigitte Azzara (Secretary)
Christina Dimopoulou
Erika Dittes (Secretary)
Rainer W. Hasse (Editor)
Fritz Nolden
Claudius Peschke
Volker Schaa (Editor)
Markus Steck
Gertrud Walter
email address: cool07@gsi.de

Imprint

Proceedings COOL 07

Published by

Gesellschaft für Schwerionenforschung mbH
Planckstraße 1
64291 Darmstadt
Germany

Editors

Rainer W. Hasse
Volker RW Schaa

JACoW version

Michaela Marx
Volker RW Schaa
http://www.jacow.org/

Printed by

some printing company
somewhere

Gesellschaft für Schwerionenforschung mbH, December 2007

Preface

The workshop COOL 07 was organized by GSI in succession to several precursor workshops on beam cooling and related techniques. It was held in the delightful neighborhood of the resort of Bad Kreuznach, Germany, between September 10 and September 14, 2007. The Park-Hotel Bad Kreuznach, located close to the spa gardens and the city, provided comfortable meeting rooms and created a relaxed atmosphere during and after the sessions.

The workshop was attended by 68 participants from 8 countries in Europe, America, and Asia. About two thirds of the contributions were presented in talks, one third on posters. The workshop was structured in 14 sessions of 3 oral presentations each, two in the morning and two in the afternoon. One afternoon was reserved for the poster presentations and ended in a special lecture by Fritz Bosch of GSI on the application of stochastic and electron cooling to prepare rare isotope beams for experiments studying the decay of single ions. One session organized by Dieter Möhl aimed at a discussion of special ion optical lattices for optimum performance of stochastic cooling.

The contributions gave a rather complete overview of recent developments in the field of beam cooling, but also some planned new projects and ideas for advanced cooling concepts were discussed. The presentations covered the range from high intensity antiproton stacks accumulated by stochastic cooling, and now also supplemented by electron cooling, down to low intensity crystalline beams achieved by means of electron or laser cooling. Beyond these well-established techniques, more advanced concepts like muon and ionization cooling and a stochastic cooling scheme based on the use of an electron beam were discussed.

A possibility to relax from the workshop and enjoy the vicinity was given on an afternoon excursion that took the participants along the Rhine Valley culminating in the conference dinner at the Eberbach Monastery. The excursion, as well as the reception on the eve of the workshop, gave plenty of time for intense and extended discussions.

The organizers would like to thank GSI, Research Centre Jülich, and Pink Vacuum for sponsoring this workshop.

Special thanks should be given to the conference secretaries Brigitte Azzara, Erika Ditter, and Paola Karampougiouki, who prepared and managed the workshop with high efficiency and great enthusiasm, and to the editors Rainer W. Hasse, Michaela Marx, and Volker RW Schaa for successfully introducing the JACOW system for the publication of the workshop and for their editorial work.

Markus Steck

Chairman of COOL 07

International Program Committee

Ilan Ben-Zvi	BNL, Brookhaven, USA
Håkan Danared	MSL, Stockholm, Sweden
Yaroslav Derbenev	TJNAF, Newport News, USA
Dan M. Kaplan	IIT, Chicago, USA
Kwang-Je Kim	ANL, Argonne, USA
Igor Meshkov	JINR, Dubna, Russia
Dieter Möhl	CERN, Geneva, Switzerland
Yoshiharu Mori	KEK, Tokyo, Japan
Sergei Nagaitsev	FNAL, Batavia, USA
Akira Noda	Kyoto University, Japan
Vasily V. Parkhomchuk	BINP, Novosibirsk, Russia
Ralph Pasquinelli	FNAL, Batavia, USA
Dieter Prasuhn	IKP, Jülich, Germany
Andrew Sessler	LBNL, Berkeley, USA
Markus Steck	GSI, Darmstadt, Germany
Gérard Tranquille	CERN, Geneva, Switzerland
Hong W. Zhao	IMP, Lanzhou, China

Local Organizing Committee

Brigitte Azzara (Secretary)	GSI, Darmstadt, Germany
Christina Dimopoulou	GSI, Darmstadt, Germany
Erika Ditter (Secretary)	GSI, Darmstadt, Germany
Rainer W. Hasse (Editor)	GSI, Darmstadt, Germany
Paola Karampougiouki (Secretary)	GSI, Darmstadt, Germany
Michaela Marx (Editorial Team)	DESY, Hamburg, Germany
Fritz Nolden	GSI, Darmstadt, Germany
Claudius Peschke	GSI, Darmstadt, Germany
Volker RW Schaa (Editor)	GSI, Darmstadt, Germany
Markus Steck (Chairman)	GSI, Darmstadt, Germany
Gertrud Walter	GSI, Darmstadt, Germany

Contents


GSI
FAIR


Sparkasse
HOTEL BURG STAHLECK

STATUS OF THE FERMILAB RECYCLER*

P.F. Derwent†, for the Recycler Department
Fermi National Accelerator Laboratory, Batavia IL 60510-0500 USA

Abstract

I present the current operational status of the Fermilab Recycler Ring. Using a mix of stochastic and electron cooling, we prepare antiproton beams for the Fermilab Tevatron Collider program. Included are discussion of stashing and cooling performance, operational scenarios, and collider performance.

THE RECYCLER RING AT FERMILAB

The Fermilab Recycler is an 8 GeV storage ring using strontium ferrite permanent magnets. It was designed to provide more antiprotons for the Tevatron collider program, though the use of stochastic and electron cooling [1]. By providing a second storage ring for the accumulation of antiprotons and allowing for the recycling of antiprotons from the Tevatron, the Recycler was a critical part of the luminosity improvements to a design goal of $2\times10^{32}/\mathrm{cm}^2/\mathrm{sec}$. The Run II luminosity upgrade program expanded on this original design, requiring the Recycler to be the repository of large stashes (6×10^{12}) with appropriate phase space characteristics to be used in the Tevatron collider stores, while abandoning the plan to recycle antiprotons. In order to maximize the stacking efficiency of the Fermilab antiproton Accumulator, small stacks of antiprotons ($\approx 5 \times 10^{11}$) are transferred every 2-3 hours to the Recycler. In the Recycler, the stash is initially cooled by stochastic cooling [2], then stored and cooled by electron cooling [3] until the antiprotons are to be used in the Tevatron. Table 1 presents basic parameters of the Recycler ring. As we inject and extract with stored beam in the Recycler, we use barrier potential wells to time separate the cold 'stashed' beam from the 'hot' injected beam (or the beam for extraction).

Table 1: Recycler Ring Design Parameters

Circumference	3310.8 m
Momentum	8.9 GeV/c
Transition γ	20.7
Average β Value	30 m
Typical Transverse Emittance	6 $\pi\mu$m rad
Number of antiprotons	$\leq 600 \times 10^{10}$
Average Pressure	0.5 nTorr

ANTIPROTON COOLING

The Recycler utilizes both stochastic and electron cooling for antiprotons. Table 2 summarizes important parameters for the different cooling systems. As electron cooling can be viewed as an energy exchange process from the hot antiproton beam to the cold electron beam, achieving transverse overlap between the two beams is essential. The stochastic cooling systems are designed to cool the antiproton beam transversely, to be contained within the transverse size of the electron beam, so as to maximize the electron cooling force (see discussion in reference [4]).

Table 2: Stochastic and Electron Cooling System Parameters. There are two independent notch filter longitudinal stochastic cooling systems, in different frequency ranges.

Longitudinal Stochastic Cooling	
Frequency Range	0.5 – 1.0 GHz
Number of Pickup/Kicker loops	16
Frequency Range	1.0 – 2.0 GHz
Number of Pickup/Kicker loops	32
Operating Temperature	300 K
Transverse Stochastic Cooling	
Horizontal Frequency Range	2.0 – 4.0 GHz
Number of Pickup/Kicker loops	32
Vertical Frequency Range	2.0 – 4.0 GHz
Number of Pickup/Kicker loops	32
Operating Temperature	300 K
Electron Cooling	
Terminal Voltage	4.34 MV
Beam Current (max)	0.5 mA
Terminal Voltage Ripple (rms)	200 V
Cooling Section Length	20 m
Cooling Section Solenoidal Field	100 G
Cooling Section Beam Radius	3.5 mm
Electron Angular Spread (rms)	≤ 0.2 mrad

The stochastic cooling systems were commissioned and integrated in operations in early 2003. There are two independent longitudinal systems, spanning the ranges 0.5 –1.0 GHz and 1.0 – 2.0 GHz, which use notch filter cooling. The transverse systems (both horizontal and vertical) are in the frequency range 2.0 – 4.0 GHz. All stochastic cooling systems use planar loops for pickups and kickers [5]. Gated cooling studies, to show that the systems met the performance requirements, were performed in 2004 [2]. In figure 1, I show the transverse cooling performance of the systems. They effectively cool 15π mm mrad [6] beams to 10π mm mrad within 25 minutes. Beams of

* Work supported by the Fermi Research Alliance, under contract DE-AC02-76CH03000 with the U. S. Dept. of Energy.
† derwent@fnal.gov

10π mm mrad fit within the designed electron beam radius.

The electron cooling system was commissioned and integrated in operations in 2005 [3, 7]. It utilizes a 4.3 MeV DC electron beam. The beam is generated by a thermionic-cathode gun, located at a potential of 4.3 MV inside of a large electrostatic accelerator. We can sustain electron beam and voltage with currents to ground of less than 100 μA. To maintain this high efficiency, we utilize a recirculation system that has an efficiency $> 99.998\%$ for currents up to 0.5 A.

The electron gun is immersed in a solenoidal magnetic field to create a beam with large angular momentum. The beam is transported through the electrostatic accelerator and to the cooling section using convential focussing elements, then is made round and parallel to the antiproton beam such that the beam radius r_b produces the same magnetic flux as at the cathode [7]. Operationally, the electron cooler is required to reduce the longitudinal emittance from up to 140 eV-sec to $\approx$ 70 eV sec in 90 minutes for stashes up to 500×10^{10} antiprotons, which is slightly different than originally foreseen [8].

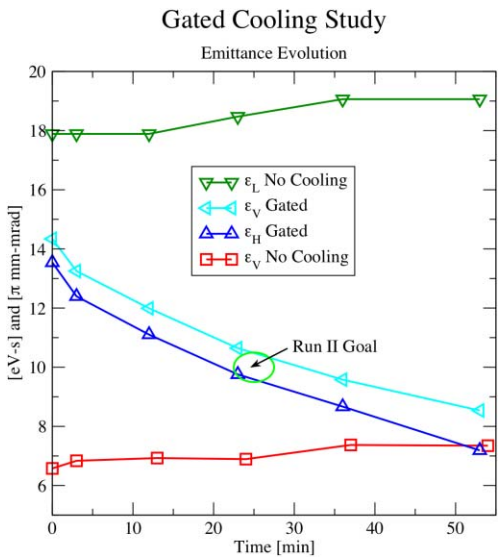

Figure 1: Gated cooling demonstration for the stochastic cooling systems. 20×10^{10} antiprotons were in a barrier potential well and the transverse stochastic cooling systems were gated to cool only the particles in that well. An additional 20×10^{10} antiprotons were in a separate potential well and were not cooled. The goal was to cool to 10πmmmrad within 30 minutes. The goal was attained, with no heating to the beam that was not in the cooled potential well.

OPERATIONAL SCENARIOS

Incoming Antiprotons from the Accumulator

The Antiproton source has made significant improvements in accumulating antiprotons through the past two years [9]. The average stacking rate has gone from 10×10^{10} antiprotons per hour to more than 17×10^{10}, with peak hours where better than 23×10^{10} antiprotons have been accumulated. There has also been significant work done in speeding up the transfers from the Accumulator to the Recycler. It is a point that often times gets lost in the shuffle, that the amount of time spent to do a transfer is time that is not spent stacking, resulting in lower total accumulation in a fixed time frame.

For transfers, we have changed our operational mindset. As antiprotons are difficult to produce, we defined success as not accepting loss of a transfer. The antiproton transfer goes from the Accumulator through a transfer line into the Main Injector, through a small energy change to match the Recycler, and into the Recycler. We did a complete detailed beam line tune up with protons from the Main Injector to the Accumulator, including the energy matching and orbit closure in the Accumulator. We had two separate sets of power supplies for the transfer line, as it is also used to transport 120 GeV protons from the Main Injector to the antiproton target, the power supply regulation at 8 GeV currents through the 120 GeV supplies was not originally good enough, and we switched supplies based on how the beamline was being used. The Run II Upgrade program included elements to improve the power supply regulation so that we no longer need to switch supplies to do antiproton transfers. The entire tuneup, plus transfers, would take on order 60 minutes, during which there was no accumulation of antiprotons in the Accumulator. To maximize performance, we would transfer when the Accumulator current reached $> 80 \times 10^{10}$ antiprotons, which required 6 separate transfers to empty the Accumulator because of bucket area constraints and longitudinal emittance in the Accumulator. Each transfer required manipulations of the barrier potential wells in the Recycler, adding time to the process. Of this 60 minutes, $\approx \frac{2}{3}$ was spent in tune up and $\frac{1}{3}$ in transferring antiprotons.

By defining success as accepting the occasional loss of a transfer, we now operate in a different mode. We use the 120 GeV beamline supplies for both protons to the antiproton target and antiprotons from the Accumulator to the Main Injector. We do a brief beamline tuneup with protons, using the efficiency of the transfer from the Main Injector to the Accumulator to define whether a more detailed tuneup is necessary (if the efficiency is $> 85\%$, we proceed). As the total preparation time is smaller, we can do transfers more frequently with less of an impact, so transfers are triggered at smaller Accumulator currents ($> 50 \times 10^{10}$ antiprotons). As the current is smaller, the Accumulator stochastic cooling systems are more efficient, lowering the longitudinal emittance and requiring fewer transfers to empty the Accumulator. With fewer transfers, the time for the barrier potential well manipulations is also smaller. We know routinely do the transfers in $\approx$ 12 minutes, with the same $\frac{2}{3}$ $\frac{1}{3}$ split between setup and transfer, with 3 separate transfers from the Accumulator to the Recycler. We estimate (given caveats discussed below with regard to inten-

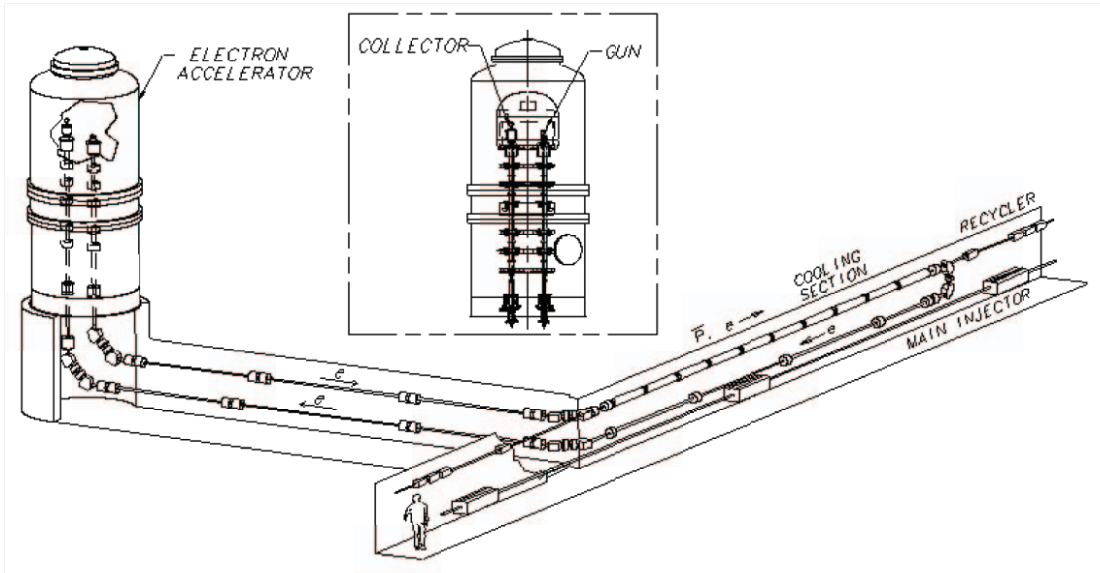

Figure 2: Electron Cooling insert in the Fermilab Recycler.

sity measures) that the transfer efficiency is $\approx 90\%$, falling slightly as intensity in the Recycler increases.

Figure 3 shows an operational week for the Recycler. In the top plot, the Recycler beam intensity is in red, the Accumulator beam intensity is in blue, and the sum is in green (all in units of 10^{10}). During this 7 day period, there were 52 transfers from the Accumulator to the Recycler, with the peak Accumulator current of $\approx 75 \times 10^{10}$ but most occurring at 50×10^{10}. There were 4 transfers to the Tevatron during this week, with Recycler current routinely $> 300 \times 10^{10}$ and peak current $> 450 \times 10^{10}$ antiprotons. There was one lost stash in the Recycler, due to a failure in a CAMAC controls crate that included the control cards for ramped trim dipoles (used to compensate for changes in the path length due to the ramping of the dipole and quadrupole busses in the Main Injector). In the bottom plot, red is the horizontal transverse emittance and blue is the vertical transverse emittance for the antiproton beam in the Recycler. Note that we were consistently able to keep the transverse emittances between 5 and 7 π mm mrad, even as the intensity reached its maximum.

Of interest in figure 3 is the behavior of the beam intensity in the Recycler between transfers from the Accumulator. One would expect the intensity to decay during this time period, due to finite beam lifetime. Close inspection of the intensity shows that it in fact rises in between transfers! Are we making antiprotons out of the vacuum? No, of course we are not. In December 2006, the main beam current measuring device (a DCCT) for the Recycler failed. We did not have a replacement in hand, so we needed an alternative method of measuring the beam current. The DCCT was the only instrument capable of making a DC measurement, but we do have additional toroids and a resistive wall monitor for making AC measurements. Because we do keep the beam in a barrier potential well,

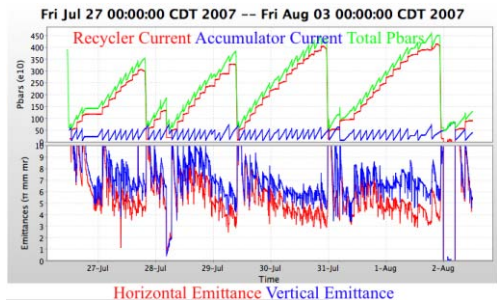

Figure 3: An operational week for the Recycler. In the top plot, blue is the Accumulator intensity, red is the Recycler intensity, and green is the sum (in units of 10^{10}. In the bottom plot, red is the horizontal transverse emittance and blue is the vertical transverse emittance (both 95% normalized π mm mrad).

there is a strong AC signal available (see figure 4).

By sampling and integrating the signal, we can calculate the beam intensity. We use 588 samples (the number of 53 MHz RF buckets in the Main Injector, which has the same circumference and serves as a convenient clock) over the 11.13 μsec time of a revolution. By looking for the minimum in the signal and correlating it with the time where we expect that there is no beam, we can define a baseline. However, if there are high momentum antiprotons (with $\Delta p > 18$ MeV/c), they will not be trapped within the barrier potential well and will be DC beam within the Recycler. This DC beam causes a baseline shift. As the beam is strongly cooled by the electron cooler, these free particles fall into the potential well, so the baseline moves down and the beam intensity over baseline increases, resulting in an 'increase' in the measured antiproton beam current. This behavior has made it difficult for us to truly define transfer

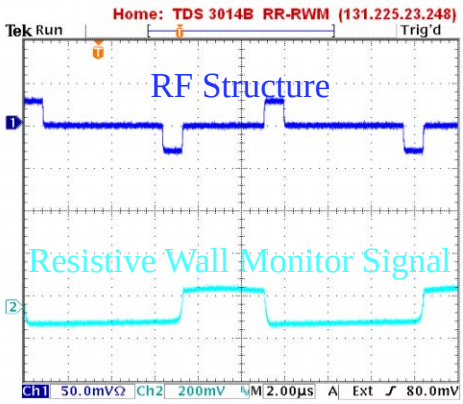

Figure 4: An oscilloscope view of the RF waveform (the integral creates a potential well) and the resistive wall monitor signal. The Recycler revolution period is 11.13 μsec, so the 20 μsec displayed shows more than 1 full turn.

efficiencies, peak intensities, beam lifetimes, or any other measures that depend upon accurate and precise measures of beam current. As all antiprotons coming in and going out travel through the Main Injector, we use the measured intensities in that machine to define some of our performance criteria.

With these caveats, the week summarized in figure 3 saw 2.72×10^{13} antiprotons transferred into the Recycler and 1.82×10^{13} transferred out of the Recycler (with loss of $\approx 1.2 \times 10^{12}$ due to the controls failure).

A standard accumulation period is approximately 25 hours. Soon after the antiprotons have been transferred from the Recycler, we accept antiprotons from the Accumulator, which has been stacking during the Recycler – Tevatron transfer process. The electron cooler is not needed until the accumulated intensity is $> 100 \times 10^{10}$, giving approximately 4 hours where beam studies can be done with the electrons without disturbing the antiprotons. Once the intensity reaches this threshold, the electron cooler is turned on with electron current of 100 mA. The electron beam is radially offset from the antiproton beam to control the cooling rate [4]. For the final hour of cooling before transfer to the Tevatron, the beam current is increased to 200 mA and slowly brought 'on–axis' with the antiproton beam. This cooling approach has been driven by the desire to control the longitudinal and transverse emittances of the antiprotons as a function of intensity so that the Tevatron can handle the antiproton beam brightness.

We have reached this operating mode by optimizing the average accumulation of antiprotons (which includes stacking performance in the Accumulator, the transfer time, and efficiency from the Accumulator to the Recycler) balanced against the integrated luminosity in the Tevatron. The integrated luminosity in the Tevatron is a complicated mix of beam intensities, emittances, and tune operating point [10], with both proton and antiproton beam brightness important inputs to the performance.

COLLIDER PERFORMANCE

The goal of the Recycler is to provide bright antiproton beams to the Tevatron Collider, to maximize the integrated luminosity for the two collider experiments. History has shown that antiproton intensity is the single strongest correlation for the collider program. Figure 5 shows the number of antiprotons (in units of 10^{10}) available at the start of a Tevatron shot. The horizontal axis is time, with the different colors representing different fiscal years (as defined by the US government, which differ from calendar years in that they go from 1 October to 30 September). The first 3 years (to the start of 2005), we only had the Accumulator available as an antiproton storage ring. Starting in 2005, we used both the Accumulator and the Recycler. During this period, the Recycler was limited to intensities of $< 175 \times 10^{10}$ because of limitations in the stochastic cooling and the lack of a transverse damper. Starting in the fall of 2005 through the present, with the commissioning of electron cooling and transverse dampers, the Recycler has become the main antiproton storage ring. The peak number of antiprotons available to the collider has doubled in the last 2 years. This doubling is a result of stacking improvements in the Accumulator [9], operational improvements in transfer time and efficiency, and the operation of electron cooling in the Recycler.

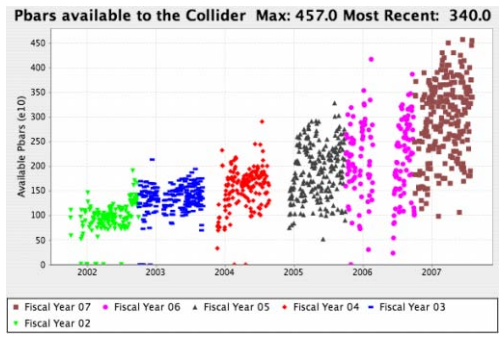

Figure 5: The number of antiprotons (by US government fiscal year) available to the Tevatron Collider. During the time period 2002-2004, antiprotons were stored only in the Accumulator. Starting in 2005, we began using both the Accumulator and the Recycler. After the commissioning of the electron cooling in the Recycler [3] in the summer and fall of 2005, the Recycler became the sole repository for antiprotons.

With the increased intensity comes the question, can the Recycler preserve the transverse and longitudinal emittance? Intrabeam scattering emittance diffusion, stochastic cooling performance, instabilities, etc., are all strongly intensity dependent. In figure 3, the lower plot shows the transverse emittances as measured for intensities ranging from $\approx 10 \times 10^{10}$ to $> 450 \times 10^{10}$. The transverse emittances are all kept within the range of 5 – 7 π mm mrad, which is the required target for the Tevatron collider. Smaller transverse emittances can actually hurt inte-

grated luminosity performance, because of changes to the beam and emittance lifetimes in the Tevatron due to beam beam effects [10]. In figure 6, the 95% longitudinal emittance (assuming a Gaussian beam distribution) is shown as a function of the Recycler antiproton intensity. Most stashes are between 54 and 70 eV secs, with the stated goal of 54 eV sec and available bucket area of 72 eV sec. As the electron cooled beam distribution is sharper than a Gaussian (for example, we measure an RMS of 2.66 MeV/c momentum spread and that the 90% width is 7.7 MeV/c, while for a Gaussian distribution we would expect a 90% width of 8.8 MeV/c), this measure is an overestimate of the 95% longitudinal emittance, which is why operationally we accept this measure up to 70 eV sec for transfers.

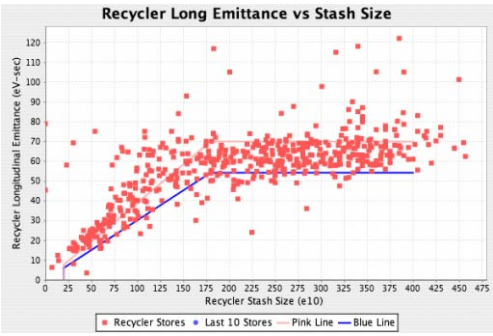

Figure 6: The calculated 95% longitudinal emittance (in units of eV-sec, assuming a Gaussian beam distribution) for the Recycler as a function of the beam intensity (units of 10^{10}). The pink and blue lines represent performance goals for cooling performance.

Figure 7 shows the peak luminosity attained in the Tevatron as a function of time. Since the Recycler and electron cooling became part of standard operations in the fall of 2005, the peak luminosity has doubled, both because of improvements in the Accumulator [9], the Tevatron [10], and the use of the Recycler and electron cooling. With continuing improvements to the Accumulator stacking performance, operational experience with the Recycler and electron cooling, and continuing work with the Tevatron, we anticipate that we will continue to push the number of antiprotons accumulated to $> 500 \times 10^{10}$ and the peak luminosity to $> 3 \times 10^{32}/\mathrm{cm}^2/\mathrm{sec}$.

ACKNOWLEDGEMENTS

I would like to acknowledge all the members of the Recycler Department at Fermilab, who have done the work to make the Recycler and the Pelletron operate so well during the previous two years. I would also like to thank the organizers of this conference for giving me the opportunity to present these results.

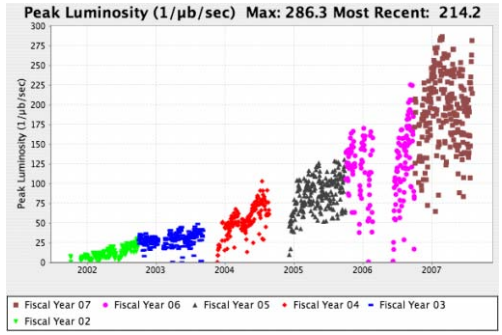

Figure 7: The peak luminosity (in units of $10^{30}/\mathrm{cm}^2/\mathrm{sec} = 1\mu\mathrm{b}^{-1}/\mathrm{sec}$) achieved in the Tevatron Collider. During the time period 2002-2004, antiprotons were stored only in the Accumulator. Starting in 2005, we began using both the Accumulator and the Recycler. After the commissioning of the electron cooling in the Recycler [3] in the summer and fall of 2005, the Recycler became the sole repository for antiprotons. There have been many improvements in the Tevatron performance to handle the higher antiproton intensities [10].

REFERENCES

[1] G. Jackson, FERMILAB-TM-1991 (1996).

[2] D. Broemmelsiek, A. V. Burov, S. Nagaitsev and D. Neuffer, "Bunched beam stochastic cooling in the Fermilab Recycler Ring," to appear in the proceedings of Particle Accelerator Conference (PAC 05), Knoxville, Tennessee, 16-20 May 2005. FERMILAB-CONF-05-132-AD, PAC-2005-FPAE009, May 2005.

[3] S. Nagaitsev, *et al.*, Phys. Rev. Lett. **96** 044801 (2006).

[4] L. Prost, these proceedings.

[5] J. Petter *et al.*, "Novel Stochastic Cooling Pickups/Kickers" in IEEE Particle Accelerator Conference, Chicago IL 1989.

[6] All transverse emittances quoted in this paper are using the standard 95% normalized emittance.

[7] S. Nagaitsev, *et al.*, "Antiproton Cooling in the Fermilab Recycler Ring", in *Beam Cooling and Related Topics, International Workshop on Beam Cooling and Related Topics COOL05*, edited by S. Nagaitsev and R.J. Pasquinelli, AIP 0-7354-0314-7/06, Galena IL Sep 2005.

[8] A. Burov, *et al.*, Phys. Rev. ST AB **3** 094002 (2000).

[9] V. Lebedev, these proceedings.

[10] R. Moore, "Review of Recent Tevatron Operations", to appear in the proceedings of Particle Accelerator Conference (PAC 07), Albuquerque, New Mexico 25-29 June 2007.

STATUS OF THE ANTIPROTON DECELERATOR AND OF THE ELENA PROJECT AT CERN

P. Belochitskii, CERN, Geneva, Switzerland

Abstract

The Antiproton Decelerator (AD) at CERN operates for physics since 2000 [1]. It delivers low energy antiprotons for production and study of antihydrogen, for atomic physics and for medical research. Two beam cooling systems, stochastic and electron, play key roles in AD operation. They make beam transverse and longitudinal emittances small, which is an obligatory condition for beam deceleration without losses, as well as for physics. The machine performance is reviewed, along with plans for the future. Significant improvement of intensity and emittances of the beam delivered to the experiments could be achieved with the addition of a small ring suitable for further deceleration and cooling. The details of this new extra low energy antiproton ring (ELENA) and its status are presented.

AD CYCLE

The 26 GeV/c proton beam from CERN PS is delivered to the target where antiprotons are produced and transferred to AD. The machine cycle is a sequence of plateaus and ramps (Figure 1).The first plateau is suited for injection of 4 bunches followed by 90° rotation in the longitudinal phase space to fit beam momentum spread to longitudinal acceptance of the stochastic cooling system. Then beam is cooled, decelerated down to 2 GeV/c and cooled again. Deceleration down to 300 MeV/c follows, where beam is cooled, now with electron cooling. Next ramp down to 100 MeV/c follows, where beam is cooled down to emittances required for AD experiments, bunched and extracted.

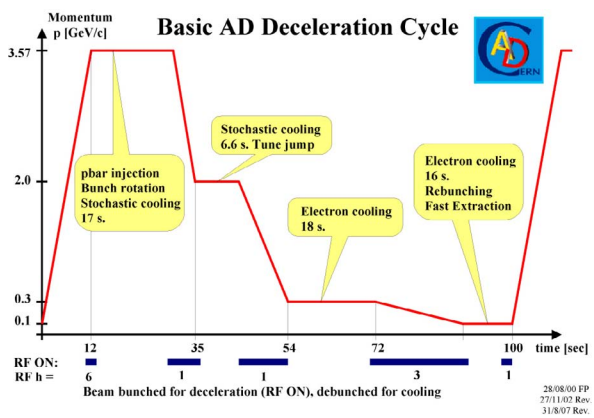

Figure 1: AD cycle.

STOCHASTIC COOLING

Due to lack of space only band I (1 - 1.65 GHz) from AC (AD predecessor) is used (H&V pickup tanks and H&V kicker tanks), bands II and III (1.65 GHz to 2.40 GHz and 2.40 GHz to 3.0 GHz) are dismantled. The momentum cooling is done by notch filter method with sum signal from both PUs sent to both kickers. The momentum acceptance of system is about ±1.0%, which is significantly smaller than momentum spread of injected beam which is ±3%. To fit the latter to the former, the advantage of short bunch length of production beam is used. Short antiproton bunches are rotated 90° in the longitudinal phase space with reduction of momentum spread to about ±1.2%. Cooling at 2 GeV/c is mainly aimed to reduce momentum spread of beam to fit the small longitudinal acceptance of RF cavity. The performance of stochastic cooling system is shown in Table 1.

Table 1: Performance of stochastic cooling system

Momentum, GeV/c	3.57	2.0
Duration, sec	17	6
$\varepsilon_x / \varepsilon_y$, π mm mrad	3 / 3	4 / 5
$\Delta p/p$	$1 \cdot 10^{-3}$	$2 \cdot 10^{-4}$

ELECTRON COOLING

The AD electron cooler (Figure 2) is recuperated from LEAR, which stopped operation in 1996, with minimal upgrade (mechanical support, change from S-shape to U-shape). The parameters of cooler are given in Table 2.

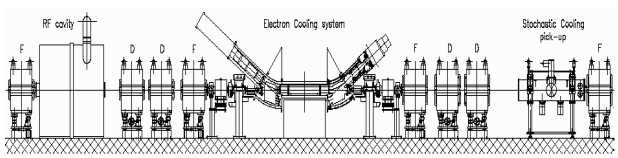

Figure 2: Layout of electron cooler.

The performance of electron cooling in AD is sensitive to orbit stability. Special procedure has been implemented to compensate slow orbit drift caused by decay of eddy currents in massive end plates of bending magnets. To avoid losses during cooling process, careful choice of tunes and coupling compensation have to be done.

Table 2: Main parameters of electron cooler

Cooling length, m	1.5
Electron beam energy, keV	2.8 - 35
Electron beam current, A	0.1 – 2.5
Field in solenoid, Gs	590
Electron beam radius, cm	2.5

The electron cooling at 300 MeV/c is accompanied by about 13% of beam losses. They can be reduced by earlier start of gun voltage, several seconds before beam arrives to plateau. In addition, both careful choice of tunes and coupling compensation have to be done to keep as much beam as possible during cooling.

Small dispersion in a cooler region is prepared at 300 MeV/c resulting in a smaller horizontal emittance compared with the vertical one. The cooling time at 300 MeV/c is about 10 sec to 15 sec. It is chosen to cool down to emittances less than 5π mm mrad in both planes to make the following deceleration lossless and also to facilitate cooling at 100 MeV/c.

Main task of cooling at 100 MeV/c is to prepare the beam for physics. Typical requirements are: $\varepsilon < 1\pi$ mm mrad and bunch length shorter than 170 nsec. Due to RF noise during beam bunching before extraction the longitudinal emittance is blown up resulting in increased bunch length. To overcome this, electron cooling is extended to overlap a part of bunching process. Unfortunately, the "cross-talk" between two systems causes beam filamentation in transverse planes with creation of core (70% to 85% of beam) and halo [2]. The compromise for overlapping time for cooling and bunching has to be carefully chosen to achieve optimal transverse and longitudinal emittances. The performance of electron cooling is given in Table 3.

Table 3: Performance of electron cooling

Momentum, MeV/c	300	100
Duration, sec	16	15
$\varepsilon_x/\ \varepsilon_y,\ \pi$ mm mrad	1.6 / 2.4	<0.5 / <0.5
$\Delta p/p$	$8\cdot10^{-5}$	$1.2\cdot10^{-4}$

MACHINE OPERATION

Since autumn 2004 AD runs without stopping on weekends to increase a time available for physics. In 2006 beam availability went down to 70% due to major faults in CERN PS and due to long start up period in AD. This year is good in view of machine performance. Unfortunately in the middle of the run the orbit started to jump from time to time causing degradation of deceleration efficiency and emittance until new readjustment. This is caused by magnetic field fluctuations in one of the dipoles on side of electron cooler. The coils in this corrector magnet are likely to be damaged and the magnet is scheduled for replacement. The operational statistics is summarized in Table 4.

Table 4: Operational statistics

	2000	2001	2002	2003	2004	2006
Total	3600	3050	2800	2800	3400	2352
Physics	1550	2250	2100	2300	3090	2185
MD	2030	800	700	500	310	167
Uptime	86%	89%	90%	90%	71%	69%

MACHINE PERFORMANCE

The performance of AD is defined by number of antiprotons per second and by beam emittances. The deceleration efficiency (number of extracted antiprotons divided by number of cooled antiprotons at injection energy) is 80% to 85% and can be improved only slightly.

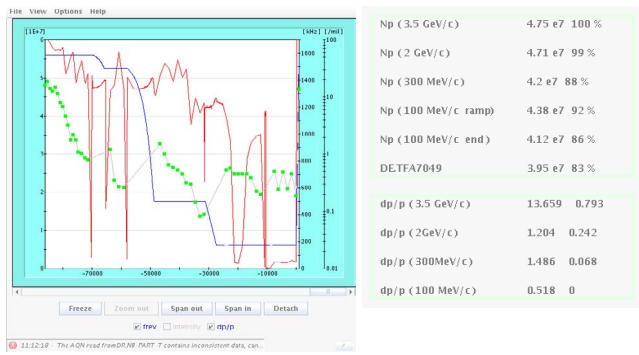

Figure 2: Beam intensity during AD cycle.

The beam intensity depends mainly on production beam from CERN PS. The potential of its increase exists but needs hardware upgrade for sophisticated RF gymnastics in PS. The ramp speed is limited by eddy currents and is already at the limit The cooling time at 100 MeV/c could be shorter which is a subject for investigations.

Yet there is another and very efficient way to increase a lot the number of antiprotons delivered to experiment. To present this proposal a short review is useful which gives more details how AD beam is used by experiments.

POSTDECELERATION OF AD BEAM BY EXPERIMENTS

The ALPHA and ATRAP experiment physics programs are focused on trapping antiprotons in Penning traps where antihydrogen is created after recombination with positrons. Typical energy range to trap antiprotons is 3 keV to 5 keV. To decelerate beam down to this range from extraction energy 5.3 MeV (momentum 100 MeV/c) several degraders are used. During passing the degrader 99.9% of AD beam is lost and the remaining beam is blown up.

The ASACUSA experiment uses RFQD (Radio Frequency Decelerating Quadrupole) for further deceleration of antiprotons down to about 100 keV kinetic energy. The use of RFQD allows to reduce significantly beam losses in degrader because much thinner one can be used. Still the deceleration efficiency in RFQD is about 25% to 40% only and beam emittances are increased.

EXTRA LOW ENERGY ANTIPROTON RING (ELENA)

Machine Main Features and Location

For efficient deceleration of antiprotons to low energy a small ring with electron cooling has been proposed [3]. The low energy limit for this machine is 100 keV. It was chosen as a compromise between requirements from experiments of ultra low energy beam and constraints given by space charge limitations in machine and cooler, requirements to vacuum of few 10^{-12} Torr and others. The availability of electron cooling system allows to keep very high phase space density which is a top priority from users. With extra ring which delivers very dense low energy beam one to two order of magnitude more trapped antiprotons expected for experiments.

ELENA ring is a small machine with circumference of 26m and can be placed inside of AD Hall (see Figure 3). Small reshuffle of experimental area is required, as well as movement of some of AD equipment and new configuration of shielding. The precise positioning of a new ring in AD Hall will be dictated by optimal conditions for injection and for extraction into existing experimental areas.

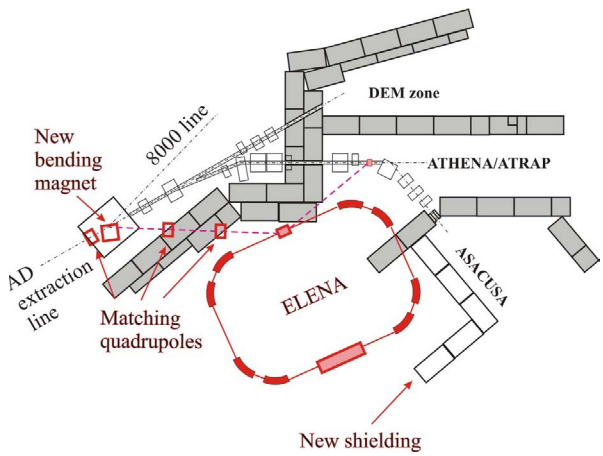

Figure 3: ELENA ring location in AD Experimental Area.

Ring Configuration

Two variants of ring configuration have been studied, triangular and rectangular [4]. For the first one possible tune range is from 0 to 1.5 and optics with suitable beta functions and working point Q_x/Q_y=1.30/1.28 can be prepared. For the second one tune range is from 0 to 2 and more choice of working points is available. The comparison of two optics shows that triangular machine is longer and provides less room in tune diagram which is essential due to space charge limitations at low energies.

As result, a machine with four straight sections has been chosen. Two long sections are suited for electron cooler and injection/ejection system, and two short sections for beam diagnostics, RF equipment and other (Figure 4).

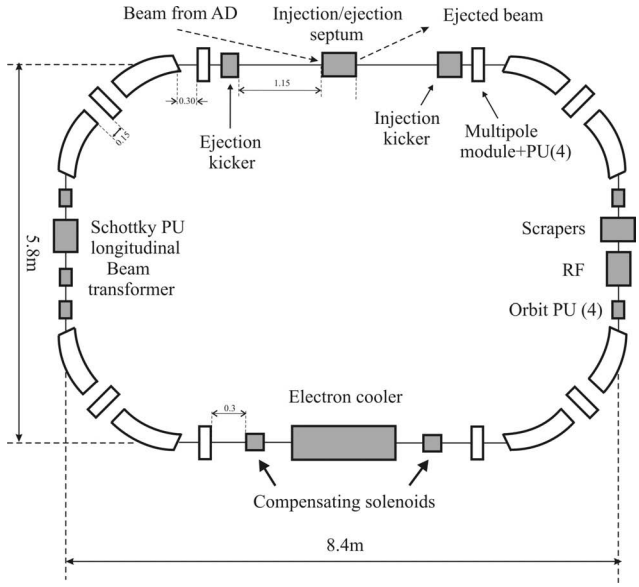

Figure 4: ELENA ring layout.

Electron Cooler

In ELENA cooling will be done at two momenta during deceleration cycle. At the intermediate momentum of 35 MeV/c the antiproton beam will be cooled to avoid beam losses during deceleration and to prepare good conditions for last cooling at 13.7 MeV/c. At extraction energy beam with small emittances is prepared by cooling to fit requirements for physics.

For fast and efficient cooling special attention must be paid to the design of the electron gun and the quality of the longitudinal magnetic field guiding the electrons from the gun to the collector [5]. The electron gun has to be designed in a way to produce a cold ($T_\perp < 0.1$ eV, $T_\parallel < 1$ meV) and relatively intense electron beam ($n_e \approx 3\text{x}10^{12}$ cm^{-3}). The gun is immersed in a longitudinal field of 700 Gs which is adiabatically reduced to maximum field of 200 Gs in the transition between the gun solenoid and the toroid. Due to this transverse temperature is reduced as well during beam adiabatic expansion. The main characteristics of the proposed device are summarized in Table 5.

Table 5: Main parameters of electron

Cooling length, m	1
Beam cooled at momentum, MeV/c	35 and 13.7
Electron beam energy, V	355 and 54
Electron beam current, mA	15 and 2
Magnetic field in solenoid, Gs	200
Electron beam radius,, cm	2.5

To compensate coupling introduced by drift solenoid, two compensators are placed on each sides of the cooler.

Two horizontal and two vertical orbit correctors are located on each side of the cooler for compensation of kicks produced by toroids and for optimal alignment of antiproton beam with respect to electron beam. The schematic layout of electron cooler for ELENA is shown in Figure 5.

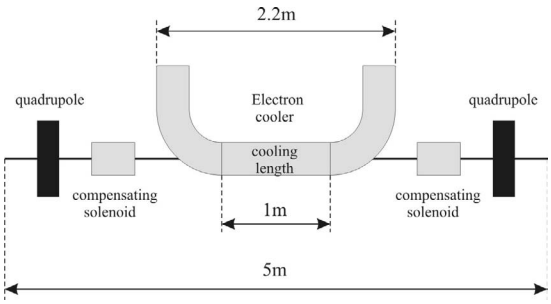

Figure 5: Layout of electron cooler for ELENA.

The simulation of electron cooling have been performed using BETACOOL code[6] to study sensitivity of cooling time to main cooler parameters like electron beam temperatures, magnetic field in drift solenoid and others. With electron beam parameters mentioned above and magnetic field 200 Gs the beam is cooled from $\varepsilon_{x,y}$ = 20π mm mrad to $\varepsilon_{x,y}$ =1π mm mrad in one second. The influence of other parameters (gas pressure, IBS) has been studied as well [7]. Due to very strong optics perturbation by solenoidal fields operation with lower magnetic field (i.e. 150 Gs) is foreseen. With proper gas pressure required final emittances are achieved in a bit longer time, which makes no effect on ELENA performance because AD cycle is much longer than ELENA cycle.

Optics of ELENA

The machine optics was designed [4] to fit the following tasks:

- Magnet system should be compact and minimizing expenses
- Operation with significant incoherent tune shift due to space charge should be foreseen
- Proper conditions for effective work of electron cooling system should be prepared, and unavoidable effects of cooler on antiproton beam carefully compensated.

Two lattices with tunes Q_x/Q_y=1.45/1.42 and Q_x/Q_y=1.64/1.62 have been compared. The first one provides moderate beta functions in cooler about 3m to 4m, the second one gives twice smaller beta function values there. As result, the first optics is much more sensitive to effect of solenoid of electron cooler and of compensating solenoids, which increases toward the end of the ramp. This effect is squared with magnetic field in a drift solenoid of cooler and breaks lattice periodicity (Figure 6). On the other side, very small beta function values in a cooler section of the second optics are not favourable for fast cooling, which could be critical at low energy. In addition, in the first machine tunes are more distanced from the limiting resonances. As result, the first variant of optics has be chosen.

The tune shift produced by electron beam is noticeable as well, but is much smaller than effect of solenoidal fields. It is independent on antiproton beam energy and can be handled more easily.

The important feature of optics is that focussing is done mainly in bending magnets by proper choice of length and edge angle. The quadrupoles are weak and suited for fine adjustment of tunes in operation, and for compensation of the effects of electron cooler on machine optics. Their location in a ring with respect to bending magnets is chosen to provide best efficiency.

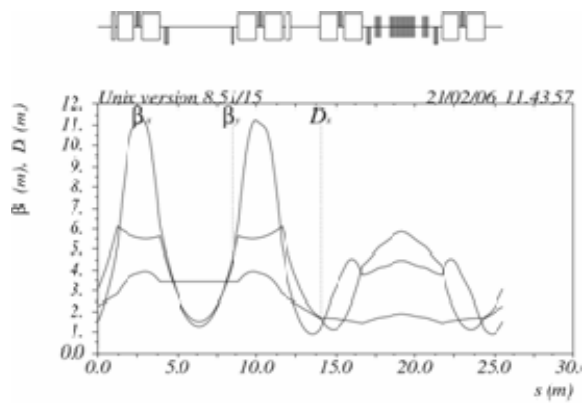

Figure 6: ELENA optics at extraction energy (effects of electron cooler and electron beam are taken into account).

Magnet System

To save space special magnet design has been proposed [8]. A horizontal and vertical dipole, normal quadrupole, skew quadrupole and sextupole are integrated into one module. The low level of required field allows to use normal conducting ironless magnets. The proper configuration of coil sectors is chosen (Figure 7) with homogeneous current density.

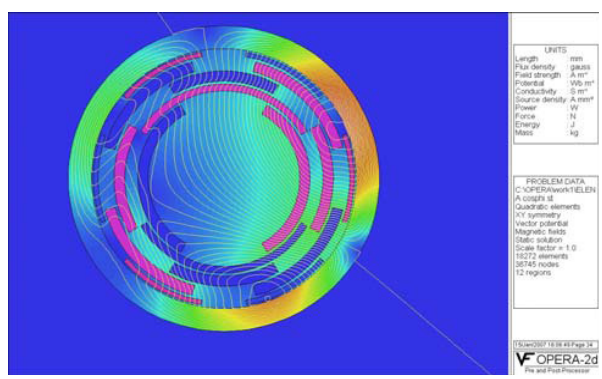

Figure 7: Multipole corrector.

All 8 modules are identical to reduce costs, but some of them may not be used, hence not connected to power supplies.

Beam Diagnostics

Eight horizontal and eight vertical PUs are foreseen to measure beam orbit. For beam intensity of 10^7 antiprotons in the bunch a resolution of 0.2mm (which is similar to AD) is expected.

An ultra low noise longitudinal Schottky PU which is a part of low level RF system [3] will be used for beam intensity measurements and for monitoring of longitudinal cooling. Signals from two units (low frequency and high frequency) are summed in an amplifier with appropriate equalizers to ensure the wide bandwidth required for intensity measurements. The transverse emittances will be measured with scrapers and scintillators.

Vacuum System

An ultra high vacuum of a few 10^{-12} Torr is required in the ELENA ring. The achieved pressure will define beam lifetime which is especially critical at low energies. Ultimate electron cooling is limited by residual gas scattering as well. To fit requirements vacuum chamber will be fully bakeable and coated with NEGs. Ions pumps will be installed in cooler section.

ELENA Main Parameters

The main machine parameters are given in Table 6. The intensity limitation by space is calculated for bunched beam at 100 keV right before extraction. The bunch length is small at the end of bunch rotation and during time needed for synchronization with ejection kicker, typically a couple of hundred msec.

Table 6: Main parameters of ELENA

Energy range, MeV	5.3 – 0.1
Circumference, m	26.062
Emittances at 100 keV, π mm mrad	5 / 5
Intensity limitation by space charge	$1.1 \cdot 10^7$
Maximal incoherent tune shift	0.10
Bunch length at 100 keV, m / nsec	1.3 / 300
Expected cooling time at 100 keV, sec	1
Required vacuum* for $\Delta\varepsilon=0.5\pi$ mm mrad/sec, Torr	$3 \cdot 10^{-12}$
IBS blow up times for bunched beam* ($\varepsilon_{x,y}=5\pi$ mm mrad, $\Delta p/p=1\ 10^{-3}$), s	1.1/- 9.1/0.85
* No electron cooling is assumed	

CONCLUSION

The AD is operating for physics since 2000 delivering more than $3 \cdot 10^7$ antiprotons per shot every 100 seconds with emittances less than 1π mm mrad and bunch length about 170 nsec. The deceleration efficiency is above 80% due to good performance of stochastic and electron cooling systems. The number of antipropons used for AD physics could be increased in one to two orders of magnitude with new small ring where further beam deceleration down to 100 keV kinetic energy will be performed together with beam cooling aimed on preparation of antiproton beam with high phase space density.

ACKNOWLEDGEMENTS

The author would like to thank the members of the AD team and CERN supporting personnel, whose contributions provide a machine with good operation and maintenance. Many people contributed to ELENA studies, particularly from operation, beam instrumentation, vacuum, RF, power converters, injection and ejection groups, and members of AD physics community. Thanks to all of them.

REFERENCES

[1] S.Maury e.a., "Commissioning and First Operation of the Antiproton Decelerator (AD)", Proceedings of the 2001 Particle Accelerator Conference, Chicago, June 18-22, 2001, p.580.

[2] P.Belochitskii, “Report on Operation of Antiproton Decelerator”. The International Workshop on Beam Cooling and Related Topics (COOL05), Eagle Ridge Resort and Spa, Galena, IL (USA), September 18 - 23, AIP Conf. Proc..: 821 (2006) pp.48-56.

[3] T.Eriksson (editor) e.a., ”ELENA – a preliminary cost and feasibility study”, to be published.

[4] P.Belochitskii, “ELENA optics”, private communication.

[5] G.Tranquille, “Electron cooler for ELENA”, private communication.

[6] I.N.Meshkov e.a. “Simulation of electron cooling process in storage rings using BETACOOL program”, in: Proceedings of beam Cooling and Related Topics, Bad Honnef, Germany, 2001.

[7] P.Belochitskii, “Simulation of electron cooling in ELENA ring with BETACOOL”, private communication.

[8] P.Belochitskii, T.Eriksson, Th.Zickler, “Magnet Design Proposal for ELENA and the Injection Transfer Line”, AT-MEL Technical Note (to be published).

PROGRESS OF HIGH-ENERGY ELECTRON COOLING FOR RHIC*

A. V. Fedotov** for the electron cooling team***, BNL, Upton, NY 11973

Abstract

The fundamental questions about QCD which can be directly answered at Relativistic Heavy Ion Collider (RHIC) call for large integrated luminosities. The major goal of RHIC-II upgrade is to achieve a 10 fold increase in luminosity of Au ions at the top energy of 100 GeV/nucleon. Such a boost in luminosity for RHIC-II is achievable with implementation of high-energy electron cooling. The design of the higher-energy cooler for RHIC [1] recently adopted a non-magnetized approach which requires a low temperature electron beam. Such electron beams will be produced with a superconducting Energy Recovery Linac (ERL). Detailed simulations of the electron cooling process and numerical simulations of the electron beam transport including the cooling section were performed. An intensive R&D of various elements of the design is presently underway. Here, we summarize progress in these electron cooling efforts.

ELECTRON COOLING FOR RHIC-II

Research towards high-energy electron cooling of RHIC includes simulations and benchmarking experiments to establish with some precision the performance of the cooler and development of hardware for cost and risk reduction. Recent progress in intensive R&D program was described in detail in numerous contributions to the 2007 Particle Accelerator Conference. An overview of these contributions is reported in Ref. [2].

The present performance of the RHIC collider with heavy ions is limited by the process of Intra-Beam Scattering (IBS) [3]. To achieve the required luminosities for the future upgrade [4] of the RHIC complex (known as RHIC-II) an electron cooling system was proposed [5].

The baseline of the heavy-ion program for RHIC-II is operation with Au ions at total energy per beam of 100 GeV/nucleon. For such an operation, the electron cooling should compensate IBS and provide an increase by about factor of 10 in an average luminosity per store.

For RHIC-II operation with the polarized protons, the electron cooling should assist in obtaining required initial transverse and longitudinal emittances or prevent their significant increase due to IBS. Although IBS is not as severe for protons as for heavy ions, a proposed increase in proton intensity for RHIC-II upgrade makes IBS an important effect as well.

Although extensive studies of the magnetized cooling approach for RHIC showed that such approach is feasible [1], the baseline was recently changed to the non-magnetized one [6, 7].

Electron cooling at RHIC using the non-magnetized electron beam significantly simplifies the cooler design. The generation and acceleration of the electron bunch without longitudinal magnetic field allows us to reach a low value of the emittance for the electron beam in the cooling section. The cooling rate required for suppression of the Intra-Beam Scattering (IBS) can be achieved with a relatively small charge of the electron bunch ~ 5 nC.

Since non-magnetized cooling requires a low temperature of the electrons, a possible problem which one can encounter in cooling of heavy ions is a high recombination rate of ions with the electrons. In the present design, suppression of the ion recombination is based on employing fields of a helical undulator in the cooling section [8]. In the presence of undulator field, electron trajectories have coherent azimuthal angle which helps to suppress recombination.

To make sure that our representation of the friction force is accurate, an undulator field was implemented in the VORPAL code [9], and numerical simulations were performed for different strength of the magnetic field B and pitch period λ [10]. In all simulated cases, it was found that the friction force scales close to predictions based on a modified logarithm [8, 11]. This confirmed our expectations that with a modest reduction of the friction force values one can introduce relatively large azimuthal coherent velocity of electrons to suppress recombination [12]. Details on VORPAL simulations about undulator effects on the friction force can be found in Ref. [13].

In its 2006-2007 baseline (which presently undergoes some changes) the proposed electron cooler uses a double pass, superconducting ERL to generate the electron beam with maximum energy of 54.3 MeV [14]. The cooling power needed requires bunch charge of 5 nC with an emittance smaller than 4 microns (rms, normalized) and a repetition frequency of 9.38 MHz. The necessary transverse and longitudinal electron beam brightness will be generated by a superconducting 703.75 MHz laser photocathode RF gun. To test the hardware and to explore various beam dynamics questions a R&D ERL is presently under construction at BNL with commissioning being planned in early 2009 [15].

The electron cooler will be located at the 2 o'clock IR of RHIC. There are various RHIC lattice modifications, which result in sufficiently large space available for cooling (up to 100 meters) [16]. The cooling section includes modules of a helical undulator to combat recombination of heavy ions with the electron beam, as well as several pairs of solenoids to counteract space-charge defocusing and control the rms angular spread within electron beam to a required level [12].

*Work supported by the U.S. Department of Energy
**Author e-mail: fedotov@bnl.gov
***http://www.bnl.gov/cad/ecooling

HARDWARE DEVELOPMENT

Electron beam needed for cooling will be delivered by superconducting ERL [14]. The superconducting RF (SRF) gun produces 5 nC electron beam with the exit energy of 4.7 MeV. The beam then goes through injection channel comes to SC RF Linac to be accelerated to 54.3 MeV. The 54.3 MeV beam is transported to RHIC for cooling of ion beams in both rings, and then is returned back to the ERL.

SRF ERL Cavity

A 5-cell ERL accelerating cavity at 703.75 MHz was developed. The cavity and cryostat were fabricated by Advanced Energy Systems (AES) [17]. It was processed and tested at Jefferson Laboratory. The process yielded a good performance with the cavity reaching 20 MV/m acceleration, with a Q of 1×10^{10} at a field of 19 MV/m (starting from a low field Q of 4×10^{10}) [18]. This "single mode" cavity has strong damping of all HOM through the 24 cm diameter beam pipe and 1 V/pC loss factor, thus it is ideal for multi-ampere current ERLs.

SRF Gun

The production of a high bunch charge with low emittance requires a high RF electric field at the cathode. For CW operation, a SRF gun is most advantageous. One and a half cell 4.7 MeV gun for RHIC-II high-energy cooler is being designed. A half cell 2.5 MeV SRF gun is under construction for the R&D ERL by BNL and AES [15].

Diamond Amplified Photocathode

RHIC-II electron cooler requires 50-100mA of electron beam current. For other future projects, currents more than 100mA will be needed. The production of CW 100 mA to 1 ampere current with a long lifetime and low thermal emittance is a challenge. The scheme used combines a high Quantum Efficiency (QE) photocathode with a diamond window, which also offers protection of the gun and cathode from each other. The amplification gain in the diamond results from the generation of a large number of electron-hole pairs. In measurements, gains of two orders of magnitude were achieved reproducibly, as well as good theoretical understanding of the gain dependence on the field using a plasma separation model [19].

The thermal emittance is a very important characteristic of cathodes. A lower thermal emittance cathode can lead to a lower beam emittance. A diamond amplified photocathode, being a negative electron affinity (NEA) cathode, promises to deliver a very small thermal emittance.

R&D ERL

A 20 MeV ERL is presently under construction at BNL. It will serve as a test-bed for future RHIC projects, including high-energy electron cooling [13]. The facility is based on a half cell superconducting 2.5 MeV RF gun, superconducting 5-cell RF accelerating cavity and about 20m long return loop. The ERL is scheduled for commissioning in early 2009 and will address many outstanding questions relevant for high current, high brightness ERLs.

COOLER DESIGN AND PARAMETERS

Design of the cooler, discussed in this paper, employs large beta-functions (400 meters for ions and 500 meters for electrons), the density of electron bunch was reduced compared to initial estimates, which in turn reduced the recombination rate. The parameters of undulator were set for magnetic field of 10 G and a period of 8 cm, corresponding to an effective temperature of 30 eV and recombination lifetime of 166 hours.

To ensure good cooling performance a quality of the electron beam should not suffer significantly as a result of the electron beam transport in the ERL, merging of the electron and ion beam, transport through the cooling section and interactions with the ion beam.

A lattice of the ERL was designed using PARMELA to provide electron beam parameters satisfying the RHIC electron cooling requirements [20]. In addition, a multi-parameter program was used for optimizing the injector and the emittance of electron bunch [21].

Table 1: 2006-2007 design parameters of electron cooler for RHIC-II.

Parameters	Units	Value
kinetic energy	MeV	54.3
rf frequency	MHz	703.75
bunch frequency	MHz	9.38
bunch charge	nC	5
rms emittance, normalized	μm	<4
rms momentum spread		3×10^{-4}
rms bunch length	cm	0.8
rms beam radius in cooling section	cm	0.4
cooling section length	m	80

With the non-magnetized cooling approach, electron angles in the cooling section should be comparable to the angular spread of the ion beam being cooled. With ion beam 95% normalized emittance of 15 μm and beta-function in the cooling section of 400 m, the rms angular spread of ion beam is 7.6 μrad.

In the baseline cooling simulations with 5nC electron beam we assumed "effective" rms angular spread of the electrons of 8.6 μrad, which, for example, corresponds to the electron beam rms normalized emittance (thermal contribution) of 4 μm if no other contributions to electron angular spread are present. An emittance of 3 μm (demonstrated in simulations [20, 21]) corresponds to rms angular spread of 7.5 μrad and allows to accommodate additional contributions from other sources. To have a minimum impact on cooling performance, the goal is to constrain total contribution to the rms angular spread of the electrons to about 10 μrad.

Beam current dependent effects such as space charge, wake fields, CSR and trapped ions may reduce electron beam quality. The defocusing effect of space charge at the cooling section led to implementation of compensating weak solenoids in the cooling section design. Summary of these effects and their impact on cooler design are given in Ref. [22].

The stability of the circulating ion beam in the presence of electrons due to two stream instabilities of various modes or due to the reduction of the Landau damping due to longitudinal cooling of the momentum spread of ions was studied. Simulations and theoretical estimates were performed to calculate the thresholds of the instabilities caused by these effects [23]. No problems were found given the present baseline parameters of the cooler.

Parameters of electron cooler which were used in simulations reported in this paper are given in Table 1.

COOLING PERFORMANCE

For heavy ions, electron cooling will provide both longitudinal and transverse cooling at the top energy of 100 GeV/nucleon. Electron cooling is more effective for particles in the core of the distribution, while stochastic cooling works best for large-amplitude particles. As a result, when fully implemented, both systems will work together to produce a significant boost in luminosity. The ultimate limitation in peak luminosity comes from the beam-beam limit. The ion intensity is currently also limited by instabilities at transition.

For protons, the goal of electron cooling is to produce required initial transverse and longitudinal emittances for high-intensity proton beam with 2×10^{11} particles per bunch mostly by pre-cooling at energy of about 30 GeV. Presently, no direct cooling at the top energy of 250 GeV is being planned, although various schemes are under investigation.

Baseline luminosities for the RHIC-II upgrade with electron cooling are summarized in Table 2 for Au ions and polarized protons. In addition, electron cooling can provide effective cooling for higher intensities of Au ions as well as for other ion species.

Table 2: Baseline RHIC-II parameters and luminosities.

Parameters	Units	p↑	Au
total beam energy	GeV/n	250	100
95% normalized emittance	μm	15	15
rms bunch length, initial	cm	16	20
ions/bunch	10^9	200	1
no of bunches		111	111
β*	m	0.5	0.5
peak luminosity	$cm^{-2}s^{-1}$	6×10^{32}	10×10^{27}
average luminosity	$cm^{-2}s^{-1}$	4×10^{32}	7×10^{27}

An accurate estimate of the cooling times for high-energy cooling requires detailed calculation of the cooling process, which takes place simultaneously with various diffusive mechanisms. This task becomes even more challenging when cooling is performed directly at a collision energy which puts special demands on the description of the beam distribution function under cooling [7].

Cooling dynamics simulations for RHIC-II presented in this paper were performed using the BETACOOL code [24]. The effects typically included in the simulations are electron cooling, IBS, particle loss in collisions (burn-up), loss from the rf bucket and recombination. An example of such a simulation with all effects being included is shown in Fig. 1.

The simulated luminosity performance in Fig. 1 is based on an electron bunch with 5nC charge and 4 μm "effective" emittance. An exact value for the average luminosity during the store may vary depending on the scheme used during the cooling. For example, an rms length of electron bunch is about 1 cm while rms length of an ion bunch is 20 cm. In order not to overcool the core and produce even cooling for particles at various amplitudes the electron bunch is being swept through the length of the ion bunch. An average luminosity per store will depend on how this sweeping is implemented. A detailed description can be found in a "RHIC-II Feasibility Study (2007)" document [1].

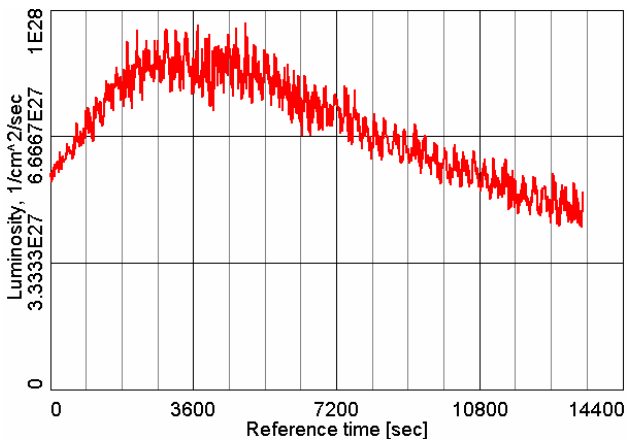

Figure 1: Electron cooling simulation of Au-Au luminosity: ion bunch intensity 1×10^9, 111 bunches; using single electron bunch per ion bunch. Average luminosity in 4 hour store is 7×10^{27} $cm^{-2}s^{-1}$.

The present design of electron cooling system (703.75 MHz) allows to have 2 electron bunches spaced by 0.4 m to be used simultaneously for the cooling of a single ion bunch. Such an approach allows us to apply shaping of the longitudinal distribution of the ions, thus avoiding long tails which are detrimental to the detector's operation. In addition, with 2 electron bunches (5nC charge each), ion bunches of higher intensity, than presently used in operation, can be cooled as well. This will allow future luminosity improvement of the complex. The present limit on bunch intensity comes from an

instability at transition limiting an average beam current per ring and resulting in about 1.1×10^9 ions per bunch with 111 bunches. Several measures are being planned which should help to elevate this limit. Figure 3 shows simulations of luminosity with and without electron cooling for bunch intensity of 2×10^9 and 111 bunches (which is a factor of 2 above an average beam current presently achieved in RHIC). The store time is limited by the burn-off of particles in collisions. In Fig. 2 an average simulated luminosity of Au ions in 3 hour store is 2×10^{28} cm^{-2} s^{-1}.

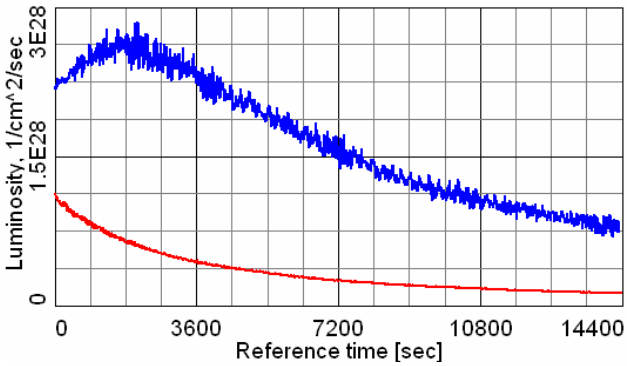

Figure 2: Simulation of Au-Au luminosity for ion bunch intensity 2×10^9 and 111 bunches using two 5nC electron bunches per single ion bunch with (blue top curve) and without (red bottom curve) electron cooling, taking β^*=0.5 m and 1 m, respectively.

For the present RHIC operation without electron cooling, the β^* is limited to about 1 meter (or slightly less) due to the fact that the emittance is increased during the store by a factor of 2 because of the IBS. Further reduction of the β^* with such an increase of emittance would lead to a significant angular spread and beam loss. On the other hand, keeping rms emittance constant (by cooling), allows us to start a store cycle with smaller values of the β^*.

An additional benefit comes from the longitudinal cooling which prevents bunch length from growing and beam loss from the bucket (as shown in Fig. 3). Also, it maximizes the useful interaction region in the detector.

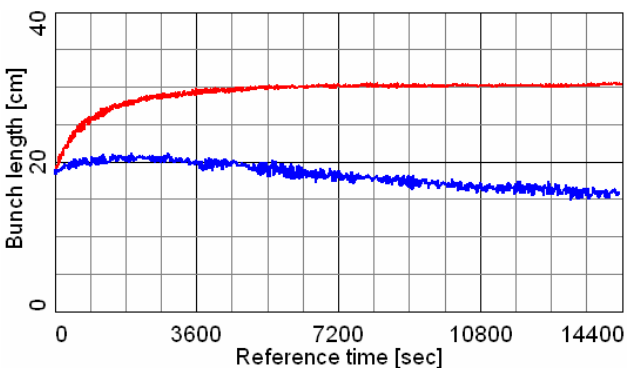

Figure 3: Simulated bunch length for ion bunch intensity 2×10^9 using two 5nC electron bunches with (blue bottom curve) and without (red upper curve) electron cooling.

Cooling of Various Ion Species

For Au-Au collisions at 100 GeV/nucleon with electron cooling, the store time is limited due to a rapid ion "burn-off" in the IP (large cross section from dissociation and bound electron-positron pair production). However, for other ion species, for which the cross section of such a "burn-off" process is small, longer stores can be tolerated. For example, Fig. 4 shows the luminosity performance for Cu-Cu collisions.

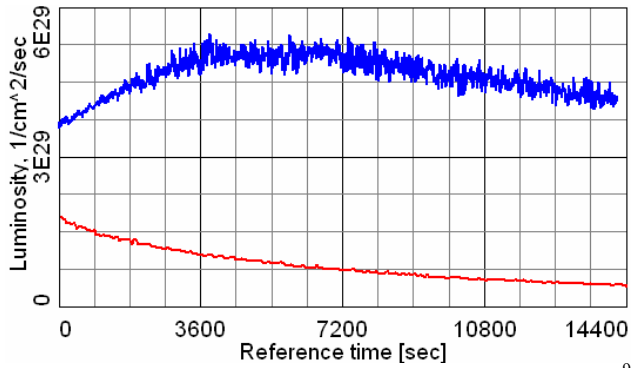

Figure 4: Cu-Cu luminosity for ion bunch intensity 8×10^9 and 111 bunches. Average luminosity in 4 hour store 4.6×10^{29} and 0.8×10^{29} $cm^{-2}s^{-1}$ with (upper blue curve) and without (low red curve) electron cooling, respectively.

For protons, in addition to pre-cooling at low energy, the present cooling system can be effectively applied to proton collisions at 100 GeV (see Fig. 5). At 100 GeV electron cooling can maintain the transverse emittance of protons, as well as keep rms bunch length to about 20 cm.

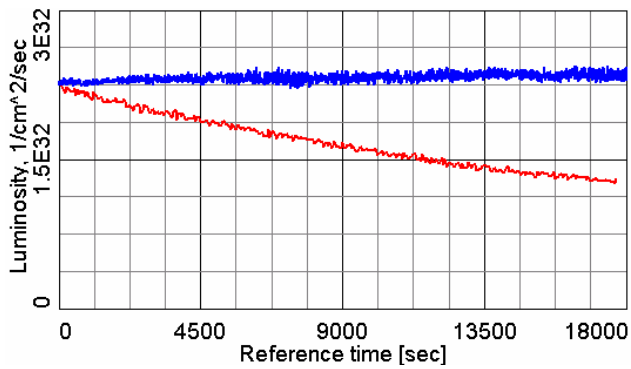

Figure 5: p-p luminosity at 100 GeV for ion bunch intensity 2×10^{11} and 111 bunches, using two 5nC electron bunches. With (upper blue curve) and without (low red curve) electron cooling, respectively.

Cooling at Various Collision Energies

Fast cooling at low energies also makes such energies attractive for collisions, which is under consideration for RHIC-II and eRHIC [25] However, rapid cooling of the beam core can lead to problems with a large beam-beam parameter. To keep the beam-beam parameter at an acceptable level, one can vary parameters of the electron beam dynamically during the cooling process.

Pre-cooling at Low Energy

Pre-cooling at low energy may be very attractive. This is due to the fact that cooling is much faster at lower energy as well as charge of the electron beam needed is smaller. Also, such a pre-cooling at low energy allows effective cooling of protons which is needed to achieve RHIC-II parameters. Pre-cooling at low energy is required to achieve present design parameters of linac-ring eRHIC collider [25]. Such pre-cooling was studied at 25 GeV/n, and cooling performance found was satisfactory.

PRESENT DEVELOPMENTS

The electron cooler for RHIC-II with parameters in Table 1 was carefully studied over the last two years. A detailed cost estimate of such a cooler was also performed. Presently, work is underway on various modifications of the cooler, such as relocation of ERL inside the RHIC tunnel and employing existing straight section in RHIC without its modification. Such changes promise significant reduction in the cost of the RHIC-II cooler. Preliminary evaluation of the new design parameters show that cooler can deliver the same performance as the one presented in this report.

In addition, the work has been started on a feasibility study of coherent electron cooling [26] for RHIC. This approach promises very good cooling performance at high energies [27].

SUMMARY

A significant progress has been made in the R&D towards high energy electron cooling of RHIC. Much of recent progress was reported in the proceedings of 2007 Particle Accelerator Conference. The feasibility of electron cooling of RHIC for a significant luminosity increase has been established and extensive R&D is being carried out on accelerator components and techniques.

ACKNOWLEDGMENTS

We would like to thank members of electron cooling team at BNL as well as many collaborators from other laboratories (FNAL, JLAB, JINR, BINP) and industry (AES, Tech-X) whose work is summarized in this progress report. The author is grateful to I. Ben-Zvi for help with preparation of this report.

REFERENCES

[1] Electron cooling for RHIC-II: http://www.bnl.gov/cad/ecooling
[2] I. Ben-Zvi, “Status of the R&D towards electron cooling of RHIC”, Proc. of PAC07, p. 1938.
[3] A. Fedotov et al, Proc. of HB2006 Workshop (KEK, Tsukuba, Japan, 2006), pub. by JACoW, p.259.
[4] A. Fedotov, “RHIC plans towards higher luminosity”, Proc. of PAC07 (Albuquerque, NM), p. 709.
[5] V. Parkhomchuk and I. Ben-Zvi, BNL C-AD Technical Report C-AD/AP/47 (2001).
[6] S. Nagaitsev et al., PRL 96, 044801 (2006).
[7] A. Fedotov et al., “High-energy electron cooling in a collider”, New Journal of Physics 8 (2006), p. 283.
[8] Ya. Derbenev, “Electron cooling in solenoid with undulator”, TJLAB Note 2001, unpublished.
[9] C. Nieter, J. Cary, J. Comp. Phys. 196 , p.448 (2004); http://www.txcorp.com.
[10] G. Bell et al., “Numerical algorithms for modeling electron cooling in the presence of external fields”, Proc. of PAC07, p. 3549.
[11] A. Fedotov et al., Proc. of PAC05 (Knoxville, TN), p. 4236.
[12] A. Fedotov et al., “Electron cooling in the presence of undulator fields”, Proc. of PAC07, p. 3696.
[13] D. Bruhwiler et al., these proceedings.
[14] I. Ben-Zvi, “The ERL high-energy cooler for RHIC”, Proceed. of EPAC06 (Edinburgh, 2006), p. 940.
[15] V. N. Litvinenko et al., “Status of R&D ERL at BNL”, Proc. of PAC07, p. 1347.
[16] D. Trbojevic et al., “A straight section design in RHIC to allow heavy ion electron cooling”, Proceed. of EPAC06 (Edinburgh, 2006), p. 279.
[17] A. Todd, Nuclear Instr. Meth. A, 557, p. 36 (2006).
[18] A. Burrill et al., “Challenges Encountered during the Processing of the BNL ERL 5 Cell Accelerating Cavity”, Proc. of PAC07, p. 2541.
[19] X. Chang et al., “Recent Progress on the Diamond Amplified Photo-cathode Experiment”, Proc. of PAC07, p. 2044.
[20] D. Kayran et al., “Optics of a Two-Pass ERL as an Electron Source for a Non-Magnetized RHIC-II Electron Cooler”, Proc. of PAC07, p. 3708.
[21] J. Kewisch et al., “Low Emittance Electron Beams for RHIC Electron Cooler”, Proc. of PAC07, p. 3187.
[22] E. Pozdeyev et al., “Collective Effects in the RHIC-II Electron Cooler”, Proc. of PAC07, p. 3717.
[23] G. Wang et al., “Coherent instability of RHIC ion beam due to electron cooling”, Proc. PAC07, p. 3726.
[24] BETACOOL code, http://lepta.jinr.ru; A. Sidorin et al., NIM A 558, p. 325 (2006).
[25] eRHIC design: http://www.bnl.gov/cad/eRhic.
[26] Ya. Derbenev, “Amplification of electron cooling by internal instability of electron beam”, Proc. of the 7th National Acc. Conf., V. 1 (Dubna, Russia, 1981), p. 269 (in Russian).
[27] V.N. Litvinenko et al., Proc. of FEL07 Conference (Novosibirsk, Russia, August 2007).

COOLING SIMULATIONS WITH THE BETACOOL CODE

A. Sidorin, JINR, Dubna, Russia

Abstract

The BETACOOL program developed by the JINR electron cooling group is a kit of algorithms based on a common format of input and output files. The general goal of the program is to simulate long term processes (in comparison with the ion revolution period) leading to a variation of the ion distribution function in six dimensional phase space. The BETACOOL program includes three algorithms for the simulation of the beam dynamics and takes into account the following processes: electron cooling, intrabeam scattering, ion scattering on residual gas atoms, interaction of the ion beam with an internal target and some others.

INTRODUCTION

The goal of the first version of the Betacool program [1] was to investigate the electron cooling process using formulae for the friction force derived in [2]. Presently the program is a kit of algorithms allowing to simulate long term processes (in comparison with the ion revolution period) leading to the variation of the ion distribution function in six dimensional phase space.

Evolution of the second order momenta of the ion distribution function is realized in the so called "*rms dynamics*" algorithm based on the assumption of a Gaussian shape of the distribution. Here all heating and cooling effects are characterized by rates of variation of the emittances or of particle loss.

The investigation of the beam dynamics at arbitrary shape of the distribution is performed using multi-particle simulation in the frame of the Model Beam algorithm. In this algorithm the ion beam is represented by an array of model particles. The heating and cooling processes involved in the simulations lead to a change of the components of the particle momentum and of the particle number.

During the last years the program was used for simulations of ion beam dynamics in the following fields of a cooling application:

- luminosity preservation in ion-ion colliders:
  RHIC-II (BNL), PAX (FZJ), NICA (JINR),
- simulations of experiments with internal pellet target:
  PANDA (GSI, FZJ), WASA at COSY (FZJ),
- benchmarking of IBS and electron cooling models:
  CELSIUS (TSL), RHIC (BNL), Recycler (FNAL), Erlangen University, TechX,
- beam ordering investigations:
  S-LSR (Kyoto University), COSY (FZJ), NAP-M (BINP), ESR (GSI),
- simulations of cooling-stacking process:
  LEIR (CERN), HIRFL-CSR (Lanzhou).

In this report a brief description of a few basic Betacool algorithms is presented.

PHASE DIAGRAMS

Usually a design of a cooling system is started from an estimation of the cooling rate required for reaching equilibrium at the necessary value of the beam emittance. By definition, the cooling (heating) rate is equal to

$$\frac{1}{\tau}=\frac{1}{\varepsilon}\frac{d\varepsilon}{dt}, \qquad (1)$$

and in the general case it is a function of the beam phase volume and intensity. Here ε are the horizontal, vertical or longitudinal emittances. An equilibrium between heating and cooling processes corresponds to a vanishing sum of the rates:

$$\sum_j \frac{1}{\tau_j}=0\cdot \qquad (2)$$

The index *j* is the number of processes involved in the calculations. Equations (2), written for each degree of freedom, form a system of non-linear algebraic equations describing the equilibrium emittance of the beam. For the solution of such systems the phase diagram method was developed in the Betacool program. In a phase diagram the sum of the rates is plotted as a function of the beam emittance (assuming that the horizontal emittance is equal to vertical one) and of the momentum spread. The crossing of the lines of vanishing sum of the rates at the phase diagrams for all three degrees of freedom corresponds to an expected equilibrium beam parameters. An analysis of the phase diagrams permits to predict some peculiarities of the cooling process without simulation of its dynamics. For example, the efficiency of this method was demonstrated in the simulations of the beam ordering process [4].

Calculation of the characteristic times is also the basis of RMS dynamics algorithm.

RMS DYNAMICS

The physical model used in the *rms* dynamics simulations is based on the following general assumptions:

1) the ion beam has a Gaussian distribution over all degrees of freedom and does not change during the process.

2) the algorithm for the analysis of the problem is considered as a solution of the equations for the *rms* values of the beam phase space volumes of three degrees of freedom.

3) the maxima of all the distribution functions coincide with the equilibrium orbit.

The evolution of the ion beam parameters during the motion in the storage ring is described by the following system of four differential equations:

$$\begin{cases} \dfrac{dN}{dt} = N\sum_j \dfrac{1}{\tau_{life,j}}, \\ \dfrac{d\varepsilon_h}{dt} = \varepsilon_h \sum_j \dfrac{1}{\tau_{h,j}}, \\ \dfrac{d\varepsilon_v}{dt} = \varepsilon_v \sum_j \dfrac{1}{\tau_{v,j}}, \\ \dfrac{d\varepsilon_{lon}}{dt} = \varepsilon_{lon} \sum_j \dfrac{1}{\tau_{lon,j}}, \end{cases} \quad (3)$$

where N is the particle number, ε_h, ε_v, ε_{lon} are root mean square values of horizontal, vertical and longitudinal beam emittance, respectively. The characteristic times are functions of all three emittances and of the particle number and have positive sign for a heating process and negative for cooling. A negative sign of a lifetime corresponds to particle loss and the sign of the lifetime can be positive in the presence of particle injection, when the particle number increases. The structure of the algorithm is designed in such a way as to allow for including any process into calculation which can be described by cooling or heating rates. Numerical solution of the system (3) is performed using the Euler method with automatic step variation. Results of the simulation are the dependences on time of the emittance and particle number.

The time step in the integration of the system (3) is determined by the characteristic times of the investigated effects and the speed of the calculation can be very fast. However, in some cases the basic physical model cannot provide a realistic simulation mainly due to the basic assumption of a Gaussian shape of the ion distribution function. This assumption is more or less realistic in an equilibrium state of the ion beam when the equilibrium is determined by many processes of stochastic nature. If there does not exist an equilibrium due to fast particle loss or in the initial stage of the beam cooling, the ion distribution function can be far from Gaussian. The same situation takes place in an experiment with internal targets which dimensions are not comparable with the ion beam dimensions. Neither can be calculated in the framework of this model correctly ionization energy losses of the ion beam in the target.

MODEL BEAM ALGORITHM

An investigation of the ion beam dynamics with an arbitrary shape of the distribution function is performed using multi-particle simulation in the frame of the Model Beam algorithm. In this algorithm the ion beam is presented by an array of modeling particles. Heating and cooling processes involved in the simulations lead to a change of the particle momentum components and of the particle number, which is calculated in accordance with the time step of the dynamical simulation. Each effect is located at some position of the ring characterized by the ring lattice functions. Transformation of the beam inside the ring is provided using a linear matrix with a random phase advance between the different objects. The results of the simulations can be presented both in form of a beam profile evolution in time or as time dependencies of the beam emittance and the particle number.

The Model Beam algorithm is based on the solution of the Langevin equation in momentum space that is realized in the Betacool program using the Euler method at fixed integration step. Action of some physical processes (IBS, scattering on gas etc.) results in a regular and (or) stochastic variation of the model particle momentum components. The momentum variation after the integration step of Δt is calculated in accordance with the following equation,

$$\Delta P_i = F_i \Delta t + \sqrt{\Delta t}\sum_{j=1}^{3} C_{i,j}\xi_j , \quad (4)$$

where $i = x, y, s$ are the horizontal, vertical and longitudinal co-ordinates, F_i are the components of the friction (or leading) term, ξ_j are three Gaussian random numbers with unit dispersion. The coefficients $C_{i,j}$ have to be calculated from the components of the diffusion tensor. In the Betacool program the component of the particle momentum are chosen to be $\left(p_x / p, p_y / p, \Delta p / p\right)$.

In the general case that the components of the diffusion tensor form a diagonal symmetric matrix,

$$\begin{pmatrix} D_{x,x} & D_{x,y} & D_{x,z} \\ D_{x,y} & D_{y,y} & D_{y,z} \\ D_{x,z} & D_{y,z} & D_{z,z} \end{pmatrix}, \quad (5)$$

and depending on the process some of them can be equal to zero. In the presence of diffusion the mean values of the variation of the components of the momentum can be expressed via components of the diffusion tensor in accordance with the definition,

$$\left\langle \frac{d\left(P_i P_j\right)}{dt} \right\rangle = D_{i,j} , \quad (6)$$

where triangular brackets mean averaging over the particles. From these expressions one can deduce the values of the coefficients $C_{i,j}$. They have to satisfy the following system of equations:

$$\sum_{k=1}^{3} C_{i,k} C_{j,k} = D_{i,j} . \quad (7)$$

This system has an infinite number of solutions but it can be simplified when the diffusion tensor has zero components. For example for a diagonal diffusion tensor (this corresponds to the case when the variations of momentum components do not correlate with each other) the simplest solution is:

$$C_{x,1} = \sqrt{D_{x,x}} , \; C_{y,2} = \sqrt{D_{y,y}} , C_{z,3} = \sqrt{D_{z,z}} ,$$

all other coefficients are equal to zero.

The Fokker-Plank approach (which is the physical basis of the Model Beam algorithm) allows for providing a uniform treatment of most of the heating and cooling effects, such as electron and stochastic cooling, interaction with residual gas and internal gas target,

intrabeam scattering process, heating due to noise of magnetic system power supply and others. However, when an accurate calculation of the distribution tail width and intensity is necessary one needs to provide direct simulations of the scattering processes. A more important example of such a situation is the simulation of an experiment with an internal pellet target.

SIMULATION OF PELLET TARGETS

When a beam interacts with an internal pellet target each particle crosses the pellet once during a few thousands of revolutions in the ring. In this case each crossing can be simulated directly. In order to simulate the variation of the components of the ion momentum the program calculates expectation values of the numbers of elementary events after a single crossing of the target, i.e. the numbers of ionizations of the target atoms and number of scattering on the nuclei. The actual numbers of the events is assumed to be distributed around its expectation values in accordance with Poisson law. In each elementary event the momentum variation is calculated as a random number distributed in accordance with corresponding law.

This algorithm can be illustrated on the example of the simulation of the ionization energy loss The variation of the longitudinal momentum component is caused mainly by the ionization energy loss distributed according to the function:

$$g(E) = \frac{(E_{\max} + I)I}{E_{\max}} \frac{1}{E^2} . \quad (8)$$

The macroscopic cross-section for ionization is

$$\Sigma = \frac{\Delta E_{BB}}{\Delta x} \frac{E_{\max}}{I(E_{\max} + I)\ln\left(\frac{E_{\max} + I}{I}\right)} . \quad (9)$$

$E_{\max}$ is the maximum transferable energy:

$$E_{\max} = \frac{2m_e c^2 \beta^2 \gamma^2}{1 + 2\gamma\frac{m_e}{M} + \left(\frac{m_e}{M}\right)^2} , \quad (10)$$

with m_e being the electron mass and M the projectile mass. I is the mean excitation energy that can be estimated as $I = 16 \cdot Z^{0.9}\ eV$, ΔE_{BB} is the mean energy loss after crossing the target calculated in accordance with the Bethe-Bloch equation and Δx is the target thickness. The number of ionization events n after single crossing the target is

$$n = \Sigma \Delta x . \quad (11)$$

The energy loss due to ionization is calculated as

$$\Delta E_{ion} = \sum_{i=1}^{n} \frac{I}{1 - h\xi_i} . \quad (12)$$

n is the integer number sampled from the Poisson distribution, ξ_i are random numbers uniformly distributed in 0 to 1, $h = \frac{E_{\max}}{E_{\max} + I}$.

The deviation of the longitudinal component of the particle momentum is calculated as:

$$\delta\frac{\Delta p}{p} = \frac{\gamma}{1+\gamma}\frac{\Delta E_{total}}{AE} , \quad (13)$$

where E is the particle kinetic energy per nucleon, A is the particle atomic number. The expectation of the energy loss ΔE_{BB} is calculated in accordance with the equation:

$$\frac{\Delta E_{BB}}{\rho \Delta x} = -KZ_P^2 \frac{Z_T}{A_T}\frac{1}{\beta^2}\left[\frac{1}{2}\ln\frac{2m_e c^2 \beta^2 \gamma^2 E_{\max}}{I^2} - \beta^2 - \frac{\delta}{2}\right] .$$

where ρ is the target density, Z_P and Z_T are the charge numbers of the projectile and target atoms, respectively, A_T is the target atomic number, δ is the density correction factor. K is a constant determined by the following expression:

$$\frac{K}{A} = \frac{4\pi N_A r_e^2 m_e c^2}{A} = 0.307075\ \text{MeV}\cdot\text{g}^{-1}\cdot\text{cm}^2,$$

r_e is the electron classic radius and N_A is the Avogadro number.

HIERARCHY OF IBS MODELS

Another physical task requiring direct simulation of a scattering process is the investigation of the beam ordering process. For this goal the simulation of the IBS process through Coulomb interaction between particles was realized in the tracking algorithm in the Betacool program. The Fokker-Plank approach is used in local and simplified kinetic models of the IBS process. To speed up the calculation a few detailed models of the IBS based on analytical expressions for the diffusion power were developed. In this chapter a brief description of the IBS simulation methods is presented.

Tracking Algorithm

A tracking algorithm is used for the simulation of the IBS process through Coulomb interaction between ions. One of the goals of this algorithm development is to simulate a formation of a crystalline state of the ion beam. In the crystalline state of the ion beam the IBS process cannot be treated in the frame of analytical models which are based on the assumption of Gaussian shape of the ion distribution function. To speed up the calculations in the tracking algorithm the IBS simulations are performed using Molecular Dynamics technique. In this case the equations of motion are solved for a small number of particles located inside a short cell. The influence of all other particles is taken into account through periodic boundary conditions in the longitudinal direction for the particle distribution function and use of Ewald's sum for the calculation of Coulomb forces. Therefore, this algorithm can be used for coasting beams only.

In the frame of the tracking algorithm the equations of motion of the particles are integrated in the real structure of the ring. The ring structure is imported from an input MAD file. Each cooling or heating effect involved in the calculations together with IBS is located in some optic element. Calculation of the variation of the particle

coordinates due to the action of an object is provided using the map of this object. The position of the object in the ring is described in the input MAD file using special markers.

Local Model of IBS and Electron Cooling

Calculation of the friction force and diffusion tensor components related with the problem of Coulomb scattering of a test particle of a mass m_t and velocity $\vec{V}$ proceeds in an array of N_{loc} field particles of mass m_f and velocities $\vec{v}_i$. The solution of this problem is well known from plasma physics. For a given distribution function $f(v)$ of the field particles in velocity space the friction force is equal to

$$\vec{F} = -\frac{4\pi n e^4 Z_t^2 Z_f^2}{\left(\frac{m_f m_t}{m_f + m_t}\right)} \int \ln\left(\frac{\rho_{\max}}{\rho_{\min}}\right) \frac{\vec{U}}{U^3} f(v) d^3 v$$

and the components of the diffusion tensor are

$$D_{\alpha,\beta} = 4\pi n e^4 Z_t^2 Z_f^2 \int \ln\left(\frac{\rho_{\max}}{\rho_{\min}}\right) \frac{U^2 \delta_{\alpha,\beta} - U_\alpha U_\beta}{U^3} f(v) dv \cdot$$

Here $\alpha, \beta = x, y, s$, the angular brackets mean averaging over the field particles, Z_t, Z_f are the charge numbers of the test and field particle, n is the mean local density of the field particles and $\vec{U} = \vec{V} - \vec{v}$ is the relative velocity of the test and field particle. The minimum and maximum impact parameters are determined as in the simulation of electron cooling.

For a particle array the distribution function of the field particles in the velocity space is given as a series of δ-functions:

$$f(v) = \frac{1}{N_{loc}} \sum_{j=1}^{N_{loc}} \delta(\vec{v} - \vec{v}_j) \cdot$$

The minimum impact parameter in the Coulomb logarithm is calculated as

$$\rho_{\min} = \frac{Z_t Z_f e^2}{\left(\frac{m_f m_t}{m_f + m_t}\right)} \frac{1}{\left|\vec{V} - \vec{v}_j\right|^2} .$$

The value of the dynamic shielding radius required for the maximum impact parameter determination is calculated using the *rms* velocity spread of the field particles.

The algorithm described above can be used for IBS as well as for electron cooling simulations. In the case of electron cooling simulation the test particle is the ion and the field particles are the electrons. In the case of IBS the test and the field particles are the same ions. For IBS simulation the friction and diffusion components have to be calculated in each optic element of the ring. Therefore the algorithm is very slow and it is suited only for large computers.

Simplified Kinetic Model

To speed up the calculations a simplified kinetic model of the IBS process was proposed in [5]. It is based on the assumption that the friction force is proportional to the particle momentum and to the diffusion constant. The friction and diffusion components can be calculated in accordance with one of the analytical IBS models. In the Betacool program the kinetic model was realized for the ring optical structure with non-zero vertical dispersion in accordance with [6].

Detailed Models

The analytical models are used as a basis for a few detailed models of the IBS process realized in the Betacool program. In Burov's model [7] the diffusion power for each ion is calculated as a function of its action variables. In the "core-tail" models the diffusion is calculated separately for the particles from a dense core of the distribution function and from low intensive tails.

Analytical Models for IBS Growth Time Calculation

For the calculation of the IBS growth rates a few analytical models are available in the Betacool program. Their description can be found in [8].

ELECTRON COOLING SIMULATION

In order to solve all the problems related with the simulation of the electron cooling process a hierarchy of objects was developed in the BETACOOL program. The cooling simulation is based on a friction force calculation in the particle rest frame. The friction force can be calculated in accordance with one of the analytical models from a library or by using results of numerical calculations imported from an external file. The next layer of the simulation is related with a cooler representation as a map, transforming particle coordinates from entrance to exit of the cooling section and calculating the ion loss probability due to recombination with electrons. Calculation of the cooler map is based on a model of the electron beam that provides transformation of the ion velocity to the frame related with the electron beam and takes into account the real geometry of the cooler. The main models of the electron beam used in the Betacool program and a description of the friction force formulae are given in [8]. The cooler model takes into account the variation of the magnetic field in the cooling section. For this purpose the coordinates of the electron beam trajectory inside cooling section are input from an additional file and the equations of motion of the ions are solved numerically inside the cooler.

The map of the cooler can be used directly in the frame of the Molecular Dynamics algorithm or in other tracking procedures. On the basis of the map one can calculate the kick of the ion momentum after crossing the cooling section that is necessary for the simulation of the ion distribution evolution in the frame of the Model Beam algorithm. The map of the cooler is also used for the calculation of the cooling rate that is necessary for the simulation of the *rms* dynamics. The calculation of the cooling rate can be performed using two different models

of the ion beam, either the cooling rates for "*rms*" particle dynamics or for the ion beam with Gaussian distributions in all degrees of freedom.

ACKNOWLEDGMENTS

Successive development of the Betacool program during a long period of time was possible only because of the help of many good friends of our group. On behalf of the Betacool team I would like to thank P. Zenkevich, T. Katayma, H.J. Stein, J. Dietrich, H. Stockhorst, A. Noda, T. Shirai, I. Ben-Zvi, A. Fedotov, D. Reistad, D. Moehl, A. Burov and many others, with the hope for future fruitful co-operation.

REFERENCES

[1] A. Lavrentev, I. Meshkov, "The computation of electron cooling process in a storage ring", preprint JINR E9-96-347, 1996.
[2] I. Meshkov, Electron cooling: Status and Perspectives, Phys. Part. Nucl., 25, (6), 1994, 631.
[3] I. Meshkov et. al., NIM A 558 (2006), 325-328.
[4] A.Smirnov et. al., Necessary condition for beam ordering, these Proceedings.
[5] P.Zenkevich, private communication.
[6] M. Venturini, Proceedings of 2001 PAC, Chicago, p. 2961 (2001).
[7] A.Burov, private communication..
[8] "BETACOOL Physics Guide", BNL Tech Note C-A/AP/#262 (Nov. 2006).

LONGITUDINAL ACCUMULATION OF ION BEAMS IN THE ESR SUPPORTED BY ELECTRON COOLING*

C. Dimopoulou, B. Franzke, T. Katayama, G. Schreiber, M. Steck, GSI, Darmstadt, Germany
D. Möhl, CERN, Geneva, Switzerland

Abstract

Recently, two longitudinal beam compression schemes have been successfully tested in the Experimental Storage Ring (ESR) at GSI with a beam of bare Ar ions at 65 MeV/u injected from the synchrotron SIS. The first employs Barrier Bucket pulses, the second makes use of multiple injections around the unstable fixed point of a sinusoidal rf bucket at h=1. In both cases, continuous application of electron cooling maintains the stack and merges it with the freshly injected beam. These experiments provide the proof of principle for the planned fast stacking of Rare Isotope Beams (RIBs) in the New Experimental Storage Ring (NESR) of the FAIR project.

INTRODUCTION

In order to reach the high intensity of RIBs required by the internal experiments in the NESR [1, 2] and in particular by the electron-ion collider [3], it is planned to stack the RIBs longitudinally at injection energy i.e. in the range 100-740 MeV/u [4]. The stacking will be supported by electron cooling. A stacking cycle time, i.e. the time between 2 successive injections, below 2 s would be optimal because of the short RIB lifetimes and in order to profit from the planned cycle time of 1.5 s of SIS100, where the primary heavy ion beam is accelerated. In this frame, two options of longitudinal beam accumulation have been investigated by beam dynamics simulations and by experiments in the existing ESR at GSI.

The first option uses a broadband Barrier Bucket (BB) rf system. Dedicated beam dynamics simulations [5] show that a maximum voltage of 2 kV is sufficient to compress cooled beams in the NESR. The stacking cycle time could be about 2 s, provided that the quality of the injected pre-cooled beam from the CR/RESR complex [2] allows cooling times below 1 s in the NESR. This is demonstrated in Fig. 1. At t=0 a bunch is injected between the BB sine pulses of 100 ns period. The injected beam debunches because the voltage is not sufficient to capture the particles. The BB pulses are decreased and switched off at t=0.2 s, while the beam is being continuously cooled. For the injected beam, an initial emittance of 0.5 π mm mrad and energy spread of 1.5 MeV/u was assumed. They correspond to the 2σ design values for the pre-cooled beam in CR with an additional 30% increase of the longitudinal emittance due to diffusion processes during the transfer through the RESR to the NESR. Parkhomchuk's formula [6] is used for the cooling rate, for an electron beam density of 3.2×10^8 cm^{-3}, a magnetic field strength of 0.2 T in the cooling section and an effective electron velocity corresponding to magnetic field errors of 5×10^{-5}. The resulting cooling time is about 0.8 s. Then, the BB pulses are adiabatically introduced into the beam and increased to 2 kV. One stays stationary while the other is shifted in phase to compress the cooled beam. At t=2 s a new bunch is injected.

The second option uses a h=1 rf system for bunching of the circulating beam and injection of a new bunch onto the unstable fixed point in longitudinal phase space [7]. The rf voltage is raised adiabatically so as to confine the bunch in a small fraction of the ring circumference. A new bunch is injected onto the free part of the circumference. Then the voltage is decreased (rather non-adiabatically in order to avoid dilution of the new bunch) to let the beam debunch.

In both schemes, continuous application of electron cooling (i) counteracts heating of the stack during the rf compression and (ii) merges the stack with the freshly injected bunch. The required rf voltages for the longitudinal beam compression are moderate since the momentum spread of the cooled stack is small (of the order of 10^{-4} or better). The cooled stack is repeatedly subjected to the same procedure until an equilibrium between beam losses and injection rate is reached.

EXPERIMENTAL PROCEDURE

Both stacking options have been tested in the ESR [8] under the same conditions. The experiments were performed with a $^{40}Ar^{18+}$ beam at 65.3 MeV/u injected from the synchrotron SIS. The SIS and ESR rf systems were synchronised to operate at f_{rf}=983 kHz, at h=2 and h=1, respectively, since the SIS has the double circumference of the ESR. One of the two bunches in SIS is fast extracted to the ESR. The bunches in SIS, measured with a sum pickup, had a FWHM between 300-350 ns. The ESR injection kicker pulse was typically 500 ns long (100 ns rise/fall time, 300 ns flat top). It was not straightforward to further reduce the kicker pulse length during the experiment, which restricted the flexibility in the longitudinal manipulation during the stacking with BB. In the case of stacking with the sinusoidal rf at h=1, a longer kicker pulse could in principle have been advantageous to reach higher injection efficiency. However, as it will be explained below, the experimental results indicate that the synchronisation of the kicker with the rf pulse at h=1 was not perfect and, as a consequence, losses occurred during stacking.

* Work supported by EU FAIR Design Study COOLSB11

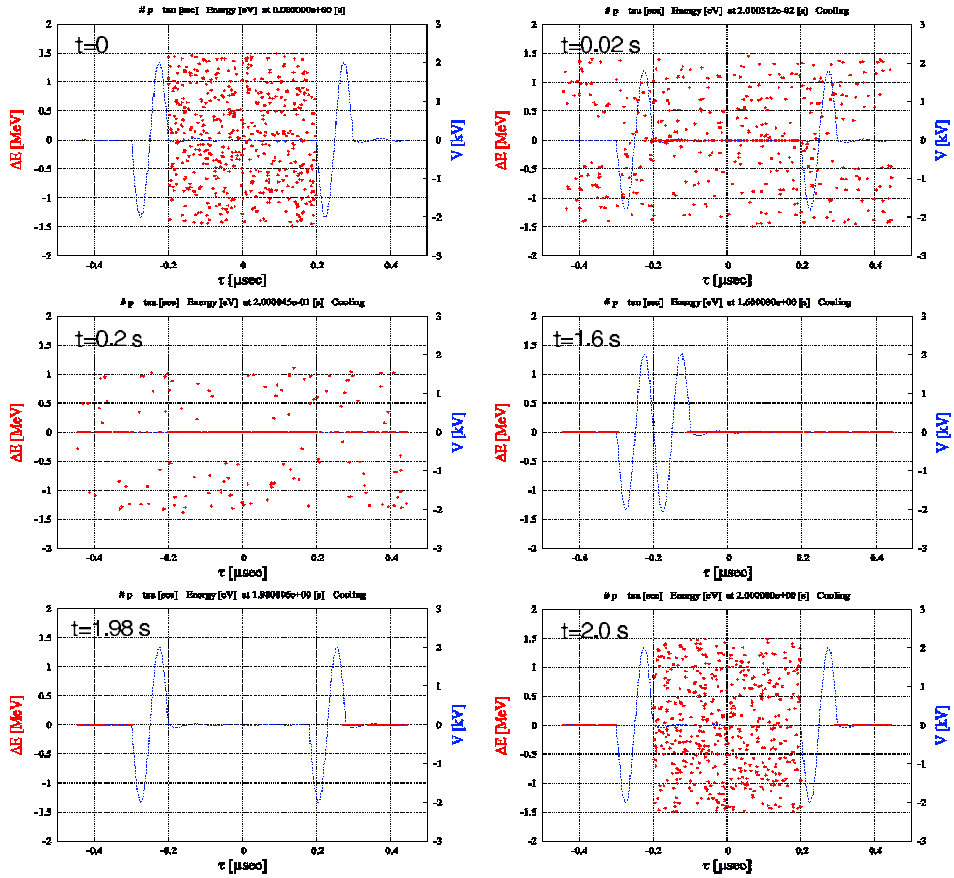

Figure 1: Accumulation of the 740 MeV/u $^{132}Sn^{50+}$ beam (0.9 μs revolution period) in the NESR by Barrier Buckets and electron cooling. Solid lines: barrier voltage; Dots: particle distribution in the longitudinal phase space. Top left to bottom right: beam injection, debunching, cooling, application of the BB pulses, compression of the stack by moving one barrier, new injection into the gap between the barriers.

Measurements of the horizontal beam profile with the rest gas monitor and of the momentum spread with the longitudinal Schottky pickup showed that the injected beam was cooled down to the equilibrium within about 13 s, for operation of the ESR electron cooler [9] with an electron beam density of $3 \times 10^6 \mathrm{cm}^{-3}$ (0.1 A, 2.5 cm beam radius) and a magnetic field strength of 0.07 T in the cooling section.

At the equilibrium between the applied electron cooling and Intra Beam Scattering (IBS), the horizontal emittance and momentum spread of the stored coasting beam were measured with the rest gas beam profile monitor and the longitudinal Schottky pickup, respectively. They were found to scale with the particle number N_i for coasting beam- more generally with the beam linear density N_i/B, where $B = T_{bunch(stack)}/T_{rev}$ is the bunching factor- and cooling current I_e as

$$(\Delta p/p)_{equil} \sim (N_i/B)^{0.36} I_e^{-0.3} \quad (1)$$

$$(\epsilon_{h,v})_{equil} \sim (N_i/B)^{0.41} I_e^{-0.3} \quad (2)$$

in accordance with the results of previous systematic experimental studies in the ESR [10]. For 10^8 ions and I_e=0.1 A, $(\Delta p/p)_{equil}$=10^{-4}, $(\epsilon_h)_{equil}$=1 π mm mrad (2σ values).

The revolution period in the ESR was T_{rev}=1.017 μs, i.e. sufficiently long to allow stacking with the sine-shaped BB pulses of T_B=200 ns period provided from the BB cavity. The maximum height (in momentum spread) of the rf barrier δ_B is given by the usual formula for a sinusoidal rf pulse

$$\delta_B = \sqrt{\frac{2QeV_{rf}}{\pi\beta^2\eta h E_{0,tot}}} \quad (3)$$

where $E_{0,tot} = \gamma A m_u c^2$ is the total energy ($m_u c^2$=931.5 MeV is the nucleon mass) and Q the charge state of the ion. The height δ_B is defined so that the maximum height of the separatrix is at $\Delta p/p = \pm\delta_B$. For the BB pulses of period T_B a "harmonic" number $h = T_{rev}/T_B \approx 5$ is defined. Hence, at the same voltage the confining potential of the BB system is $\sqrt{5}$ lower than for the h=1 rf.

For both methods, the increase of beam intensity in the ESR during the stacking was measured with the dc beam current transformer. An example is shown in Fig. 3. The corresponding accumulation efficiency curves i.e. the increment of the ESR beam current per injected shot are also shown. A beam current of 0.3 mA corresponds to 10^8 $^{40}Ar^{18+}$ ions at 65.3 MeV/u in the ESR.

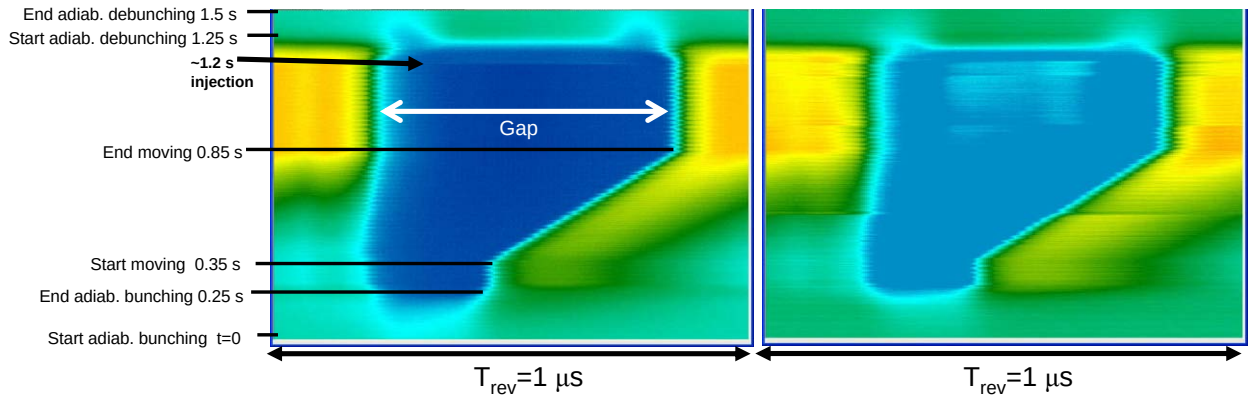

Figure 2: Longitudinal beam accumulation with Barrier Bucket pulses and electron cooling. Signal (arbitrary units) registered in the ESR beam position monitor. Colour code (dark blue to orange): zero to high beam signal. One frame was recorded every 200 revolutions for a total time of 1.5 s. The stacking cycle was 9 s and the electron beam current in the cooler 0.1 A. The period of the barrier pulses was 200 ns. Left: BB voltage=120 V; Right: BB Voltage=20 V.

STACKING WITH BARRIER BUCKETS

Fig. 2 shows the $^{40}Ar^{18+}$ beam signal measured in the ESR pickup during the stacking with BB and illustrates the experimental procedure, which was similar to the one in Fig. 1. For 120 V BB voltage, the stack and the injected bunch are well separated at the instant of the new injection (t∼1.2 s), whereas the lower voltage of 20 V is not sufficient to confine the stack particles with high momentum spread. The barrier pulse moves in phase by 400 ns (141.6°) within 0.5 s i.e. with a rate of 8×10^{-7} much slower than the synchrotron motion rate $\Delta f/f = \eta \Delta p/p \approx 7 \times 10^{-5}$ of the cooled stack with $\Delta p/p \approx 10^{-4}$. The saturated value I_{ESR} of the stacked beam intensity in the ESR was measured with the current transformer for different parameters of the rf system (voltage, T_B) and electron currents. As expected, I_{ESR} increases with increasing available rf bucket height δ_B and cooling strength. In a further analysis, the momentum spread of the stacked beam at equilibrium between cooling and IBS can be estimated by applying the measured scaling law of Eq. 1, where N_i is now the measured saturated stack intenstity and taking into account the bunching factor $B = T_{stack}/T_{rev}$. The distribution of the stack measured in the pickup (see also Fig. 2) was uniform with a length (including 75% of the distribution) T_{stack}=400 ns, 300 ns for pulses of T_B=200 ns, 300 ns, respectively. The resulting $\Delta p/p$ of the saturated stack is plotted in Fig. 4 versus δ_B , for different I_e. For the largest δ_B and strong cooling the accumulated beam intensity was limited due to the onset of observed coherent transverse instabilities. Comparison of the experimental results with beam dynamics simulations is given in [5].

STACKING WITH THE HARMONIC H=1

Stacking by multiple injections on the unstable fixed point of the sinosoidal rf at h=1 was investigated experimentally in a similar way: The cooled coasting beam is

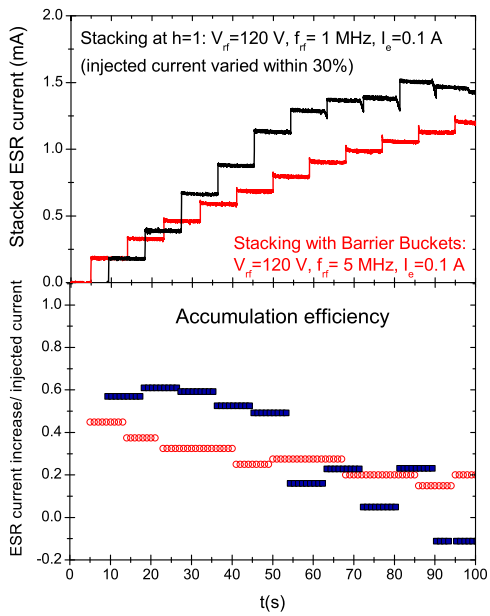

Figure 3: Experimental demonstration of the two proposed longitudinal accumulation methods with an $^{40}Ar^{18+}$ beam at 65.3 MeV/u in the ESR. The stacking cycle was 9 s, the electron cooling current 0.1 A. Because of the different rf frequency, for the same voltage, stacking at h=1 offers $\sqrt{5}$ stronger confinement than with BB. Variations of the injected current are due to source current variations.

bunched adiabatically within 0.25 s. Then, the new beam is injected. The rf voltage is switched off within 1 ms after injection to allow fast debunching and merging of the bunch with the stack for cooling. The energy of the electron cooler was finely adjusted to the energy of the synchronous particle in the rf bucket by minimising the bunch length measured with the pickup.

Surprisingly, as shown in Fig. 5, the dependence of the accumulated intensity on I_e is very slight, in contrast to the results for the BB stacking. At saturation intensity, the

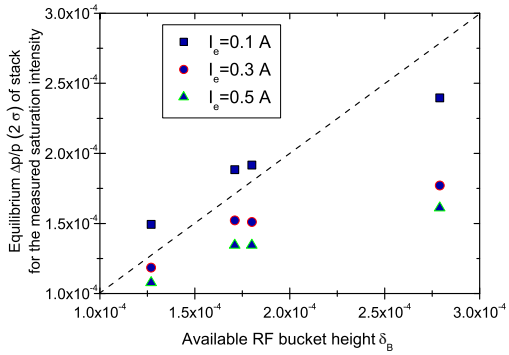

Figure 4: Longitudinal beam accumulation with Barrier Bucket pulses and electron cooling. Momentum spread of the accumulated $^{40}Ar^{18+}$ beam in comparison with the rf bucket height for different electron cooling currents.

stacked bunch length was measured in the pickup and the corresponding $\Delta p/p$ was calculated from the rf bucket formula:

$$\frac{\sigma_t}{T_{rev}} = \sqrt{\frac{\beta^2 \eta E_{0,tot}}{2\pi Q e h V_{rf}}} \frac{\Delta p}{p} \qquad (4)$$

It is compared in Fig. 5 with δ_B for the corresponding rf voltage. Within the pickup resolution (10 ns), the bunch length was found to be independent on I_e. The conclusion is that at saturation intensity the stacked bunch occupied about 20% of the ring circumference and filled essentially 50-60% of the momentum acceptance of the rf bucket at h=1, for all applied voltages in the range 30-120 V.

The results in Fig. 3 suggest that the injection efficiency was not optimal. In particular, from the relative phase of the stacked bunch with respect to the freshly injected bunch as measured in the pickup, it follows that the kicker pulse overlapped in time with the tail of the stack, so that stack particles were lost at every new injection. In other words, the new bunch was not injected exactly on the unstable fixed point of the separatrix but rather close to the stack. Another remark concerns the bunching time of 0.25 s: It was indeed adiabatic with respect to the synchrotron motion but might have been rather fast with respect to the cooling time of the stack. A dedicated experiment is planned in the ESR in order to improve the stacking procedure at h=1.

We have checked that, for both stacking methods, the maximum accumulated intensity of $4 - 5 \times 10^8$ ions was not limited by space charge effects. Typically, for bunching factors of 0.2-0.4 and strong cooling (I_e=0.5 A), the stack transverse emittance calculated from the scaling law in Eq. 2 was 2 mm mrad. For a maximum incoherent Laslett tune shift of 0.1, the space charge limit was $2-3\times10^9$ ions i.e. well above the considered maximum stacked intensity. The longitudinal space charge limit from the Keil-Schnell-Boussard criterion [12] was even higher i.e. $\approx 4 \times 10^{10}$ ions for a cooled stack with $\Delta p/p \approx 10^{-4}$.

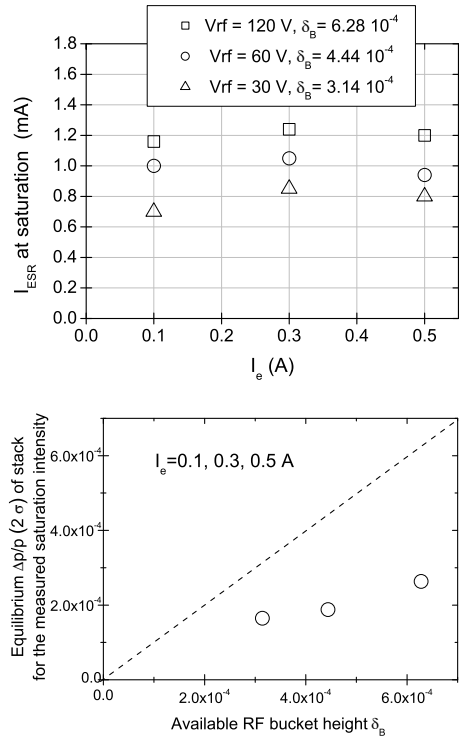

Figure 5: Longitudinal beam accumulation with h=1 rf and electron cooling. Upper part: Stacked beam intensity measured with the current transformer for different rf voltages and electron currents. Lower part: Momentum spread of the stacked $^{40}Ar^{18+}$ beam (proportional to its measured bunch length) compared to the rf bucket height.

OUTLOOK

These results confirm the requirements for the NESR systems, namely, faster electron cooling [11], a BB system with 2 kV peak voltage, adjustable injection kicker pulse and appropriate beam diagnostics.

REFERENCES

[1] C. Dimopoulou et al., Phys. Rev. ST Accel. Beams 10 (2007) 020101.

[2] FAIR Baseline Technical Design Report, GSI (2006). http://www.gsi.de/fair/reports/.

[3] I.A. Koop et al., Proc. of EPAC, Paris (2002) 620.

[4] B. Franzke et al., NIM A 532 (2004) 97.

[5] T. Katayama, these proceedings.

[6] V.V. Parkhomchuk, NIM A 441 (2000) 9.

[7] S. Baird et al., IEEE Proc. of PAC (1989) 645.

[8] B. Franzke, NIM B 24/25 (1987) 18.

[9] M. Steck et al., NIM A 532 (2004) 357.

[10] M. Steck et al, CERN Yellow Report 94-03 (1993) 395.

[11] V.V. Parkhomchuk et al., GSI-Acc-Report-2005-04-001.

[12] J. Bosser et al., NIM A 441 (2000) 1.

BUNCHED BEAM STOCHASTIC COOLING AT RHIC*

J.M. Brennan+, M.Blaskiewicz, Brookhaven National Lab 11973, U.S.A.

Abstract

Stochastic cooling of ions in RHIC has been implemented to counteract Intra-Beam Scattering and prevent debunching during stores for luminosity production. The two main challenges in cooling bunched beam at 100 GeV/n are the coherent components in the Schottky spectra and producing the high voltage for the kicker in the 5 - 8 GHz band required for optimal cooling. The technical solutions to these challenges are described. Results of cooling proton beam in a test run and cooling gold ions in the FY07 production run are presented.

INTRODUCTION

Stochastic cooling is an effective and well-established accelerator technology for improving beam quality. However, stochastic cooling of high frequency bunched beam has always proved problematic due to strong coherent components in the Schottky spectra of bunched beam.[1] We have built a stochastic cooling system for RHIC employing specialized techniques to overcome the problem of coherent components. The system works in the 5-8 GHz band and cooling in the longitudinal plane. The kicker of the system is realized in an unusual way by creating the kick voltage with 16 high-Q cavities. Even though the bandwidths of the cavities are much smaller than their separation in frequency the effective bandwidth of the cooling system is sufficiently covered. This follows from the fact the beam bunches are 5 ns long and the separation between cavity frequencies is 200 MHz, that is; the reciprocal of the bunch length.[2] The high-Q cavities greatly reduce the microwave power needed to operate the system. The system was first tested with protons during the FY06 polarized proton run. In the FY07 gold-on-gold run the cooling system was commissioned and proved effective in reducing the beam loss rate and debunching during 5 hour stores.

BUNCHED BEAM COOLING

Coasting beam formulae can be used to calculate cooling rate for bunched beam if the number of particles is replaced by an effective number which is the number that would be in the ring if it were filled at density equal to bunch density. For RHIC this is about 2e12, and implies a cooling time of about one hour for a 5-8 GHz system. This is an adequate cooling rate to counteract Intra-Beam Scattering in RHIC.

*Work performed under US DOE contract No DE-AC02-98CH1-886.

+ brennan@bnl.gov

Bunched beam cooling differs from coasting beam also in that mixing is strongly influenced by synchrotron motion. Particles tend to return to the sample in a half synchrotron period and with their same neighbours. In RHIC we are cooling the beam while it is stored in essentially full buckets and the spread of synchrotron frequencies for large amplitude particles tends to make the mixing comparable to coasting beam.

The key challenge of bunched beam cooling is to overcome the difficulties caused by the coherent components in the Schottky spectra. Figure 1 shows a spectrum with coherent components.

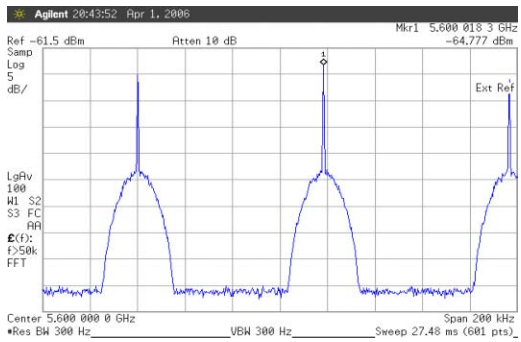

Figure 1: A Schottky spectrum showing coherent components.

Dealing with the Coherent Components

The true significance of the coherent components is not revealed in the frequency domain. However, their existence indicates that large instantaneous voltages are present in the time domain where they may easily overdrive active electronic components such as, low noise amplifiers, causing inter-modulation distortion which defeats the cooling loop. In order to reduce the peak voltages we employ the filter shown in figure 2, which is built from coaxial cables, in the cable lengths are adjusted to precise 5.000 ns intervals with small 100 ps coaxial trombones.

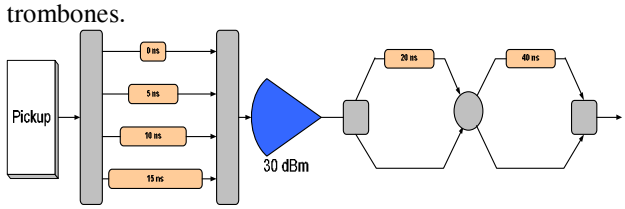

Figure 2: Coax filter used to reduce peak voltages from the pickup before the low noise amplifier and electrical to optical converter.

The filter repeats the beam pulse at reduced voltage at 5 ns intervals 16 times as shown in figure 3 and creates the

insertion loss of ~3 dB which reduces the signal to noise ratio but for gold ions with charge 79 the pick up signal is inherently strong.

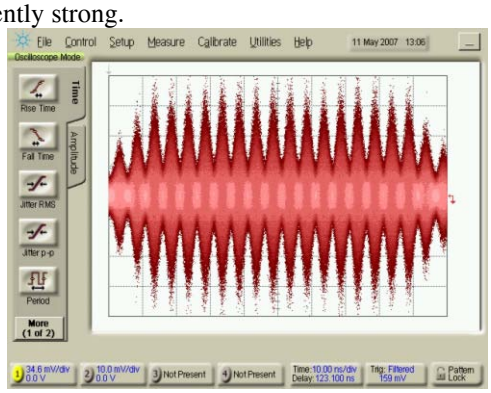

Figure 3: time domain output of traversal filter.

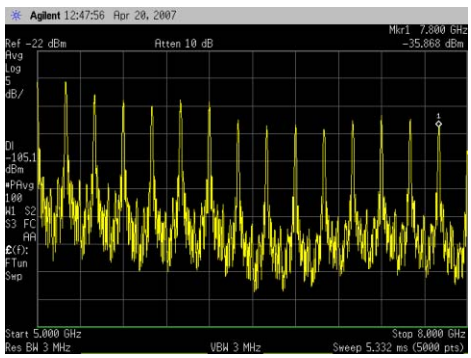

Figure 4: Frequency domain showing 16 lines between 5 to 8 GHz, spaced at 200 MHz.

The signal is sent from the pickup to the kicker via an AM modulated analogue fiber optic link of 6 microsecond length. We have found much better linearity in the link when the source DFB laser is modulated with an external electro-absorption modulator (PHOTONICSystems, inc.) compared to direct modulation of the laser current. Direct modulation causes excessive chirp for large signals, which distorts the signal because of the dispersion (18 ps/nm/km) in the fiber, SMF28.

The Cooling Filter

For momentum cooling a correlator notch filter is employed to create the correct phase of the kick so as to correct the measured energy fluctuations. The filter essentially differentiates the pickup signal to extract the sign of the energy error from the deviation of the beam signal from the synchronous revolution frequency. The concept is shown schematically in figure 5.

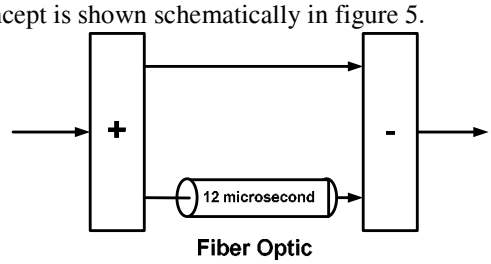

Figure 5: The concept of the notch cooling filter.

The notches it makes at revolution harmonics of the Schottky spectrum are seen in figure 6. The symptom of the distortion in the analogue fiber optic link is that the frequencies of the notches depend on signal amplitude.

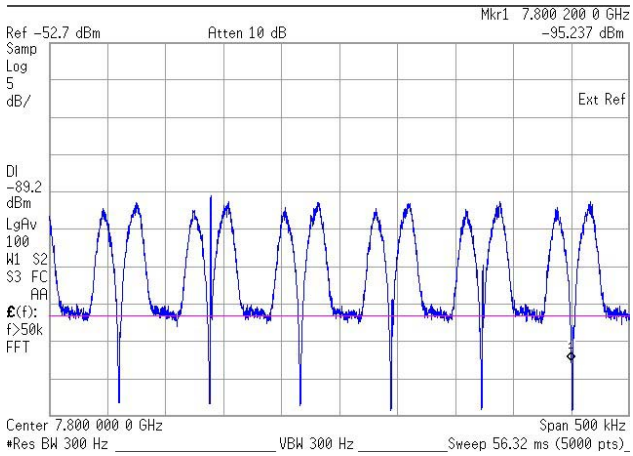

Figure 6: Notches made by the cooling filter.

From the system transfer function shown in figure 7 one sees that the real part (bottom display) changes sign at the revolution frequency (where the notch is). This causes the system to extract energy from the high energy particles and conversely.

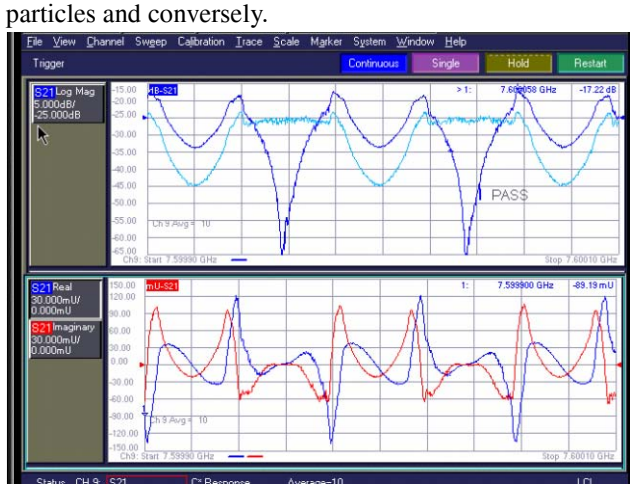

Figure 7: System open loop transfer function, including beam response. The real part is anti-symmetric about the revolution frequency.

Because the delay corresponding to one revolution period is 12.8 microseconds the filter must be realized with a fiber optic cable, in order to have constant frequency response across the 5 to 8 GHz band. The scheme for realizing the cooling filter is shown in figure 8. Matched pairs of photodiodes with >35 dB of common mode rejection assure consistent notch depth across the 5–8 GHz band with no equalizer.

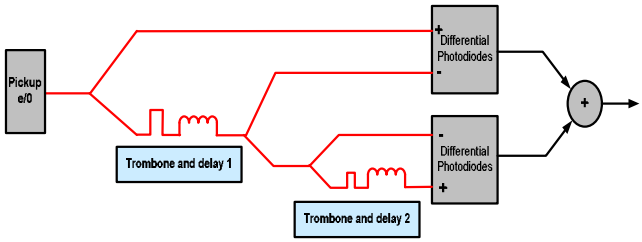

Figure 8: Realization of cooling filter. The four branches synthesize two filters in cascade.

Halo Cooling and the Two-turn Filter

The primary goal of the cooling system is to counteract IBS to prevent beam loss and debunching. This means that the most important particles to cool are those close to the separatrix. These particles have the greatest momentum offsets and are considered in the halo. A two-turn notch filter is used to concentrate the cooling power on the halo particles. The two-turn filter has a wider notch to exclude particles in core of the bunch and also to extend the momentum reach of the stable part of the cooling force. The cooling force from a one-turn filter (red) is compared to that from a two-turn filter in figure 9.

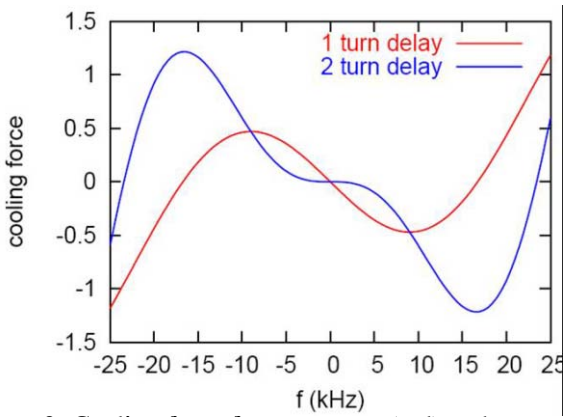

Figure 9: Cooling force for a one-turn (red) and two-turn filter.

The two-turn filter is just two one-turn filters in cascade. One can see how the four branches of the filter in figure 8 constitute two filters cascaded filters by expanding the expression for the product of two one-turn filters.

$$S(\omega) = \left(1 - e^{-j\omega T_{rev}}\right)^2$$

$$= 1 - e^{-j\omega T_{rev}} - e^{-j\omega T_{rev}} + e^{-j\omega 2 T_{rev}}$$

In figure 10 the response of the two-turn filter (red) is compared to that of the one-turn.

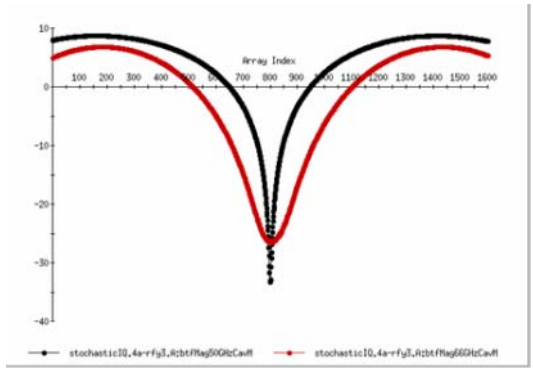

Figure 10: The response of the two-turn filter (red) compared to that of the one turn.

The Kicker Cavities

For optimal cooling of gold ions at 100 GeV/nucleon up to 250 keV must be supplied from the kicker. Although the ion charge is 79 this would require, nevertheless, 3 kV. One could consider a 50 Ohm kicker to cover the 3 GHz span of the system but the required power would then be 90 kW. We synthesize the kick with much less power by employing high-Q cavities to generate the kicks. The cavity frequencies are spaced at 200 MHz intervals in the 5 to 8 GHz band of the system. One can think of these frequencies as a Fourier synthesis of the kick, and because the bunch is 5 ns long the basic harmonic of the series is 200 MHz. The bandwidth of the cavities is chosen to allow filling and emptying the cavities between bunches (100 ns). This determines the Q of the cavities and a high shunt impedance is achieved by using a four-cell TM_{010} like structures with R/Q ~ 100 Ohm. A computer model of a typical cavity is shown in figure 11. They have equal two coaxial ports, one for incoupling and one for an external load (located outside the vacuum) which sets the desired loaded Q. They have a 20 mm beam bore hole, which is unacceptability small for the collider during filling and ramping. They are split on a vertical midplane and opened during filling and ramping and then closed for operation during the store.

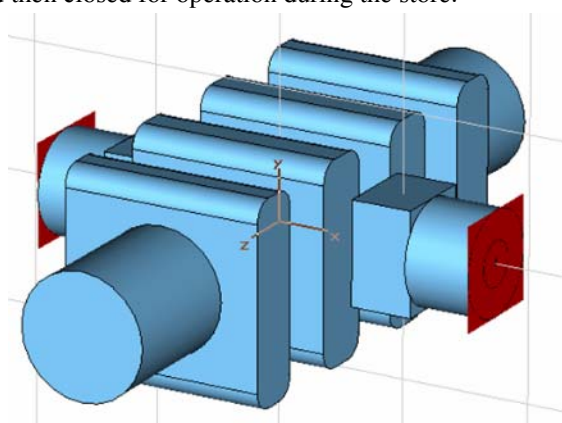

Figure 11:Computer model of a kicker cavity. It has a 20 mm bore and two matched coaxial coupling ports.

The Low-Level System

The low level system resembles a typical rf system with 16 cavities. Each cavity has an IQ modulator and rf power supply (40 Watts). The correct setting of IQs are obtained by measuring the system open loop response function including the beam(Beam Transfer Function). This is done automatically by the network analyzer. Software running in the embedded Window XP PC analyzes the BTF results and calculates settings for the IQs. This is done periodically (about every 15 minutes) during the store to adapt the system gain to cooling of the beam and to compensate drifts in phase. Phase drifts come about because of heating on the cavities and changes in the long fiber optic cables. The network analyzer also monitors the delays in the notch filters and sends commands to motorized optical trombones. Corrections are typically less than 1 ps in 15 minutes. The operation takes about one minute for a cavity and since the process takes one cavity out of the 16 at a time off line, every 15 minutes, it amounts to a negligible degradation of the cooling rate. Figure 12 shows a typical system response function result.

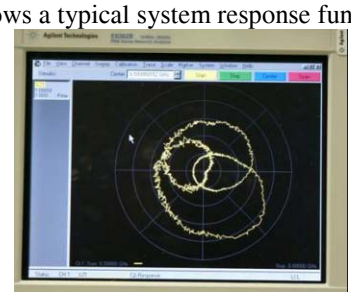

Figure 12: Cooling system response function including BTF and filters.

RESULTS

Tests with Protons

The first system tests were carried out with protons in the polarized proton run at RHIC of FY06. Since the proton bunch intensity is 10^{11} a special low intensity bunch with 10^{9} was prepared as an analogue to an ion bunch. By gating the cooling system before the first low noise amplifier the development and testing of the cooling system could be carried out parasitically during production stores. This was the first successful test of bunched beam stochastic cooling. [3] Figure 13 shows the proton bunch before and after cooling for two hours.

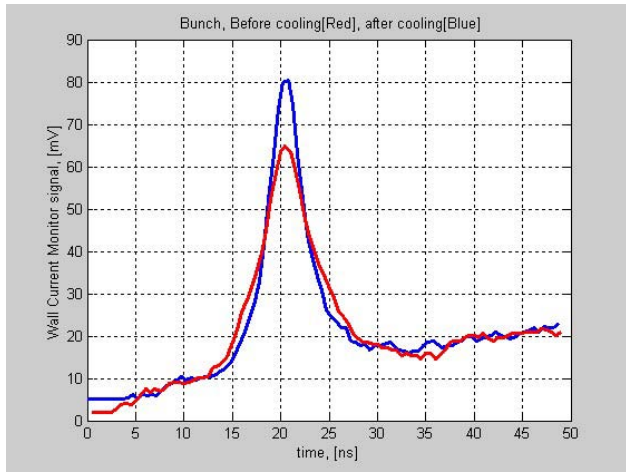

Figure 13: Proton bunched before (red) and after (blue) cooling.

Operational Cooling of Gold Ions

The system was commissioned and made operational in the Yellow ring of RHIC in May FY07. Cooling showed the desired benefit of reducing losses and preventing debunching from the storage buckets. In fact, the losses in the Yellow ring when cooling became operational reached the level of "burn-off" losses. That is the situation when all the particles that are lost are consumed by collisions. Figure 14 shows the stored beam in RHIC for several stores of duration about 5 hours each. In the middle store stochastic cooling was used in the operation mode for the first time. It is clear that the loss rate in the Yellow ring was markedly reduced compared to previous stores and that of the Blue ring.

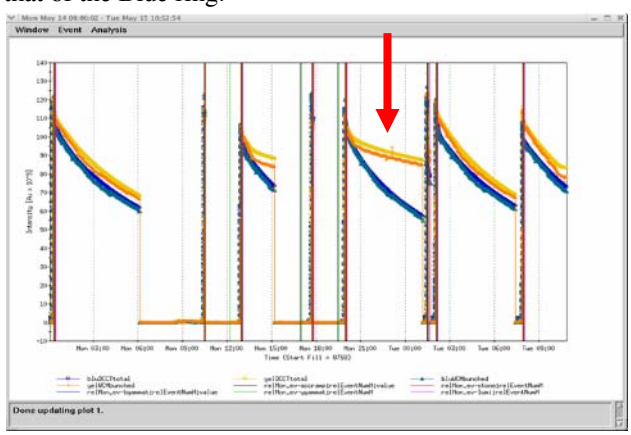

Figure 14: Five stores at RHIC, typically 5 hours. Stochastic cooling was operating for the middle two stores in the Yellow ring.

It is apparent that the cooling not only stops losses but also cools the beam to a smaller emittance. In a preliminary test we cooled only half of the bunches in the ring by gating the system at the pickup. In this way we could compare the cooled and un-cooled bunches under the same conditions. Figure 15 shows a scope trace of all the bunches after about 2 hours of cooling. It is clear that the cooled bunches attained higher peak current. Figure

16 compares a detailed view of the bunch profiles. The un-cooled bunch shows beam in the adjacent 197 MHz buckets. These satellite bunches are populated in the imperfect transfer of beam from the 28 MHz accelerating system to the storage rf system. Beam in the satellite buckets is also cooled.

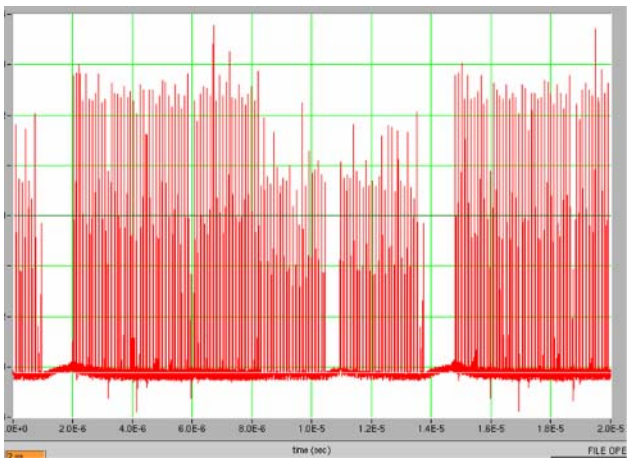

Figure 15: Wall current monitor of all 100 bunches. The first 50 were cooled for two hours.

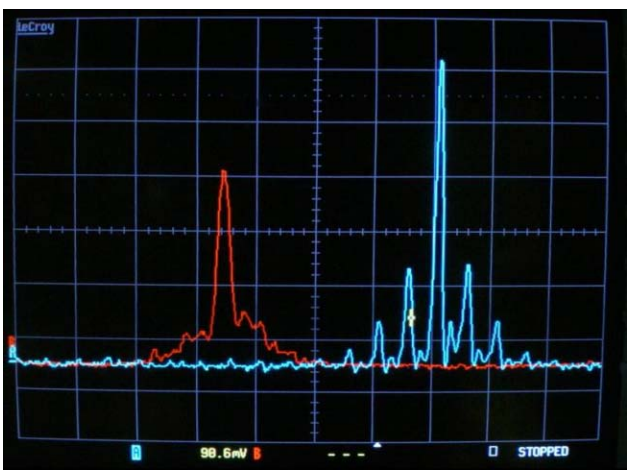

Figure 16: Expanded scale of bunch profiles comparing cooled (blue) and un-cooled bunches.

CONCLUSIONS

Bunched beam stochastic cooling at 100 GeV/nucleon has been achieved at RHIC. A cooling system is operational in the Yellow ring and cools Gold beam to eliminate debunching and reduces beam losses to the burn-off level. The longitudinal phase area of the bunches is reduced by the cooling system.

REFERENCES

[1] G. Jackson et al, "A Test of Bunched Beam Stochastic Cooling in the Tevatron Collider", PAC91, p. 1759.

[2] D. Boussard, "Schottky Noise and Beam Transfer Function Diagnostics", The Queen's College, Oxford, England, 1985, CERN 87-03 Vol. II.

[3] M. Blaskiewicz, J. M. Brennan and J. Wei, "Stochastic Cooling in RHIC II", EPAC06, Lucerne p. 2861.

STOCHASTIC COOLING FOR THE HESR AT FAIR

H. Stockhorst, R. Stassen, R. Maier and D. Prasuhn, FZ Jülich GmbH, Jülich, Germany
T. Katayama, University of Tokyo, Saitama, Japan, L. Thorndahl, CERN, Geneva, Switzerland

Abstract

The High-Energy Storage Ring (HESR) of the future International Facility for Antiproton and Ion Research (FAIR) at GSI in Darmstadt is planned as an anti-proton cooler ring in the momentum range from 1.5 to 15 GeV/c. An important and challenging feature of the new facility is the combination of phase space cooled beams with internal targets. The required beam parameters and intensities are prepared in two operation modes: the high luminosity mode with beam intensities up to 10^{11} anti-protons, and the high resolution mode with 10^{10} anti-protons cooled down to a relative momentum spread of only a few 10^{-5}. Consequently, powerful phase space cooling is needed, taking advantage of high-energy electron cooling and high-bandwidth transverse and longitudinal stochastic cooling. A detailed numerical and analytical approach to the Fokker-Planck equation for longitudinal filter cooling including an internal target has been carried out to demonstrate the stochastic cooling capability. The great benefit of the stochastic cooling system is that it can be adjusted in all phase planes independently to achieve the requested beam spot and the high momentum resolution at the internal target within reasonable cooling down times for both HESR modes even in the presence of intra-beam scattering. Experimental stochastic cooling studies with the internal ANKE target to test the model predictions for longitudinal cooling were carried out at the cooler synchrotron COSY. The routinely operating longitudinal stochastic cooling system applies the optical notch filter method in the frequency band I from 1-1.8 GHz.

INTRODUCTION

The High-Energy Storage Ring (HESR) [1] of the future International Facility for Antiproton and Ion Research (FAIR) at GSI in Darmstadt [2] is planned as an antiproton cooler ring in the momentum range from 1.5 *to* 15 GeV/c. The circumference of the ring is 574 m with two arcs of length 155 m each. The long straight sections each of length 132 m contain the electron cooler solenoid and on the opposite side the Panda experiment. The stochastic cooling tanks will be located in the long straights and in one arc. Two injection lines are foreseen, one coming from the RESR [2] to inject cooled anti-protons [3] with 3 GeV kinetic energy and the other one to inject protons from SIS 18. An overview on the HESR ring is given in figure 1. Using a target thickness of $4 \cdot 10^{15}$ atoms cm^{-2} the high luminosity mode (HL) is attained with 10^{11} antiprotons yielding a luminosity of $2 \cdot 10^{32}$ cm^{-2} s^{-1}. The HL-mode has to be prepared in the whole energy range and beam cooling is needed to particularly prevent beam heating by the beam target interaction. Much higher requirements are necessary in the high resolution mode (HR) with 10^{10} antiprotons. The same target thickness yields here a luminosity of $2 \cdot 10^{31}$ cm^{-2} s^{-1}. This mode is requested up to 8.9 GeV/c with a rms-relative momentum spread down to about $4 \cdot 10^{-5}$.

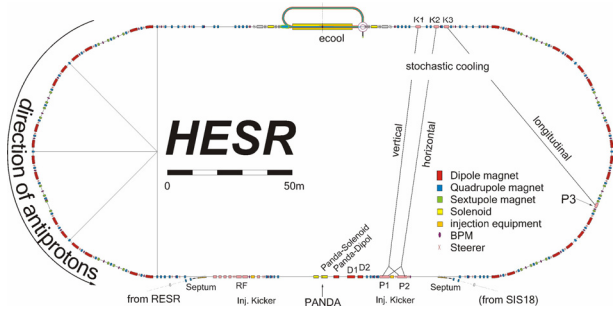

Figure 1: Layout of the HESR ring including the signal paths for transverse and longitudinal cooling.

The injected beam in the HESR at $p = 3.8\ GeV/c$ has the following emittance and relative momentum spread in HR-Mode: $\varepsilon_{rms,HR} = 0.1\,mm\,mrad$ $\delta_{rms,HR} = 2 \cdot 10^{-4}$ and HL-Mode: $\varepsilon_{rms,HL} = 0.6\,mm\,mrad$ $\delta_{rms,HL} = 5 \cdot 10^{-4}$.

The injected beam is then accelerated with an acceleration rate of 0.1 (GeV/c)/s to the desired experiment momentum.

COOLING SYSTEMS

In general a very broad cooling bandwidth must be chosen for fast cooling. However the upper frequency of the cooling system is restricted when considering the filter cooling method [4]. In this case a proper functioning is only achieved if there is no overlap of adjacent revolution harmonics so that each band can be covered separately by the notch filter. As a reasonable compromise a (2 – 4) GHz system has been chosen that can be operated in the whole momentum range from 3.8 GeV/c up to maximum momentum. The simulations assume quarter wave pickup and kicker loops [5]. For longitudinal stochastic cooling an optical notch filter will be implemented in the signal path. In figure 1 the cooling signal paths are shown. Cooling simulations applying a linear notch filter have been already presented in [6]. In this contribution the model utilizes a more realistic non-linear notch filter. The HESR optics [1] that has been used throughout has an imaginary transition energy with $\gamma_{tr} = 6.0\,i$. The target-beam interaction is treated in the formalism as outlined elaborately in [7].

Transverse Cooling

The theory of transverse cooling used in this contribution is outlined in detail in [8]. The formalism has

been extended to include the beam interaction with an internal target. The time development of the horizontal or vertical beam emittance ε during cooling and beam target interaction is governed by a first order differential equation. This equation can be solved for the rms-equilibrium emittance which yields for a low thermal noise cooling system

$$\varepsilon_{eq,rms} = \frac{1}{4\sqrt{2\pi}} \frac{f_0^2 N \beta_T \theta_{rms}^2}{|\eta| \delta_{rms} W f_C} \qquad [1]$$

under the assumption of no position and angle dispersion at the target location where the beta function is β_T. θ_{rms} is the rms value of the Gaussian small angle scattering distribution [7]. The quantity θ_{rms}^2 is proportional to the target area density N_T. The revolution frequency of a particle with nominal momentum p_0 is f_0. The center frequency of the cooling system with bandwidth W is f_C. The particle number is N, η is the frequency slip factor and δ_{rms} is the rms relative momentum spread of the (longitudinally cooled) beam. Note that eq. (1) does not depend on the initial emittance of the beam as well as pickup and kicker sensitivity. Simulations have shown [9] that an additional contribution to the equilibrium emittance due to beam heating by intra beam scattering (IBS) can be neglected here. IBS becomes only important if the beam is cooled to very low emittances. This can be avoided by a proper adjustment of the electronic gain.

Longitudinal Cooling

The time development of the momentum distribution during longitudinal filter cooling and beam target interaction is found by numerically solving a Fokker-Planck equation (FPE) [10] with an initial condition and a boundary condition that takes into account the acceptance limit. The FPE contains not only the coherent cooling force but also the mean energy loss in the target leading to a shift of the distribution as a whole towards lower momenta. Beam diffusion due to electronic and Schottky beam noise as well as diffusion by the target determined by δ_{loss}^2, the mean square relative momentum deviation per target traversal [7] is included. Diffusion results in a broadening of the beam distributions. The quantity δ_{loss}^2 is directly proportional to the target area density. Under the assumptions of an initial centered Gaussian beam that remains almost Gaussian during cooling, no thermal noise, mean energy loss compensated and no unwanted mixing one can derive a simple first order differential equation for the rms relative momentum spread from the FPE. From this equation the smallest equilibrium value

$$\delta_{eq,rms} = \frac{4}{5}\left(\frac{3}{16} \cdot \frac{N f_0^2}{|\eta| W f_C} \delta_{loss}^2 \right)^{1/3} \qquad [2]$$

for the rms relative momentum spread can be found where the electronic gain is to be adjusted accordingly. Again the final equilibrium does not depend on the initial momentum spread of the beam.

COOLING SIMULATION RESULTS

Figure 2 shows longitudinal beam distributions resulting from solutions of the FPE at several times *t = 0 s (black), 50 s, 100 s, 150 s, 2000 s (blue)* for the HL-mode at *T = 3 GeV*. The mean square relative momentum deviation per target traversal is $\delta_{loss}^2 = 3.84 \cdot 10^{-16}$. The emittance increase with time due to the target beam interaction amounts to $d\varepsilon / dt = 3.6 \cdot 10^{-4}\, mm\, mrad / s$ resulting in a beam

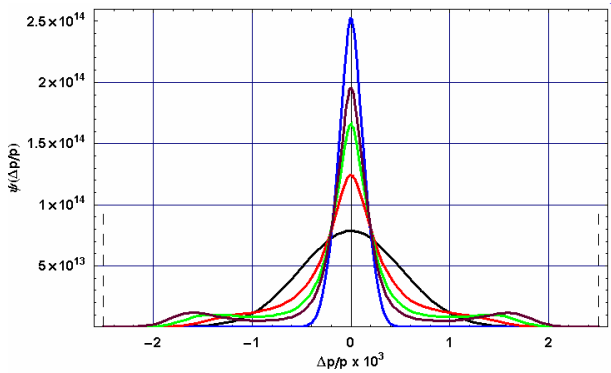

Figure 2: Beam distributions at t = 0 s (black), 50 s, 100 s, 150 s, 2000 s (blue) for the HL-mode at *T = 3 GeV*. The mean energy loss is assumed to be compensated. The acceptance limit (dashed lines) is ± 2.5 · 10^{-3}.

emittance of about *1 mm mrad* within one hour when transverse cooling is off. It is assumed that the strong mean energy loss $\bar{\varepsilon} = -2.73 \cdot 10^{-2}\, eV / turn$ can be compensated by an rf-barrier bucket cavity or by TOF cooling as explained below. In figure 3 the rms relative momentum spread (red dots) versus time is shown.

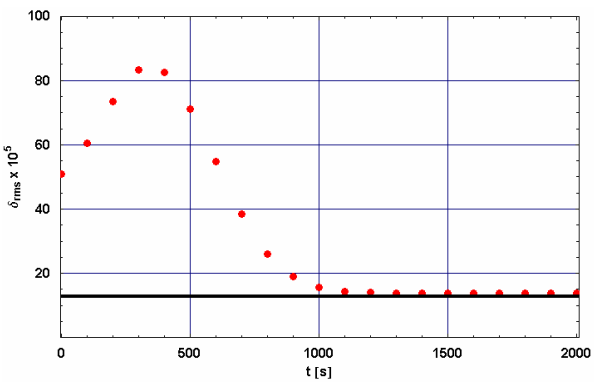

Figure 3: Rms-relative momentum spread (red dots) during cooling with an internal target at T = 3 GeV for the HL-mode. Horizontal line: eq. (2)

The rms values of the distributions exhibit an increase during the first 400 s and then drop down to the equilibrium value, $\delta_{rms} = 1.4 \cdot 10^{-4}$, which is attained in nearly 1200 s. This growth is due to the tails in the distributions that evolve in the first 400 s as can be seen in figure 2. Particles are moved towards the acceptance limit where they are lost mainly due to the enhanced diffusion induced by the unwanted mixing between

pickup and kicker when their relative momentum spread is larger then $\pm\ 7 \cdot 10^{-4}$. A short period of the larger acceptance TOF cooling prior to filter cooling can avoid these losses. Bad mixing plays a minor role at only slightly larger beam momenta as well as in the HR-mode where the initial momentum spread prior to cooling is significantly smaller. The beam loss amounts about 20% at $T = 3\ GeV$ in the HL-mode. Figure 3 shows that the beam distributions in equilibrium are nearly Gaussian. Here the rms-value is quite well predicted by the formula given in eq. (2). Table 1 and 2 summarize for two beam energies the expected equilibrium values and cooling down times in the HR- and HL-mode, respectively. The necessary electronic gain lies in the range 95 dB to 110 dB. The particle power ranges up to 15 W.

Table 1: HR-Mode Stochastic Cooling

p [GeV/c]:	**3.8**	**8.9**	**14.9**
rms rel. momentum spread δ_{rms}:	$7 \cdot 10^{-5}$	$6 \cdot 10^{-5}$	$5 \cdot 10^{-5}$
rms transverse emittance ε_{rms} [mm mrad]:	$2 \cdot 10^{-2}$	$7 \cdot 10^{-3}$	$4 \cdot 10^{-3}$
cooling down time [s]:	≈100	≈200	≈250

Table 2: HL-Mode Stochastic Cooling

p [GeV/c]:	**3.8**	**8.9**	**14.9**
rms rel. momentum spread δ_{rms}:	$1.3 \cdot 10^{-4}$	$1.2 \cdot 10^{-4}$	$1.0 \cdot 10^{-4}$
rms transverse emittance ε_{rms} [mm mrad]:	$8 \cdot 10^{-2}$	$4 \cdot 10^{-2}$	$2 \cdot 10^{-2}$
cooling down time [s]:	≈500	≈800	≈1000

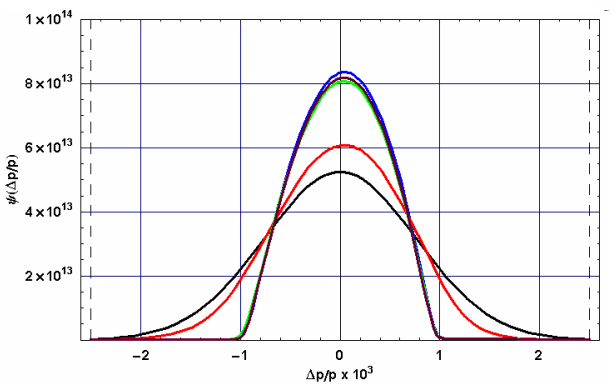

Figure 4: TOF momentum cooling at T = 3 GeV for the HL-mode. The mean energy loss due to the target-beam interaction is compensated. The initial distribution (black) is cooled down to a stable equilibrium without tails in about 300 s (brown curve).

All simulation and experimental results show that the dominant process due to the target-beam interaction is the mean energy loss in the target. The stochastic cooling predictions were deduced under the assumption that the mean energy loss can be compensated by a suitable method. An interesting and promising method to accomplish this goal is the time of flight discrimination cooling method (TOF cooling). Here the notch filter in the cooling chain is replaced by a ninety degree broadband phase shifter. This method prefers a high bandwidth and a low electronic gain. An example using the (2 - 4) GHz system is shown in figure 4. After proper adjusting the electron gain (98 dB) and the system delay ($\Delta T_D = -0.195\,ns$) the initial beam distribution with even a 50% larger initial momentum spread in the HL-mode at $T = 3\ GeV$ is cooled down to a stable equilibrium beam momentum spread within 300 s. No particle losses occur and the mean energy loss is compensated as can be seen in figure 4. The corresponding rms-relative momentum spread during TOF cooling shows an exponentional decrease and attains an equilibrium value $\delta_{rms} = 4.5 \cdot 10^{-4}$ after 300 s. The value is larger as compared to that in figure 3 due to the absence of the notch filter which strongly suppresses the particle and thermal noise in the center of the distributions. Consequently the particle power is larger and amounts up to 30 W. The TOF cooling method also helps to prevent the development of low momentum tails in the beam distribution. By adjusting the system delay it is also possible to accelerate or decelerate the beam in flat top if a small energy change should be necessary.

STOCHASTIC COOLING EXPERIMENTS

In order to gain confidence in the stochastic momentum cooling predictions with internal targets cooling experiments [10] have been carried out at COSY with the present cooling system [11]. The cooling experiments were carried out at beam momentum 3.2 GeV/c with about 10^{10} stored protons. The frequency slip factor was measured and resulted in $\eta = -0.1$, i.e. the machine was operated above transition. Longitudinal cooling was carried out with band I ranging from 1 to 1.8 GHz. Particle distributions were measured in the frequency range of the harmonic number 1500 with the band II system (1.8 – 3) GHz and can be converted to momentum distributions using the relation $\Delta f / f_0 = \eta \cdot \Delta p / p_0$. The frequency distributions were measured every 2.5 min or 5 min in flat top with a duration of about 30 min.

Beam Target Interaction

First the target beam interaction was investigated in order to determine the mean energy loss per turn ε and the mean square relative momentum deviation per turn δ^2_{loss} . The results are shown in the figures 5 and 6. In figure 5 the measured center of the frequency distributions are shown from which the revolution frequency of the protons can derived by dividing the values by the harmonic number 1500. At time zero this gives $f_0 \approx 1.568\ MHz$.

The measured data (black symbols) in figure 5 show the expected behavior that the beam distributions are

shifted linearly towards lower energies due to the beam target interaction.

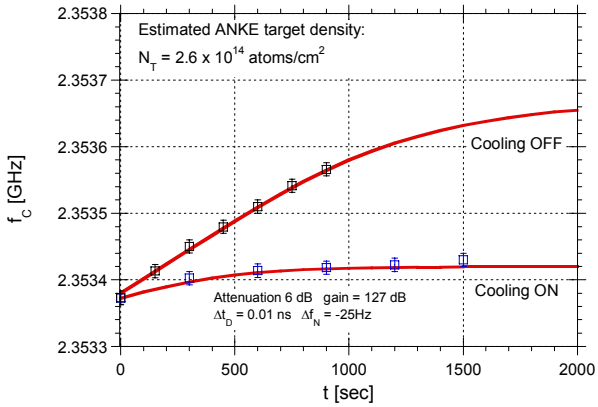

Figure 5: The measured center frequency at harmonic 1500 (blue symbols: cooling ON, black symbols: cooling OFF) in comparison with the model predictions (red curves).

Due to the negative frequency slip factor this corresponds to a linear increase in frequency. Thus the revolution frequency of the protons increases with increasing energy loss. From the slope of the data (black symbols) in figure 5 the mean energy loss per turn was determined to $\delta^2_{loss} = 2 \cdot 10^{-17} / turn$. The relative momentum spread in figure 6 (black symbols) shows only a small increase. From the linear increase of δ^2_{rms} the mean square relative momentum deviation per turn $\delta^2_{loss} = 2 \cdot 10^{-17} / turn$ was derived.

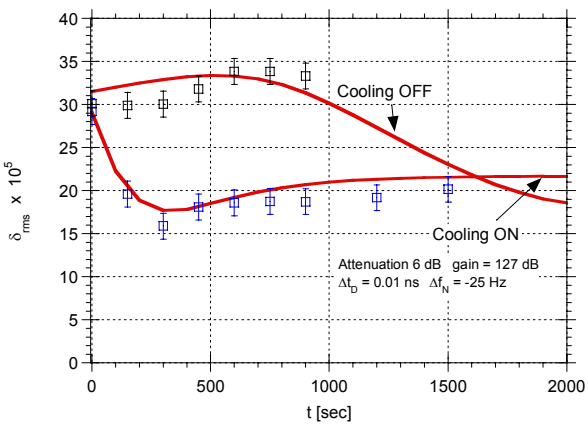

Figure 6: The measured relative momentum spread at harmonic 1500 (blue symbols: cooling ON, black symbols: cooling OFF) in comparison with the model predictions (red curves). The linear increase of the squared momentum spread determines the mean square relative momentum deviation per turn when cooling is switched off.

The indicated error bars result from three consecutive measurements and reflect the uncertainties due to the finite frequency resolution of the spectrum analyzer. The values for ε and δ^2_{loss} have been then used in the FPE when cooling is switched off to determine the beam distributions versus time. A Gaussian initial distribution in the calculations was assumed. The results are shown in figure 5 and 6 as red curves. As can be seen the model deviates from the linear behavior at about 600 s which is due to particle losses when the shifted distributions reach the momentum acceptance of the machine. This becomes clearly visible when the measured frequency distributions are compared with the distributions predicted by the model as is depicted in figure 7 for $t = 900\ s$.

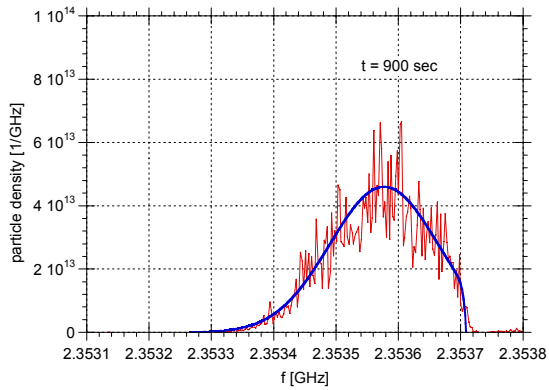

Figure 7: Measured frequency distributions (red) at harmonic number 1500 for $t = 900\ s$ in comparison with the model prediction (blue curve). The sharp cut-off at about 2.3537 GHz corresponds to the acceptance limit.

The measurement as well as the model prediction show a cut off in the distributions at about 2.3537 GHz which corresponds to the negative relative momentum acceptance limit $\delta_{acc} = -1.4 \cdot 10^{-3}$. It is seen that this value is reached after about 600 s. Particle losses are increasing then with time as indicated by the increase in the slope at the high frequency side of the distributions. Measured and predicted distributions agree remarkable well. The measured mean energy loss yielded a target thickness $N_T \approx 3 \cdot 10^{14}\ atoms / cm^2$.

Momentum Cooling with Internal Target

After determining the parameters of the beam target interaction stochastic cooling was switched on. The system delay was adjusted for cooling by means of BTF measurements and the notch filter was set 25 Hz below the center frequency of the distribution at harmonic one. In momentum space this means that the filter was set above the mean momentum of the protons. Measurements for different attenuations of the electronic gain of the cooling system were then carried out. As an example the figures 5 and 6 show the results for the attenuation set to 6 dB which corresponds to a model gain and an additional delay of 127 dB and $\Delta T_D = 0.01 ns$, respectively. Figure 5 shows the center frequency measured at harmonic number 1500 (blue data points) in comparison with the model prediction. The figure clearly shows the cooling effect. The ANKE target thickness is more than an order of magnitude smaller as compared to the HESR case. The mean energy loss is nearly compensated by cooling. The time development of the relative moment spread during

cooling and ANKE target on (blue data points) is fairly well predicted by the model as shown in figure 6. Initially the momentum spread drops down and increases until an equilibrium value $\delta_{rms} = 2.2 \cdot 10^{-4}$ between target beam interaction and cooling is attained after about 1000 s. Again the cooling effect is clearly visible when the data with cooling on and off are compared.

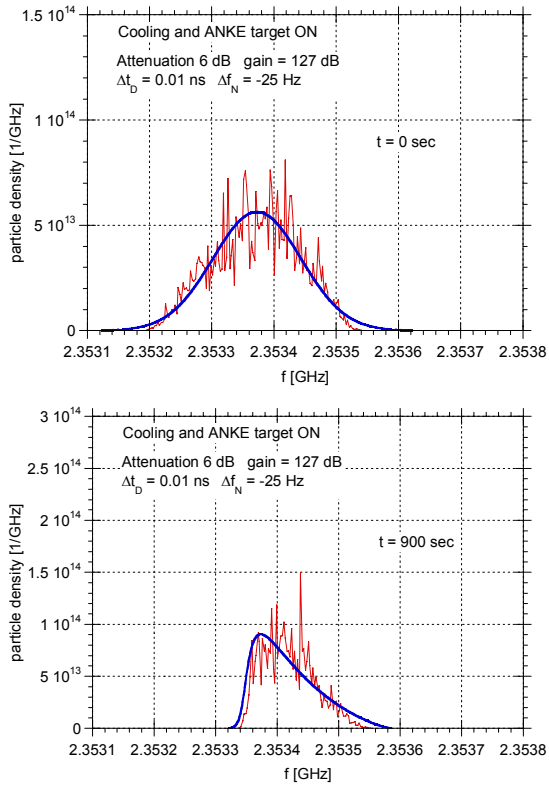

Figure 8: Measured beam distributions (red) during cooling in comparison with model predictions (blue). Initially a Gaussian distribution has been assumed with values for the center frequency and variance determined from the measured initial distribution.

Figure 8 presents a comparison of the measured distribution with the model prediction at $t = 0\ s$ and $t = 600\ s$. Initially a Gaussian distribution has been assumed with values for the center frequency and variance determined from the measured initial distribution. The particle distributions are normalized to the number of protons in the ring. The Fokker-Planck solutions present the absolute beam distributions. There are no scaling factors to adjust the solutions to the measured distributions. A more detailed discussion of the cooling experiment can be found in [10].

SUMMARY AND OUTLOOK

The stochastic filter cooling model developed for the investigation of stochastic cooling at the HESR receives a remarkable good agreement with the experimental results at COSY when the internal ANKE target is in operation. The beam target interaction is well described by the model through the quantities mean energy loss and mean square relative momentum deviation per turn. Both quantities can be measured. Once the main parameters are known the model can be employed to predict the cooling properties under different conditions, e.g. if the target thickness is increased, different beam energy, etc.. The good agreement of the model with the experimental results at COSY gives a save confidence that the model will also fairly well predict the cooling properties in the case of the planned HESR at the FAIR facility. However more investigation are needed concerning the undesired mixing that is here much more severe as at COSY. The available equilibrium values for the HESR are close to the desired beam quality. Beam heating due to the internal target can be compensated with stochastic cooling in the whole momentum range. The promising TOF cooling method will be further investigated in theory as well as in experiment especially including the feedback via the beam. Also other methods to compensate the mean energy loss have to be studied. A further method to compensate the mean energy loss by a barrier bucket cavity will be investigated theoretically and will be soon tested at COSY. The stochastic cooling model will be further developed to include the characteristics of the newly designed pickup and kicker structures [12] as well.

REFERENCES

[1] HESR, “Baseline Technical Report”, http://www.fz-juelich.de/ikp/hesr/2-11-HESR.pdf
[2] M. Steck, “Status of the FAIR Facility”, COOL 05, Galena, USA, 18-23 Sept. 2005
[3] F. Nolden et al., “Stochastic Cooling Developments at GSI”, COOL05, Galena, USA, 18-23 Sept. 2005
[4] D. Möhl et al., Phys. Rep. Vol. 58, No.2, Feb. 1980
[5] G. Lambertson, “Dynamic Devices – Pickup and Kickers”, in AIP Conf. Proc. 153, p. 1413
[6] H. Stockhorst et al., “Stochastic Cooling for the HESR at the GSI-FAIR Complex”, Proc. EPAC 2006, Edinburgh, Scotland, 26-30 June 2006, p. 231
[7] F. Hinterberger, “Beam-Target Interaction and Intrabeam Scattering in the HESR Ring”, 2006, Jül-4206, ISSN 0944-2952
[8] B. Autin, ”Fast Betatron Cooling in an Antiproton Accumulator”, CERN/PS-AA/82-20
[9] H. Stockhorst et al., “Cooling Scenario for the HESR Complex”, COOL 05, Galena, USA, 18-23 Sept. 2005
[10] H. Stockhorst et al., “Experimental Test of Momentum Cooling Model Predictions at COSY and Conclusions for WASA and HESR”, Proc. of the Symposium on Meson Physics at COSY-11 and WASA-at-COSY, Krakow, Poland, 17-22 June 2007, to be published in AIP Conf. Proceedings
[11] P. Brittner, H.U. Hacker, R. Maier, U. Pfister, D. Prasuhn, H. Singer, W. Spiess, R. Stassen, H. Stockhorst, A. Zumloh, “The stochastic cooling system for COSY”, proceedings of EPAC92, Berlin
[12] R. Stassen et al., this conference

STOCHASTIC COOLING FOR THE FAIR PROJECT *

F. Nolden, A. Dolinskii, C. Peschke, GSI, Darmstadt, Germany

Abstract

Stochastic cooling is used in the framework of the FAIR project at GSI for the first stage of phase space compression for both rare isotope and antiproton beams. The collector ring CR serves for the precooling of rare isotope and antiproton beams. The paper discusses mainly the stochastic accumulation in the RESR based on a new lattice design.

STORAGE RINGS IN THE FAIR PROJECT

The storage rings in the FAIR project are designed for the preparation of experiments with rare isotope (RI) or antiproton beams, which are produced by bombardment of short high intensity bunches from the SIS100 synchrotron [1] on appropriate production targets. As these beams have large longitudinal and transverse emittances, stochastic precooling is foreseen in the Collector Ring (CR) [2].

The antiprototon beams are accumulated in the RESR storage ring [3]. High energy antiproton experiments make use of stochastic cooling in the HESR storage ring [4].

PRECOOLING IN THE COLLECTOR RING

The stochastic cooling systems in the CR have been described in [5] and [2].

The development of slotline electrodes for the CR is described in [6]. A prototype of the 1 GHz - 2 GHz power amplifier has been built and will be tested at GSI in the near future. The integration of the slotline structures into a complete pick-up tank is presently prepared.

STOCHASTIC ACCUMULATION IN THE RESR RING

Overview

Stochastic accumulation in the RESR makes use of the same principle which has successfully been used in the AA at CERN [7], [8] and in the Accumulator at FNAL [9]. In any case, the accumulation works in the longitudinal phase subspace. Figure 1 shows a sketch of the vacuum chamber at the pick-up which is used for accumulation.

The beam is injected at the injection orbit (i). It is then deposited by rf to a deposition orbit (d). Before the next shot arrives, the stochastic cooling system must be fast enough to shift these particles to the stack tail (t). The repetition interval between single injection shots is mainly given by the time it takes to perform the shift between (d) and (t). Then the same pick-up signal is used to shift the particles gradually into the core. The pick-up sensitivity of the stack tail cooling pick-up should decrease exponentially towards the core.

In order to achieve this goal, the vertical β function at the pick-up must be small and the dispersion large (see below). However, experience from the CERN AA shows that in addition a twofold staggered notch filter may be needed in order to get the system gain down in the core region.

New RESR Lattice

The new lattice of the RESR [10] has the following advantageous properties with respect to antiproton accumulation:

- The lattice enables a flexible choice of the transition gamma up to $\gamma_t = 6.3$.
- There are straight sections with large dispersion and small vertical betatron function for the accumulation pick-up.
- There is enough space in dispersion free sections to take up the stochastic cooling kicker tanks.

RESR Cooling Systems

Four cooling systems are envisaged for the RESR:

1. The stack tail cooling system (longitudinal, see above)
2. The core cooling system (longitudinal)
3. A horizontal betatron cooling system
4. A vertical betatron cooling system

Figure 2 shows the locations for pick-ups and kickers in the new RESR lattice. Figure 3 shows the Twiss functions of an optical setting with $\gamma_t = 5.3$.

In a first stage, the system will work in the 1 GHz - 2 GHz band. Due to the chosen η value, an upgrade up to 4 GHz is feasible. The pick-ups and kickers will be of the Faltin [11] type. The core cooling system will use the same kicker as the stack tail system, just with an additional quadruplet of pick-up electrodes in the accumulation pick-up structure, and a low gain amplification.

* Work supported by EU design study (contract 515873 - DIRACsecondary-Beams)

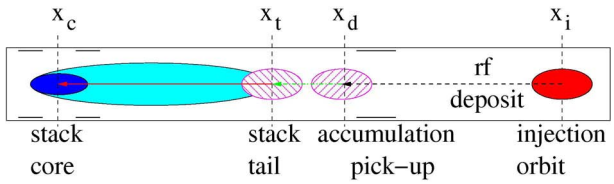

Figure 1: Sketch of vacuum chamber at accumulation pick-up

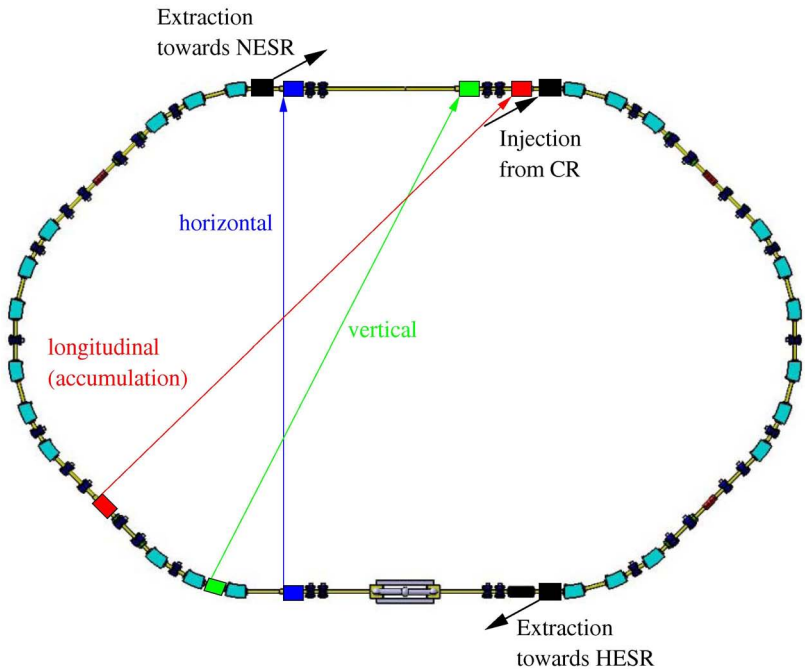

Figure 2: Stochastic cooling paths in the RESR

Exponential Gain Profile and Vertical Chamber Height

For optimum accumulation we need an exponential gain profile [12] with the property

$$g(x) = g_t \exp\left(\frac{x - x_t}{\delta x}\right) \tag{1}$$

leading to an exponential particle distribution

$$\Psi(x) = \Psi_t \exp\left(-\frac{x - x_t}{\delta x}\right) \tag{2}$$

with $\delta x > 0$. Accumulation proceeds towards negative x (Figure 1). g_t and Ψ_t are the values of the gain and distribution functions at the stack tail orbit x_t. If Ψ_c is the distribution at the core x_c, then

$$\delta x = (x_c - x_t) \ln\left(\frac{\Psi_t}{\Psi_c}\right) \tag{3}$$

and

$$\frac{\Psi_t}{\Psi_c} = \frac{g_c}{g_t} \tag{4}$$

For the RESR, we want to inject 10^8 antiprotons per shot and accumulate up to at most $2 \cdot 10^{11}$ particles. Hence we must achieve a (voltage) gain drop of 66 dB over $x_c - x_t$. This can only be achieved if the chamber height h is small compared to $x_c - x_t$. An electrostatic model of the electrode sensitivity $S(x)$ yields in the vertical midplane of a sum pick-up

$$S(x) = \frac{2}{\pi} \arctan\left(\frac{\sinh(\pi w/2h)}{\cosh(\pi x/h)}\right) \tag{5}$$

h is the vertical separation between pick-up plates, w is their horizontal width. For large $|x|/h$, this scales as

$$S(x) \propto \exp\left(-\frac{\pi|x|}{h}\right) \tag{6}$$

In case of the RESR

$$\frac{x_c - x_t}{h} \approx \frac{\ln\left(2 \times 10^3\right)}{\pi} \approx 2.42 \tag{7}$$

In other words: If the gain profile is realized only by the sensitivity drop from the pick-up to the core (and not by additional notch filters), then the distance between the stack tail and the stack core should be about 2.4 times the chamber height. This leads to rather tight requirements for the chamber height. In the straight sections inside the arcs of

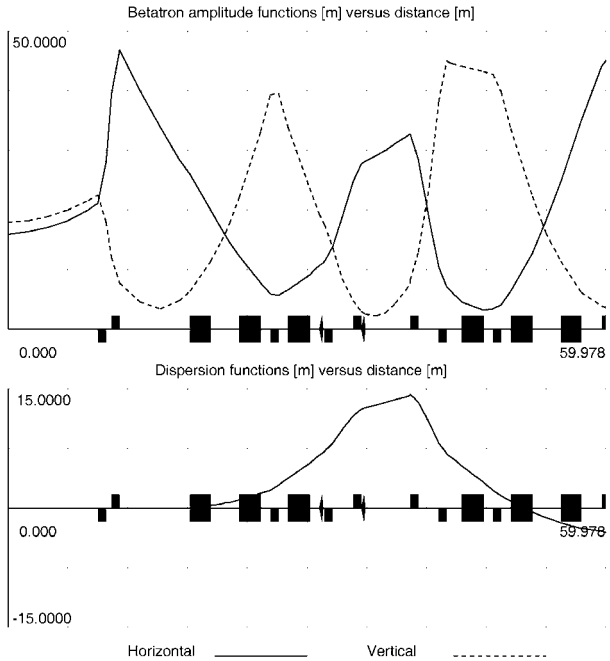

Figure 3: Twiss functions in one quarter of the RESR, beginning in the middle of a long straight section.

the RESR, the dispersion is about 13 m, and the vertical beta function is below 3 m along a distance of 3 m. These are almost ideal conditions for an accumulation pick-up. With the vertical emittance ϵ_y of 10 mm mrad, one gets a beam height of $\Delta y = 2\sqrt{\beta_y \epsilon_y} = 11$ mm. Adding a safety margin of ± 3 mm on each side, one arrives at a chamber height of 17 mm. With these parameters, one then would get a distance of at least 41 mm from the stack tail to the core. An analog requirement is that the stray field of the injection kicker must not disturb the beam at the stack tail. This requirement gives a limit for $x_i - x_d$ (see Figure 1).

Desired and Undesired Mixing

Once the distance $x_c - x_t$ is given, the product

$$x_c - x_t = D(\delta p/p)_{ct} \tag{8}$$

is also fixed. Here $(\delta p/p)_{ct}$ is the relative momentum difference between tail and core, and D is the dispersion at the pick-up. For the RESR pick-up it follows that $(\delta p/p)_{ct} = 3.2 \times 10^{-3}$.

This number is important as the product $|\eta|(\delta p/p)_{ct}$ is important for the mixing number

$$M = (m_c |\eta| (\delta p/p)_{ct})^{-1} \tag{9}$$

which should be of the order of unity. Here $\eta = (\delta f/f) \,/\, (\delta p/p)$ is the frequency slip factor, and m_c is the harmonic number in the center of the cooling band. On the other hand, the undesired mixing (bad mixing)

$$B = \cos\left(\pi m_c x \eta_{pk} (\delta p/p)_{cd}\right) \tag{10}$$

must not be too small of even get negative. Here $(\delta p/p)_{cd} \approx 4 \times 10^{-3}$ is the momentum width between the deposit and the core orbits. This number enters into the cooling rate equation for transverse cooling. In this equation $x = (s_k - s_p)/C$ is the ratio of the path between pick-up and kicker along the closed orbit and the circumference of the closed orbit. η_{pk} is the *local* frequency slip factor between pick-up and kicker. It is assumed for simplicity that the cooling system is adjusted to the time of flight of a particle at the position $(x_c + x_d)/2$. One should require that the cooling decrement as a function of frequency should not have the wrong sign even at the upper limit of the cooling band, leading to an upper frequency limit:

$$f_G = \frac{f_{\rm rev}}{2x\eta_{pk}(\delta p/p)_{cd}} \tag{11}$$

where $f_{\rm rev}$ is the revolution frequency.

In the long straight straight sections, the dispersion vanishes. These sections are used for the kickers. The section consists of a central part with a total length of 18m, delimited by a quadrupole doublet on each side. Between each doublet and the adjacent dipole there are additional dipersion free straight sections (7 m) with a vertical waist (β_y at most 7.8 m). The vertical phase advance here amounts almost exactly to 90 degrees. Of these straight sections, three are occupied by injection or extraction septa, which are located close to the dipoles. The horizontal pick-up is located close to the next dipole (Figure 2), reserving space for an optional electron cooler. Because the vertical cooling pick-up should be at moderate beta functions. it is placed at the beginning of the northern arc, where the dispersion is still below 0.7 m.

Table 1 shows some parameters of the new stochastic cooling paths. $s_k - s_p$ is the length of the central closed orbit between pick-up and kicker. Shortcut is the length of

Table 1: Important parameters of the stochastic cooling paths

path	$s_k - s_p$ [m]	shortcut [m]	γ_t	η_{pk}	f_G [GHz]	T_{free} [ns]
horizontal	89.476	62.149	4.604	0.010	42	89
vertical	102.588	57.298	4.946	0.016	22	151
accumulation	95.292	67.297	6.030	0.029	13	91

the straight connection across the ring between the end of the pick-up and the beginning of the kicker. This number is needed for the evaluation of the time which is available for electronic processing (amplifiers, filters, etc.). The free signal processing time T_{free} is calculated by assuming a signal transmission velocity of 0.95 c across the ring. γ_t and η are the local parameters between pick-up and kicker. f_G is the upper operating frequency limit (see eq. 11).

The longitudinal kicker could be placed at the oppsite side of the long straight section, just before the injection septum magnet. This choice leaves a comfortable time interval of 91 ns for signal processing, but still allows for increasing the operating bandwidth in a possible future system upgrade.

Approximate Optimum Frequency Slip Factor

The transverse cooling rate can be written

$$\frac{1}{\tau_\perp} \approx \frac{2W}{N}\left[2Bg_\perp - (M+U)\left|g_\perp\right|^2\right] \tag{12}$$

If one works at the optimum gain

$$|g_\perp|_{\mathrm{opt}} = \frac{B}{(M+U)} \tag{13}$$

the optimum cooling rate is

$$\left(\frac{1}{\tau_\perp}\right)_{\mathrm{opt}} = \frac{2WB^2}{N(M+U)} \tag{14}$$

Under these conditions one can deduce an approximate optimum value for the frequency slip factor, if one assumes in addition that

1. the diffusion due to Schottky noise dominates the diffusion due to thermal noise, i.e. $M \gg U$,
2. if we vary η then we vary η_{pk} proportionally, i.e if we change the optical setting then the ratio of these values remains approximately constant.

Then the optimum cooling rate can be written in the form

$$\left(\frac{1}{\tau_\perp}\right)_{\mathrm{opt}} = a\eta\cos^2 b\eta \tag{15}$$

where a is independent of η and $b = \pi m_c x \left(\delta p/p\right)_{\mathrm{tot}}$. Here $\left(\delta p/p\right)_{\mathrm{tot}}$ is the total range of momenta to be cooled. This expression can be treated as a function of η It has a maximum if $2b\eta\tan b\eta = 1$ or if

$$\left|\left(\eta\right)_{\mathrm{opt}}\right| = \frac{0.208}{m_c x \left(\delta p/p\right)_{\mathrm{tot}}} \tag{16}$$

This expression can serve as a guide to estimate the optimum η value. It should be noted that it is independent of $\Delta p/p$. For example we get for the RESR ($m_c = 1236$, $\left(\delta p/p\right)_{\mathrm{tot}} \approx 4 \times 10^{-3}$, and $x \approx 0.5$) an optimum value of $\left(\eta\right)_{\mathrm{opt}} \approx 0.084$, wheras the actual value with $\gamma_t = 5.3$ is $\eta = 0.022$.

If U has the same order of magnitude as M, then the optimum η becomes smaller than the analytic estimate, it is zero in the case $U \gg M$, because then the desired mixing is worthless.

On the other hand, because during the process of cooling the momentum width becomes smaller, larger values of η become desirable. If one cannot or does not wish to ramp the quadrupoles during cooling, one would have to chose whether fast initial cooling or high equilibrium phase space density are more important issues.

REFERENCES

[1] J. Stadlmann, K. Blasche, B. Franczak,C. Omet, N. Pyka, P.J. Spiller, A.D. Kovalenko, Ion Optical Design of the Heavy Ion Synchrotron SIS100 *Proc. EPAC '06* (2006) 214-216

[2] F. Nolden, et al., The Collector Ring CR of the FAIR project, *Proc. EPAC '06* (2006) 208-210

[3] P. Beller, K. Beckert, C. Dimopoulou, A. Dolinskii, F. Nolden, M. Steck, J. Yang, Layout for an Accumulator and Decelerator Ring for FAIR, *Proc. EPAC '06* (2006) 199-201

[4] H. Stockhorst, R. Maier, D. Prasuhn, R. Stassen, T. Katayama, L. Thorndahl, Stochastic Cooling for the HESR at FAIR, this conference

[5] F. Nolden et al., Stochastic Cooling Developments at GSI, *AIP Conference Proceedings*, **821** (2005), 177-184.

[6] C. Peschke, F. Nolden, Pick-Up Electrode System for the CR Stochastic Cooling System, this conference

[7] S. van der Meer, Design study of a proton-antiproton colliding beam facility, internal report CERN/PS/78-3

[8] B. Autin et al., Antiproton Accumulator Complex (AAC) Performance, *Proc. EPAC '90* (1990) 614-616

[9] R.J. Pasquinelli et al., Stacktail Momentum Cooling in the Fermilab Antiproton Source, *Proc. PAC '87* (1990) 1132-1134

[10] A. Dolinskii, F. Nolden, M. Steck, Lattice Considerations for Collector and Accumulator Rings of the FAIR, this conference

[11] L. Faltin, Slot-type Pick-up and Kicker for Stochastic Beam Cooling, *Nucl. Inst. Meth.*, **148** (1978), 449

[12] D. Möhl, GSI internal report, 2004

ANTIPROTON PRODUCTION AND ACCUMULATION *

V. Lebedev #, FNAL, Batavia, IL 60510, U.S.A.

Abstract

In the course of Tevatron Run II (2001-2007) improvements of antiproton production have been one of major contributors to collider luminosity growth. Commissioning of Recycler ring in 2004 and making electron cooling operational in 2005 freed Antiproton source from the necessity to keep large stacks in the Accumulator and allowed us to boost the antiproton production. That resulted in doubling average antiproton production during last two years. The paper discusses improvements and upgrades of the Antiproton source during last two years and future developments aimed at further stacking improvements.

INTRODUCTION

Improvements in the Tevatron resulted in that the fraction of antiprotons burned in collisions achieved ~40% in 2004. Since that time this number was not changed, and its further increase is limited by intrabeam scattering (IBS) in the proton and antiproton beams. Further growth of the collider luminosity would not be possible without growth of antiproton production. For past two years increased antiproton production has been our highest priority in Tevatron Run II. Figure 1 demonstrates the results of these efforts culminating in ~1.7 times antiproton production growth in FY'07 alone. Further growth is expected in FY'08.

The following items contributed to this growth of antiproton production. First, there has been an improvement of the proton source. A reduction of longitudinal emittance in the Booster allowed us to optimize slip-stacking in the Main injector [1], which resulted in an increase in the number of protons on the antiproton production target from $6.5\cdot10^{12}$ to $8\cdot10^{12}$ per pulse. Second, an optics correction in the transfer line from the Main Injector to the antiproton production target allowed us to reduce the rms beam size on the target to ~200 μm. The resulting increased target depletion rate limits further reduction of the beam size. Third, stabilization of the proton beam position on the antiproton production target resulted in more stable operation and ~5% growth in the average antiproton production (it did not change the peak production). Fourth, an upgrade of the lithium lens allowed us to increase its gradient from 60 to 75 kG/cm, which resulted in ~10% growth in the antiproton yield. Fifth, optics correction in the Debuncher [2] resulted in an increase in Debuncher acceptance from 30/25 to 35/34 mm mrad, correspondingly for horizontal and vertical degrees of freedom. This resulted in ~10% improvement of the antiproton yield.

After the above upgrades were finished by the end of FY'06 the remaining major limitation to the stacking rate was the Stacktail system. Therefore its improvement became the highest priority item for the last year. This project combines a few separate improvements that are described in detail below. The implementation of these improvements resulted in a growth of peak stacking rate from $20\cdot10^{10}$ to $23.2\cdot10^{10}$ hour^{-1} in FY'07 and positioned us well for further improvements of stacking rate. Figure 2 shows how the dependence of stacking rate on stack size has changed during the course of Run II. As one can see, the stacking rate drops fast with the stack size. Too minimize this harmful effect the transfer time from Accumulator to MI injector was decreased from ~50 to 9 min. That allowed us to reduce the maximum stack size to ~$50\cdot10^{10}$ and greatly decrease the difference between the peak and average stacking rates. This resulted in the best average weekly stacking rate of $16.5\cdot10^{10}$ hour^{-1}, which is only ~28% below the peak stacking rate. This number looks quite impressive if one takes into account that it also includes all interruptions to the stacking.

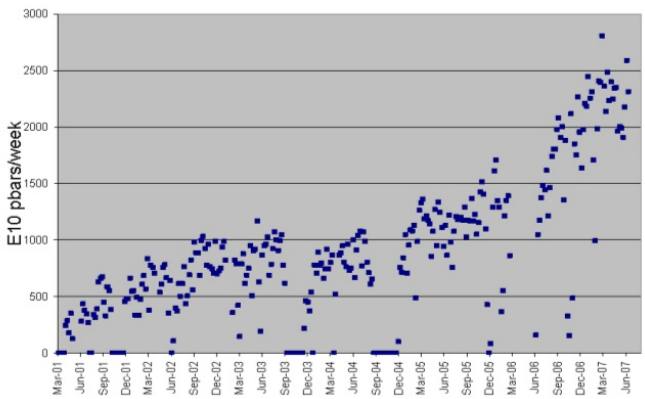

Figure 1: Weekly antiproton production rate during Run II (2001-2007).

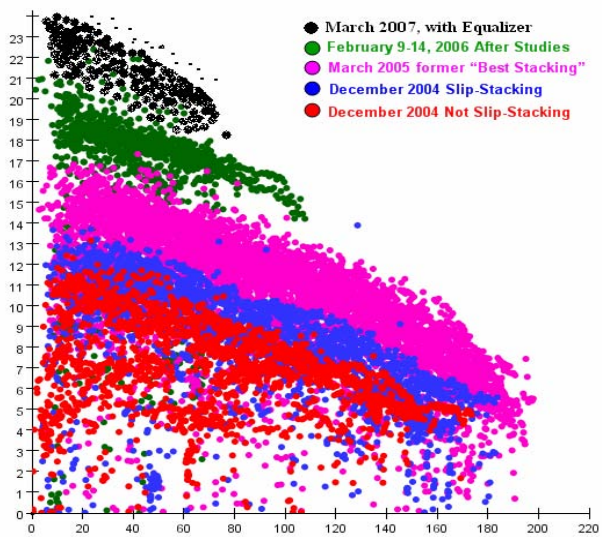

Figure 2: Dependence of antiproton production rate (units of 10^{10} hour^{-1}) on stack size (units of 10^{10}) during Run II.

* Work supported by Fermi Research Alliance, LLC., under contract DE-AC02-76CH03000 with the U.S. Dept. of Energy.
# val@fnal..gov

The upgrade of the Stacktail system [3] has also included a few other systems which are logically connected to Stacktail operation. It has consisted of a few steps. First, we optimized tuning of the existing system. This included a large increase of the gain for 4-8 GHz longitudinal core cooling system (February 2006). There was also a polarity flip for the Stacktail amplifier (October 2006). That corrected the phase intercept and, consequently, increased the bandwidth. Second, we corrected phase and magnitude of the system gain by installation an equalizer [4, 5]. An equalizer prototype was installed in March of 2007 and the final equalizer was installed in June 2007. The equalizer increased the bandwidth of the Stacktail, which resulted in faster stacking but also caused stronger transverse and longitudinal heating of the core. Third, the transverse heating was mitigated by an Accumulator optics correction [6]. That increased the slip factor and resulted in less heating (see below). If unaddressed the slip factor increase would also result in a larger phase variation of the gain on the way from the deposition orbit to the core orbit. To reduce this phase variation we moved the pickups of legs 2 and 3 closer to the leg 1 pickups and began using leg 3 pickups[1]. Fourth, to mitigate the longitudinal heating we replaced one of three Stacktail BAW (bulk acoustic wave) notch filters by the superconducting notch filter, and we will install the equalizer for the longitudinal 4-8 GHz core cooling system by the end of the 2007 shutdown (October 2007).

STACKTAIL MODEL

Improvements of the stacktail system would not be possible without its detailed model. The model is based on the beam measurements [4] and includes all the important features of the system.

Evolution of the beam longitudinal distribution is described by the Fokker-Planck equation [6]:

$$\frac{\partial f}{\partial t}+\frac{\partial}{\partial x}\left(F(x)\psi\right)=\frac{1}{2}\frac{\partial}{\partial x}\left(D(x)\frac{\partial \psi}{\partial x}\right)\ , \qquad (1)$$

where $x \equiv \Delta p/p$ is the relative momentum deviation, $\psi(x)$ is the distribution function $\left(\int \psi(x)dx = N\right)$, N is the number of particles in the beam,

$$F(x)=f_0\sum_{n=-\infty}^{\infty}\frac{G_{tot}(x,\omega_n)}{\varepsilon(\omega_n)}\exp\left(i\omega_n T_2\eta_2 x\right) \qquad (2)$$

is the cooling force,

$$D(x)=f_0\psi(x)\sum_{n=-\infty}^{\infty}\frac{1}{|n\eta|}\frac{1}{|\varepsilon(\omega_n)|^2}|G_{tot}(x,\omega_n)|^2 \qquad (3)$$

describes the diffusion due to the beam noise, f_0 is the revolution frequency, $\omega_n = 2\pi f_0(1-\eta x)n$, η is the slip factor, T_2 is the pickup-to-kicker travel time, η_2 is the partial pickup-to-kicker slip factor, and $\varepsilon(\omega)$ is the beam dielectric permeability. The Stacktail system has a sufficiently large signal-to-noise ratio allowing us to neglect diffusion due to noise of electronics.

[1] Only Legs 1 and 2 were used before this modification

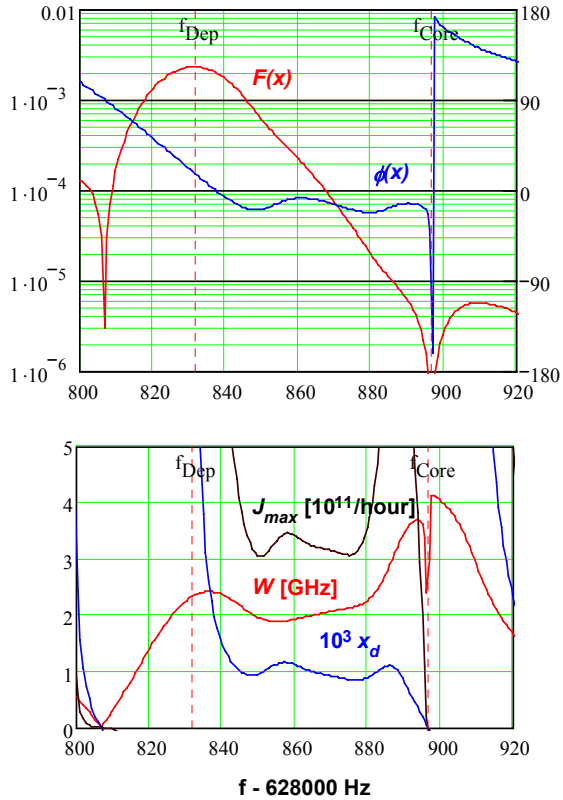

Figure 3: Dependence of Stacktail parameters on the revolution frequency; top: red line – cooling force, blue line – phase of the cooling force; bottom: red line – effective bandwidth, blue line – x_d, black line – maximum flux computed using Eq. (7).

The total gain of the system is combined from the gains of three pickup systems (legs 1, 2 &3) belonging to the Stacktail system and two core systems (2-4 GHz and 4-8 GHz). Each leg is centered on its own momentum, and the gains and delays for each leg are independently controlled. The block diagram of the Stacktail system is presented in Figure 2 of Ref. [4]. The corresponding total gain can be presented in the following form

$$\begin{aligned} G_1(x,\omega) &= K_{24}(\omega)G_{24}(x,x_{core}) + K_{48}(\omega)G_{48}(x,x_{core}) \\ &+ \left(1-A_3(\omega)e^{-i\omega T_{03}}\right)\left\{K_1(\omega)G_1(x,x_1)\left(1-A_1(\omega)e^{-i\omega T_{01}}\right)\right. \\ &\left.+\left[K_2(\omega)G_2(x,x_2)+K_3(\omega)G_3(x,x_3)\right]\left(1-A_2(\omega)e^{-i\omega T_{02}}\right)\right\}. \end{aligned} \qquad (4)$$

Here terms in the parenthesis describe the effect of notch filters, $K_k(\omega)$ and $K_{xx}(\omega)$ are the electronics gains, and $G_k(\ldots)$and $G_{xx}(\ldots)$ are the space gains of Stacktail and core systems, correspondingly. The space gain of each leg is parameterized as following:

$$\begin{aligned} G_k(x,x_k) &= (1/\pi)\left[\operatorname{atan}\left(\sinh\left((\pi/h_k)(x-x_k+w_k/2)\right)\right)\right. \\ &\left.-\operatorname{atan}\left(\sinh\left((\pi/h_k)(x-x_k-w_k/2)\right)\right)\right]\ , \quad k=1,2,3. \end{aligned} \qquad (5)$$

where h_k and w_k are the effective gaps and widths of pickups, and x_k are the positions of pickup centers. Each of the core cooling systems consists of two pickups with design similar to the stacktail pickups. These pickups are located on the different sides of the core orbit and are wired in difference mode. Their space gains are presented

as difference of two terms. Each term is given by Eq. (5) but the terms have opposite sign offsets relative to the core orbit. Table 1 presents the parameters for all pickups. Parameter A presents relative gains of different pickups at their maximum sensitivities. In normal operating conditions the ratios for the Stacktail legs are fixed while the core cooling gains are changed with beam current.

Table 1: Parameters of Stacktail pickups

	X [cm]	W [cm]	H [cm]	A
Leg 1	0.97	3	3.2	1
Leg 2	-0.29	3	3	0.34
Leg 3	-2	3	3	0.023
Core 2-4 GHz	-3.45/-8.42	2	2.7	$2\cdot10^{-3}$
Core 2-4 GHz	-5.06/-6.58	0.76	3.2	$1.6\cdot10^{-3}$

Eq. (5) describes well the beam based measurements in the entire stacktail region (see Figures 5 and 6 in Ref. [4]). The only exception is the Leg 1 response on the core orbit, where the Leg 1 pickup sensitivity at the high frequency end is ~2 times higher than predictions of Eq. (5). Taking into account that the Leg 1 sensitivity at the core orbit is ~50 dB smaller than at its center, and that it contributes to the gain at the core orbit less than other two legs, this complication was neglected in the model.

As was proved in Ref. [7] the notch filter terms have to be outside the integral in the dielectric permeability calculation. This results in:

$$\varepsilon(\omega) = 1 + \left(1 - A_3(\omega)e^{-i\omega T_{03}}\right)\left\{\left(1 - A_1(\omega)e^{-i\omega T_{01}}\right)\right.$$
$$\int_{\delta\to 0_+} \frac{d\psi(x)}{dx}\frac{K_1(\omega)G_1(x,x_1)e^{i\omega T_2\eta_2 x}}{e^{i\omega T_0(1+\eta x)} - (1-\delta)}dx + \left(1 - A_2(\omega)e^{-i\omega T_{02}}\right) \qquad (6)$$
$$\left.\int_{\delta\to 0_+} \frac{d\psi(x)}{dx}\frac{K_2(\omega)G_2(x,x_2) + K_3(\omega)G_3(x,x_3)}{e^{i\omega T_0(1+\eta x)} - (1-\delta)}e^{i\omega T_2\eta_2 x}dx\right\} +$$
$$\int_{\delta\to 0_+} \frac{d\psi(x)}{dx}\frac{K_{24}(\omega)G_{24}(x,x_{core}) + K_{48}(\omega)G_{48}(x,x_{core})}{e^{i\omega T_0(1+\eta x)} - (1-\delta)}e^{i\omega T_2\eta_2 x}dx.$$

The system optimization has been based on a static solution of Eq. (1) in Van deer Myer approximation. That results in the maximum flux:

$$J_{\max}(x) = |\eta| W(x)^2 x_d(x) / f_0 \quad , \qquad (7)$$

where

$$W(x) = \sqrt{\left(\int_0^\infty \mathrm{Re}\left(G_{tot}(x, 2\pi f)\right)df\right)^2 \Big/ \int_0^\infty \left|G_{tot}(x, 2\pi f)\right|^2 \frac{df}{f}} \qquad (8)$$

is the effective bandwidth, and $x_d(x)=F(dF/dx)^{-1}$ is the inverse rate of the relative gain change. Parameters of the system were adjusted to maximize the total flux with an approximately constant $x_d(x)$ in the central part of the Stacktail, which for a given flux maximizes the gain difference between the deposition and core orbits. Figure 3 presents the results of calculations with this static model after all upgrades. One can see that the cooling force achieves its maximum at the deposition orbit and then exponentially decays in direction of the core orbit with $p\,x_d \approx 9$ MeV. It approaches zero at the core due to notch filters which minimize heating of the core by Stacktail. Because the addends in Eq. (2) for positive and negative n are complex conjugates of one other, $F(x)$ is a real function. To compute the phase of the cooling force, ϕ, we compute the sum in Eq. (2) for positive n only and denote the result as F_p; then $F = 2\mathrm{Re}(F_p)$ and $\exp(i\phi) = F_p / |F_p|$. The effective bandwidth is changing through the Stacktail due to the notch filters. It starts at ~2.4 GHz at the deposition orbit, slightly decreases and then goes up to ~4 GHz in at the core where the 4-8 GHz core cooling system dominates. The static model predicts maximum stacking rate of $\sim 30\cdot10^{10}$ hour^{-1}.

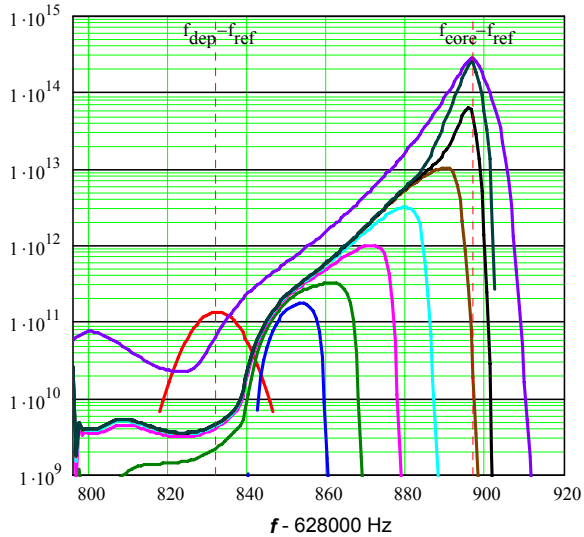

Figure 4: Results of stacking simulations for the system after all upgrades; $2\cdot10^8$ antiprotons are injected every 2.4 s; red line – distribution function after injection of the first antiproton pulse, other lines present distributions just before injection of pulses with numbers: 2, 4, 11, 31, 101, 301, 1001, 2001, 3001.

After system parameters were optimized Eq. (1) was solved numerically. The results of the calculations are presented in Figure 4. One can see that at the beginning the Stacktail pushes particles to the core. Then the core starts to be formed after ~20 min (core size $\sim 10\cdot10^{10}$); and finally the core becomes too large and back-streaming starts at the core size of $\sim 25\cdot10^{10}$ antiprotons (1 hour after stacking start). The simulations predict the same stacking rate of $\sim 30\cdot10^{10}$ hour^{-1} as the static model described above. Nevertheless, in addition to the limitation of Eq. (7), there appears to be another effect which can limit the stacking rate. It is the deposition orbit clearing requiring the Stacktail to remove antiprotons from the deposition area before the next injection happens. As one can see from the stack evolution the deposition orbit clearing and the stacktail throughput of Eq. (7) are well balanced for the parameters of the Accumulator Stacktail system.

To make an estimate of the deposition orbit clearing we ignore the dependence of the cooling force on momentum and assume that the gain is equal to zero outside of the band $[f_1, f_2]$ while it is set to its maximum value (limited by the beam stability) inside the band. For beam with a Gaussian distribution the maximum gain is:

$$G(\omega_n) = C_s \sigma^2 \eta n / N \ , \quad C_s \approx 9.011 , \tag{9}$$

where σ is the rms relative momentum spread. Substitution of Eq. (9) into Eq. (2) results in:

$$F = C_s \frac{\sigma^2 \eta}{N} \frac{f_2^{\,2} - f_1^{\,2}}{f_0} = 2C_s \frac{\sigma^2 \eta}{N} \frac{W^2}{f_0} \ , \tag{10}$$

where we took into account that $W = \sqrt{\left(f_2^{\,2} - f_1^{\,2}\right)/2}$. Requiring the distribution to be moved by distance $C_\sigma \sigma$ ($C_s \approx 2.5$) during one stacking cycle ($F \Delta T = C_\sigma \sigma$) one finally obtains a stacking rate estimate from the point of view of deposition orbit clearing:

$$J \approx \frac{C_s}{C_\sigma} \frac{f_2^{\,2} - f_1^{\,2}}{f_0} \sigma\eta = \frac{2C_s}{C_\sigma} \frac{W^2}{f_0} \sigma\eta \approx 6 \frac{W^2}{f_0} \sigma\eta \ . \tag{11}$$

This estimate yields ~5 times larger result than the numerical solution described above because the distribution widening due to diffusion and the cooling force drop at the distribution edges (3 times at 2.5σ) were neglected. Eq. (11) yields that if the stacking rate is limited by the deposition orbit clearing it can be mitigated by an increase of σ. Nevertheless this requires larger power which is not always available. Taking into account that in the case of Accumulator the fluxes of Eqs. (7) and (11) are well balanced; that both of them are proportional to the slip factor; that the operation of stacktail system is power limited; and that the stacking rate increase by the slip factor increase does not change the stacktail power we increased η by 15% from 0.0131 to 0.015 [6]. Further increase is limited by the band overlap and by variation of the cooling force phase through the stacktail region.

Before the equalizer installation the model predicted a peak stacking rate of ~$22 \cdot 10^{10}$ hour^{-1}, which is close to the experimental value. Nevertheless after the equalizer installation the stacking rate grew to only ~$24 \cdot 10^{10}$ hour^{-1} instead of the expected ~$30 \cdot 10^{10}$ hour^{-1}. The stacking rate has been limited by strong transverse and longitudinal core heating excited by stacktail operation. This heating limits the stacktail power to about half of the pre-equalizer operation (0.9 kW instead of 1.8 kW). A few steps were made to mitigate this. First results are already seen and more improvements are expected in the future.

TRANSVERSE CORE HEATING

There are two major sources of core heating due to stacktail operation. The first one is a consequence of non-zero dispersion at the stacktail kickers; and the second one is related to the quadrupole kicks excited together with longitudinal kick due to the finite size of the pickup loops. Stacktail kickers have similar design and geometry to the stacktail pickups and therefore in accordance with the reciprocity theorem [8] the longitudinal kick and the pickup sensitivity depend similarly on the transverse coordinate. Expending Eq. (5) in Tailor series one obtains the dependence of longitudinal kick on the particle transverse coordinates:

$$U(X,Y) = U_0 \left(1 + \kappa \left(X^2 - Y^2\right) / 2a_{eff}^{\,2}\right) + \ldots \ . \tag{12}$$

Here $\kappa = \pm 1$ with signs "+" and "-" assigned to the kickers rolled so that in the difference mode they would be the horizontal or vertical kickers correspondingly, and the effective gap is

$$a_{eff} = \frac{h}{\pi} \cosh(\pi w / 2h) \sqrt{\frac{\operatorname{atan}(\sinh(\pi w / 2h))}{\sinh(\pi w / 2h)}} \ . \tag{13}$$

a_{eff} = 1.7 cm for the Accumulator stack-tail kickers. In the case where the particle velocity, v_0, coincides with the phase velocity of the kicker wave, the transverse and longitudinal kicks are related so that [8]:

$$\frac{\Delta p_x}{p} = \kappa \frac{i v_0}{\omega} \frac{\Delta p_x}{p} \frac{x}{a_{eff}^{\,2}} , \quad \frac{\Delta p_y}{p} = -\kappa \frac{i v_0}{\omega} \frac{\Delta p_x}{p} \frac{y}{a_{eff}^{\,2}} \ . \tag{14}$$

Each kicker tank has four kickers located in the same plane so that the higher order modes could be damped. To mitigate the kick non-uniformity each next kicker tank is rolled to the orthogonal plane.

The transverse kicks described above introduce two mechanisms for the emittance growth. The first one is related to offsets of kickers from the beam center resulting in the transverse kicks proportional to the kicker offset and, consequently, the emittance growth excited by noise on the betatron sidebands. The second mechanism is related to the quadrupole kicks. That result in the parametric excitation of betatron motion and, consequently, the emittance growth excited by sidebands of doubled betatron frequency. Comparatively straight forward calculations yield the following expression for the emittance growth rate excited by the stacktail:

$$\left.\frac{d\varepsilon}{dt}\right|_{param} = \left.\frac{d\varepsilon}{dt}\right|_{dip} + \left.\frac{d\varepsilon}{dt}\right|_{param} \ ,$$

$$\left.\frac{d\varepsilon}{dt}\right|_{dip} = \frac{f_0 \beta_{kick}}{2} \sum_{k,m=-\infty}^{\infty} \frac{\psi(p_{km})}{|\eta k|} \left|G(p_{km}, \omega_{km})\right|^2 \left|D_{eff}(\omega_{km})\right|^2 ,$$

$$\left.\frac{1}{\varepsilon}\frac{d\varepsilon}{dt}\right|_{param} = \frac{v_0^{\,2} \beta_{eff}^{\,2}}{8\pi^2 f_0 a_{eff}^{\,4}} \sum_{k,m=-\infty}^{\infty} \frac{\psi(\tilde{x}_{km})}{|\eta k^3|} \left|G_{tot}(\tilde{x}_{km}, \tilde{\omega}_{km})\right|^2 \ . \tag{15}$$

Here $x_{km} = x - (\nu + m)/\eta k$, $\tilde{x}_{km} = x - (2\nu + m)/\eta k$, $\omega_{km} = \omega_0(\nu + m + k(1 - \eta x))$, $\tilde{\omega}_{km} = \omega_0(2\nu + m + k(1 - \eta x))$ are the resonant momenta and frequencies. The term,

$$D_{eff}(\omega) = \frac{v_0 \hat{X}(\omega)}{\omega a_{eff}^{\,2}} + \frac{D'_{kick}\beta_{kick} + \alpha_{kick} D_{kick} - i D_{kick}}{\beta_{kick}} \ , \tag{16}$$

accounts for the effective offset of kickers, $\hat{X}(\omega)$, and the finite value of the dispersion in the kicker section. Here $\beta_{kick}, \alpha_{kick}, D_{kick}$, and D'_{kick} are the beta- and alpha-functions, the dispersion and the dispersion prime in the kicker section center. The positions of kicker electrical centers, $X_i(\omega)$, depend on frequency resulting in the frequency dependence of the effective offset:

$$\hat{X}(\omega) = \left(\sum_{i=1}^{N_{kick}} \kappa_i X_i(\omega) + \frac{\alpha_{kick} - i}{\beta_{kick}} \sum_{i=1}^{N_{kick}} \kappa_i s_i X_i(\omega) \right) \Bigg/ \sum_{i=1}^{N_{kick}} |\kappa_i| \ , \tag{17}$$

where s_i is the longitudinal coordinate of the i-th kicker relative to the kicker section center. The effective beta-function of the parametric excitation is equal to:

$$\beta_{eff}^{\,2} = \frac{1}{N_{kick}^{\,2}} \sum_{i,j=1}^{N_{kick}} \kappa_i \kappa_j \left(\beta_0^{\,2} + 2 s'_i s'_j + \frac{s'^2_i s'^2_j}{\beta_0^{\,2}} - \left(s'_i - s'_j\right)^2 \right) \ , \tag{18}$$

where s_i' is the longitudinal coordinate of i-th kicker relative to the location of beta-function minimum, β_0.

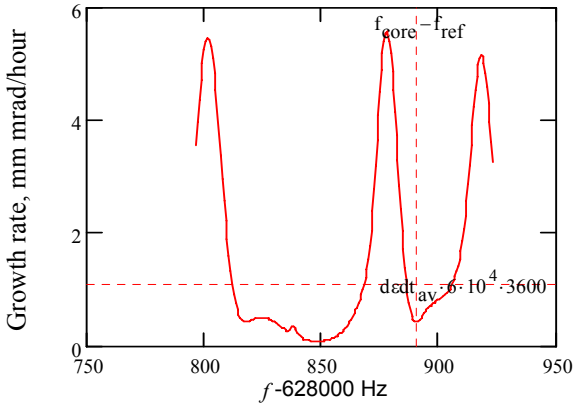

Figure 5: Dependence of transverse heating rate on the revolution frequency before Accumulator optics upgrade. Horizontal line marks the heating rate averaged over particle distribution.

Table 2: Heating and cooling rates at normal operation

Heating mechanisms	mm mrad/hour
IBS heating at 50 mA	~3
Stacktail heating	5-6
Noise of core systems	~2
Total heating = Total cooling	~10

Table 3: Estimate of Stacktail heating

Heating mechanisms	mm mrad/hour
Parametric heating	~0.25
Dispersion mismatch	~2.4
Kicker offset (res. at 3.25 GHz)	~1.2 - 2.2
Unaccounted (most probably due to geometric kicker offset)	~1.1 mm

The Stacktail system uses 8 kicker tanks located close to each other in one straight section. Each tank has four kickers. One of these 32 kickers is used for the longitudinal core cooling other 31 for the stacktail. It has became apparent that parametric heating has been a problem for a long time. The problem was resolved after two kickers on each side of kicker straight section were switched off. That reduced the effective beta-function of the parametric heating, β_{eff}, from 2.3 to 0.6 m resulting in negligible parametric heating. After the equalizer installation we observed the strong transverse heating again. This time it was excited by a resonance in the kickers which became much more apparent with the increased bandwidth. The resonance occurs at 3.25 GHz and results in a resonant displacement of kicker electrical center with frequency. The amplitude of the displacement is ~2 mm and the quality factor is ~27. Figure 5 presents dependence of computed horizontal heating rate on the revolution frequency. Tables 2 and 3 present measured heating and cooling rates for the horizontal degree of freedom before the optics upgrade.

The optics upgrade increased the slip factor and resulted in the displacement of heating peaks (related to lower and upper betatron sidebands) so that the core became better centered between the peaks. That reduced the heating. In addition it reduced IBS and improved the core cooling resulting in acceptable values for transverse emittances.

PLANS

The following upgrades will be introduced after the 2007 shutdown end in the first half of October. First, the upgrade of Debuncher transverse and longitudinal cooling systems should improve their cooling times by about 10%. Second, a Debuncher optics correction should improve vertical cooling by additional 5%. Third, an improved equalizer will be installed into 4-8 GHz core cooling systems resulting in more than a 50% improvement in its damping rate. Fourth, faster Accumulator-to-Recycler transfers will allow us to reduce the stack size, which should additionally mitigate transverse and longitudinal heatings. Together with a few other operational improvements we expect the average stacking rate be above $20 \cdot 10^{10}$ /hour by the next summer.

ACKNOWLEDGMENTS

The author would like to thank A. Burov for multiple discussions devoted to the stochastic cooling theory and K. Gollwitzer, V. Nagaslaev, R. Pasquinelli, D. Sun, S. Werkema, D. Vander Meulen as well as the entire Antiproton source department for help in measurements, data analysis and operational support of the Antiproton source. Without their work and devotion this work could not happen.

REFERENCES

[1] K. Seiya, *et. al.*, "Multi-batch Slip Stacking in the Main Injector at Fermilab," PAC-2007, p. 742.

[2] V.P. Nagaslaev, *et. al.*, "Measurement and Optimization of the Lattice Functions in the Debuncher Ring at Fermilab," EPAC-2006, p. 2050.

[3] R. Pasquinelli, D. McGinnis, "Performance of the Upgraded Stacktail Momentum Cooling System in the Fermilab Antiproton Source," Proceedings of the 1993 Part. Accel. Conference, p. 2361-2363

[4] R. Pasquinelli, V. Lebedev, S. Werkema, "Beam Based measurements for Stochastic Cooling Systems at Fermilab," This conference.

[5] D. Sun, *et. el.*, "New Equalizer for Antiproton Stochastic Cooling at Fermilab at Fermilab," This conference.

[6] V. Nagaslaev, *et. al.*, "Lattice Optimization for the Stochastic cooling in the Accumulator ring at Fermilab," This conference.

[7] V. Lebedev, "Stochastic Cooling with Schottky Band Overlap," COOL'05, AIP Conf. proc., v. 821, p. 231.

[8] J. Bisognano and C. Leemann, "Stochastic Cooling," 1981 Summer School on High Energy Particle Accelerators, AIP Conf. Proceedings, N. 87, New York, 1982, p.584.

CALCULATIONS ON HIGH-ENERGY ELECTRON COOLING IN THE HESR*

D. Reistad, B. Gålnander, K. Rathsman, The Svedberg Laboratory, Uppsala University, Sweden
A. Sidorin, Joint Institute of Nuclear Research, Dubna, Russia

Abstract

PANDA will make use of a hydrogen pellet target. We discuss the choice of beam size at the target and emittance stabilization, and show some results of simulations made with BETACOOL. The simulations include the effects of the internal target, intra-beam scattering, electron cooling and in some cases also stochastic cooling.

HYDROGEN PELLET TARGET

In order to achieve luminosities in PANDA in the range $2\times10^{31} - 2\times10^{32}$ cm^{-2}s^{-1} with $10^{10} - 10^{11}$ stored antiprotons in HESR, an internal hydrogen target with thickness 4×10^{15} cm^{-2} is required. A hydrogen pellet target [1] is the only known kind of internal target, which meets this requirement. At the same time, the granular nature of this target will cause a temporally varying luminosity, particularly if the antiproton beam has small transverse dimensions compared to the vertical separation between pellets or the diameter of the pellet stream.

The hydrogen pellets move in a well-collimated cylindrical flow in which they are distributed rather uniformly, see figure 1. Experience from the use of the pellet target at CELSIUS [2] shows that the pellet flux diameter can be varied between about 1.5 and 3 mm by changing the size of a skimmer in the pellet generator. Since PANDA requires a very big luminosity, we have here chosen to assume that the pellet stream will have a diameter of 3 mm.

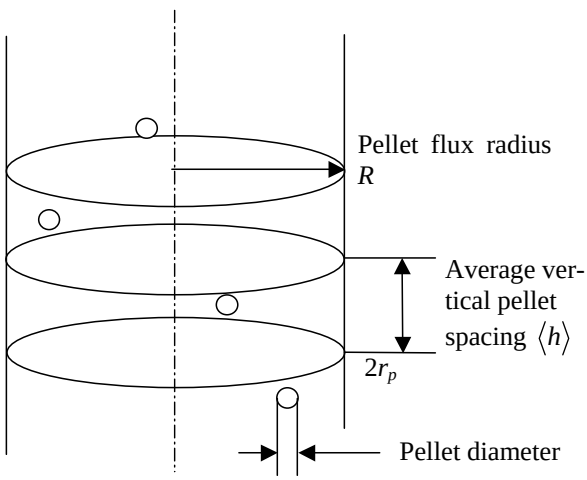

Figure 1: Schematics of the pellet target geometry. The pellets move from top to bottom with the same speed.

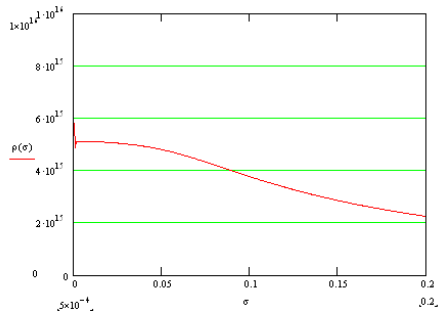

Figure 2: Mean effective target thickness in atoms/cm^3 as a function of the horizontal rms. beam size (in cm). Calculated for Gaussian distribution.

The required target thickness is then met if the average vertical separation between the pellets $\langle h \rangle$ is about 4 mm, which is what we have assumed in the following. With a pellet speed of 60 m/s, this corresponds to a pellet rate of 15,000 s^{-1}, which is well within the achieved performance of the hydrogen pellet target.

CHOICE OF BEAM SIZE AT TARGET

If the horizontal antiproton beam size on the target is made too large, then the luminosity will be reduced due to poor overlap between the beam and the target. The expression for a Gaussian beam is

$$\rho_{\text{eff,mean}} = \frac{\langle \Re \rangle}{\sqrt{2\pi}\sigma_x} \int_{-R}^{R} 2\sqrt{R^2 - x^2}\, \exp\left(-\frac{x^2}{2\sigma_x^2}\right) dx$$

where

$$\langle \Re \rangle = \frac{\frac{4}{3}\pi r_p^3}{\pi R^2 \langle h \rangle} \Re; \quad \Re = 4.3\times10^{22} \text{ atoms/cm}^3$$

This effect is illustrated for our parameters in figure 2. We see that the horizontal r.m.s. beam size should not be chosen bigger than about 0.8 mm in order to keep the effective luminosity above 80 % of the maximum possible.

At the same time, if the beam size is chosen too small, then the granular nature of the pellet target will cause fluctuations in the effective target thickness. For a Gaussian beam, the maximum instantaneous effective target thickness, which occurs when the beam hits a pellet head-on, is given by

* Work supported by Uppsala University and by EU Design Study Contract 515873, DIRACSecondary-Beams

$$\rho_{\text{eff,max}} = \frac{\Re}{2\pi\sigma_x\sigma_y}\int_{-r_p}^{r_p}\int_{-\sqrt{r_p^2-x^2}}^{\sqrt{r_p^2-x^2}} 2\sqrt{r_p^2-x^2-y^2}\times$$

$$\times\exp\left(-\frac{x^2}{2\sigma_x^2}-\frac{y^2}{2\sigma_y^2}\right)dydx$$

The ratio between the maximum and average luminosity is plotted as the ratio between $\rho_{\text{eff,max}}$ and $\rho_{\text{eff,mean}}$ according to these formulae, and also according to the approximate formula given in [3], is shown in figure 3.

In fact, the beam distribution is not going to be Gaussian, but more like a square with rather homogeneous density of antiprotons up to a certain dimension, see figure 10 below. In the following, we define our transverse beam size as the beam size, which contains 50 % of the particles.

We choose a "square" beam spot with side $2\times0.8=1.6\,\text{mm}$ in both planes, which gives a ratio between maximum and mean luminosity of about 3 and about 80 % of the maximum possible average luminosity, which we believe is an acceptable compromise.

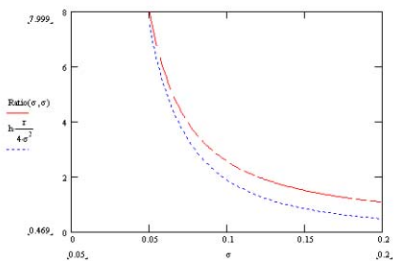

Figure 3: Ratio between maximum and mean effective luminosity as a function of rms beam size (in cm), assumed to be the same in both planes. The lower curve is according to the simplified formula in [3].

CHOICE OF BETA VALUE AT TARGET

Conventional wisdom tells that the beta value at the target should be chosen as small as possible, in order to get the best single-scattering lifetime of the beam. We have

$$\sigma_{\text{single scattering}} = \pi\left(\frac{2r_e m_e c^2}{cp\beta}\right)^2\cdot\frac{\beta_T}{A}$$

where *A* is the acceptance of the ring. However, choosing very small β_T will make the maximum beta value in the neighbouring quadrupoles large, which may make the acceptance small, see figure 4. In HESR, the diameter of the quadrupole vacuum chambers is planned to be 89 mm, and PANDA requires the diameter of the vacuum chamber at the pellet target to be 20 mm. Therefore, we can assume that the horizontal and vertical acceptances are given by:

$$A_{x,y} = \min\left(\frac{(44.5\,\text{mm})^2}{\beta_{x,y,\max}},\frac{(10\,\text{mm})^2}{\beta_{x,y,T}}\right)$$

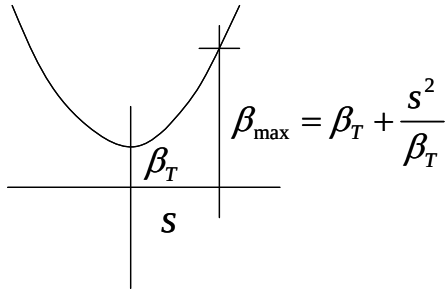

Figure 4: Choosing the beta value at the target too small does not significantly improve single-scattering lifetime, because the beta value in the neighbouring quadrupoles becomes correspondingly larger.

Inspecting a MAD file for HESR [4] indicates the following approximate relationships between $\beta_{\max}$ and β_T:

$$\beta_{x,\max}=\beta_{x,T}+\frac{300\,\text{m}^2}{\beta_{x,T}};\ \beta_{y,\max}=\beta_{y,T}+\frac{550\,\text{m}^2}{\beta_{y,T}}$$

Inspecting these formulae shows that if the beta values at the target are chosen below 4 m, then they have almost no effect on the single scattering cross section. On the other hand, if the beta values are chosen above 4 m, then the single-scattering cross section will grow as β_T^2. We choose $\beta_{x,T}=\beta_{y,T}=4\,\text{m}$ for 1.5 GeV/*c*, but 8 m for intermediate energies and 16 m for 15 GeV/*c*. The single-scattering cross section remains much smaller than the nuclear cross section for all momenta from 3.8 GeV/*c* and up.

TRANSVERSE EMITTANCE

The choice of $\beta_{x,T}=\beta_{y,T}=8\,\text{m}$ at intermediate energies together with the chosen beam spot on the target of 0.8 mm implies that the transverse emittance should be 8×10^{-8} m. For the lowest and highest energies required transverse emittances are 1.6×10^{-7} m and 4×10^{-8} m respectively.

ELECTRON BEAM

The task of the electron cooling system is to reduce the energy spread of the antiproton beam to a few 10^{-5}. This corresponds to a longitudinal temperature of the antiprotons of about 0.1 eV, and can only be achieved with magnetized electron cooling. The magnetic flux in the electron beam is limited for technical reasons to $0.07\times\pi\times0.0085^2\,\text{Tm}$ [5]. We have chosen an electron beam diameter on the cooling section of 10 mm and a magnetic field of 0.2 T. For a transverse electron temperature of 1 eV this magnetic field strength gives a cyclotron radius of 1.7×10^{-5} m and at 8 GeV a typical distance between electrons $n_e^{-1/3}$ of 7.7×10^{-4} m, which means that magnetized electron cooling can take place. The reason for the choice of electron beam diameter is that we wish the antiproton beam to remain essentially inside of the electron beam in order to avoid any effects of non-linear

electrical fields outside of the electron beam, which in our opinion still remain to be fully understood [6,7]. We have therefore also chosen the beta value in the electron cooler to be only $10 \times \beta_T$, i.e. 80 m at intermediate energies. Then, the "square" antiproton beam will have a side of half of the electron beam diameter, and thus the antiprotons will essentially go inside of the electron beam.

SUMMARY OF PARAMETERS USED IN COMPUTATIONS

The following parameters have been used in the computations reported here:

effective length of electron cooler	20 m
electron current	1 A (0.2 A @ 1.5 GeV/*c*
electron beam radius, uniform cylinder	5 mm
magnetic field in electron cooler	0.2 T
beta value at electron cooler (both H and V)	80 m (40, 160 m @ 1.5, 15 GeV/*c*)
transverse electron temperature (in centre of electron beam)	1 eV
Transverse gradient of electron velocity (in order to take unavoidable envelope oscillations into account. The chosen value corresponds to a cyclotron radius at the edge of the electron beam of 0.1 mm, or 35 eV)	7×10^8 s^{-1}
longitudinal electron temperature	0.5 meV
electron beam neutralization	nil
cooling force model	Parkhomchuk
rms. straightness of magnetic field lines	1×10^5 radians
hydrogen pellet target, pellet size	30 μm
pellet stream diameter	3 mm
vertical separation between pellets	4 mm
beta value (both planes) at target	8 m (4, 16 m @ 1.5, 15 GeV/*c*)
nuclear reaction cross section	100, 70, 55, 50 mbarn @ 1.5, 3.8, 8.9, 15 GeV/*c*.
intra-beam scattering	Martini model
barrier bucket voltage	200 V
barrier duration (relative to circumference)	10 %

EMITTANCE STABILIZATION

If special precautions were not to be taken, then the electron cooling would reduce the transverse emittance below the wanted value. This would make the antiproton beam size on the target too small and also the momentum spread increase due to intra-beam scattering.

Three different methods for stabilization of the emittance have been discussed:

- use of a "hollow" electron beam [8]
- application of white noise in the transverse degrees of freedom
- intentional misalignment ("tilt") of the electron beam with respect to the antiproton beam.

The "hollow" electron beam will be efficient for ion beam storage using cooling-stacking procedure. The low electron density in the stack region avoids overcooling of the stack and decreases (for heavy ions) recombination in the cooling section. In the HESR, where very small momentum spread is wanted, the hollow beam will not be suitable, because cooled antiprotons will only see a small

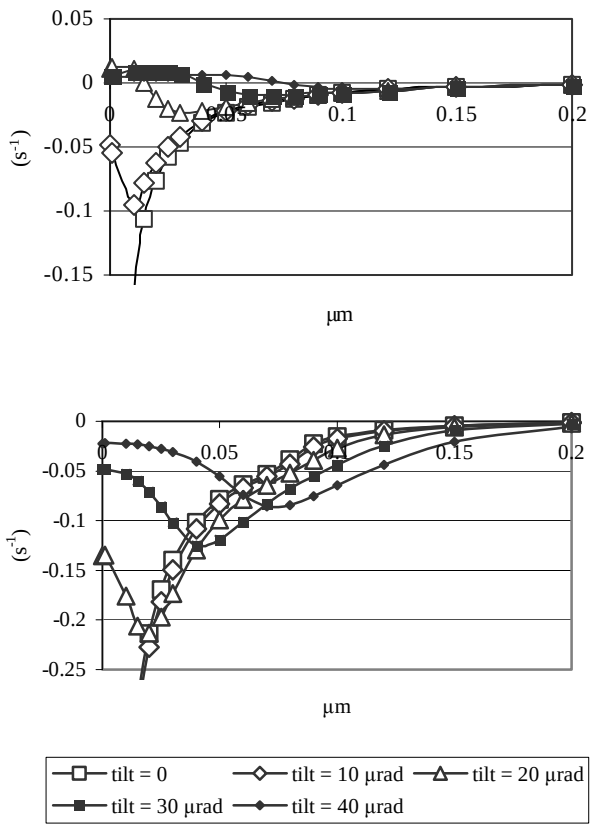

Figures 4 – 5: Transverse and longitudinal cooler rates at 8 GeV for different tilts.

electron density and the longitudinal cooling force will therefore be correspondingly smaller.

Another unknown with the hollow electron beam will be due to the non-linear electrical fields, that the antiprotons will be seeing. These fields may be particularly damaging in the case of hollow beam [9].

Transverse heating by additional noise has been tried at a few rings to suppress coherent instabilities. However, the experience has been, that the transverse heating decreases the beam lifetime, and leads to increase not only of emittance, but also of momentum spread.

Many experiments have shown, that a controlled misalignment is a powerful tool to control the transverse emittance of a stored beam. When the tilt reaches a cer-

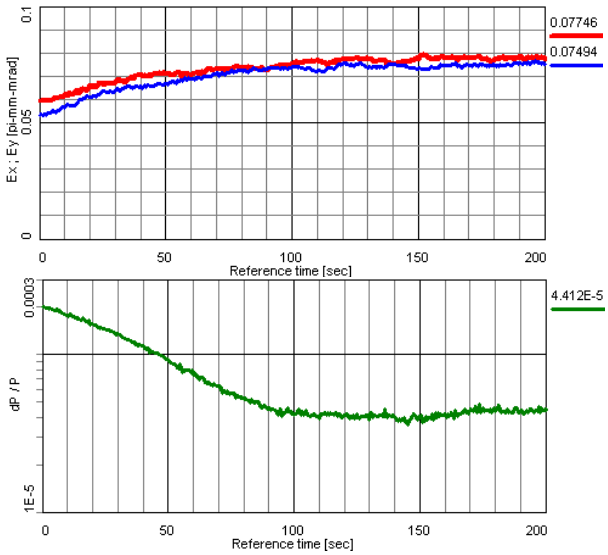

Figures 6–7: The calculated evolution of the beam under the influence of the hydrogen pellet target, electron cooling and intra-beam scattering of horizontal and vertical emittances and momentum spread of a beam of 10^{10} antiprotons of 8.9 GeV/c.

tain threshold the particles start to oscillate with a certain value of betatron amplitude [10]. This amplitude depends on the tilt angle, and the beam emittance cannot be less than the value corresponding to the oscillation amplitude. In absence of other effects, the beam profile has a specific double-peak structure.

These oscillations are caused by the non-linearity of the friction force. The force has a maximum at a certain relative velocity, and the oscillations begin when the transverse velocity of the misaligned electron beam is equal to the velocity, which is corresponding to the maximum of the force. This transition from stable particle motion, described by a fix-point attractor in the centre of phase space, to oscillating motion corresponding to a circular attractor is known as a "Hopf bifurcation".

In the absence of the internal target, the beam distributions become significantly denser near the circular attractor. The density does become smeared by the target and typically gets rather flat. However, if the dip in the middle of the distribution would become too important, then a solution can be to turn off the intentional tilt during short

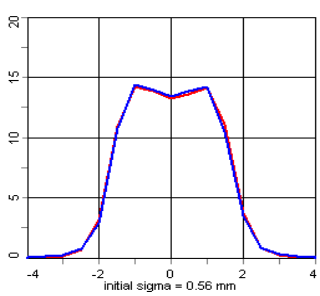

Figure 8: Calculated equilibrium transverse beam profiles of 10^{10} 8 GeV electron-cooled antiprotons on target in units of the initial rms. beam size of 0.56 mm.

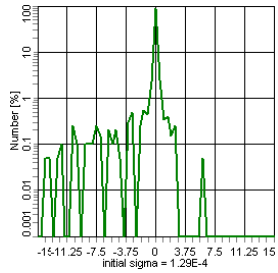

Figure 9: Calculated equilibrium momentum distribution of 10^{10} 8 GeV electron-cooled antiprotons on target in units of the initial rms. momentum spread of 1.29×10^{-4}.

intervals. This will re-create the attractor in the middle of the distribution.

The emittance stabilization by tilting the electron beam with respect to the antiproton beam illustrated in figures 4 – 5, where the growth rates due to electron cooling are shown as a function of transverse Courant-Snyder invariant for different tilts. The calculation is made in BETACOOL [11] using the Parkhomchuk cooling model [8]. The rates can be compared to the heating rates caused by the hydrogen pellet target, which for this energy are approximately 5×10^{-10} m$/\varepsilon$ s^{-1} in the transverse planes (where ε is the Courant-Snyder invariant), and $3\times10^{-10}\Big/\left(\frac{\Delta p}{p}\right)^2$ s^{-1} in the longitudinal plane. This indicates that at $\varepsilon = 0.08$ μm the equilibrium $\Delta p/p$ between target heating and electron cooling would be about 7×10^{-5}. In the tracking computation, we arrive at 4.4×10^{-5} for 90 % of the antiprotons.

RESULTS

Calculations were made with BETACOOL [11]. They were carried out for a beam of 10^{10} antiprotons (except when stated otherwise) at 1.5, 3.8, 8.9, and 15 GeV/*c*. All calculations were made assuming that the hydrogen pellet target was continuously turned on. At 1.5 GeV/*c* we reduced the electron current to avoid instabilities. We found the tilt angles as stated in the table below. At 15 GeV/*c*, the situation dramatically improved when we included longitudinal stochastic cooling as well as electron cooling in the simulation, see below:

momentum GeV/c	β_T (m)	β_C (m)	tilt (radians)	I_e (A)	$\Delta p/p$ (90 %)
1.5	4	40	6×10^{-5}	0.2	1.3×10^{-5}
3.8	8	80	3.5×10^{-5}	1	9.3×10^{-6}
8.9	8	80	3.5×10^{-5}	1	4.4×10^{-5}
15	16	160	8×10^{-6}	1	1.9×10^{-4}

In agreement with others in the project [12] we have defined the momentum spread as the spread, which contains 90 % of the antiprotons. The transverse emittances

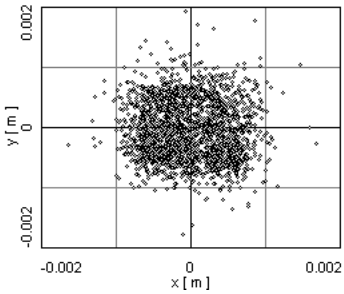

Figure 10: Calculated aspect of the beam on the target for 10^{10} 8 GeV electron-cooled antiprotons on target.

are defined as the areas of the ellipses in phase space, which contain 50 % of the particles, divided by π.

The calculated evolution of horizontal and vertical emittances and momentum spread of a beam of 10^{10} antiprotons of 8.9 GeV/*c* are shown in figures 6 – 7, the calculated equilibrium transverse beam profiles and momentum distribution are shown in figures 8 – 9, and the calculated aspect of the beam on the target in figure 10.

The beam lifetime was ranging from about 3,000 s at 1.5 GeV/*c* to about 7,000 s at 15 GeV/*c*, considering nuclear cross sections and transverse acceptances as discussed above and momentum acceptance 2×10^{-3} [13].

We repeated the calculation at 8.9 GeV/*c* also for 10^{11} antiprotons, see figures 11 – 12. We note that the equilibrium 90 % momentum spread increased from 4.4×10^{-5} to 6.6×10^{-5}.

We note that at high energies the momentum distribution (figure 9) develops a pronounced low-energy tail. We therefore have made another simulation, where we have included longitudinal stochastic cooling as well as electron cooling. For the longitudinal stochastic cooling we used a bandwidth from 2 to 4 GHz [14]. The resulting longitudinal evolution and equilibrium distribution are

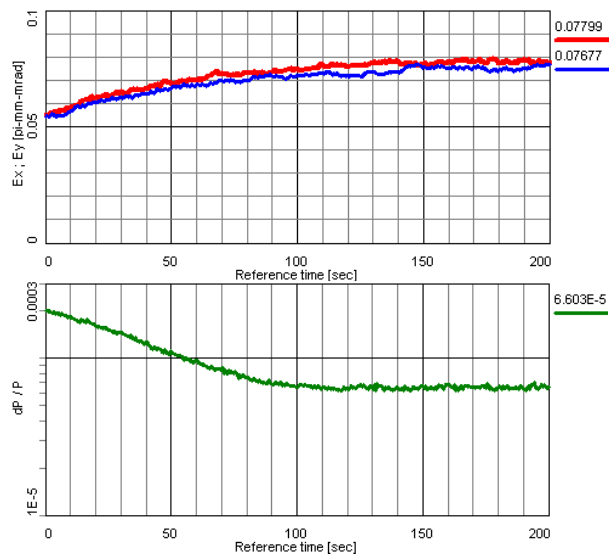

Figures 11 – 12: The calculated evolution of the beam under the influence of the hydrogen pellet target, electron cooling and intra-beam scattering of horizontal and vertical emittances and momentum spread of a beam of 10^{11} antiprotons of 8.9 GeV/c.

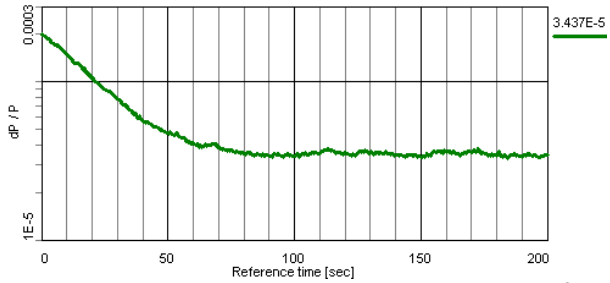

Figure 13: Calculated longitudinal evolution of the beam under the same conditions as in figure 7, but with stochastic cooling as well as electron cooling assumed.

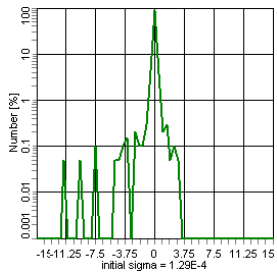

Figure 14: As figure 9 but with stochastic cooling as well as longitudinal cooling.

shown in figures 13-14. The equilibrium 90 % momentum spread went down from 4.4×10^{-5} to 3.4×10^{-5}

We also made a calculation at 15 GeV/*c* where we again included longitudinal stochastic cooling with bandwidth from 2 to 4 GHz as well as electron cooling. The equilibrium momentum spread improved dramatically: from 1.9×10^{-4} to 3.4×10^{-5}.

CONCLUSIONS

We have chosen a "square" beam spot with side 1.6 mm on the pellet target, and shown that by appropriate choice of beta value at the target and suitably tilting the electron beam, this can be combined with achieving very small momentum spread. At high energies, a combination of electron cooling and longitudinal stochastic cooling gives the best performance.

REFERENCES

[1] C. Ekström et al., NIMA 371 (1996) 572.
[2] G. Norman, private communication.
[3] V. Ziemann, NIMA 556 (2006) 641.
[4] Y. Senichev, private communication.
[5] T. Bergmark et al., EPAC2006.
[6] D. Reistad et al., CERN94-03, 183.
[7] J. Dietrich et al., COOL05, 270.
[8] V.V. Parkhomchuk, COOL05, 249.
[9] V. Ziemann, NIMA 556 (2006) 45.
[10] H. Danared et al., EPAC2000.
[11] A. Sidorin, these proceedings.
[12] A. Lehrach, private communication.
[13] R. Maier, private communication.
[14] H. Stockhorst, private communication.

ELECTRON COOLING STATUS AND CHARACTERIZATION AT FERMILAB'S RECYCLER*

L.R. Prost#, A. Burov, K. Carlson, A. Shemyakin, M. Sutherland, A. Warner, FNAL, Batavia, IL 60510, U.S.A.

Abstract

FNAL's electron cooler (4.3 MV, 0.1 A DC) has been integrated to the collider operation for almost two years, improving the storage and cooling capability of the Recycler ring (8 GeV antiprotons). In parallel, efforts are carried out to characterize the cooler and its cooling performance.

This paper discusses various aspects of the cooler performance and operational functionality: high voltage stability of the accelerator (Pelletron), quality of the electron beam generated, operational procedures (off-axis cooling, electron beam energy measurements and calibration) and cooling properties (in the longitudinal and transverse directions).

INTRODUCTION

The Recycler Electron Cooler (REC) [1] has been fully integrated to the collider operation since January 2005. However, over the past year, the average antiproton production rate in the Accumulator ring has almost doubled, reducing the average time between successive injections into the Recycler from 4 to 2.5 hours, hence increasing the need for fast cooling. In turn, the REC has been heavily relied upon for the storage and cooling of 8 GeV antiprotons destined for collisions in the Tevatron.

In this paper, we report on the status of the electron cooler, which has proved to be very reliable over the past year. We also discuss its overall cooling performance, through dedicated friction force and cooling rate measurements.

THE REC IN OPERATION

The REC employs a DC electron beam generated in an electrostatic accelerator, Pelletron [2], operated in the energy- recovery mode. The beam is immersed into a longitudinal magnetic field at the gun and in the cooling section (CS); other parts of the beam line use lumped focusing. The main parameters of the cooler can be found in Ref. [1].

Cooling Procedure

The cooling procedure described in Ref. [3] remains the norm to this date: the electron beam is used when needed and the cooling rate is being adjusted by increasing or decreasing the fraction of the antiproton beam that the electron beam overlaps (through parallel shifts). The driving consideration for this procedure is to avoid overcooling the center of the antiproton beam and preserve its lifetime.

A cooling sequence is illustrated on Figure 1 and in this particular case the electron beam was turned on just before the 3rd injection (out of 11) and kept on until extraction to the Tevatron. Throughout the storage cycle, the electron beam position is adjusted regularly according to the needs for longitudinal cooling. Note that stochastic cooling is always on (both the longitudinal and transverse systems).

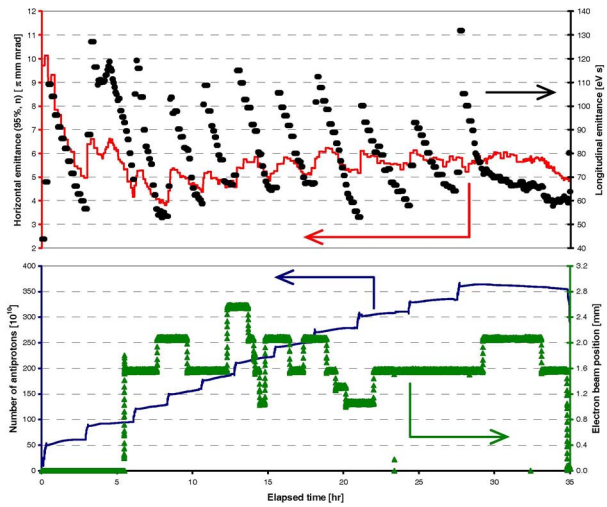

Figure 1: Example of the cooling sequence and electron beam utilization during a storage cycle. Bottom plot - Solid blue: Number of antiprotons; Green triangles: Electron beam position; Top plot – Solid red: Transverse (horizontal) emittance measured by the 1.75 GHz Schottky detector; Black circles: Longitudinal emittance measured by the 1.75 GHz Schottky detector. The electron beam current is kept constant (100 mA).

At the end of the storage cycle, just before mining [4], the beam is brought 'on-axis' (i.e. the electron beam trajectory coincides with the antiprotons central orbit) to provide maximum cooling when lifetime preservation is no longer an issue since the antiprotons are about to be extracted to the Tevatron. Recently, to accommodate the large number of particles often present in the Recycler ($>300\times10^{10}$), the electron beam current is increased from 100 mA to 200 mA after the last injection of fresh antiprotons. The additional cooling strength obtained from the increased beam current is required to reach the longitudinal emittance needed for high transfer efficiencies in the downstream machines all the way to collision in the Tevatron.

The final cooling sequence (between the last injection from the Accumulator to extraction to the Tevatron) takes 2-2h30 (Figure 2). It is dictated by the needs for reducing the longitudinal emittance from 110-120 eV s (just after

*Operated by Fermi Research Alliance, LLC under Contract No. DE-AC02-07CH11359 with the United States Department of Energy
#lprost@fnal.gov

the last injection) to 60-70 eV s before extraction to the Tevatron [5], while maintaining a decent beam lifetime (> 100 hours). However, in this case, cooling ultimately takes priority on lifetime preservation, although the cooling strength is increased in steps. On Figure 2, one can see how moving the electron beam closer to the antiprotons central orbit decreases both the longitudinal and transverse emittances but also affects the lifetime.

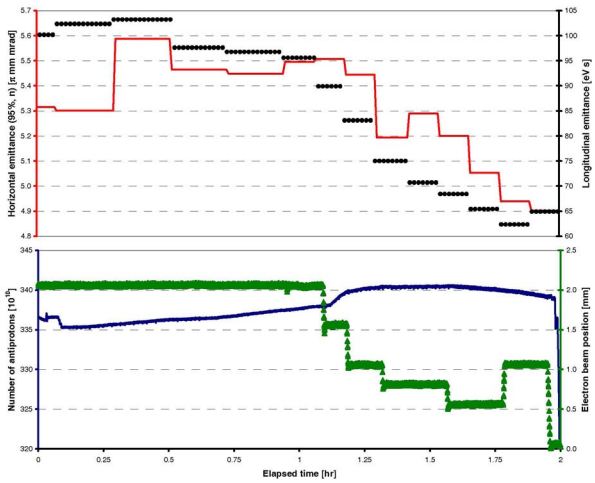

Figure 2: Example of a final cooling sequence. The legend is the same as for Figure 1. Electron beam is kept constant (200 mA).

The antiproton beam lifetime is currently difficult to extract quantitatively because the main beam current diagnostic, a DCCT, failed and the alternate beam current monitor does not perform reliably with the barrier-bucket RF structure. Nevertheless, the fact that the beam current signal turns over indicates a real degradation of the antiproton lifetime. Note that a new DCCT has been installed during our latest shutdown period, which will give us back the ability to investigate lifetime issues in the Recycler (induced or not by the presence of the electron beam).

Availability and Performance Stability

Due to the increased demand on electron cooling, it is imperative that the cooler be very reliable. A storage cycle (between extractions to the Tevatron) typically lasts 25-35 hours and, on average, the electron beam is used 75% of this time, with an electron current I_b = 100-200 mA. During our recent run (~past 8 months), the number of downtimes needed for conditioning of the acceleration tubes was approximately once every two months. Conditioning usually followed a series (2-3) of full discharges, when the Pelletron voltage drops to zero in a sub-μs time, and the pressure in one of the acceleration tubes increases by several orders of magnitude. When they occur, full discharges take 30-60 minutes to recover from while conditioning takes 4-8 hours. However, note that when possible, conditioning is carried out during times when the electron beam is not absolutely required, limiting its operational impact. In addition, routine maintenance requiring opening of the Pelletron tank (~3 days of downtime) were carried out once every 5-6 months, when the whole complex undergoes some downtime, mainly for cleaning of the charging circuitry (chain, pulleys, sheaves, corona needles replacement). Other sources of beam downtime were mostly related to issues with the controls system. Short recirculation interruptions (<1 min with low impact on the operation performance) have also been sparse (~2-10 per day) and many of them were false-positive due to losses from the Main Injector (i.e. proton loss during acceleration) being recorded by the electron cooler protection system. The latter has been resolved by masking (in the software) the Main Injector losses during acceleration.

Besides the intrinsic cooling performance to be discussed in the following section, being able to maintain (or quickly return to) optimum conditions for efficient cooling during operation is critical. The main three reasons that hinder the cooling performance were found to be the degradation of the cooling section magnetic field straightness, the antiproton trajectory drift and the Pelletron HV stability.

Once the electron beam trajectory has been optimized, we find that, over time, it changes in a fashion consistent with a degradation of the straightness of the magnetic field from solenoid to solenoid. To correct for this misalignment, a beam-based procedure was developed, relying on cooling rate and/or friction force measurements [6]. Over the past year, this procedure was repeated twice and the cooling efficiency increased both time.

While for storing purposes the antiproton trajectories only need to be stable to the ~1 mm level, for cooling purposes, any misalignment between the electron and antiproton beam trajectories introduces a shift and/or adds an effective angle which impacts the cooling performance. For reason not well determined (but ground motion is a possible candidate along with failing power supplies), we find that the antiproton beam trajectories need to be adjusted regularly, once every 1-2 months, or when a significant piece of hardware has been changed out (i.e. a corrector bulk power supply). To do so, a localized 3-bumps has been implemented, which allows for steering the antiproton beam in the cooling section both for its position and its average tilt, while maintaining a closed orbit around the ring.

Finally, the Pelletron high voltage stability may be the one parameter that can have a significant impact on operation in various ways.

First, the most detrimental events for the integrity of the cooler are the full discharges. Specific efforts to reduce their frequency are reported in Ref. [7,8]. As mentioned in the first section of this paper, during our recent run (~past 8 months), the number of full discharges was limited to ~2-3 every two months, with successive discharges typically occurring over a few days, at which point, conditioning of the tubes was undertaken. In all cases, the conditioning process revealed that the

weakened region was located in the top half of the acceleration tubes (low kinetic energy).

Then, besides high voltage events leading to beam interruptions, the question of the Pelletron energy stability (relative and absolute) arises. We found that the average energy of the electron beam drifts over long period of times (by up to 1-2 keV), which reduces greatly the cooling efficiency. In addition, it is sensitive to the Pelletron temperature and the energy changes at the rate of ~ -300 V/°C. This is mostly an issue at turn on since it takes 6-10 hours for the Pelletron to reach its equilibrium temperature. Figure 3 shows an example of the typical flattened antiproton longitudinal distribution measured with a Schottky pickup when the electron beam momentum is offset by some significant amount with respect to the antiproton momentum (left). For comparison, Figure 3 also shows the much sharper peak (right) that one obtains when the electron beam energy is close to being optimal. Although the antiproton momentum distribution is a good indication that the electron beam energy is not adequate *a posteriori*, it does not provide the magnitude and the sign of the mismatch.

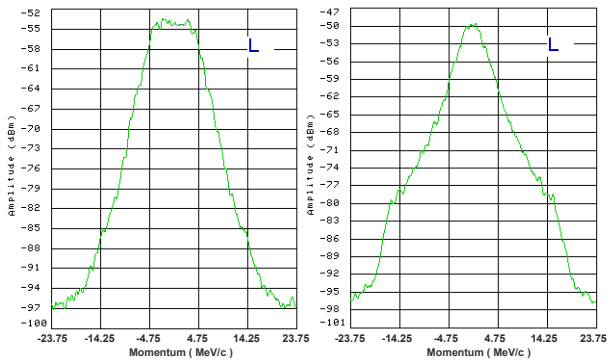

Figure 3: Antiproton longitudinal distributions measured with the 1.75 GHz Schottky detector. In both cases, the electron beam was on axis for ~2h at 100 mA. Bunch length = 6.1 μs. $N_p = 200\times10^{10}$ (left) and 280×10^{10} (right) particles.

The absolute electron beam energy calibration is done using un-bunched antiprotons (no RF structure) and measuring its longitudinal Schottky distribution, for which the frequency of the peak with respect to the revolution frequency indicates the absolute momentum shift between the two beams. However, this method can only be used with a very low number of antiprotons in the ring ($<20\times10^{10}$) and does not allow for opportune checks. Instead, we are able to utilize the 180° bend magnet following the cooling section and a beam position monitor (BPM) just downstream (R01) as an energy analyzer. Again using antiprotons for calibration purposes, the absolute vertical (y) position is recorded, as well as the relative displacement of the beam as a function of the electron beam energy. Figure 4 shows the Pelletron's high voltage read back and the corresponding beam displacement at R01 when a step function is applied. While the relative calibration (0.31 mm/kV) is very stable, the absolute position at R01 for a fixed energy does vary with time also and needs to be recalibrated with antiprotons ~once a month. This is because the position at the entrance of the bend is not exactly fixed due to upstream drifts (BPM electronics, power supplies stability, ground motion).

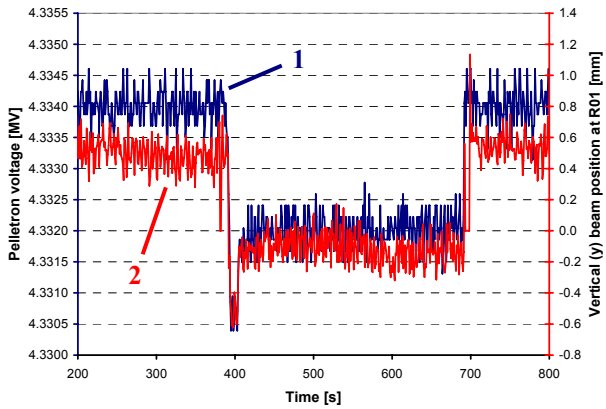

Figure 4: Pelletron voltage (1-blue) and electron beam vertical (y) position at R01 (2-red) as function of time during a voltage jump. The corresponding calibration is 0.31 mm/kV.

The use of the beam position at R01 as a measure of the electron beam energy also revealed some limitations to the generator volt meter (GVM) that is used to regulate the Pelletron high voltage. Figure 5 shows the time evolution of the Pelletron voltage (average value being subtracted) as measured by the GVM, a capacitive pickup (CPO) and the displacement at R01. Both the CPO and the R01 BPM indicate a ~1 kV voltage drop of several seconds at t ≈ 60 s, while the GVM remains unperturbed. This could be the result of micro-discharges with nano-Amperes current flowing directly to the GVM plate and we are considering implementing a magnetic shielding of the GVM. Note that at this time, the CPO signals are not used for regulation of the high voltage.

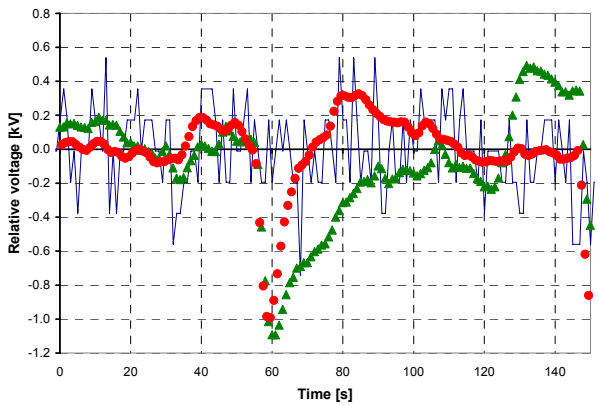

Figure 5: Relative (AC) Pelletron voltage as a function of time. Blue: GVM; Red circled: Capacitive pickup (CPO); Green triangles: position at R01.

Because these drops in voltage are of short period of times, their impact on cooling is low. However, they can

be a problem during drag rate measurements by the voltage jump method.

Electron Beam Related Operational Issues

Since we started to use the electron beam for cooling, we dealt with three major issues: transverse emittance growth, fast beam loss and lifetime degradation of the antiprotons.

Transverse emittance growth was observed during the mining process where both the physical (i.e. peak current) and phase space density become relatively large [3]. A change of our operating point from 25.414/24.422 (H/V) to 25.452/24.469, suggested from the analysis of quadrupole instabilities in the presence of an electron beam [9], eliminated almost entirely the emittance growth problem. However, we now believe that the quadrupole instability was not the mechanism by which emittance growth was induced but rather a single particle resonance mechanism [10], which could also explain the different beam lifetime observed for different working points in tune space [11].

Fast antiprotons loss is typically the result of one of two different beam conditions, both of which become more difficult to avoid as the number of antiprotons increases: high phase-space density or high peak current of the antiproton beam. With the addition of dampers [12], the threshold for resistive wall dipole instabilities [13] has greatly increased [11] and has not been an issue recently. To deal with high peak currents occurring during mining of large stacks, the RF structure of the mined buckets has been modified [14], reducing by a factor of 2 the maximum peak current of any single bunch. The new RF structured allowed to successfully mine and extract up to ~450×10^{10} antiprotons.

Because of the problem related above with our beam current monitor, no recent observations were made regarding the lifetime degradation of the antiproton beam undergoing electron cooling. It is clear, however, that it remains the biggest issue when the number of antiprotons in the Recycler exceeds 350-400×10^{10}. It is also important to note that the history of how the antiproton beam is cooled (i.e. relative position of the electron beam w.r.t. the antiproton beam as a function of time) leads to very different lifetimes for nearly the same antiproton beam parameters. As was noted in Ref. [3], the lifetime appeared to improve at the new tunes, although no good explanation has been developed as for why. In that respect, exploring other tune regions may prove to be beneficial. Thus, additional quadrupoles are being installed in the Recycler to increase its tune phase-space range.

We are also investigating a novel procedure for cooling which relies on a modified RF bucket structure, the so-called compound bucket, which separates in the longitudinal direction the high transverse emittance, high momentum spread particles (i.e. hot particles) from the low transverse emittance, low momentum spread particles (i.e. cold particles). Then, gated stochastic cooling is applied on the hot particles, while the electron beam remains on axis cooling more efficiently the cold particles. Details of this technique are presented in Ref. [15] along with preliminary results. The purpose of this procedure would be to provide strong cooling while maintaining a good lifetime.

COOLING PERFORMANCE

Longitudinal Cooling Force

The cooling properties of the electron beam are first evaluated with drag rate measurements by a voltage jump method [16]. Details on the methodology and results of these measurements can be found in Ref. [3], and more recent measurements of the drag force as a function the antiproton momentum offset $p \equiv P\text{-}P_0 = \gamma M_p V_{pz}$ are plotted on Figure 6. For $p \approx 4$ MeV/c, the typical rms momentum spread of the antiproton beam during operation, the drag rate ranges from 25 to 50 MeV/c per hour. This difference appears to be correlated to the transverse emittance of the antiproton beam. For the measurements presented in Ref. [3], the antiproton transverse emittance was relatively large (2-6 π mm mrad, 95%, normalized, measured with a Schottky detector) and not accurately monitored during the data acquisition. In Figure 6, the starting initial transverse emittances, as measured with flying wires, are similar for both data sets (< 0.5 π mm mrad, 95%, normalized). However, for the blue diamond data points, the extent of the antiproton beam in the transverse direction was further limited with a scraper, which was moved in between each measurement.

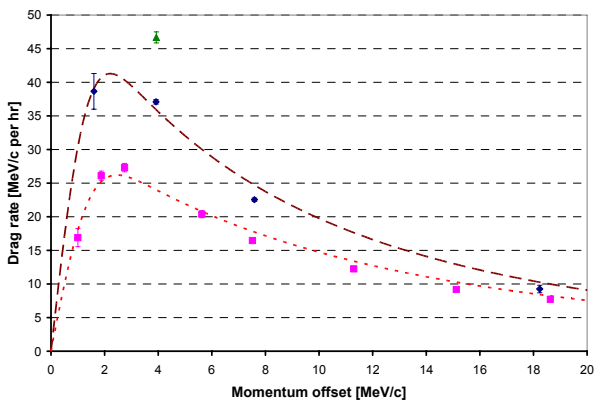

Figure 6: Longitudinal cooling force (negated) as a function of the antiproton momentum deviation. Points are data with error bars representing the statistical error (1σ) of the measurement procedure. Dashed lines are a fit to the data using a non-magnetized model. Pink squares: no scraper limiting the aperture; Blue diamonds: Scraper was brought in to the same transverse location between measurements; Green triangle: Measurement immediately after moving in and out the scraper. For all measurements, transverse stochastic cooling was applied, I_b = 100 mA, on-axis.

Because of various calibration issues, it is difficult to relate the acceptance limitation technique to a quantitative

measure of the emittance. Nonetheless, the data point at 46.9 MeV/c per hour obtained immediately after a scrape shows the extreme sensitivity of the friction force to the transverse distribution of the antiproton beam. More details on the friction force measurements, their interpretation and comparison with non-magnetized models can be found in Ref. [17].

Correlation to the Electron Beam Properties

The electron beam cooling capability depends on the beam energy spread σ_E, rms value of the electron angles in the cooling section θ_e, and beam current density J_{cs} (or beam size at a fixed beam current). As such, one would expect to be able to correlate the drag rate measurements with the electron beam parameters independently measured [3,8,11,18].

Fitting the data from Figure 6 with the usual non-magnetized model [19,20] does not lead to any significant disagreement (to within a factor of two) with previously reported fitted parameters [3, Table 2]. In fact, at 1.0 A cm^{-2} (for both curves in Figure 6), the fitted current density is closer to the theoretical calculation than previously reported. Also, the fitted rms electron angle is 150 and 120 μrad for the brown and red curves, respectively, which could be explained by the fact that the smaller antiproton beam experiences a better quality beam on average. On the other hand, the fitted rms energy spread (600-650 eV) is quite larger than what we would expect from the Pelletron HV ripple, $\delta U = 250$ eV rms and multiple-coulomb scattering and electron beam density fluctuations [21] which are estimated to contribute ~100 eV, added in quadrature.

However, it should be noted that the extraction of the friction force F from the drag rate measurements assumes that the second derivative of the friction force w.r.t. p is small so that $F(p) \approx \dot{p}$. This latter assumption becomes questionable with the increasing amplitude of the maximum friction force and a more complex analysis of the drag rate data is being considered.

Preliminary Measurements with a Scintillator Screen

Although the cooling performance proved that the beam quality was overall adequate for regular operation, we still lack a consistent model which would explain all of our measurements.

Firstly, the beam size measured with scrapers was ~1.4 time larger than expected based on conservation of the magnetic flux (Bush's theorem) [8]. On the other hand, friction force measurements showed that the effective electron beam radius was much smaller than both the direct measurement with scrapers and the expected value [18], of the order of 1 mm. In Ref. [3], it was pointed out that our estimation of the envelope scalloping could be an underestimate for the core particles, which could explain the smaller measured effective radius. We also proposed that secondary electrons be responsible for the larger than expected beam size [8]. In addition, during the optics optimization process, we observed that the cooling force had a shallow maximum when plotted against the matching solenoid strength just upstream of the cooling section. This was unexpected considering that they should affect the electron beam envelope considerably.

Preliminary measurements of the beam profile at the exit of the cooling section with a scintillator screen (a YAG crystal [22]) and gated CID camera (Figure 7) revealed interesting features that would explain the inconsistencies mentioned above. First, the beam core (saturated region) is elliptical. This indicates envelope oscillations in the cooling section, hence larger scalloping angles than estimated and a faster drop of the cooling force away from the axis than if the beam was self-similar.

Second, there is a clear halo of electrons more round than its core. The boundary of the halo is what the scrapers measure, thus explaining the large radius measured by this method.

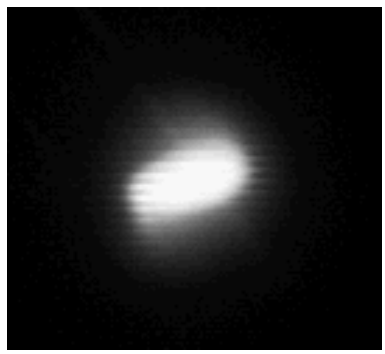

Figure 7: Picture of the electron beam at the exit of the cooling section taken with YAG screen and CID camera. The pulse amplitude was 3.2 kV (i.e. ~100 mA).

At this time, neither the ellipticity of the distribution nor the presence of the halo is completely understood. Further measurements with OTRs and the YAG are planned for the near future.

Cooling Rates

Although friction force measurements are necessary to understand the ultimate cooling capabilities of the electron cooler, cooling rate measurements are more adequate to qualify the cooler performance for operation purposes. Cooling rates measurements were discussed in detail in Ref. [18] and typical results were found to be -8 MeV/c per hour; for the longitudinal cooling rate, -6 π mm mrad /hr for the average transverse cooling rate for flying wire data and -2 π mm mrad /hr for the average transverse cooling rate for the Schottky detector data. However, as for the drag rates, we found the cooling rates (both longitudinally and transversely) to be sensitive to the antiproton transverse emittance. This is illustrated in Figure 8, where the longitudinal cooling rate is plotted against the antiproton transverse emittance measured by flying wires.

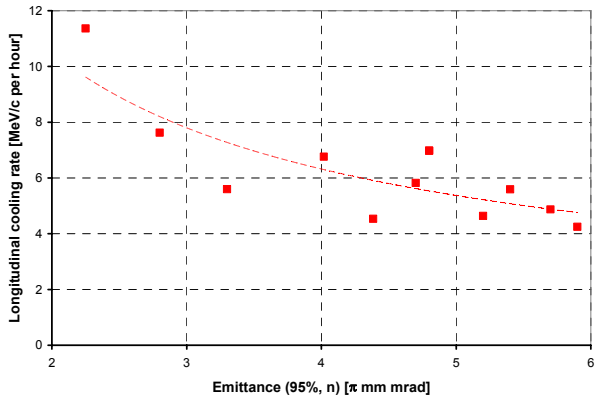

Figure 8: Longitudinal cooling rate (negated) as a function of the antiproton transverse emittance (from flying wire measurements). The dashed line is an arbitrary power law fit (for illustration only). The electron beam was on axis for all measurements (100 mA).

Once again, the image of the electron beam on the YAG screen suggests that this dependence may be due to the lack of homogeneity in the electron beam properties.

At this point, in order to assess the cooling properties of the electron beam more precisely and in an understandable fashion, the beam line optics need to be corrected. This work will take place this fall.

CONCLUSION

Electron cooling plays a preeminent role in Fermilab's latest luminosity achievements. The electron cooler high voltage stability and reliability has proven to be exceptionally good and the electron beam characteristics adequate and sufficiently stable to provide the necessary cooling performance.

Full discharges are sparse and conditioning of the accelerating columns is only required every ~2-3 months. In addition, long shutdowns for Pelletron maintenance (2-3 days) are only needed every ~6 months.

The measured longitudinal friction force and cooling rates were found to depend greatly on the antiproton transverse emittance. Recent YAG measurements indicate that the electron beam distribution may be the main culprit. Thus, correcting the electron beam line optics could significantly improve the cooling performance further (now planned).

The antiproton lifetime under strong electron cooling remains the main issue and may be dealt with another change of the Recycler working point.

ACKNOWLEDGMENTS

We are grateful to the entire Recycler department for helping with many aspects of the work and measurements discussed in this paper and countless productive discussions.

REFERENCES

[1] A Shemyakin *et al.*, AIP Conf. Proc. **821** (2006) 280.
[2] Pelletrons are manufactured by the National Electrostatics Corporation, www.pelletron.com.
[3] L. Prost *et al.*, in Proc. of HB2006, Tsukuba, Japan, May 29-June 2, 2006, WEAY02, p 182.
[4] 'Mining' is the first step in the extraction process that consists of capturing the core of the antiproton beam in 9 individual square buckets, leaving out the high momentum particles.
[5] P. Derwent *et al.*, Status of the Recycler Ring, *these proceedings*.
[6] L. Prost *et al.*, Beam-Based Field Alignment of the Cooling Solenoids for Fermilab's Electron Cooler, *these proceedings*.
[7] L. Prost and A. Shemyakin, AIP Conf. Proc. **821** (2006) 391.
[8] A. Shemyakin *et al.*, Proc. of EPAC'06, Edinburgh, UK, June 26-30, 2006, TUPLS069, p 1654.
[9] A. Burov *et al.*, in Proc. of HB2006, Tsukuba, Japan, May 29-June 2, 2006, THAW07, p 334
[10] A. Burov and V. Lebedev, in Proc. of PAC'07, Albuquerque, New Mexico, June 25-29, 2007, WEYC01, p 2009.
[11] L. Prost *et al.*, Proc. RuPAC'06, Novosibirsk, Russia, September 10-14, 2006, WEBO02.
[12] A. Burov, FERMILAB-TM-2336-AD (2005).
[13] Laslett, K. Neil and A. Sessler, Rev. Sci. Instr. **36** (1965) 436.
[14] C. Bhat *et al.*, in Proc. of PAC'07, Albuquerque, New Mexico, June 25-29, 2007, WEOCKI04, p 1941.
[15] A. Shemyakin *et al.*, Cooling in compound buckets, *these proceedings*.
[16] H. Danared *et al.*, Phys. Rev. Lett. **72** (1994) 3775.
[17] A. Shemyakin *et al.*, Electron Cooling in the Recycler Cooler, *these proceedings*.
[18] L. Prost and A. Shemyakin, in Proc. of PAC'07, Albuquerque, New Mexico, June 25-29, 2007, TUPAS030, p 1715.
[19] Ya.S. Derbenev and A.N. Skrinsky, Particle Accelerators **8** (1977) 1.
[20] S. Nagaitsev *et al.*, Phys. Rev. Lett. **96**, 044801 (2006).
[21] A. Burov *et al.*, AIP Conf. Proc. **821** (2006) 159.
[22] A. Warner *et al.*, Proc. of DIPAC'07, Venice, Italy, May 20-23, 2007, WEPB18, *to be published*.

COOLING RESULTS FROM LEIR

G. Tranquille, CERN, Geneva, Switzerland

Abstract

The LEIR electron cooler has been successfully commissioned for the cooling and stacking of Pb^{54+} ions in LEIR during 2006. The emphasis of the three short commissioning runs was to produce the so-called "early" beam needed for the first LHC ion run. In addition some time was spent investigating the difficulties that one might encounter in producing the nominal LHC ion beam.

Cooling studies were also made whenever the machine operational mode made it possible, and we report on the preliminary results of the different measurements (cooling-down time, lifetime etc.) performed on the LEIR cooler. Our investigations also included a study of the influence of variable electron density distributions on the cooling performance.

INTRODUCTION

The LHC program foresees lead-lead collisions in 2009 with luminosities up to 10^{27} $cm^{-2}s^{-1}$. In LEIR, ion beam pulses from the LINAC3 are transformed into short high-brightness bunches needed for the LHC. This is obtained through multi-turn injection, cooling and accumulation. The electron cooler plays an essential role in producing the required beam brightness by rapidly cooling down the newly injected beam and then dragging it to the stack.

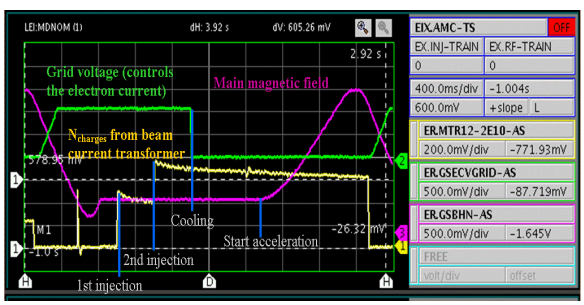

Figure 1: A standard 3.6s LEIR cycle during which 2 LINAC pulses are cooled-stacked in 800ms at an energy of 4.2 MeV/n. After bunching the Pb ions are accelerated to 72 MeV/n for extraction and transfer to the PS.

The goal of the LEIR commissioning runs in 2006 was to produce the Pb ion beam with the characteristics required for the first LHC ion run (N_{ions} = 2.2x10^8, $\varepsilon_{h,v}$ < 0.7 μm) and to subsequently transfer this beam to the next accelerator in the injection chain, the Proton Synchrotron (PS), for beam studies. Figure 1 shows a typical LEIR cycle in which two pulses are cooled and stacked to obtain the required intensity and emittance after which the beam is accelerated to top energy and extracted to the PS. These tests were so successful that the Pb ion beam was also extracted towards the Super Proton Synchrotron (SPS) for tests of the beam transport system and the stripping foil. Initial investigations into the production of the optimum beam (N_{ions} = 1.2x10^9, $\varepsilon_{h,v}$ < 0.7 μm) for LHC were also made on dedicated machine cycles. A full report of the LEIR commissioning can be found in [1].

ELECTRON COOLER HARDWARE COMMISSIONING

Hardware commissioning of the electron cooler concentrated on ensuring the vacuum [2] compatibility of the new device as well as exploring the performance limits. The main parameters of the cooler have been given in previous papers [3]. Two operational regimes can be used depending on the momentum of the ions to be cooled. If the small normalized emittances required cannot be reached at injection energy e.g. due to direct space charge detuning, operation of the cooler at the extraction energy will be necessary. In this scenario (unlikely for Pb ion operation, but a possible option for an eventual later upgrade to lighter ions), the LEIR magnetic cycle must contain an additional plateau at a suitable higher energy.

Electron Gun Characteristics

The high perveance gun provides an intense electron beam in order to decrease the cooling rate. However, in theory, increasing the electron density induces first an increase of the recombination rate (capture by the ion of an electron from the cooler), which is detrimental to the ion beam lifetime, and secondly increases the electron azimuthal drift velocity, thus increasing the cooling time. To combat the increase in electron-ion recombination, the electron gun has a "control electrode" used to vary the density distribution of the electron beam. The beam profile is adjusted in such a way that the density at the centre, where the cold stack sits, is smaller and thus the recombination rate is reduced. At larger radii, the density is large and allows efficient cooling of the injected beam executing large betatron oscillations.

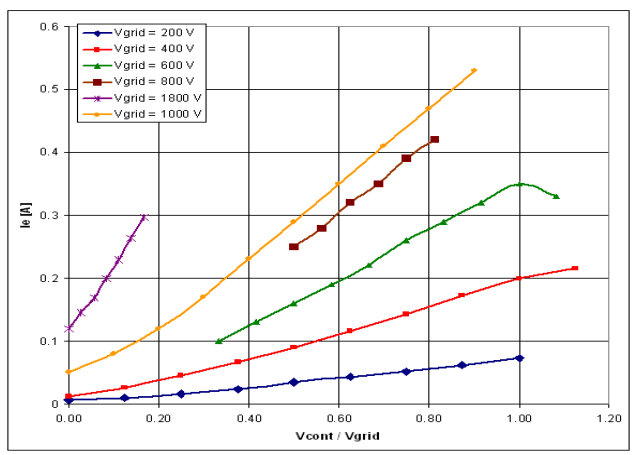

Figure 2: Electron beam current as a function of Vcont/Vgrid for Ee = 2.3 keV.

Figure 2 shows the measured electron beam intensity as a function of the control to grid voltage ratio. As the control electrode voltage is increased, the electron beam distribution changes from a parabolic beam ($V_{cont} < 0.2$ V_{grid}) to a completely hollow beam ($V_{cont} = V_{grid}$). A maximum stable current of 530 mA with a hollow distribution has been obtained but for operational purposes only 200 to 300 mA are used.

The effectiveness of the electrostatic bend has also been demonstrated when trying to obtain the highest electron currents. With only the B field in the toroids the relative losses are an order of magnitude higher than with a crossed electrostatic and magnetic field and it is very difficult to obtain a stable beam. With a polarisation voltage of 240 V and a careful steering of the electron beam into the collector, currents of up to 530 mA can be obtained. Figure 3 shows the dependence of the relative beam losses on the electron current for the two regimes.

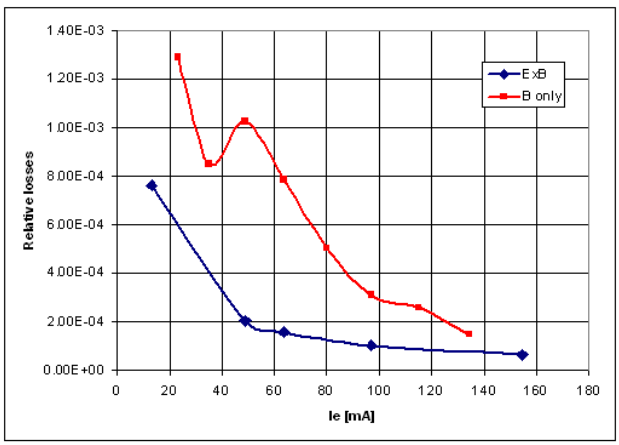

Figure 3: Relative electron beam loss as a function of the electron current, showing the influence of the electrostatic bend on the electron collection efficiency.

A system for measuring the beam position was also implemented and is used to align the electron and ion beams more efficiently. The measurement is done by the direct modulation of the electron intensity by a high frequency sine wave applied on the grid electrode. The sum and difference signals from the two position pick-ups installed in the cooling section are then acquired and calibration coefficients and offsets are applied to obtain the electron beam position. Using the different correction coils, the electron beam position and angle are adjusted such that the alignment with the circulating ion beam is optimum.

COOLING AND LIFETIME STUDIES

The cooling of ion beams was studied in parallel with the commissioning of the LEIR ring. Schottky diagnostics, ionisation profile monitors (IPM) and beam current transformers (BCT) were used to measure the phase-space cooling characteristics and to investigate the influence of the electron beam profile on the ion beam lifetime [4,5]. During the measurement we encountered many problems with the ionisation profile monitors which severely limited the quality of our measurements and limited the measurements to the horizontal plane only. These monitors have been redesigned and will be used in future measurement sessions.

As many of the LEIR systems had to be commissioned at the same time it was difficult to obtain long cycles dedicated to electron cooling studies. Almost all our measurements were performed on the standard magnetic cycle lasting 2.4 or 3.6 seconds during which 2 to 4 Linac pulses are cooled and stacked at 4.2 MeV/u. Due to the short duration of the injection plateau the momentum spread and the horizontal beam size after 400 ms were used as the measured parameters to characterise the cooling performance.

Influence of Beam Expansion

On the LEIR electron cooler the beam size can be varied by applying a stronger longitudinal field in the gun region. A maximum expansion factor of 3 is available thus making it possible to vary the electron beam radius from 14 mm to 24 mm. Figure 4 shows the result of a series of measurements made for two electron beam distributions (uniform for Vc/Vg = 0.2 and hollow for Vc/Vg = 0.5) with similar currents (~150 mA).

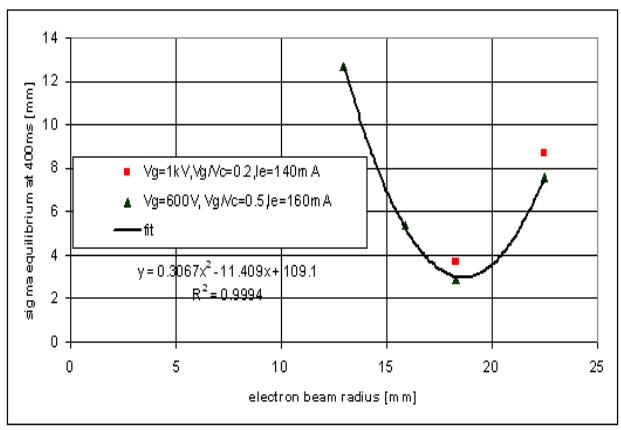

Figure 4: Beam size 400 ms after first injection as a function of the electron beam radius.

What one sees is that beam expansion becomes less useful when the electron beam radius is greater than 20 mm, roughly the size of the injected beam. Another phenomenon that was observed with larger electron beams is the relatively bad cooling of the first injected beam. In all our measurements, regardless of the number of injections, the first beam was never fully cooled to make space for another injection. Subsequent injections were cooled to dimensions almost twice smaller than the first one.

Influence of the Density Distribution

The electron beam density distribution can be varied from a parabolic distribution to a completely hollow one by applying a voltage on “control electrode” in the gun. For a grid voltage to control voltage ratio (Vg/Vc) below 0.2 the electron beam essentially has a parabolic distribution. Above this ratio the distribution changes

from uniform to hollow. In figure 5 the electron beam distribution is varied as the intensity is increased. Again we observe a minimum in the curve corresponding to a slightly hollow distribution.

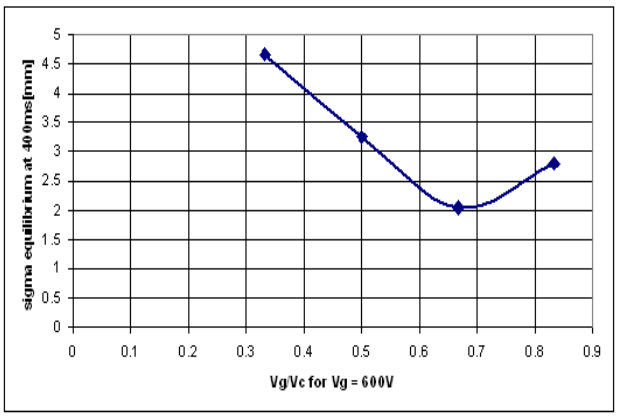

Figure 5: Beam size after 400 ms as a function of the electron beam distribution for the operational value of expansion (k=1.7, r=18 mm).

It is clear from the above measurements that a more detailed study of the interplay between beam size, intensity and density distribution needs to be made in order to optimise the transverse cooling.

Longitudinal Cooling

The momentum spread after 400 ms of cooling was measured using a down-mixed longitudinal Schottky signal captured with a fast ADC and treated mathematically to produce the spectral density distribution as a function of time. The results shown on the scatter plot of figure 6 do not exhibit any particularly strange behaviour, with a decreasing momentum spread as the electron current is increased.

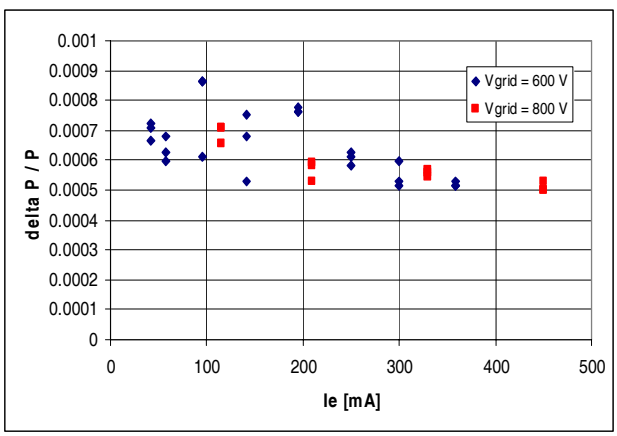

Figure 6: Momentum spread of the cooled ion beam after 400 ms as a function of electron current.

If we look more closely at the actual Schottky spectra (Figures 7a and 7b) then we see that, as the intensity goes up, and the distribution becomes more hollow, the final energy of the cooled ions vary well after the equilibrium momentum spread has been reached.

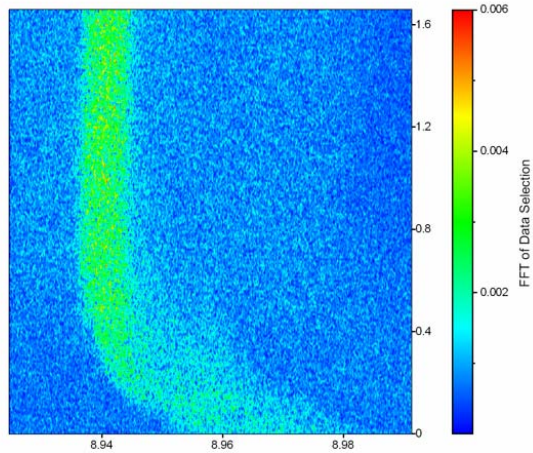

Figure 7a: Longitudinal Schottky evolution for uniform electron beam distribution.

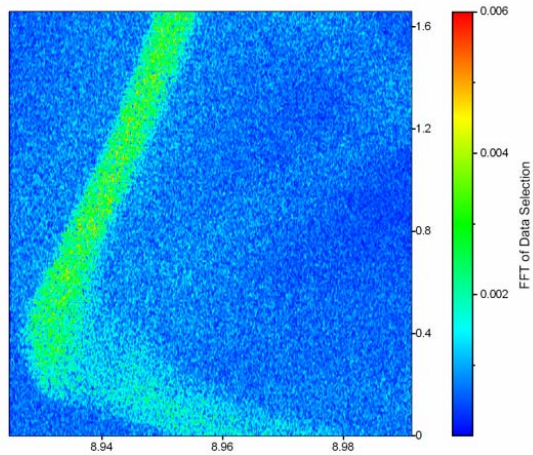

Figure 7b: Longitudinal Schottky evolution for a hollow electron beam distribution.

Lifetime Studies

In previous tests [6] the maximum accumulated intensity was a factor 2 lower than that required for the nominal LHC ion beam (1.2×10^9 ions). This was in part attributed to a short lifetime due to the recombination of ions with the cooling electrons and also to the limited electron current that could be obtained for effective cooling with the old electron gun.

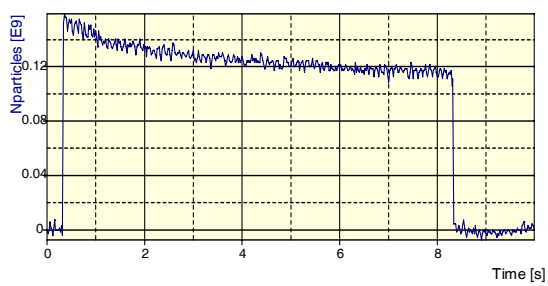

Figure 8: Example of the BCT signal for lifetime measurements.

In our measurements intensities well above $1.2x10^9$ ions could easily be accumulated with an injection repetition rate of 1.6 Hz and an electron current of 110 mA. If the repetition rate is increased, the maximum number of stacked ions decreases proportionally for the same electron current.

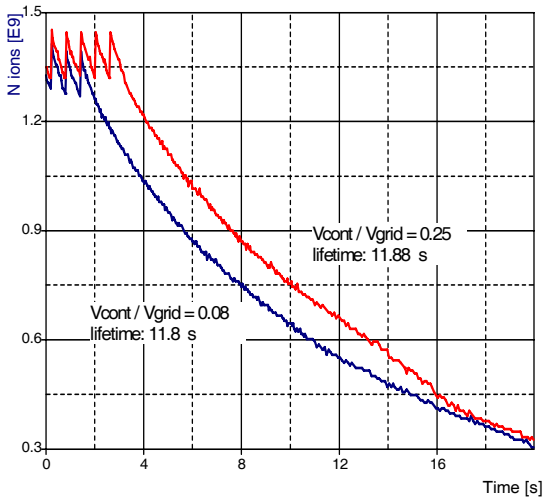

Figure 9: Beam lifetime for a parabolic (blue) and hollow (red) electron beam distribution.

The lifetime of the cooled ion beam can be measured by recording the evolution of the BCT signal as a function of time (Figure 8). The lifetime of the circulating beam was also compared for a parabolic and a hollow electron beam distribution (Figure 9). From the plot we see that the electron beam distribution does not significantly influence the lifetime indicating that recombination may not be after all the main cause of the short lifetime measured in the 1997 tests. Other processes related to the vacuum conditions or the injection scheme could be more dominant.

A complete plot of all our lifetime measurements for different intensities and density distributions is shown in figure 10. The slope of the curves gives the lifetime due to the electron beam whilst the intersection with the y-axis gives the vacuum lifetime. Comparing with the measurements made in 1997, we see a definite gain by a factor of 2 in the vacuum lifetime. The lifetime due to the electron beam is also slightly improved but does not seem to be influenced by the electron beam distribution.

CONCLUSIONS

The new electron cooler for LEIR has been successfully integrated in the LEIR environment and commissioned. It has been used routinely for the LEIR ring commissioning with O^{4+} and Pb^{54+} ions where its role has been central in obtaining the Pb ion beam characteristics required for the first LHC ion run planned for 2009. First investigations on the cooling performance and ion beam lifetime clearly indicate of the usefulness of high-intensity electron beams with variable density distributions [7] but the expected gain in ion beam lifetime with hollow electron beams is not clearly observed. More systematic studies of the influence of the different variables on the cooling performance still need to be done making use of the recently upgraded diagnostic systems (IPM and spectrum analysers).

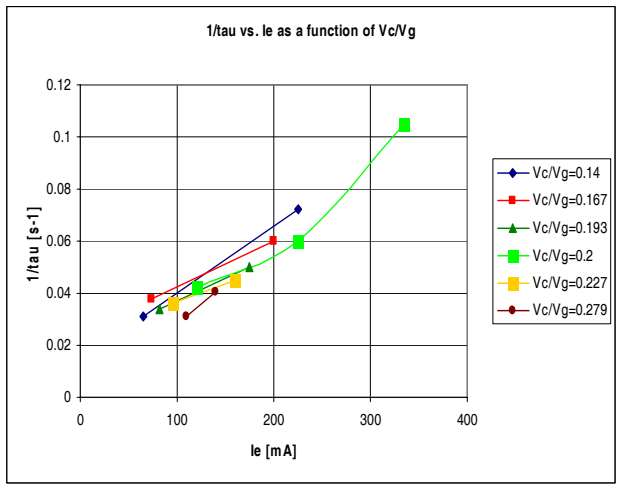

Figure 10: Inverse lifetime of Pb54+ ions as a function of electron current and density distribution.

REFERENCES

[1] C. Carli, "Commissioning and Performance of LEIR", These proceedings.

[2] E. Mahner, "The Vacuum System of the Low Energy Ion Ring at CERN: Requirements, Design and Challenges", CERN AT-2005-013.

[3] G. Tranquille, "Specification of a new Electron Cooler for the Low Energy ion Ring, LEIR", Proceedings of COOL03, Yamanashi, Japan, 2003.

[4] J. Tan and G. Tranquille, "Beam Diagnostics with Schottky Noise in LEIR", EPAC'06, Edinburgh, June 2006, p. 1214.

[5] C. Bal, V. Prieto, R. Sautier, G. Tranquille, "First Results from the LEIR Ionisation Profile Monitors", To be published in the DIPAC07 proceedings.

[6] J. Bosser, C. Carli, M. Chanel, R. Maccaferri, D. Mohl, G. Molinari, S. Maury, G. Tranquille , "The Production of Dense Lead-ion Beams for the CERN LHC", Proceedings of ECOOL99, Uppsala, Sweden, 1999, and CERN/PS 99-042 (BD).

[7] V. Parkhomchuk, "Comparison of Hollow Electron Device and Electron Heating", These proceedings.

COMMISSIONING OF ELECTRON COOLING IN CSRM*

X.D. Yang[#,1], V.V. Parkhomchuk[2], W.L. Zhan[1], J.W. Xia[1], H.W. Zhao[1], G.Q Xiao[1], Y.J. Yuan[1], M.T. Song[1], Y. Liu[1], J.C. Yang[1], L.J. Mao[1], J. Li[1], G.H. Li[1], D.Q. Gao[1], Z.Z. Zhou[1], Y. He[1], W. Zhang[1] , X. T. Yang[1], J.H. Zheng[1], R.S. Mao[1], T.C. Zhao[1]

1. Institute of Modern Physics, 730000 Lanzhou, CAS, China
2. Budker institute of Nuclear Physics,630090 Novosibirsk, RAS, Russia

Abstract

A new generation electron cooler has started operation in the heavy ion synchrotron CSRm which is used to increase the intensity of heavy ions. Transverse cooling of the ion beam after horizontal multiturn injection allows beam accumulation at the injection energy. After optimization of the accumulation process an intensity increase in a synchrotron pulse by more than one order of magnitude has been achieved. In given accumulation time interval of 10 seconds, 10^8 particles have been accumulated and accelerated to the final energy. The momentum spread after accumulation and acceleration in the 10^{-4} range has been demonstrated in five species of ion beams. Primary measurements of accumulation process varying with electron energy, electron beam current, electron beam profile, expansion factor and injection interval have been performed. The lifetimes of ion beam in the presence of electron beam were roughly measured with the help of DCCT signal.

INSTRUCTION

HIRFL-CSR is a new ion cooler-storage-ring system in IMP China. It consists of a main ring (CSRm) and an experimental ring (CSRe). The two existing cyclotrons SFC (K=69) and SSC (K=450) of the Heavy Ion Research Facility in Lanzhou (HIRFL) are used as its injector system. The heavy ion beams from HIRFL is injected into CSRm, then accumulated, e-cooled and accelerated, finally extracted to CSRe for internal-target experiments and other physics experiments.

Table 1: Parameters of the CSRm electron cooler

Maximum electron energy	35 keV
Maximum electron current	3A
Gun perveance	29 μP
Cathode diameter	29mm
Current collection efficiency	≥99.99%
Maximum magnetic field in gun section	0.25T
Maximum magnetic field in cooling section	0.15T
Field parallelism in cooling section	4×10^{-5}
Effective length of cooling section	3.4m
Vacuum pressure	$\leq 3\times10^{-11}$mbar

CSRm is a 161m circumference cooler storage ring with sixteen 22.5 degree H-type bending dipole magnets. The maximum betatron functions are 15.3m and 30.5m in horizontal and vertical respectively. The maximum dispersion is 5.4m, and the dispersion at injection point is 4m. The betatron functions at electron cooler are 10m and 17m in the two transverse directions respectively, the dispersion is zero here. The emittance of ion beam from SFC and SSC is about 20πmmmrad and 10 π mmmrad, and the acceptance of CSRm is about 150πmmmrad.

Two modes of injection are used in CSRm, stripping for lighter ions and repeated multiturn for heavier ones. The accumulation duration of CSRm is about 10s, and the acceleration time of CSRm is nearly 3s, and the one whole cycle period is about 17s.

In CSRm, the electron cooling device plays an important role in the heavy ion beam accumulation at injection energy. The new state-of-the-art electron cooling device was designed and manufactured in the collaboration between BINP and IMP, it has three distinctive characteristics, namely high magnetic field parallelism in cooling section, variable electron beam profile and electrostatic bending in toroids. The main parameters are listed in table 1.

In 2005 the main construction of the CSR project was completed, and from then the preliminary commissioning of CSRm was performed, including the first turn commissioning as a beam line, the stripping injection, and the zero-bumping orbit test, fixed-bumping orbit test with four in-dipole coils, bumping orbit test, C-beam accumulation and some investigations of the closed orbit with BPM.

Shortly after last workshop of COOL2005, the cooler started routine operation during CSR commissioning. Up to now five species of ion were cooled and accumulated with the help of electron cooling. In this paper the recent results of commissioning of CSRm and its cooler are presented. The previous results have been given in the APAC2007-THXMA03 [1]

BEAM DIAGNOSTICS

The closed orbit is monitored by 16 shoebox-shaped BPMs, the length of electrodes is 150mm, the cross-section is rectangular, and the width and height are 170mm and 100mm respectively. Two additional cylindrical BPMs were installed at the ends of cooling section to measure the positions of electron beam and ion beam. A Schottky pickup was placed behind the cooler, the length of the plate electrodes is 395mm, and the widths are 160mm in horizontal and 100mm in vertical directions, the gaps between electrodes are 110mm in vertical and 160mm in horizontal. A DCCT developed by company Bergoz is used to monitor the ion beam current in the ring, with precision of about 0.5μA. The direct determination of beam's transverse emittance was presently ruled out due to the magnesium jet monitor was out of order during commission. In order to measure the work-point, the Schottky pickup electrodes were used to

*Work supported by the central government of China
#yangxd@impcas.ac.cn

excite the ion beam, a BPM was used to monitor the Schottky signal, the length of its electrodes is smaller than Schottky pickup electrodes. The lifetime of ion beam was measured by DCCT signal roughly. The work point of ring was monitored during the process of acceleration. Due to lack of the transverse ion beam monitors, the transverse profile of the ion beam was not measured during the commissioning.

CLOSED-ORBIT CORRECTION

The closed-orbit is monitored during acceleration by the BPM system. 16 steering in-dipole coils, 8 pairs of horizontal and vertical bidirectional correction dipoles and 6 additional vertical correction dipoles are used to correct the closed-orbit.

The longitudinal field produced by electron cooler is compensated by two compensation solenoids at the both ends of cooler. The transverse field introduced by the toroids is corrected by four pairs of horizontal and vertical correction dipoles. The displacement and direction of ion beam in the cooling section can be adjusted by these dipoles.

The global closed-orbit correction was performed according to the ion beam decay in the ring after accumulation process. After turning on the magnetic field of electron cooler and related correction coils, the local closed-orbit correction was carried out in the region of electron cooler.

BEAM ACCUMULATION

Stripping Injection of $^{12}C^{6+}$

Firstly, the 7MeV/u $^{12}C^{4+}$ was injected into CSRm from small cyclotron SFC through a stripping foil with thickness of 15μg/cm^2 placed in the first dipole of the ring, the average pulse intensity was about 12μA in the injection line. In the absent of magnetic field of electron cooler, the single-turn stripping injection beam was tested in CSRm with bumping orbit, the stored beam signal was observed from BPM signal, the closed orbit correction was done roughly, the machine parameter such as working point was measured and tuned, acceleration was attempted.

The average particle number of stored $^{12}C^{6+}$ was about 4.7×10^8 in one standard multiturn injection. With the help of electron cooling of partially hollow electron beam, 2.5×10^9 particles were accumulated in the ring after 10 times injection in 10 seconds, and 2.2×10^9 particles were accelerated to final energy of 1GeV/u. The momentum spread of injected beam was about 1.5×10^{-3}, after electron cooling the momentum spread rapidly reduced to 5.5×10^{-5} in a second at first shot, and then final momentum spread increased linearly with the stored particle number. The Schottky noise signal of $^{12}C^{6+}$ during accumulation was presented in Figure 1, and the dependence of momentum spread upon the stored ion number was shown in Figure 2. The momentum cooling time was about 0.3sec. About 1.6×10^{10} particles were stored in the ring after longer time accumulation which is displayed in Figure 3.

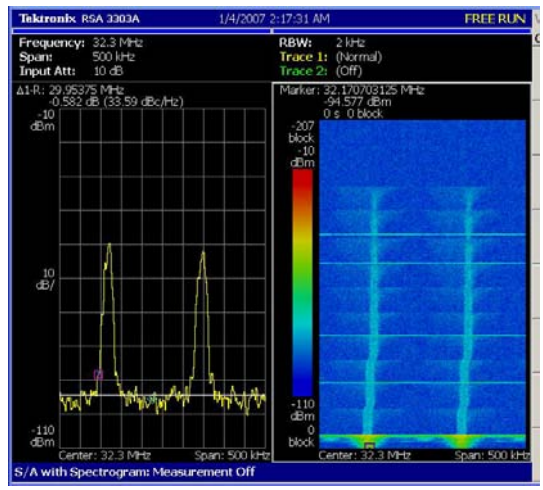

Figure 1: Schottky signal of $^{12}C^{6+}$ during accumulation.

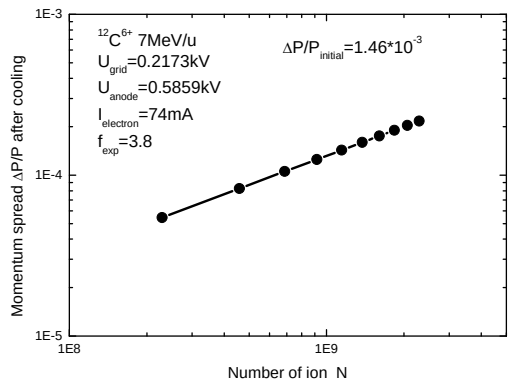

Figure 2: Momentum spread of cooled $^{12}C^{6+}$ as a function of the stored particle number at the injection energy determined by Schottky signal of a coasting beam in Fig.1.

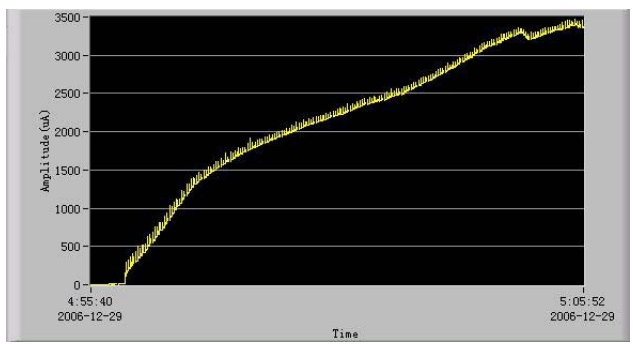

Figure 3: $^{12}C^{6+}$ beam accumulation.

Multiturn Injection of $^{12}C^{4+}$

At the end of the transfer line one magnetic septum and an electrostatic septum inflector guides the beam parallel to the ring orbit; four in-dipole coils create a DC bump of 50mm amplitude at the electrostatic septum. For multiturn injection four fast bump magnets produce a time dependent bump orbit to fill the horizontal acceptance of the ring.

In order to test the performance of the elements for multiturn injection, repeated multiturn injection was carried out with 7MeV/u $^{12}C^{4+}$ without stripping. The average pulse intensity was about 6μA in the injection

line. Only 47% of beam intensity left after turned on the cooler magnetic field and related correction, it is smaller than the results of SIS. The average particle number of $^{12}C^{4+}$ per pulse is about 1.2×10^8 in one standard multiturn injection, with the help of electron cooling of partially hollow electron beam, 5.8×10^8 particles were accumulated in the ring after 10 times injection in 10 seconds, and 4.6×10^8 particles were accelerated to final energy of 300MeV/u. The measured lifetime of $^{12}C^{4+}$ is 28 seconds, which is shorter comparing with 255s of $^{12}C^{6+}$, after longer time accumulation, the particle number was saturated at 7.0×10^8.

Multiturn Injection of $^{36}Ar^{18+}$

For the sake of the performance of accelerator complex of HIRFL, 22MeV/u $^{36}Ar^{8+}$ beam extracted from SSC was stripped into $^{36}Ar^{18+}$ by the foil with thickness of 350μg/cm^2, and then injected to CSRm, the average pulse intensity was about 4μA in the injection line. The average pulse particle number of $^{36}Ar^{18+}$ was about 5.4×10^6 in one standard multiturn injection. With the help of electron cooling of partially hollow electron beam, 1.2×10^8 particles were accumulated in the ring after 29 times injection in 10 seconds, and 1.1×10^8 particles were accelerated to final energy of 1GeV/u. 3.8×10^8 particles were stored for long time accumulation. The best results were demonstrated in Figure 4. Comparing with the results in reference[2], accumulation rate which is defined as the increase of circulating current per unit of time divided by the current in the injection line to the synchrotron, was achieved 6 in the commissioning of CSRm. It seems slightly better than the maximal value 5 in the reference.

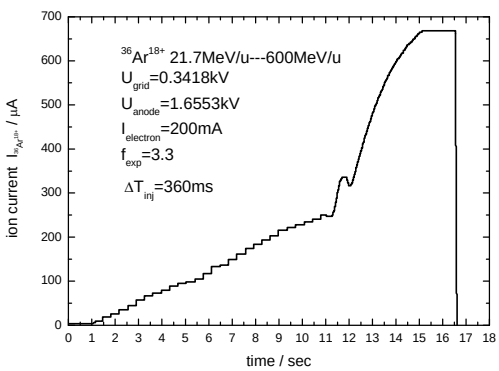

Figure 4: A complete cycle of accumulation and acceleration of $^{36}Ar^{18+}$ with electron beam.

Multiturn Injection of $^{129}Xe^{27+}$

It should be mentioned that a new superconducting ECR ion source SECRAL developed by IMP has started operation to provide high intensity heavier ion beam[3]. $^{129}Xe^{27+}$ delivered by the SECRAL was accelerated by SFC to 2.9MeV/u and then injected into CSRm, the average pulse intensity was about 3.0μA in the injection line. The average pulse particle number of $^{129}Xe^{27+}$ was about 1.0×10^7 in one standard multiturn injection. With the help of electron cooling of partially hollow electron beam, 1.2×10^8 particles were accumulated in the ring after 29 times injection in 10 seconds, and 1.0×10^8 particles were accelerated to final energy of 235GeV/u. 1.1×10^8 particles were stored after long time accumulation.

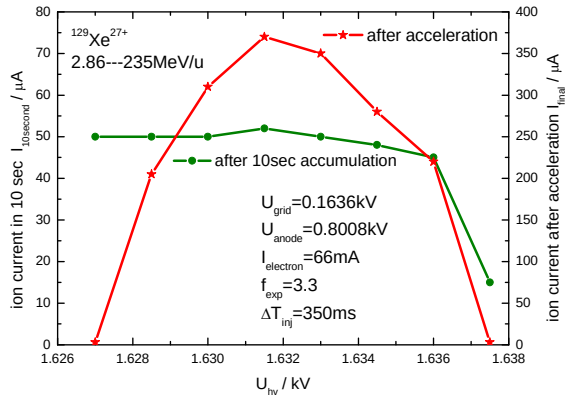

Figure 5: $^{129}Xe^{27+}$ intensity after accumulation and acceleration as a function of electron beam energy.

The ion intensity after 10s accumulation and acceleration depending on the electron beam energy was investigated in case of fixed electron beam current and profile, the results are illustrated in Figure 5. The accumulated intensity in 10s does not critically rely on the electron energy compared with the intensity after acceleration. The reason was that the RF capture frequency is more precise than the velocity of electrons. The same phenomena were observed in the commissioning of $^{12}C^{5+}$. The potential drop caused by space charge of electron with different profile was taken into account at the time of finely tuning the velocity of the electron beam.

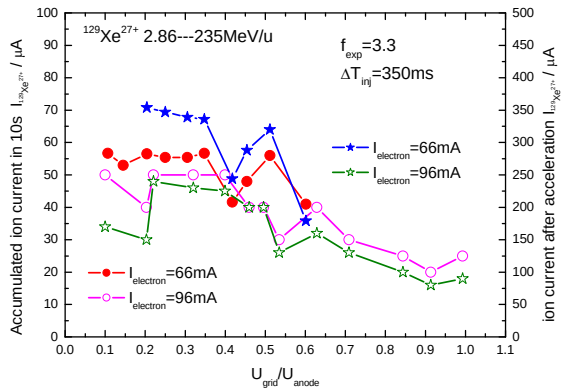

Figure 6: $^{129}Xe^{27+}$ intensity after 10 seconds accumulation and acceleration as a function of the ratio U_{grid}/U_{anode} of electron gun.

In the interest of optimization the electron beam profile for accumulation, the electron beam profile was changed at fixed electron beam current. The results were shown in Figure 6. One can see that at the larger ratio U_{grid}/U_{anode}, the electron density in the centre of electron beam becomes smaller than that at the edge. The ion beam was

weakly cooled in this case, and the accumulated ion becomes smaller. When the electron beam current increases, the electron density in the centre slightly increases, and the accumulated ion beam also increase. Optimum accumulation happened when the ratio U_{grid}/U_{anode} is near 0.2.

Multiturn Injection of $^{12}C^{5+}$

In order to examine the performance of the elements for fast extraction, repeated multiturn injection was done with 8.26MeV/u $^{12}C^{5+}$ without stripping. The average pulse intensity was about 3μA in the injection line. The average pulse particle number of $^{12}C^{5+}$ was about 4.0×10^7 in one standard multiturn injection, with the help of electron cooling of partially hollow electron beam, 3.5×10^8 particles were accumulated in the ring after 10 times injection in 10 seconds, and 4.6×10^8 particles were accelerated to final energy 100MeV/u. The lifetime of 16 seconds of $^{12}C^{5+}$ is short compared with 255s of $^{12}C^{6+}$, after longer time accumulation only 4.6×10^8 particles were accumulated and saturation was reached.

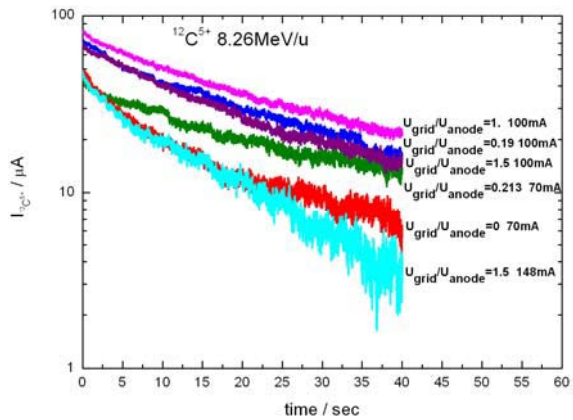

Figure 7: Decrease of the stored $^{12}C^{5+}$ intensity with time for different profile electron beam at different current.

The charge state of ion $^{12}C^{5+}$ is medial, so that the possibilities of ion loss due to various mechanisms exist in the ring. In the absence of electron beam, the ionization and electron capture process due to residual gas determines the lifetime of ion beam in the ring. In the presence of electron beam, the electron capture process will dominate. Figure 7 reveals the decrease of the stored $^{12}C^{5+}$ ion current during cooling at different electron current and profile. Figure 8 shows the lifetime of the stored $^{12}C^{5+}$ ion with the ratio U_{grid}/U_{anode} in electron gun at different electron current. It is clear that the lifetime is longer in the case of partially hollow electron beam. The accumulation efficiency demonstrated is higher for hollow electron beam in 10 seconds. In the case of bigger current of hollow electron beam, the lifetime becomes shorter, but accumulation becomes higher. Much higher accumulation efficiency for higher ratio U_{grid}/U_{anode} can be explained by improving the vacuum conditions. Vacuum condition along ring depends on the degasification by action of ion beam and it will be improved with time.

The effect of the electron beam expansion factor on the accumulation is shown in Figure 9. After repeated multiturn injection, the emittance of ion beam will be close to the transverse acceptance of the ring. And the radius of ion beam will be 3.8cm in the cooling section. The ion beam is completely surrounded by the electron. The accumulation is improved in the case of bigger expansion factor. The experimental results don't change smoothly and regularly because of the fluctuation of injected ion beam.

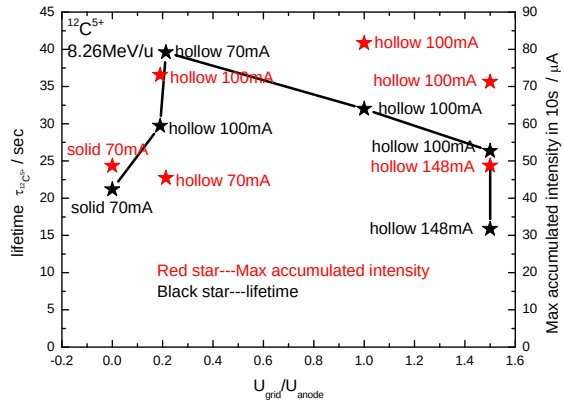

Figure 8: Lifetime of the stored $^{12}C^{5+}$ ion as a function of the ratio U_{grid}/U_{anode} of electron gun at different electron current.

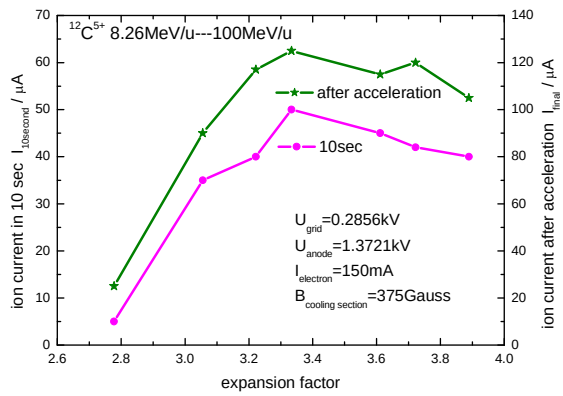

Figure 9: $^{12}C^{5+}$ intensity after 10 seconds accumulation and acceleration as a function of expansion factor.

The accumulation rate subjects to the cooling time and injection repetition rate. It is determined by the electron beam parameters and injected ion beam stability. Variation of the time between two successive multiturn injections is illustrated in Figure 10. The optimum time interval between the two adjacent multiturn injections corresponds to the transverse cooling time of ion.

The influence of the electron beam current on the accumulation is illustrated in Figure 11, The accumulated ion intensity in 10s was measured as a function of the electron current for the different electron beam profile. For the hollow electron beam, because the electron density in the centre decreases, higher electron current is

needed for the same cooling. The effects of higher electron beam current on the work-point should be taken into account.

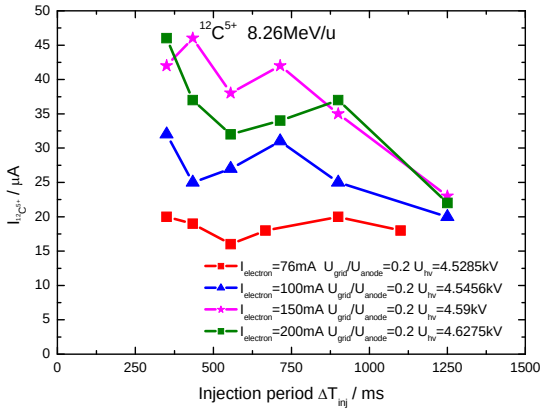

Figure 10: $^{12}C^{5+}$ intensity after 10 seconds accumulation as a function of the time interval between subsequent multiturn injections at different electron current in case of the same electron beam profile.

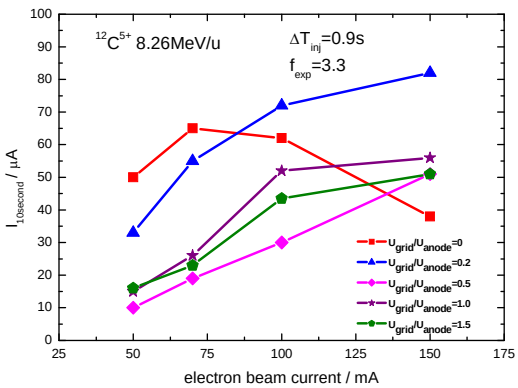

Figure 11: $^{12}C^{5+}$ intensity after 10 seconds accumulation as a function of the electron current at different ratio between U_{grid} and U_{anode} of electron gun.

The impact of the electron beam profile on the accumulation is shown in Figure 12. The accumulated ion intensity in 10s was measured as a function of the ratio U_{grid} /U_{anode} of electron gun at different electron current. It is clear that optimum accumulation happened in the partially hollow electron beam, the ratio U_{grid} /U_{anode} is close to 0.2. In this case, the central density is 2 times less than the edge one in the electron beam.

Table 2: Accumulation parameters of ion beam

Ion	E_{inj}	M	I_{inj} μA	Foil μg/cm^2	ΔT_{inj} ms	Lifetime sec	I_e mA
$^{12}C^{6+}$	7.09	ST	12	15	1000	255	70
$^{12}C^{4+}$	7.1	MI	6		1000	27.7	124
$^{36}Ar^{18+}$	21.7	MI	4	350	350	554.7	97
$^{129}Xe^{27+}$	2.9	MI	3		350	12	70
$^{12}C^{5+}$	8.26	MI	3		900	16	151

The injection parameters of ion are enumerated in table 2, I_{inj} is the intensity of single multiturn shot, ΔT_{inj} is the injection period, and the lifetime of the ion beams with the electron beam is listed in the penultimate column.

The momentum spread of the ion beams are summarized in table 3, after accumulation and acceleration it is in the range of 10^{-4}.

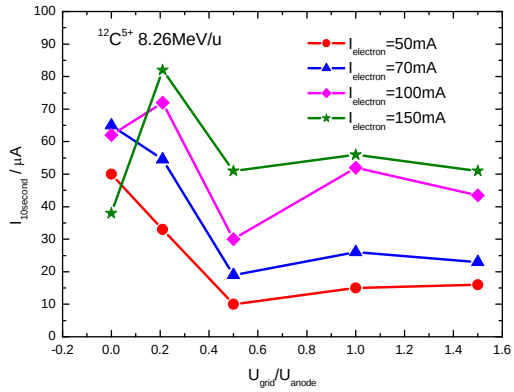

Figure 12: $^{12}C^{5+}$ intensity after 10 seconds accumulation as a function of the ratio U_{grid} /U_{anode} of electron gun at different electron current.

Table 3: Momentum spread of ion beam

Ion	E_{ion}	Mode	$\Delta P/P_{inj}$	$\Delta P/P_{10sec}$	$\Delta P/P_{final}$
$^{12}C^{6+}$	7.09---1000	ST	1.46×10^{-3}	3.9×10^{-3}	3.6×10^{-4}
$^{36}Ar^{18+}$	21.7---1000	MI	6.98×10^{-4}	3.2×10^{-4}	2.5×10^{-4}
$^{129}Xe^{27+}$	2.9---235	MI		2.4×10^{-4}	1.8×10^{-4}
$^{12}C^{5+}$	8.26---100	MI		2.3×10^{-4}	1.3×10^{-4}

SUMMARY AND OUTLOOK

Experimental results indicate that the partially hollow electron beam has an advantage in beam accumulation. The optimal ratio U_{grid}/U_{anode} is near 0.2. In this case, the centre density is 2 times less than the edge density in the electron beam. The equilibrium momentum spread increases with the number of accumulated ions; the result is unanimous contrasted with the SIS cooler. The optimal electron currents are well agreed with simulated one with the help of Vasily's electron cooling simulation code. Systematic investigation of cooling with hollow electron beam will be performed in the future.

REFERENCES

[1] J.W. Xia et al, "Construction and Commissioning of the HIRFL-CSR", APAC'2007, Indore, India, January 2007

[2] M. Steck et al, "Beam Accumulation with the SIS Electron Cooler", NIM A441(2000) 175-182.

[3] H. W. Zhao et al, "First Results of SECRAL at 18GHz for Intense Beam Production Highly Charged Ions", HEPNP Vol (31) S1 (2007)8-12.

COMPARISON OF THE HOLLOW ELECTRON BEAM DEVICES AND ELECTRON HEATING

V. Parkhomchuk, BINP, Novosibirsk, Russia

Abstract

In the previous two years after COOL05 a new generation of low energy electron coolers with variable electron beam profile was successfully commissioned with Pb^{+54} ion beams at CERN LEIR and at IMP (China, Lanzhou) CSRm with C^{+6}. A hollow electron beam profile with low electron beam density at the center helps to suppress recombination at the accumulation zone and to increase the lifetime of the ion beam. First experiments with a vertically offset electron beam (with aim to control overcooling the storage stack of ion beam) were made at the RECYCLER high energy electron cooler (FNAL) with very different conditions for accumulation and cooling antiprotons. In this paper the parameters of these different experiments with electron cooling are discussed in the frame of a model of electron heating. The aim is to integrate the experience of using the hollow electron beam cooling, test model and to find recommendations for the next generation electron coolers for the FAIR p.

ELECTRON COOLING AND HEATING

Cooling manifests itself in damping single particle oscillations and coherent oscillations of ion beams. The presence of the electrons in the cooling section and high phase space density of the ion beam after cooling can be sources of the development of instabilities and beam losses [1]. These problems were the subjects of discussions of many reports [2,3] but their final understanding is still far in future. Modulation of the electron beam energy helps to increase the threshold current of the ions [4]. The square-wave modulation of the electron beam energy decreases the cooling rate for the central (equilibrium) energy but helps cooling of the tail energy ions. Control of the transverses ion beam profile after cooling was not so easy because of a very fast increase of the cooling power for small amplitude radial oscillations of the ions.

In order to avoid overcooling in the transverse direction a so called "painted" electron beam position has been proposed. A fast manipulation of the transverse positions and angle of the electron beam in a high energy cooler so that tails cooled more intensively was discussed for the projected cooler for RHIC [5]. At high voltage the cooling time is about a few hours and fast manipulation of the electron beam energy and of the transverse positions can be made relatively easyly. But for the low energy coolers with cooling times of a few milliseconds the electron gun with a special control electrode was designed to produce electron beams with variable profiles [6]. In this electron gun the control electrode voltage can produce a practically hollow electron beam in a steady mode. In the moment of passing the cooling section the ions with not have an equilibrium energy but move in the rest electron gas. By the action of the friction force they lose momentum as:

$$\delta p = -\frac{4\pi e^4 Z^2 n_e \ln(\frac{\rho_{\max}}{\rho_{\min}})\tau}{mMV^3} p = -\lambda \times p\,, \qquad (1)$$

where e is the electron charge, Z is the ion charge in units e, n_e is the electron beam density, m and M are the electron and ion masses, respectively, t is the time of flight through the cooling section in the reference frame of the beam system, r_{max}, r_{min} are the maximum and minimal impact distances, and l is the single pass cooling decrement. There is normal cooling interaction, but the neighbouring ions inside distance r_{max} obtain almost the same momentum kick δp and a slight increase of the kinetic energy in the ion beam (these ions do not have a correlation $\delta p\, V$ and the term $<\delta p * V>=0$ is equal to 0):

$$\delta E_{ion} = -\delta p V + \frac{\delta p^2}{2M} n_i \frac{4\pi}{3} \rho_{\max}^3 = \qquad ,(2)$$

$$(-2\lambda + \lambda^2 \times N^*) E_{ion} = -2\lambda(1 - \omega_e^2 \omega_i^2 \tau^4 g) E_{ion}$$

where ω_e , ω_i are the plasma frequencies of the electron and ion beams, N^* is the number of neighbouring ions inside the distance r_{max} , g is a numerical factor close to unity which can be calculated more carefully by numerical integration in the interaction zone of the ion. The meaning of this equation is that the single pass cooling decrement should be limited by the number of ions in the interaction zone $l<2/N^*$. Practically there exists a limit of the product of electron and ion beam densities [7]:

$$n_i \times n_e \le \frac{6}{r_e r_i (c\tau)^4 * g(4\pi)^2 \ln(\rho_{\max}/\rho_{\min})} \,. \qquad (3)$$

Decreasing the electron beam density at the center of the storage zone opens additional space for the accumulation of a more intense ion beam.

FNAL COOLER EXPERIMENTS

In september 2005 cooling experiments have been performed with the RECYCLER cooler with a vertical offset of the electron beam. Initially the electron beam was shifted by 9 mm and then moved step by step inside the antiproton beam as demonstrated in fig.1. Straight lines along the longitudinal emittance data were used for the calculation of the longitudinal cooling time which changed from 40 hours for 9 mm offset to 2 hours for 1.5 mm offset. The experience of using electron cooling in

the RECYCLER shows the too strong overcooling of the antiproton beam that leads to a degradation of the lifetime and to a fast loss of antiprotons. With offset cooling it was possible to cool the tail of the beam without overcooling the centre zone of the beam. On 4 oct. 2005 the RECYCLER operators had achieved a record number of antiprotons and a world record of initial luminosity of the hadron collider TEVATRON: $1.413\times10^{32}(1/cm^2 sec)$ with using a vertical offset of the electron beam. It was complicated gymnastics with the vertical position of the electron beam so that the lifetime was high but the antiproton beam was cooled before injection into the TEVATRON.

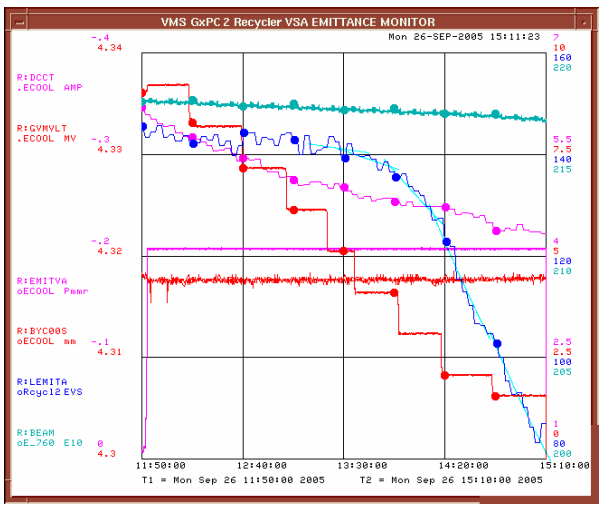

Figure 1: The RECYCLER cooling with vertical offset of the electron beam: red line: position of electron beam - 9,8,7,6,5,4,3,2,1.5 mm, blue line: cooling of longitudinal emittance (80-160 eV*s scale).

These were the first experiments with using the technique of "painting" in the transverse direction for the distribution of the electron beam cooling power.

LEIR EXPERIMENTS AT CERN

Experiments with comparison of cooling with two different settings of the voltage in the electron gun are done for the accumulation of an ion beam of Pb^{+54} for (Ucontr=0, Uanode=1800 V, parabolic shape of the electron beam with maximum at center) and (U_{contr}=200 V, U_{anode}=900 V slightly hollow electron beam with 20% decrease of the density at the center of the electron beam). For both settings the electron beam current was close to 0.1 A but the accumulated ion beam current increased from $0.7\text{x}10^9$ up to $1.3\ \text{x}10^9$ Pb ions as is shown in figs. 2a and 2b. The main reason of this increase of the ion beam current is clearly seen in the figures as an improved lifetime from 6 sec to 12 sec. after end of injection.

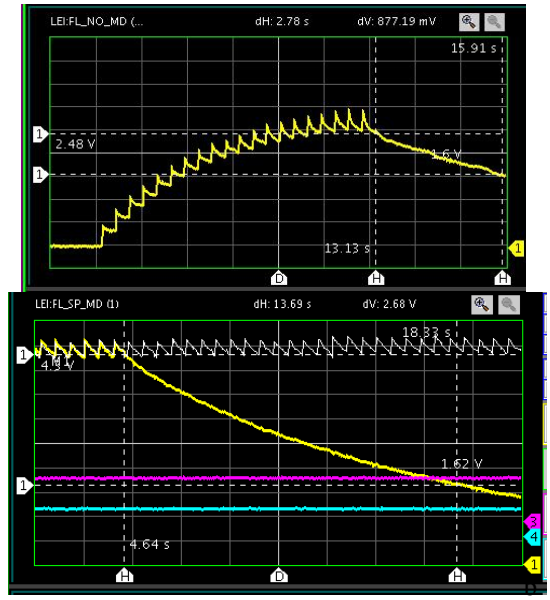

Figure 2 (a,b): Ion beam accumulation at maximum density at center (a), and minimum density at the center (b).

The lifetime after end of injection is 6.3 s for an "a" profile of the electron beam and with initial decay at several times faster (1-2 sec). For a "b" shape profile the lifetime is 13.8 s and without fast losses just after injection. There are basic problems of "electron heating" and decreasing the decay rate for the electron beam profile with lower density at the center which support this plasma oscillations model. For these first experiments, the lifetime in the LEIR ring varies by no evident reasons and in the next experiments, this phenomenon should be studied more carefully.

Almost all our measurements were performed with the standard magnetic cycle lasting 3.6 seconds during which 2 linac pulses are cooled and stacked at 4.2 MeV/u, then accelerated to 72 MeV/u before being extracted to the PS ring. Fig. 3 shows the typical magnet cycle used for our measure of the number of ions in the beam.

Figure 3: The standard magnet cycle of acceleration: magenta line: magnet field value (3), green line: anode voltage for the control of the electron beam current (2), yellow line: number of ion (1) at beam.

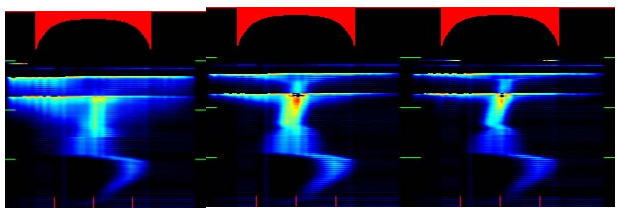

Figure 4: Cooling with the same profile but different electron beam current Uanode(V)=300,600,900, Ucontr(V)=150,300,450, Je(mA)=60,110,260, emittance (mm*mrad)=0.15,0.05,0.03, cooling time (s)= 0.5, 0.08, 0.05. Red color shows the profile of the electron beam.

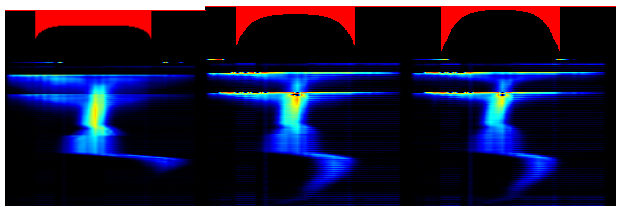

Figure 5: Cooling with different profiles, Uanode(V)= 1000,600,500, Ucontr(V)=200,300,600 Je(mA)= 140, 160, 280, e (mm*mrad)= 0.07, 0.07, 0.07, tcooling(s)=0.3, 0.1, 0.07.

Figs. 4 and 5 show signals of the ion beam profile monitor measured for different shapes of the electron beam profile. From fig.5c is clearly seen that a hollow electron beam cools very effectively ions with high amplitude (up to 2.5 cm) and without large increase of the equilibrium emittance. Fig.6 shows that the cooling time is about 0.2 s and after switch off the electron beam, the emittance blows up from 0.1 to 0.35 mm*mrad*π (2-2.2 sec) by the action IBS .

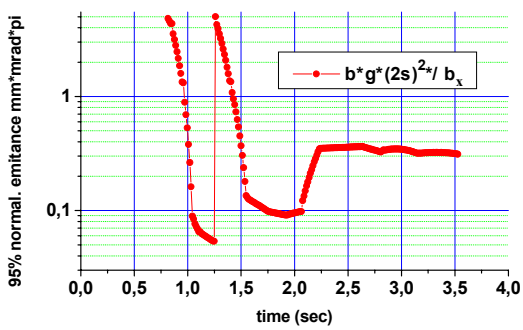

Figure 6: Variation of the normalized emittance (95%) variation vs. time inside the magnet cycle. (ooling current 0.1 A)

At time of acceleration the normalized emittance stays constant close to 0.35 *mm*mrad*π within measuring accuracy.

CSR (IMP) EXPERIMENTS

A first demonstration of successful electron cooling and accumulation of an C^{+6} ion beam was made in july 2006. At the beginning of 2007 a systematic study of the accumulation and acceleration at high energy and with da ifferent ion beam was started. Let us discuss just some experiments with electron cooling with a hollow electron beam. From fig.7 we can clearly see that the optimum of accumulation and acceleration is near Ucontr/Ugrid=0.4 when the ratio of the electron beam density at the center to the average density is near 0.5. This acceleration was made after accumulation with electron cooling and with 10 injections.

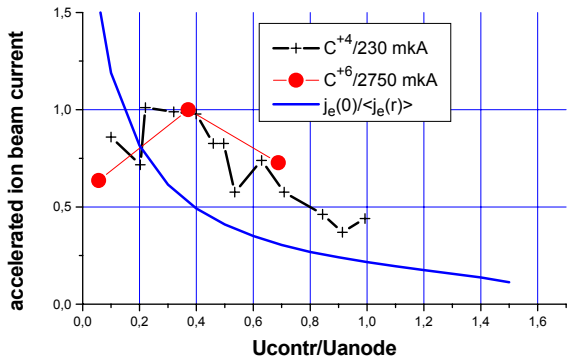

Figure 7: Maximum ion beam currents for ions C^{+4},C^{+6} accelerated at CSRm vs. the ratio of grid anode voltage which change of the shape of the electron beam profile. Blue line: ratio of the electron beam density at the center to the average density (for a flat beam j(0)/<j(r)>=g_e=1).

An experiment with accumulation of maximal C^{+6} is shown in fig. 8. For fitting the data is used a model with two components. The cooled ion beam has a decay time of 10 sec but some part of the newly injected ions have decay times of just 0.2 sec. This fast decay fraction increases with accumulating more current and for an 600μA ion beam current almost all newly injected beam beam was lost. After this further accumulation is stopped- all newly injected ions are lost.

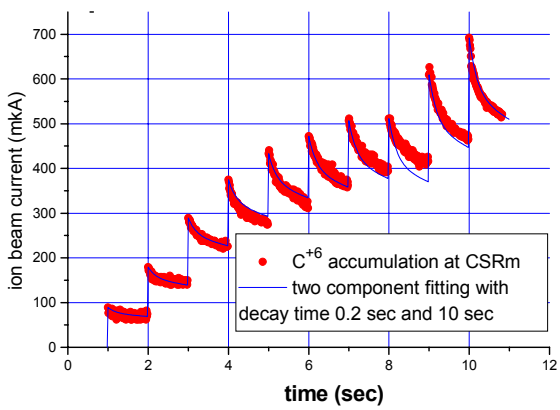

Figure 8: Example of accumulation at CSRm: C^{+6} ion beam with fitting to the two component model.

Increasing the ratio Ucontr/Uanode= 0.217kV /0.586kV demonstrates accumulation up to 1500μA. After stop of injection the initial lifetime was very short but

after decay of the ion beam to a current of less then 600μA the lifetime became very long ~400 sec. This high lifetime (400s) means that the fast losse is generated by space charge fluctuations in the accumulated intensive ion beam. The diffusion by this space charge noise of the plasma oscillations at the core of the ion beam killed all newly injected ions with high amplitudes that have weak cooling.

LIFETIME WITH ELECTRON COOLING

The presence of plasma oscillations can be demonstrated by the variation of the lifetime with different electron coolers. Fig. 9 shows the lifetimes in different rings with electron cooler in units of number of turns vs. the parameter which characterises the interactions of the ions with the electrons: $\delta = \omega_e^2 \omega_i^2 \tau^4$. The data in for the coolers are listed at table.1.

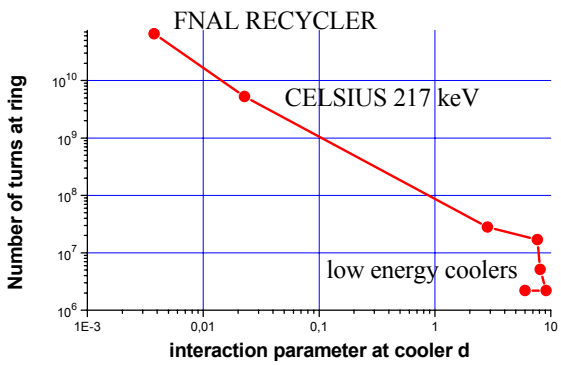

Figure 9: Ion lifetime vs. the parameter δ for the different coolers.

Table 1: Parameters of different coolers

ring	E_e keV	J_e mA	a_e cm(g)	Ion	J_i mA	a_i mm	ΔQ_L	τ	δ
SIS	6.5	400	2.2(1)	Kr^{+34}	5	4.5	0.12	62	6
LEIR	2.5	100	2.12(2)	Pb^{+54}	2.5	2	0.12	67	9
LEIR	2.5	100	2.12(0.5)	Pb^{+54}	5	3	0.11	67	8
CSRm	3.8	100	2.12(0.4)	C^{+6}	1.5	5	0.05	100	7.6
CELSIUS	6	60	1(1)	He^{+2}	0.5	1	0.05	43	2.8
CELSIUS	217	600	1(1)	p^{+1}	6	0.7	0.01	6	0.023
RECYCLER	4300	200	0.3(1)	$\bar{p}^{-1}$	32	2.5	0.008	7	0.003

The effect of electron heating is very similar to so called beam-beam effects in colliders. Usually the life-time of luminosity decreases with the beam-beam tune shift ΔQ_{bb} as $N_{turns} \sim 1/(\Delta Q_{bb})^3$[9]. The relation between tune shift for a symmetric collider and δ is determined as: $\delta = \omega_e^2 \omega_i^2 \tau^4 = (4\pi \Delta Q_{bb} l_b / \beta^*)^2$. From fig. 9 we can see the fast decrease of the lifetime under electron cooling for high values of the space charge parameter δ. For next generation storage rings (e.g. HESR) will be used electron cooler systems with long coolers and high intensity electron beams. The proper distribution the of the electron beam profile can help to optimise the luminosity and the ion beam lifetime.

CONCLUSION

First successful cooling experiments with using hollow electron beams demonstrated the high potential of these coolers with variable profiles of thr electron beam. Effects from the nonlinear electric field that were discussed as source of problems for hollow electron beams [10] were not detected. Parameters of ion beams after cooling obtained at LEIR and CSRm are close to the proposed ones. The technique of hollow electron beam cooling has a high potential for optimization. It will be interesting to test this cooling in experiments with internal targets.

REFERENCES

[1] D. Reistad, L.Hermansson, T. Bergmark, O. Johanson, A.Simonsson, A.V. Burov, "Measurements of electron cooling and electron heating at CELSIUS", Proceedings of the Workshop on Beam Cooling and Related Topics, Montreux, Switzerland, 4-8 October 1993,CERN 94-03,p.183.

[2] V.V. Parkhomchuk, A.N. Skrinsky, "Electron cooling: 35 years of development", Physics-Uspehi 43,(5) 433-452 (2000)

[3] 3. V. Parkhomchuk, L. Hermansson, D. Reistad "Problems of Electron Cooling of High Brightness Ion Beams", IICFA Beam Dynamics Newsletters, No21, April 2000 pp.106-110.

[4] L.Hermansson, D.Reistad, "Electron cooling at CELSIUS", NIM in Phys.Res. A 441(2000) 140-144.

[5] Eectron cooling for RHIC, BNL, C-A/AP 47 April 2001. "RHIC, 50 MeV cooling", http://www.agsrhichome.bnl.gov/AP/ap_notes/ap_note_47.pdf

[6] A. Bubley, "The electron gun with variable beam profile for optimisation of electron cooling", EPAC02, http://www.jacow.org/e02/PAPERS/WEPRI049.PDF

[7] V.V. Parkhomchuk, Cool05, 18-23 Sept.2005, AIP conference proceedings, 821, p.249-258. http://conferences.fnal.gov/cool05/Presentations/Thursday/R01_Parkhomchuk.pdf

[8] L.R.Prost, "Status of high energy electron cooler in FNAL's RECYCLING ring". RUPAC06, http://www.jacow.org/r06/PAPERS/WEB002.PDF

[9] P.M. Ivanov, I.A. Koop, "Luminosity and the beam beam effects", Third advanced ICFA beam dynamics workshop on beam-beam effects in circular colliders", 29 May- 3June 1989, Novosibirsk.

[10] V.Ziemann, "Electron cooler driven transverse resonances". EPAC98. http://www.jacow.org/e98/PAPERS/THP27F.PDF

IONIZATION COOLING*

Rolland P. Johnson#, Muons, Inc., 552 N. Batavia Ave., Batavia, IL 60510, USA

Abstract

All three components of a particle's momentum are reduced as a particle passes through and ionizes some energy absorbing material. If the longitudinal momentum is regenerated by RF cavities, the angular divergence of the particle is reduced. This is the basic concept of ionization cooling. What can be done for a muon beam with this simple idea is almost amazing, especially considering that the muon lifetime is only 2.2 μs in its rest frame. In this paper we discuss the evolution and present status of this idea, where we are now ready to design muon colliders, neutrino factories, and intense muon beams with very effective cooling in all three dimensions. The discussion will include the heating effects and absorber Z-dependence of multiple scattering, numerical simulation programs, the accuracy of scattering models, emittance exchange, helical cooling channels, parametric-resonance ionization cooling, and the ionization cooling demonstration experiments, MICE and MANX.

INTRODUCTION

In the last year, several things have come together to reinvigorate muon collider enthusiasts: 1) There is a great interest to have a plan for a next-generation project that would continue the energy-frontier accelerator tradition in the US. 2) The uncertainties in need, cost, and siting of the International Linear Collider (ILC) have made it clear even to strong ILC supporters that a "Plan B" is prudent. 3) While impressive work has been done toward a neutrino factory based on a muon storage ring [1,2], the physics case for such a machine will have to wait for results of experiments that are just getting started. Thus there is some muon-related accelerator expertise that is available for muon collider development. 4) As discussed below, several new ideas have arisen in the last five years for six-dimensional (6D) muon beam cooling. The advantage of achieving high luminosity in a muon collider with beams of smaller emittance and fewer muons has been recognized as a great advantage for many reasons [3], including less proton driver power on target, fewer detector background issues, and relaxed site boundary radiation limitations.

Another advantage of small 6D emittance for a collider is that the cost of muon acceleration can be reduced by using the high frequency RF techniques being developed for the ILC. To the extent that muon beams can be cooled well enough, the muon collider is an upgrade path for the ILC or its natural evolution if LHC results imply that the ILC energy is too low or if its cost is too great.

Effective 6D cooling and the recirculating of muons in the same RF structures that are used for the proton driver may enable a powerful new way to feed a storage ring for a neutrino factory [4]. This would put neutrino factory and muon collider development on a common path such that a muon collider could be realized in several stages, each independently funded and driven by high-energy physics goals, e.g. a very cool stopping muon beam, neutrino factory, Higgs factory, energy frontier collider.

IONIZATION COOLING PRICIPLES

The idea that the transverse emittance of a beam could be reduced by passing it through an energy absorber originated in Novosibirsk many years ago [5,6]. Figure 1 is a schematic of the concept, showing how the angular divergence of a beam can be reduced.

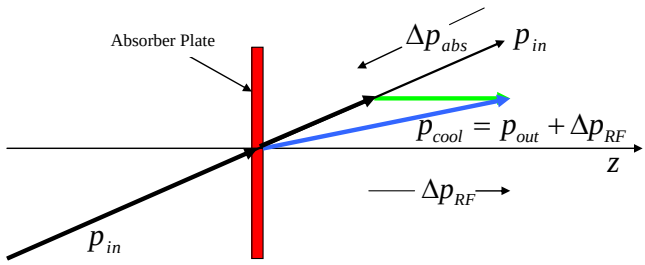

Figure 1: Conceptual picture of the principle of Ionization Cooling. Each particle loses momentum by ionizing an energy absorber, where only the longitudinal momentum is restored by RF cavities. The angular divergence is reduced until limited by multiple scattering, so that a low-Z absorber is favored.

Ionization cooling of a muon beam involves passing a magnetically focused beam through an energy absorber, where the muon transverse and longitudinal momentum components are reduced, and through RF cavities, where only the longitudinal component is regenerated. After some distance, the transverse components shrink to the point where they come into equilibrium with the heating caused by multiple coulomb scattering. The equation describing the rate of cooling is a balance between these cooling (first term) and heating (second term) effects:

$$\frac{d\varepsilon_n}{ds} = -\frac{1}{\beta^2}\frac{dE_\mu}{ds}\frac{\varepsilon_n}{E_\mu} + \frac{1}{\beta^3}\frac{\beta_\perp (0.014)^2}{2E_\mu m_\mu X_0} \quad [1].$$

Here ε_n is the normalized emittance, E_μ is the muon energy in GeV, dE_μ/ds and X_0 are the energy loss and radiation length of the absorber medium, $\beta_\perp$ is the transverse beta-function of the magnetic channel, and β is the particle velocity. Muons passing through an absorber experience energy and momentum loss due to collisions with electrons. The derivations and discussions of the basic formulae of ionization cooling can be found in many places [7,8], where the energy loss is described by the Bethe-Bloch theory and the multiple-scattering heating is

*Supported by DOE SBIR/STTR grants DE-FG02-03ER83722, 04ER86191, 04ER84016, 05ER86252, 05ER86253 and 06ER86282.
#rol@muonsinc.gov

described by the Moliere theory [9].

Setting the heating and cooling terms equal defines the equilibrium emittance, the very smallest possible with the given parameters:

$$\varepsilon_n^{(equ.)} = \frac{\beta_\perp (0.014)^2}{2\beta m_\mu \frac{dE_\mu}{ds} X_0} \quad [2].$$

A cooling factor ($F_{cool} = X_0 dE_\mu/ds$) can be uniquely defined for each material, and since cooling takes place in each transverse plane, the figure of merit is F_{cool}^2. For a particular material, F_{cool} is independent of density, since energy loss is proportional to density, and radiation length is inversely proportional to density. The inverse of F_{cool}^2 corresponds to the best equilibrium emittance that can be achieved. Super-conducting solenoidal focusing is used to give a value of $\beta_\perp$ as low as 10 cm. Figure 2 shows F_{cool}^2 for many materials of interest.

Gaseous hydrogen is the very best material that one can use from the standpoint of the final equilibrium emittance. Also, since the exponential cooling rate depends on the difference between the initial and final emittances, it provides the very best cooling rate.

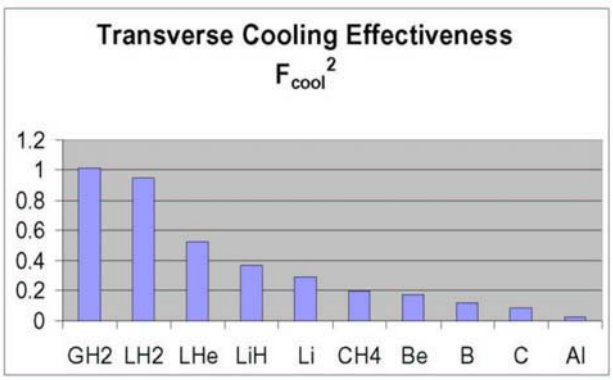

Figure 2: A comparison of the cooling figure of merit for light materials. The equilibrium beam emittance in each transverse plane is inversely proportional to the product of the energy loss and the radiation length. The graph indicates the total figure of merit,

Fundamental Limitations

The transverse beta function, $\beta_\perp$, is proportional to the ratio of momentum divided by the magnetic field. So the lowest equilibrium emittance requires the lowest momentum and the highest field.

As implied by the Bethe-Bloch equation and shown on figure 3, the fact that *dE/dx* increases as the momentum decreases means that once the momentum is below a few hundred MeV/c, any transverse cooling is necessarily accompanied by longitudinal heating. To a certain extent, this unwanted heating can be mitigated by modifying the dispersion function [10] and/or changing the profile of an absorber with shaped edges.

The maximum magnetic field is a technological problem discussed below. One solution is the use of High Temperature Superconducting (HTS) magnets that can develop large fields at low temperatures.

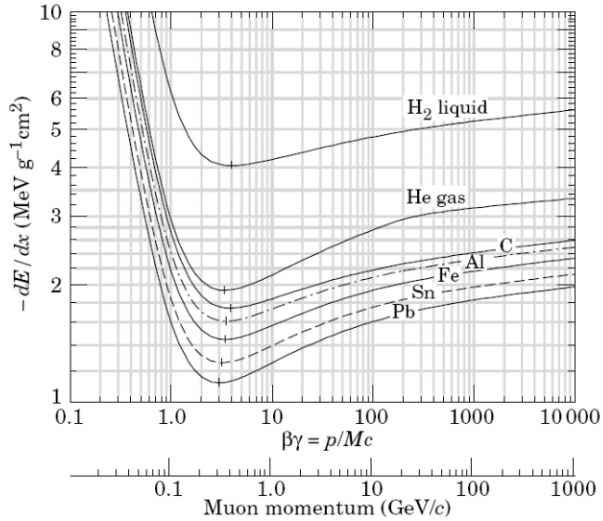

Figure 3: Energy loss for muons in various materials taken from the Particle Data Group [11], where the minimum *dE/dx* for hydrogen occurs near 300 MeV/c.

Multiple Scattering

Investigations of the deficiencies of the Moliere theory for low-Z materials [12] and other models [13] have been vindicated by recent measurements, as shown in figure 4. These seemingly small differences in the tails of the scattering distributions can have large consequences for long cooling channels. An ICOOL investigation indicated that as much as a factor of 3 improvement in cooling factor could be achieved with scattering models that agreed with the MuScat [14] data compared to the Geant4 models that we have used up to now.

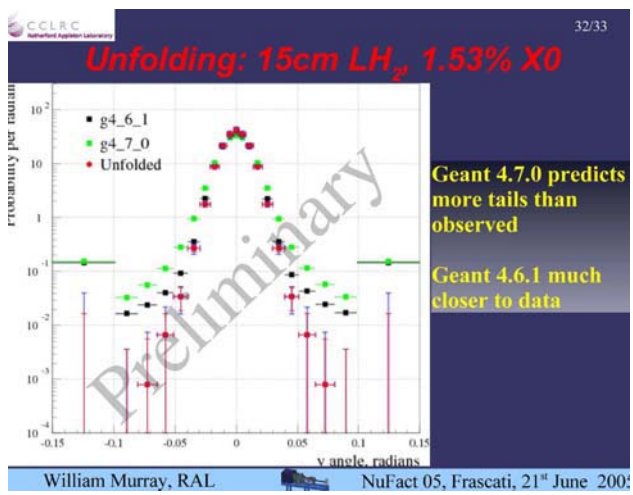

Figure 4: Comparison of angular distributions of the MuScat experiment for muons scattering off of hydrogen with two different releases of the Geant4 simulation program. The (red) experimental data show smaller tails.

Charge Sign Effects

As a post-doc I was fortunate to experimentally discover that a 500 to 1500 MeV/c muon's range depends on its charge sign [15]. Although Hans Bethe assured me in a telephone call in 1971 that such an effect must be

down by 6 orders of magnitude, later discussions with David Jackson substantiated my claim that the range difference was three orders of magnitude larger than Bethe believed. The effects of the interference between one- and two-photon exchange diagrams were calculated [16] and gave good agreement with our measurements. A range difference for very low energy muons had previously been noted by Barkas [17] but apparently not understood. The extreme ionization cooling required for muon colliders may require that effects as small as the charge-sign interference be included in the simulation cross-sections to get the energy loss and multiple scattering right.

Emittance Exchange

To achieve longitudinal cooling requires emittance exchange with transverse oscillations. Emittance exchange, in turn, requires the introduction of a beam bend that creates dispersion, a correlation between the orbit and energy of a particle. Figure 5 shows the conceptual pictures of the two approaches that have recently been studied most. In the left of figure 5 the use of a wedge absorber is shown, where the beam is dispersed across a wedge of energy absorbing material such that higher momentum particles lose more energy. The muons become more monoenergetic after they pass through the wedge, while the transverse emittance is increased as part of the emittance exchange process.

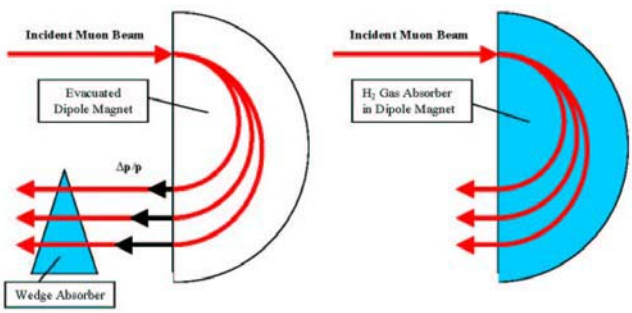

Figure 5: Emittance exchange. LEFT: Wedge Absorber Technique. RIGHT: Homogeneous Absorber Technique where dispersion causes higher energy particles to have longer path length and thus more ionization energy loss.

Gas-filled Helical Cooling Channel (HCC)

The HCC is an attractive example of a cooling channel based on this idea of energy loss dependence on path length in a continuous absorber. One version of the HCC uses a series of high-gradient RF cavities filled with dense hydrogen gas, where the cavities are in a magnetic channel composed of a solenoidal field with superimposed helical transverse dipole and quadrupole fields [18,19]. In this scheme, energy loss, RF energy regeneration, emittance exchange, and longitudinal and transverse cooling happen simultaneously.

The helical dipole magnet creates an outward radial force due to the longitudinal momentum of the particle while the solenoidal magnet creates an inward radial force due to the transverse momentum of the particle, or

$$F_{h-dipole} \approx p_z \times B_\perp; \quad b \equiv B_\perp$$
$$F_{solenoid} \approx -p_\perp \times B_z; \quad B \equiv B_z ,$$

where B is the field of the solenoid, the axis of which defines the z axis, and b is the field of the transverse helical dipole at the particle position. By moving to the rotating frame of the helical fields, a time and z-independent Hamiltonian can be formed to derive the beam stability and cooling behavior [20].

Use of a continuous homogeneous absorber as shown on the right side of figure 5, rather than wedges at discrete points, implies a positive dispersion along the entire cooling path, a condition that has been shown to exist for an appropriately designed helical dipole channel. We have also shown that this condition is compatible with stable periodic orbits. The simple idea that emittance exchange can occur in a practical homogeneous absorber without shaped edges followed from the observation that RF cavities pressurized with a low Z gas are possible [21,22].

The analytic relationships derived from this analysis were used to guide simulations using a code developed based on the GEANT4 [23] program called G4Beamline [24] and also using ICOOL [25] developed at BNL.

Simulation results [10] show cooling factors or 50,000 for a series of 4 250 MeV/c HCC segments, where the magnet diameters are decreased and fields are increased as the beam cools. In this example the final field would be 17 T with a hydrogen gas pressure of 400 atmospheres.

Momentum-dependent HCC

While the HCC described above operates at constant energy, another set of applications follows from HCC designs where the strengths of the fields are allowed to change with the muon momentum. The first example was a 6D precooler, where the beam is slowed in a liquid hydrogen absorber at the end of the pion decay channel, with 6D emittance reduction by a factor of 6. Another example is a stopping muon beam based on a HCC [26].

Parametric Resonance Ionization Cooling

Parametric-resonance Ionization Cooling (PIC) [27], requires a half integer resonance to be induced in a ring or beam line such that the normal elliptical motion of particles in $x - x'$ phase space becomes hyperbolic, with particles moving to smaller x and larger x' as they pass down the beam line. (This is almost identical to the technique used for half integer extraction from a synchrotron where the hyperbolic trajectories go to small x' and larger x to pass the wires of an extraction septum.) Thin absorbers placed at the focal points of the channel then cool the angular divergence of the beam by the usual ionization cooling mechanism, where each absorber is followed by RF cavities. Thus in PIC the phase space area is reduced in x due to the dynamics of

the parametric resonance and x' is reduced or constrained by ionization cooling. The basic theory of PIC is being developed to include aberrations and higher order effects. Simulations using linear channels of alternating dipoles, quadrupoles, solenoids, or HCC's are now underway [28].

PHASE SP ACE REPARTITIONS

Reverse Emittance Exchange Using Absorbers

A muon beam that is well cooled at one or two hundred MeV/c will have its unnormalized longitudinal emittance reduced by a factor of a thousand or more at 100 or more GeV collider energy. At the interaction point in the collider the bunch length would then be much shorter than the IR focal length. In reverse emittance exchange (REMEX), we propose to repartition the emittances to lengthen each bunch and narrow the transverse emittances using beryllium wedge energy absorbers.

Calculations show that two stages of reverse emittance exchange, one at low energy and one at a higher energy before energy straggling becomes significant, can reduce each transverse emittance by an order of magnitude.

Muon Bunch Coalescing

One of the newest ideas is to cool less intense bunches at low energy and to recombine them into intense bunches at higher energy where wake fields, beam loading, and space charge tune shifts are less problematic [29].

Beryllium Wedges

Both PIC and REMEX techniques involve the focusing of a beam onto an energy absorber for which beryllium is better suited than the lower-Z materials shown in figure 2. First, the higher density of beryllium allows the thickness of the absorber to be a smaller fraction of a betatron wavelength and thereby more effective since the average betatron function in the region of the absorber is closer to the minimum value. Second, the energy straggling in the absorbers leads to longitudinal heating that must be controlled by emittance exchange. Thus the absorbers should be thin wedges made of beryllium which can easily be refrigerated to handle the heat deposition of the bright beams required by a muon collider.

NEW COOLING TECHNOLOGY

Pressurized RF Cavities

A gaseous energy absorber enables an entirely new technology to generate high accelerating gradients for muons by using the high-pressure region of the Paschen curve [30]. This idea of filling RF cavities with gas is new for particle accelerators and is only possible for muons because they do not scatter as do strongly interacting protons or shower as do less-massive electrons. Measurements by Muons, Inc. and IIT at Fermilab have demonstrated that hydrogen gas suppresses RF breakdown very well, about a factor six better than helium at the same temperature and pressure. Consequently, much more gradient is possible in a hydrogen-filled RF cavity than is needed to overcome the ionization energy loss, provided one can supply the required RF power. Hydrogen is also twice as good as helium in ionization cooling effectiveness, viscosity, and heat capacity. Present research efforts include tests of materials in pressurized RF Cavities in magnetic fields [31] as shown in Figure 6, where an external field causes no apparent reduction in maximum achievable gradient. Crucial beam tests of the concept are scheduled in 2008.

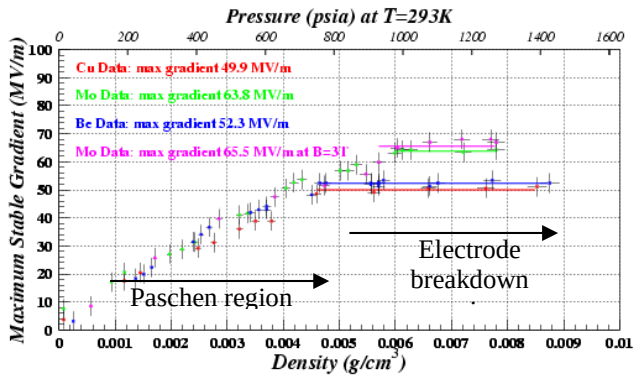

Figure 6: Measurements of the maximum stable RF gradient as a function of hydrogen gas pressure at 805 MHz with no magnetic field for three different electrode materials: Cu (red), Mo (green), and Be (blue). The cavity was also operated at the same gradients in a 3T field with Mo electrodes (magenta).

High-pressure RF cavities near the pion production target can be used to simultaneously capture, bunch rotate, and cool the muon beam as it emerges from the decaying pions [32]. We have started an R & D effort to develop RF cavities that will operate in the extreme conditions near a production target and an effort to simulate the simultaneous capture, phase rotation, and cooling of muons as they are created from pion decay.

High Temperature Superconductor

Magnets made with high-temperature superconducting (HTS) coils operating at low temperatures have the potential to produce extremely high fields for use in accelerators and beam lines. The specific application of interest is to use a very high field (greater than 30 Tesla) solenoid to provide a very small beta region for the final stages of cooling for a muon collider. With the commercial availability of HTS conductor based on BSCCO or YBCO technology with high current carrying capacity at 4.2 K, very high field solenoid magnets should be possible. We are evaluating the technical issues associated with building this magnet [33]. In particular we are addressing how to mitigate the high Lorentz stresses associated with this high field magnet.

Helical Solenoid

The original concept of the HCC involved a rather complex magnet with separate coils to provide the required solenoidal, helical dipole, and helical quadrupole fields. Figure 7 shows a new design [34] called a Helical

Solenoid (HS) which uses simple offset coils to generate the three required components.

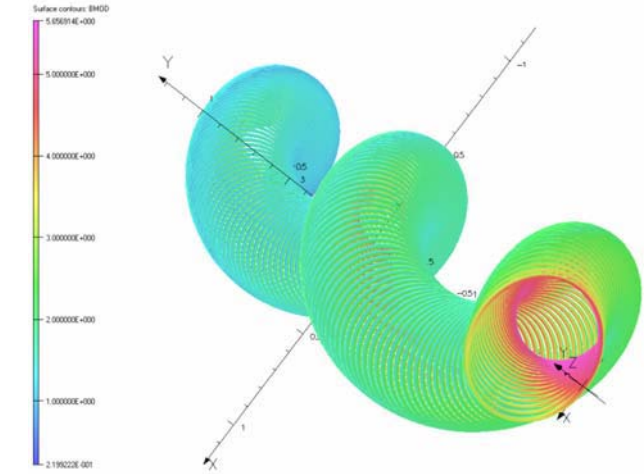

Figure 7: Helical Solenoid geometry and flux density for the Helical Solenoid magnet for MANX.

Muon Cooling Demonstration Experiments

The MICE project, designed primarily to develop transverse cooling to reduce neutrino factory cost, is described in another paper at this meeting. Figure 8 shows MANX, a 6D muon cooling demonstration experiment based on a HCC with variable field strengths. It is being designed to slow a 300 MeV/c muon beam to about 150 MeV/c in a HCC filled with liquid helium [35].

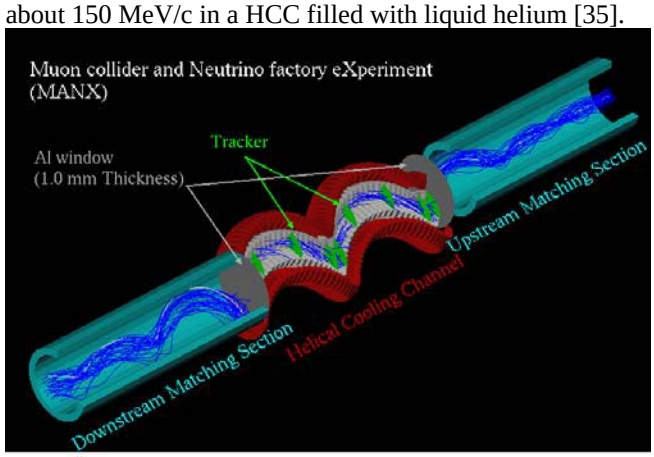

Figure 8: Conceptual picture of the MANX apparatus. The helical solenoidal magnets shown in red enclose the LHe ionization energy absorber, which is separated from the vacuum of the matching sections by thin Al windows.

SUMMARY

New 6D muon cooling ideas described above and a new enthusiasm to build an energy frontier lepton collider to follow the LHC are creating an exciting environment for muon collider research. More new ideas are described by Robert Palmer in another COOL07 contribution. High-pressure RF experiments are underway, with encouraging results. A 6D HCC demonstration experiment is being designed and plans for 1.5 TeV and higher center of mass muon colliders are being studied at Fermilab.

REFERENCES

[1] http://www.fnal.gov/projects/muon collider/nu/study/report/machine report/
[2] http://www.cap.bnl.gov/mumu/studyii/FS2-report
[3] http://www.muonsinc.com/mcwfeb07
[4] M. Popovic et al., Linac06
[5] M. Ado, V. I. Balbekov, Sov. At. Energy 31, 731,'71
[6] A. N. Skrinsky and V. V. Parkhomchuk, Sov. J. Part. Nucl. 12, 223 (1981).
[7]D. M. Kaplan, http://www.slac.stanford.edu/econf/C010630/papers/M102.PDF
[8] P. Gruber, CERN/NUFACT Note 023, http://slap.web.cern.ch/slap/NuFact/NuFact/nf23.pdf
[9] Bethe, H. A.: Molière's Theory of Multiple Scattering, Phys Rev. **89**, 1256 (1953)
[10] K. Yonehara et al., EPAC06
[11] http://pdg.lbl.gov/2007/reviews/passagerpp.pdf
[12] A. V. Tollestrup & J. Monroe, MUCOOL note 176
[13] W. W. M. Allison et al., arxiv.org/PS_ cache/physics/pdf/0609/0609195v1.pdf
[14] W. Murray, NuFact05, Frascati
[15] A. R. Clark et al., OBSERVED DIFFERENCES IN THE RANGES OF POSITIVE AND NEGATIVE MUONS, PL 41B, 229 (1972)
[16] J. D. Jackson and R. L. McCarthy, "Z3 Corrections to Energy Loss and Range", Phys. Rev. B6, 4131 http://link aps org/abstract/PRB/v6/p4131
[17] See PDG discussion of the "Barkas effect", http://pdg.lbl.gov/2007/reviews/passagerpp.pdf
[18] V. Kashikhin et al., Magnets for the MANX Cooling Demonstration Experiment, MOPAS012, PAC07
[19] S. A. Kahn et al., Magnet Systems for Helical Muon Cooling Channels, MOPAN117, PAC07
[20] Y. Derbenev and R. P. Johnson, Phys. Rev. Spec. Topics Accel. and Beams 8, 041002 (2005)
[21] R. P. Johnson et al., Linac04
[22] M. BastaniNejad et al.,RF Breakdown in Pressurized RF Cavities, WEPMS071, PAC07
[23] http://wwwasd.web.cern.ch/wwwasd/geant4/geant4
[24] T. J. Roberts et al., G4BL Simulation, PAC07
[25] R. Fernow, ICOOL, http://pubweb.bnl.gov/users/fernow/www/icool/readme.html
[26] M. A. C. Cummings et al., Stopping Muons Beams, THPMN096, PAC07
[27] Yaroslav Derbenev et al., COOL05
[28] D. Newsham et al., Simulations of PIC, PAC07
[29] C. M. Ankenbrandt et al., Muon Bunch Coalescing,, THMN095, PAC07
[30] Meek and Craggs, Electrical Breakdown in Gases, John Wiley & Sons, 1978, p. 557
[31] P. Hanlet et al., EPAC06
[32] D. Neuffer et al., Use of Gas-filled Cavities in Muon Capture, THPMN106, PAC07
[33] S. A. Kahn et al., High Field HTS Solenoid for Muon Cooling, MOPAN118, PAC07
[34] V. Kashikhin et al., PAC07
[35] K. Yonehara et al., Design of the MANX Demonstration Experiment, PAC07

MICE: THE INTERNATIONAL MUON IONIZATION COOLING EXPERIMENT

J.S. Graulich and A. Blondel#, Université de Genève, Geneva, Switzerland

Abstract

An international experiment to demonstrate muon ionization cooling is scheduled for beam at Rutherford Appleton Laboratory (RAL) in 2008. The experiment comprises one cell of the neutrino factory cooling channel, along with upstream and downstream detectors to identify individual muons and measure their initial and final 6D emittance to a precision of 0.1%. Magnetic design of the beam line and cooling channel are complete and portions are under construction. This paper describes the experiment, including cooling channel hardware designs, fabrication status, and running plans. Phase 1 of the experiment will prepare the beam line and provide detector systems, including time-of-flight, Cherenkov, scintillating-fiber trackers and their spectrometer solenoids, and an electromagnetic calorimeter. The Phase 2 system will add the cooling channel components, including liquid-hydrogen absorbers embedded in superconducting Focus Coil solenoids, 201-MHz normal-conducting RF cavities, and their surrounding Coupling Coil solenoids. The goal of MICE Collaboration is to complete the experiment by 2010.

INTRODUCTION

The MICE experiment is part of the R&D programme towards a neutrino factory based on a muon storage ring, largely considered as the most precise tool to probe neutrino physics in the future. The cooling of muon beam is largely unexplored and is a major source of uncertainty on the cost and construction time of a neutrino factory. MICE has been designed to demonstrate that it is possible to engineer, build and operate safely and reliably a section of linear muon ionization cooling channel similar to the one proposed in the US Feasibility Studies [1].

The MICE collaboration started in 2001 [2] and now rallies about 140 people, engineers, accelerator and particle physicists from more than 40 institutes in Europe, USA, China and Japan. The MICE collaboration is also working together with the US MuCool Collaboration with whom we are sharing several objectives.

GENERAL DESIGN

An introduction to Ionization Cooling can be found in [3]. Basically, under certain conditions, cooling is obtained when the beam passes through some energy absorbing material where it loses energy by ionization. The conditions are 1) the Z of the material is low, in order to maximize the ratio between the stopping power, responsible for cooling, and the multiple scattering cross section, responsible for heating; 2) The transverse β function is small at the position of the absorber. Additionally, in order to avoid de-bunching effects, the energy loss in the forward direction should be compensated for. In line with these principles, the MICE cooling channel is made of three liquid hydrogen absorbers alternating with two linac sections, each composed of four RF cavities. Rapid evaluation has shown that this system should be able to cool a 6π mm rad beam by about 10% [4]. The aim of the experiment is to measure this cooling effect with a precision of 1%, requiring a precision of 0.1% on the emittance measurement before and after the cooling channel. Such a precision can't be obtained with standard beam diagnostic instrumentation hence we had to adopt a particle per particle tracking approach. It has been shown as well [5] that pion and electron contamination in the beam introduces a bias on the emittance measurement, imposing the presence of some detectors dedicated to Particle Identification (PID), both upstream and downstream. The tracker and PID detectors have been designed using a simulation code based on GEANT4 [6] but developed especially for MICE. This code, called G4MICE, after validation by precise experimental data, can be considered as one of the most important deliverable of the experiment since it should become a reliable tool for the design of future cooling channels.

THE BEAM LINE

MICE will be hosted by the Rutherford Appleton Laboratory (RAL) in the UK. A new muon beam line is under construction using the existing, 800 MeV, 300 μA, proton synchrotron, ISIS. The beam line components are shown in Figure 1 and detailed in [7]. A short description is given below.

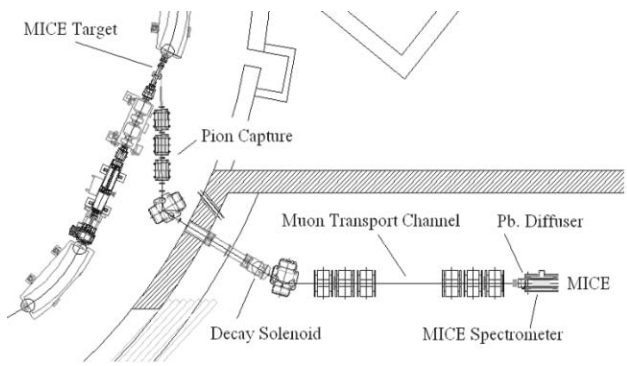

Figure 1: Schematic view of the MICE beam line at ISIS, Rutherford Appleton Laboratory, UK.

The Target System

A dedicated system has been designed in Sheffield to dip the Ti target into the halo of the beam in the few milliseconds preceding the extraction of the primary

#Alain.Blondel@cern.ch

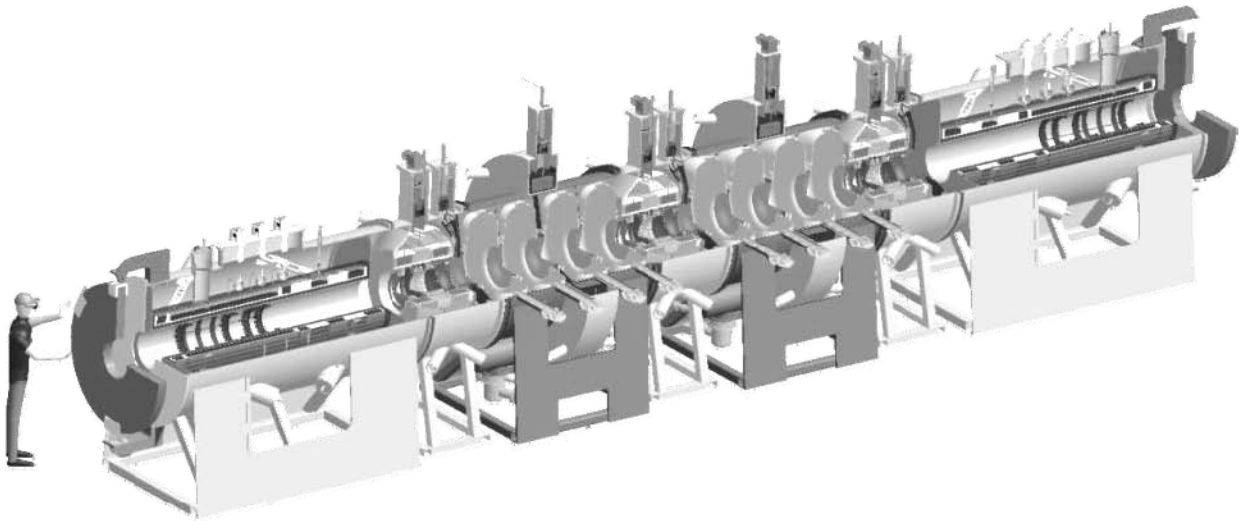

Figure 2: 3-D cutaway rendering of the MICE apparatus, showing, from left to right, the first spectrometer module, the first LH_2 absorber module, the RF module and, at the centre of symmetry, the second absorber module.

proton beam. The main constraint was that the target should be completely out of the way when the injection of the next ISIS bunch starts. The acceleration of $80g$ m/s^2 necessary to meet this requirement has been achieved recently with the target attached to a leaded bronze shaft driven by induction coils. The system has been running reliably for more than 12 weeks at a rate of 1 Hz, producing more than 5 millions actuations. However, the observation of a small amount of dust produced by the wearing of the shaft and bearings has led to the decision to test a diamond-like carbon coated shaft.

Pion Collection and decay

The pions produced by the collision of the protons on the target are captured by a triplet of quadrupoles, followed by a dipole selecting the pion's momentum. The pions then decay in a 5 m long, 12 cm bore, supra-conducting (SC) solenoid (5 T) which is the contribution to the experiment from the Paul Scherrer Institute, Switzerland. All the magnetic elements in the ISIS vault have been put in place before the accelerator start-up in August 2007. Unfortunately, a vacuum leak in the cooling system of the solenoid prevented us to install it and forced us to add temporary radiation shielding in the hall, disturbing the plan for subsequent installations.

Muon optics

After the decay solenoid, a second dipole selects muons with half the momentum of the original pions (backward muons). This particular setting ensures a very large reduction of the pion content in the muon beam. Muon beam central momentum will be selectable from 140 MeV/c to 240 MeV/c. The entire beam line has been designed to obtain about 600 muons traversing the cooling channel per target shot.

The second dipole is already mounted on rails, allowing transverse translation and necessary clearance for the decay solenoid installation. After the second dipole, two triplets of quadrupoles transport the beam up to the entrance of the cooling channel where a lead diffuser distribution system provides variable beam emittance from less than 1π mm rad up to 10π mm rad.

THE COOLING CHANNEL

The MICE cooling channel is illustrated in Figure 2, together with the upstream and downstream trackers that are also part of the main magnetic channel.

Absorber Module

The absorber module (Fig. 3) is made of two main components. The first is the liquid hydrogen container and distribution system. It represents a considerable safety challenge. It has been designed and prototyped in KEK and is now under test at the MuCool Test Area (MTA) in Fermilab, USA. The container is 35 cm long for a volume of 20 litters. It is sealed by 0.18 mm, curved

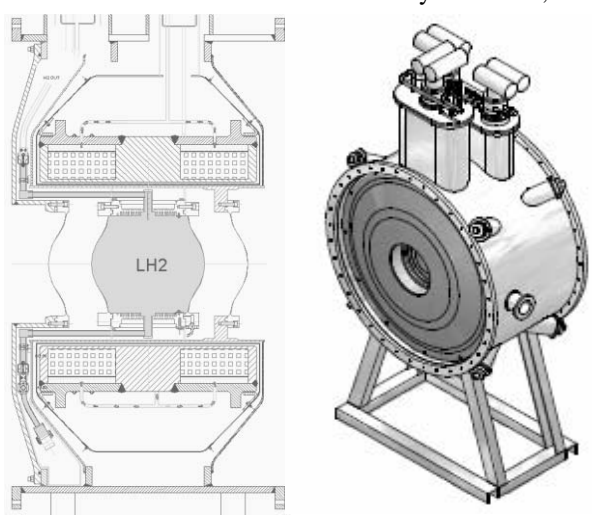

Figure 3: Left: a sketch of the LH_2 absorber. Right: 3D rendering of the Focus Coil Module.

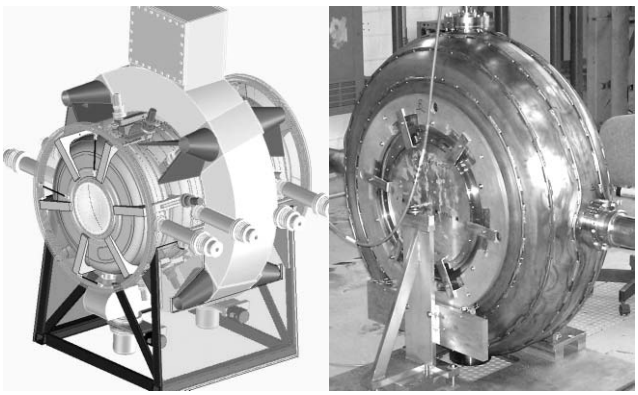

Figure 4: The RF and Coupling Coil Module. Left: three-dimensional rendering of the preliminary design. Right: The prototype 201 MHz RF Cavity.

aluminium windows. The entire LH2 system is double walled for safety reasons. Each muon looses about 12 MeV in the absorber, that is 1 W for a beam of 5 10^{11} muons per second. The system has been designed to absorb up to 15 W of power.

The second main component of the absorber module is the set of two SC focus coils, providing the required small β function inside the absorber. The two coils can be operated with identical or opposite polarities, allowing a rapid field flip inside the absorber. The absorber modules are now out for tender and should be delivered in mid 2009.

RF Module

Relatively low RF frequency (201 MHz) has been chosen to handle the extended muon beam. A large SC coil surrounds the cavities allowing for magnetic coupling with the neighbouring focus coils. The magnetic field inside the RF cavities reaches a few Tesla, precluding the use of SC cavities and enhancing field emission.

Large, water cooled, copper cavity has been prototyped and tested at the MTA. It has reached easily 16 MV/m without magnetic field. Further tests are needed to validate the pre-curved beryllium windows used to isolate the individual cavities and to study the behaviour under large magnetic field. Simulations have shown that the RF background stays at an acceptable level in the condition of the experiment. The RF and Coupling Coil Module (RFCC) is still in the design phase but the production of the coupling coils should start shortly, thanks to a fruitful collaboration with ICST in Harbin, China. The delivery of the first RFCC is scheduled for summer 2009.

THE PARTICLE DETECTORS

The particle detectors are based on standard particle physics techniques. Apart from the tracker, the data digitalization and readout use commercial VME electronics controlled by PCs running Linux.

Spectrometers

The two spectrometers modules are fully symmetrical. Each is made of a cylindrical tracker immerged into a solenoid field of 4 T. The main solenoid coil is flanked by two correcting coils ensuring field uniformity. Two additional coils on the absorber side provide matching optics with the cooling channel. These magnets are in the manufacturing process with delivery of the first coil expected for spring 2008.

The tracker inside has been optimized to minimize the amount of material in the beam. It is made of 5 stations of 350 μm scintillating fibres, exploiting the technology of the Fermilab-D0 tracker [8]. Each station is perpendicular to the beam axis and is made of three plans of fibres rotated by 60° in order to resolve degeneracy in case of multiple hits. By recording hit positions in the five stations, it is possible to reconstruct the full helix track of the particle and obtain the longitudinal and transverse momentum. A four-station prototype has been constructed and tested in beam at KEK in 2005 with magnetic field. It has shown a spatial resolution better than 440 μm, allowing a momentum resolution of 1.5 Mev/c in p_T and 3 Mev/c in p_z for a typical muon at 200 MeV/c. The first tracker, completed with the fifth station will be tested with comics ray in November 2007 and installed in the beam early 2008. The two complete spectrometers are expected for summer 2008.

Time of Flight Stations

Three Time-of-Flight (TOF) stations are placed along the beam line in the experimental hall, respectively between the two triplets of quadrupoles, just before the diffuser and just after the downstream spectrometer. They are made of two crossed plans of plastic scintillator slabs, 1" thick and a few centimetres wide (Fig. 5). Each slab is equipped with standard light guides and Photomultiplier Tubes (PMT). Tests in beam have shown that this design

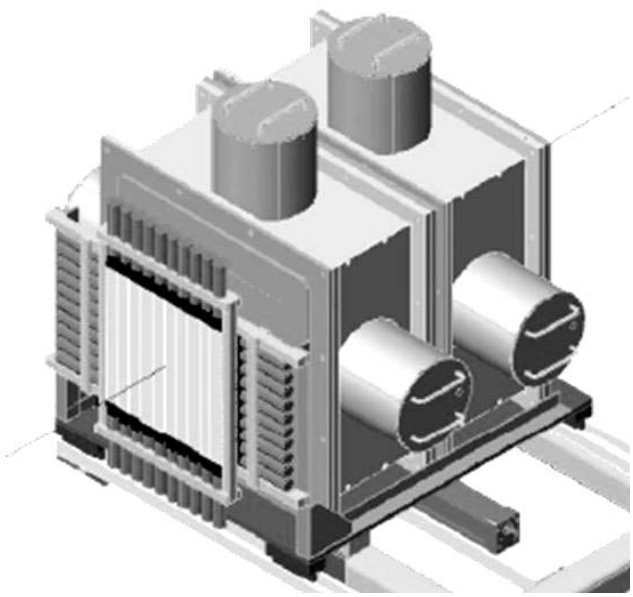

Figure 5: 3-D rendering of the upstream PID module, showing the first TOF station (foreground) and the two Cherenkov counters (background).

allows a resolution on the time of flight between two stations of 70 ps [9]. The first two stations provide a good muon/pion separation at low energy while the second two provide the time information needed for 6D emittance measurement as well as the time of arrival with respect to the RF phase. The main problem encountered with the design of the TOF stations is the intense fringe field coming from the solenoid coils and imposing a heavy iron magnetic shielding. The first two stations are under construction and will be delivered in November 2007.

Cherenkov Counters

The two Cherenkov counters share the same design. A three dimensional view is shown in Figure 5. The Cherenkov light produced in a 2.3 cm thick layer of hydrophobic aerogel is collected by four intersecting conical mirrors reflecting it on four 8" PMTs. Refractive indices of 1.07 and 1.12 are used respectively for the two aerogel plans, ensuring a good muon/pion/electron separation at high momentum when electrons trigger both counters, muons only one and pions none. At lower momentum, the TOF counters can be used to complete the PID. The first Cherenkov counter is already assembled at RAL and will be tested in November 2007 together with the first tracker and the TOF stations. The second counter is under construction in the US and will be delivered to RAL later this year.

Electron Muon Calorimeter

The last particle detector is dedicated to the separation between the muons and the electrons produced by muon decaying in the cooling channel. A careful design study [10] has demonstrated that a better PID is obtained with a detector made of two parts. The first part is a 4 cm thick conventional sampling calorimeter similar to the one used for the KLOE experiment [11]. Grooved lead foils interleaved with scintillating fibres force the electrons to shower while most of the muons are going through. The second part is a fully active plastic scintillator wall, thick enough to stop all the muons and segmented along the beam axis (z axis) to allow range measurement. The layer thickness also increases along the z axis to improve the performance of the system for low energy muons, almost stopped in the first layer. Muons and electrons behave very differently in such a device. Electrons lose more energy in the first layer while muons exhibit the Bragg peak in the last layer. In general, the energy deposit of the muon is much larger than that of the electron for which a significant part of the kinetic energy is radiated as gamma rays and is not detected by the scintillator. Apart for the last layer, the energy deposit is also much more homogenous since the muon tack angle is conserved. Last but not least, for the muons, there is a well defined relation between the total energy deposit and the range which is less pronounced from the electron distribution.

A prototype of the first part, manufactured in Rome III has been tested in beam in the summer 2006. The final production is nearly finished. The second part is still at the prototyping stage in Trieste, Italy. The plan is to use extruded scintillator with individual wavelength shifter fibres coupled to standard or solid sate (Si) PMTs.

CONCLUSION

The installation of the MICE experiment is underway at RAL, UK. The major challenge of the experiment is the operation of large gradient RF cavities in intense magnetic field and in the vicinity of liquid hydrogen cells.

The beam line commissioning will start in early 2008. In the meanwhile, the particle detectors will be commissioned with cosmic rays. The first observation of ionization cooling with a partial setup is expected for mid 2009, after the delivery of the first absorber. The complete setup should be operational by the end of 2009 and the final result, the first performance measurement of a realistic muon ionization cooling channel, delivered in 2010.

REFERENCES

[1] M. Zisman, "Review of U.S. Neutrino Factory Studies", Nuclear Physics B155-1, May 2006, pp. 336-338, and references there in.

[2] The MICE web site, http//mice.iit.edu offers very complete documentation links and references.

[3] R.P. Johnson, "Ionization Cooling", COOL07, Bad Kreuznach, September 2007, TUM2I04.

[4] P. Drumm, Proceedings of PAC'05, Knoxville, May 2005, pp. 398-400

[5] R. Sandström, "Background and Instrumentation in MICE", PhD Thesis, Geneva, 2007.

[6] GEANT4 Collaboration, Nuclear Instruments and Methods in Physics Research A 506 (2003) 250-303, and IEEE Transactions on Nuclear Science 53-1 (2006) 270-278.

[7] K. Tilley et al, Proceedings of EPAC'06, Edinburgh, WEPLS002, pp. 2397-2399

[8] T. Hart, "MICE Tracker Data Acquisition Using D0 Analog Front End IIt Boards", MICE Note 139, April 2006 and
The MICE tracker group, "Specification of the scintillating and clear fibre for the MICE scintillating fibre trackers", MICE Note 135, December 2005, http://mice.iit.edu/notes/notes.html

[9] M. Bonesini et al, "Study of the MICE TOF prototypes performance at the BTF test beam", MICE Note 163, February 2007, http://mice.iit.edu/notes/notes.html

[10] R. Sandström, "Comparison of two calorimeter designs", MICE Note 146, September 2006, http://mice.iit.edu/notes/notes.html

[11] J. Lee-Franzini, "The KLOE electromagnetic calorimeter", Nuclear Instruments and Methods in Physics Research A 360 (1995) 201-205

A COMPLETE SCHEME FOR A MUON COLLIDER *

Robert B. Palmer, J. Scott Berg, Richard C. Fernow, Juan Carlos Gallardo, Harold G. Kirk
BNL, Upton, NY, U.S.A.
Yuri Alexahin, David Neuffer, Fermilab, Batavia, IL, U.S.A.
Stephen Alan Kahn, Muons Inc, Batavia, IL, U.S.A.
Don J. Summers, University of Mississippi, Oxford, MS, U.S.A.

Abstract

A complete scheme for production, cooling, acceleration, and ring for a 1.5 TeV center of mass muon collider is presented, together with parameters for two higher energy machines. The schemes starts with the front end of a proposed neutrino factory that yields bunch trains of both muon signs. Six dimensional cooling in long-period helical lattices reduces the longitudinal emittance until it becomes possible to merge the trains into single bunches, one of each sign. Further cooling in all dimensions is applied to the single bunches in further helical lattices. Final transverse cooling to the required parameters is achieved in 50 T solenoids.

Table 1: Parameters of three muon colliders. Note 1: Depth is relative to any nearby low land, e.g. Fox river at FNAL. Note 2: Survival is from the end of phase rotation to the collider ring.

$E_{\rm c.m.s}$ (TeV)	1.5	4	8
$\mathcal{L}$ (10^{34} cm^{2}sec^{-1})	1	4	8
Beam-beam $\Delta\nu$	0.1	0.1	0.1
μ/bunch (10^{12})	2	2	2
$< B_{\rm ring} >$ (T)	5.2	5.2	10.4
$\beta^* = \sigma_z$ (mm)	10	3	3
rms dp/p (%)	0.09	0.12	0.06
Depth for ν rad [1] (m)	13	135	540
Muon Survival [2]	≈0.07	≈0.07	≈0.07
Rep. rate (Hz)	13	6	3
$P_{\rm driver}$ (MW)	≈4	≈ 1.8	≈ 0.8
$\epsilon_\perp$ (π mm mrad)	25	25	25
$\epsilon_\parallel$ (π mm rad)	72	72	72

INTRODUCTION

Muon colliders were first proposed by Budker in 1969 [1], and later discussed by others [3]. A more detailed study was done for Snowmass 96 [4], but in none of these was a complete scheme defined for the manipulation and cooling of the required muons.

Muon colliders would allow the high energy study of point-like collisions of leptons without some of the difficulties associated with high energy electrons; e.g. the synchrotron radiation requiring their acceleration to be essentially linear, and as a result, long. Muons can be accelerated in smaller rings and offer other advantages, but they are produced only diffusely and they decay rapidly, making the detailed design of such machines difficult. In this paper, we outline a complete scheme for capture, phase manipulation and cooling of the muons, every component of which has been simulated at some level.

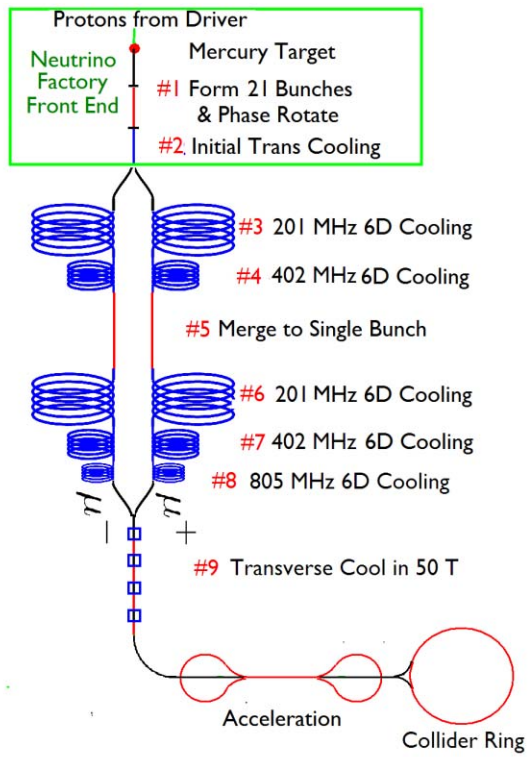

Figure 1: (Color) Schematic of the components of a Muon Collider.

The work in this paper was performed as part of the NFMCC collaboration [5], the recently formed MCTF [6], and Muons Inc. [7].

COLLIDER PARAMETERS

Table 1 gives parameters for muon colliders at three energies. Those at 1.5 TeV correspond to a recent collider ring design [9]. The 4 TeV example is taken from the 96–

* This work was presented by A. Sessler at the workshop. This work was supported by US Department of Energy under contracts AC02-98CH10886 and DE-AC02-76CH03000

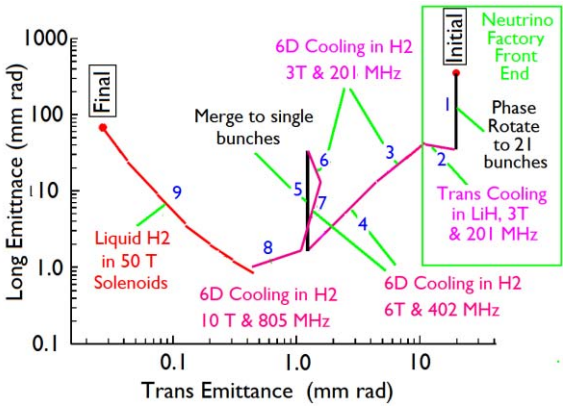

Figure 2: (Color) Transverse vs. longitudinal emittances before and after each stage. The nine stages are indicated with the numeral 1–9.

study [4]. The 8 TeV is an extrapolation assuming higher bending fields and more challenging interaction point parameters. All three use the same muon intensities and emittances, although the repetition rates for the higher energy machines are reduced to control neutrino radiation.

PROPOSED SYSTEM

Figure 1 shows a schematic of the components of the system. Figure 2 shows a plot of the longitudinal and transverse emittances of the muons as they progress from production to the specified requirements for the colliders. The subsystems used to manipulate and cool the beams to meet these requirements are indicated by the numerals 1–9 on the figures.

Proton Driver

The proton driver requirements depend on the muon survival estimates that will be discussed in a later section. We further assume, from the neutrino factory studies, that pion production in the 21 best bunches, at the end of phase rotation, is 1.7% per proton per GeV. The resulting required proton bunches, for different energies, are given in Tb. 2. For efficiency in the following phase rotation, an rms bunch length of 3 ns is required. The space charge tune shift and required longitudinal phase space densities are challenging at the lower proton energies, but easier at the higher energies.

Table 2: Proton bunch intensity for three different proton energies

E (GeV)	8	24	60
N_p (10^{13})	21	7	2.8

Production, Phase Rotation, and Initial Cooling

The muons are generated by the decay of pions produced by proton bunches interacting in a mercury jet target [8]. These pions are captured by a 20 T solenoid surrounding the target, followed by an adiabatic lowering of the field to 3 T in a decay channel.

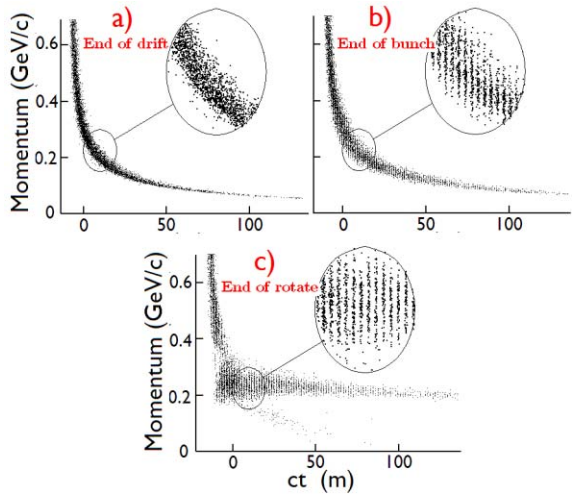

Figure 3: Phase spaces during phase rotation a) before bunching, b) after bunching, c) after rotation.

The first manipulation (#1), referred to as phase rotation [10], converts the initial single short muon bunch with very large energy spread into a train of bunches with much reduced energy spread of which we use only 21. The initial bunch is allowed to lengthen and develop a time-energy correlation in a 110 m drift. It is then bunched into a train, without changing the time-energy correlation, using rf cavities whose frequency varies with location, falling from 333 MHz to 234 MHz. Then, by phase and frequency control, the rf accelerates the low energy bunches and decelerates the high energy ones. Figure 3 shows ICOOL [11] simulations of the phase spaces before bunching, after bunching, and after rotation.

Muons of both signs are captured and then (#2) cooled transversely in a linear channel using LiH absorbers, periodic alternating 2.8 T solenoids, and pillbox 201 MHz rf cavities. All the components up to this point are identical to those described in a recent study [12] for a Neutrino Factory.

6D Cooling Before Merge

The next stage (#3) cools simultaneously in all 6 dimensions. The lattice [13], shown in figure 4, uses 3 T solenoids for focus, weak dipoles (generated by tilting the solenoids) to generate bending and dispersion, wedge shaped liquid hydrogen filled absorbers where the cooling takes place, and 201 MHz rf, to replenish the energy lost in the absorbers. The dipole fields cause the lattices to curve, forming a slow upward or downward helix (see inset in Fig. 5). The following stage (#4) uses a lattice essentially

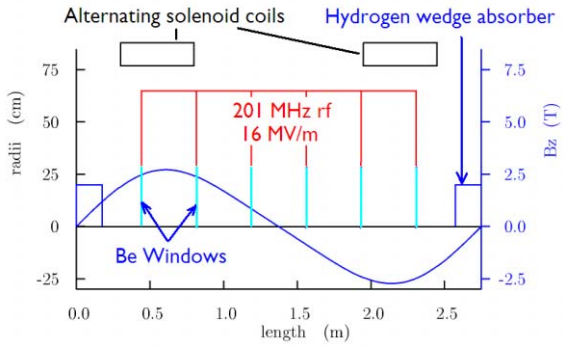

Figure 4: (Color) One cell of the first 6D cooling lattice.

the same as (#3), but with twice the field strength, half the geometric dimensions, and 402 instead of 201 MHz rf. Figure 5 shows the results of a simulation of both systems using ICOOL. Although this simulation was done for circular, rather than the helical geometry, it used realistic coil and rf geometries. Preliminary studies [14] suggest that the differences introduced by the helical, instead of circular, geometries will be negligible. The simulation did not include the required matching between the two stages. The simulations also used fields that, while they satisfied Maxwell's equations and had realistic strengths, were not actually calculated from specified coils. Simulations reported in reference [13], using fields from actual coils, gave slightly better results.

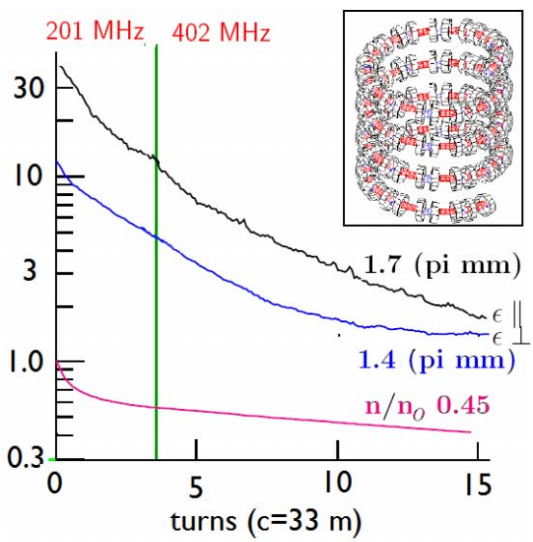

Figure 5: (Color) ICOOL simulation of 6D cooling in stages (#3) & (#4). Inset: long pitch helical geometry of (#3).

Bunch Merge

Since collider luminosity is proportional to the square of the number of muons per bunch, it is important to use relatively few bunches with many muons per bunch. Capturing

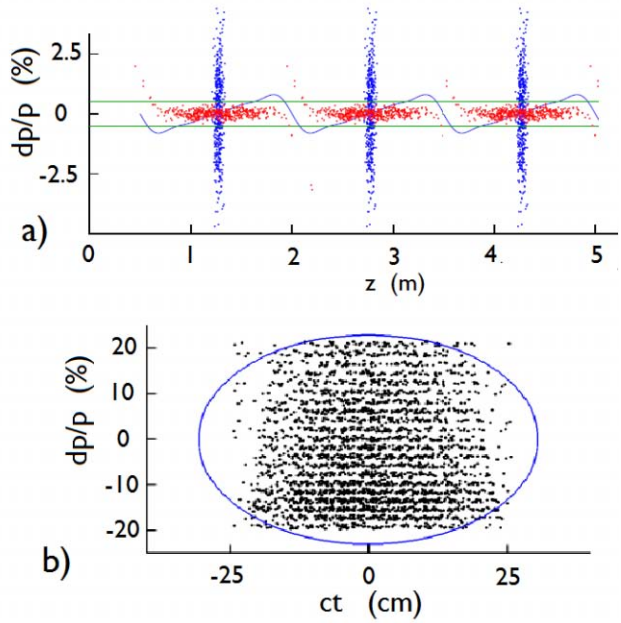

Figure 6: (Color) 1D Simulation of merge (#5): a) before (blue) and after (red) first rotation, b) after second rotation.

the initial muon phase space directly into single bunches requires low frequency ($\approx$ 30 MHz) rf, and thus low gradients, resulting in slow initial cooling. It is thus advantageous to capture initially into multiple bunches at 201 MHz and merge them after cooling allows them to be recombined into a single bunch at that frequency. This recombination (#5) is done in two stages: a) using a drift followed by 201 MHz rf, with harmonics, the individual bunches are phase rotated to fill the spaces between bunches and lower their energy spread; followed by b) 5 MHz rf, plus harmonics, interspersed along a long drift to phase rotate the train into a single bunch that can be captured using 201 MHz. Results of an initial one dimensional simulation of this process is shown in Fig. 6. Work is ongoing on the design and simulation of a system with the low frequency rf separated from a following drift in a wiggler system with negative momentum compaction to reduce the length and decay losses.

6D Cooling After Merge

After the bunch merging, the longitudinal emittance of the single bunch is now similar to that at the start of cooling. It can thus be taken through the same, or similar, cooling systems as (#3) and (#4): now numbered (#6) and (#7). One more (#8) stage of 6D cooling has been designed (Fig. 7), using 10 T magnets, hydrogen wedge absorbers, and 805 MHz rf. Its ICOOL simulated performance is show in Fig. 8. Again, the simulation shown used fields that, while they satisfied Maxwell's equations and had realistic strengths, were not actually calculated from specified coil configuration.

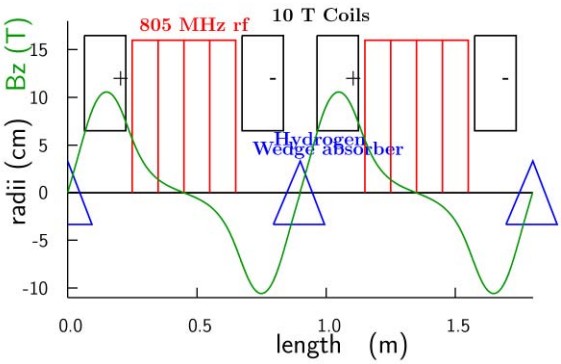

Figure 7: (Color) One cell of the last 6D cooling lattice.

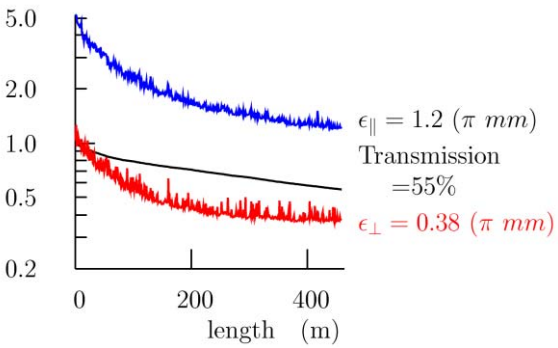

Figure 8: (Color) ICOOL simulation of final 6D cooling lattice (#8) using 10 T solenoids and 805 MHz rf.

Final Transverse Cooling in High Field Solenoids

To attain the required final transverse emittance, the cooling needs stronger focusing than is achievable in the 6D cooling lattices used in the earlier stages. It can be obtained in liquid hydrogen in strong solenoids, if the momentum is allowed to fall sufficiently low. But at the lower momenta the momentum spread, and thus longitudinal emittance, rises relatively rapidly. However, as we see from Fig. 2, the longitudinal emittance after (#8) is far less than that required, so such a rise is acceptable. Figure 9 shows the results of ICOOL simulation of cooling in seven 50 T solenoids. The simulation did not include the required matching and re-accelerations between the solenoids.

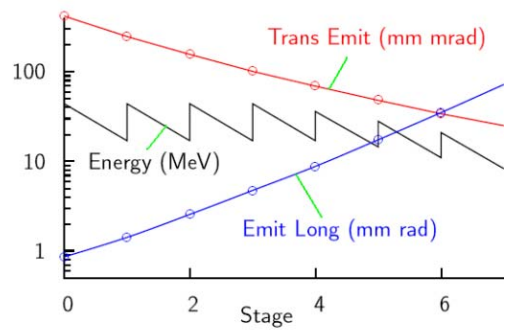

Figure 9: (Color) Results of ICOOL simulations of transverse cooling in liquid hydrogen in 7 sequential 50 T solenoids.

A 45 T hybrid Cu and superconductor solenoid[15] is currently operating at NHFML and an upgrade to 50 T is planned, but this magnet uses a lot of power. A 27 T solenoid using an 8 T YBCO insert at 4K has recently been successfully tested [16]. There is a conceptual design of an all superconducting 50 T solenoid [17].

Acceleration

Sufficiently rapid acceleration is straightforward in linacs and recirculating linear accelerators (RLAs). Lower cost solutions might use fixed field alternating gradient (FFAG) accelerators, rapidly pulsed magnet synchrotrons, and/or hybrid SC and pulsed magnet synchrotrons[18].

Muon Losses

The estimate of muon losses is very preliminary. The simulations assumed Gaussian initial distributions and were not very well matched into each lattice, leading to larger initial losses. And no tapering of the focus parameters as function of length was included, leading to larger losses as the emittances approached their equilibrium. As a result, the losses observed were larger than those deduced using the performances in the mid range of each simulation. Table 3 shows the result of an attempt to estimate realistic losses, but this remains very preliminary. Since it is this estimate that was used to determine the required proton driver specifications used above, these too must be considered very preliminary.

Table 3: Calculated transmission tune shifts at different stages in the system.

	Transmission	Cumulative
Linear transverse pre-cooling	0.7	0.7
Pre-merge RFOFO cooling	≈ 0.5	0.35
Merging	0.8	0.28
Post-merge RFOFO cooling	≈ 0.5	0.14
Final 50 T solenoid cooling	0.7	0.1
Acceleration to 0.75 TeV	0.7	0.07

Collider Ring

For the 1.5 TeV c.m.s, a lattice has been developed [9]. The parameters as given in Tb. 1 were achieved with adequate momentum acceptance but with dynamic transverse acceptance of only at little over 2σ for the specified final emittance. We note however that since luminosity is dependent on the square of the bunch densities, there would be little luminosity loss if the larger amplitudes were collimated prior to injection into the ring.

Space Charge Tune Shifts

For bunches with Gaussian distributions in all dimensions:

$$\frac{\Delta\nu}{\nu_{\rm cell}} = \left(\frac{N_\mu}{\epsilon_\perp}\right) \frac{\beta_{\perp\ \rm ave}\, r_\mu}{2\sqrt{2\pi}\sigma_z\ \ \beta_v\gamma^2}$$

where $\beta_{\perp\ \rm ave} = \left(\frac{L_{\rm cell}}{2\pi\ \nu_{\rm cell}}\right)$ and $r_\mu = 1.35\ 10^{-17}$ m

Then at the the ends of a number of stages in this system, one obtains the tune shifts given in Tb. 4.

Table 4: Calculated maximum space charge tune shifts at different stages in the system.

	N_μ 10^{12}	$\beta_{\perp\rm ave}$ mm	σ_z mm	$\epsilon_\perp$ π μm	p MeV/c	$\Delta\nu/\nu$ %
(#4)	2	292	27	1500	200	0.9
(#6)	12	584	199	1500	200	1.6
(#7)	9	292	20	1500	200	5.9
(#8)	6	191	13	400	200	14.5
(#9_1)	6	222	27	400	100	26.1
(#9_7)	3	93	354	25	42	20.0

Note that N_μ is larger at earlier cooling stages to allow for losses. The first order shifts can be corrected by increasing the focus strength, but tune spreads of half the shifts cannot be corrected.

Before the merge, the shifts are small because the numbers of muons per bunch are small. The only 6D cooling stage with significant tune shift is the last (#8). Its tune accepted $\Delta\nu/\nu \approx 0.7$ which is 5 times the calculated maximum full tune spread of $\pm$ 7.3%, and is not expected to be a problem.

The tune shifts in the 50 T cooling will be significant only during the reaccelerations, where we have assumed $\beta_\perp$s corresponding to 3 T focusing fields. The design of these lattices to accept such tune shifts appears possible, although we are clearly nearing the limit.

ONGOING STUDIES

There is a serious question as to whether the specified gradients of rf cavities operating under vacuum would operate in the specified magnetic fields. This is under study by NFMCC collaboration [5] and alternative designs using high pressure hydrogen gas, or open cell rf with solenoids in the irises, are being considered. The bunching and phase rotation will be optimized for the muon collider, instead of being copied from a neutrino factory. Instead of the slow helices, a planar wiggler lattice is being studied that would cool both muon signs simultaneously, thus greatly simplifying the system. The use of more, but lower field (e.g., 35 T) final cooling solenoids is also under study. Experiments are underway to demonstrate two of the new technologies: mercury target [8], ionization cooling [19]. Further experimental studies are needed.

CONCLUSION

Although much work remains to be done, the scenario outlined here appears to be a plausible solution to the problems of capturing, manipulating, and cooling muons to the specifications for muon colliders with useful luminosities and energies, even up to 8 TeV in the center of mass.

REFERENCES

[1] G. I. Budker, quoted and translated in [2].

[2] D. Cline, in *Physics Potential and Development of $\mu^+\mu^-$ Colliders: Second Workshop; Sausalito, CA 1994*, edited by D. Cline (American Institute of Physics, Woodbury, NY, 1996), pp. 3–6.

[3] A. N. Skrinsky, quoted and translated in [2]; V. V. Parkhomchuk and A. N. Skrinsky, in *Proceedings of the 12th International Conference on High Energy Accelerators, 1983*, edited by F. T. Cole and R. Donaldson, 485; D. Neuffer, Fermilab report FN-319, 1979; D. Neuffer, Part. Accel. **14**, 75 (1983); D. V. Neuffer and R. B. Palmer, in *Fourth European Particle Accelerator Conference*, edited by V. Suller and Ch. Petit-Jean-Genaz (World Scientific, Singapore, 1994), p. 52.

[4] The $\mu^+\mu^-$ Collaboration, reports BNL-52503, Fermi Lab-Conf. 96/092, LBNL-38946, 1996.

[5] http://www.cap.bnl.gov/mumu

[6] http://mctf.fnal.gov

[7] http://www.muonsinc.com

[8] H. G. Kirk *et al.*, *A High-Power Target Experiment at the CERN PS* PAC07, Albuquerque, NM, (MOPAS094).

[9] Y. Alexahin and E. Gianfelice-Wendt, Fermilab report Beams-doc-2724-v1, 2007. URL: http://beamdocs.fnal.gov/AD-public/DocDB/DocumentDatabase

[10] D. Neuffer, report NFMCC-doc-269-v1, 2003. URL: http://nfmcc-docdb.fnal.gov/cgi-bin/DocumentDatabase/

[11] ICOOL, http://pubweb.bnl.gov/people/fernow/icool/readme.html

[12] J. S. Berg *et al.*, Phys. Rev. ST Accel. Beams **9**, 011001 (2006).

[13] R. Palmer *et al.*, Phys. Rev. ST Accel. Beams **8**, 061003 (2005).

[14] Amit Klier, presentation at the Low Emittance Muon Collider Workshop, Fermilab (6-10 Feb 2006). URL: http://www.muonsinc.com/mcwfeb06/

[15] G. B. Lubkin, Phys. Today 47N12, 21 (1994).

[16] http://www.magnet.fsu.edu/mediacenter/news/pressreleases/2007august7.html; http://www.superpower-inc.com/20070807.aspx

[17] S. A. Kahn *et al.*, *A High Field HTS Solenoid for Muon Cooling* PAC07, Albuquerque NM, (MOPAN118).

[18] D.J. Summers *et al.*, *Muon Acceleration to 750 GeV in the Tevatron tunnel for a 1.5 TeV $\mu^+ - \mu^-$ Collider*, PAC07, Albuquerque NM, (THPMS082); also arXiv:0707.0302.

[19] M. Zisman, *Status of the International Muon Ionization Cooling Experiment*, PAC07, Albuquerque NM, (THPMN119); P. Drumm, *MICE: The International Muon Ionisation Cooling experiment*, PAC07, Albuquerque NM, (ROAA004).

THEORETICAL STUDY OF EMITTANCE TRANSFER*

H. Okamoto, K. Kaneta,
Hiroshima University, 1-3-1 Kagamiyama, Higashi-Hiroshima 739-8530, Japan

A. M. Sessler,
LBNL, 1 Cyclotron Road, Berkeley, CA94720, U.S.A.

Abstract

The beam emittance, i.e. the volume of a charged-particle ensemble in six dimensional phase space, is approximately conserved in common accelerators. The concept of "cooling" is thus crucial in improving the beam quality for various machine users. In contrast to cooling, it is rather easy to change the ratios of emittance projections on to the three spatial degrees of freedom. This paper addresses a possible method of controlling the projected emittances with conservative interactions; not only a full emittance exchange but also a partial emittance transfer can readily be achieved in a dedicated storage ring operating near resonance. In a process of eimttance transfer, strong correlations between three directions are naturally developed, which may be useful for specific purposes.

INTRODUCTION

Liouville's theorem implies that the six-dimensional (6D) phase-space volume occupied by a charged-particle beam is an approximate invariant unless the beam is subjected to dissipative interactions (such as in cooling). Symplectic conditions, in a Hamiltonian system (once again, no dissipation), put constraints upon emittance transfer between the various degrees of freedom [1]. We can, however, even in non-dissipative Hamiltonian systems arrange for partial emittance transfers. This process results in phase space correlations and change in the emittance projections on to various phase planes; namely, the projected emittances in three degrees of freedom are controllable while the direction and amount of a possible emittance flow are not very flexible because of the symplectic nature of Hamiltonian systems. In some applications, it is clearly advantageous to optimize the ratios of projected emittances despite the effect of correlations. Since the three emittances are not always equally important, we may consider reducing the emittance of one direction at the sacrifice of the other emittance(s). Emittance exchanging systems have been seriously discussed these days to improve the performance of free electron lasers (FELs) [2,3].

As a possible scheme to achieve efficient emittance control, we study a compact storage ring operating near resonance. The basic features of linear and nonlinear emittance flow are briefly described with numerical examples. A general discussion touching on some of these matters was made over ten years ago and recently published in Ref. [4].

COUPLING STORAGE RING

For a full emittance exchange between the longitudinal and transverse directions, Cornacchia and Emma designed a beam transport channel that employs a special radio-frequency (rf) cavity placed in the middle of a magnetic chicane [5]. Their rectangular rf cavity, excited in a deflective mode, is identical to the *coupling cavity* previously considered for three-dimensional (3D) laser cooling [6]. Although the present scheme is based on a compact ring rather than a short beam transport, we have much higher flexibility in manipulating phase spaces. It is actually straightforward to accomplish a wide range of emittance ratios simply by switching coupling potentials on and off. Furthermore, various linear and nonlinear correlations can be introduced in phase spaces if we switch off coupling (or extract the beam) on the way to a full emittance exchange.

Neglecting interparticle Coulomb interactions, the dynamic motion of a particle in a storage ring can be approximated as the superposition of three harmonic oscillators. The Hamiltonian of interest to us is given by

$$H = \frac{1}{2}\sum_{q=x,y,z}\left[p_q^2 + \left(\frac{\nu_q}{R}\right)^2 q^2\right] + \phi_c(x,y,z;s), \qquad (1)$$

where x, y, and z stand, respectively, for the horizontal, vertical, and longitudinal directions, ν_q $(q = x, y, z)$ is the tune of each direction, R is the average radius of the ring, and the independent variable s is the path length measured along the design beam orbit. Here, $\phi_c(x,y,z;s)$ is an artificial potential that couples three degrees of freedom if required. As an example, let us take a symmetric coupling

$$\phi_c / R = g_x x^m z^n \delta_p(s - s_x) + g_y y^m z^n \delta_p(s - s_y), \qquad (2)$$

where m and n are positive integers, and $g_{x(y)}$ are coupling constants. Since coupling sources are generally electromagnetic devices localized and fixed at specific positions of the ring, we have multiplied each coupling term by a periodic delta function $\delta_p(s)$ with periodicity $2\pi R$. For the sake of simplicity, we assume that the two

*Work supported in part by Japan Society for the Promotion of Science, and by the U.S. Department of Energy, Office of Basic Energy Sciences, under Contract No. DE-AC02-05CH11231.

coupling sources are sitting side by side; namely, $s_x \approx s_y$. Without loss of generality, we set the origin of the s-coordinate at the position of the coupling potential.

The coupling itself can be strengthened by increasing $g_{x(y)}$, but that is not practical, nor necessary. We can prove that, in order to expedite an emittance flow from one direction to another, the two directions have to be on coupling resonance. Typically, we employ difference resonance:

$$m\nu_x - n\nu_z \approx \ell_x, \tag{3a}$$

$$m\nu_y - n\nu_z \approx \ell_y, \tag{3b}$$

where $\ell_{x(y)}$ are integers. The efficiency of the emittance transfer can be controlled by changing the distance from the resonance or the coupling constant. Although most accelerator designers try to avoid such resonances, we rather exploit them here. It is straightforward to derive the following invariant under the conditions (3):

$$I \equiv \frac{\varepsilon_x + \varepsilon_y}{m} + \frac{\varepsilon_z}{n} = \text{const.}, \tag{4}$$

where ε_q $(q = x, y, z)$ is the projected emittance in q-direction. Due to the existence of this invariant, the sum of all three projected emittances is always bounded. Figure 1 shows an example of typical emittance flow when a linear coupling potential ($m = n = 1$) is taken into account. Clearly, the sum of the three projected emittances is conserved; namely, $\varepsilon_x + \varepsilon_y + \varepsilon_z = \text{const.}$ Needless to say, we can stop the emittance flow at any timing by shutting down the coupling sources, which allows us to choose various ratios of projected emittances.

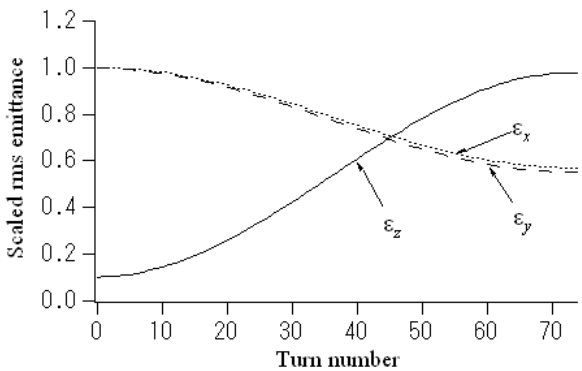

Figure 1: Time evolution of root-mean-squared (rms) projected emittances in the x, y, and z directions. A linear coupling ($m = n = 1$) with $g_x = g_y = 0.01$ and $R = 1$ has been assumed in this example. The tunes are $(\nu_x, \nu_y, \nu_z) = (1.1, 1.1, 0.1)$ satisfying the resonance conditions in Eqs. (3). The initial distributions of particles are Gaussian and upright in all phase planes. At injection, the emittance ratio is $\varepsilon_{x(y)} / \varepsilon_z = 10$.

There is a particularly simple scaling law in the case of symmetric coupling where $g_x = g_y (\equiv g)$ and $\nu_x = \nu_y$ $(\equiv \nu_\perp)$. When the ring is exactly on resonance, the emittance-evolution pattern itself is basically independent of the fundamental parameters (g, $\nu_\perp$, and R) and only the exchange period varies. We can, therefore, carry out a desired beam optimization sooner or later even if it is difficult to increase the coupling strength in practice. An identical emittance-transfer process can be expected under the condition $g(mR/\nu_\perp)^{m/2}(nR/\nu_z)^{n/2} = \text{const.}$

PHASE-SPACE CORRELATIONS

Linear Correlation

In a linear situation as shown in Fig. 1, the direction of a possible emittance flow is strictly limited due to symplecticity [1]; provided the beam is initially matched to the uncoupled system where $\phi_c = 0$, the projected emittances only start to flow from a "hot" to a "cold" degree of freedom. We, however, notice that the emittance flow is eventually reversed after the three emittances become equal. This suggests the development of correlation among the degrees of freedom during the emittance exchanging process, which is confirmed in Fig. 2. The correlation disappears when a full emittance transfer is accomplished.

The projected emittance of a particular direction can be diminished if we could somehow produce a beam with such a correlation. It is, however, impossible to introduce the necessary correlation into phase space (with conservative forces) while preserving the three projected emittances; the sum of the three projected emittances inevitably grows. As a result, the minimum emittance of any direction will be larger than the level achievable with the original uncorrelated distribution.

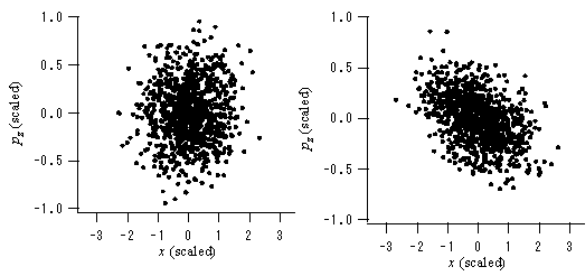

Figure 2: Phase-space correlation developed in the coupled harmonic-oscillator system under a linear difference resonance. The particle distributions at injection (left) and at the 40th turn (right) in Fig. 1 are plotted on a correlation phase plane spanned by x and p_z.

Nonlinear Correlation

When the coupling source is nonlinear, the direction of emittance flow can be made more flexible. The quality of a beam is, in a practical sense, somewhat deteriorated by "smearing" in phase space. (The 6D volume of the beam is, of course, unchanged as long as the nonlinear force is

conservative.) The coupling constant has to be moderate to avoid too much a shrinkage of the dynamic aperture. The direction and amount of a nonlinear emittance flow depend basically on initial beam conditions (the three projected emittances) as well as lattice parameters (tunes and coupling constants). Unlike linear coupling cases where particle distributions in 2D phase space are always elliptic as shown in Fig. 2, complex correlations can be developed with nonlinear potentials because of the amplitude dependence of single-particle tunes. An example of nonlinear correlation is given in Fig. 3 where third-order coupling ($m=1$, $n=2$) has been assumed. To be on resonance, the tunes have been set at $(\nu_x, \nu_y, \nu_z) = (1.2, 1.2, 0.1)$. These distributions in p_x-p_z and z-p_x phase planes correspond to what we observe at the 120th turn after injection. The correlation tends to be less pronounced due to nonlinear smearing as the beam stays in the coupling ring for a longer period.

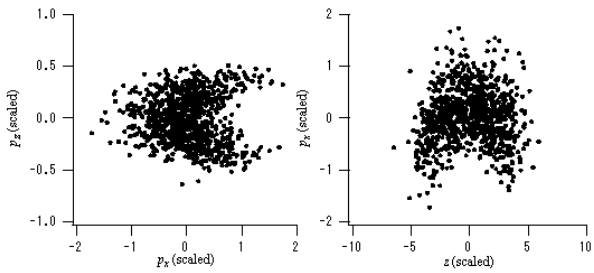

Figure 3: Phase-space correlation developed in the coupled harmonic-oscillator system under a nonlinear (third-order) difference resonance. The coupling constants and average ring radius have been chosen to be $g_x = g_y = 1$ and $R = 1$. The initial emittance ratio assumed here is $\varepsilon_{x(y)} / \varepsilon_z = 0.1$.

COUPLING SOURCES

Transverse-transverse Coupling

In order to introduce linear or nonlinear coupling between the two transverse directions, we can simply employ multipole magnets. For linear coupling, a skew quadrupole magnet can be used. (A solenoid is another good candidate as a linear coupling source.) Multipole magnetic fields are derivable from vector potentials that generally have only longitudinal components. For instance, the potential of a skew quadrupole is given by

$$\mathbf{A}_{skew} = \left(0, \quad 0, \quad g_{skew} xy \delta_p(s)\right), \tag{5}$$

where g_{skew} is proportional to the strength of the magnetic field. For nonlinear coupling, we excite a sextupole (third order) or an octupole (fourth order) magnet.

Transverse-longitudinal Coupling

Special rf cavities can be utilized to correlate the longitudinal motion with the transverse. The coupling cavity mentioned above is a simple solution for generating linear synchro-betatron coupling [6]. Even a regular accelerating cavity can be a linear coupling source when it is placed at a position with finite momentum dispersion [7]. The rectangular coupling cavity operating in TM_{210} mode produces a longitudinal electric field proportional to x, which establishes a linear correlation between the horizontal and longitudinal directions. To make a direct coupling with the vertical direction, we just rotate the cavity by 90 degrees around its axis of symmetry.

As to nonlinear coupling, we may exploit a cylindrical cavity rather than a rectangular type. The electromagnetic fields of a cylindrical resonator excited in $TM_{k\ell 0}$ mode can again be obtained from a vector potential with no transverse components:

$$\mathbf{A}_{rf} = \left(0, \quad 0, \quad \frac{V}{\omega} J_k(\zeta_{k\ell} r / r_0) \cos(m\theta) \sin(\omega t) \delta_p(s)\right), \tag{6}$$

where ω and V are the angular frequency and amplitude of rf, r_0 is the radius of the resonator cross section, $J_k(r)$ denotes the Bessel function of kth order, and $\zeta_{k\ell}$ is the ℓ th root of the algebraic equation $J_k(r) = 0$. We see that a third-order coupling can be developed in TM_{010} -mode operation. In fact, when $r / r_0 \ll 1$, the longitudinal component of Eq. (6) can be approximated by

$$A_z \approx \frac{V}{\omega}\left[1 - \left(\frac{\zeta_{01}}{2}\frac{r}{r_0}\right)^2\right] \sin(\omega t) \delta_p(s), \tag{7}$$

indicating that A_z depends quadratically on the transverse coordinates. Since time t is regarded as the longitudinal canonical coordinate in the present coordinate system where the path length s is the independent variable, the potential (7) yields a third-order synchro-betatron coupling corresponding to $(m,\ n) = (2,\ 1)$ in Eq. (2). It is indeed possible to provide different types of nonlinear coupling by using other excitation modes.

APPLICATION

Whenever the emittance of a particular direction is more important than those of the other directions or emittances ratios rather than their magnitudes themselves play an essential role, the present idea merits attention. Among a wide range of choices, we here briefly study FELs as a possible application of the coupling ring. After a proper emittance-transfer procedure, the electron beam from the ring is injected into a short transport channel to match the Twiss parameters to a subsequent FEL system. In what follows, we employ the simulation code "GENESIS" [8] to figure out the usefulness of a coupling storage ring. The FEL parameters assumed here are summarized in Table 1.

Table 1: FEL design parameters

Radiation wavelength λ [nm]	6
Beam energy [GeV]	1
Beam current (peak) [A]	250
Undulator period λ_w [cm]	2
Undulator parameter K	1.14

Emittance Optimization for FEL

In order to attain high power from FEL, the current of the electron beam should be as high as possible. In addition, the following conditions are generally required for the beam quality [9]:

(a) The transverse normalized emittances must be less than $\lambda / 4\pi$ where λ is the wavelength of radiation.

(b) The energy spread must be less than the FEL parameter ρ.

These requirements indicate that a possible performance of FEL is critically limited by the condition of an incident electron beam; even if the 6D volume is maintained, the FEL gain can be reduced considerably unless the ratios of three projected emittances are properly chosen.

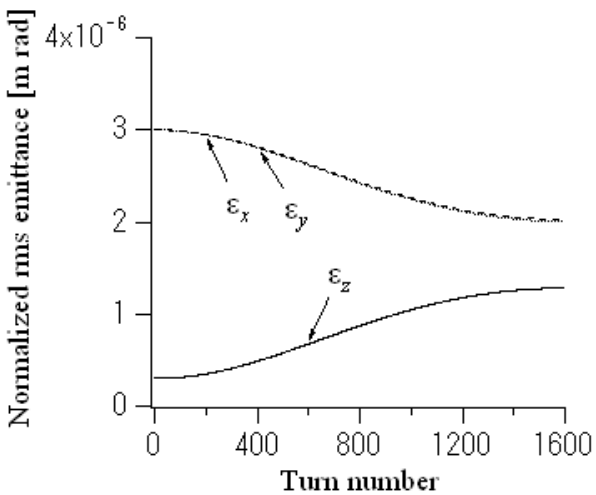

Figure 4: Nonlinear emittance transfer in a coupling storage ring where $(\nu_x, \nu_y, \nu_z) = (3.55,\ 3.55,\ 0.1)$.

The recent progress in accelerator technologies has made it feasible to produce an electron beam with a very low longitudinal emittance [2,3]. The FEL performance is then limited by the transverse beam properties rather than the longitudinal. If the energy spread is much smaller than ρ, the system can tolerate some longitudinal emittance growth with no reduction of the FEL gain. It should then be advantageous to transfer a portion of the phase-space volume from the transverse to the longitudinal direction, so that the condition (a) is more securely fulfilled. Figure 4 shows an emittance exchange process in a coupling ring where a third-order potential ($m = 2, n = 1$) is switched on. The transverse projected emittances have been reduced from 3μm to 2μm after a emittance exchange, while the longitudinal emittance becomes three times greater. The results of GENESIS simulations based on the electron beams before and after this emittance transfer are displayed in Fig. 5 that clearly demonstrates the advantage of the emittance manipulation. Some numerical results concerning linear emittance transfer can also be found in Ref. [4].

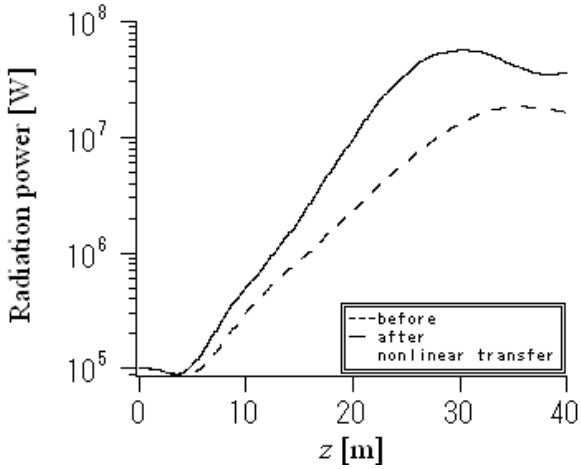

Figure 5: Results of GENESIS simulations. The broken curve was obtained with an original electron beam whose rms emittances are $(\varepsilon_x, \varepsilon_y, \varepsilon_z) = (3\,\mu\text{m}, 3\,\mu\text{m}, 0.3\,\mu\text{m})$. As shown in Fig. 4, this emittance combination is altered, after a nonlinear emittance exchange, to $(\varepsilon_x, \varepsilon_y, \varepsilon_z) = (2.09\,\mu\text{m}, 2.06\,\mu\text{m}, 1.23\,\mu\text{m})$ with which the solid curve was obtained. The power of the seed laser, which is not essential to the present study, is 10^5 W.

Optimum Correlation for FEL

As is well-known, the resonant wavelength λ is determined ideally by $\lambda \approx (1 + K^2)\lambda_w / 2\gamma^2$ where λ_w and K are the spatial period and normalized strength of the undulator. In reality, however, the beam has a finite energy spread and, furthermore, individual electrons execute betatron oscillations that can modify their average longitudinal velocities. Incorporating the effect of the betatron amplitude in the resonance condition, we obtain

$$\lambda \approx \frac{1}{2}\left(\frac{1+K^2}{\gamma^2} + \frac{2J_x}{\beta_x} + \frac{2J_y}{\beta_y}\right)\lambda_w, \qquad (8)$$

where $J_{x(y)}$ denotes the transverse action, and $\beta_{x(y)}$ is the betatron function. This condition implies that, even if the energy of an electron is deviated from the design value by the amount of $\Delta\gamma$, it can still be on resonance with the laser, provided [10]

$$\Delta\gamma / \gamma \approx \kappa_x J_x + \kappa_y J_y, \qquad (9)$$

where $\kappa_{x(y)}$ is a constant often referred to as the "conditioning" parameter. Assuming the parameters in

Table. 1, Eq. (9) requires the conditioned phase space as depicted in Fig. 6(a) [10]. Such a special correlation can roughly be established in a coupling ring by exciting nonlinear sources. For instance, let us again take a third-order situation considered in Fig. 4. It is then possible to develop a correlation as shown in Fig. 6(b), by intentionally applying a mismatch to an initial beam. The resultant distribution is not highly conditioned but clearly has a preferable correlation between the energy spread and transverse actions (unlike an electron beam provided by the linear scheme in Ref. [3] where the projected emittances are not partially but only fully exchanged and no correlation remains). Results of GENESIS simulations plotted in Fig. 7 actually confirm that the FEL performance can be considerably improved by such an approximate conditioning procedure.

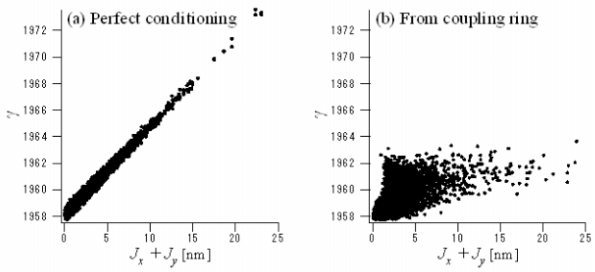

Figure 6: Phase-space correlations corresponding to the perfectly conditioned beam (left) and to an approximately conditioned beam extracted from a third-order coupling ring (right). The same FEL parameters as listed in Table 1 have been taken into account.

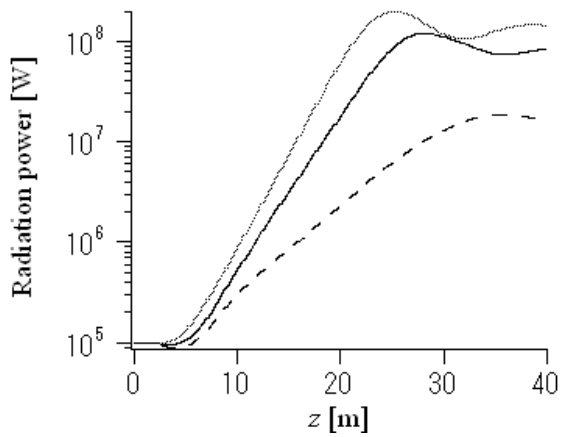

Figure 7: Results of GENESIS simulations. The broken curve was obtained with an original unconditioned electron beam, while the solid curve with the correlated beam shown in Fig. 6(b). The dotted curve is the evolution of the FEL power achievable with the perfectly conditioned beam in Fig. 6(a).

SUMMARY

We have studied a method of manipulating a charged-particle beam in 6D phase space. The present scheme is based on a dedicated storage ring containing linear and nonlinear coupling sources through which the projected emittance of one direction can be transferred to the other directions. The emittance transfer becomes most efficient when the ring operates on coupling resonances. Since the speed of an emittance flow is controllable with lattice parameters such as the coupling constant and tunes, the ratios of projected emittances can be well optimized for diverse purposes. Another important feature of this method is the automatic development of various correlations between degrees of freedom, which may open up a possibility of controlling not only emittance ratios but also even details of the particle distribution in 6D phase space.

As a typical application of the coupling storage ring, we considered FELs where the achievable radiation power is quite sensitive to the transverse and longitudinal projected emittances of an electron beam. Numerical simulations demonstrated that the FEL performance could be improved by a partial emittance transfer. It was also pointed out that the use of a nonlinear coupling enables us to correlate the transverse action with the energy spread of a beam. Although the beam conditioning achieved in the present simulation was not perfect, the resultant FEL gain actually got better compared to an unconditioned case. A further study is, however, needed incorporating detailed lattice structures and more accurate effects of coupling cavities.

ACKNOWLEDGMENT

One of the authors (K.K.) is indebted to Drs. G. Penn, W. M. Fawley, and S. Reiche for valuable comments on FEL designs and GENESIS simulations.

REFERENCES

[1] E.D. Courant, "Conservation of Phase Space in Hamiltonian Systems and Particle Beams", in Perspectives in Modern Physics, edited by R.E. Marshak (1966).

[2] K.-J. Kim and A. M. Sessler, in *AIP Conf. Proc.* **821**, edited by S. Nagaitsev and R. J. Pasquinelli (2006) 115.

[3] P. Emma, Z. Huang, K.-J. Kim and P. Piot, Phys. Rev. ST Accel. Beams **9** (2006) 100702.

[4] H. Okamoto, K. Kaneta and A. M. Sessler, J. Phys. Soc. Jpn. **76**, No. 7 (2007) 074501; H. Okamoto, unpublished report (February, 1995).

[5] M. Cornacchia and P. Emma, Phys. Rev. ST Accel. Beams **5** (2002) 084001.

[6] H. Okamoto, A. M. Sessler and D. Möhl, Phys. Rev. Lett. **72** (1994) 3977.

[7] H. Okamoto, Phys. Rev. E **50** (1994) 4982.

[8] S. Reiche, "Numerical Studies for a Single Pass High Gain Free-Electron Laser", Ph.D thesis (Hamburg, 1999).

[9] See, e.g., C. A. Brau, "Free-Electron Lasers", *Advances in Electronics and Electron Physics* (suppl. 22), published by Academic Press Inc. (1990).

[10] A. M. Sessler, D. H. Whittum and L.-H. Yu, Phys. Rev. Lett. **68** (1992) 309.

NECESSARY CONDITION FOR BEAM ORDERING

I.Meshkov, A.Sidorin, A.Smirnov[#], JINR, Dubna, Russia
A. Noda, T. Shirai, H. Souda, H. Tongu, ICR, Kyoto Univ., Japan
K.Noda, NIRS, Chiba, Japan
J.Dietrich, IKP, Juelich, Germany

Abstract

The very low momentum spread for small number of particle was reached on different storage rings. When the sudden reduction of the momentum spread ("phase transition") was observed during decreasing of the particle number it was interpreted as ordered state of ion beams. The most extensive study of ordered ion beams was done on storage rings ESR (GSI, Darmstadt) [1] and CRYRING (MSL, Stockholm) [2]. Recently, for the first time, the ordered proton beam has been observed on S-LSR (ICR, Kyoto University) [3].

This article presents the experimental investigation of low intensity proton beams on COSY (IKP, Juelich) and S-LSR which have the aim to formulate the necessary conditions for the achievement of the ordering state. The experimental studies on S-LSR and numerical simulation with the BETACOOL code [4] were done for the dependence of the momentum spread and transverse emittances on particle number with different misalignments of the magnetic field at the cooler section.

INTRODUCTION

Since very low momentum spread of proton beam was obtained with a help of electron cooling in NAP-M experiments [5] (BINP, Novosibirsk) the deep cooling of low intensity ion beams was studied in a few scientific centres. Essence of the experiments is a measurement of an ion beam momentum spread under cooling during long period of time when the beam intensity slowly decreases. At given value of the particle number the momentum spread is determined by equilibrium between the electron cooling and heating effects, main of which is an intrabeam scattering in the ion beam. The intrabeam heating rates decrease with the particle number that leads to decrease of the equilibrium momentum spread. At large intensity the momentum spread $\Delta p/p$ is scaled with the particle number N in accordance with a power law $\Delta p/p \sim N^{\xi}$, where ξ is some constant depending on settings of a storage ring and cooling system. When the particle number becomes less than certain threshold value the momentum spread can saturate (like in NAP-M, COSY experiments) or suddenly drop down by about one order of magnitude (ESR, SIS, CRYRING, S-LSR), which was interpreted as a phase transition to the ordered state.

Initially the ordered state was observed at ESR for heavy ions only [6], for light ions C^{6+}, Ne^{10+}, Ti^{22+} (except protons) the ordering was reached much later [7]. A few attempts for ordering of the proton beam were made at COSY (FZJ, Juelich), however the sudden reduction of the momentum spread was not observed [8]. Firstly the proton beam ordering was reached at S-LSR (Kyoto University) [3].

From analysis of the ESR experimental results one can conclude that the ordered state was reached when the dependence of momentum spread on particle number had a power coefficient $\xi \leq 0.3$ [6, 7]. In the first experiments at ESR with the light ions this condition was not satisfied and the beam ordering did not occur. This condition can explain why in experiments at COSY (where ξ was larger than 0.5) and NAP-M (where ξ was about 1) a sudden reduction of the proton beam momentum spread was not observed. First attempt to reach ordered proton beam at S-LSR in 2006 was not successive also, the ξ value in this experiment was about 0.4 [10].

EXPERIMENTS AT COSY

A few attempts for searching of the ordered proton beams were made at COSY ring [8]. The Schottky spectrum of proton beam was measured at injection energy (45 MeV) at different electron current values for different proton number in the beam. After injection the proton number was being reduced with introducing of the horizontal scraper that decreased the ring aperture and led to a fast proton loss.

The last measurements have shown that minimum value of the proton momentum spread can be reached at proton number below $1 \cdot 10^6$ protons and does not decrease below $2 \cdot 10^{-6}$ (Figure 1). The result does not depend actually on the feedback of high voltage power supply. The value ξ was about 0.5 in these experiments and the sudden reduction of the momentum spread was not observed.

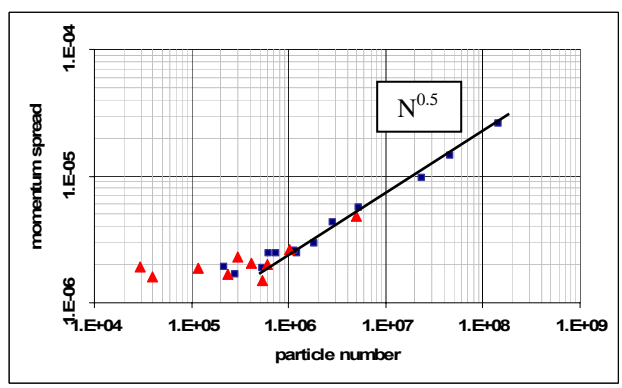

Figure 1: Momentum spread vs particle number: squares - fedback OFF, triangles – feedback ON. I_e=70 mA.

smirnov@jinr.ru

OREDERED PROTON BEAMS AT S-LSR

The successful achievement of the ordered state of the proton beam on S-LSR [3] permitted to start careful studies of the low temperature ion beam at different experimental settings. The describing experiments were performed with 7 MeV proton beam. The measured beam parameters was a momentum spread and a horizontal beam profile. They were measured by a Schottky monitor and a residual gas ionization monitor, respectively. The particle number in the ring was measured by the residual gas ionization monitor and a beam intensity monitor. At first, an electron beam alignment was done to maximize the longitudinal cooling force measured by the induction accelerator. This setting was defined as "0 mrad". Then, the misalignment between the electron and proton beams was created by the Helmholtz coils in the horizontal and vertical directions.

In the experiments the variation of the ξ value was realized by introduction of well-controlled angular deviation of the electron beam in respect to the proton beam equilibrium orbit. At small angles the electron beam misalignment leads to decrease of the cooling efficiency only. When the misalignment reaches a certain threshold value a qualitatively different situation is obtained. The ions start to oscillate with a certain value of betatron amplitude. The amplitude of the oscillations depends on the misalignment angle and the beam emittance can not be less than the value corresponding to the oscillation amplitude. In absence of another effects leading to heating of the beam, the beam profile has specific double-peak structure, and sudden appearance of this structure at variation of misalignment angle is called "chromatic instability".

Intrabeam scattering heating rate linearly scales with the particle number and inversely proportional to the beam phase volume $\varepsilon_x\varepsilon_y(\Delta p/p)$. Electron cooling rates have constant values at small temperature. At perfectly aligned electron beam a thermal equilibrium between degrees of freedom corresponds to $\varepsilon_x \sim \varepsilon_y \sim (\Delta p/p)^2$. In the case of equilibrium between the electron cooling and intrabeam scattering rates and after substitution $(\Delta p/p)^2$ instead ε_x and ε_y we have $(\Delta p/p) \sim N^{0.2}$.

At large misalignment in one transverse plane (for instance in the horizontal) we have ε_x=const, $\varepsilon_y \sim (\Delta p/p)^2$ and $(\Delta p/p) \sim N^{0.33}$. The large misalignment in both transverse planes leads to $(\Delta p/p) \sim N$. At small misalignment angle one can expect some intermediate value of the power coefficient. Thus the electron beam misalignment in one transverse plane permits to vary the ξ value from about 0.2 to 0.33, two dimensional misalignments can lead to variation of the ξ value from about 0.33 to 1.

Evolution of the momentum spread with decrease of the proton number was measured for different misalignment angles in the horizontal direction (Figure 2) and in both (horizontal and vertical) directions (Figure 3) with electron current 25.5 mA. For small misalignment (<0.5 mrad), the momentum spread was proportional to $N^{0.29}$.

When the misalignment was larger (>0.5 mrad), the momentum spread scaled with $N^{0.44}$ at large particle number and saturated (or changed the slope) below 3×10^5 particles. Especially, the behaviours at the horizontal and vertical misalignment were similar. A misalignment in both directions leads to saturation of the momentum spread at the larger value (Figure 3). In this case the dependence of the momentum spread on proton number is similar to the results obtained at COSY and NAP-M.

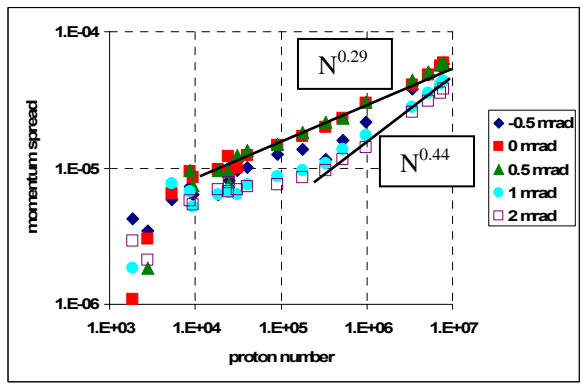

Figure 2: The dependence of momentum spread on the particle number for different horizontal misalignment angles (-0.5, 0, 0.5, 1, 2 mrad), I_e=25.5 mA.

The drop of the momentum spread, which indicates the ordered state, was observed at different horizontal or vertical misalignments (Figure 2), but it was not noticed at large misalignments (>0.5 mrad) in both directions (Figure 3).

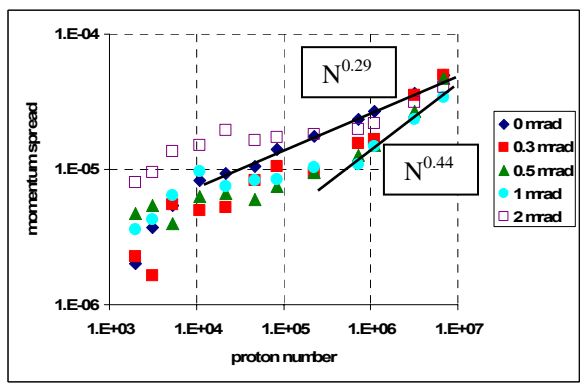

Figure 3: The dependence of momentum spread on the particle number for different angles in both directions (0, 0.3, 0.5, 1, 2 mrad), I_e=25.5 mA.

NUMERICAL SIMULATION

The dependence of the momentum spread on the particle number for different values of the misalignment angle was simulated with BETACOOL code. The friction force in the electron beam was calculated using Parkhomchuk's formula [11] with the effective electron velocity spread determined by the magnetic field imperfection. Intrabeam scattering was simulated in

accordance with Martini model [12]. This model presumes Gaussian distribution of the ions that can lead to some mistake at large misalignment angles.

The simulations show that a transverse misalignment can change the power coefficient ξ in the range from 0.21 up to 0.53 (Figure 4). In the case of a large horizontal misalignment only (horizontal/vertical = 1/0, 1/0.2 mrad) the power coefficient ξ can be changed up to values of about 0.45, however the low temperature can be reached.

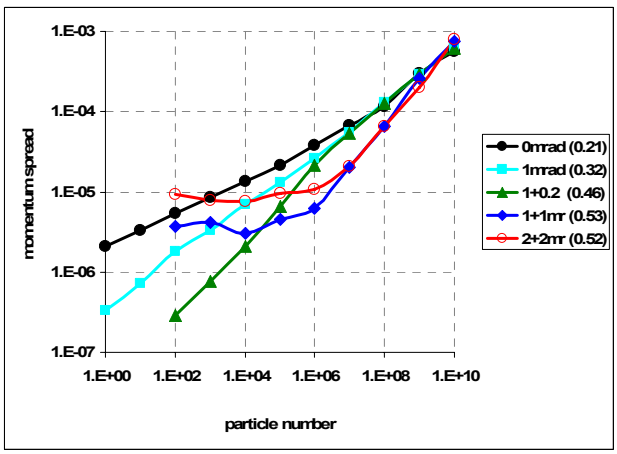

Figure 4: The dependence of the momentum spread on the particle number for different misalignments. I_e=25 mA, (0/0, 1/0, 1/0.2, 1/1 mrad, ξ=0.21, 0.32, 0.46, 0.53, 0.52).

In the case of a large misalignment in both transverse directions (Figure 5, 1/1, 2/2 mrad) the saturation of the momentum spread exists due to large influence of the space charge of the electron beam [10]. Misalignments in both transverse directions leads to the large transverse size of proton beam even at small number of particles. Protons with large amplitude of the transverse oscillation have the momentum deviation which is comparable with the momentum spread. In this case the momentum spread does not decrease with particle number and its sudden reduction can not take a place.

The use of an additional field misalignment can change the power coefficient ξ but this behaviour can not fully explain the variation of the ξ value measured in experiments and predicted by the theory. Beam parameters for different particle number are shown on the phase diagram (Figure 5) which presents the sum of the transverse and longitudinal components of the intrabeam scattering and electron cooling rates. Different colours of the diagram correspond to the values of growth rates from 10^{-5} to 10^{5} sec^{-1} at the particle number $N_p = 10^3$. Boundary between white and colour regions means the equilibrium between intrabeam scattering and electron cooling. Gray straight line means the equilibrium of transverse and longitudinal temperatures of the proton beam, black straight line – ordering criterion Γ_2 [13].

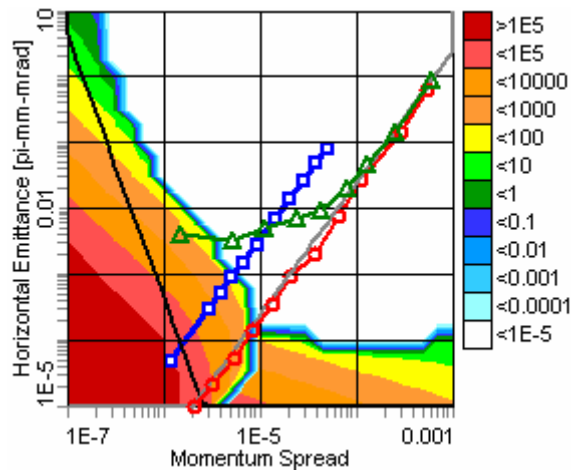

Figure 5: The dependence of horizontal emittance and momentum spread on the particle number. I_e = 25 mA. Blue square – experiment, red circles – simulation with zero misalignment, green triangle – simulation with 0.2/0.2 mrad misalignment.

The simulation results without any misalignment shows that the beam parameters are cool down along the thermal equilibrium between transverse and longitudinal degrees of freedom of the proton beam (Figure 5, red circles) and the power coefficient is ξ=0.21. The experimental results when the ordered state was observed (Figure 5, blue squares) show that the transverse temperature is much higher then the longitudinal one and the power coefficient is ξ=0.29.

Application of some misalignment in the transverse direction increases the power coefficient ξ=0.3. But this additional transverse heating changes the behaviour of the beam parameters (Figure 5, green triangles). It means that the experimental behaviour of beam parameters can not be explained by the misalignment only.

Martini model of intrabeam scattering can not describe the ordered state of the ion beam. For the simulation of the crystalline beam the Molecular Dynamics method [14] was used in BETACOOL code. Simulation results show that the longitudinal component of the intrabeam scattering heating rates has a specific behaviour for small number of particles (Figure 6).

Left part of the IBS longitudinal component is described by the shear force which always exists in bend magnets. The boundary of this part is dependent on the particle number (dashed black-gray line on Figure 6, 7) and region, where crystalline state is prohibited, is:

$$\frac{\Delta p}{p} < \frac{2N^3 r_{ion}\sigma_\perp}{\pi Q^2 \gamma_0^3 \beta_0^2 C^2}, \qquad (1)$$

where N – particle number, r_{ion} – classical ion radius, $\sigma_\perp = \sqrt{\varepsilon_\perp \beta_\perp}$ - transverse beam size, Q – betatron value, β_0, γ_0 – relativistic factors, C – ring circumference.

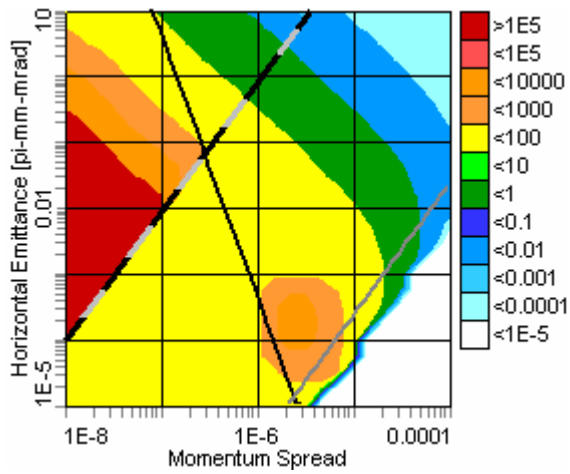

Figure 6: Intrabeam scattering rates for S-LSR ring (Molecular Dynamics, $N = 10^3$). Black line – ordering criteria (4), gray line – temperature equilibrium, dashed black-gray line – shear force boundary (5).

Ordering criteria Γ_2 [13] describes the transition to the ordered state when a relaxation between transverse and longitudinal degrees of freedom is switched off. This region is placed below the following condition (black line on Figure 6, 7):

$$\left(\frac{\Delta p}{p}\right)^2 < \frac{r_{ion}}{\pi\beta_0^2\sigma_\perp}, \qquad (2)$$

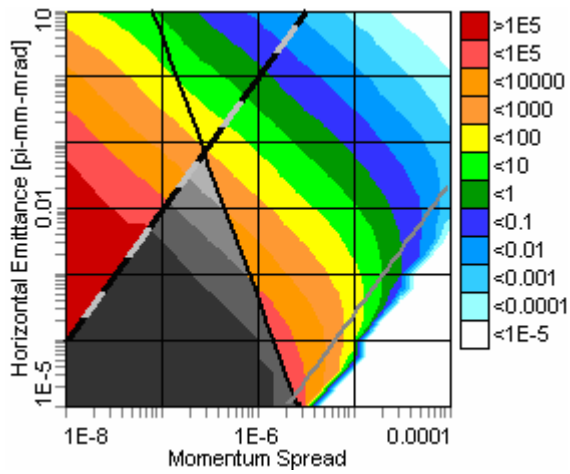

Figure 7: Intrabeam scattering rates for S-LSR ring (Martini model, $N = 10^3$).

Phase diagram (Figure 6) has a specific peculiarity: there is a region of high heating rate value surrounded by regions where the heating rate is sufficiently less. Origin of this "island" can be explained from the phase diagram calculated with Martini model (Figure 7) if we assume that in the region between conditions (1) and (2) the IBS process is suppressed due to the beam ordering (black-gray region on Figure 7). IBS island takes a place due to different angles on the phase diagram between ordering criteria (2) and the lines of equal heating rates.

CONCLUSION

The theoretical and experimental investigation of the ordered ion beam shows that the ordered state can be reached for a power coefficient $\xi \leq 0.3$, describing the dependence of the momentum spread on the particle number. A large misalignment of the magnetic field at electron cooling section increases the power coefficient up to 0.5 and the ordered state of the ion beam can not be reached due to influence of the electron beam space charge.

The specific island of the IBS longitudinal component is described by different angles between lines of equal heating rates and ordered criteria Γ_2. In real experiments when the transverse temperature of the ion beams much higher then longitudinal one the cooling "around the IBS island" can help to reach the ordered state.

REFERENCES

[1] M.Steck, K.Beckert, H.Eickhoff et al. Anomalous temperature reduction of electron-cooled heavy ion beams in the storage ring ESR. PRL **77**, 3803 (1996).

[2] H.Danared, A.Kallberg, K.G. Rensfelt, A.Simonsson. Observation of ordered ion beams in CRYRING. Proc. of PAC'2001.

[3] T. Shirai, M. Ikegami, A. Noda, I.Meshkov, A. Smirnov, et al. One-Dimensional Beam Ordering of Protons in a Storage Ring. PRL **98**, 204801 (2007).

[4] A. Sidorin, I. Meshkov, I. Seleznev, A. Smirnov, E. Syresin, A. Smirnov, G. Trubnikov. BETACOOL Program for Simulation of Beam Dynamics in Storage Rings. NIM A **558**, 325 (2006).

[5] V. Parkhomchuk. Proceedings of the Workshop on Electron Cooling and Related Applications (ECOOL'84), 71, (1984).

[6] R. Hasse. Theoretical Verification of Coulomb Order of Ions in a Storage Ring. PRL **83**, 3430 (1999).

[7] M. Steck, P. Beller, K. Beckert, B. Franzke, F. Nolden. Electron cooling experiments at the ESR. NIM A **532**, 357 (2004).

[8] J.Dietrich, I.Meshkov, A.Sidorin, A.Smirnov, J.Stein. Studies of Beam Dynamics in Cooler Rings. Proc. of COOL'2005.

[10] I.Meshkov, A.Noda, A.Smirnov, T.Shirai et al. Investigation of ordered proton beams at S-LSR. NIRS Preprint, to be published.

[11] V.Parkhomchuk, New insights in the theory of electron cooling, NIM A **441**, 9 (2000).

[12] M. Martini. Intrabeam scattering in the ACOOL-AA machines, CERN PS/84-9 AA, Geneva (1984).

[13] I.Meshkov, A.Sidorin, A.Smirnov, E.Syresin, T.Katayama. Ordered state of ion beams. Preprint RIKEN-AF-AC-34, Japan (2002).

[14] V.Avilov. Calculation of Electrostatic Energy of Planar Lattices. Solid State Communications, **44**, No.4, 555 (1982).

HIGH-ENERGY COLLIDING CRYSTALS - A THEORETICAL STUDY*

Jie Wei†, Institute of High Energy Physics, China and Brookhaven National Laboratory, USA
Hiromi Okamoto, Hiroshi Sugimoto, Hiroshima University, Japan
Yosuke Yuri, Japan Atomic Energy Agency, Japan
Andrew Sessler, Lawrence Berkeley National Laboratory, USA

Abstract

Recent theoretical investigations of beam crystallization using computer modeling based on the method of molecular dynamics (MD) and analytical approach based on the phonon theory [1, 2, 3] are motivated by the study of colliding crystalline beams [4]. Analytical study of crystal stability in an alternating-gradient (AG) focusing ring was previously limited to the smooth approximation. In a typical ring, results obtained under such approximation largely agrees with that obtained with the MD simulation. However, as we explore ring lattices appropriate for beam crystallization at high energies (Lorentz factor γ much larger than the transverse tunes ν_x, ν_y) [5], this approximation fails. Here, we present a newly developed phonon theory in a time-dependent Hamiltonian system representing the actual AG-focusing ring and predict the stability of 1D crystals at high energies. Luminosity enhancement is illustrated in examples of rare-ion colliders based on ordered 1D strings of ions.

INTRODUCTION

It is well-known that to create a crystal, two conditions need to be satisfied. First, the storage ring must operate below the transition energy so that the particle motion is in a positive-mass regime. Second, resonances between the oscillations of a crystal and the AG-focusing lattice structure must be avoided so as to prevent heating and thus destruction of the crystal. This requires that the phase advance per lattice period must not exceed 127° (in practice not more than 90° [6, 7]).

In this work, we are motivated by the desire to collide one ion crystal with another or to collide an electron beam with an ion crystal. We desire to do so because in such colliders the usual beam-beam limit can be greatly exceeded. The usual limit is roughly a change in tune, $\Delta\nu_{bb}$ of less than 0.01, but for a crystal the limit (destruction of the crystal or an ordered avoidance of ions colliding) occurs for $\Delta\nu_{bb} \sim 1$. Since the luminosity varies as the square of $\Delta\nu_{bb}$, the enhancement is of the order of 10^4.

Colliders are of significant interests at high energies. So, the very first question we want to address is can we make crystals at high energy. We shall show that the answer is positive. Then we go on to explore lattices appropriate for high energy and, in particular, low-momentum-compaction compact lattices where the transverse tunes are relatively low, i.e., $\gamma_T^{-2} \ll \nu_x^{-2}$. These lattices can not be described by the smooth approximation based on which previous phonon theory was developed [3]. We develop a new formalism appropriate for studying 1D crystal stability in general AG lattices. In comparison, we study both 1D and multi-dimensional high-energy crystals using the MD method. Finally, we present examples of ion-ion and electron-ion colliders with 1D ordered ions.

COLLIDING-BEAM HAMILTONIAN

The rest-frame motions of particles interacting through the Coulomb fields are governed by the Hamiltonian [8]

$$\begin{aligned} H &= \frac{1}{2}\sum_\ell \left(P_{x,\ell}^2 + P_{y,\ell}^2 + P_{z,\ell}^2\right) - \sum_\ell \gamma x_\ell P_{z,\ell} \\ &\quad + \frac{1}{2}\sum_\ell \left(\nu_x^2 x_\ell^2 + \nu_y^2 y_\ell^2\right) + V_C + V_{bb}, \end{aligned} \tag{1}$$

where ν_x and ν_y are the transverse tunes, γ is the Lorentz factor, and the summation extends over all particles l in the beam traveling in one direction. In Eq. (1), all canonical variables are scaled as dimensionless by expressing the time, t, in units of $\rho/\beta\gamma c$, the spatial coordinates x, y, and z in units of the characteristic inter-particle distance $\xi \equiv \left(r_0\rho^2/\beta^2\gamma^2\right)^{1/3}$, and the energy in units of $\beta^2\gamma^2 e^2/\xi$, where βc is the velocity of the reference particle, r_0 is its classical radius, and ρ is the bending radius of the ring under the dipole magnetic field. The Coulomb potential is given by

$$V_C = \frac{1}{2}\sum_{\ell\neq m} \frac{1}{|\mathbf{r}_\ell - \mathbf{r}_m|}, \tag{2}$$

where

$$|\mathbf{r}_\ell - \mathbf{r}_m| = \left[(x_\ell - x_m)^2 + (y_\ell - y_m)^2 + (z_\ell - z_m)^2\right]^{1/2}.$$

Interaction with the colliding beam occurs once per lattice period in a very short time, so it is treated as a lumped kick in momentum. The kick on particle l can be represented by

$$V_{bb} = \sum_j \frac{(1+\beta^2)\gamma\xi}{\rho\sqrt{b_{min}^2 + b_{lj}^2}} \tag{3}$$

where $b_{lj}^2 = (x_l - x_j)^2 + (y_l - y_j)^2$ is the square of the transverse separation and $b_{min} = (1+\beta^2)r_0/(4\beta^2\gamma^2\xi)$ is the minimum separation in the beam rest frame, and the summation, j, is over all the particles in the opposite beam. We find that if the kick is large comparing with that of the crystalline space charge, then the ground state is two crystals separated in space at the crossing point; i.e. there are

* Work performed under the auspices of the Chinese Academy of Sciences and the U.S. Department of Energy.

† weijie@ihep.ac.cn and jwei@bnl.gov

no overlapping. If, however, the beam-beam effect is not too large then the two crystals do overlap and beam-beam nuclear interactions can occur.

A convenient measure of both the beam-beam and the space-charge forces is given by assuming a uniform charge distribution within the beam. This is usually an underestimate of the actual space-charge and beam-beam forces when the beam is crystallized. Let R be the average radius of the machine, β^*_{xy} be the β values at the crossing point, N_B be the number of crossing per revolution, N_0 be the number of ions per bunch, λ_0 be the peak number of ions per unit length, and a be the full transverse radius of the bunch, we have:

$$\Delta\nu_{sc}=\frac{-\lambda_0 R r_0 \beta_{xy}}{\beta^2\gamma^3 a^2},\ \Delta\nu_{bb}=\frac{-N_B N_0(1+\beta^2) r_0 \beta^*_{xy}}{4\pi\beta^2\gamma a^2} \quad (4)$$

Fig. 1 shows an example of colliding multi-shell crystals obtained by computer simulation based on Eq. 1 using the MD method [4].

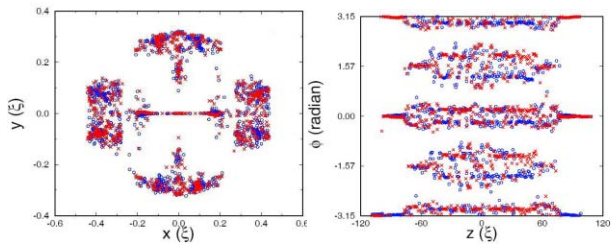

Figure 1: Formation of colliding crystalline beams with 1000 macro particles in each beam. The space charge tune shift $\Delta\nu_{sc} = -3.8$ and the beam-beam tune shift $\Delta\nu_{bb} = 0.27$. The crosses correspond to one beam while the circles correspond to the other. ϕ is the polar angle.

LATTICE FOR HIGH-ENERGY CRYSTAL

To form crystals at high energy for enhanced luminosity, we explore ring lattices with high ($\gamma_T \gg \nu_{x,y}$) or imaginary ($\gamma_T^2 < 0$) transition energy. A low-momentum-compaction lattice (i.e., $\gamma_T^{-2} \ll \nu_x^{-2}$) that satisfies the maintenance condition is shown in Fig. 2. The short, negative-bend dipoles at the high-dispersion region compensate for the long, regular dipoles at the low-dispersion region. Such lattice was proposed in 1955 to avoid transition crossing [9]. A variation of the structure was recently proposed for the Fixed Field Alternating Gradient (FFAG) accelerator. The cell phase advance is kept below 90° [10].

THEORETICAL APPROACHES

Theoretical investigation of crystal stability mainly consists of three methods all based on the beam-rest-frame Hamiltonian. The first is phonon spectrum analysis under the smooth approximation of the machine lattice [3]. The second is generalized phonon spectrum analysis for the actual machine lattice. The third is computer simulation using the MD method for the actual machine lattice.

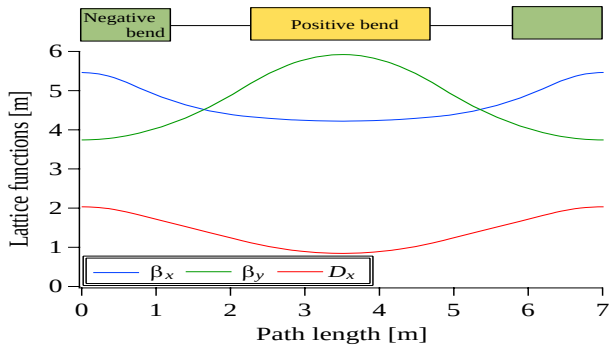

Figure 2: Imaginary-γ_T negative-bend lattice with 87° horizontal phase advance. The middle (positive) bend is of combined-function (dipole and defocusing quadrupole).

Phonon Theory under the Smooth Approximation

The analysis is based on linearized Coulomb forces around the equilibrium positions of the particles. Write the spatial coordinates of ℓ-th ion in a crystalline state as (X_ℓ, Y_ℓ, Z_ℓ),

$$\begin{aligned} x_\ell &= X_\ell + \delta x_\ell,\ \delta x_\ell = \tilde{x}_\ell \exp\left[i(\omega t - kZ_\ell)\right], \\ y_\ell &= Y_\ell + \delta y_\ell,\ \delta y_\ell = \tilde{y}_\ell \exp\left[i(\omega t - kZ_\ell)\right], \\ z_\ell &= Z_\ell + \delta z_\ell,\ \delta z_\ell = \tilde{z}_\ell \exp\left[i(\omega t - kZ_\ell)\right]. \end{aligned} \quad (5)$$

When there are N particles per unit cell of length L, we obtain the linearized equations of motion in a storage ring,

$$\begin{aligned} \omega^2\tilde{x}_\ell &= -i\gamma\omega\tilde{z}_\ell + (\nu_x^2-\gamma^2)\tilde{x}_\ell + \sum_{n=-\infty}^{\infty}\sum_{m=1}^{N} \quad (6) \\ &\left\{\left[\frac{1}{R^3_{\ell mn}} - \frac{3\left(X_\ell - X_m\right)^2}{R^5_{\ell mn}}\right]\left[e^{ik(Z_\ell - Z_m - nL)}\tilde{x}_m - \tilde{x}_\ell\right]\right. \\ &-\frac{3\left(X_\ell - X_m\right)\left(Y_\ell - Y_m\right)}{R^5_{\ell mn}}\left[e^{ik(Z_\ell - Z_m - nL)}\tilde{y}_m - \tilde{y}_\ell\right] \\ &\left.-\frac{3\left(X_\ell - X_m\right)\left(Z_\ell - Z_m - nL\right)}{R^5_{\ell mn}}\left[e^{ik(Z_\ell - Z_m - nL)}\tilde{z}_m - \tilde{z}_\ell\right]\right\} \end{aligned}$$

$$\begin{aligned} \omega^2\tilde{y}_\ell &= \nu_y^2\tilde{y}_\ell + \sum_{n=-\infty}^{\infty}\sum_{m=1}^{N} \quad (7) \\ &\left\{-\frac{3\left(X_\ell - X_m\right)\left(Y_\ell - Y_m\right)}{R^5_{\ell mn}}\left[e^{ik(Z_\ell - Z_m - nL)}\tilde{x}_m - \tilde{x}_\ell\right]\right. \\ &+\left[\frac{1}{R^3_{\ell mn}} - \frac{3\left(Y_\ell - Y_m\right)^2}{R^5_{\ell mn}}\right]\left[e^{ik(Z_\ell - Z_m - nL)}\tilde{y}_m - \tilde{y}_\ell\right] \\ &\left.-\frac{3\left(Y_\ell - Y_m\right)\left(Z_\ell - Z_m - nL\right)}{R^5_{\ell mn}}\left[e^{ik(Z_\ell - Z_m - nL)}\tilde{z}_m - \tilde{z}_\ell\right]\right\} \end{aligned}$$

$$\begin{aligned} \omega^2\tilde{z}_\ell &= i\gamma\omega\tilde{x}_\ell + \sum_{n=-\infty}^{\infty}\sum_{m=1}^{N} \quad (8) \\ &\left\{-\frac{3\left(X_\ell - X_m\right)\left(Z_\ell - Z_m - nL\right)}{R^5_{\ell mn}}\left[e^{ik(Z_\ell - Z_m - nL)}\tilde{x}_m - \tilde{x}_\ell\right]\right. \\ &-\frac{3\left(Y_\ell - Y_m\right)\left(Z_\ell - Z_m - nL\right)}{R^5_{\ell mn}}\left[e^{ik(Z_\ell - Z_m - nL)}\tilde{y}_m - \tilde{y}_\ell\right] \\ &\left.+\left[\frac{1}{R^3_{\ell mn}} - \frac{3\left(Z_\ell - Z_m - nL\right)^2}{R^5_{\ell mn}}\right]\left[e^{ik(Z_\ell - Z_m - nL)}\tilde{z}_m - \tilde{z}_\ell\right]\right\} \end{aligned}$$

where

$$R_{\ell mn} = \sqrt{(X_\ell - X_m)^2 + (Y_\ell - Y_m)^2 + (Z_\ell - Z_m - nL)^2}$$

$\ell = 1, \ldots, N$, and $R_{\ell mn} = 0$ term is excluded from the double sum. A computer algorithm was developed to obtain the eigenvalues of the system for a general crystalline structure beyond 1D, Practically, systems of up to $N = 50$ particles per MD supercell were studied.

For 1D crystals, $N = 1$, Eqs. 6, 7, and 8 can be solved analytically. The phonon bands are calculated as

$$\begin{aligned}
\omega_1^2 &= \frac{1}{2}\left\{\nu_x^2 + \Omega^2 + \sqrt{(\nu_x^2+\Omega^2)^2 - 8\Omega^2(\nu_x^2 - \gamma^2 - \Omega^2)}\right\} \\
\omega_2^2 &= \nu_y^2 - \Omega^2 \\
\omega_3^2 &= \frac{1}{2}\left\{\nu_x^2 + \Omega^2 - \sqrt{(\nu_x^2+\Omega^2)^2 - 8\Omega^2(\nu_x^2 - \gamma^2 - \Omega^2)}\right\}
\end{aligned} \tag{9}$$

where

$$\Omega^2 = 2\sum_{n=1}^{\infty} \frac{1 - \cos(kn/\Lambda)}{(n/\Lambda)^3} \geq 0 \tag{10}$$

with Λ being the scaled dimensionless line density defined by $\Lambda = N/L$, and the wave number k varies from $-\pi\Lambda$ to $\pi\Lambda$. The actual line density λ in the laboratory frame can be related to Λ as $\lambda = \Lambda/(\gamma\xi)$. The 1D structure is stable if all the eigenvalues are real for any k.

Fig. 3 shows the stability of 1D crystalline beams at different line densities as functions of the beam energy. Stable 1D structure exists for energies up to a threshold γ_{th} corresponding to the transition energy of the machine, i.e., $\gamma_{th} = \gamma_T = \nu_x$. For energies below transition ($\gamma < \gamma_{th}$), there exists a threshold density beyond which the crystalline structure is beyond 1D.

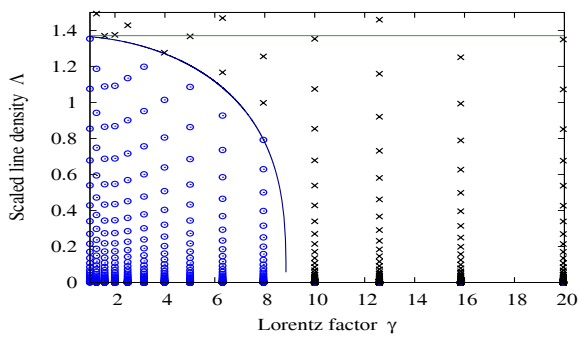

Figure 3: Stable region (blue circles) of 1D crystals evaluated using the smooth approximation. The transverse tunes are $\nu_x = \nu_y = 8.85$. The threshold energy corresponds to $\gamma_{th} = \gamma_T = 8.85$ beyond which no crystals are predicted.

Phonon Theory for a General Lattice

The smooth approximation with $\gamma_T = \nu_x$ fails to describe features of machine lattices where the transition energy is either high ($\gamma_T \gg \nu_x$) or imaginary. We hereby develop the phonon theory applicable to a general machine lattice where γ_T may deviate significantly from ν_x and ν_y.

Divide the machine into sections along the circumference; within each section the external force (i.e. magnetic focusing and bending) is constant. The one-turn transfer M is the product of the transfer matrices across each section i,

$$M = \Pi_{i=1}^{N_{lat}} M_i \tag{11}$$

where N_{lat} is the number of sections along the machine. In the case of a 1D crystal under regular bending and focusing forces, the vertical motion (y) is decoupled from the motion in the other two directions (x, z). The one-turn transfer matrices in y and x, z are

$$M_y = \Pi_{i=1}^{N_{lat}} M_{y,i}, \quad M_{xz} = \Pi_{i=1}^{N_{lat}} M_{xz,i} \tag{12}$$

Within each section, the transfer matrices may be obtained by linearizing the Coulomb forces around the equilibrium positions of the particles,

$$M_{y,i} = \begin{bmatrix} \cos\omega_{2i}t_i & \dfrac{\sin\omega_{2i}t_i}{\omega_{2i}} \\ -\omega_{2i}\sin\omega_{2i}t_i & \cos\omega_{2i}t_i \end{bmatrix} \tag{13}$$

and

$$M_{xz,i} = \bar{M}_{xz,i}\bar{M}_{xz,i}^{-1}(0) \tag{14}$$

where

$$\bar{M}_{xz,i} = \begin{bmatrix} \bar{M}_{xz,i}^{11} & \bar{M}_{xz,i}^{12} \\ \bar{M}_{xz,i}^{21} & \bar{M}_{xz,i}^{21} \end{bmatrix} \tag{15}$$

with the sub-matrices given by

$$\bar{M}_{xz,i}^{11} = \begin{bmatrix} e^{i\omega_{1i}t_i} & e^{-i\omega_{1i}t_i} \\ i\omega_{1i}t_i e^{i\omega_{1i}t_i} & -i\omega_{1i}t_i e^{-i\omega_{1i}t_i} \end{bmatrix} \tag{16}$$

$$\bar{M}_{xz,i}^{12} = \begin{bmatrix} e^{i\omega_{3i}t_i} & e^{-i\omega_{3i}t_i} \\ i\omega_{3i}t_i e^{i\omega_{3i}t_i} & -i\omega_{3i}t_i e^{-i\omega_{3i}t_i} \end{bmatrix} \tag{17}$$

$$\bar{M}_{xz,i}^{21} = \begin{bmatrix} c_{31}e^{i\omega_{1i}t_i} & -c_{31}e^{-i\omega_{1i}t_i} \\ c_{41}e^{i\omega_{1i}t_i} & c_{41}e^{-i\omega_{1i}t_i} \end{bmatrix} \tag{18}$$

$$\bar{M}_{xz,i}^{22} = \begin{bmatrix} c_{33}e^{i\omega_{3i}t_i} & -c_{33}e^{-i\omega_{3i}t_i} \\ c_{43}e^{i\omega_{3i}t_i} & c_{43}e^{-i\omega_{3i}t_i} \end{bmatrix} \tag{19}$$

and

$$\bar{M}_{xz,i}(0) = \begin{bmatrix} 1 & 1 & 1 & 1 \\ i\omega_{1i}t_i & -i\omega_{1i}t_i & i\omega_{3i}t_i & -i\omega_{3i}t_i \\ c_{31} & -c_{31} & c_{33} & -c_{33} \\ c_{41} & c_{41} & c_{43} & c_{43} \end{bmatrix} \tag{20}$$

where the coefficients are given by

$$c_{3n} = \frac{i\omega_{ni}\gamma}{\omega_{ni}^2 - 2\Omega^2}, \; c_{4n} = \frac{-2\Omega^2\gamma}{\omega_{ni}^2 - 2\Omega^2}, \; n = 1, 3 \tag{21}$$

with ω_{ni} in each section i given by

$$\begin{aligned}
\omega_{1i}^2 &= \frac{1}{2}\left\{\nu_{xi}^2 + \Omega^2 + \sqrt{(\nu_{xi}^2+\Omega^2)^2 - 8\Omega^2(\nu_{xi}^2 - \gamma^2 - \Omega^2)}\right\} \\
\omega_{2i}^2 &= \nu_{yi}^2 - \Omega^2 \\
\omega_{3i}^2 &= \frac{1}{2}\left\{\nu_{xi}^2 + \Omega^2 - \sqrt{(\nu_{xi}^2+\Omega^2)^2 - 8\Omega^2(\nu_{xi}^2 - \gamma^2 - \Omega^2)}\right\}
\end{aligned} \tag{22}$$

where Ω^2 is given by Eq. 10. The 1D crystalline structure is defined to be stable if all the eigenvalues of the one-turn matrix (Eq. 11) are real for any wave number k.

Fig. 4 shows the stability of the 1D crystalline beams in a high-transition lattice with $\gamma_T = 105$ much higher than the transverse tunes ($\nu_x = \nu_y = 8.85$). At low energy,

$\gamma < \nu_x$, the stable region is similar to that predicted by the phonon theory using the smooth approximation (Fig. 3). However, at energies beyond ($\gamma > \nu_x$) stable 1D structures are also predicted, although the threshold density decreases with energy. A narrow stable region exists even when the energy is above transition ($\gamma > \gamma_T$).

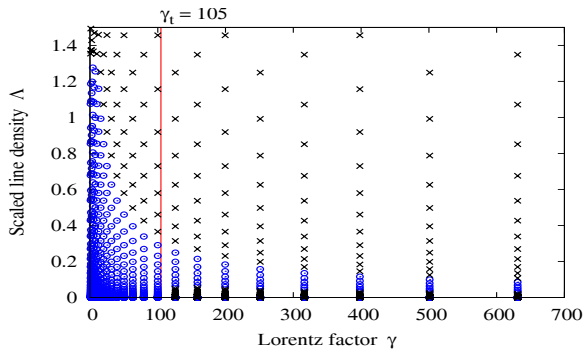

Figure 4: Stable region (blue circles) of 1D crystals evaluated with the phonon theory based on the actual lattice. The ring consists of 36 lattice periods each containing four uniform-external-force sections as illustrated in Fig. 2. Here, $\nu_x = \nu_y = 8.85$, and $\gamma_T = 105$.

Molecular Dynamics Method

Using the MD method [1, 2], Fig. 5 shows the region where crystalline structures are obtained in the high-transition lattice ($\gamma_T = 105$, $\nu_x = \nu_y = 8.85$). At energies up to $\gamma \approx \nu_{x,y}$, stable crystals from 1D string to 3D multi-shell are formed depending on the line density of the beam, as shown in Fig. 6. Formation of stable 3D crystals becomes increasingly difficult for higher beam energies. At $\gamma = 20$, only 2D crystals are formed. Due to reduction of the effective horizontal focusing [3], the zig-zag structure extends in the horizontal plane. Stable 1D structures are obtained at energies up to the transition but not beyond.

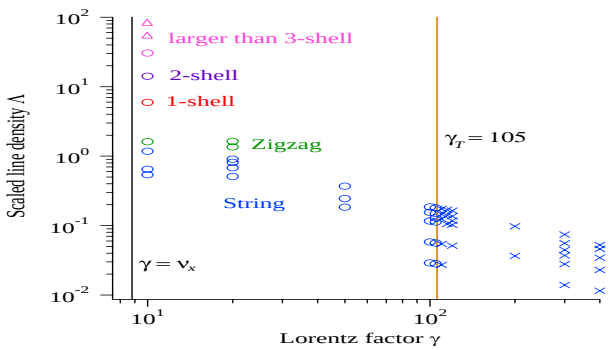

Figure 5: Stable region (non-crosses) of 1D, 2D, and 3D crystals evaluated using the MD method for the high-transition lattice. The machine lattice is the same as that used for Fig. 4 with $\nu_x = \nu_y = 8.85$, and $\gamma_T = 105$.

MD simulations are also used to study the crystal formation in an imaginary-γ_T lattice. Lattice functions of a ring lattice period is shown in Fig. 2. The phase advances per lattice period are $\mu_x = \mu_y = 87°$. Fig. 7 shows the region where crystalline structures are obtained. Again, at energies up to $\gamma \approx \nu_{x,y}$, stable crystals from 1D string to 3D multi-shell are formed depending on the line density of the beam. Formation of stable 3D crystals becomes increasingly difficult for higher beam energies. On the other hand, stable 1D structures are obtained at very high energies.

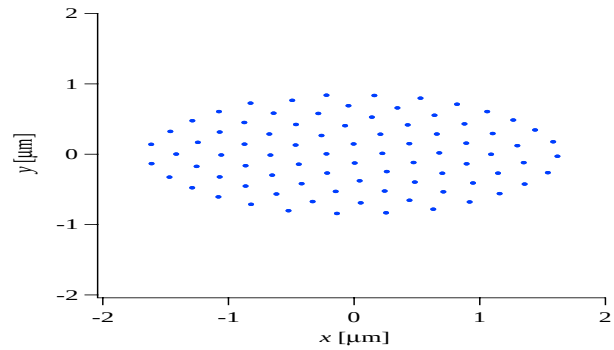

Figure 6: A multi-shell crystalline beam of $^{24}Mg^{+}$ ions formed with the high-transition ($\gamma_T = 105$, $\nu_x = \nu_y = 8.85$) lattice at the energy corresponding to $\gamma = 10$ and density of 6.2×10^9/m in the laboratory frame. During simulation, both the transverse and tapered cooling are applied [11]. If a crystalline state is reached, the cooling force is removed to test the stability of the formed crystal.

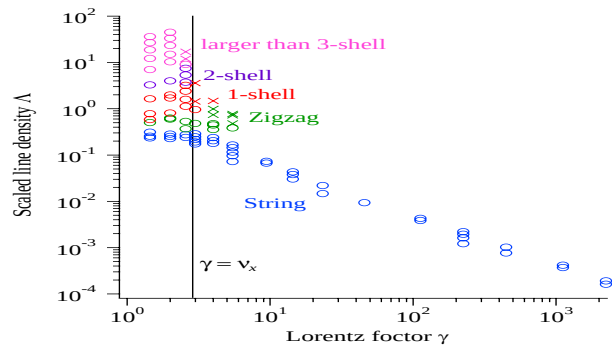

Figure 7: Stable region (non-crosses) of 1D, 2D, and 3D crystals evaluated using the MD method for the imaginary-transition lattice. The transverse tunes are $\nu_x = \nu_y = 2.90$. The transition energy corresponds to $\gamma_T = i13$. The machine of 84 m circumference consists of 12 lattice periods.

COLLIDING CRYSTALS

We provide two examples using 1D ordered ion beams in a collider to achieve significant luminosity with a small number of ions.

Rare-ion Collider with Ordered Ions

We adopt the main machine parameters of the Relativistic Heavy Ion Collider (RHIC) to illustrate the performance of a rare-ion collider with two counter-circulating beams of 360 bunches each containing 4×10^6 ions. At the beam energy of $\gamma = 20$ below transition, the characteristic distance

in the rest frame is $\xi = 19$ μm. For the beam to be an ordered 1D string, the line density in the laboratory frame must be below $\Lambda_{\rm th}\gamma/\xi$ where

$$\Lambda_{\rm th} = 0.62\nu_{eff}^{2/3}, \quad \nu_{eff}^2 = \min(\nu_x^2 - \gamma^2, \nu_y^2) \qquad (23)$$

and the amplitude $\sigma_{x,y}$ of the transverse motion must be much smaller than the distance between the ions in the rest frame. The luminosity is given by

$$L = \frac{f_0 N_B N_0^2}{4\pi\sigma_{x,y}^*} \qquad (24)$$

where $f_0 = \beta c/2\pi R$. Under sufficient beam cooling, Table 1 shows that significant luminosity can be attained.

With relatively few number of particles and significant luminosity, the lifetime of the beam is usual short due to the event of collisions. Fast beam cooling like optical-frequency-range stochastic cooling and high-energy electron cooling is necessary. Ref. [12] indicates that with efficient beam cooling, the ordered state can be maintained in the presence of significant event rate.

Electron-ion Collider with Ordered Ions

Following the example presented in Ref. [13], significant luminosity can be achieved when a beam of rare ions formed as 1D ordered string collides with an electron beam of similar beam radius (Table 2) [13, 14]. Electron cooling is proposed to cool the ion beam to an ordered state.

SUMMARY AND DISCUSSIONS

For regular machine lattices, multi-shell crystals can be formed for energies (γ) up to the machine tunes ($\gamma_{th} \approx \nu_{x,y}$). Special lattices can be designed – they are AG-focusing, low-momentum-compaction lattices that have very high or even imaginary transition energy. Thus, it is not necessary to make very large rings to achieve high-energy crystals.

We have developed a phonon formalism for analyzing 1D crystals in such AG-focusing lattices. Stability analysis based on this formalism is compared with the MD simulations. In such lattices, lower-density crystals can be formed at energies much higher than the machine tunes ($\gamma_{th} \gg \nu_{x,y}$). In particular, 1D crystals can be formed in low-momentum-compaction lattices even if $\gamma \gg \nu_{x,y}$. However, we find that it is impossible to form multi-shell crystals in this energy regime possibly due to the sensitivity of the effective momentum compaction to the transverse force between the particles.

Even 1D crystals, when made to collide, would have a very interesting luminosity. We have presented two examples of such rare-ion colliders. Performance of an ion-ion collider may be demonstrated by implementing a trap with a storage ring and force the ordered beam in the ring to interact with the crystal formed in the trap.

Table 1: Major parameters of a rare-ion collider with ordered ions.

Ring circumference, $2\pi R$ [m]	3834
Ring transition energy, γ_T	23
Ring transverse tunes, ν_x, ν_y	29.18, 28.19
Ion charge Z, mass number A	79, 197
Ion beam energy, γ	20
Number of bunches in each ring, N_B	360
Bunch length in laboratory frame [m]	1
Number of ions per bunch, N_0	10^6
Transverse amplitude (ave.), $\sigma_{x,y}$ [m]	10^{-6}
Transverse amplitude at IR, $\sigma_{x,y}^*$ [m]	0.22×10^{-6}
Momentum spread, $\Delta p/p$	0.9×10^{-6}
Inc. space-charge tune shift, $\Delta\nu_{sc}$	-19.5
Beam-beam tune shift, $\Delta\nu_{bb}$	-4.1
Instan. luminosity, L [cm^{-1}s^{-1}]	4.7×10^{27}

Table 2: Major parameters of an electron-ion collider with ordered ions [13].

Ring circumference [m]	108
Ion charge Z, mass number A	82, 208
Ion kinetic energy [MeV/n]	180
Total Number of ions in the ring	3×10^6
Interaction region length [m]	1
Tran. amplitude at IR [m]	6×10^{-6}
Momentum spread, $\Delta p/p$	1.3×10^{-6}
Inc. space charge tune shift	-0.25
Beam-beam parameter	1
Instan. luminosity [cm^{-1}s^{-1}]	1.4×10^{27}

We thank X.-P. Li, S. Machida, D. Moehl, and D. Trbojevic for helpful discussions. One of the authors (JW) is grateful to M. Steck, D. Moehl and the COOL07 organizing committee for the invitation and support to the workshop.

REFERENCES

[1] J. Wei, X-P. Li, and A. M. Sessler, Phys. Rev. Lett., **73** (1994) 3089
[2] J. Wei, H. Okamoto, and A.M. Sessler, Phys. Rev. Lett., **80** (1998) 2606
[3] X.-P. Li, H. Enokizono, H. Okamoto, Y. Yuri, A.M. Sessler, and J. Wei, Phys. Rev. ST-AB, **9** (2006) 034201
[4] J. Wei, A.M. Sessler, EPAC (1998) 862
[5] J. Wei, H. Okamoto, S. Ochi et al, EPAC (2006) 2841
[6] K. Okabe, H. Okamoto, Jpn. J. Appl. Phys. **42** (2003) 4584
[7] I. Hofmann, L. Laslett, L. Smith, and I. Haber, Part. Accel. **13** (1983) 145
[8] J. Wei, X.-P. Li, and A.M. Sessler, Proc. 6th Adv. Accel. Conf. (1994) 224
[9] V.V. Vladimirski, E.K. Tarasov, Theoretical problems of the ring accelerators, USSR Academy of Science (1955)
[10] C. Johhnstone, E. Keil, and D. Trbojevic, private communications
[11] H. Okamoto, J. Wei, Phys. Rev. E, **58** (1998) 3817
[12] J. Wei, A.M. Sessler, EPAC (1996) 1179
[13] T. Katayama, D. Moehl, RIKEN Report (2002)
[14] I. Meshkov, A. Sidorin, A. Smirnov, E. Syresin, and T. Katayama, Inst. of Phys. & Chem. Res. (RIKEN) Report: RIKEN-AF-AC-34 (2002)

INTRODUCTION TO THE SESSION ON LATTICE OPTIMIZATION FOR STOCHASTIC COOLING

D. Möhl, CERN, Geneva, Switzerland

Abstract

Lattices that circumvent the 'mixing dilemma' for stochastic cooling have repeatedly been considered but were not adopted in the original design of existing cooling rings. Recently new interest has arisen to modify existing machines and to design future 'optimum mixing rings'. This talk is meant to summarize the advantages and disadvantages with the aim to introduce the discussion.

INTRODUCTION

For efficient stochastic cooling a small dispersion (η_{PK}) in the time of flight is desirable on the beam-path from pickup to kicker and a large dispersion (η_{KP}) on the way kicker to pickup. For a regular lattice one has (at least approximately)

$$\eta_{PK} = \eta_{KP} = \eta = \gamma_{tr}^{-2} - \gamma^{-2}$$

i.e. the local η-factors are equal to each other and given by the off-momentum factor of the whole ring. Then the spread of the flight times ΔT_{PK} (leading to undesired mixing) and ΔT_{KP} (desired mixing) are related by the corresponding lengths L_{PK} and L_{KP} along the circumference

$$\Delta T_{PK} = \eta (L_{PK} / \beta c)(\Delta p / p)$$
$$\Delta T_{KP} = \eta (L_{KP} / \beta c)(\Delta p / p)$$

Thus in the special case of a regular lattice and a cooling loop that cuts diagonally through the ring one has $\Delta T_{PK} = \Delta T_{KP}$. One can however design an 'asymmetric' (also called 'split ring-' or 'optimum mixing-') lattice [1], which combines sections with small local η in one part with large η-sections in the other part. In this way ΔT_{PK} and ΔT_{KP} can be adjusted independent of each other. In addition if the local momentum compaction factors $\alpha = \gamma_{tr}^{-2}$ are tuneable, then optimum mixing can be envisaged for different energies and one can even envisage η-tuning dynamically during cooling at fixed energy. The potentially large gain in cooling speed has to be balanced against difficulties such as complexity of the lattice, and 'single particle' and collective beam stability.

GAIN WITH AN ASYMMETRIC LATTICE

It can be concluded from [1] that by optimising the mixing one can gain a factor of ~3.4 in the initial cooling rate. This is when the system noise is negligible and the cooling loop cuts diagonally through the ring. To ease the discussion this 'standard case' will mostly be assumed in the following. For low energy rings where the distance L_{PK} can be made considerably smaller than L_{KP} and also for cooling systems with poor signal to noise ratio, the gain is less pronounced. On the other hand for momentum the cooling the improvement factor can be larger than 3.4 because with a regular lattice the mixing situation degrades as the Δp decreases. For momentum spread reduction by e^{-1} (e^{-2}) the overall improvement turns out to be 4.4 (5.8) in our standard case.

The gain concerns transverse cooling and longitudinal cooling by the "Palmer method" [2] where the momentum error is detected via the transverse displacement of the particle. For the filter method of Thorndahl [3] where the in essence the momentum error is deduced from the change in time of flight for a whole revolution, the "split lattice" is not helpful. However for the further momentum cooling methods, that use the time of flight over part of the circumference [4,5], the advantage remains. In this case one has to provide a well chosen finite, and if possible even tuneable η (instead of η=0) over the distance where the flight time is observed, and again large η for the section kicker to pickup. This can be achieved, at least in principle, by placing the observation interval partly into the low mixing and partly into the strong mixing branch of the lattice.

In summary: a factor of three to six in cooling speed can be gained with an optimum mixing lattice. The gain concerns transverse cooling as well as longitudinal cooling by the Palmer and local time of flight approaches but not the filter method.

LATTICE MODULES

Small η_{PK} requires a local momentum compaction $\alpha_{PK} = \gamma_{tr\,PK}^{-2}$ close to the beam's γ^{-2}. Big η_{KP} can be realized by large negative α_{KP}. There is a long list of references that deal with adjusting the momentum compaction (starting with the 1955 paper of Vladimirski and Tarasov [6] who proposed reverse bend dipoles to make the momentum compaction negative). The original aim was to avoid crossing of transition energy by making γ_{tr} large or even imaginary (α negative). In the 1970s the additional task of performing a jump of γ_{tr} without a too large change of the betatron tune [7-9] came up. The aim of the jump is to cross transition rapidly and this was achieved successfully, first in 1969 and operationally since 1974 in the CERN PS [7]. Later γ_{tr}-jumps were incorporated in the Booster and the Main Injector at

FERMILAB, as well as in the AGS and RHIC at BNL. Examples of synchrotrons that worked with imaginary transition energy are LEAR and STURN II.

In these applications negative closed orbit dispersion (D(s)<0) in bending magnets is of prime importance. Basically two methods, the 'harmonic-' and 'modular approach', are used to enhance D. In the harmonic method one excites a 'dispersion oscillation' by introducing a super-periodicity S in the bending or the focussing with S close to the betatron tune. In the modular approach local 'dispersion bumps' are generated via quadrupoles or bends. Both methods affect not only the dispersion but also the betatron functions, the tunes and other lattice properties. It is the aim of the designer to keep the unwanted perturbations small. This is more difficult in the existing machines (the PS, AGS, FNAL-booster) where, to maintain constant tune, a large number of γ_{tr}-jump quadrupoles has to be used and the maximum excursions of the dispersion and the β–functions are large. In designs, where flexible momentum compaction is included from the start, these problems are alleviated, although not completely removed.

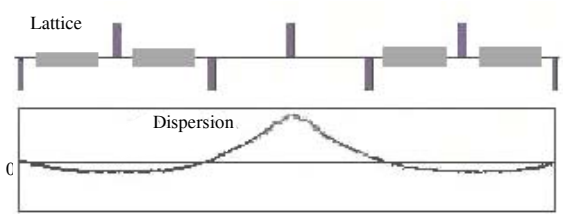

Figure 1: Layout of a simple Flexible Momentum Compaction (FMC) lattice module (adapted from [11]).

Already in 1972 L. Teng [10] proposed modules with a negative dispersion at dipole locations bridged by straight sections where the dispersion wave was positive (Fig. 1). Such a concept forms the basis of flexible momentum compaction (FMC) modules. More recently Trbojevic and co-workers [12-15] extended the modular approach. Their FMC sections consist of a FODO part where a negative dispersion in the dipoles provides negative α_p and a matching section, where the optical functions are re-matched to avoid excessive excursions.

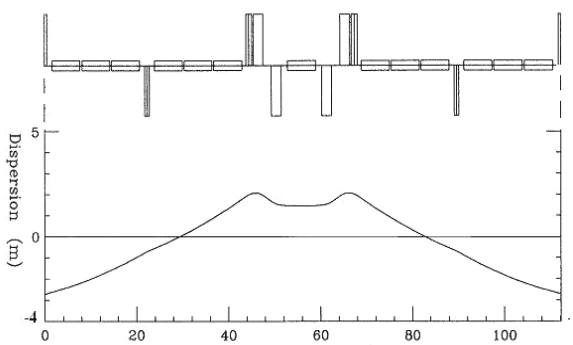

Figure 2: Example of an advanced FMC module (adapted from [13]).

The authors of [13] find that "…the modules can be made very compact without much unwanted empty space, and at the same time, the maximum of the dispersion function can be controlled to less than that of the regular …FODO lattice, thus overcoming … the difficulties of Teng's original idea". The phase advance of the module can be adjusted to be an odd multiple of quarter betatron waves and modules can be positioned one after another to create long sections with small or large negative momentum compaction. Designs for large momentum compaction [12], isochronous [14] and adjustable momentum compaction [15] lattices have been established.

In summary: It appears that the modular approach is well suited, to construct a cooling ring lattice consisting of small momentum compaction modules for the (low mixing, quasi-isochronous) part pickup to kicker and negative momentum compaction modules for the (strong mixing) part kicker to pickup. For a cooling ring that has to work at different energies, the isochronous part has to be tuneable. Here techniques used for the γ_{tr} jump can be helpful.

DISADVANTAGES

The FMC modules require extra quadrupoles. For example: the module of Fig. 2 needs 7 quadrupoles (on the assumption that the 2x2 adjacent quads near the centre are combined into a single lens each) compared to 6 in the corresponding regular FODO lattice. The number of different *quadrupole families* is 4 instead of 2 for the FODO structure. In fact the problems are similar to those of other lattice insertions like long straight sectors or low beta sections.

In the 'Teng structure' of Fig.1, the number of quadrupoles is the same as for the FODO lattice but the number of families is again larger, probably also 4 instead of 2 because in the 'missing magnet sections' the phase advance is specific and the horizontal defocusing of the dipoles is absent.

Moreover, a machine with *simple* FMC modules will have larger excursions of the optical function and hence reduced acceptances. With the advanced modules this drawback is absent or less pronounced. Yet there remains the problem that one will have several pieces of straight section and low betas at locations where one cannot always make use of them.

It is a question of detailed design to conceive a lattice which incorporates other basic blocks like injection/ejection, long straight sections, and locations for experimental apparatus. Lee, Ng, and Trbojevic [13] designed a complete accelerator ring using FMC modules. They found "…that this lattice is extremely tunable and is insensitive to misalignment errors. Its chromatic properties are at least comparable to that of a regular FODO lattice. … it provides dynamical aperture as large as that of a regular … lattice".

The 'optimum mixing lattice' will however have a basic periodicity of 1 and thus many systematic resonances will

be present. This perturbation is similar to the disturbance due to other insertions like e.g. a low beta section.

Finally the large η of the ring influences some RF-parameters e.g. the voltage necessary to produce a bucket of given size (U proportional to η) and the synchrotron oscillation frequency ($f_s \alpha \eta^{1/2}$)

In summary: "Optimum mixing lattices" need extra qudrupoles and extra quadrupole families. Compared to a regular FODO lattice they are more complicated, both in their design and their operation, especially when the advanced FMC modules are used. With simpler modules the acceptance will suffer. Other quantities depending on the ring η change.

COHERENT BEAM STABILITY

Damping of longitudinal instabilities is lost close to the transition energy (η –> 0). In fact the "Keil-Schnell-Boussard" stability criterion [16] requires coupling impedances Zn/n smaller than a maximum that is proportional to η and thus unattainably small for small η. However -- because the growth of the instability takes a great number of turns -- it is the η of the entire ring that counts. For the "split ring" (with circumference C) we have

$$\eta = \frac{L_{pk}}{C}\eta_{pk} + \frac{L_{kp}}{C}\eta_{kp} \approx \frac{L_{kp}}{C}\eta_{kp}$$

Then, if the mixing kicker to pickup is large (η_{kp} large as desired) we preserve a good margin for tolerable coupling impedance, frequently even higher than the in a regular lattice.

In summary: The "optimum mixing lattice" has automatically a large "whole ring η" and the longitudinal stability threshold is usually equal or even more favourable than in a regular lattice.

CONCLUSION

In the design of a new generation of stochastic cooling rings, the "optimum mixing concept" should be taken into consideration. FMC modules, originally developed to move up transition energy, are appropriate to construct lattices optimised for mixing. One can even think of tuning transition energy during a cooling cycle, taking advantage of concepts developed for a γ_{tr}–jump. The benefits have to be weighed against complexity, lager number of quadrupoles and, for simple FMC modules, larger required aperture or reduced acceptance.

REFERENCES

[1] D. Möhl, "The status of stochastic cooling", Nucl. Instr. Meth. A 391, 1997 p. 164-171 see also "Stochastic cooling for beginners", in CERN 84 -15, (see p. 113/ 114 and fig. 11).

[2] R.B. Palmer, "Stochastic cooling", Brookhaven Nat. Lab.internal Report BNL 18305 1973.

[3] G. Carron and L. Thorndahl, "Stochast cooling of momentum spread with filter techniques", internal Reports CERN/ISR–RF/78-12 and ISR-RF/Note LT/ps 78 1978.

[4] B. Kells' "Filterless fast momentum cooling", in Proc. 11th Internat. International Conference on High Energy Accelerators., Geneva 1980,(Birkhauser, Basel, ed. Company 1980) p. 777

[5] D. Möhl, "Stochastic cooling", in CERN 95-06, p. 587-671 1995, see also "Stochastic cooling for beginners", in CERN 84 -15, p. 151/152

[6] V.V. Vladimirski and E.K. Tarasov, "Theoretical problems of the ring accelerators" (USSR Academy of Sciences, Moscow, 1955).

[7] W. Hardt and D. Möhl, "Q-jump at transition", CERN internal Report ISR 300/GS/69 16; W. Hardt, "Gamma transition jump scheme of the CPS", in Proceedings of the 9th International Conference on High Energy Accelerators, Stanford, 1974, (edited by R. Nelson),p. 434-438

[8] L.C. Teng, " Compensation of space-charge mismatch at transition of booster using the transition jump method", Fermilab internal Report FN-207 April 1970; W.W. Lee and L.C. Teng, "Bunch length matching at transition energy in the FNAL booster", in Proceedings of the 8th International Conference on High Energy Accelerators, Geneva, 1971, (CERN), p. 327-330.

[9] T. Risselada, "Gamma transition jump schemes", in CERN 94-1, p. 161-174.

[10] L.C. Teng, "Infinite transition energy synchrotron lattice using π straight sections", Part. Accel. **4**, 1972 p. 81.

[11] J. Wei et al., "Lattices for high-power beam acceleration, secondary beam collection and cooling" , in Proc. EPAC 2006 (Edinburgh), p. 2074.

[12] D. Trbojevic, et al., "Design method for high energy accelerator without transition energy", in Proc. EPAC 1990 (Nice), p. 1536

[13] S.Y. Lee, K.Y. Ng and D. Trbojevic, "Minimizing dispersion in flexible-momentum-compaction lattices", Phys. Rev. E 48, 1993, p. 3040-3048.

[14] S.Y. Lee, K.Y. Ng and D. Trbojevic, "A design of a quasi-isochronous storage ring", in Proc. PAC1993 (Waschington) , p. 102-104.

[15] D. Trbojevic, E. Courant, "A standart FODO lattice with adjustable momentum compaction", in Proc. PAC 1997 (Vancouver) , p. 1371-1372.

[16] J. Bosser et al. , "Stability of cooled beams", Nucl. Instr.. Meth. A441, 2000, p. 1-8.

A SPLIT-FUNCTION LATTICE FOR STOCHASTIC COOLING *

Sheng Wang†, Institute of High Energy Physics, Chinese Academy of Sciences
Jie Wei‡, Institute of High Energy Physics, China and Brookhaven National Laboratory, USA

Abstract

Lattice for a 3-GeV cooler ring with split functions is presented. The ring consists of two half-rings of different properties: in one half-ring, the phase-slip factor is near-zero; in the other half-ring, the phase-slip factor is large. The near-zero phase slip minimizes the "bad mixing" between the stochastic-cooling pick-ups and kickers, while the high phase slip maximizes the "good mixing" between the kickers and the next-turn pick-ups.

INTRODUCTION

In Ref. [1] we reported the lattice design for rapid-cycling synchrotrons used to accelerate high-intensity proton beams to energy of tens of GeV for secondary beam production. After primary beam collision with a target, the secondary beam can be collected, cooled, accelerated or decelerated by ancillary synchrotrons (or cooler rings) for various applications [2, 3, 4].

To increase the efficiency of stochastic cooling in the cooler ring, the phase-slip factor between the cooling pick-ups and kickers shall be small to minimize the "bad mixing", and the phase-slip factor between the kickers and the next-turn pick-ups should be large to enhance the "good mixing" [5, 6]. In this paper, we present the preliminary lattice design for a 3-GeV cooler ring with split functions. The ring consists of two half-rings of different properties: in one half-ring, the phase-slip factor is near-zero; in the other half-ring, the phase-slip factor is large.

LATTICE LAYOUT AND FUNCTIONS

Two different lattice structures are adopted for each half of the split-function ring. We choose a normal FODO structure to achieve near-zero phase-slip factor in one half-ring, and choose Flexible Momentum Compaction (FMC) lattice to achieve large phase-slip factor in the other half-ring [7, 8, 9, 10]. The magnet layout of the ring is shown in Figure 1.

FMC Module Structure for Large Phase Slip

We use the FMC lattice to realize a small momentum compaction factor α_p, so that the absolute value $|\eta|$ of the phase-slip factor

$$\eta = \alpha_p - \frac{1}{\gamma^2} \tag{1}$$

is large. Here, γ is the Lorentz factor. For protons or anti-protons of 3-GeV kinetic energy, $\gamma = 4.2$.

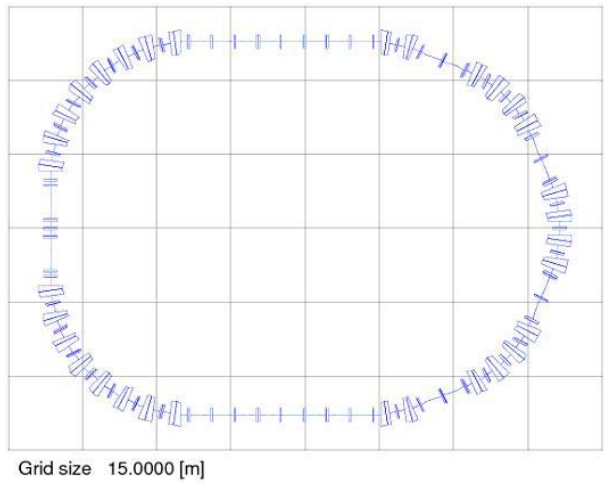

Figure 1: Main magnet layout of the cooler ring.

A FMC lattice without negative bending requires negative dispersion at locations of bending dipoles. Figure 2 shows the lattice module consisting of three FODO cells with missing dipole in the middle cell. The horizontal phase-advance of about 90° per cell excites dispersion oscillation so that high dispersion occurs at locations of missing dipoles.

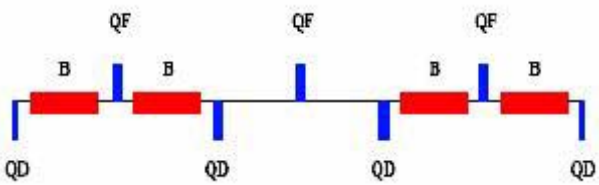

Figure 2: FMC module with missing dipoles.

The half-ring of large phase-slip factor is designed by using the modules shown in Figure 2. The lattice consists of four modules, as shown in the right-hand-side of Figure 1. The horizontal phase advance is near but not equal to 270° across each three-cell module. The horizontal phase advance across the four-module arc is exactly 6π, so that the dispersion is completely suppressed outside of the arc.

* Work performed under the auspices of the Chinese Academy of Sciences and the U.S. Department of Energy.
† wangs@ihep.ac.cn
‡ weijie@ihep.ac.cn and jwei@bnl.gov

The momentum compaction factor can be easily adjusted by varying the strength of the quadrupole families in the arc. The momentum compaction across this 180° bend is 0.001. The phase-slip factor of the lattice is -0.055. The lattice function is shown in the Figure 3.

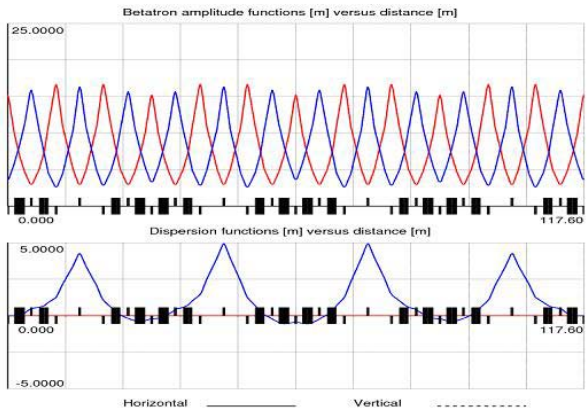

Figure 3: Lattice functions of the large phase-slip half-ring with FMC modules (blue in top chart: β_H; red in top chart: β_V; bottom chart: D_p).

Normal FODO Structure for Small Phase Slip

As shown in the Figure 1, the left-hand-side of the cooler ring contains two bending arcs, each containing four FODO cells. The horizontal phase advance is exactly 2π across each of these normal arcs. Two arcs are connected by a dispersion-free straight section with triplet-quadrupole focusing structure. By tuning the strength of the quadrupole families and the distance between the magnets, the momentum compaction across this 180° bend is adjusted to 0.0562 so that the phase-slip factor of the lattice is small ($\eta = 0.0005$). The lattice function is shown in Figure 4.

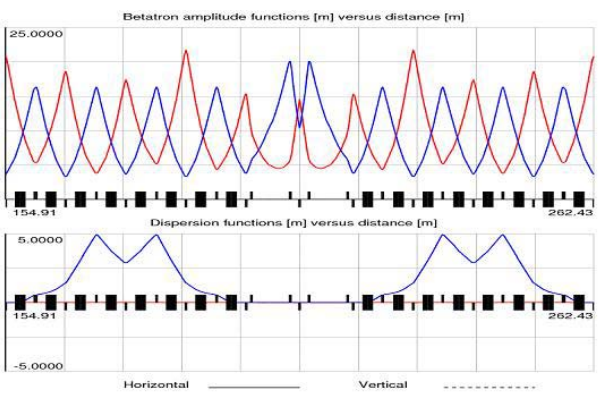

Figure 4: Lattice functions of part of the small phase-slip half-ring with FODO and triplet structure (blue in top chart: β_H; red in top chart: β_V; bottom chart: D_p).

Main Parameters

Corresponding to the kinetic energy of the 3 GeV beam and the circumference of the main accelerator, the circumference of the cooler ring is selected to be 299.7 m [1]. The maximum β-function is less than 23 m. The maximum dispersion is about 5 m. The lattice super-periodicity is 1. The focusing structures in the straight sections are FODO and triplet, providing drift spaces with uninterrupted length up to about 4 m to accommodate stochastic-cooling pickups and kickers, electron cooling, injection, extraction, and RF systems. Figure 5 shows the lattice function of entire ring. Table 1 gives the primary parameters.

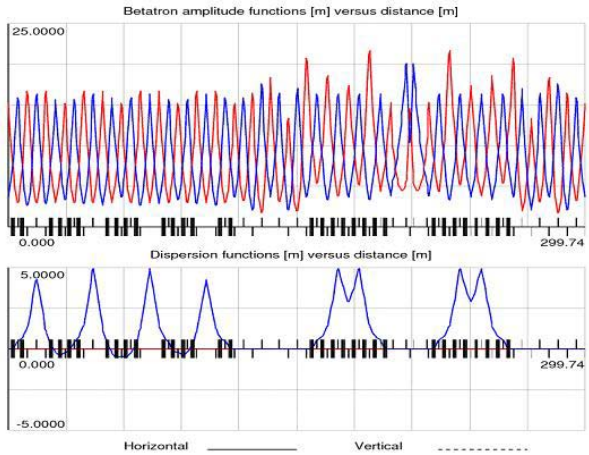

Figure 5: Lattice function of the entire cooler ring (blue in top chart: β_H; red in top chart: β_V; bottom chart: D_p).

Table 1: Primary parameters of the cooler ring.

Ion type	proton/anti-proton
Beam kinetic energy [GeV]	3
Ring circumference [m]	299.7
Lattice type - small phase-slip half	FODO/triplet
Lattice type - large phase-slip half	FMC
Uninterrupted drift length in straight [m]	< 4.2
Nominal betatron tune (H)	7.30
Nominal betatron tune (V)	7.34
Transition energy, γ_T	31.6
Natural chromaticity (H)	-8.7
Natural chromaticity (V)	-9.5
Maximum dispersion [m]	4.94
Momentum compaction factor	0.022

SUMMARY

Based on the Flexible Momentum Compaction lattice modules and FODO/triplet structures, we designed a split-function lattice for 3-GeV proton or anti-proton beams. As an example to facilitate stochastic cooling with high efficiency, we set the phase-slip factor between the cooling

pick-ups and kickers to near-zero (0.0005) to minimize the "bad mixing", and set the phase-slip factor between the kickers and the next-turn pick-ups to -0.055 to enhance the "good mixing".

In the case that the pick-ups or kickers need to be placed in high-dispersion locations, drifted spaces of dispersion near 5 m are available. The strengths of the quadrupole families may be adjusted to again realize the split-function features.

The lattice study presented is preliminary. Detailed work including dynamic-aperture evaluation is yet to be performed.

We thank S. Peggs, T. Satogata, S. Tepikian, and D. Trbojevic for many helpful discussions. We are deeply grateful to M. Steck, D. Moehl and the organizing committee of the COOL07 workshop for the invitation and support to the workshop.

REFERENCES

[1] S. Wang, J. Wei, K. Brown, C. Gardner, Y.-Y. Lee, D. Lowenstein, S. Peggs, N. Simos, *Lattices for High-Power Proton Beam Acceleration and Secondary Beam Collection and Cooling*, EPAC06, Edinburgh (2006)

[2] B. Autin et al, CERN/PS/AA78-3 (1978) ; E.J. Wilson et al, CERN 83-10 (1983)

[3] M.D. Church, J. Marriner, Ann. Rev. Nucl. Part. Sci. 43 (1993) 253; Fermilab Design Report, Tevatron I Project (1984)

[4] W.F. Henning, EPAC04 (2004) 50; http://www-aix.gsi.de/GSI-Future/cdr/

[5] *Handbook of Accelerator Physics and Engineering: a Compilation of Formulae and Data*, edited by A.W. Chao and M. Tigner (World Scientific, Singapore, 1998)

[6] D. Moehl, these proceedings

[7] L.C. Teng, Part. Accel., **4** (1972) 81

[8] R.C. Gupta et al, IEEE Tran. Nucl. Sci. NS-32 (1985) 2308

[9] D. Trbojevic et al, EPAC90 (1990) 1536

[10] E.D. Courant et al PAC91 (1991) 2829

ADVANCED HESR LATTICE WITH NON-SIMILAR ARCS FOR IMPROVED STOCHASTIC COOLING

Yu.Senichev, Forschungszentrum Jülich, Germany.

Abstract

The advanced HESR lattice with two arcs of identical layout and different slip factors has been developed. The conception of arcs with three families of quadrupoles makes it easy to adjust the imaginary transition energy in one arc and the real transition energy in another arc with the absolute value close to the beam energy in the whole required region from 3.0 GeV to 14 GeV. The arcs have the special feature that the high order non-linearities are fully compensated inside each arc, and therefore the dynamic aperture of the whole machine is conserved. We consider and compare two lattices with the same absolute value of transition energy: the current lattice with a negative momentum compaction factor in both arcs and correspondingly the lattice with negative and positive momentum compaction factors in different arcs. Simultaneously, we analyzed the 4- and 6- fold symmetry arc machine. Thus allows us to conclude that the 4-fold symmetry lattice is more suitable for acquiring slip factors. At the lowest energy 3 GeV, this is $\eta_{imag} / \eta_{real} \approx 4 \div 5$ in the imaginary and the real arc, respectively. For the higher beam energy this ratio is much bigger.

INTRODUCTION

To intensify the stochastic cooling process it is desirable to have the mixing factor between the pick-up and kicker as large as possible, and, on the contrary, in the case of mixing between the kicker and pick-up we should try to make it smaller. This option can be realized if the lattice has different local optical features between pick-up – kicker and kicker – pick-up.

The idea with different slip factors was first proposed by Möhl [1,2]. Later many authors tried to design such a lattice, for instance [3, 4]. However, this involved a more complicated lattice with a large number of quadrupole and sextupole families and the need to have different optical settings at different energies. As result the dynamic aperture in such lattices is usually unacceptably small, and it has very difficult tuning. Therefore the compromise was to scarify some of the desired re-randomization in order to avoid too much unwanted mixing. In the classical lattice the slip factors between pick-up and kicker η_{pk}, kicker and pick-up η_{kp} are similar, and by Möhl's definition [2] the mixing factors are approximately equal. In paper [5] the comprehensive analysis of the stochastic cooling was done in the HESR lattice with similar arcs and the negative momentum compaction factor ($\gamma_{tr} = 6.5i$) [6]. In this paper, we consider the advanced HESR lattice with different slip factors η_{pk}, η_{kp} in two arcs.

ARCS WITH DIFFERENT SLIP FACTOR

The HESR lattice consists of two arcs and two straight sections for the target and cooling facilities with a circumference ~500÷600 m. The arcs have 6-fold (or 4-fold) symmetry with superperiodicity S=6 (or 4). The phase advance per arc is $\nu_{x,y} = 5.0$ (or $\nu_{x,y} = 3.0$) in both planes. Each superperiod consists of three FODO cells with 4 superconducting bending magnets (B=3.6T) and superconducting quadrupoles with G<60T/m (see fig. 1).

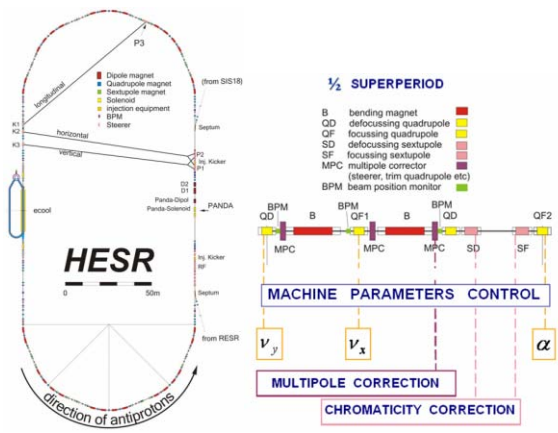

Figure 1: HESR layout and half super-period.

The momentum compaction factor is one of the most important characteristics of any accelerator, and defines its transition energy. The slip factor, $\eta = 1/\gamma^2 - 1/\gamma_{tr}^2$ determined by transition γ_{tr} and current γ energy, should be as high as possible in order to increase the microwave stability threshold.

The most successful solution for the control of the momentum compaction factor has achieved in [7] by simultaneously correlated curvature and gradient modulations. This lattice was used in the following projects: the Moscow Kaon Factory, the TRIUMF Kaon Factory, the SSC Low Energy Booster, the CERN Neutrino Factory and in the Main Ring of the Japan Proton Accelerator Research Complex facility constructed now [8]. In the HESR lattice the same idea was used [6].

In the advanced HESR lattice for the stochastic cooling we propose modifying the conception to provide different slip factors in two arcs, but with conservation of sequence of all bending, focusing elements and drift between them.

The proposed lattices meet the following requirements:

- momentum compaction factor is about $1/\nu^2$ in one arc (the slip factor close to zero, isochronous structure) and it is negative in the other arc $-1/\nu^2$; the total slip factor is enough high to provide a minimum spread in incoherent frequencies for the longitudinal motion stability requirements;
- dispersion-free straight sections;
- convenient method of correcting the chromaticity by the sextupoles;
- sufficiently large dynamic aperture after chromaticity correction.

The momentum compaction factor is usually determined from the integral

$$\alpha = \frac{1}{\gamma_t^2} = \frac{1}{2\pi}\int_0^{2\pi} \frac{D(\phi)}{\rho(\phi)} d\phi, \qquad (1)$$

where $D(s)$ is the dispersion function and $\rho(s)$ is the curvature radius of the equilibrium trajectory.

To achieve the required momentum compaction factor we make a correlated modulation of the quadrupole gradients

$$\varepsilon \cdot k(\phi) = \sum_{k=0}^{\infty} g_k \cos\, k\phi \qquad (2)$$

and the orbit curvature

$$\frac{1}{\rho(\phi)} = \frac{1}{R}\left(1 + \sum_{k=1}^{\infty} r_k \cos k\phi\right) \qquad (3)$$

with superperiodicity S_{arc}.

The radius curvature modulation r_n is provided by the missing magnet and it is performed once and is then fixed. However, the gradient modulation is the variable parameter. Due to the FODO structure with mirror symmetry we realize:

$$\begin{aligned} &\frac{\partial\alpha}{\partial G_{QF2}} >> \frac{\partial\alpha}{\partial G_{QF1}} \approx \frac{\partial\alpha}{\partial G_{QD}} \\ &\frac{\partial\nu_x}{\partial G_{QF1}} > \frac{\partial\nu_x}{\partial G_{QF2}} >> \frac{\partial\nu_x}{\partial G_{QD}} \\ &\frac{\partial\nu_y}{\partial G_{QD}} >> \frac{\partial\nu_y}{\partial G_{QF1}} \approx \frac{\partial\nu_y}{\partial G_{QF2}} \end{aligned} \qquad (4)$$

Therefore, the lattice provides independent control of α, ν_x, ν_y by gradients of quadrupoles QF2, QF1 and QD, respectively.

In paper [7], the dispersion equation was solved for the case of both the quadrupole gradients and the orbit curvature modulation:

$$\alpha_s = \frac{1}{\nu^2}\left\{1 + \frac{1}{4(1-kS/\nu)} \cdot \left[\left(\frac{\overline{R}}{\nu}\right)^2 \frac{g_k}{\left[1-(1-kS/\nu)^2\right]} - r_k\right]^2\right\} \qquad (5)$$

where $\overline{R}$ is the average radius of machine, and ν is the horizontal tune. We can see that the sign of the momentum compaction factor depends on the term $1-kS/\nu$. The negative momentum compaction factor is achieved in lattice with superperiodicity S and ν, when $1-kS/\nu < 0$ and it is determined by the kS-th harmonic.

It can be seen that this lattice has a remarkable feature: the gradient and the curvature modulation amplify each other if they have opposite signs $g_k \cdot r_k < 0$, and, on the contrary, they can compensate each other when they have the same sign. We use this feature to make arcs with different slip factors. Hereinafter, we will call the arc between the pick-up and the kicker in the line of beam the real arc $\alpha = 1/\gamma_t^2 > 0$. Correspondingly, the arc between the kicker and the pick-up will be called the imaginary arc $\alpha = 1/\gamma_t^2 < 0$, because the transition energy is imaginary.

First of all, in both arcs we create the resonant curvature modulation by the usual method of the "missing magnet" in the center of the superperiod. Then the quadrupole gradient is modulated with the opposite sign and the value determined by the gradient modulation when the ratio between them is:

$$|r_k| \le \left(\frac{\overline{R}}{\nu}\right)^2 \left|\frac{g_k}{1-(1-kS)^2}\right| \qquad (6)$$

In principle, the curvature modulation can be made much higher, but since in the real arc we need full compensation of the curvature modulation by the gradient modulation, and we would like to have an identical sequence of magneto-optic elements in both arcs, it is not desirable to increase the first arc. At the same time, the gradient modulation is restricted by the parametric resonance of the envelope, when the second harmonic $kS/\nu = 2$.

Therefore, from this point of view it is desirable to have such g_k when the ratio has value:

$$\frac{1}{4(kS/\nu - 1)} \cdot \left(\frac{g_k}{[1-(1-kS/\nu)^2]} - r_k\right)^2 \approx 2 \qquad (7)$$

Then the momentum compaction factor in the imaginary arc takes the form $\alpha_{kp} \approx -1/\nu^2$, and the momentum compaction in the real arc is $\alpha_{pk} \approx 1/\nu^2$. Thus, in such a lattice, we can make two arcs with different slip factors: $\eta_{pk} = 1/\gamma^2 - 1/\gamma_{tr}^2$; $\eta_{kp} = 1/\gamma^2 + 1/\gamma_{tr}^2$. In case $\gamma \approx \nu$, one of the arcs is isochronous when the slip factor

is $\eta_{pk} \approx 0$, and the other slip factor is $\eta_{kp} \approx 2/\nu^2$. However, together with the advantage of two different arcs for stochastic cooling we lose the lattice mirror symmetry, which makes the probability of the structure resonance excitation higher.

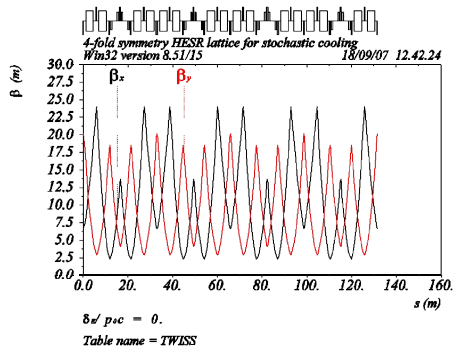

Figure 2: $\beta_{x,y}$-functions on the imaginary arc.

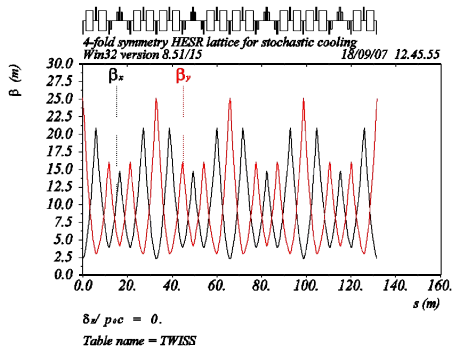

Figure 3: $\beta_{x,y}$-functions on the real arc.

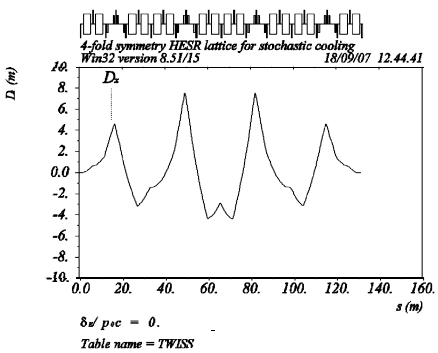

Figure 4: Dispersion-functions on the imaginary arc.

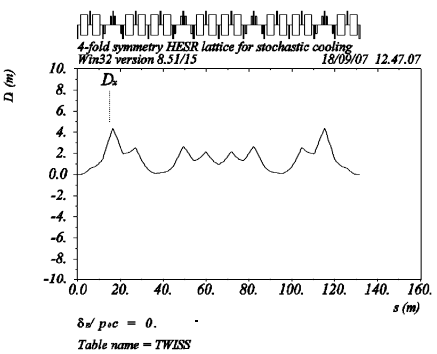

Figure 5: Dispersion-functions on the real arc.

However, the lattice developed here has the fundamental feature, since the both arcs have the same tunes and the similar phase advance between all elements located on arc. Since any order resonance strength is determined by the integral

$$\left\langle h_{k_x,k_y,p} \right\rangle \propto \int_0^C \beta_x^{k_x/2} \beta_y^{k_y/2} \frac{\partial^{(k_x+k_y-1)} B_{y,x}}{\partial (x,y)^{(k_x+k_y-1)}}(s) \exp i(k_x\mu_x + k_y\mu_y) ds \quad (8)$$

and, as we can see, in the subintegral expression the $\beta_{x,y}$-functions are the multipliers of field errors, the resonance excitation probability is determined only by the difference of $\beta_{x,y}$-function behaviour in the arcs.

Figures 2-5 show the $\beta_{x,y}, D_x$ functions for the real and imaginary 4-fold symmetry arcs. In both arcs the dispersion is suppressed to have the zero-dispersion straight sections. We can see from these figures that the different momentum compaction factors are reached mainly due to the dispersion function change, and that the β-function itself changes insignificantly.

Two families of sextupoles are used for the chromaticity correction (see fig. 1). To make the sextupoles self-compensating in the first approach we have to have an even number of arc superperiods S_{arc} and as a consequence nearest to S_{arc} the arc tune $\nu_{arc} = S_{arc} - 1$. Then the phase advance between similar sextupoles of $i-th$ and $(i + S_{arc}/2) - th$ superperiods equals $\nu_{arc}/2$. This means we have an exact condition for compensating each sextuplet's non-linear action by another one. Thus, there are the combinations: $\{S_{arc}, \nu_{arc}\} = \{4,3;\ 6,5;\ 8,7;\ldots\}$.

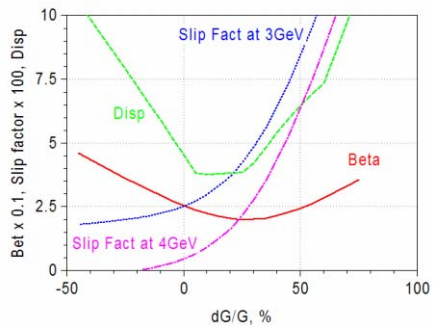

Figure 6: β_x, D_x, η vs. gradient modulation.

The optimum set for our case should be around a value $\nu = 2\nu_{arc} \approx \gamma$ and depends on the lowest energy. For instance, for energy E=3 GeV ($\gamma \approx 4.2$) the 4-fold arc with a tune of arc $\nu_{arc} = 3$ gives the best fit. Figure 6 shows Twiss parameters together with the slip factor dependence on the gradient modulation. We can see that for an energy 3 GeV at acceptable Twiss parameter

behavior the maximum ratio is $\eta_{imag} / \eta_{real} \approx 4 \div 5$, while at 4 GeV this ratio can be significantly higher.

DYNAMIC APERTURE

At the end of this paper, we will discuss the numerical calculation results. Since the indicator of any structure is the dynamic aperture, we performed the tracking simulation in the lattice with non-similar arcs and compare this with the lattice where the arcs are similar. Of course, due to the loss of mirror symmetry in the whole ring lattice the dynamic aperture becomes smaller. But the significant reserve of the dynamic aperture still allows the large right value in the horizontal plane ~270 mm mrad and in the vertical plane ~500 mm mrad. Both values satisfy the required ratio between the dynamic and physical apertures very well.

CONCLUSION

We developed the advanced lattice for stochastic cooling. The lattice has two similar arcs with different mixing factors due to the different slip factors with conservation of the optic geometry. Each arc has two families of focusing quadrupoles and one family of defocusing quadrupoles. The transition energy is adjusted by the quadrupole gradient modulation. The natural chromaticity is corrected by one family of focusing and defocusing sextupoles. After the chromaticity correction the dynamic aperture remains very large. The straight section allows stochastic and electron cooling to be performed simultaneously.

The author would like to thank D. Möhl, A. Sidorin and A. Dolinsky for reading the article and useful discussions.

REFERENCES

[1] D. Möhl, G. Petrucci, L. Thorndahl and S. van der Meer, Phys. Rep. 58 (1980) 75

[2] D. Möhl, Nuclear Instruments and Methods in Physics Research A 391 (1997), 164-171

[3] R. Giannini, P. Lefevre, D. Möhl, SuperLear, Conceptual machine design, Nuclear Physics A558(1993), 519c

[4] A. Dolinskii, et al., Optimized lattice for the Collector Ring, NIM A532 (2004) 483-487

[5] H. Stockhorst et al., Stochastic cooling for the HESR at the GSI-FAIR complex, EPAC 2006

[6] Yu. Senichev et al., Lattice Design Study for HESR, Proc. of EPAC 2004, p.653, Lucerne, Swiss (2004)

[7] Yu. Senichev, ICANS, KEK Tsukuba, 1990, p.

[8] Y. Ischi, et al. paper 5D002.pdf http://hadron.kek.jp/jhf/apac98/

LATTICE CONSIDERATIONS FOR THE COLLECTOR AND THE ACCUMULATOR RING OF THE FAIR PROJECT*

A. Dolinskii, F. Nolden, M. Steck,
GSI, Darmstadt, 64291, Germany

Abstract

Two storage rings (Collector Ring (CR) and Recycled Experimental Storage Ring (RESR)) have been designed for efficient cooling, accumulation and deceleration of antiproton and rare isotopes beams at the FAIR project (Darmstadt, Germany). The large acceptance CR must provide efficient stochastic cooling of hot radioactive ions as well as antiproton beams. The RESR will be used as an accumulator of high intensity antiproton beams and as decelerator of rare isotopes. Different lattice structures have been considered in order to achieve good properties for the stochastic cooling and at the same time the maximum dynamic aperture. The structure of the ring lattices and its ion optical properties are described in this contribution. The beam dynamics stability and flexibility for operation in the different modes are discussed.

INTRODUCTION

Production, fast cooling, and accumulation of intense secondary beams, antiprotons and rare isotopes are key issues of the FAIR accelerator facility [1]. The rather hot secondary particles, rare isotopes coming out of the Super-FRS [2] or antiprotons coming out of the antiproton separator will be injected into the Collector Ring (CR), where fast RF bunch rotation and debunching followed by fast stochastic pre-cooling in all phase planes is foreseen. The envisaged total precooling times are 10 s for 3 GeV antiprotons and 1.5 s for fully stripped radioactive isotopes at 740 MeV/u. The CR will be operated at static magnetic field corresponding to the magnet rigidity of 13 Tm. After precooling in the CR the batches of 10^8 antiprotons will be delivered to the RESR, where the accumulation up the 10^{11} particles takes place during several hours at the beam energy of 3 GeV. Then accumulated antiprotons are either transferred to the HESR [3] for further acceleration/ deceleration or transferred to the NESR [4] for experiments with low energy antiprotons at FLAIR [5]. The accumulation scheme in the RESR foresees longitudinal stacking in combination with stochastic cooling. This will be achieved by a momentum stacking scheme. The RESR will be used also as the fast decelerator of rare isotopes from an energy of 740 MeV/u to energies between 100 MeV/u and 500 MeV/u within 1 s in order to be able to provide short-lived rare isotope beams at low energy for electron-ion collision experiments in the NESR. As an

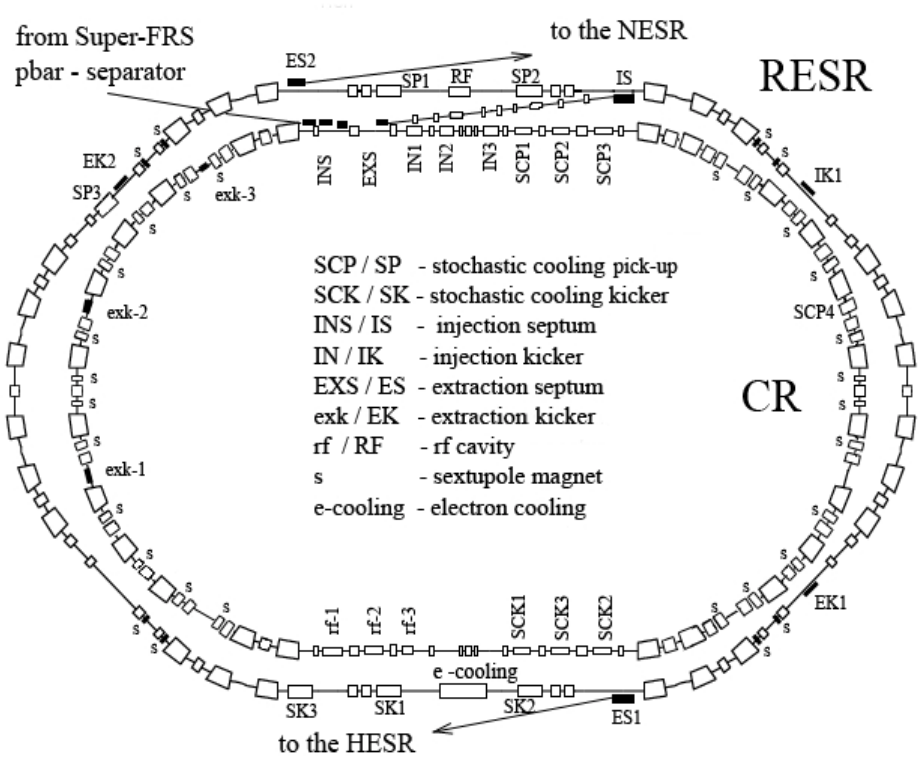

Figure 1: Layout of the CR – RESR rings.

* Work supported by EU design study (contract 515873 – DIRAC Secondary-Beams)

option the RESR can be used to decelerate antiprotons as well. This will be necessary if antiprotons for antiproton-ion collision experiments have to be provided to the NESR. For this mode the antiprotons are cooled and accumulated below the RESR transition energy to avoid crossing of the transition energy during deceleration. An additional electron cooling system in the RESR then compensates diffusion during deceleration. As this option is expected to be realized at a later stage of the FAIR project, the required space for the installation is taken into account during the present planning.

Here we consider the lattices of the two rings: the CR and RESR, where the stochastic cooling technique will be used for efficient cooling and accumulation of antiprotons. The RESR and CR are located in a common building as depicted in Figure 1.

THE COLLECTOR RING

The Lattice Consideration

On an early stage of the CR design we have considered two solutions for the CR lattice: a "symmetric ring" with identical lattice functions in the arcs and the "split ring" with different lattice functions in the arcs. The detailed consideration of both lattices is given in ref.[6]. In both cases the CR ring layout should follow these requirements

- setting different γ_{tr} values for antiprotons and radioactive ion beams to reach optimized mixing parameters for stochastic cooling, both for desired and undesired mixing;
- setting γ_{tr} value exactly equal to the energy of radioactive isotopes to have the so-called isochronous condition in the ring for TOF mass measurements [7];
- accommodation of stochastic cooling pick-up and kickers as well as the RF cavities in regions of zero dispersion;
- controlling the horizontal and vertical betatron phase advance between pickups and kickers of the transverse stochastic cooling systems;
- reducing chromaticity over the whole momentum range;
- the arrangement of sextupoles and higher order correctors has to be applicable for all three (different) ion optical settings;
- sufficient places to house the injection/extraction devices.

One can see that the ring must operate in three different optical modes in order to have good properties for stochastic cooling. In this paper we call the optics of the CR needed for antiproton cooling as "pbar-mode", for radioactive isotope beams – "rib-mode", and for the isochronous condition – "iso-mode". After many optimisations it was found that the "symmetric ring" lattice is much favourable because of different reasons. This layout of the CR gives the possibility to choose optimal ring optics for both pbar and rib-modes and the CR can be easily adjusted to iso-mode with relatively large transverse and momentum acceptance. Table 1 lists the main specification of the symmetric ring and the beam parameters before and after cooling.

Table 1: Main Specifications of the CR

Circumference	215 m	
Magnetic rigidity	13 Tm	
	antiprotons	Rare Isotopes
Max. number of particles	10^8	10^9
Kinetic energy	3 GeV	740 MeV/u
Transition, γ_{tr}	3.6	2.7
Betatron tunes Q_h/Q_v	4.42 / 4.44	3.11 / 3.10
Natural chromati., ξ_x / ξ_y	-7.8 / -8.4	-5.6 / -4.6
Revolution frequency	1.38 MHz	1.18 MHz
RF amplitude	100 kV	200 kV
Beam emittance (2σ) after injection after cooling	 240 mm mrad 5 mm mrad	 200 mm mrad 0.5 mm mrad
Momentum spread (2σ) after injection after cooling	 3 % 0.1 %	 1.5 % 0.05%
Overall cooling time	10 s	1.5 s

The Chromatic Correction

Since hot ion beams must be injected into the CR efficient chromatic correction must be done for a large off-momentum dynamic aperture. Therefore the CR lattice requires strong sextupole correctors. In the present layout of the CR design normalconducting quadrupole magnets with a number of separate sextupoles are considered. A method to control the natural chromaticity of a synchrotron, while keeping the tunes $Q_{x,y}$ constant, is to introduce two families of sextupoles for example placed at location of the ring, where the values of the function $\beta_{x,y}$ and D_x are high. But two sextupole families however may strongly affect the first and second order dependence on the momentum spread of the $\beta_{x,y}$ and D_x functions as well as of the chromaticity. This dependence of the functions $\beta_{x,y}$ and D_x on $\delta p/p$ introduces strong "beta/dispersion waves", which reduces the dynamic aperture of the ring. In addition the beta/dispersion waves will affect the horizontal and vertical chromaticities $\xi_{x,y,t}(\delta p)$ through the first and higher order terms of the chromaticity expression [8]. In order to minimize the dependence of $\beta_{x,y}$, D_x and the chromaticity on the $\delta p/p$, several sextupole families are required. Presently 6 independently powered sextupole families (totally 24) are foreseen in order to control the chromaticity and at the same time to minimize the dependence of the $\beta_{x,y}$ and D_x on $\delta p/p$. The side effect of using such a large number of sextupoles is the introduction of additional non-linearities

in the ring such as increasing the amplitude dependence and nonlinear chromatic aberration. These effects tend to reduce the dynamic aperture. In case of the split optics in the CR the dynamic aperture is smaller then the required ring acceptance in pbar-mode operation [6]. The symmetric ring layout gives optimal properties of the optics for the stochastic cooling and at the same time the maximum dynamic aperture in all modes of operation.

Stochastic Cooling in the CR

The injection and extraction beam parameters (Table 1) for both stochastic cooling tasks in pbar and rib-modes are determined by the longitudinal, horizontal and vertical beam emittances at the end of the transport lines from the antiproton target and from the Super-FRS. The optical layout of the ring is chosen to meet the requirements for most efficient cooling. It has turned out that flexibility in setting transition γ_{tr} to an optimal value is extremely important. This is due to the necessity to find a compromise for the required mixing between kicker and pick-up (which should be large) and the undesired mixing between pick-up and kicker (which should be small). In a simplified model, one can write the stochastic cooling rate

$$\frac{1}{\tau} = \frac{W}{2N}\left[2gB - g^2(M+U)\right], \quad (1)$$

where W is the electronic bandwidth, N is the number of particles in the beam, g is the system gain, B is the undesired mixing parameter, which can be written in the form

$$B = \cos(m_c \varphi_u), \quad (2)$$

here m_c is the central harmonic in the cooling frequency band, φ_u is undesired mixing phase angle

$$\varphi_u = k\eta_{pk}\frac{\delta p}{p}. \quad (3)$$

k is the ratio between the path from pickup to kicker and the circumference, $\delta p/p$ is the maximum momentum width to be cooled, η_{pk} is the local frequency slip factor between pick-up and kicker

$$\eta_{pk} = \left|\frac{1}{\gamma^2} - \frac{1}{\gamma_{tr,pk}^2}\right|, \quad (4)$$

with the local $\gamma_{tr,pk}$

$$\frac{1}{\gamma_{tr,pk}^2} = \frac{1}{\Delta L_{pk}}\int_{s_p}^{s_k} D(s)\frac{ds}{\rho(s)}. \quad (5)$$

In this equation s_p and s_k denote the azimuthal positions of the pick-up and the kicker, $D(s)$ is the dispersion function, and $\rho(s)$ is the radius of curvature. The desired mixing parameter can be approximated by

$$M = \left(m_c \eta_{kp}\frac{\delta p}{p}\right)^{-1}. \quad (6)$$

U is the noise to signal ratio. If the parameter $m_c\varphi_u$ becomes larger than $\pi/2$, the cooling force changes sign,

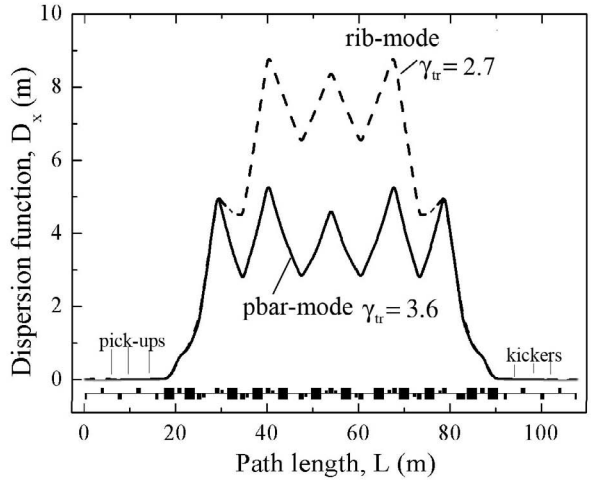

Figure 2: Dispersion function of the CR over half of the ring.

i.e. heats up the beam. This is minimized by making γ_{tr} as low as possible by increasing the dispersion in the dipole magnets. Also, the ratio k is minimized by placing pick-up and kicker as close together as possible. Rare isotope beams (γ = 1.79) and antiproton beams (γ = 4.2) require different γ_{tr}. For the antiproton beams one has to keep a certain distance between γ and γ_{tr} in order to make the mixing parameter M small enough. For antiproton cooling, the CR will be operated above transition with γ_{tr} = 3.6. In rib-mode the CR will be operated bellow transition with γ_{tr} = 2.7. In Fig.2 the shape of the dispersion functions over half of the ring for both pbar-mode and rib-mode is shown. For the rare isotope beams, the undesired mixing effect limits the momentum acceptance of the system because of the larger dispersion function in the arcs (Fig.2).

THE RECYCLED EXPERIMENTAL STORAGE RING

The RESR layout is dominated by the requirements of the stochastic cooling system in combination with momentum stacking. Beams are always transferred from the CR. This means the injection septum has to be positioned on the inner side of the RESR (Fig.1). The momentum stacking scheme requires a kicker which covers only half of the RESR aperture at a location in a dispersive section of the ring. The beam is injected on an inner orbit at a momentum offset of approximately $\Delta p/p$ = -0.8 % with respect to the central orbit, while the stacked beam circulates on an outer orbit with $\Delta p/p$ = +0.8 %. Although no stacking for rare isotopes is foreseen, the injection scheme is the same as for antiprotons.

The new version of the RESR has been designed with emphasis on strong stochastic accumulation rate. The structure of the ring is sketched in Fig. 1. The boundary conditions follow the requirements

- adjustable transition energy to provide good ion optical properties of the ring for antiproton

accumulation as well as for radioactive ion deceleration;
- to have a large dispersion function at the longitudinal stochastic pick-up to provide the good separation between injection and stacking orbits;
- small vertical beta function at longitudinal pick-up position
- long drift sections to provide injection from the CR as well as extraction from the RESR
- the phase advance in all pairs between kicker and septum for inj/ext must be close to $\pi/2$.

The current layout shown in Fig.1 fulfils all these requirements. This lattice is also suitable for fast deceleration of rare isotopes. Therefore, the optical mode of the RESR can remain unchanged for this task. Required acceptances of the RESR are moderate since only pre-cooled beams are injected from the CR. The actual RESR lattice and beam parameters are given in the Table 2.

Table 2: Main Specifications of the RESR

Circumference	240 m	
Magnetic rigidity	13 Tm	
	Antiprotons	Rare Isotopes
Max. number of particles	10^{11}	10^{9}
Accumulation time	up to 3 h	no accum.
Kinetic energy	3 GeV	740 MeV/u
Transition, γ_{tr}	6.0	3.3
Betatron tunes Q_h/Q_v	3.11 / 4.10	
Momentum acceptance	1.6 %	
Trans. acceptance, H/V	40 / 35 mm mrad	
Revolution frequency	1.17 MHz	1.0 MHz
Beam emittance (2σ) after extraction	5 mm mrad	1 mm mrad

The chromaticity correction is done by two families of sextupole magnets. Each family consists of 4 sextupole magnets. The lattice functions have a basic superperiodicity of 2. The adjustment of γ_{tr} is obtained by tuning the quadrupoles, which are located between injection (IK1) and extraction kickers (EK1, Fig.1). Using 6 independently powered quadupoles families in arc one can create a local dispersion bump in 6 dipole magnets as shown in Fig.3 such that the γ_{tr} can be chosen in the range of 3.3 – 6.4 and the betatron tunes remain unchanged.

Stochastic Cooling in the RESR

A crucial point of the accumulation scheme is the reduction of emittance and momentum spread of the injected antiproton beam within the time between successive injections. The stochastic cooling system therefore must be capable of cooling a batch of 10^8 antiprotons to its final values with respect to emittance and momentum spread within 10 s. The foreseen momentum stacking scheme is very similar to the CERN AA stacking scheme [9], where such as system has been used successfully. A study on a CERN AA like system for the RESR has shown that the RESR lattice is well suited for this task. Furthermore, the results led to the definition of the gain profile for the pickups of the longitudinal cooling system. The momentum cooling system is divided into three different systems: the hand-over system, the stack-tail system and the stack-core system. An injected beam will be transferred from the injection orbit to an orbit which is covered by the hand-over system using the standard RF-cavity of the RESR. The different cooling systems then are cooling this beam towards the stack-core [10].

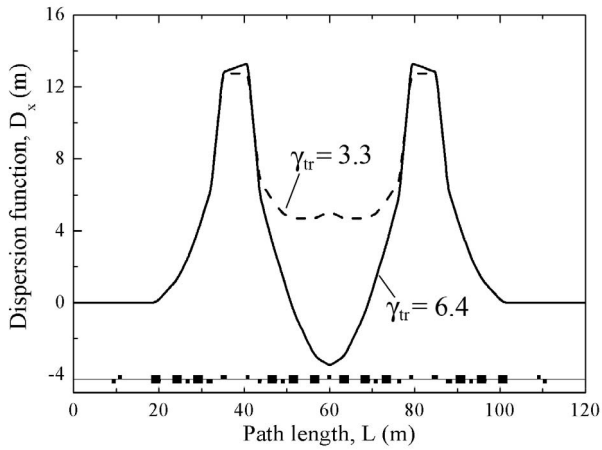

Figure 3: Dispersion function bump in the RESR arc.

REFERENCES

[1] An International Accelerator Facility for Beams of Ions and Antiprotons, Conseptual Design Report, GSI, 2001, and Baseline Technical Design Report, GSI, 2006. Both reports are available at www.gsi.de/fair/reports.

[2] H. Geissel et.al., Nucl. Instr. Methods Phys. Res., Sec. B 204 (2003) 71.

[3] Y. Senichev et al., Lattice Design Study for HESR, EPAC'2004, Lucerne, (2004) 653.

[4] C. Dimopoulou, K. Beckert, P. Beller, A. Dolinskii, U. Laier, F. Nolden, G. Schreiber, M. Steck, J. Yang, Phys. Rev. STAB 10, 020101 (2007)

[5] C. P. Welsch, M. Grieser, J. Ullrich, A. Wolf, Nucl. Inst. and Meth. A 546 (2005) 405.

[6] A. Dolinskii, P. Beller, K. Beckert, B. Franzke, F. Nolden, M. Steck, Nucl. Inst. and Meth. A 532 (2004) 483.

[7] A. Dolinskii, S. Litvinov, M. Steck, H. Weick, Nucl. Inst. and Meth. A 574 (2007) 207.

[8] E. D. Courant and H. S. Snyder. Theory of alternating gradient synchrotron. Annals of Physics, V3 (1958), p.1

[9] H. Koziol, S. Maury, CERN-PS 95-15 (AR/BD), 199.

[10] F. Nolden, A. Dolinskii, C. Peshke. Stochastic cooling for the FAIR project, this conference.

LATTICE OPTIMIZATION FOR THE STOCHASTIC COOLING IN THE ACCUMULATOR RING AT FERMILAB

V.Lebedev, V.Nagaslaev*, S.Werkema
Fermilab, PO Box 500, Batavia IL 60510, USA

Abstract

New efforts are under way at Fermilab to increase the rate of antiproton production. This program includes optimization of machine optics in the Antiproton Accumulator to improve stochastic cooling. The new lattice was implemented in May of this year. Results are discussed, as well as some aspects of model development and lattice measurements.

INTRODUCTION

A broad effort to increase antiproton production for the Tevatron accelerator complex at Fermilab was initiated in 2005. The goal was to optimize the performance of all machines in the production chain: Booster, Main Injector, Debuncher, Accumulator and beam lines, in order to maximize the flux of antiprotons to the Accumulator. This effort succeeded in reaching the peak rate of 20 mA/hr in February 2006.

Further increase of the stacking rate was limited by the capability of the stacktail stochastic cooling system in the Accumulator such that any further increase in the incoming flux would not result in an appreciable increase in the antiproton accumulation rate.

The new effort that started after the shutdown of 2006 concentrated primarily on the stacktail cooling system. Subsequently, there was a further increase in the peak rate (23mA/hr in April, 2007), but more importantly, also the average stacking rate. This progress, combined with very successful improvements in the Fast Transfer Protocol [1], resulted in nearly doubled average weekly production of antiprotons for the Tevatron in March, 2007.

A significant outcome of this effort was the development of an integrated physics model of Accumulator stochastic cooling [2] that identified physical and technological limitations of the system, as well as the way to improve its performance. Here we discuss the optimization of the Accumulator lattice as suggested by this model, the implementation of the optimized lattice, and first results.

ACCUMULATOR LATTICE

The Accumulator has a periodicity of 3, and mirror symmetry in each of 3 sectors. It has 3 straight sections and 3 arcs. The Accumulator lattice functions are shown in Figure 1. Continuous injection of the antiproton beam from the Debuncher is maintained using stochastic stacking. Beam arrives at the injection orbit at an energy that is approximately 140 MeV higher than that of the circulating core beam. 100 msec later the injected beam is adiabatically bunched and RF displaced to the deposition orbit, which is approximately at the center of aperture. From this point it falls under the action of the stochastic cooling force (Stacktail system) that starts pushing it towards the main core beam (60 MeV below the central orbit energy). A 6D-cooling of the main core beam is performed by separate core stochastic cooling systems.

Large dispersion in the arcs (10m) separates the beam according to energy, whereas in straight sections beams of all energies are merged together and compressed in order to fit into the very narrow aperture of the stochastic cooling tanks. Beam focusing and flattop dispersion in the arcs are maintained by the quad quadruplets on each side of the small straight sections inside the arcs. These high dispersion sections house extraction/injection kickers and the momentum stochastic cooling pickups. In the long straight sections the dispersion is cancelled at the small bend magnets on each side. These low dispersion sections accommodate stochastic cooling kickers, RF cavities, a DCCT transformer, and dampers.

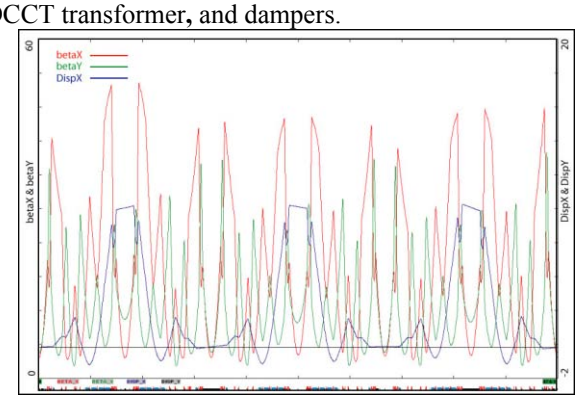

Figure 1: Accumulator Twiss-functions. Red and green traces show the horizontal and vertical beta-functions. The horizontal dispersion is shown with the blue trace.

It is important to keep dispersion as low as possible in the long straight sections. Any residual dispersion here would couple the longitudinal kicks of the stacktail kickers into the transverse dimensions causing transverse heating of the beam.

LATTICE OPTIMIZATION

Objectives

The main objective for the lattice optimization was to increase the slip factor (η). This would directly help the stack tail cooling as the maximum flux is proportional to η [2]:

$$J_{\max} = |\eta| T_0 W^2 x_d$$

** Work supported by FRA, LLC under Contract No. DE-AC02-07CH11359 with the United States Department of Energy.
#vnagasl@fnal.gov

The maximum useful value of η is limited by overlapping schottky bands at high harmonics ("bad mixing"), but there is still some room (15-20%) available, according to the model of the stacktail cooling [2].

Another benefit of raising the slip factor is additional separation of the stacktail and core revolution frequencies. This would mitigate the effects of resonant heating of the core. It has been found recently that the electrical center of the core momentum kickers depends on frequency and shifts to about 2mm at 3.3GHz [2]. This heats particles in the core whose transverse sidebands overlap with the stacktail harmonics at 3.3 GHz. Figure 2 shows the calculated emittance growth rate for a particle with a given revolution frequency. The vertical dash marker shows the center position of the core particles. Separation of the core and stacktail would better center the core between the two sideband peaks, thus reducing the heating of the core particles.

Great attention has been paid to the dispersion reduction in the long straight sections. As the standard mults affect the slip factor, they are only used for the fine

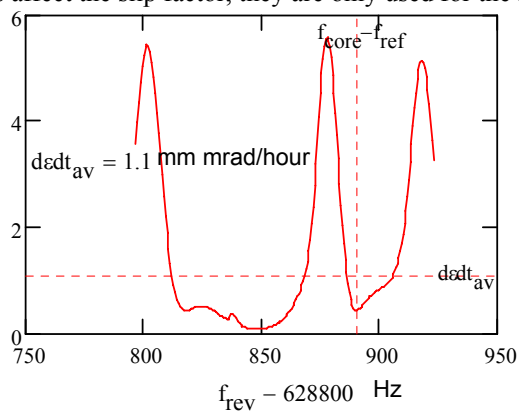

Figure 2: Emittance growth rate versus the particle frequency due to resonant heating at 3.3GHz. Vertical dash line shows the location of the core. Horizontal dash line shows average core heating rate due to this effect.

tuning, and the main corrections were made within the lattice change.

It was very desirable also to increase the design machine aperture to at least 14-15π mm-mrad. Presently the machine admittance is limited at 8-10π mm-mrad and is not very well understood. Compressing the beam size at most narrow locations may improve the admittance.

Lattice Model

For optics calculations in the Accumulator ring we utilized a model based on the OptiM program [3]. The model parameters were fit to the measured data taken in May, 2007. The method is similar to that we used earlier for the Debuncher ring [4].

Model calibration data was taken as difference between positive and negative closed orbit bumps produced by each corrector magnet in the machine. In this case small orbit drifts during the measurement cancel out. As the orbit measurement precision is crucial for the calculations, each orbit was sampled 15-20 times. The combined response at each Beam Position Monitor (BPM) to the excitation of each corrector determines the Response Matrix (RM). For the dispersion measurement a revolution frequency scan of 5 steps around the equilibrium orbit was taken making the maximum variation of momentum equal to 0.1%. Figure 3 shows these measurements for the BPMs located at low dispersion regions. The estimated sensitivity of this method is about 1mm in dispersion units. The whole process of measurement is automated and takes about 1-1.5 hours.

The data have been analyzed using the *SRLOCOFitting* program. This package has been developed at ANL [5] and recently adopted at FNAL [6,4]. It fits the model parameters to minimize the differences between the calculated and the measured RMs.

The main difficulties of lattice fitting are the limited precision of the BPMs and a very limited number of the correction elements in the Accumulator. In this case the Singular Value Decomposition (SVD) algorithm used by *SRLOCOFitting* turned out to be very efficient.

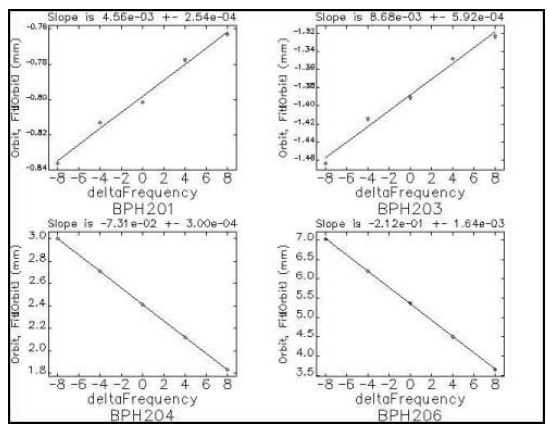

Figure 3: Dispersion measurement as a slope of orbit displacement with momentum varied within ±0.1%.

The average residual rms on the response matrix fit is 10-15 micron. From this we estimate the accuracy of the beta-function calculations to be about 5% or better. The method was used not only to find out the quad errors, but also to determine separately instrumentation errors (like BPM calibration and trim magnet strength corrections). Also, many other variables can be included in the fit, as long as they can serve as model parameters.

Optimization

In order simulate the desired solution for the new lattice we have started with the existing model with the new fitted parameters in the beam line mode. In this case one can model sequential changes that shape only the downstream lattice functions. At the end of the process, when reaching the end of the line, final functions have to be matched to functions at the beam line beginning to satisfy the closure condition. This procedure is repeated iteratively until an acceptable solution is reached. Flattop dispersion in the arcs is constrained to be kept at the same

level. In order to increase the slip factor we varied the dispersion function in the negative wells, see Figure 4.

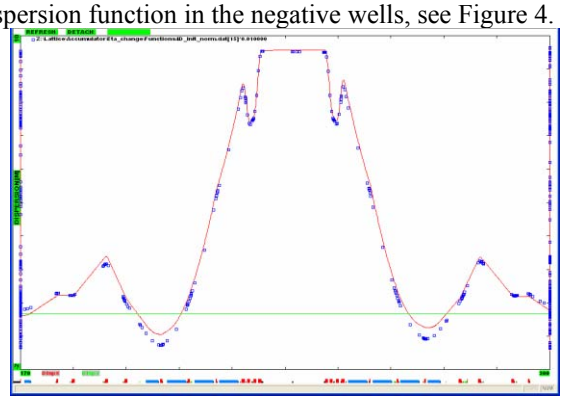

Figure 4: Dispersion corrections made to increase the slip factor. Red trace shows the new dispersion and blue data points correspond to the old lattice. Dispersion is changed in the negative wells and preserved at the flattop.

The slip factor has been increased by 15% in the final lattice design (0.012 → 0.015). Also we reduced the beam size at 6 most narrow locations (4 of them in horizontal plane and 2 – in vertical plane). This brought the minimum design aperture from 11 π up to 15 π. The new design also has smaller average beta-functions which reduces the IBS heating term by 12%. Stochastic cooling pickup to kicker phase advances were corrected also, although those were already fairly close to required values.

Results

Direct implementation of the new lattice design was complicated due to an additional operational step that we had to do in parallel. We had to change the bus cycling protocol, because it contained the historically obsolete procedure of double lattice ramping. So, the hysteresis protocol was not the same as for the old lattice. However it turned out that the difference was limited to just tune corrections, so we proceeded smoothly after this was taken into account.

The new slip factor was measured to be very close to the design one. This was proved by using two independent methods of slip factor measurement. One method was the direct measurement of gamma-t factor from the measurement of revolution frequency response to bend bus variations**;** and another method extracted the slip factor from the synchrotron frequency dependence on the RF voltage.

Because the requirement on dispersion suppression in the straight sections is so tight (<5cm, compared to the flattop dispersion of 10m!), it took 2 iterations of dispersion corrections. In the final measurement this dispersion was made lower than 2.5 cm. Final measurements have also shown that the minimum design aperture in the Accumulator ring has increased to 15 π.

The new lattice was implemented in the Accumulator and made operational as of May 16 this year. The observations of its immediate effect on stacking are not very conclusive because it was made concurrently with other changes in the stack tail system as well as temporary degradation of the incoming flux to the Debuncher. A better evaluation will be available later this year at the completion of the whole project. However a very important immediate effect of new lattice was in the substantial reduction of the transverse heating. Figure 5 shows average core emittances within a period of one month before and one month after the optics change.

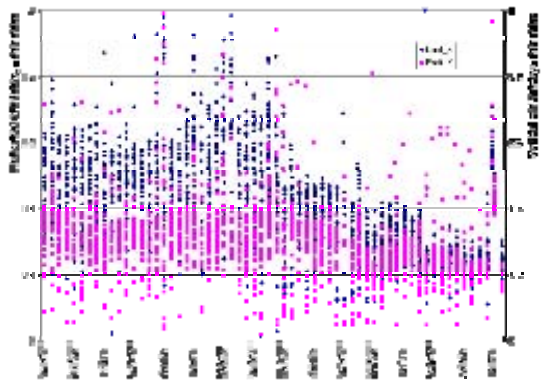

Figure 5: Accumulator transverse emittances. The break point corresponds to the day of the new lattice implementation.

High transverse emittances affect the efficiency of antiprotons transport to Recycler and, therefore, the Tevatron operations. Stacktail performance is also constrained by the core heating, so reduction of emittances gave more freedom for the stacktail optimization.

Conclusions

The new model of the Accumulator lattice has been developed using the OptiM and *SRLOCOFitting* software. Based on this model lattice optimization has been performed in order to help stochastic cooling. The new lattice design was implemented and subsequent measurements have shown that design parameters were achieved. Substantial reduction in the core transverse heating has been observed.

REFERENCES

[1] K.Gollwitzer, Antiproton Source. DOE Review report, March 2007.

[2] V.Lebedev, Antiproton Production and Accumulation. COOL'07, Bad Kreuznach.

[3] http://www-bdnew.fnal.gov/pbar/organizationalchart/lebedev/OptiM/optim.htm

[4] V.Nagaslaev et al., Measurement and optimization of the lattice functions in the Debuncher ring at Fermilab. EPAC'06, Edinburgh.

[5] V.Sajaev and L. Emery, "Determination and correction of the linear lattice of the APS Storage Ring", EPAC2002, Paris, France. P742-744

[6] V. Lebedev et al., Measurement and correction of linear optics and coupling at Tevatron complex. ICAP-04, St. Petersburg; NIM A558 (2006), p299.

STATUS OF THE LEPTA PROJECT*

V.Bykovsky, E.Ahmanova, A.Kobets#, Y. Korotaev, V.Lokhmatov,V.Malakhov, I.Meshkov, V.Pavlov, R.Pivin, A.Rudakov,A.Sidorin, A.Smirnov, G.Trubnikov, S.Yakovenko, JINR, Dubna

Abstract

The Low Energy Positron Toroidal Accumulator (LEPTA) is under commissioning at JINR. The LEPTA facility is a small positron storage ring equipped with the electron cooling system. The project positron energy is of 4-10 keV. The main goal of the facility is to generate an intense flow of positronium atoms–the bound state of electron and positron. The focusing system of the LEPTA ring after solenoidal magnetic field remeasurement and correction has been tested with pulsed electron beam by elements. Some resonant effects of beam focusing have been observed.

The experiments aiming to increase the life time of the circulating electron beam and test the electron cooling elector beam are in progress. Construction of the pulsed injector of the low energy positrons is close to the completion.

The injector is based on ^{22}Na radioactive isotope and consists of the cryogenic positron source (CPS), the positron trap and the acceleration section. In the CPS positrons from the ^{22}Na tablet are moderated in the solid neon and transported into the trap, where they are accumulated during about 80 seconds. Then accumulated positrons are extracted by the pulsed electric field and accelerated in electrostatic field up to required energy (the injector as a whole is suspended at a positive potential that corresponds to required positron energy in the range of 4-10 keV). In injection pulse duration is about 300 nsec. The CPS has been tested at the low activity of isotope ^{22}Na tablet (100 MBq). The continuous positron beam with average energy of 1.2 eV and spectrum width of 1 eV has been obtained. The achieved moderation efficiency is about 1 %, that exceeds the level known from literature. The accumulation process in the positron trap was studied with electron flux. The life time of the electrons in the trap is 80 s and capture efficiency is about 0.4. The maximum number of the accumulated particles is $2\cdot10^8$ at the initial flux of $5\cdot10^6$ electrons per second.

LEPTA RING DEVELOPMENT

The Low Energy Particle Toroidal Accumulator (LEPTA) is designed for studies of particle beam dynamics in a storage ring with longitudinal magnetic field focusing (so called "stellatron"), application of circulating electron beam to electron cooling of antiprotons and ions in adjoining storage electron cooling of positrons and positronium in-flight generation.

For the first time a circulating electron beam was obtained in the LEPTA ring in September 2004 [1]. Experience of the LEPTA operation demonstrated main advantage of the focusing system using longitudinal magnetic field: long life-time of the circulating beam in a low energy range. At average pressure on the ring orbit of about 10^{-8} Torr the life-time of 4 keV electron beam of about 20 ms was achieved that is about 2 orders of magnitude longer than in usual strong focusing system. However, experiments showed a decrease of the beam life-time at increase of its energy. So at the beam energy of 10 keV the life time was not longer than 0.1 ms. The possible reasons of this effect are the magnetic field errors and resonant behaviors of the beam focusing.

Magnetic System Improvements

The first experiments were performed without correction coils at junctions of solenoid sections of different cross-section. Moreover, the initial design of reverse current bars didn't provide the necessary distribution of the current between bars that led to an additional imperfection of the magnetic field. During testing of the straight section the electron beam didn't pass through the vacuum chamber due to influence of the magnetic fields of the reverse bars, and they were disconnected from the power supply. Therefore the whole magnetic system of the LEPTA ring was assembled without the reverse current bars, as result a magnetization of magnetic shields took a place.

To improve the magnetic field quality the LEPTA was disassembled at the end of 2005. The longitudinal magnetic field was measured on the axis of the magnetic system with Hole probe. The measured imperfections of the magnetic field were on the level of about 20% at the junctions of solenoids (Figure 1). On the basis of the measurement results the correction coils were designed using SAM program. After installation of the coils the homogeneity of the magnetic filed was achieved on the level of 2.5%.

During the disassembling of the LEPTA ring the design of the reverse current bars was improved. The using of the reverse bars permitted to improve reproducibility of experimental results.

The LEPTA injection system consists of septum windings and electric kicker located inside a septum solenoid. The injection system testing with an electron beam showed that the magnetic axis doesn't coincide with the geometry axis of the vacuum chamber. The vacuum chamber diameter in the septum windings is 50 mm and one needs a high precise adjustment of the septum winding position inside the septum solenoid. In the initial design the possibility of the septum winding displacement was restricted. The horizontal size of the septum windings was decreased by 36 mm that permitted to shift them by

* The work is supported by RFBR grant # 05-02-16320.
# kobets@jinr.ru

25 mm in the vertical direction and to adjust the vacuum chamber axis with necessary accuracy.

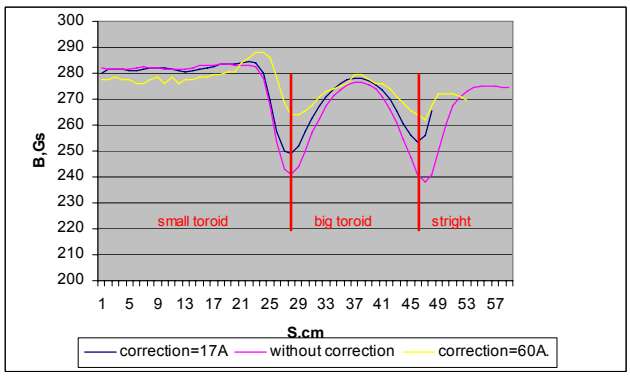

Figure 1: Magnetic field distribution along the toroidal solenoid axis at different currents of the correction coils. The design current is 60 A.

Upgrade of Diagnostic System

The Lepta diagnostic system was sufficiently modified. To adjust the beam orbit inside helical quadrupole (the optic element providing long term stability of the circulating beam) with more high precision an additional pick-up station was installed at the exit of the straight section. After crossing the straight section the electron beam can be directed into the especially installed luminescence screen. The diaphragm system at the septum entrance was made over to pick-up station.

The focusing system of the LEPTA ring after corrections of the magnetic field has been tested with pulsed electron beam by elements. For the adjustment of the beam orbit the luminescent screen was used. In front of the luminescence screen the diaphragm with 0.5 mm hole was installed. During the tests the resonance behavior of the electron gun optics was investigated. Figure 2 shows the dependence of the magnetic field on the electron energy corresponding to minimum beam spot size on the luminescent screen.

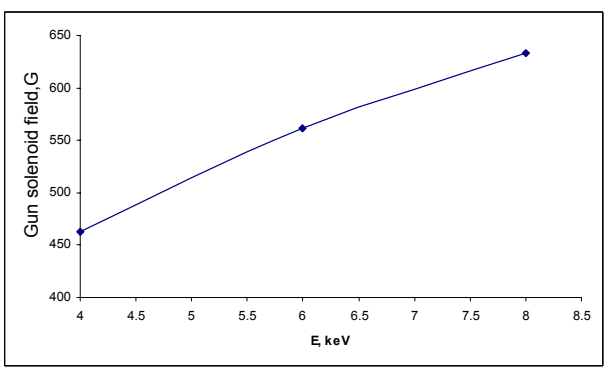

Figure 2: Dependence of Resonant Magnetic Field Value in Gun Solenoid on Electron Energy.

TEST OF THE CPS

Positrons emitted from radioactive source ^{22}Na have a very broad energy spectrum up to 0,5 MeV. To generate monochromatic beam of slow positrons the solid neon as moderator is used [2]. When positron pass trough the moderator the part of the broad energy spectrum are slowed down to thermal speeds. A small longitudinal magnetic field is used for transport of continuous beam of slow positrons (fig.3).

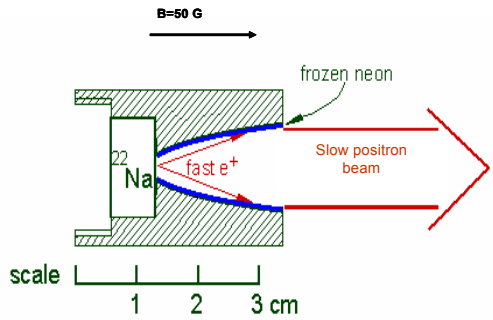

Figure 3: Slow positron getting principle.

The cryogenic source of slow positrons has been developed and made at JINR (Fig.4).

For realization of experiments with a cryogenic positron source a stand was constructed. The positron source is located in the vacuum chamber pumped to the pressure $4*10^{-8}$ Torr.

The stand includes neon and liquid helium lines. The slow positron beam flux is detected by a microchannel plate (MCP).

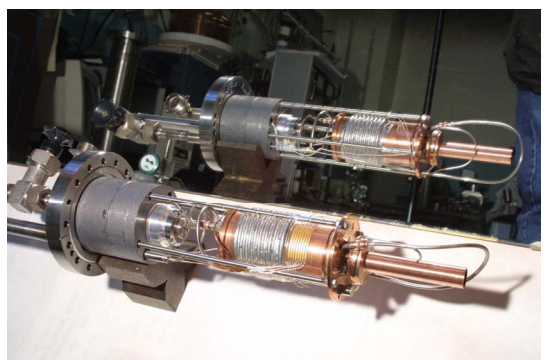

Figure 4: The cryogenic source of slow positrons.

During experiments with a test isotope ^{22}Na of activity 100 μCi, the frosting of neon was carried out on a substrate and cone. The dependence of the slow positron output on the thickness of the moderator was investigated (Fig,5). Dependence of slow positron spectrum on the thickness of the moderator was measured (Fig.6).

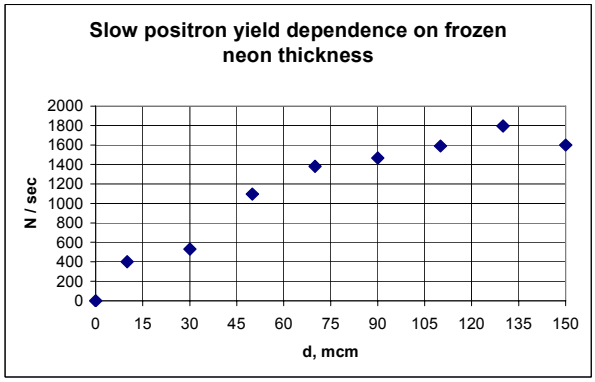

Figure 5: Slow positron yield vs moderator thickness.

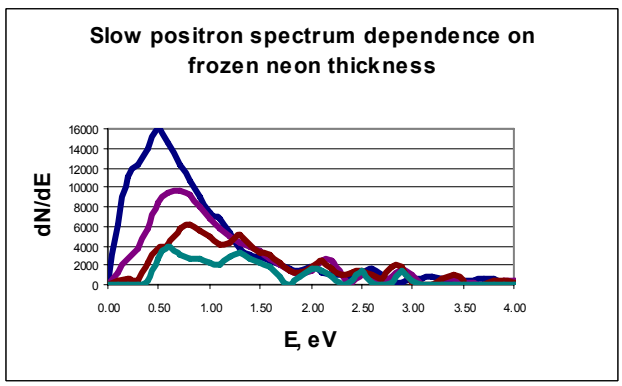

Figure 6: Slow positron spectrum vs moderator thickness.

The continuous slow positron beam at intensity of $1.75*10^3$ positrons per second has been obtained. The average energy is 1.2 eV, width of a spectrum is 1 eV. The achieved moderator efficiency is 1 %, that exceeds the level known from literature.

THE POSITRON TRAP

When slow positron beam has been formed, it enters to Penning-Malmberg trap were the positron cloud is accumulated [3]. The Penning-Malmberg trap is a device which uses static electric and magnetic fields to confine charged particles using the principle of buffer gas trapping. The confinement time for particles in Penning-Malmberg traps can easily extend into hours allowing for unprecedented measurement accuracy. Such devices have been used to measure the properties of atoms and fundamental particles, to capture antimatter, to ascertain reaction rate constants and in the study of fluid dynamics. The JINR positron trap (Fig. 7) was constructed to inject positron bunch into the LEPTA ring.

The research of the accumulation process was carried out using electron flux. For this purpose the test electron gun allowing to emit $dN/dt = 1*10^6$ electrons per second with energy 50 eV and spectrum width of distribution a few eV was made. These parameters correspond to slow monochromatic positron beam which we expect from a radioactive source at activity of 50 mCi.

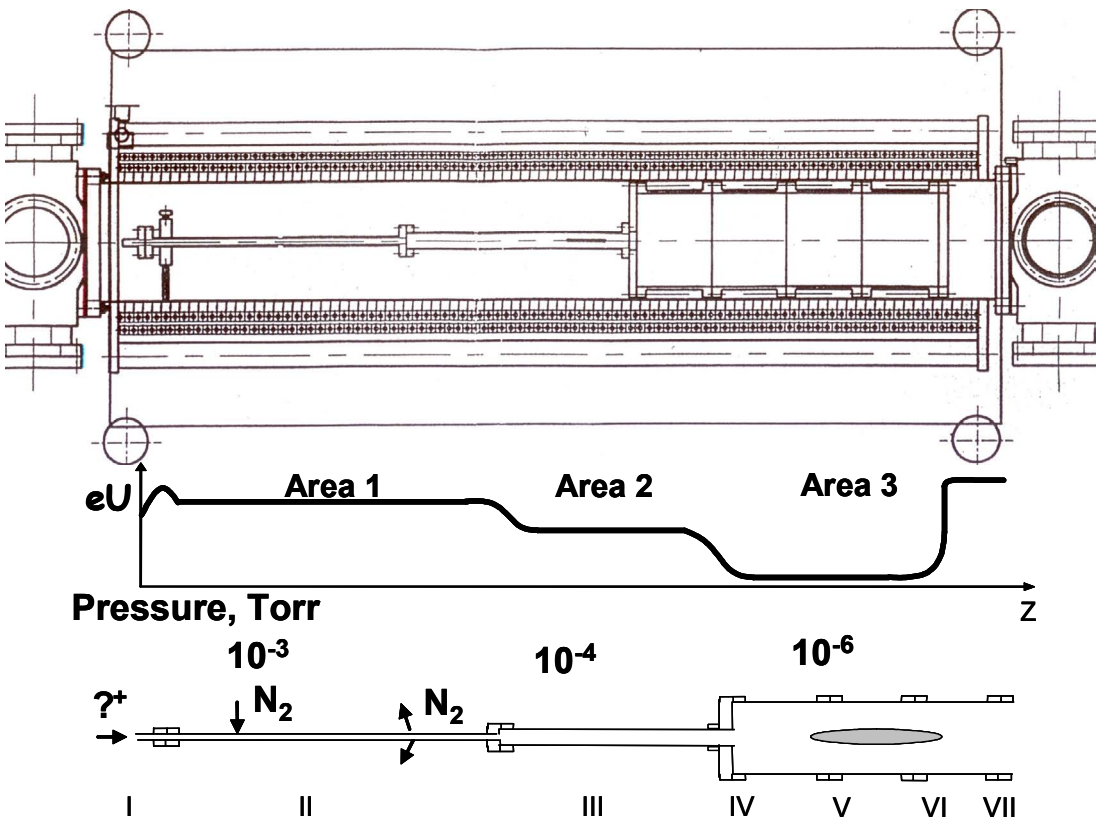

Figure 7: Assembly drawing of the positron trap (upper picture), potential and pressure distributions along the electrode system.

Electron accumulation in the trap with application of rotating electrical field was studied during December 2006. One of the trap electrodes (electrode 2) consists of four isolated segments (Fig. 1), which are connected with sine voltage generator of amplitude *A* and frequency *f*. The phases of the voltage applied to each segment are shifted by 900 one to another one that forms rotating transverse electric field

The dependence *N(t)* of the of accumulated electron number on accumulation time has been measured at different conditions (Fig.8). The curve 1 presents the function *N(t)* after optimization of distribution of pressure and electrode potentials. The curve 2 presents *N(t)* after optimization of the transverse correction magnetic field. The rotating field is OFF in both cases. The curve 3 gives *N(t)* after optimization of frequency and amplitude of the rotating electric field. The optimum frequency of rotation has been found equal to 650 kHz at the amplitude of 1V

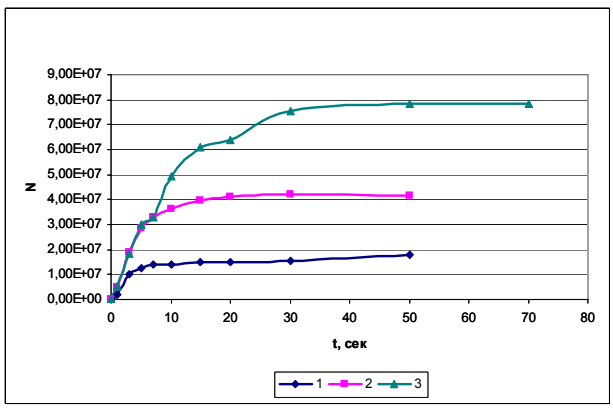

Figure 8: The total trapped charge as a function of filling time.

CONCLUDING REMARK

In the nearest future we plan to provide

1. Test of the LEPTA ring with improvement magnetic field
2. Test and tuning of electron cooling system with continuous electron beam
3. Assembling of the positron injector.

After receiving of ^{22}Na source from iThemba Labs (RSA) (expected in October 2007) the electron cooling of positrons and positromium generation will be realized.

REFERENCES

[1] A.Kobets, et. al., Status of the LEPTA project, proceeding of Beam Cooling and Related Topics

[2] A. P. Mills, Jr. and E. M. Gullikson, “Solid Neon Moderator for Producing Slow Positrons”. Appl. Phys. Lett. 49, 1121 (1986)

[3] M. Amoretti et al., The ATHENA antihydrogen apparatus, Nucl. Inst.Meth. Phys. Res. A 518 (2004) 679-711

[4] I. Meshkov, LEPTA project: generation and study of positronium in directed fluxes, NIM B 221 (2004) 168-173

OPTICAL STOCHASTIC COOLING EXPERIMENT AT THE MIT-BATES SOUTH HALL RING

W. Franklin, W. Barletta, P. Demos, K. Dow, J. Hays-Wehle, F. Kaertner, J. van der Laan, R. Milner, R. Redwine, A. Siddiqui, C. Tschalaer, E. Tsentalovich, D. Wang, F. Wang,
Massachusetts Institute of Technology, Cambridge, MA 02139, U.S.A. and
MIT-Bates Linear Accelerator Center, Middleton, MA 01949, U.S.A.

M. Bai, M. Blaskewicz, W. Fischer, B. Podobedov, V. Yakimenko,
Brookhaven National Laboratory, Upton, NY 11973, U.S.A.

A. Zholents, M. Zolotorev,
Lawrence Berkeley National Laboratory, Berkeley, CA 94720, U.S.A.

S.Y. Lee,
Indiana University Cyclotron Facility, Bloomington, IN 47405, U.S.A.

Abstract

Optical stochastic cooling (OSC) is a technique formulated for very fast cooling of charged particle beams of high energy and high brightness which has yet to be experimentally realized. An experiment to demonstrate the principle of OSC has been designed using electrons at 300 MeV in the MIT-Bates South Hall Ring (SHR). The SHR is a particularly suitable location for studying OSC physics due to its layout, energy range, and availability for dedicated use. The experiment will operate the SHR in a configuration designed for simultaneous transverse and longitudinal cooling. The cooling apparatus including a magnetic chicane, undulator system, and optical amplifier has been designed for compatibility with existing technology. Such studies are a necessary prerequisite to implementation in a high-energy collider environment.

INTRODUCTION

Many of the proven techniques for beam cooling diminish in effectiveness for beams of high energy and high brightness. Stochastic cooling [1], a beam-based feed-forward technique for cooling of stored particle beams, encounters limits on the cooling time of very intense bunched beams due to the bandwidth of RF amplification systems. The use of higher bandwidth feed-forward systems would effectively divide bunches into a larger number of samples with fewer particles in each to be cooled, thereby allowing for more rapid cooling.

The yet-to-be-demonstrated technique of optical stochastic cooling [2] combines aspects of microwave stochastic cooling with techniques developed for coherent radiation in light sources. Based on an ultra-broadband feed-forward system, OSC would significantly reduce the bandwidth-limited cooling time present for microwave stochastic cooling. The transit-time method of OSC, formulated by Zolotorev and Zholents [3], would provide momentum kicks to a stored charged particle beam via interaction with its own amplified radiation while traversing a magnetic undulator for reduction of the emittance. Successful implementation of the OSC technique is expected to yield fast cooling of protons/antiprotons and heavy ions at energies in excess of several hundred GeV per nucleon.

The OSC technique, shown schematically in Figure 1, entails construction of a nearly isochronous magnetic delay line for charged particles, installation of two undulators, development of a high gain optical amplifier, and use of fast diagnostic and feedback systems. Estimates of OSC times and design parameters have been made for existing facilities, including RHIC [4], and the technique has been considered for future facilities such as a muon collider.

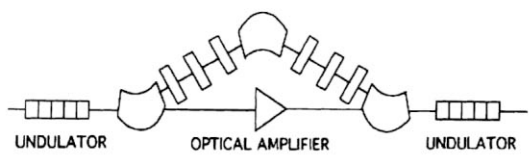

Figure 1: Schematic of an optical stochastic cooling insertion in a storage ring.

There are significant technical challenges in producing a working OSC system. The costs and time required for implementation of such systems in a new or existing high-energy hadron machine will be high. For hadrons or ions, presently achievable optical amplifier output power would necessitate operation of an OSC system well below optimal gain, thereby limiting the achievable cooling time. The development of necessary OSC diagnostic

techniques could proceed more readily in a system in which OSC can be achieved in real time. Thus, a demonstration of OSC physics using electrons, which can be much more quickly cooled than high-energy hadrons, is an essential step prior to implementation at a high-energy facility.

A unique opportunity for such a study presently exists using the MIT-Bates South Hall Ring (SHR), shown in Figure 2, which has a particularly suitable geometry. For an OSC experiment with electrons, it is essential to operate at an energy at which the ring's synchrotron radiation damping time is long compared to the expected OSC cooling time. Because of the large radius of curvature (9.1 m) in its dipole arcs, operation of the SHR near 300 MeV yields a beam with a synchrotron radiation damping time of approximately 5 seconds. This synchrotron damping time and the counteracting growth rate of the beam due to intrabeam scattering (IBS) are both long compared to the cooling time for an OSC system operating at optimal gain. The SHR contains two long straight sections with sizable gaps between magnetic elements for installation of the OSC experimental apparatus. The location permits placement of beam diagnostics for the experiment in a shielded area of the SHR northern arc. Furthermore, an experiment to study OSC physics can be performed as a dedicated experiment without impacting ongoing operations. Although beam operations for nuclear physics experiments at MIT-Bates ceased in 2005, a recent test run of the accelerator established the continuing viability of stored beams in the SHR for this energy regime.

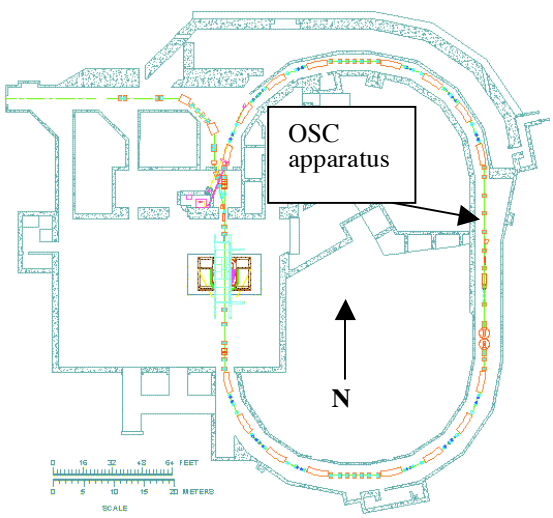

Figure 2: Layout of the South Hall Ring. The OSC experiment will be located in its eastern straight section.

EXPERIMENT

The primary goal of this experiment is to demonstrate optical stochastic cooling for the first time. A secondary goal is to produce apparatus with the potential for scaling to the high-energy high-brightness regime. Hence beam conditions and features of the experimental apparatus have been chosen specifically so as to maximize the chance of a successful demonstration of OSC. The strategy for this experiment will be to observe effects of cooling on equilibrium properties of a stored beam.

Electron Beam

An overview of design parameters for the electron beam for the OSC experiment is given in Table 1. Previous experimental studies of SHR lattices have confirmed the accuracy of past models of the SHR beam to a high degree [5].

Table 1: Design SHR beam parameters for an OSC demo.

Beam Property	**Design Value**
SHR Energy (MeV)	300
RF Voltage (kV)	14
Particles/bunch	1×10^{8}
Average current (mA)	0.3
Equilibrium emittance, ε_x (nm)	96
Energy Spread	1.67×10^{-4}
rms bunch length (mm)	9.8
Synchrotron damping τ_x (sec.)	4.83
Touschek lifetime (min)	1.45
Lattice para. at OSC Insertion	β=3m, η= 6m, $\eta'=\eta/\beta$

One of the challenges in observing OSC with electrons is to separate its effect from other beam heating and cooling forces, which act on a comparable time scale. While the damping effects due to synchrotron radiation can be readily controlled with low energy operation, heating due to intrabeam scattering must be carefully modeled as a function of bunch intensity. The effects of intrabeam scattering for the SHR have been calculated [6] using *elegant* [7] and are included in Table 1. The cooling effects will be observed by measuring changes of beam profile (transverse and longitudinal) in equilibrium before and after cooling.

The calculations also consider the effect of Touschek scattering on the beam lifetime for low-energy stored electron beam equilibrium properties. During the most recent SHR study, stored electron beams were established at 325 MeV with average intensities comparable to those which will be needed for the OSC experiment. Sustained SHR operation at energies near 300 MeV appears to be feasible and not to be prohibited by Touschek lifetime considerations.

The OSC experiment will use a few-bunch pulsed mode for beams circulating in the SHR, with up to 12 (out of 1812) RF buckets populated with electrons. Each bunch traverses the OSC apparatus at the SHR revolution frequency of 1.576 MHz. Operation of the electron beam in pulsed mode permits the use of pulsed amplification for the cooling system. It also reduces the effects of multi-bunch instabilities, which can affect the beam profile. The

bunch structure of the SHR electron beam will be set to match the maximum repetition rate for the OSC amplifier system to allow efficient cooling. A mode-locked laser system [8] has been developed to serve as a new driver for the Bates photoinjector to be phase locked to the accelerator RF systems and to the OSC amplifier. This system will provide considerable freedom to vary the bunch intensity through stacking. A nominal initial bunch intensity of $1.0*10^8$ particles has been chosen.

An OSC lattice has been designed with a horizontal equilibrium emittance of ε_x=96 nm for this intensity. This relatively large value mitigates the initial effect of intrabeam scattering. An x-y coupling of 10% is chosen. The OSC lattice has been designed with a high dispersion (η=6m) at the exit of the OSC apparatus to couple longitudinal and transverse cooling. In combination these two features should permit strong transverse damping of the beam.

OSC Apparatus

The OSC demonstration will utilize a compact experimental apparatus. A summary of selected parameters for the apparatus is given in Table 2.

Table 2: Parameters for the OSC apparatus.

Parameter	Value
Chicane length (m)	6
Chicane dipole bend (mrad)	65
Chicane Optics: R51/R52/R56	8.6×10^{-4} / 2.52 mm / -12 mm
Undulator length L_u (m)	2.0
Undulator periods	10
Radiation wavelength λ (μm)	2.06

Its centerpiece is an ultra- broadband short pulse optical parametric amplifier [9] for the undulator radiation, which has several virtues. Optical stochastic cooling requires an ultra-broad optical amplification bandwidth, which is present with well- established nonlinear optical materials. Short pulse OPA relies on the beating of a signal pulse and pump pulse with an idler to produce large gain within a very short medium. Power gains in excess of 10^3 are readily achievable in only a few millimeters of crystal length and these amplifiers can be scaled to yield large average power output. They also introduce minimal phase delay in the amplification and the phase delay over the optical bandwidth can be controlled to a fraction of an optical cycle as needed to achieve OSC.

The low delay time required for this method of amplification permits the design of a compact magnetic chicane for the electron beam with fixed optics, shown schematically in Figure 3. The bypass must preserve a small well-defined correlation between particle momentum and transit time to define the path length difference between electrons in the bypass and the amplified radiation from the first undulator to a fraction of the wavelength of the undulator radiation. Calculations of electron optics for the magnetic bypass have been performed using TRANSPORT for a small angle (ψ=65mrad) chicane including four dipole magnets and a split lens quadrupole. The optical amplifier will be housed within the same enlarged vacuum chamber as electrons traversing the magnetic bypass.

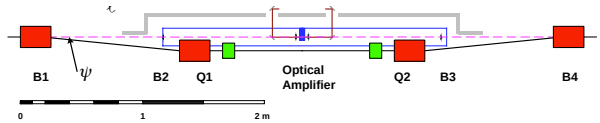

Figure 3: Schematic design for the OSC chicane.

The installation of a chicane for electrons effectively changes the circumference of the SHR. The total change in electron path length introduced by this chicane is only about 6 mm. Such a change can be accommodated with slight modifications (Δf=90 kHz) to the RF frequency of the SHR cavity (f_0 = 2856 MHz) and the injection linac, as was successfully demonstrated in a recent test. The chicane design also does not require sextupoles to control the chromaticity. Power supply accuracy and stability ($\Delta I/I \sim 10^{-4}$ over 1 hour) requirements for the magnets are at a level which can be met by commercially available devices. Alignment tolerances for the chicane magnets are also modest.

The OSC experiment requires fabrication and installation of two identical planar permanent magnet undulators. The undulator design includes adjustable operating gaps which will be tuned to yield radiation peaked at a wavelength of 2.06 μm. The overall gain of the cooling system depends on the undulator parameter and the gain of the optical amplifier. Estimates have been made for the amplifier requirements to achieve OSC of a 300 MeV beam in 500 ms have been based on two dipole undulators with 200 mm period with 2.0 m total length. For cooling a single bunch of 10^8 particles circulating in the SHR, an amplifier with gain of less than 40 dB and output power below 100 mW will suffice for an initial demonstration of OSC. The design of the optical system, which uses a direct pump source, is shown in Figure 4.

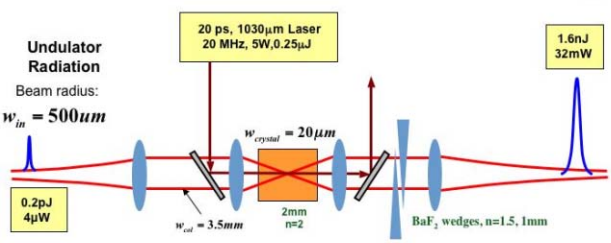

Figure 4: Layout of the optical amplifier.

Operation at a wavelength where the amplified signal is at about twice the pump wavelength, ensures ultra-broadband amplification. The pump laser will consist of a femtosecond Yb:fiber laser at 1030 nm with a fraction of

the output pulse stream tapped off and stretched to 20-100 ps in single-mode fiber. The pulses can than be directly amplified with a robust amplifier [10].

The amplifier optical line will be instrumented with a thin set of barium fluoride wedges permitting finely controlled variation of the phase shift between the amplified radiation and electrons from the chicane. Interferometry between amplified radiation from the first undulator and radiation produced in the second undulator can be performed by variation of the relative phase. In the limit of a nearly isochronous chicane and a low gain amplification system, the phase shift needed for OSC to occur can be optimized using the interference signal from a power detector with a spectrometer used as a filter to suppress background. With the amplifier operating initially in a low-gain regime, the experiment will seek to demonstrate correlation of the interference signal with the establishment of OSC. Feedback techniques to optimize the amplifier phase and gain during the OSC process will be studied.

Measurements

The OSC experiment will perform accurate measurements of cooling rates as a function of initial bunch intensity, transverse size, and momentum spread of the beam. Figure 5 shows the expected horizontal beam size reduction during the OSC process for a bunch intensity of 10^8 particles. The red curve represents a case in which the gain of the OSC system is dynamically optimized as the beam cools. Starting from the equilibrium state, cooling is expected to reduce σ_x from 0.54 mm to a new equilibrium of 0.34 mm in under 2 seconds. For the second case (blue curve) the optical amplification is fixed at a value corresponding to the initial beam profile, resulting in a reduction of only 13% in horizontal size. Development of techniques for dynamical gain adjustments during the cooling process will be pursued as a central part of the experimental program.

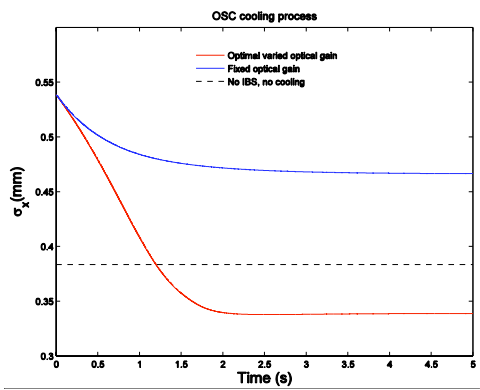

Figure 5: Calculated transverse size change due to OSC.

The required time-dependent variation of the optical gain to achieve optimal cooling is shown in Figure 6. An increase in gain of approximately 30% over the course of 2 seconds suffices to achieve optimal cooling. Similar results can be calculated for the momentum profile of the beam as a function of time as it cools, with the effects of cooling strongly dependent on the choice of chicane and lattice parameters.

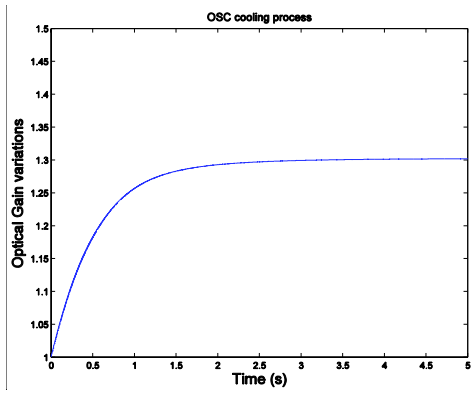

Figure 6: Optimal optical gain as beam cools

Confirmation of OSC will enable a host of additional measurements including investigation of the effects of changes in bunch intensity, lattice parameters, and beam energy.

SUMMARY

An experiment to demonstrate the principle of optical stochastic cooling using stored electrons is underway. The experiment will study the extension of cooling formalism to the optical regime with a desired reduction in cooling time depending inversely on the bandwidth of the cooling system. Recent design studies and beam development studies have reinforced the approach of carrying out this experiment in the MIT-Bates South Hall Ring with a compact apparatus based on existing technology. Such a demonstration will provide a firm basis for evaluating the applicability of this technique in higher power regimes as needed for high-energy hadron beams.

REFERENCES

[1] S. van der Meer, Rev. Mod. Phys. **57** (1985) 689.
[2] A. Mikhalichenko and M. Zolotorev, Phys. Rev. Lett., **71** (1993) 4146
[3] M. Zolotorev and A. Zholents, Phys. Rev. E **50** (1994) 3087
[4] M. Babzien et al., Phys. Rev. ST Accel. Beams, **7** (2004) 012801
[5] F. Wang et al., Phys. Rev. Lett. **96** (2006) 064801
[6] F. Wang et al., Proceedings of the 2007 Particle Accelerator Conference, Albuquerque, NM.
[7] M. Borland et al., APS LS-287, 2000.
[8] J. Buckley et al., Opt. Lett. **30** (2005) 1888
[9] I. Ross et al., Appl. Opt.. **39** (2000) 2422
[10] F. Ö. Ilday et al., "High-Energy, Single-Mode, Femtosecond Fiber Lasers", ASSP Conference, Vienna, Austria, Feb. 6-9 (2005)

ANALYSIS OF RESONANCES INDUCED BY THE SIS-18 ELECTRON COOLER*

S. Sorge†, O. Boine-Frankenheim, and G. Franchetti, GSI, Darmstadt, Germany

Abstract

Besides the beam cooling effect, an electron cooler also acts as a non-linear optical element. This may lead to the excitation of resonances possibly resulting in an increase of the beam emittance. The aim of this work is the calculation of resonances driven by the electron space charge field in the cooler installed in the SIS heavy ion synchrotron at GSI Darmstadt. For our calculations, we used a numerical model consisting of a rotation matrix representing the ideal lattice together with a non-linear transverse kick element representing the electron cooler. Within this model, we studied the non-linear tune shift and the dominant resonance lines resulting from the interaction with the cooler.

INTRODUCTION

The space charge field in an electron cooler acts as a non-linear optical element in the lattice of a storage ring. This may lead to the excitation of additional ring resonances. Depending on the machine working point these resonances cause emittance growth and an effective heating of the beam, as it was observed e.g. in the CELSIUS cooler storage ring [1].

Electron cooling at medium energies will play an essential role in the proposed FAIR storage rings [2]. Electron cooling is already available to improve the beam quality of the intense ion beams at low energy in the existing SIS synchrotron. At low or medium beam energies, the transverse tune shift due to the direct space charge force plays an important role. The resonances excited by the non-linear space charge field of the cooler electron can potentially limit the reachable beam intensity and quality.

In this work, the excitation of resonances driven by an electron cooler is calculated within a simplified numerical model. The electron cooler is represented through a non-linear kick element in an otherwise ideal lattice. This enabled us to study only the resonances driven by the electron cooler. The MAD-X code [3] was used to perform resonance scans over a large working point area. The study is performed for parameters relevant to the electron cooler in the the SIS heavy ion synchrotron at GSI Darmstadt. This theoretical study provides the necessary information for dedicated measurements of cooler induced resonances and effects in SIS.

* Work supported by the European Community RESEARCH INFRASTRUCTURES ACTION under the FP6 programme: Structuring the European Research Area - Specific Support Action - DESIGN STUDY (contract 515873 - DIRACsecondary-Beams)

† S.Sorge@gsi.de

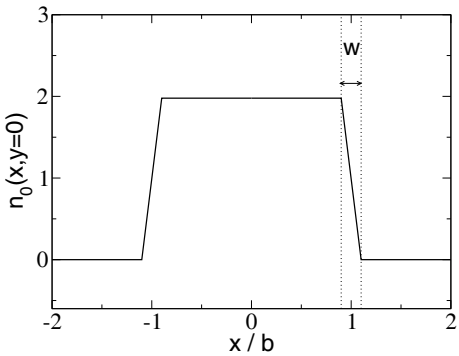

Figure 1: Normalised charge density profile used for the electron beam as provided by the beambeam element of MAD-X [3] as a function of x for $y = 0$. An edge layer with a width $w = 0.01\ b$ was used in the calculations.

PARTICLE TRACKING MODEL

In our calculations we used a simple model consisting of a rotation matrix providing the phase advance of the lattice of SIS–18 and a non-linear transverse kick introducing the force of the electron cooler in the thin lens approximation. The coordinates of a particle after the $(n+1)$-st revolution are calculated from those of the n-th revolution by

$$\begin{pmatrix} z_{n+1} \\ z^{'}_{n+1} \end{pmatrix} = \begin{pmatrix} \cos 2\pi\nu_z & \hat{\beta}_z \sin 2\pi\nu_z \\ -\frac{1}{\hat{\beta}_z}\sin 2\pi\nu_z & \cos 2\pi\nu_z \end{pmatrix} \times \begin{pmatrix} z_n \\ z^{'}_n + \Delta z^{'}(x_n, y_n) \end{pmatrix} \quad (1)$$

with $z = x, y$. Here, ν_z is the bare tune of the lattice, $\hat{\beta}_z$ is the unperturbed beta function in z direction at the location of the electron cooler, and

$$\Delta z^{'}(x,y) = \frac{q q^{'} N^{'}}{2\pi\varepsilon_0 m_0 c^2 \beta_0^2 \gamma_0^3} \frac{z}{R^2} \int_0^R \mathrm{d}r\ r\ n_0(r) \quad (2)$$

with $R = \sqrt{x^2 + y^2}$ is the transverse momentum kick depending on both spatial direction x, y. Here,

$$N^{'} = \left| \frac{I_e L_{\mathrm{cool}}}{q^{'} \beta_0 c} \right| \quad (3)$$

is the number of electrons in the electron cooler. $q, q^{'}$ are the charges of the particles in the beam considered and in the electron beam, i.e. it is $q^{'} = -e$. n_0 is the normalised radial current distribution in the electron beam.

The electron beam of an electron cooler usually has a radial shape with a constant current density in the centre

Table 1: Parameter of SIS–18 used in the calculations and taken from [4] and [5], and quantities calculated with them. K_1 corresponds to equation (4) and $\Delta\nu_x, \Delta\nu_y$ to equation (5).

Particle	U^{73+}
Injection energy E	11.4 MeV/u
Relativistic factors $\beta_0,\ \gamma_0$	$0.15,\ 1.01$
Cooling length L_{cool}	3 m
Electron current I_e	0.3 A
Cathode radius r_{cath}	12.7 mm
Adiab. expansion factor f_E: used, (range)	$3,\ (1 \ldots 8)$
Electron beam radius ($b = r_{\mathrm{cath}}\sqrt{f_E}$)	22 mm
Beta function in the cooler ($\hat{\beta}_x,\ \hat{\beta}_y$)	8 m, 15 m
Eff. focal strength K_1	$-0.010\,\mathrm{m}^{-1}$
Resulting tune shift $\Delta\nu_x, \Delta\nu_y$	0.0066, 0.012
Eigen space charge tune shift $\Delta\nu_{sc}$	up to -0.25

and a thin edge layer. We could use the beambeam element of the MAD-X code for the representation of the electron cooler. The profile is shown in figure 1.

In the region of constant current density, a momentum kick of this shape acts as an element with a field gradient having an effective focal strength K_1. For a sufficiently small width of the edge layer w, the focal strength is given by

$$K_1 := k_1 L_{\mathrm{cool}} = \frac{\Delta z^{'}}{z} \approx \frac{qeN^{'}}{2\pi\varepsilon_0 m_0 c^2 \beta_0^2 \gamma_0^3 b^2}. \quad (4)$$

For the resulting linear tune shift, one can write

$$\Delta\nu_z = -\frac{\hat{\beta}_x K_1}{4\pi}. \quad (5)$$

Our calculations were performed for U^{73+} ions using the parameters given in table 1.

RESULTS

To make the resonances visible, the relative rms beam radius variation

$$w_{z,\mathrm{rel}} = \frac{\sigma_{f,z}}{\sigma_{i,z}}, \quad z = x, y, \quad (6)$$

with

$$\sigma_{(i,f),z} = \sqrt{\bar{z^2}} = \frac{1}{N}\sqrt{\sum_{k=1}^{N} z_{k,(i,f)}^2} \quad (7)$$

was calculated as a function of the tune values ν_x, ν_y of the rotation matrix. N is the number of the test particles tracked. We used a particle beam with a Gaussian initial profile.

To have a realistic tune range, we searched for resonances in a tune window defined by $\nu_x \in [4.05, 4.3]$ and $\nu_y \in [3.2, 3.45]$, which is near the working point $(\nu_x, \nu_y) = (4.2, 3.4)$ given in [4], and which does not contain a half integer resonance. On the other hand, it was

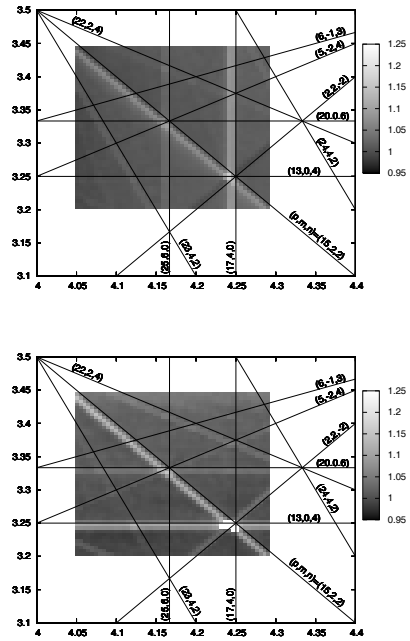

Figure 2: Relative rms beam width in x and y direction, upper and lower picture, respectively. The colour scale is within $w_{\mathrm{rel}} \leq 1$ (dark grey) and $w_{\mathrm{rel}} \geq 2$ (white).

pointed out in [1] within an analytic model, that an electron cooler, with a round electron beam, excites only resonances of even order, where, additionally, the resonances strength decreases with increasing order. Hence, we searched only for resonances of order 4 and 6.

The initial rms beam width in both spatial directions were chosen to be equal to the radius of the electron beam, i.e. $\sigma_{i,x} = \sigma_{i,y} = b = 22\,\mathrm{mm}$, see table 1. The resulting initial rms emittances are different due to the different emittances, it is $\epsilon_x = 61.0\,\mathrm{mm\ mrad}$ and $\epsilon_y = 32.3\,\mathrm{mm\ mrad}$.

The resonances found can be seen in figure 2. The straight black lines denoting the resonances satisfy the relation

$$p = m\nu_x + n\nu_y. \quad (8)$$

The positions of the resonances found in our tune scan by detecting the enhancement of the beam width are near these lines, which denote the positions of the resonances with respect to the unperturbed tune ν_x, ν_y of the rotation matrix. So, we could identify every resonance line found. The resonances found in the tune scan are slightly shifted to smaller tunes compared to the resonance lines of the rotation matrix. The reason for that is, that an electron cooler contrary to higher order multipoles yields also a linear tune shift $\Delta\nu_z(x, y)$. On the other hand, the position of the resonances depend on the total tune $\nu_{z,\mathrm{tot}} = \nu_z + \Delta\nu_z(x, y)$. So, the corresponding tune of the rotation matrix ν_z is smaller than the total tune $\nu_{z,\mathrm{tot}}$.

As expected, we found resonances of order 4 generally being the strongest resonances followed by resonances of

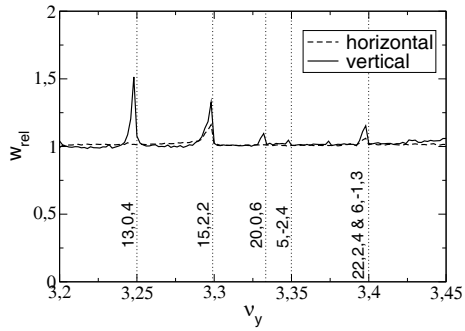

Figure 3: Relative beam width as a function of the vertical tune within the range $\nu_y \in [3.1, 3.45]$ for one horizontal tune $\nu_x = 4.2$. So, this figure is an extract of figure 2.

the order 6. Additionally, only so called sum resonances and resonances depending only on the tune of one direction lead to a significant beam blow up, what seems to be reasonable, see e.g. [6]. Here, latter lead to an enhancement of the beam size only in one direction. So, the resonances $(p, m, n) = (17, 4, 0)$ and $(25, 6, 0)$ are visible only in the upper picture of figure 2 showing the relative beam width in horizontal direction, whereas the resonances with $(p, m, n) = (13, 0, 4)$ and $(20, 0, 6)$ appear only in the lower picture of that figure and in the solid line in figure 3 showing the relative extension of the beam width in vertical direction. Figure 3 also shows, that the widths of resonances of different order do not significantly differ from each other. For that reason, a quantitative verification of the widths using the analytic model in [1] is not possible.

Under the conditions defined in table 1, we obtained a tune shift due to the electron cooler of $\Delta\nu_x = 0.0066, \Delta\nu_y = 0.012$, what is so small, that the according tune spread does not cross any resonance found in our calculation. On the other hand, the tune shift due to the eigen space charge of the beam has an size up to $\Delta\nu_{sc} \approx -0.25$. Therefore, the according tune spread will cross some of the strong resonances shown in figure 2. For that reason, we observed the beam behaviour at a working point near a strong resonance in more detail. In particular, we investigated the growth of the beam width depending on the initial beam width and the number of revolutions. One can see in figure 4 the increase of the beam width occurring only in vertical direction because of the working point $\nu_x = 4.1$, $\nu_y = 3.245$ close to the resonance given by $(p, m, n) = (13, 0, 4)$. We found, that only particles being initially at the edge of the beam increase their distance from the beam centre, whereas particles in the core stay there. So, the number of test particles having a betatron amplitude larger than the radius of the electron beam changed from 2049 at the beginning to 2056 after 100000 revolutions, what is an increase by 0.3 %. Here, the total number of test particles was 5000, and it was $\sigma_{i,x} = \sigma_{i.y} = 0.5\ b$. The according vertical rms width increased from $\sigma_{i,y} = 22$ mm to $\sigma_{f,y} = 26.4$ mm and so, by about 20 %. Note, that we have a 4-dimensional Gaussian distribution in a round

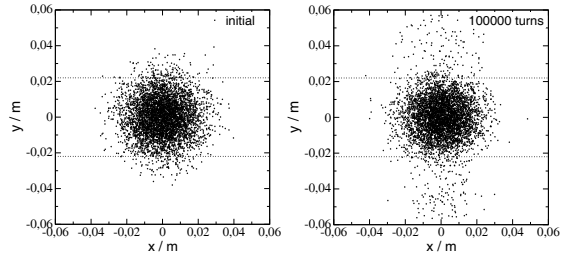

Figure 4: Spatial beam profile for $\sigma_{i,x} = \sigma_{i,y} = 0.5b$ at the beginning of a run and after 100000 revolutions. The working point is $\nu_x = 4.1$, $\nu_y = 3.245$.

beam, where the number of particles N_{in} being always closer to the beam centre than a certain distance R is given by

$$N_{in} \propto \int_0^{R/\sigma} x^3 \mathrm{e}^{-\frac{x^2}{2}} \mathrm{d}x. \tag{9}$$

The observation coincides with the statement, that resonances are driven only by the non-linear part of the electric field of the electron beam.

One exception from that general statement is the growth of the beam width due to an half-integer resonance. A resonance of this kind is driven by its nature by a quadrupole error in the lattice, i.e. by a purely linear perturbation. Such a perturbation can not cause an emittance growth. The beam blow up is caused by the growth of the beta function, see e.g. [6]. Hence, the condition $\sigma_z \propto \sqrt{\beta_z}$ is valid. Here, the full width of the tune range with a beta function enhanced by a factor 2 or more is given by the half-integer stopband integral

$$J_p = \frac{1}{2\pi} \oint \hat{\beta} k(s) \mathrm{e}^{-\mathrm{i}p\phi} \mathrm{d}s. \tag{10}$$

This provides the possibility to compare tracking results to an analytic expression. So, we performed calculations with a particle beam having an initial extension $\sigma_{i,x} = \sigma_{i,y} =$

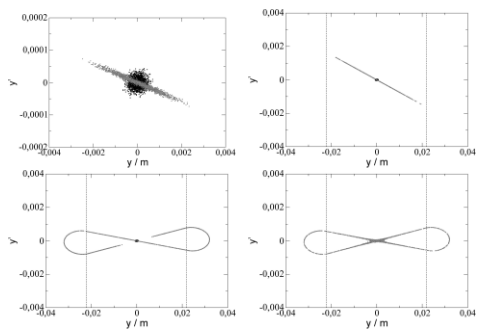

Figure 5: Vertical phase space plot for an initial beam width $\sigma_{i,y} = 0.01\ b \ll b$ at $\nu_x = 4.2$, $\nu_y = 3.45$ after several number of revolutions: $N_{\mathrm{rev}} = 20,\ 50,\ 100,\ 10000$. The vertical straight lines in pictures 2 – 4 denote the radius of the electron beam b. The black points in the centre denote the initial positions of the particles in phase space.

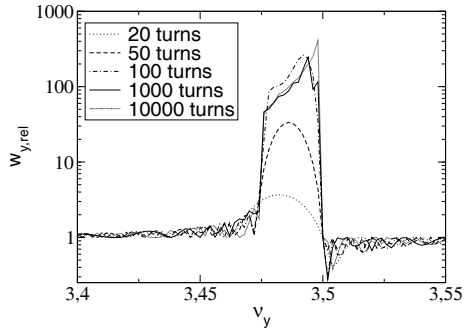

Figure 6: Relative vertical rms beam width $w_{y,\mathrm{rel}}$ after different numbers of revolutions. Note, that it is $\sigma_{i,y} = 0.01\ b$ and, so $w_{y,\mathrm{rel}} = 100$ refers to an absolute final rms beam width $\sigma_{f,y} = b$. It is $\nu_x = 4.2$.

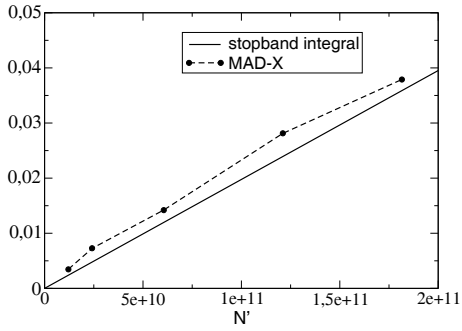

Figure 7: Full rms beam width after 1000 revolutions calculated using MAD-X compared to the half integer stopband integral J_7 from equation 10.

$0.01\ b \ll b$ to satisfy the condition of a pure linear perturbation. Due to the momentum kick, the beam extension in vertical direction started to increase. Here, the phase space ellipse became only stretched without increasing its area, as long as the vertical beam size had not exceeded the radius of the electron beam. After about 50 revolutions, the beam size exceeded the electron beam leading to the deformation of the phase space ellipse, as figure 5 shows. So, the condition for the applicability of the stopband integral was principally no longer valid. Fortunately, the width of the tune range with enhanced beam width remained almost constant also when the beam width exceeded the electron beam radius, see figure 6. So, it was possible to evaluate the full width of this range and compare it to the half-integer stopband integral. We found a very good agreement between them for several values of the electron number in the cooler, as one can see in figure 7.

SUMMARY

We studied the resonances generated by the space charge force of the electron beam in the SIS–18 cooler. The initial rms radius of the ion beam was adjusted to the radius of the electron beam. Resonances up to the 6th order could be identified. Furthermore, we could qualitatively reproduce the dependency of the resonance width on the resonance order as given by an analytic model in reference [1]. This model predicts that the resonance width decreased, when the order of a the resonances is enhanced. A quantitative reproduction of the beam width using an analytic model was possible only for the half integer resonance. Here, we found a good agreement between the resonance width and the width given by the analytic half-integer stopband integral.

Beyond that, we found, that the resonances driven by the electron cooler are of a similar width as those driven by higher order multipoles in the lattice of SIS–18 [7].

An important result is that the resonances induced by the electron cooler can lead to a strong increase of the width and the emittance of an ion beam. This can lead to a reduced cooling rate and so to an effective heating mechanism. Furthermore, the resonances are an additional possible constraint for the choice of the tune, because they could limit the extension of the space charge tune spread due to the self fields of the beam and therefore leading to the reduction of the space charge limit. On the other hand, this effect could be weakened by the fact, that an emittance growth due to the interplay of the direct space charge tune shift and spread on one hand and the resonances on the other hand arises only from particles having from the beginning a betatron amplitude larger than the radius of the electron beam. The number of these particles can be chosen by choosing a proper value for the width of the ion beam. On the other hand, it is desirable to keep this number small in any case to avoid a reduction of the electron cooling rate. So, the limiting influence of the resonance on the size of the direct space charge tune spread might possibly minimised by proper initial conditions.

Nevertheless, the interplay of the cooler induced resonances, the direct space charge tune shift, and other machine resonances requires further investigations. This will be the topic of future studies.

REFERENCES

[1] V. Ziemann, “Resonances driven by the electric field of the electron cooler”, TSL Note 98-43

[2] FAIR Baseline Technical Report Sept. 2006, GSI

[3] MAD-X: see `http://mad.web.cern.ch/mad` and `http://mad.web.cern.ch/mad/sindex.html`

[4] B. Franczak, Parameter list of SIS–18, GSI-SIS-TN / 87-13, September 10, 1987

[5] L. Groening, “Untersuchung zur Elektronenkühlung und Rekombination hochgeladener Ionen am Schwerionensynchrotron SIS”, GSI Dissertation 98-20, November 1998

[6] S. Y. Lee, “Accelerator Physics” 2nd ed., World Scientific Publishing Co. Pte. Ltd. 2004

[7] G. Franchetti, A. Franchi, T. Giacomini, M. Kirk, A. Parfenova, and A. Redelbach, “Experimental investigation of resonance induced effects in SIS18”, GSI scientific report 2005

BUNCHED BEAM STOCHASTIC COOLING SIMULATIONS AND COMPARISON WITH DATA*

M. Blaskiewicz†, J. M. Brennan
BNL 911B, Upton, NY 11973, USA

Abstract

With the experimental success of longitudinal, bunched beam stochastic cooling in RHIC [1] it is natural to ask whether the system works as well as it might and whether upgrades or new systems are warranted. A computer code, very similar to those used for multi-particle coherent instability simulations, has been written and is being used to address these questions.

INTRODUCTION

A stochastic cooling system is a wide band feedback loop[2, 3]. A pickup signal is processed, amplified and used to drive a kicker. The difference between coasting and bunch beam stochastic cooling theory is similar to the difference between coasting and bunched beam instability theory. While the former is quite simple, the latter is still evolving.

A theory of bunched beam cooling was developed in the early eighties [4, 5, 6]. As with bunched beam stability theory, there are parameter regimes in which accurate, closed form results can be obtained. In other regimes the bunched beams act like coasting beams [7, 8]. These sort of considerations were used in the design of the RHIC longitudinal cooling system, which is now operational. Uncooled and cooled bunches are shown in Figures 1 and 2, respectively. While the general beam parameters are in line with expectations, we know of no theory capable of explaining the detailed evolution of the cooled beam. Simulations of proton test bunch cooling were fairly successful [9]. We have generalized to code to include intrabeam scattering (IBS) and transverse cooling. This note gives a detailed account of the algorithms and compares data with simulation.

Table 1: Machine and Beam Parameters for Gold

parameter	value
h=360 voltage	300 kV
h=2520 voltage	3 MV
initial FWHM bunch length	3 ns
particles/bunch	10^9
initial emittance	$15\pi\mu$m
betatron tunes	$Q_x = 28.2, Q_y = 27.2$
Lorentz factor	107
circumference	3834 m
transition gamma	22.89

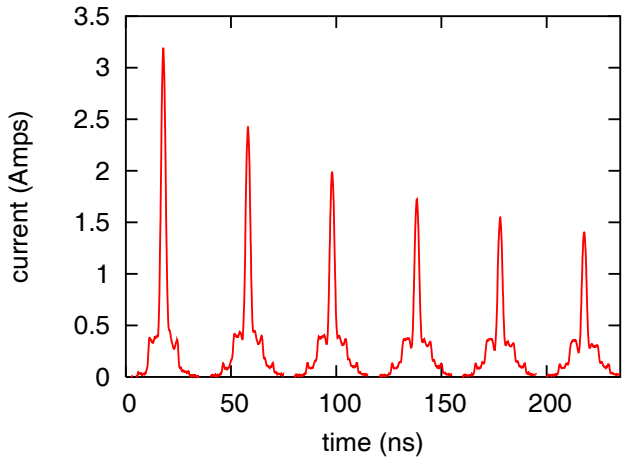

Figure 1: Evolution of the average bunch profile over a five hour RHIC store with gold beam and no cooling. Initial conditions are shown on the left and each trace to the right is one hour later.

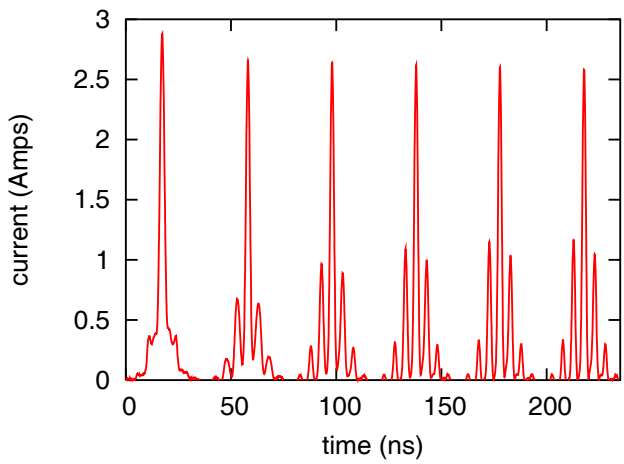

Figure 2: Evolution of the average bunch profile over a five hour RHIC store with gold beam and good longitudinal cooling. Initial conditions are shown on the left and each trace to the right is one hour later.

SIMULATIONS

The code involves single particle dynamics and multiparticle kicks. First consider the single particle motion. The longitudinal update for a fraction of a turn χ is

$$\bar{\epsilon} = \epsilon + \chi \frac{q}{mc^2} V_{rf}(\tau) \quad (1)$$

$$\bar{\tau} = \tau + \chi \frac{T_0 \eta}{\beta^2 \gamma_0} \bar{\epsilon} \quad (2)$$

* Work performed under the auspices of the United States Department of Energy.

† blaskiewicz@bnl.gov

where τ is the arrival time of the particle with respect to the synchronous phase, $\epsilon = \gamma - \gamma_0$ is proportional to the energy deviation, γ_0 is the reference Lorentz factor for a particle of mass m and charge q, $V_{rf}(\tau)$ is the RF voltage, $\beta = v/c$, $T_0 = 1/f_0$ is the revolution period, and η is the frequency slip factor. Since the RHIC synchrotron tune is $O(10^{-3})$, the distribution of the rf voltage is not important.

Only one transverse variable is considered and it will be referred to as x. The single particle transverse update for a fraction of a turn χ is

$$\bar{x} = x\cos\psi + p\sin\psi \quad (3)$$

$$\bar{p} = -x\sin\psi + p\cos\psi \quad (4)$$

$$\psi = \chi\psi_0 + \chi\frac{2\pi\xi}{\beta^2\gamma_0}\epsilon \quad (5)$$

where p is the transverse momentum variable, $\psi_0 = 2\pi Q_x$ is the on-momentum phase advance per turn, and ξ is the chromaticity. It is assumed that the rms emittance of the neglected transverse dimension is the same as the rms emittance of the dimension tracked. For no transverse cooling this is a fairly good approximation under normal RHIC conditions. With transverse cooling we invoke sufficient coupling, or cooling in both transverse dimensions.

The effect of IBS was included by first calculating the rms growth rates for the beam being simulated. This was done using Piwinski's formulae [10] with the smooth lattice approximation. The emittance growth rates are

$$\frac{1}{\sigma_j^2}\frac{d\sigma_j^2}{dt} = \alpha_{j0}, \quad (6)$$

where $j = x, y, p$. The growth rates in the handbook are for amplitudes, with *eg* $1/T_p = \alpha_{p0}/2$. For the actual RHIC beam one finds comparable growth in the two transverse directions, $\alpha_x \approx \alpha_y$, so the next step is to define an average transverse growth rate for the physical beam $\alpha_{\perp 0} = (\alpha_{x0} + \alpha_{y0})/2$. Typical rms growth times are of order an hour, but there is no need to directly simulate such a large number of turns. Instead, one can simply choose the number of simulation turns one wishes to calculate in order to model a given number of turns in the actual machine. Suppose we wish to model N_m turns in the real machine with N_c turns in a computer simulation. Let $R = N_m/N_c > 1$ be the number of machine turns divided by the number of simulation turns. By using the rms growth rates $\alpha_{p1} = R\alpha_{p0}$ and $\alpha_{\perp 1} = R\alpha_{\perp 0}$, the simulation will show the same growth with R fewer computations than a direct simulation. The final modification is due to the fact that the line densities in Figure 1 are not close to gaussian, while equation (6) is defined for gaussian bunches. The IBS rates are proportional to the beam density and, correspondingly, the local value of beam current. Define a form factor $F(t) = I(t)\sigma_t 2\sqrt{\pi}/Q$ where $I(t)$ is the instantaneous beam current, σ_t is the rms bunch length, and Q is the total bunch charge. The IBS momentum kick given to a particle on a given turn is $\Delta p = \sigma_p\sqrt{\alpha_{p1}T_0F(t)}rand$, where $rand$ is a gaussian random deviate with zero mean and unit standard deviation. The rms value of Δp for gaussian $I(t)$ equals Piwinski's value, and the same form factor is used for transverse kicks. This is equivalent to applying coasting beam formulas to longitudinal slices within the beam, with the caveat that the rms momentum spread and rms transverse emittance are calculated for the beam as a whole.

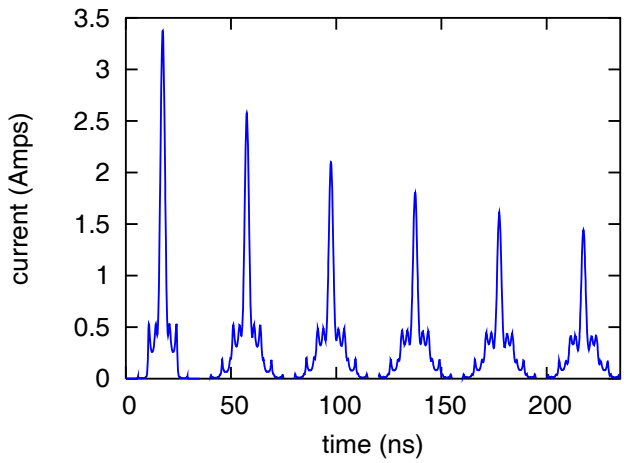

Figure 3: Simulation of the average bunch profile over a five hour RHIC store with gold beam and no cooling. Initial conditions are shown on the left and each trace to the right is one hour later.

The cooling algorithm exploits the fact that, for fixed gain and bandwidth, the cooling time is proportional to the number of particles [2, 11, 12, 4, 5, 6, 3]. While this is a well known result we will present an alternate derivation.

Consider $N \gg 1$ harmonic oscilliators with frequencies $\Omega_j = \Omega_0 + \omega_j$, with $|\omega_j| \ll \Omega_0$. The equation of motion for oscillator j is

$$\ddot{x}_j + \Omega_j^2 x_j = -\frac{2g\Omega_0}{N}\sum_{m=1}^{N}\dot{x}_m, \quad (7)$$

where $\dot{x} = dx/dt$ and g is the cooling gain. In this model N represents the number of particles per sample in an actual cooling system, and we consider a large mixing factor. Set $x_j = a_j\exp(-\lambda t - i\Omega_0 t)$ and keep leading order terms to yield

$$(\lambda - i\omega_j)a_j = \frac{g\Omega_0}{N}\sum_{m=1}^{N}a_m. \quad (8)$$

dividing through by $\lambda - i\omega_j$ and summing over j yields the dispersion relation

$$1 = \frac{g\Omega_0}{N}\sum_{m=1}^{N}\frac{1}{\lambda - i\omega_m}. \quad (9)$$

For almost all values of g equation (9) has N distinct solutions, so no information has been lost. Let the coarse

grained, normalized distribution for the frequencies be $f(\omega)$ and limit the discussion to the case were

$$\int_{-\infty}^{\omega_j} f(\omega)d\omega = \frac{j-1/2}{N}, \tag{10}$$

so that the frequencies are nearly evenly spaced when viewed over short ranges of ω. In the vicinity of frequency ω the spacing is $\Delta\omega = 1/(Nf(\omega))$. Assume the existence of an inertial range M with $1 \ll M \ll N$. Consider a solution to equation (9) with $|Im(\lambda) - \omega_K| \lesssim \Delta\omega_K = 1/Nf(\omega_K)$. For frequencies near ω_K the sum in (9) resembles a "picket fence" , while for frequencies far from ω_K the sum is well approximated by an integral. Then

$$\begin{aligned}
&\sum_{m=1}^{N} \frac{1}{\lambda - i\omega_m} \\
= &\sum_{|m-K|<M} \frac{1}{\lambda - i\omega_m} + \sum_{|m-K|\geq M} \frac{1}{\lambda - i\omega_m} \\
\approx &\sum_{|m|<M} \frac{1}{\lambda - i\omega_K - im\Delta\omega_K} + \sum_{|m-K|>M} \frac{i}{\omega_m - \omega_K} \\
\approx &\sum_{k=-\infty}^{\infty} \frac{1}{\lambda - i\omega_K - ik\Delta\omega_K} \\
+ &iN \int_{-\infty}^{\infty} \frac{\omega - \omega_K}{0^+ + (\omega - \omega_K)^2} f(\omega)d\omega.
\end{aligned} \tag{11}$$

Use the identity [13]

$$\lim_{M\to\infty} \sum_{k=-M}^{M} \frac{1}{z - ik} = \pi \frac{\exp(2\pi z) + 1}{\exp(2\pi z) - 1},$$

set

$$X(\omega_K) = \Omega_0 \int_{-\infty}^{\infty} \frac{\omega - \omega_K}{0^+ + (\omega - \omega_K)^2} f(\omega)d\omega,$$

and set $R(\omega_K) = \pi\Omega_0 f(\omega_K)$ to obtain

$$\exp[2\pi N f(\omega_K)(\lambda - i\omega_K)] = \frac{1 + gR - igX}{1 - gR - igX}. \tag{12}$$

The right hand side of (12) is independent of N so $Re(\lambda) \propto 1/N$. Equation (12) with $X = 0$ is compared with the eigenvalues obtained from exact, numerical solution of equation (8) in Figure 4. Figure 5 shows a close in view comparing the exact and approximate eigenvalues as a parametric function of g. The excellent agreement suggests that the $1/N$ scaling is robust for $N \gtrsim 50$.

By exploiting the scaling with N a comparatively small number of macroparticles can be tracked over a reasonable number of turns and the results scaled to the real beam being modeled [9]. It is then possible to simulate an accurate model of the cooling system. Consider the longitudinal cooling system in RHIC. Let $I_0(t)$ be the beam current

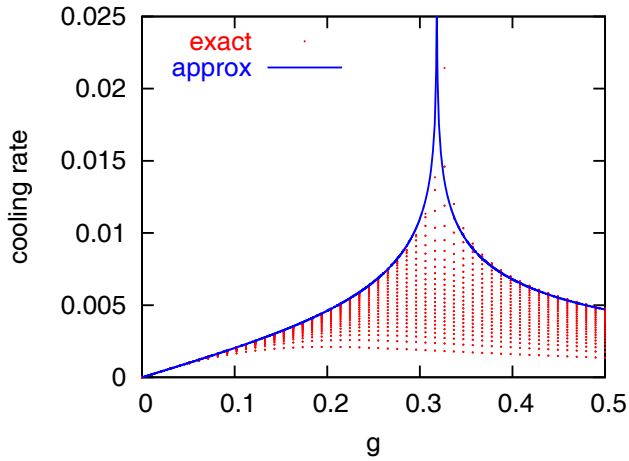

Figure 4: Comparison of actual values of $Re(\lambda)$ versus gain with those obtained from equation (12) with $X = 0$ for a rectangular frequency distribution with $N = 51$. The numerical solution had one eigenmode with a monotonically growing eigenvalue, which is not fully shown.

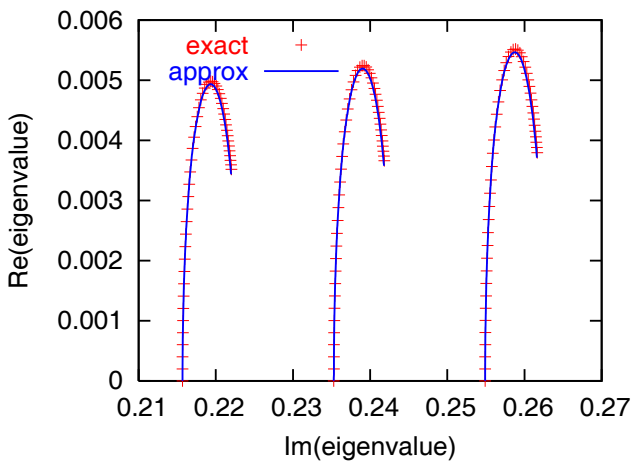

Figure 5: Evolution of λ as a function of gain for the exact, numerical solution and equation (12). The oscillator frequencies were uniformly spaced with $\omega_j = j/N$ and $N = 51$. Comparable agreement is obtained with a gaussian distribution.

at the pickup as a function of time. This is sampled on a fine grid with $t_k = k\Delta t$. For N_m macroparticles the beam current at the pickup on turn n is

$$I_0(t_k, n) = \frac{q_m}{\Delta t} \sum_{m=1}^{N_m} \hat{\delta}(\tau_m^p(n) - t_k), \tag{13}$$

where $\tau_m^p(n)$ is the arrival time of macroparticle m at the pickup on turn n, q_m is the charge of a macroparticle, and $\hat{\delta}(t)$ is a triangle function of full width $2\Delta t$ and height one. The macroparticle charge is $q_m = Q/N_m$, with Q the total charge on the real beam being modeled. We use two, cascaded one turn delay filters so the effective current driving the kicker on turn n is

$$I_1(t_k, n) = I_0(t_k, n) - 2I_0(t_k, n-1) + I_0(t_k, n-2). \tag{14}$$

The RHIC system uses a bank of cavities with frequencies spaced by 200 MHz, and a traversal filter drive. The cavity bandwidths of 10 MHz are sufficient so that the kick decays between bunches, but within a single bunch on a single turn the kick is nearly periodic with period $\tau_0 = 5$ ns. The simulation takes this periodicity to be perfect and uses the kicker drive current,

$$I_2(t_k, n) = \sum_m I_1(t_k - m\tau_0, n), \tag{15}$$

where the limits on m are chosen so that I_2 is correct for $0 \le t_k \le \tau_0$. The current I_2 drives the effective wakefield. The wakefield is defined by a lower frequency f_1, an upper frequency f_2, and the effective longitudinal resistance at these two frequencies, R_1 and R_2, respectively. The needed phase shift is incorporated yielding a longitudinal wakefield

$$W(\tau) = 2\int_{f_1}^{f_2} df\, R(f)\sin(2\pi f\tau), \tag{16}$$

where $R(f)$ is linear between f_1 and f_2. The voltage is obtained by convolving I_2 with $W(\tau)$ using a fast Fourier transform with an interval τ_0. This defines the voltage on $[0, \tau_0]$. The particles are then tracked from the pickup to the kicker and the kick is applied. For particles that arrive outside $[0, \tau_0]$, the kick is taken as periodic with period τ_0. Figure 6 shows a simulation of longitudinal cooling for the data in Figure 2. The simulations are in fair agreement with the data. The simulations do not include the few percent burn-off losses, which are of order the difference between the simulation and the data. We will treat this as an estimation error and go on to develop the algorithms for transverse cooling.

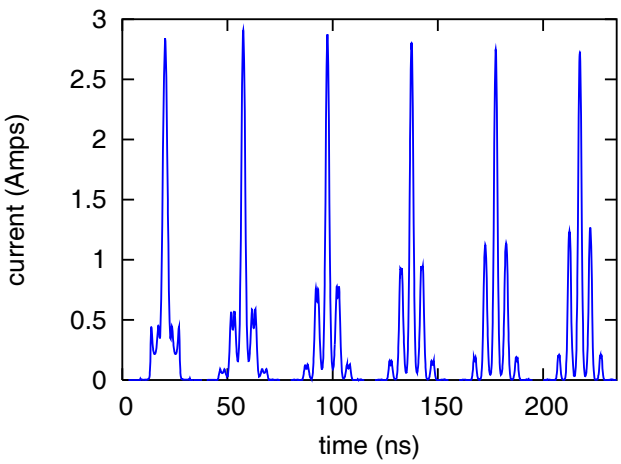

Figure 6: Simulation of the average bunch profile over a five hour RHIC store with gold beam and good cooling. Initial conditions are shown on the left and each trace to the right is one hour later.

For N_m macroparticles, the dipole weighted beam current at the pickup on turn n is

$$D_0(t_k, n) = \frac{q_m}{\Delta t}\sum_{m=1}^{N_m} x_m^p(n)\hat{\delta}(\tau_m^p(n) - t_k), \tag{17}$$

where $x_m^p(n)$ is the transverse offset for particle m at the pickup on turn n and all other symbols are the same as in equation (13). A lower frequency $(f_{1\perp})$, upper frequency $(f_{2\perp})$, and transverse impedances $R_{\perp 1}$ and $R_{\perp 2}$ are defined. The transverse wakefield is

$$W_\perp(\tau) = 2\int_{f_{1\perp}}^{f_{2\perp}} R_\perp(f)df\cos(2\pi f\tau). \tag{18}$$

As of now there is no filtering on D_0 and the kick is obtained by convolving D_0 and $W_\perp$. We assume cavity kickers with same $1/\tau_0$ frequency spacing.

As a starting point we simulated transverse cooling without longitudinal cooling or intrabeam scattering. This parameter regime allows for a particularly clean test of the scaling law for cooling rate as a function of macroparticle number, as shown in Figure 7. The horizontal scale is the normalized longitudinal energy,

$$H_s(\epsilon, \tau) = \frac{T_0\eta mc^2}{2\beta^2\gamma_0}\epsilon^2 - \int_0^\tau dtqV_{rf}(t). \tag{19}$$

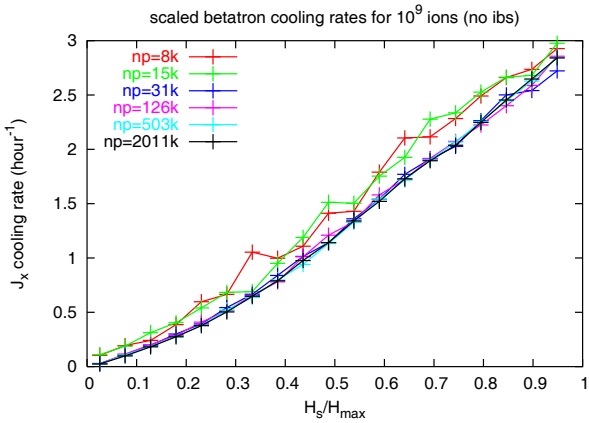

Figure 7: Transverse cooling rate versus the value of the longitudinal hamiltonian. Similar results are shown in [4, 5]

The strong dependence of transverse cooling rate on longitudinal energy was predicted by Chattopadhyay [4, 5], and design options for transverse cooling in the SPS included a higher harmonic RF cavity in an attempt to fix the problem [14]. In RHIC this problem is solved by longitudinal diffusion, from both IBS and the longitudinal stochastic cooling system. Diffusion causes the longitudinal energy of individual particles to migrate. For RHIC parameters the cooled beam shows almost no correlation of transverse action with longitudinal energy.

In addition to the large scale migration of the particles in H_s, the inclusion of IBS in the simulation can enhance the short term mixing [15]. Simulations with too few macroparticles would overestimate the effectiveness of the cooling system. Figure 8 shows that our simulations with $50,000$ macroparticles should be fine.

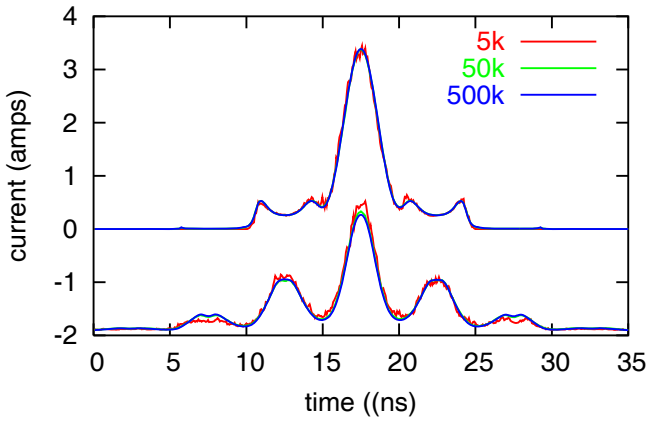

Figure 8: Test of convergence with both cooling and IBS. The initial profiles for 5000, $50,000$, and $500,000$ macroparticles are shown in the upper traces. The lower traces show the profiles at 2000, $20,000$, and $200,000$ turns, respectively. This corresponds to 10^9 gold ions evolving over 85 minutes.

Simulations for 10^9 gold ions per bunch, with both longitudinal and transverse cooling are shown in Figures 9 and 10. We assumed 5 MV on the $h = 2520$ RF system and clean rebucketing. The $1/6$th turn delay for the longitudinal cooling system will utilize the 70 GHz microwave link we are currently developing.

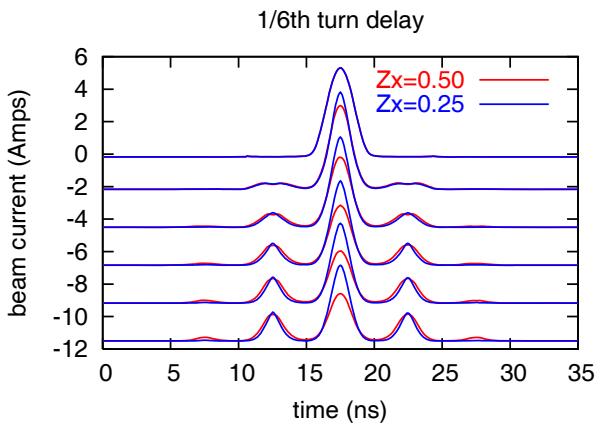

Figure 9: Simulated longitudinal profiles over 5 hours with two different transverse cooling gains and $1/6$th turn delay. The transverse gain of 0.25 utilized only a single one turn delay in the longitudinal cooling system, while the gain of 0.5 used the same cascaded delays we use now.

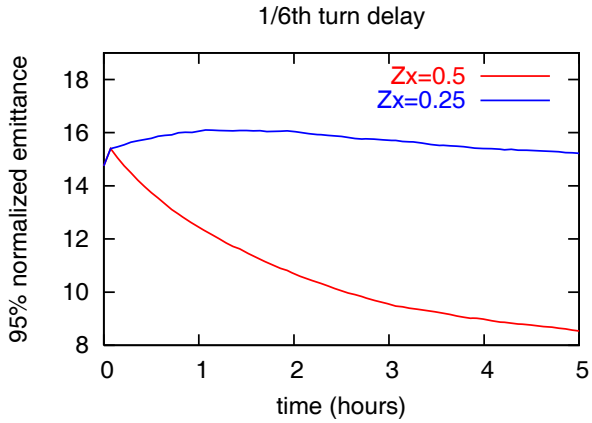

Figure 10: Simulated transverse emmittance over 5 hours with two different transverse cooling gains. The parameters are the same as those in Fig 9.

ACKNOWLEDGEMENTS

We thank Wolfram Fischer, Alexi Fedotov, Vladimir Litvinenko, Derek Lowenstein, and Thomas Roser for difficult questions and encouragement. The cooling system proper relied on the help of Freddy Severino, Fritz Caspers, Dave Mcginnis, Ralph Pasquinelli,Flemming Pedersen, Jie Wei and members of the RHIC RF and beam components groups.

REFERENCES

[1] J.M. Brennan, M. Blaskiewicz *these proceedings*

[2] S. Van de Meer, *Rev. Mod. Phys* **57**, No. 3, part 1, p689 (1985).

[3] D. Mohl, CERN 87-03, p 453 (1987).

[4] S. Chattopadhyay, LBL-14826, (1982).

[5] S. Chattopadhyay, IEEE TNS **30**, No. 4, p2646, 1983.

[6] S. Chattopadhyay, IEEE TNS **30**, No. 4, p2649, 1983.

[7] J. Wei, A.G. Ruggiero, BNL/AD/RHIC-71 (1990).

[8] J. Wei, Workshop on Beam Cooling, Montreux, 1993, CERN 94-03, (1994).

[9] M. Blaskiewicz, J.M. Brennan *Phys. Rev. ST Accel. Beams* 061001 (2007) .

[10] see *e.g.* pg 126 in 'Handbook of Accelerator Physics and Engineering', A. Chao, M. Tigner *eds.* World Scientific, 1999.

[11] F. Sacherer CERN-ISR-TH/78-11 (1978).

[12] J. Bisognano, C. Leemann, AIP conf 87, p583, AIP New York, (1982).

[13] Gradshteyn and Ryzhik, Table of Integrals, Series and Products, Academic Press, Inc, (1980).

[14] S. Chattopadhyay, IEEE TNS **30**, No. 4, p2334, 1983.

[15] D. Broemmelsiek, A. Burov, S. Nagaitsev, D. Neuffer *Phys. Rev. ST Accel. Beams* 124404 (2005).

SIMULATION OF COOLING MECHANISMS OF HIGHLY-CHARGED IONS IN THE HITRAP COOLER TRAP

G. Maero*, F. Herfurth, O. K. Kester, H.-J. Kluge, S. Koszudowski, W. Quint,
GSI, Darmstadt, Germany
S. Schwarz, NSCL, East Lansing, Michigan, USA

Abstract

The use of heavy and highly-charged ions gives access to unprecedented investigations in the field of atomic physics. The HITRAP facility at GSI will be able to slow down and cool ion species up to bare uranium to the temperature of 4 K. The Cooler Trap, a confinement device for large numbers of particles, is designed to store and cool bunches of 10^5 highly-charged ions. Electron cooling with 10^{10} simultaneously trapped electrons and successive resistive cooling lead to extraction in both pulsed and quasi-continuous mode with a duty cycle of 10 s. After an introduction to HITRAP and overview of the setup, the dynamics of the processes investigated via a Particle-In-Cell (PIC) code are shown, with emphasis on the peculiarities of our case, namely the space charge effects and the modelling of the cooling techniques.

INTRODUCTION - SCIENTIFIC GOALS

At the HITRAP facility in GSI, a series of precision experiments will be possible via the use of heavy and highly-charged ions; species up to U^{92+} can be produced and delivered by the accelerator complex, and radioactive nuclides can be provided by the Fragment Separator (FRS). Heavy atoms that have been previously stripped of all or most of their electrons allow indeed studies on residual electrons in the so-called high-field regime, where tests on the theory of quantum electrodynamics (QED) can reach new levels of accuracy; among these experiments we can mention the *g-factor* measurement of the bound electron or the width of the ground-state hyperfine splitting in H-like ions. Other planned experiments include nuclear mass measurements, collision studies and more [1].

The HITRAP setup will also be part of the Facility for Low-energy Antiproton and Ion Research (FLAIR); there $\overline{p}$ will allow fundamental symmetry tests.

THE HITRAP FACILITY

The HITRAP facility is located in the Reinjection Tunnel between the Esperimental Storage Ring (ESR) and the Heavy Ion Synchrotron (SIS); ions are accelerated and partially stripped in the Universal Linear Accelerator (UNILAC) and taken up to 400 MeV/u in the SIS. The particles lose all electrons on a thin target; deceleration to 4 MeV/u in the ESR allows their injection in the HITRAP decelerating section, where a double-drift buncher shapes them for improved acceptance into a IH-Linac operated in deceleration mode. A RadioFrequency Quadrupole (RFQ) structure further slows the bunch from 0.5 Mev/u to 6 KeV/u, after which the ions can be stored in the Cooler Trap that cools them down to 4 K and ejects them in pulsed or quasi-continuous mode. A bending magnet and a vertical beam line guide the beam to the platform on top of the tunnel, where a distribution beam line delivers the cold ions to the various experiments.

THE COOLER TRAP

The Cooler Trap, currently in the construction stage, is the element where the ion beam is not only decelerated but also cooled and shaped in such a form to fit the experiments' requirements. It consists of a cryogenic, cylindrical Penning trap, i.e. a series of cylindrical electrodes immersed in a longitudinally directed magnetic field provided by a superconducting solenoid. The latter, with a strength of 6 T and a maximum inhomogeneity below 0.1% over a volume of 10-mm diameter and 400-mm length, allows for the radial confinement via the Lorentz' $\vec{v} \times \vec{B}$ force. The longitudinal trapping of the 10^5 ions is obtained by lifting the last electrode's potential, so that the bunch is reflected back at the end of the trap. If the first electrode's potential is raised before the ions reach the entrance, the bunch is trapped. The energy and length of the incoming bunch (6 KeV/u $\approx$ 15.5 KV/q, $\approx$ 400 ns) dictate the length of the electrode stack (400 mm excluding the outermost trapping electrodes) and the trapping potential, that is about 20 KV.

The manipulation of the potential of the 21 equally-shaped internal electrodes gives the possibility to create nested traps where simultaneous confinement of ions and electrons is achieved. Indeed, as many as 10^{10} electrons, created in a pulsed laser source located in the downstream beam line, are injected in order to perform electron cooling (see Fig. 1). Due to the presence of a strong magnetic field, the electrons maintain the low temperature of the cryogenic environment (4 K) losing energy via synchrotron radiation with a time constant $\tau_s = 3\pi\varepsilon_o \frac{m^3c^3}{e^4B^2} \approx 0.1$ s [2]. The axial bounce of the ion cloud through the electron-filled regions lowers the ions' energy via Coulomb collision [4]; to avoid radiative recombination as the electrons' and ions' energies get closer, the process must be stopped at some point and a different cooling scheme has to be introduced:

* G.Maero@gsi.de

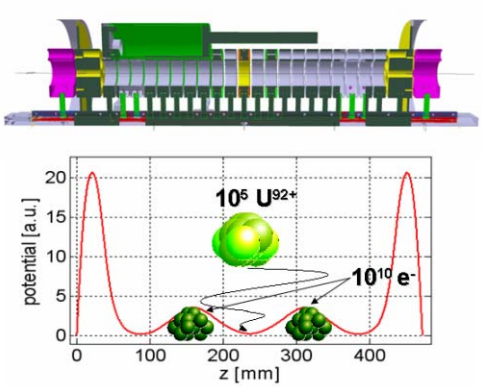

Figure 1: Section of the Cooler Trap, a large-scale storing device with an inner diameter of 35 mm and a length of 400 mm of trapping region. Inner electrodes are 17-mm long and are separated by 2-mm gaps. The box for cryogenic electronics is placed in the upper-left part. A sketch of the nested-trap configuration is shown below.

resistive cooling. Ions are collected in the central region of the trap, where radially-split electrodes allow detection of motion frequencies and manipulation of the cloud via resonant excitation (e.g. 'rotating wall' radial compression [5]). Then resistive cooling with an external RLC circuit (whose quality factor is about 800) at the resonant axial oscillation frequency ω_z takes place. This provides the cooling of the axial motion only, RF coupling to the radial motions is obviously foreseen; the ions' energy is brought down to the level of the environment temperature, that is why the trap is in thermal contact with the magnet cold head at 4 K.

Some questions have already become apparent, and will be dealt with in the next section:

- the survival probability to radiative recombination;
- the space charge and its effects (frequency shifts and frequency range broadening);
- the time constants of the abovementioned processes.

THEORY AND SIMULATION OF COOLING PROCESSES

Electron Cooling

For electron cooling in a trap, electrons are not renewed like in a storage ring, but cooled via synchrotron radiation in the magnetic field; nevertheless the energy exchange by Coulomb collisions with the ions produces a strong feedback depending on particle densities. The dependence is not trivial: to model the phenomenon, the energy lost by hot ions is considered as instantaneously converted into the temperature of an isotropic e^- distribution. On the other hand, the latter will be the result of this positive contribution and the radiation decay; furthermore, the stopping force affecting the ions is density-dependent, too. Hence a denser electron cloud will have a stronger stopping and consequently the electrons will heat up more (typical numbers show a rise from the initial meV range to a few eV), leading then to a slower cooling of the ions. Therefore the cooling times do not reduce linearly with the electron density.

To summarize, from former investigations it appears possible to cool the ion bunch in about 1 s, keeping radiative recombination losses within $10 \div 15\%$ [2], [3].

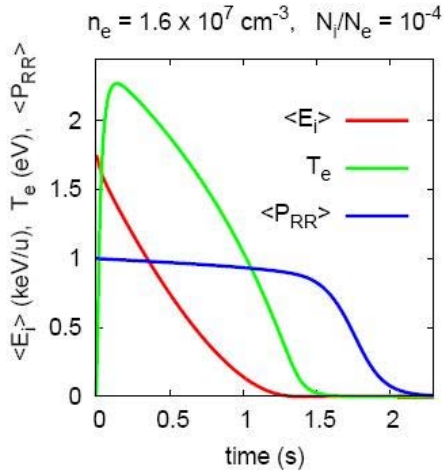

Figure 2: Example of electron cooling: 10^5 U^{92+} ions are cooled in about 1 s without significant losses by recombination ($\langle P_{RR} \rangle$ is the ion survival probability). The strong heating and successive cooling of the e^- temperature T_e by synchrotron radiation is also evident [3].

The Particle-In-Cell Code

A Particle-In-Cell (PIC) code is used to investigate the issues of space charge and resistive cooling. A PIC code essentially solves the Poisson equation, i.e. calculates the electrostatic potential with assigned boundary conditions including the charge of the ions. Then the particles are advanced in time with a suitable propagation algorithm within the obtained electrostatic potential and the given $\vec{B}$ field, and the process is looped ad libitum [6].

The Poisson equation is solved in an rz-symmetric geometry with a Fast-Fourier-Transform (FFT) method [7]. The charge of each particle is smeared on a radial ring when it is included in the charge distribution, but the motion is treated in full 3d. The $\vec{B}$ field creates an additional problem, as an ion of charge q performs cyclotron oscillations of frequency $\omega_c = qB/m$ and common advancement algorithms, as leapfrog or time-adaptive Runge-Kutta routines, would require too small time steps Δt to keep a sufficient level of accuracy, depending on the B strength. On the contrary, a Velocity Verlet (VV) scheme, adapted to the specific case of ions in electromagnetic fields, allows for a B-independent choice of Δt s [8]. Our simulations show that with $\Delta t = 5^{-9}$ s one gets an energy nonconservation

$\Delta E/E \approx 10^{-4}$ after a simulation time of 50 ms for $B = 6$ T, while using a leapfrog algorithm the particle is radially lost much before.

Since the simulation of 10^5 trajectories would be too expensive in terms of computing time, the method of charge scaling is used: a limited number of simulation 'superparticles' is chosen, carrying the total amount of charge of the real bunch when the charge distribution has to be calculated for the Poisson equation, but behaving as normal particles when advanced in time with the VV routine. $500 \div 1000$ superparticles are already enough to reproduce well the statistical properties of the cloud.

Resistive Cooling

A particle placed in the vicinity of a conductor induces a surface charge density on the conductor itself; if the latter is kept at a fixed potential, one can cancel the apparent contradiction with the creation of a so-called 'image charge' of opposite sign, so that the global effect is null at the conductor's surface. If an ion is placed between two conducting elements, the image charge induced on the first will have an effect on the second, generating a second image and so on and so forth, so that a whole series of images is created. An analytical calculation of the image sequence is possible for simple cases, like for instance that of an ion placed between two parallel plates (a capacitor) [9]; the net difference $\Delta q^{(N)} = q^L_{im} - q^R_{im}$ between the charge collected on the two plates (when the series of images is truncated at the $N - th$ order) varies depending on the ion's axial position (see Fig. 3) and connecting the plates to an external circuit this turns out to be an 'image current' oscillating with the ion bounce, that can be detected with LC elements (resonant or 'bolometric' detection [10]), or damped in amplitude if the LC ('tank') circuit has a dissipative component (resistive cooling).

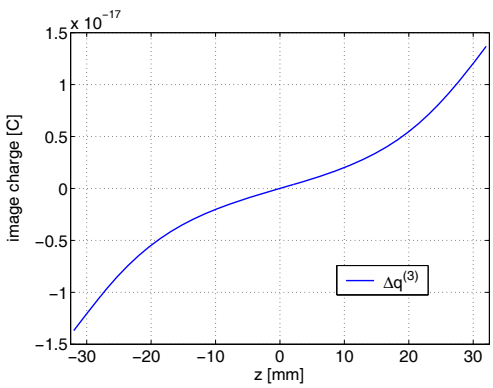

Figure 3: Net image charge $\Delta q^{(N)}$ accumulated on two parallel plates at a distance $d = 64$ mm, versus the position of a U^{92+} ion. The charge is calculated up to the third image ($N = 3$).

In the Cooler Trap the detection and cooling are performed creating a nested trap in the center of the electrode stack and connecting the two electrodes adjacent to the central one to the tank circuit; we have calculated the image charge that is collected on the cylindrical surface following the same approach as described for the capacitor [9], i.e. writing the Gauss' law for a cylinder; integration on an axially-finite region $[z_1 - z, z_2 - z]$ where z is the particle position with respect the the center of the trap and z_1, z_2 are the axial coordinates of the desired electrode, the result yields

$$q_{ring} = \frac{qR^2}{2} \int_{z_1-z}^{z_2-z} \frac{1}{\left(R^2 + z^2\right)^{3/2}} \mathrm{d}z' = \\ = \frac{qR^2}{2} \left[\frac{z' \left(1 + \frac{z'^2}{R^2}\right)^{3/2}}{\left(R^2 + z'^2\right)^{3/2} \left(1 + \frac{z'^2}{R^2}\right)^{1/2}} \right]_{z_1-z}^{z_2-z}, \qquad (1)$$

and again the net Δq_{ring} is the difference between the charge on the two collecting electrodes (see Fig. 4).

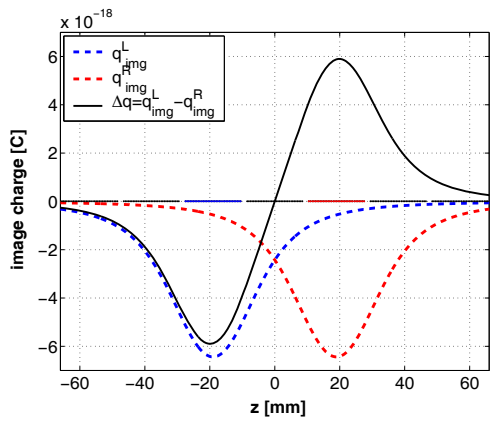

Figure 4: Net image charge accumulated on the electrodes of a multi-ring trap versus the position of a U^{92+} ion. The charge on the two pick-up electrodes and the difference (net charge) is shown. The geometrical parameters reproduce the Cooler Trap characteristics.

It can be shown that the damping of the ion motion (i.e. its energy) is exponential [11], with a decay constant $\tau = mD^2_{eff}/\left(Rq^2\right)$, where R is the resistance of the tank circuit and D the *effective electrode distance*, that would be the equivalent distance between the parallel plates in the capacitor case. This guides us to the implementation in the PIC code: the instantaneous image current is I gives a voltage drop on the external resistance $\Delta V = RI$, and the cooling is fed back via a restoring force $F_z = qE_z \approx -q\Delta V/D_{eff}$ acting on the particle. In our case, with an effective resistance of 72.7 $M\Omega$, the theoretical value is $\tau = 110$ ms; simulations give a pretty good agreement (125 ms) if we imagine to have parallel plates at the ends of the central nested trap, while using the cylindrical rings as pick-ups affects the detected signal and gives a cooling time constant of 250 ms.

Space Charge

The picture changes significantly moving from a single particle to a cloud of 10^5 ions. First of all, they will fill the potential well, flattening its bottom (see Fig. 5). As a consequence, the axial motion will not have a fixed eigenfrequency $\omega_z = (qV/(md^2))^{1/2}$ (with d a geometrical trap parameter) anymore. The energy spread of the particles will result in an energy-dependent range of frequencies. The estimate of this effect is crucial, since the resistive cooling will be performed via an RLC circuit, whose effective resistance has a peak at the characteristic frequency $\omega_{LC} = 1/(2\pi)(LC)^{-1/2}$; this means that full cooling will be reached only by ions within the bandwidth of the tank, that is inversely proportional to its Q value. Simulations of an ion column (1 mm radius, ≈ 10 eV energy) in a potential well of 100 V show that as the number of ions increases, ω_z shifts from the eigenvalue of 383.15 KHz and the frequency range $\Delta\omega/\omega = (\omega' - \omega)/\omega$ broadens (see Table 1).

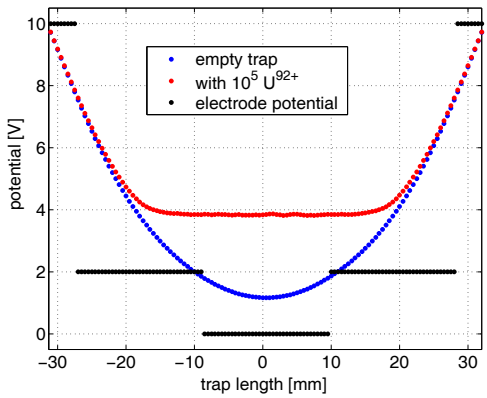

Figure 5: Space-charge effect of column of 10^5 bare Uranium ions with a radius of 1 mm. The potential on the longitudinal axis is visibly flattened. The voltage applied to the electrodes is also shown.

Table 1: Axial frequency shifts

No. ions	$\overline{\omega}'$	$-\Delta\omega/\omega$	$\sigma(\omega)$
10^3	379.72 KHz	$8.95 \cdot 10^{-3}$	1.77 KHz
10^4	374.91 KHz	$2.15 \cdot 10^{-2}$	6.93 KHz
10^5	362.05 KHz	$5.51 \cdot 10^{-2}$	24.70 KHz

As far as resistive cooling is concerned, it can be shown that considerations similar to the single-particle case apply to the center-of-mass (CoM) motion, that should be damped at the abovementioned rates; however other internal motions (e.g. a 'breathing'-like expansion and contraction of the cloud around the center) could be totally or almost invisible in the present coupling scheme and therefore much slower to damp. It has been suggested that natural or artificial imperfections could render them apparent (for instance, recombined ions would displace the CoM with respect to the center of charge) [9]. Cooling of a cloud of C^{5+} ions has been experimentally proved, but there is not a complete theoretical understanding of the phenomenon yet [12]. Again, investigation of these processes is of high interest and it is being considered within our PIC code. Since the potential is distorted by the space charge, the restoring force cannot be inserted as done above for one ion, but it should be fed back directly into the boundary conditions as a potential difference due to the drop on the external circuit. The implementation is under way.

CONCLUSIONS

We have shown that a PIC code is a powerful tool for investigations of ion dynamics in a Penning trap. Further improvements of the code are under way as they are not only required within the HITRAP project, but of interest in the whole trap community for the development of new setups and understanding of experimental results.

REFERENCES

[1] F. Herfurth, K. Blaum, S. Eliseev, O. Kester, H.-J. Kluge, S. Koszudowski, C. Kozhuharov, G. Maero, D. Neidherr, W. Quint, S. Schwarz, S. Stahl, G. Vorobjev, "The HITRAP project at GSI: trapping and cooling of highly-charged ions in a Penning trap", Hyp. Int. 173 (2006) 93.

[2] H. Nersisyan, C. Toepffer and G. Zwicknagel, "Interactions between charged particles in a magnetic field", Springer (2007) 151.

[3] G. Zwicknagel, "Electron cooling of highly charged ions in Penning traps", AIP Conf. Proc. 862 (2006) 281.

[4] H. Poth, "Electron Cooling: Theory, Experiment, Application", Phys. Rep. 196 (1990) 135.

[5] F. Ames, G. Bollen, P. Delahaye, O. Forstner, G. Huber, O. Kester, K. Reisinger and P. Smith, "Cooling of radioactive ions with the Penning Trap REXTRAP", Nucl. Instr. Meth. Phys. Res. A 538 (2005) 17.

[6] D.W. Mitchell and R.D.Smith, "Two dimensional many particle simulation of trapped ions", Int. J. Mass Spectrom. Ion Proc. 166/167 (1997) 271.

[7] R.W. Hockney, "A fast direct solution of Poisson's equation using Fourier analysis", J. Ass. Comp. Mach. 12 (1965) 95.

[8] Q. Spreiter and M. Walter, "Classical Molecular Dynamics simulation with the Velocity Verlet algorithm at strong external magnetic fields", J. Comp. Phys. 152 (1999) 102.

[9] D.F.A. Winters, M. Vogel, D.M. Segal and R.C. Thompson, "Electronic detection of charged particle effects in a Panning trap", J. Phys. B 39 (2006) 3131.

[10] H. G. Dehmelt, F. L. Walls, "Bolometric technique for the rf spectroscopy of stored ions", Phys. Rev. Lett. 21 (1968) 127.

[11] M.H. Holzscheiter, "Cooling of particles stored in electromagnetic traps", Phys. Scripta 22 (1988) 73.

[12] H. Häffner, T. Beier, S. Djekić, H. Hermanspahn, H.-J. Kluge, W. Quint, S. Stahl, J. Verdú, T. Valenzuela and G. Werth, "Double Penning trap technique for precise g factor determinations in highly charged ions", Eur. Phys. J. D 22 (2003) 163.

COMMISSIONING AND PERFORMANCE OF LEIR

C. Carli, CERN, Geneva, Switzerland,
on behalf of the LEIR and I-LHC teams

Abstract

The Low Energy Ion Ring (LEIR) is a key element of the LHC ion injector chain. Under fast electron cooling, several long pulses from the ion Linac 3 are accumulated and cooled, and transformed into short bunches with a density sufficient for the needs of the LHC. Experience from LEIR commissioning and the first runs in autumn 2006 and summer 2007 to provide the so-called "early LHC ion beam" for setting-up in the PS and the SPS will be reported. Studies in view of the beam needed for nominal LHC ion operation are carried out in parallel to operation with lower priority.

INTRODUCTION

The LHC [1,2], presently under construction at CERN will, in addition to proton operation, provide ion collisions for physics experiments. For the moment, only lead ion operation is part of the approved program, but other species may be used as well. The ion accelerator chain existing before the LHC era was not capable to provide the ion beams needed for the LHC.

Thus, fundamental upgrades of the CERN ion accelerator complex, based on ion accumulation experiments [3] carried out with LEAR, had to be implemented. The resulting ion accelerator chain is depicted in Fig. 1 and nominal values for some key parameters are listed in Tab. 1.

Since nominal LHC ion operation is very demanding for both the LHC and the injector chain, first LHC ion operation will take place with a lower luminosity and less bunches using the so-called “early scheme” [3-5]. In this scheme, every LEIR/PS pulse will provide only one LHC bunch, the SPS will accumulate only up to four batches and the LHC will be filled with 62 bunches per ring.

OVERVIEW OF LEIR

The most fundamental upgrade of the CERN ion accelerator chain [4-6] for the LHC was the addition of the Low Energy Ion Ring LEIR (reconstructed and upgraded LEAR). The role of this small accumulator ring, equipped with a new state-of-the-art electron cooler (constructed in the frame of a collaboration by BINP), is to convert several 200 µs long Linac3 pulses into short high brilliance bunches needed for LHC ion operation.

Fig.2 shows the LEIR ring after installation. A typical 3.6 s LEIR cycle needed for nominal operation and producing the beam intensity for four LHC bunches is shown in Fig. 3. On an accumulation plateau several Pb^{54+} pulses from Linac3 are accumulated alternating:

- An elaborate multiturn injection of the 200 µs long Linac pulses with stacking in momentum and in both transverse phase spaces [4]. For this injection scheme, momentum ramping of the Linac3 (mean beam energy increases by ~4 10^{-3} during the duration of the Linac3 pulse) is required as well as a large dispersion at the injection and an inclined injection septum.
- Fast (in 200 ms to 400 ms) electron cooling [4,7,8] .

After accumulation of a sufficient intensity, the beam is bunched with harmonic number two and accelerated during about 1 s. Finally the two bunches, each one corresponding to two LHC bunches, are ejected and

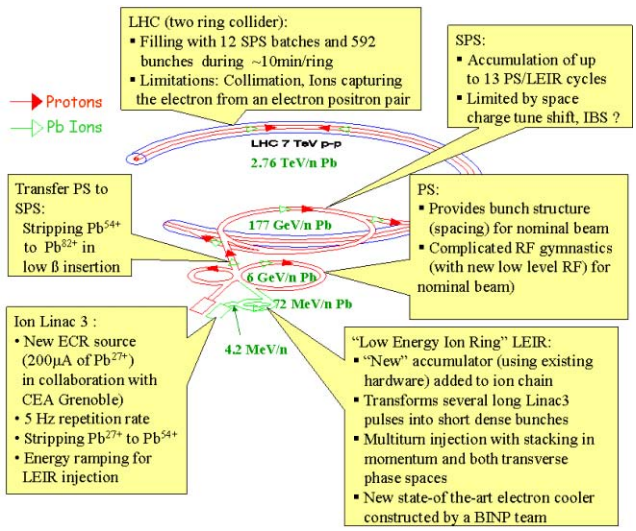

Figure 1: Overview of the LHC ion injector chain.

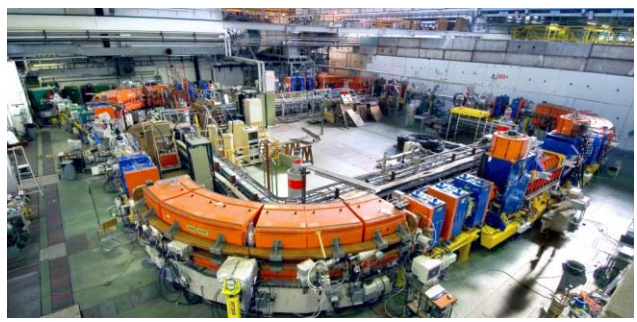

Figure 2: LEIR ring after completion of installation.

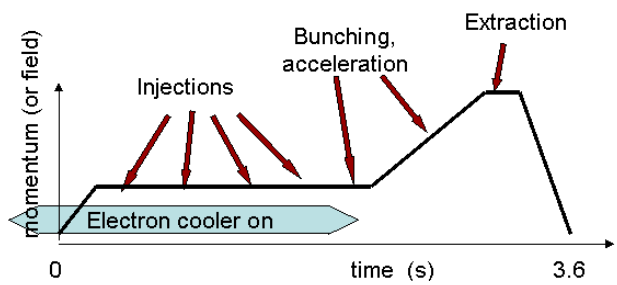

Figure 3: Nominal LEIR cycle.

transferred to the PS, the next machine in the chain. The PS has to provide already four bunches with the spacing needed in the LHC with the help of RF gymnastics. 12 SPS shots, each one accumulating up to 13 LEIR/PS shots, fill the LHC.

The "early" beam provides, with a 2.4 s cycle and only one injection, only one bunch for the PS and the LHC. Only four LEIR/PS batches are accumulated in the SPS.

LEIR optics

The basic shape of LEIR (see Fig. 2) is a "square" with long 90° bending sections in the corners separating four straight sections.

Rather different lattice parameters are needed in the injection section (large dispersion and small horizontal ß-function) and the electron cooler section (ß-function of about 5m in both planes and small dispersion). These requirements can be fulfilled by installing injection and the cooler in adjacent straight sections and a basic (without perturbation by the cooler) lattice with twofold periodicity and symmetry.

The electron cooler introduces strong lattice perturbations especially at low energy during accumulation. The coupling between the two transverse planes induced by the cooler solenoid is compensated with short compensation solenoids; those add significant additional focusing. This additional focusing is compensated globally by readjusting all quadrupole families and trim power supplies close to the cooler, rather than locally just by changing quadrupole gradients close to the perturbation. The lattice functions of the lattice obtained are shown in Fig. 4 for one half of the ring (second half is the mirror image) extending from the section opposite to the cooler, through the injection section to the electron cooler section.

Another perturbation of the lattice, which had been considered a challenge, occurs during acceleration. Since the LEIR bending sections are C-shaped and the vacuum chamber is connected to ground at many locations (fully bakeable and constructed initially for a slow cycling

Table 1: Key beam parameters along the accelerator chain for LHC ion operation with the "early" and nominal scheme.

	Linac 3	LEIR		PS		SPS		LHC	
Parameter		nominal	early	nominal	early	nominal	early	nominal	early
energy per nucleon	4.2 MeV	4.2 MeV		5.9 GeV		72 MeV		2.76 TeV	
Charge state	27→54	27 → 54		54 → 82		82		82	
Shots accumulated		~5-7	1	1	1	8,12,13	4	12	16
LHC bunches/shot	≤ 1	4	1	4	1	≤ 52	4	592	62
Ions/LHC bunch		$2.25\ 10^8$		$1.2\ 10^8$		$0.9\ 10^8$		$0.7\ 10^8$	
Ions/shot (filling)	$11.5\ 10^8$	$9\ 10^8$	$2.25\ 10^8$	$4.8\ 10^8$	$1.2\ 10^8$	$\leq 47\ 10^8$	$3.6\ 10^8$		
Bunch spacing		350 ns		99.8 ns	1350ns	99.8 ns	1350ns	99.8 ns	1350 ns
Norm. rms emittance	0.25 µm	0.7 µm		1.0 µm		1.2 µm		1.5 µm	
Long. emitt./LHC bunch ($4\ \pi\ \sigma_E\ \sigma_\tau$)		0.025 eVs/n		0.05 eVs/n		0.24 eVs/n		1 eVs/n	
rms bunch length		50 ns		1 ns		0.41 ns		0.25 ns	
Cycle/Filling time	>200ms	3.6s	2.4s	3.6s	2.4s	~50s	~16s	~10 min	~4 min
β*								0.5 m	1.0 m
Initial luminosity								10^{27} cm^{-2}s^{-1}	$5\ 10^{25}$ cm^{-2}s^{-1}
Initial lumi. decay time (2 experiments)								~5.5 hrs	~ 10 hrs

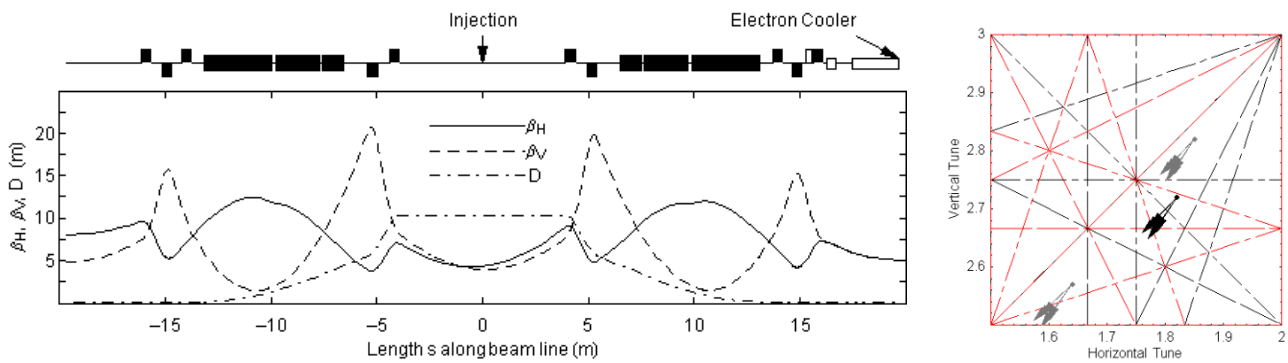

Figure 4: LEIR lattice. The left image shows Twiss parameters for the nominal lattice for one half of the circumference; the right image shows a resonance diagram with the nominal working point (black) and two other envisaged working points. The arrows point from the zero intensity working point to the one with the largest space charge tune shift.

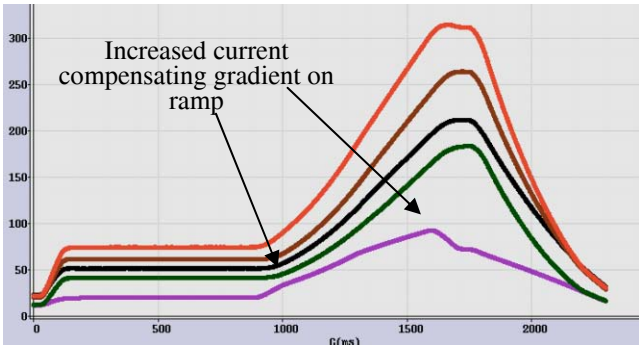

Figure 5: Time evolution of quadrupole currents with corrections to compensate gradients due to ramping.

machine), ramping induces net currents flowing along the chamber inducing, in turn, defocusing gradients acting on the lattice. Thus a compensation scheme, adjusting the quadrupole currents during the ramp has been implemented. The effect of these corrections is clearly visible on the acquisitions of quadrupole current versus time shown in Fig. 5.

LEIR COMMISSIONING AND PERFORMANCE

LEIR Commissioning

LEIR commissioning [9] has taken place in stages partly in parallel with installations. Commissioning of the Linac3 to LEIR transfer line has taken place in spring 2005 and has suffered from "teething" problems of the new controls system and first difficulties with injection matching. After bringing the beam up to the LEIR injection in July 2005, LEIR commissioning has been interrupted to complete the installations of the ring.

Commissioning of the LEIR ring started in autumn 2005 with O^{4+} (beam rigidity very close to Pb^{54+}, but longer life-times had been expected). First circulating beam and satisfactory injection efficiency could be obtained quickly after work on improving the transfer line optics. However, due short life-times, which later-on were traced back to ions hitting a piece of the vertical ionization profile monitor and degrading the vacuum, only weak signs of cooling and no accumulation have been observed. Another problem encountered during this period was that cables between position pick-up and their head-amplifiers were damaged by currents induced by the ramp [9]. In consequence, the ramp rate had to be reduced.

During a short shutdown at the beginning of 2006, the machine has been opened to install a new vertical ionisation profile monitor with collimators intercepting circulating ions before they hit surfaces with high beam loss induced outgassing yields. The damage of pick-up cables due to ramp induced currents has been cured by insulating the head amplifier boxes from ground.

Ring commissioning resumed in the middle of February 2006 with Pb^{54+} ions. At the very beginning, progress was slowed down by difficulties to tune the injection efficiency with Pb^{54+} ions, again due to problems with injection matching. After improving the injection line setting [10] and setting-up of the transverse damper, clear signs of cooling could be observed on 3rd March without particular difficulties.

LEIR commissioning has been completed, almost as scheduled, in May 2006 with the proof that the early LHC ion beam can be produced and transported to a region just upstream from the PS injection.

Experience from first LEIR Runs

The first regular LEIR run has taken place in autumn 2006 in order to provide the beam for setting up the PS with the "early LHC ion beam". The beginning of the start-up had been delayed due to technical problems (vacuum leak at the collector of the electron cooler). However, the start-up with beam was smooth and the beam was available almost on time for the PS. The machine has been running in general with good reliability. Strong fluctuations of the trajectory in the injection line, caused by stray field of the PS ring and lead to a jitter of the injection efficiency.

The second LEIR run started at the beginning of August 2007. Again, the start-up with beam has been carried without particular difficulties. The fluctuations of the injection trajectory and efficiency have been reduced to an acceptable level by magnetic shielding of the beam pipe in regions close to the PS. LEIR now delivers routinely the beam needed for SPS setting-up with the "early LHC ion beam". Work to sort out various minor technical problems and, with lower priority, to produce the not yet demonstrated nominal LEIR beam is going on in parallel.

LEIR Performance

Table 2: Comparison of LEIR design performance and obtained performance for the nominal beam and the beam needed for first LHC ion run(s).

	Nominal		"early"	
Parameter	design	obtained	design	obtained
Linac3 current (μA)	50	25	50	25
Cycle time (s)	3.6	3.6	2.4	2.4
Inj. efficiency (%)	50	50	50	50
Accumulated. Int. (10^8 Pb^{54+})		~10		~2.5
Int. for PS (10^8 Pb^{54+})	9	~7	2.25	2.25
Hor. norm. rms emitt. (μm)	0.7	0.5	0.7	0.52
Vert. norm. rms emit. (μm)	0.7	0.2	0.7	0.24
Long. emitt. $4\pi\,\sigma_E\sigma_\tau$ per bunch (eVs/n)	0.05	0.04	0.025	0.025

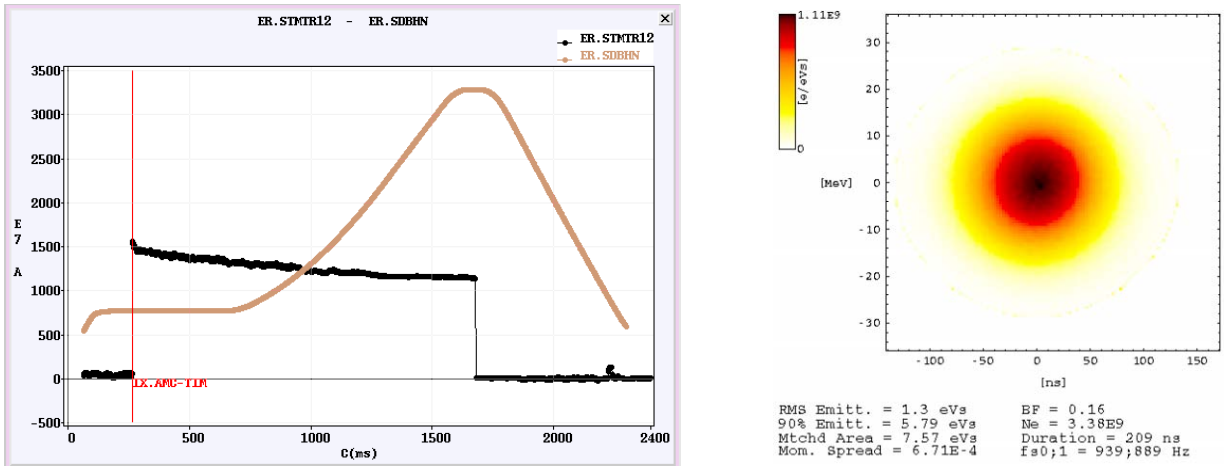

(a) (b)

Figure 6: LEIR performance for the "early" beam used routinely for setting-up of the PS and SPS with the beam needed for the first LHC ion run. The images show the evolution of the beam current (a) and a tomographic reconstruction of the longitudinal phase space (b).

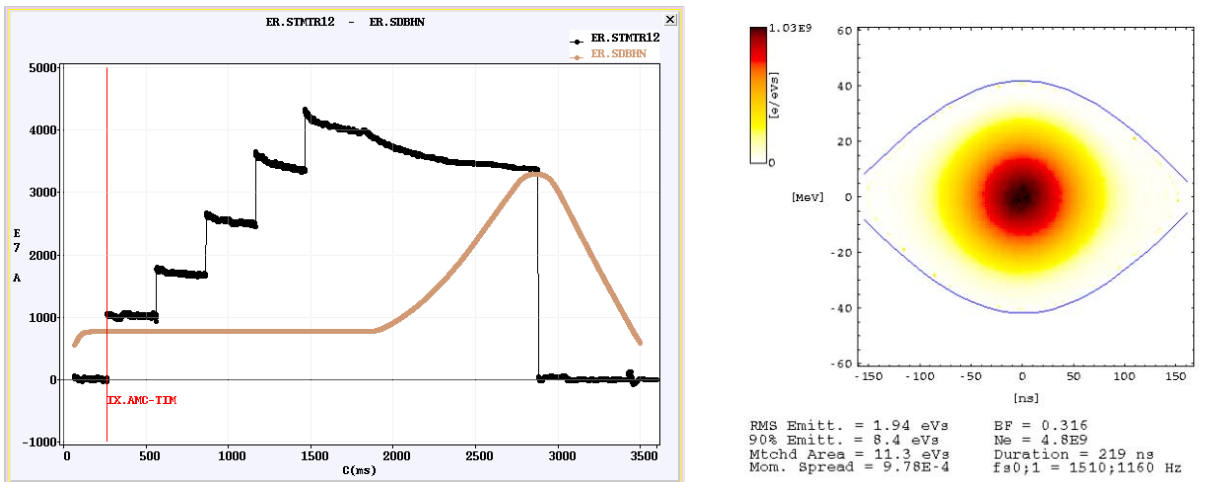

(a) (b)

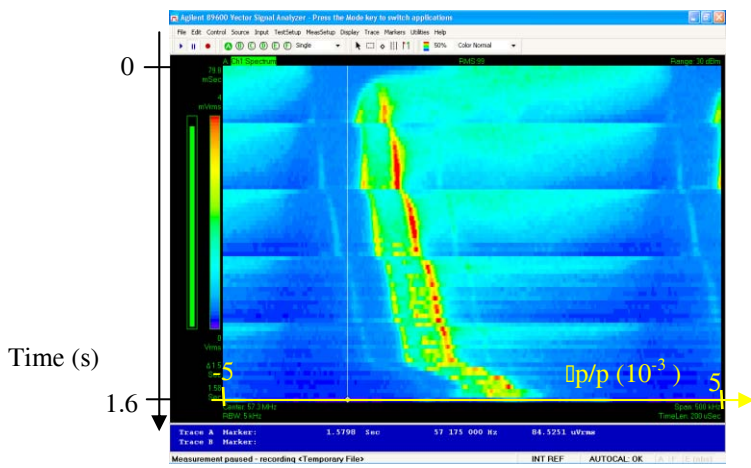

(c)

Figure 7: LEIR performance with a high intensity beam. The images show the evolution of the beam current (a), a tomographic reconstruction of the longitudinal phase space (b) and the evolution of longitudinal Schottky spectra(c).

Tab. 2 compares LEIR performance as observed during the present run 2007 with design values for the "early" beam needed for the first LHC ion runs and the nominal beam. One observes that the design performance has been reached for the "early" beam with transverse emittances significantly below specifications. Fig. 6a shows some details. After injection, a bit more than the design intensity is circulating; with some losses mainly during the cooling plateau, the design intensity is ejected. The tomographic reconstruction of longitudinal phase space show that the design longitudinal emittance (the number quoted in the figure is the rms for all 208 nucleons) is reached.

Fig. 7 shows some measurements for high intensity beams obtained so far. The evolution of the beam current (with higher Linac3 currents, higher beam currents, exceeding the design value at ejection, have been obtained at the end of the accumulation plateau) shows a loss at the beginning of the ramp. This loss is more pronounced for higher beam currents and, thus, the design current has not yet been obtained at ejection. However, investigations on these losses and the nominal LEIR beam are carried out only with low priority and in parallel to operation. The emittances in all three phase spaces are well within specifications.

Vacuum Limitations

Beam loss induced vacuum degradation had been a fundamental limitation of proof of principle experiments [3]. Thus systematic investigations of beam loss induced outgassing have been carried out [11]. Based on these results, the LEAR vacuum system has been upgraded carefully and, in particular, Au coated collimators [12] with a low outgassing yield, intercepting lost ions before they can hit the normal vacuum chamber, have been installed and, where it was possible, the vacuum chamber was coated with low temperature NEG. Fig. 8 shows that beam life-times, sufficient for accumulation the nominal intensity, have been obtained. During the 2006 run, intensities by more than a factor two larger than the design nominal intensity have been accumulated on very long plateaus.

CONCLUSIONS AND OUTLOOK

LEIR has been successfully installed and commissioned. The second regular run takes place at present. The beam needed for the first LHC ion runs is delivered reliably during routine operation for setting up the PS and the SPS for the first LHC ion run. The present run aims at (i) demonstrating that the "early" LHC ion beam can be obtained at SPS extraction and (ii) carrying out machine studies to better understand potential SPS limitations (IBS, direct space charge tune shift during a long front porch) with the nominal LHC ion beam. The first LHC ion run is expected to take place in 2009.

Even though no fundamental limitation has been identified so far, further work on the production of the nominal beam has still to be carried in parallel to operation. Experiments have expressed strong interest in

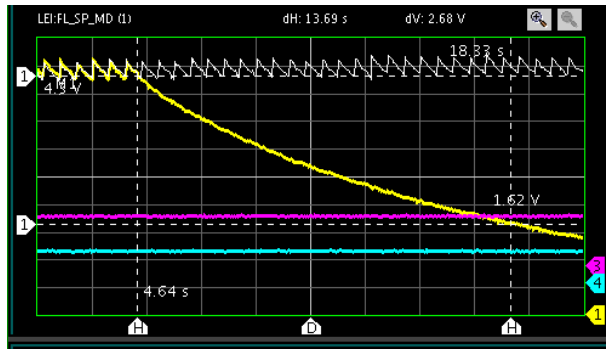

Figure 8: Beam intensity (yellow trace) versus time (2s/div) after accumulation on a very long plateau. The peak intensity is about 16 10^8 Pb^{54+} ions; and the beam life-time about 14 s.

LHC runs with lighter ions, even though this is not foreseen in the LHC program. Furthermore, first studies on using LEIR to provide various ions species for SPS fixed target experiments have started recently.

REFERENCES

[1] O. Brüning et al. (eds), "LHC design report" Vol. 1, CERN-2004-003.

[2] O. Brüning, "LHC progress and commissioning plans", Proceedings of EPAC 2006, Edinburgh.

[3] J. Bosser et al., "Experimental Investigations of Electron Cooling and Stacking in a low Energy Accumulation Ring", Part. Acc. Vol. 63, p. 171-210.

[4] M. Benedikt et al. (eds), "LHC design report", Chapters 32 to 38 of Vol. 3, CERN-2004-003.

[5] A. Beuret et al., "The LHC lead injector chain", Proceedings of EPAC 2004, Lucerne 2004.

[6] M.E. Angoletta et. al., "Ions for LHC: Physics and Engineering Challenges", Proceedings of PAC05, Knoxville, 2005.

[7] A. Bubley, V. Parkhomchuk, V. Prieto, R. Sautier, G. Tranquille, "LEIR Electron Cooler Status", Proceedings of EPAC 2006, Edinburgh.

[8] G. Tranquille, "Cooling Results from LEIR", these Proceedings.

[9] P. Belochitskii, L. Bojtar, C. Carli, M. Chanel, K. Cornelis, B. Dupuy, J. Duran-Lopez, T. Eriksson, S. Gilardoni, D. Manglunki, E. Matli, S. Maury, C. Oliveira, S. Pasinelli, J. Pasternak, F. Roncarolo, G. Tranquille,, "LEIR Commissioning", Proceedings of EPAC 2006, Edinburgh.

[10] F. Roncarolo, C. Carli, M. Chanel, L. Dumas, R. Scrivens, "Design and Validation with Measurements of the LEIR Injection Line", Proceedings of EPAC 2006, Edinburgh.

[11] E. Mahner et al., "Ion Stimulated Gas Desorption Yields of Coated (Au, Agm Pd) Stainless Steel Vacuum Chambers irradiated with 4.2 MeV/u Lead Ions", CERN/AT 2003-006 (VAC).

[12] C. Bal, C. Carli, M. Chanel, E. Mahner, J. Pasternak, "A Collimation Scheme for Ions Changing Charge State in the LEIR Ring", Proceedings of PAC 2005.

ELECTRON COOLING EXPERIMENTS AT S-LSR

T. Shirai#, S. Fujimoto, M. Ikegami, H. Tongu, M. Tanabe, H. Souda, A. Noda
ICR, Kyoto-U, Uji, Kyoto, Japan,
K. Noda, NIRS, Anagawa, Inage, Chiba, Japan,
T. Fujimoto, S. Iwata, S. Shibuya, AEC, Anagawa, Inage, Chiba, Japan,
E. Syresin, A. Smirnov, I. Meshkov, JINR, Dubna, Moscow Region, Russia
H. Fadil, M. Grieser, MPI Kernphysik, Saupfercheckweg, Heidelberg, Germany

Abstract

The electron cooler for S-LSR was designed to maximize the cooling length in the limited drift space of the ring. The effective cooling length is 0.44 m, while the total length of the cooler is 1.63 m. The one-dimensional ordering of protons is one of the subjects of S-LSR. Abrupt jumps in the momentum spread and the Schottky noise power have been observed for protons at a particle number of around 2000. The beam temperature was 0.17 meV and 1 meV in the longitudinal and transverse directions at the transition, respectively. The normalized transition temperature of protons is close to those of heavy ions at ESR. The lowest momentum spread below the transition was 1.4×10^{-6}, which corresponded to the longitudinal beam temperature of 26 μeV (0.3 K). It is close to the longitudinal electron temperature.

INTRODUCTION

S-LSR is a compact ion storage/cooler ring at Kyoto University to study physics of cooled ion beams and applications of beam cooling. S-LSR has an electron beam cooler and a laser cooling system. The laser cooling system has been developed for the study of the crystalline beam [1] and the laser cooling experiments have been carried out since 2007 [2].

The commissioning of the electron cooling was started from October 2005. The 7 MeV proton beam from the linac was used and the first cooling was observed on October 31. The proton and electron beam current were 50 μA and 60 mA, respectively. The initial momentum spread of 4×10^{-3} was reduced to 2×10^{-4} after the cooling. The initial beam size of 26 mm was reduced to 1.2 mm.

In 2006 and 2007, the following experiments have been carried out using the electron cooling:

- Development of the induction accelerator sweep cooling for the hot ion beam with large momentum spread [3].
- Short pulse generation using the electron cooling and the RF phase rotation [4].
- Study of the coherent instability of the electron cooled proton beam with high intensity and the damping by the feedback system [5].
- One-dimensional ordering experiments of electron cooled protons [6, 7].

In this paper, the electron cooler at S-LSR is introduced at first. Figure 1 shows the cross-sectional view of the electron cooler and table 1 shows the main parameters of S-LSR and the electron cooler. Then, the results of the one-dimensional ordering of protons are mainly reported.

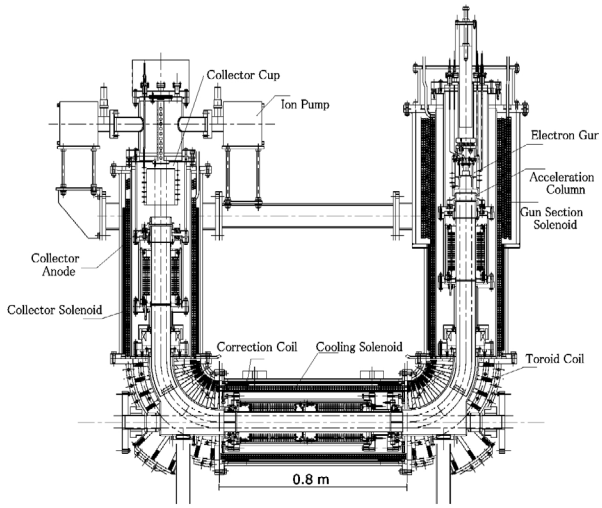

Figure 1: Cross-sectional view of the electron cooler at S-LSR.

Table 1: Main parameters of S-LSR and the electron cooler.

Ring	
Circumference	22.557 m
Length of Drift Space	1.86 m
Number of Periods	6
Average Vacuum Pressure	1×10^{-8} Pa
Electron Cooler	
Maximum Electron Energy	5 keV
Electron Beam Current	25 mA - 300 mA
Beam Diameter	50 mm
Solenoid Field in the central	500 Gauss
Expansion Factor	3
Cooler Solenoid Length	800 mm
Effective Cooling Length	440 mm

#shirai@kyticr.kuicr.kyoto-u.ac.jp

ELECTRON COOLER

The design issues of the electron cooler at S-LSR were a high cooling force and a compactness in order to install the short drift space (1.86 m). The following design methods and devices were adopted:

- Precise three-dimensional magnetic field simulation of the whole system of the cooler using TOSCA [8].
- High perveance electron gun. The typical perveance is 2.3 μP [8].
- Small toroid radius (0.25 m) and the elliptical vacuum chamber in the central solenoid for the compactness of the toroid section.
- Six vertical correction coils in the central solenoid in order to extend the effective cooling length.
- Electrostatic deflectors in the toroid coils in order to compensate the drift motion of the electron beam [9].

Using the vertical correction coils, the effective length of the cooling section becomes 440 mm, while the lengths of the cooler solenoid and the overall electron cooler are 0.80 m and 1.63 m, respectively. The electrostatic deflectors reduce a secondary electron loss. Figure 2 shows the electron loss rate and the maximum cooling force with various deflector voltages in the toroid. The cooling force was measured by the induction accelerator. When the deflector voltage was changed, the dipole magnetic field in the toroid was also changed to keep the electron orbit constant. When the voltage was 1.25 kV, there was no dipole magnetic field for the compensation. The loss rate is reduced with the deflectors, while the cooling force is almost constant. It shows that the electron temperature gets no effect from the electrostatic potential. The small change of the cooling force was induced by the vertical closed orbit distortion due to the dipole magnetic field in the toroid.

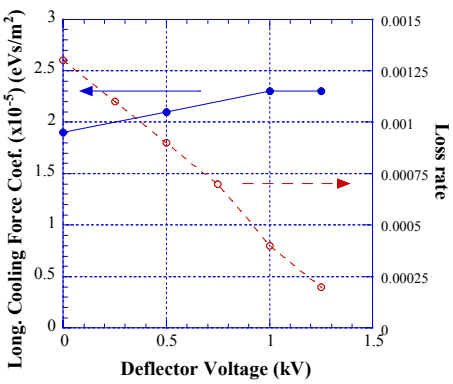

Figure 2: Longitudinal cooling force coefficient in the linear region and the electron loss rate with various deflector voltages with the electron current of 107mA.

The systematic cooling force measurements have been carried out to evaluate the cooler. The ion is 7 MeV proton and the induction accelerator is used. Figure 3(a) shows the cooling force at the electron current of 25, 50 and 100 mA. The cooling forces have maximum values at the relative velocity of around 4000 m/sec. It shows that the electron temperature is almost constant between 25 mA and 100 mA. Figure 3(b) shows the electron current dependence of the maximum longitudinal cooling force. The cooling force is proportional to the electron current.

Figure 4 shows the comparison between the measured longitudinal cooling force and the cooling force model at the electron current of 100 mA. The electron temperature is assumed to be 40 μeV in the models. The measured one is different by a factor of 10 from the magnetized and non-magnetized cooling models. It is about two times smaller than the Parkhomchuk's formula [10].

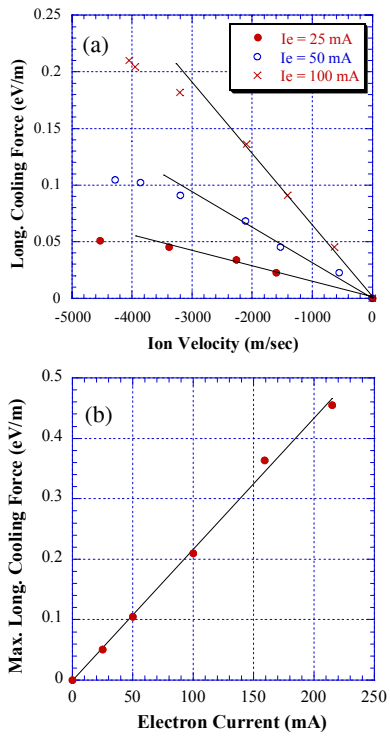

Figure 3 (a): Longitudinal cooling force with the electron current of 25, 50 and 100 mA (2.2, 4.4 and 8.8x10^6 e$^-$/cm^3) as a function of the relative ion velocity. (b): Electron current dependence of the maximum longitudinal cooling force.

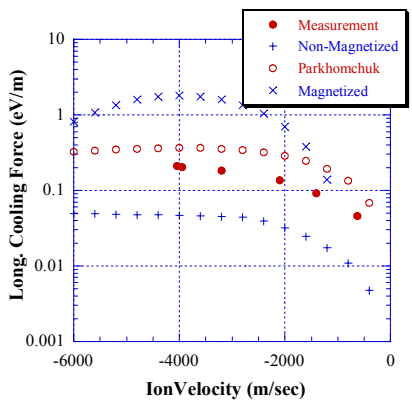

Figure 4: Comparison between the measured longitudinal cooling force and the cooling force models, such as non-magnetized, Parkhomchuk and magnetized cooling model. The electron current is 100 mA (8.8x10^6 e$^-$/cm^3).

ONE-DIMENSIONAL ORDERING FOR PROTONS

The ion ordering by the electron cooling was reported at NAP-M [11] and the abrupt jump of the momentum spread was found at ESR for highly charged heavy ions [12]. The similar jump of the momentum spread was also confirmed at CRYRING for other heavy ions [13]. However, the jump of the momentum spread has not been found for protons. The parameters of the one-dimensional ordering experiments for protons at S-LSR are shown in Table 2.

Table 2: Parameters of the one-dimensional ordering experiments for protons.

Beam	Proton, 7 MeV
Revolution frequency	1.61 MHz
Lifetime with cooling	1.7 x 10^4 sec
Ring	
Betatron tune	(1.645, 1.206)
Max. β-function	(3.9 m, 3.2 m)
Max. dispersion	1.8 m
Electron Cooler	
Energy	3.8 keV
Beam Current	25, 50, 100 mA
Expansion Factor	3

Experimental Setup

In the one-dimensional ordering experiment, a momentum spread and an emittance of the cooled beam were measured as a function of a particle number. Since the typical particle number at the ordering transition was expected to be some thousands, special beam diagnostics were necessary for such very low intensity, especially for singly charged protons.

The particle number was measured by the two independent methods. One is an ionization residual gas monitor and the other is a bunch signal monitor. The results of the two methods agree within 10 % from 10^8 to 500 protons. The momentum spread was measured from the frequency spread of the Schottky noise spectrum. A helical pickup was used for the measurement, which had been developed for the storage ring, TARN at INS, Tokyo University [14]. Figure 5 shows the schematic view of the electrode. It is a travelling-wave type electrode and the phase velocity of the electric signal coincides with the ion velocity (7 MeV proton).

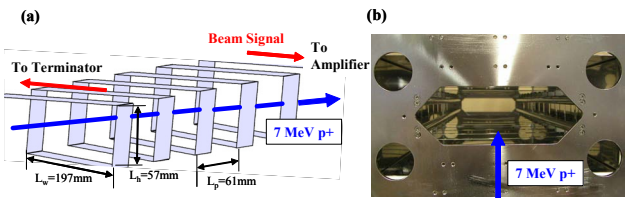

Figure 5 (a): Schematic view of the helical electrode. (b): Photo of the helical pickup.

The beam radius was measured by a beam scraper. At first, the protons of 10^8 was injected and cooled. The typical beam diameter was around 1 mm. The scraper was moved into the circulating beam and stopped at a certain position for 0.1 second, and then removed back away. It killed a part of the beam and reduced the particle number. The rms beam radius σ was determined from the distance L between the scraper position and the beam centre. The ratio between L and σ was calculated by the beam simulation using BETACOOL code [15] and it was found to be 3.5.

Momentum Spread Measurement

Figure 6(a) shows momentum spreads of the protons as a function of the particle numbers in the ring. The electron current was 25 mA, 50 mA and 100 mA. The momentum spread is defined as 1σ of the fitted Gaussian function to the momentum distribution. The momentum spread is proportional to $N^{0.29}$ above a particle number of 4000. At the particle number of around 2000, the momentum spread drops abruptly. The transition momentum spread at the electron current of 25 mA is 3.5×10^{-6}, which corresponds to the ion temperature of 0.17 meV. It is considered that this abrupt drop is evidence of ordering of the protons. The lowest momentum spread below the transition is 1.4×10^{-6}, which corresponds to the longitudinal ion temperature of 26 μeV (0.3 K). It is close to the longitudinal electron temperature.

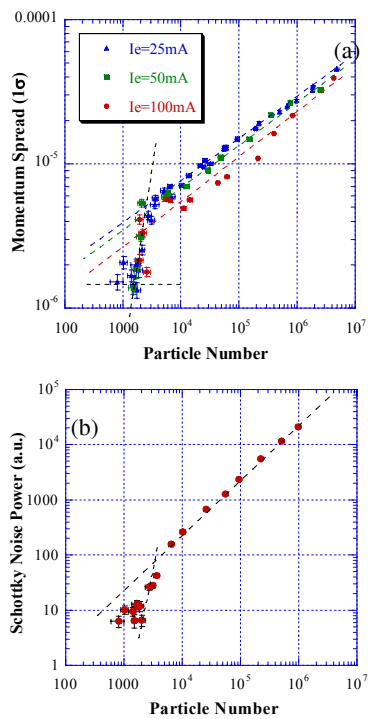

Figure 6(a): Momentum spread as a function of the particle numbers with three different electron currents, 25 mA, 50 mA and 100 mA. (b): Schottky noise power as a function of a particle numbers with electron current of 25 mA. The Schottky noise power is defined as the integrated area of the spectrum [6].

Figure 6(b) shows the Schottky noise power as a function of the particle number with an electron current of 25 mA. It is proportional to $N^{0.99}$ above a particle number of 6000. At the transition point, it drops by one order of magnitude. Similar phenomena have been observed for highly charged heavy ions at CRYRING [13].

Transverse Beam Size Measurement

The transverse beam temperature can be estimated from the beam size measurements. Figure 7 shows the measured horizontal beam size as a function of the particle numbers. The beam size was measured by the ionization residual gas monitor and the beam scraper. The electron current of the cooler was 25 mA. The beam radius is proportional to $N^{0.28}$, and monotonically decreased. The beam radius is 17 μm at a particle number of 4000, which is the transition point of the momentum spread. It is impossible to determine whether there is an abrupt jump of the beam size, because of the insufficient resolution of the scraper. The corresponding horizontal emittance is $1.7\text{x}10^{-4}$ π.mm.mrad with the β-function of 1.7 m at the scraper. If it is assumed that the horizontal and vertical emittances were equal, the transverse temperature is 1 meV. On the other hand, the transverse electron temperature is 34 meV with the expansion factor of 3. The transverse proton temperature of 1 meV is much smaller than that of the electron. It is the result of the magnetized cooling [16] and the key for the ordering of the proton beam.

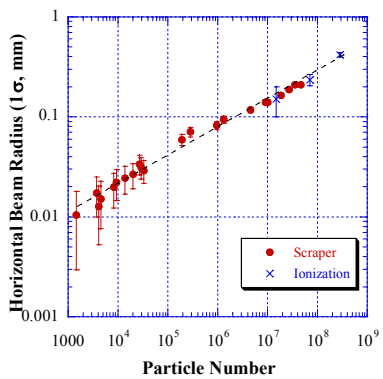

Figure 7: Horizontal beam radius as a function of the particle numbers with electron current of 25 mA. They were measured by the scraper and the ionization residual gas monitor [6].

Heavy ions and Proton

The conditions of the one-dimensional ordering for heavy ions are explained by the reflection probability between two particles [17]. The momentum spread of the heavy ions has a transition at the reflection probability between 60 % and 80 % [18]. In order to compare the heavy ions and proton, the normalized temperature was introduced as the following definition [18],

$$\widehat{T}_{//,\perp} = \frac{2}{m_i c^2}\left(2r_i \beta\gamma \frac{\nu}{R}\right)^{-2/3} k_B T_{//,\perp}, \qquad (1)$$

where m_i is the mass of the ion, r_i is the classical ion radius, βγ is the relativistic factor, ν is the betatron tune and R is the average radius of the ring. Table 3 shows the transition temperatures and normalized ones for the proton at S-LSR [6] and for the heavy ions at ESR [19]. Although the transition temperatures are different by a factor of 1000 between U^{92+} and p^+, the normalized transition temperatures are very close and both have the similar reflection probabilities [6]. It suggests that the transition of the momentum spread occurs by the same mechanism from highly charged heavy ions to proton. It is a general phenomenon for the ion beam. The low transverse ion temperature by the magnetized cooling is the essential condition of the ordering for the light ions, because the transverse transition temperature is usually lower than the transverse electron temperature.

Table 3: Transition temperatures and the normalized temperatures for heavy ions and proton.

Ions	$T_{//}$	$T_{\perp}$	$\widehat{T}_{//}$	$\widehat{T}_{\perp}$
p^+ [6]	0.17 meV	1 meV	1.2	6.5
C^{6+} [19]	4.0 meV	11 meV	0.62	1.6
Zn^{30+}[19]	78 meV	0.64 eV	0.78	7.6
U^{92+} [19]	470 meV	3.4 eV	0.70	5.1

Beam Simulation

The molecular dynamics simulations were carried out for the proton ordering to analyze more precisely. The program code was BETACOOL [15] and the electron cooling was treated as the constant cooling rate, which was calculated from the cooling force measurements. Figure 8(a) shows the trajectories in the cooling process on the phase space of the horizontal emittance and the momentum spread. The particle numbers are 2000 and 6000, respectively. In both cases, the beams are cooled down along the similar trajectories but the beam at the particle number of 6000 stops at the point with the momentum spread of $6\text{x}10^{-6}$. It reaches the equilibrium state, where the electron cooling rate and the IBS heating rate are equal. On the other hand, the momentum spread at the particle number of 2000 decreases monotonically and there is no limit of the lowest momentum spread. The reduction rate of the momentum spread is almost the same as the input cooling rate.

Figure 8(b) shows the final momentum spread obtained by the molecular dynamic simulation with various particle numbers. The measured momentum spread is also shown in the same figure. The momentum spread drops at the particle number of 4000 in the simulation, while it drops between the particle number of 4000 and 2000 in the measurement. The simulation is globally consistent with the measurement.

These simulations suggest that the cooling rate is close to the maximum IBS heating rate with the particle number of 4000. At the particle number of 2000, the cooling rate

exceeds the maximum heating rate. Concerning the transition, the mechanism in the one-dimensional ordering is similar to that of the crystalline beam. This result also explains why the one-dimensional ordering occurs at the very small particle number. Because of the small cooling rate of the electron cooling, it can exceed the IBS heating rate only with the very small particle number. It is different from the crystalline beam simulation by laser cooling. The laser cooling has a high cooling rate and can overcome the intrabeam scattering even with the large particle number.

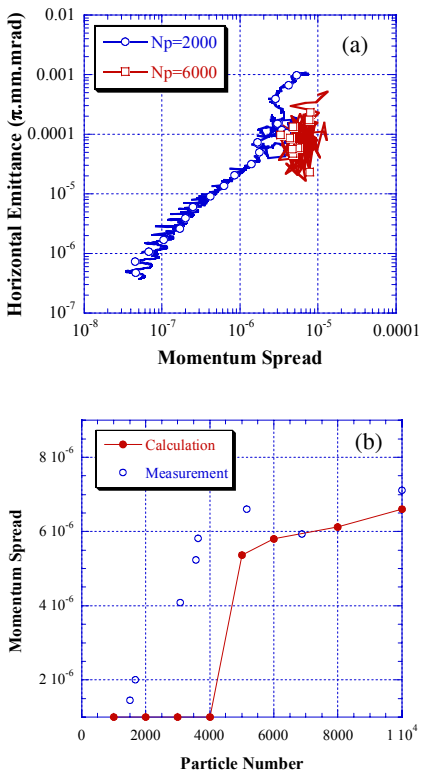

Figure 8(a): Beam trajectories in the cooling process on the phase space of the horizontal emittance and the momentum spread. The particle number is 2000 and 6000. (b): Final momentum spread obtained by the molecular dynamic simulation with various particle numbers. The measured momentum spread is also shown in the figure.

ACKNOWLEDGEMENTS

This work was supported by the Advanced Compact Accelerator Development project by MEXT of the Japanese Government and 21st Century COE at Kyoto University - Diversity and Universality in Physics.

REFERENCES

[1] J. P. Schiffer and P. Kienle, "Could there be an ordered Condensed State in Beams of Fully Stripped Heavy Ions", Zeitschrift for Physik A, **321** (1985) p.181.

[2] A. Noda et al., "Present Status and Recent Activity on Laser Cooling at S-LSR", in Proceedings of this workshop.

[3] H. Fadil et al., "Electron Beam Cooling Experiments at S-LSR", HIMAC Report-111 (2006).

[4] T. Fujimoto et al., "Fast extraction of the short bunched proton beam for investigation of free radicals behaviour", to be submitted to Jpn. J. Appl. Phys.

[5] S. Fujimoto et al., "Feedback Damping of a Coherent Instability at Small-Laser Equipped Storage Ring, S-LSR", Jpn. J. Appl. Phys., **45** (2006) p.1307.

[6] T. Shirai et al., "One dimensional beam ordering of protons in a storage ring", Phys. Rev. Lett., **98** (2007) 204801.

[7] A. Smirnov et al., "Necessary Condition for Beam Ordering", in Proceedings of this workshop.

[8] H. Fadil et al., "Design of a compact electron cooler for the S-LSR", Nucl. Instrum. Methods Phys. Res. Sect. A, **532** (2004) p.446.

[9] V. V. Parkhomchuk, "Development of a New Generation of Coolers with a Hollow Electron Beam and Electrostatic Bending", Proc. of COOL05, Galena (2005) p.249.

[10] V. V. Parkhomchuk, "New insights in the theory of electron cooling", Nucl. Instrum. Methods Phys. Res. Sect. A, **441** (2000) p.9.

[11] V. V. Parkhomchuk, "Physics of Fast Electron Cooling", Proc. of ECOOL84, Karlsruhe (1984) p.71.

[12] M. Steck et al., "Anomalous Temperature Reduction of Electron-Cooled Heavy Ion Beams in the Storage Ring ESR", Phys. Rev. Lett., **77** (1996) p.3803.

[13] H. Danared et al., "Model and Observations of Schottky-Noise Suppression in a Cold Heavy-Ion Beam", Phys. Rev. Lett., **88** (2002) 174801.

[14] H. Yonehara et al., "Equipments For Momentum Cooling at TARN", INS Report No. INS-NUMA-49, (1983).

[15] I. Meshkov et al., "Physics guide of BETACOOL code Version 1.1", BNL Note C-A/AP/262 (2006).

[16] Ya. S. Derbenev and A. N. Skrinsky, "The Physics of Electron Cooling", Physics Reviews (Soviet Scientific Reviews), **3** (1981) p.165.

[17] R. W. Hasse, "Theoretical Verification of Coulomb Order of Ions in a Storage Ring", Phys. Rev. Lett., **83** (1999) p.3430.

[18] H. Okamoto et al., "One-dimensional Ordering of Ultra-Low-Density Ion Beams in a Storage Ring", Phys. Rev. E, **69** (2004) 066504.

[19] M. Steck et al., "Electron cooling experiments at the ESR", Nucl. Instrum. Methods Phys. Res. Sect. A, **532** (2004) p.357.

PROGRESS WITH TEVATRON ELECTRON LENSES*

Yu. Alexahin, V. Kamerdzhiev#, G. Kuznetsov, G. Saewert, V. Shiltsev, A. Valishev, X.L. Zhang,
FNAL, Batavia, IL 60510, U.S.A.

Abstract

The Tevatron Electron Lenses (TELs) were initially proposed for compensation of long-range and head-on beam-beam effects of the antiproton beam at 980 GeV. Recent advances in antiproton production and electron cooling led to a significant increase of antiproton beam brightness. It is now the proton beam that suffers most from the beam-beam effects. Discussed are the motivation for beam-beam compensation, the concept of Electron Lenses and commissioning of the second TEL in 2006. The latest experimental results obtained during studies with high energy proton beam are presented along with the LIFETRAC simulation results.

MOTIVATION

The luminosity of storage ring colliders is limited by the effects of electromagnetic (EM) interaction of one beam with another which leads to a blowup of beam sizes, a reduction of beam intensities and unacceptable background rates in HEP detectors. This beam-beam interaction is described by a beam-beam parameter $\xi \equiv r_0 N/4\pi\varepsilon$, where $r_0 = e^2/mc^2$ denotes the particle's classical radius, N is the number of particles in the opposing bunch and ε is its rms normalized emittance. This dimensionless parameter is equal to the tune shift of the core particles caused by beam-beam forces. While the core particles undergo a significant tune shift, halo particles with large oscillation amplitudes experience negligible tune shift. The EM forces drive nonlinear resonances which can result in instability of particle motion and loss. The beam-beam limit in modern hadron colliders is $\xi^{max} \cdot N_{IP} \approx 0.01$ - 0.02 (N_{IP} is the number of IPs), while it can exceed $\xi^{max} \cdot N_{IP} \approx 0.1$ in high energy electron-positron colliders [1].

Operation with a greater number of bunches allows a proportional increase of luminosity but requires careful spatial separation of two beams everywhere except at the main IPs. Long-range EM interaction of separated beams is also nonlinear and also limits the collider performance. These long-range effects usually vary from bunch to bunch, making their treatment even more difficult.

One of the most detrimental effects of the beam-beam interaction in the Tevatron is the significant loss rate of protons due to their interaction with the antiproton bunches in the main IPs (B0 and D0) and due to numerous long-range interactions [2]. The effect is especially large at the beginning of HEP stores when the positive proton tune shift due to focusing by antiprotons at the main IPs can reach $2\xi^p = 0.016$. Figure 1 shows a typical bunch-to-bunch distribution of proton loss rates at the beginning of an HEP store.

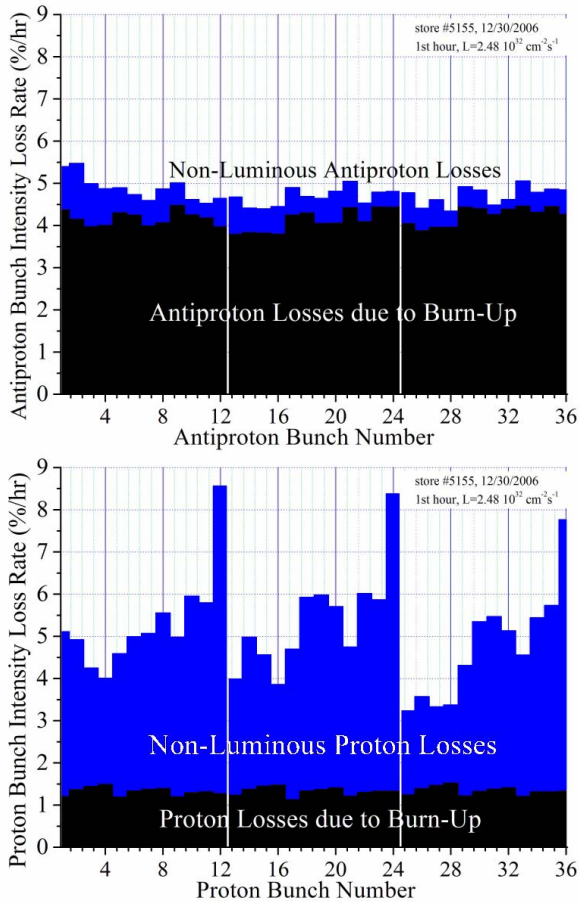

Figure 1: Proton bunch intensity loss rates at the beginning of store #5155.

In the Tevatron, 36 bunches in each beam are arranged in 3 trains of 12 bunches separated by 2.6 μs long abort gaps. Proton bunches P12, P24, and P36 at the end of each bunch train typically lose about 9 % of their intensity per hour while other bunches lose only (4-6) %/hr. In the beginning of high luminosity stores these losses are a very significant part of the total luminosity decay rate of about 20 % per hour. The losses due to burn-up at the two main IPs are much smaller (1.1–1.5%/hr). Figure 1 shows large bunch-to-bunch variations in the beam-beam induced proton losses within each bunch train but similar rates for equivalent bunches in different trains, e.g. P12, P24, and P36. Figure 2 shows the vertical proton bunch-by-bunch tunes about six hours into a store. Proton bunches at the end of each train have the lowest vertical tune due to the missing long-range collisions in the proximity of the main IPs.

*Work supported by the U.S. Department of Energy under contract No. DE-AC02-07CH11359.
#vsevolod@fnal.gov

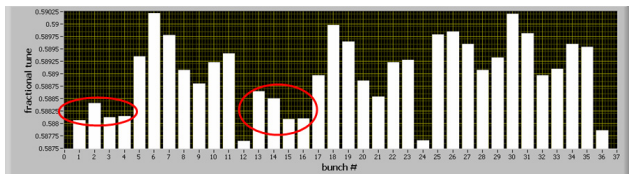

Figure 2: Vertical proton bunch-by-bunch tunes 6 hrs into store #5592 measured by the Digital Tune Monitor. Circled are the proton bunches affected by the four missing antiproton bunches. Full scale: 0.5875 – 0.59025.

This translates in the highest loss rates for this proton bunches (see Figure 1). Due to injection problems, the antiproton bunches A25-A28 were lost, so in store #5592 36 proton bunches collided with only 32 antiproton bunches. Proton bunches missing collisions (head-on and long-range) at one IP had lower tunes (circled red).

ELECTRON LENSES

Electron lenses were proposed for compensation of both long-range and head-on beam-beam effects in the Tevatron collider [3]. The lens employs a low energy $\beta_e = v/c << 1$ electron beam whose space charge forces act on the high-energy hadron beam. These forces are linear at distances smaller than the characteristic beam radius $r < a_e$ but scale as $1/r$ for $r > a_e$. Correspondingly, such a lens can be used for linear and nonlinear beam-beam compensation depending on the beam-size ratio a_e/σ and the current density distribution $j_e(r)$. Main advantages of beam-beam compensation by the electron lenses are: a) the electron beam acts on high-energy beams only through EM forces (no nuclear interaction), eliminating radiation issues; b) unused electrons interact with the high-energy particles each turn, leaving no possibility for coherent instabilities; c) the electron current profile can be optimized for different applications; d) the electron current can be adjusted for individual bunches, equalizing the bunch-to-bunch differences and optimizing the performance of all of the bunches in multi-bunch colliders.

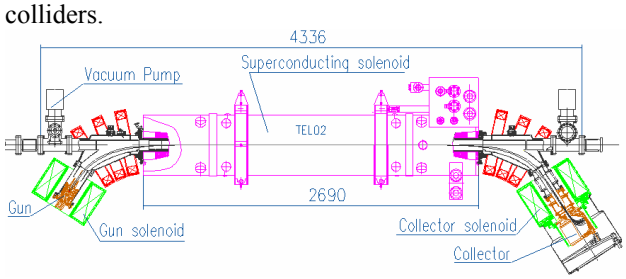

Figure 3: TEL2 layout.

Two Tevatron Electron Lenses (TELs) were built and installed at two locations of the Tevatron ring, A11 and F48. Figure 3 shows the layout of TEL2 [4]. Relevant parameters of the Tevatron and the TELs are given in Table 1.

In order to keep the electron beam straight and its distribution unaffected by its own space-charge and the EM fields of the circulating beam, the electron beam is immersed in a strong magnetic field. The conventional solenoids generate up to 4.5 kG in the electron gun and collector regions, while the superconducting (SC) one generates up to 65 kG in the interaction region. The deviations of the magnetic field lines from a straight line are less than ±100 μm over the entire length of the SC solenoid. Therefore the electron beam, following the field lines, does not deviate from the straight Tevatron beam trajectory by more than 20% of the Tevatron beam rms size $\sigma \approx 0.5$ mm at the TEL locations.

The electron beam's transverse alignment on the proton or antiproton bunches (within 0.2–0.5 mm all along the interaction length) is crucial for successful BBC. The electron beam steering is done by adjusting currents in the SC dipole correctors installed inside the main solenoid cryostat. It is also important that the transverse electron current distribution utilizes wide flat top and smooth radial edges.

The high-energy protons are focused by the TEL and experience a positive betatron tune shift given by [3]:

$$dQ_{x,y} = +\frac{\beta_{x,y} L_e r_p}{2\gamma e c} \cdot j_e \cdot \left(\frac{1-\beta_e}{\beta_e}\right) \qquad (1)$$

Table 1: Electron Lens and Tevatron collider parameters.

Parameter	Symbol	Value	Unit
Tevatron Electron Lens			
Electron energy (oper./max)	U_e,	5/10	kV
Peak electron current (oper./max)	J_e	0.6/3	A
Magnetic field in main/gun solenoid	B_{main} B_{gun}	30 3	kG
Radii: cathode/*e*-beam in main solenoid	a_c a_e	7.5 2.3	mm
e-pulse period/width, "0-to-0"	T_0 T_e	21 ≈0.6	μs
Interaction length	L_e	2.0	m
Tevatron Collider Parameters			
Circumference	C	6.28	km
Proton/antiproton beam energy	E	980	GeV
Proton bunch intensity	N_p	250	10^9
Antiproton bunch intensity	N_a	50-100	10^9
Emittance proton, antiprot. (norm., rms)	ε_p ε_a	≈2.8 ≈1.4	μm
Number of bunches, bunch spacing	N_B T_b	36 396	ns
Initial luminosity	L_0	1.5-2.9	10^{32} cm^{-2}s^{-1}
Beta functions, TEL2	β_y/β_x	150/68	m
Beta functions, TEL1	β_y/β_x	29/104	m
Proton/antiproton head-on tuneshift	ξ^p ξ^a	≈0.008 ≈0.011	max., per IP
Proton/antiproton long-range tuneshift	ΔQ^p ΔQ^a	≈0.003 ≈0.006	max.

Electron Gun

A charge density distribution required for tune shift compensation is generated by the electron gun utilizing a convex dispenser cathode and optimized electrode

geometry [5]. The convex cathode shape allows for high perveance (≈ 4.2 μP) even at high electron currents.

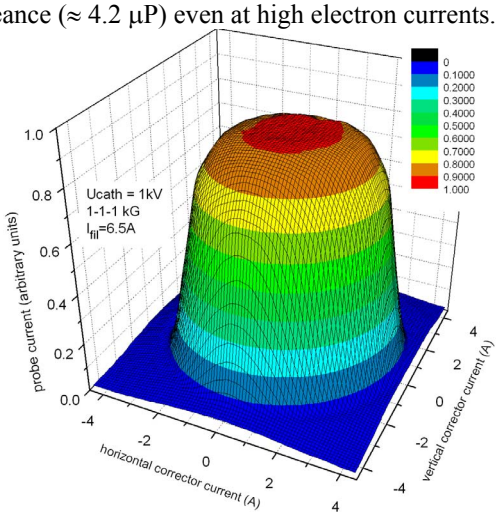

Figure 4: 2D charge density distribution generated by the SEFT (smooth edge flat top) electron gun.

The electron beam profile shown in Figure 4 was measured on the test bench by recording the electron current passing through a 0.2 mm hole while scanning the beam over the hole using the corrector coils [5]. The TEL magnetic system compresses the electron-beam cross-section area in the interaction region by the factor of $B_{main}/B_{gun} \approx 10$ (variable from 2 to 30), proportionally increasing the current density of the electron beam in the interaction region. Most recent experiments have not required more than 0.6 A of electron current, however tests with up to 3.0 A have been performed.

Electron Gun Drivers

To make compensation of individual bunches separated by 396 ns possible, the anode voltage, and consequently the electron beam current, are modulated with 500-600 ns pulses and a repetition rate equal to the Tevatron revolution frequency of $f_0 = 47.7$ kHz by using a newly developed Marx generator [6] or a HV RF tube based modulator [7].

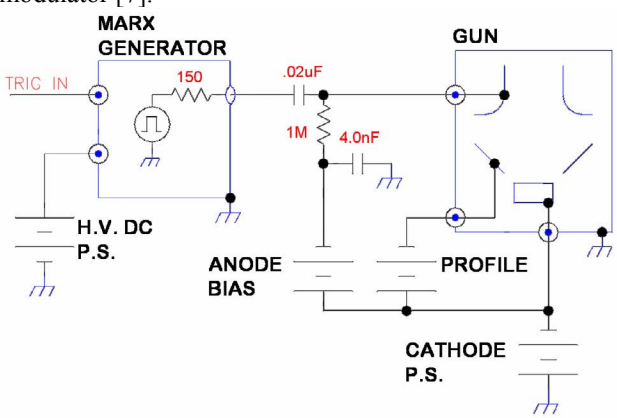

Figure 5: A schematic representation of the electron gun driving circuit.

Figure 5 shows the electron gun driving circuitry. In order to insure the shortest possible pulse rise and fall times the driver was installed in the Tevatron tunnel close to the electron gun [8]. All the dc power supplies, however are located outside the tunnel.

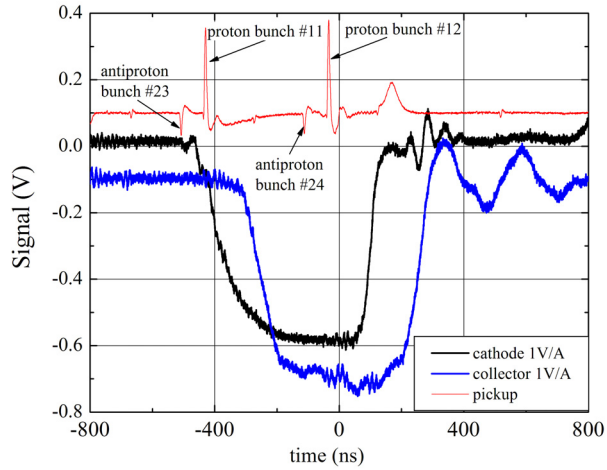

Figure 6: TEL2 timing for P12 compensation.

Figure 6 shows how the TEL2 timing is set up for single bunch compensation. Plotted are electron current leaving the cathode and the one arriving at the collector, measured by the current transformers, and a pickup signal. The capacitive pickup reports proton, antiproton and electron signals. Only proton bunch P12 was affected by the TEL during this experiment. The electron pulse timing jitter is less than 1 ns and the peak current is stable to better than 1%, so, the TEL operation does not cause any measureable emittance growth.

An improved Marx generator capable of driving the electron gun at repetition rates up to 150 kHz and a high voltage modulator utilizing a summed pulse transformer scheme [9] are being built. The latter is designed to add all-bunch compensation capabilities to the TELs.

EXPERIMENTAL RESULTS

Preliminary alignment of the electron beam was done by relying on the TEL beam position measurement system. However, additional fine tuning was necessary to achieve best possible compensation. Measurements of the proton loss rate versus electron beam position at increased electron current were performed at the very end of a store, when no beam-beam related losses occur. This approach allowed to determine the optimal electron beam position. Since the Tevatron orbit is kept stable by the orbit feedback system within 100 μm the end-of-store values can be used throughout other stores, unless an optics change is introduced.

The tune shift is about the same for most protons in the bunch since $a_e \approx 3\sigma$. Figure 7 shows the results of the vertical tune shift measurement of 980 GeV protons versus TEL2 electron current which are in good agreement with Equation 1 for the parameters summarized in Table 1– see solid line.

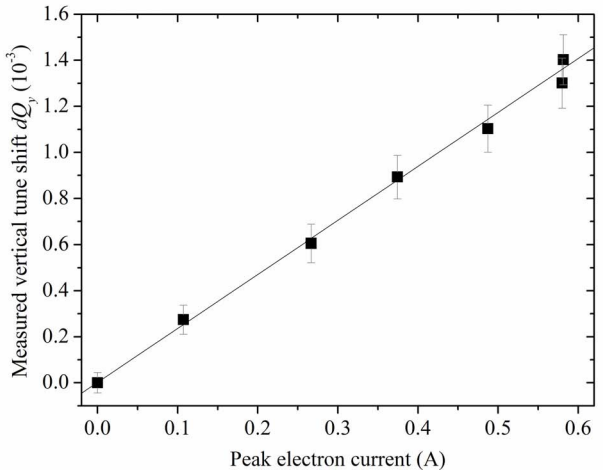

Figure 7: Vertical tune shift vs TEL2 electron current.

The beam-beam compensation studies were performed in the beginning of stores. As soon as TEL2 electron current was turned on (affecting P12 only) a significant change of slope of P12 intensity decay was observed (see Figure 8). This change corresponds to a lifetime improvement of about 100%. This result has been confirmed in several beam studies.

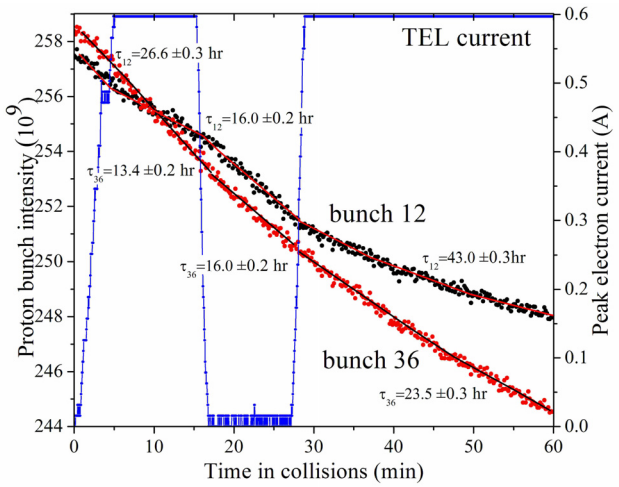

Figure 8: Dependence of the proton intensity decay rate on TEL2 peak electron current.

Another way to look at the same phenomena is to measure the effect of the TEL on the proton loss rate. Both HEP experiments D0 and CDF routinely measure loss rates (halos) around their detectors on a bunch-by-bunch basis. Figure 9 shows the dependence of D0 proton loss rate on TEL1 electron current. In this experiment TEL1, being a horizontal beam-beam compensation device, was acting on P13 which has the lowest horizontal tune. P14 was chosen as a reference bunch because its behavior in terms of halo and lifetime was very similar to P13. The loss rate of P13 dropped by about 35% once the electron current was turned on, while P14 loss rate stayed unaffected (TEL1 is not acting on P14). The P13 loss rate actually became smaller before the final e-current value (0.6 A peak, 19mA AVG) was reached. After about 12 min the e-current was turned off which made P13 loss rate return to the reference level. This result has been confirmed in several beam studies.

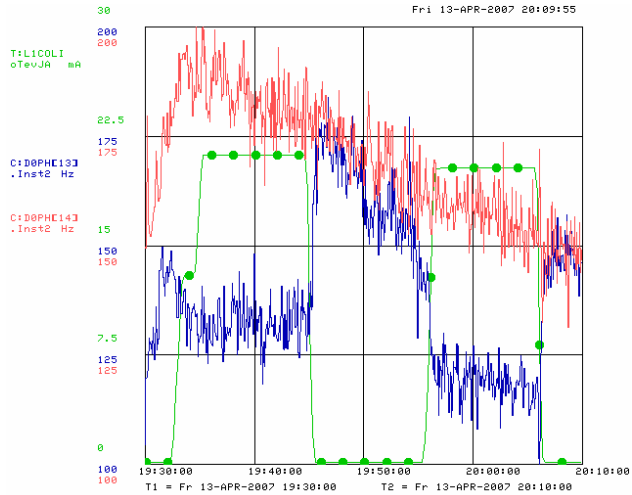

Figure 9: Dependence of proton loss rate of P13 (C:D0PH[13]) and P14 (C:D0PH[13]) on TEL1 average electron current (T:L1COLI).

The effect of the TEL2 and TEL1 improving the proton intensity lifetime, can be explained by a positive tune shift introduced by the TEL (see Figure 7) pushing the tune away from the 12th order resonance. However, it is not yet clear whether it is the only mechanism responsible for the significant lifetime improvement.

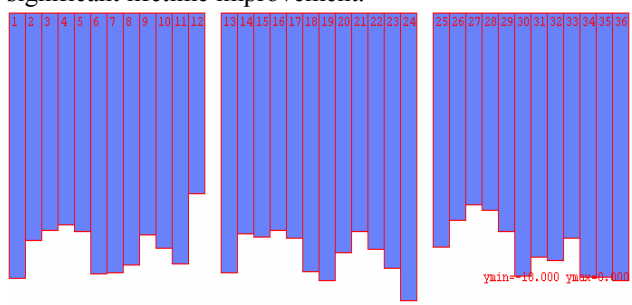

Figure 10: Lost bunch intensity as reported by T:SBDPIS for the first 1.5 hours of a store. TEL2 was acting on P12, $J_e = 0.3$ A. Scale:-18·10^9 – 0 protons.

Furthermore, another beam study with TEL2 at $J_e = 0.3$ A on P12 showed that this bunch experienced the smallest intensity loss as compared to any other proton bunch (see Figure 10). The tune shift caused by such a moderate electron current is not sufficient for P12 to reach the average tune value. Nevertheless, P12 had the best lifetime among all proton bunches. This single result is not fully understood yet.

LIFETRAC SIMULATION

To simulate the effect of the TEL on dynamics of the proton beam we used the weak-strong code LIFETRAC [10] which has been extensively used to study beam-beam effects in the Tevatron [11]. This is a multi-particle simulation code where a single bunch of particles is tracked through a sequence of maps and points of beam-beam interaction reproducing the real pattern of collisions

in the machine. The code takes full advantage of the current knowledge of the Tevatron optics by using the measured beta-functions and helical orbits in order to compute the transfer maps for tracking particles between the IPs and to calculate the beam-beam kick.

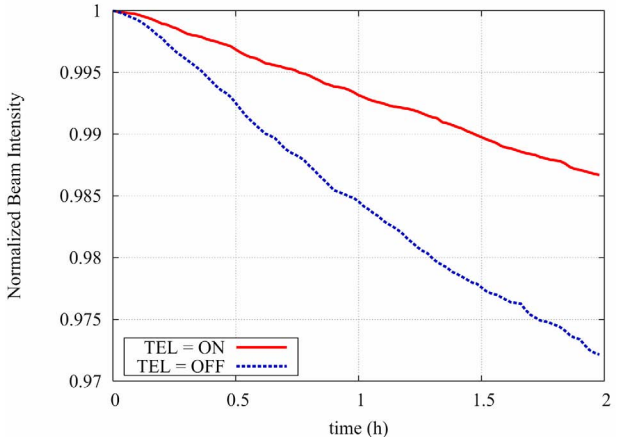

Figure 11: Normalized proton beam intensity, first two hours of an HEP store, simulated with LIFETRAC code.

In the simulation, the TEL was represented by a thin kick generated by the electron beam with the transverse density distribution described by the formula

$$\rho(r) = \rho_0 \left(1 + \left(r / r_0\right)^8\right)^{-1} \qquad (2)$$

Particle diffusion in the Tevatron is dominated by the intrabeam scattering which however may be enhanced significantly by the beam-beam effects, especially when the betatron tune is close to strong resonances. Still, the strength of the random noise can be used to set the time scale for tracking simulations. With the present computing capacity it is possible to track a bunch of 10,000 macro particles for up to 10^6 turns. With the real Tevatron revolution frequency this corresponds to roughly 2 minutes. By artificially increasing the IBS diffusion rate we are stretching this time to about 2 hours. Hence, calculating the number of particles lost from the beam during the time of simulation can be used to estimate the non-luminous beam lifetime. Although this method does not give a very accurate absolute result it is quite effective for relative comparison of various conditions. This approach has been applied to the beam-beam compensation with the TELs. Figure 11 shows the evolution of intensity of a single proton bunch with and without the TELs acting on it.

The simulation shows that the TELs improve non-luminous proton lifetime by about a factor of 2. The TELs push the betatron tunes away from the 12^{th} order resonance thus improving the beam lifetime.

SUMMARY

The Tevatron Electron Lenses equipped with SEFT electron guns were operated in pulsed mode to perform single bunch beam-beam compensation. Significant proton intensity lifetime improvement achieved in numerous beam studies is consistent with computer simulations carried out using weak-strong code LIFETRAC. However, a single result indicating that TEL2 made the lifetime of a proton bunch it was acting on better than the lifetime of any other proton bunch is not fully understood yet. BBC with dc electron beam using TEL2 has been performed as well with positive results, however they were not treated in this paper. The high voltage pulse generators being built are expected to add multi-bunch compensation capabilities to the TELs. Preparations for the beam studies using the electron gun with Gaussian charge density distribution are underway.

ACKNOWLEDGEMENTS

The authors would like to thank B. Fellenz, R. Hively, A. Klebaner, S. Kozub, M. Kufer, A. Martinez, N. Mokhov, M. Olson, H. Pfeffer, V. Scarpine, A. Semenov, D. Shatilov, A. Shemyakin, N. Solyak, V. Sytnik, M. Tiunov, L. Tkachenko, D. Wildman and D. Wolff for their contribution to the project.

REFERENCES

[1] W.Fischer and T.Sen, Beam-Beam'03 Summary, HALO'03 Workshop, New York, 2003.
[2] V.Shiltsev et al., Beam-beam effects in the Tevatron, Phys. Rev. ST Accel. Beams 8, 101001 (2005).
[3] V.Shiltsev et al., Considerations on compensation of beam-beam effects in the Tevatron with electron beams, Phys. Rev. ST Accel. Beams 2, 071001 (1999).
[4] V. Kamerdzhiev et al, Commissioning of the second Tevatron Electron Lens and beam study results, PAC'07, Albuquerque, July 2007.
[5] V. Kamerdzhiev et al., Electron beam generation in Tevatron electron lenses, AAC'06, New York, 2006.
[6] R. Cassel, A new type high voltage fast rise/fall time solid state Marx pulse modulator, PAC'07, Albuquerque, July 2007.
[7] Y. Terechkine et al, Pulser for the Tevatron electron lens gun, FERMILAB-CONF-04-062-TD.
[8] V. Kamerdzhiev, A solid state Marx generator for TEL2, PAC'07, Albuquerque, July 2007
[9] G. Saewert, TEL Fast High Voltage Modulator Design Proposal, Fermilab TM-2390-AD.
[10] D. Shatilov et al, LIFETRAC Code for the Weak-Strong Simulation of the Beam-Beam Effect in the Tevatron, PAC'05, Knoxville, Tennessee, 2005.
[11] A. Valishev et al, Computational Study of the Beam-Beam Effect in Tevatron using the LIFETRAC Code, PAC'05, Knoxville, Tennessee, 2005.

USE OF AN ELECTRON BEAM FOR STOCHASTIC COOLING*

Y. Derbenev, TJNAF, Newport News, VA 23606, U.S.A.

Abstract

Microwave instability of an electron beam can be used for a multiple increase in the collective response for the perturbation caused by a particle of a co-moving ion beam, i.e. for enhancement of friction force in electron cooling method. The low scale (hundreds GHz and higher frequency range) space charge or FEL type instabilities can be produced (depending on conditions) by introducing an alternating magnetic field along the electron beam path. Beams' optics and noise conditioning for obtaining a maximal cooling effect and related limitations will be discussed. The method promises to increase by a few orders of magnitude the cooling rate for heavy particle beams with a large emittance for a wide energy range with respect to either electron and conventional stochastic cooling.

INTRODUCTION

The high-energy cooling plays a critical role in raising the efficiency of existing and future projects of hadron and lepton-hadron colliders: RHIC with heavy ion and polarized proton-proton colliding beams [1] and electron-ion collider eRHIC [2,3] of Brookhaven National Laboratory; ELIC [2,4] of Jefferson Laboratory; the proton-antiproton collider of Fermilab; and, perhaps, even the LHC of CERN.

Electron cooling proved to be very efficient method of cooling intense hadron- and ion-beams at low and medium energies [5]. The electron cooler of 9 GeV antiprotons in the Fermilab recycler represents state-of-the-art technology [6] and already led to significant increase luminosity in the proton-antiproton collider. Development of the ERL-based electron cooler at BNL promises effective cooling of gold ions with energies of 100 GeV per nucleon [7].

Realization of effective cooling in hadron (proton, antiproton) colliders of higher energies requires new conceptual solutions and techniques. Currently, an ERL-based EC scheme is under study which includes a circulator-cooler ring as a way to reduce the necessary electron current delivered by an ERL [8]. It should be noted, that the ERL-based electron cooling should be operated in staged regime (cooling starts at an intermediate energy e.g. injection energy of a collider ring) to be continued in the collider mode after acceleration. Finally, for best performance of a collider an initial transverse stochastic cooling of a coasted beam should precede use of EC [8].

An extremely challenging character of high energy cooling projects for hadron beams quests to search for possible ways to enhance efficiency of existing cooling methods or invent new techniques.

It was noted by earlier works [9], that potential of an electron beam-based cooling techniques may not be exhausted by the classical electron cooling scheme. Namely, the idea of *coherent electron cooling* (CEC) encompasses various possibilities of using collective instabilities in the electron beam to enhance the effectiveness of interaction between hadrons and electrons. CEC combines the advantages of two existing methods, electron cooling (microscopic scale of interaction between ion beam and cooling media, the electron beam) and stochastic cooling (amplification of media response to ions). It is based on use of a co-transported electron beam in three roles – a receiver, amplifier and kicker. Such principle seems flexible for implementation in hadron facilities of various applications in a wide energy range from non-relativistic beams to beams in colliders.

Below we will review the CEC principles and limitations referring to earlier works [9] as well as recent work [10] which is specifically devoted to development of CEC system for colliding beams by use of SASE FEL as amplifier.

PREREQUISITES OF CEC

A General CEC Idea

The electron cooling-a method of damping the angular and energy spread of the beams of heavy charged particles- is, as known, [11-13] that the beam in the straight section of an orbit is passing through an accompanying electron beam having lower temperature. In this case, heavy particles are decelerated with respect to electron medium similarly to that as is occurred in usual plasma at Ti >Te .

A principle suggested here of an amplification is naturally inserted into logical scheme of the method. On the cooling section such conditions should be arranged that the moving "electron plasma" should become unstable in the given range of the wave lengths. Then, an excitation caused by an input ion will be transferred by electron flux developing exponentially independent of the ion; at the output from electron beam the ion acquires the momentum correlated with its input velocity (Figure 1).

A firm correlation between input and output signals is maintaned unless the excitation reaches the nonlinear regime, i.e. the density modulation within the required scale of distances remains relatively small. It is, of course, necessary to provide the optimum output phase relations in the position, and velocity of an ion with respect to electron "avalanche" produced by the ion. Such a task is facilitated by the motion of ions and electrons in the fields

* Authored by Jefferson Science Associates, LLC under U.S. DOE Contract No. DE-AC05-06OR23177. The U.S. Government retains a non-exclusive, paid-up, irrevocable, world-wide license to publish or reproduce this manuscript for U.S. Government purposes.

given are absolutely different. In particular, after interaction at the "input" the beams can be separated and then can be made interacting again at the "output".

Another important condition is the noise level in electron flux at the input i.e. the electron density fluctuations of which will also be increased is sufficiently small. We will discuss some possibilities to provide this condition.

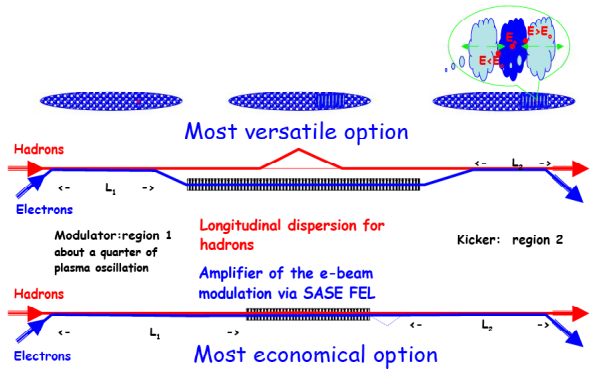

Figure1: Schematic layout of the CEC with three sections: a) A modulator, where the electron beam is polarized (density modulated) by presence of hadrons; b) A gain section, where density modulation in the electron beam is amplified; c) A kicker, where the amplified longitudinal electrostatic field in the electron beam accelerates or decelerates hadrons. [10]

Polarization of Plasma by a Fast Ion

Under condition that the spread of electron velocities is small compared to that of the ion beam, we will consider the electron beam as homogeneous, isotropic plasma of density n_e We then derive a hydrodynamic equation (in a co-moving frame) for perturbation of electron density, $\tilde{n}(\vec{r},t)$ by an ion of a charge Ze which arrives in the beam at initial moment $t=0$:

$$\ddot{\tilde{n}} + \omega_e^2 \tilde{n} = -Ze\omega_e^2 \delta(\vec{r} - \vec{\upsilon}t) \qquad (1)$$

Here $\omega_e = \sqrt{4\pi n_e e^2/m}$ is plasma oscillation frequency. Solution of this equation with zero initial conditions is as follows:

$$\tilde{n} = -Ze\omega_e \int_0^t \delta(\vec{r} - \vec{\upsilon}\tau)\sin\omega_e(t-\tau)d\tau \qquad (2)$$

We then can find the related electric field:

$$\tilde{\vec{E}} = -Ze\omega_e \int_0^t d\tau \frac{\vec{r} - \vec{\upsilon}\tau}{|\vec{r} - \vec{\upsilon}\tau|^3}\sin\omega_e(t-\tau) \qquad (3)$$

In particular, by taking this field along ion trajectory $\vec{r} = \vec{\upsilon}t$, we immediately obtain the well-known drag force of electron cooling, in this case associated with the collective response of electrons to a fast ion:

$$\vec{F} = -(Ze)^2\omega_e^2 \frac{\vec{\upsilon}}{\upsilon^3}\int_{\tau_{\min}}^t \frac{d\tau}{\tau}\frac{\sin\omega_e\tau}{\omega_e\tau} \qquad (4)$$

with $\tau_{\min}$ here should be equal to r_D/v.

Equations (2) through (4) clearly show the importance of taking into account plasma oscillations in dynamics of the collective electron response to the ion. It also should be noted that the solution (2) and (3) suggest a paradox: an ion does not perturb the electron density anywhere but only along its trajectory – yet creating a non-zero charge along its string wake! Apparently, the paradox is removed by taking into account the plasma boundaries where the excited electric field (3) creates the correspondent surface charge. In other words, one has to explicitly compute the polarization problem for an electron beam of finite transverse sizes. Other important factor will be electron beam non-isotropy connected to a focusing either solenoidal at low energies or quadrupole at high energies. Both these factors, non-isotropy and boundaries, will contribute in appearance of electron space charge perturbation distributed around the ion.

Possible Micro-instabilities of the Electron Beam

Electron polarization and the collective response to an ion could be increased proportionally to the number of electrons in the interaction region if the initial excitations could increase spontaneously. For this, the electron plasma should be able to self-bunching, i.e. should be unstable in the region of the wave-lengths exceeding the electron Debye distance $r_D = \Delta v_e/\omega_e$. There exist possibilities for a few different type of this scale microwave instabilities depending on energy and beam transport conditions [9,14].

A. A microwave Coulomb instability that seems easy to realize at low energies is the parametric instability of longitudinal plasmas oscillation of the electron beam; it occurs when plasma parameter of the electron beam ω_e is modulated with the frequency $\omega = 2\omega_e$. Such a modulation can be realized via modulation of electron beam size by varying strength of a solenoid in which the electron beam is immersed (magnetized).

B. The mechanism of instability with the properties required could be precluded if in the cooling section the transverse alternating magnetic field (undulator) of relatively small amplitude is introduced into the longitudinal magnetic field B_s accompanying an electron beam. For the sake of simplicity let us take this transverse field as a helically-variable; in the complex form:

$$B_x + iB_y = \alpha B_u \exp(iz/\lambda\!\!\!^{-}_u)$$

where x and y are transverse coordinates, z is the longitudinal coordinate, B_u and α are respectively the magnitude and angular deviation of a total magnetic field; $\lambda_u = 2\pi\lambda\!\!\!^{-}_u$ is a helical step. If the transverse size of an electron beam is small compared to $\lambda\!\!\!^{-}_u$, one can neglect the transverse inhomogeneity of the magnetic field. The field should be so large that the cyclotron frequency of electrons should significantly be larger than that of a plasma (the suppression condition of the space charge influence or magnetizing):

$$\Omega \equiv \frac{eB_s}{m_e c} >> \omega_e$$

where the frequencies are related to the beam rest frame. For a particle motion in such a field a constant parameter

is an energy in laboratory frame or the total velocity $v=\beta c$, but the transverse and longitudinal velocity dependence of energy may change sign at sufficiently strong magnetic field. Then, instability of the *negative longitudinal mass* is realized in the region

$$\frac{1}{\mu} \equiv \gamma^3 m \frac{d\upsilon_z}{dp_z} = [1 - \frac{(\gamma\beta\theta_u)^2}{\Delta}\frac{\lambda_c}{\lambda_u}]/(1+\frac{\theta_u^2}{\Delta}) < 0$$

$$\Delta \equiv 1 - \frac{2\pi p_z c}{eB\lambda_0} \qquad \theta_u = \frac{\alpha}{\Delta}$$

i.e. when an average velocity becomes a decreasing function of energy because of an increase in the forced transverse velocity. When the resonance $\Delta=0$ is far enough ($\Delta >> \Lambda/\Omega$), one can neglect the transverse mobility of electrons; at this approximation the increment length (in laboratory frame) is given by formula

$$l_\mu = \frac{\gamma}{\sqrt{1+\gamma^2\theta_u^2}}\left|\frac{k\sqrt{\mu}}{k_z\omega_e}\right|$$

where $\vec{k} = (k_z, \vec{k}_\perp)$ is a wave vector of Fourier space harmonics of an excited electric field [9,14].

C. In ultra-relativistic region the mechanism of radiation instability can be effective [9] which is connected to generation of coherent radiation with wave lengths satisfying the following condition:

$$k - k_z v_z \approx k_0 v_z$$

The systems based on this principle acquired the name "free electron lasers" (FEL). The increment length of this instability is equal to (here we use a notation J for electron peak current and notation J_A for *Alfven current* $m_e c^3/e \approx 17kA$) [15,16]:

$$l_g \approx \lambda\!\!\!^{-}_u [\frac{\gamma J_A}{J(1+2\ln\frac{\sigma_{cr}}{\sigma_\perp})}]^{1/2} \tag{5}$$

at $\sigma_\perp << \sqrt{\lambda\!\!\!^{-} l_g}$, while

$$l_g \approx \lambda\!\!\!^{-}_u (\frac{\gamma J_A}{J})^{1/2} (\frac{\sigma_\perp}{\sigma_{cr}})^{2/3} \tag{6}$$

at $\sigma_\perp >> \sqrt{\lambda\!\!\!^{-} l_g}$, where $\sqrt{\lambda\!\!\!^{-} l_g}$ is the *diffraction size* of the *self-amplified spontaneous emission* of FEL [15,16]. By comparison (5) and (6) one can find the critical transverse electron beam size σ_{cr}, at which $\sqrt{\lambda\!\!\!^{-} l_g} \approx \sigma_\perp$ [15]:

$$\sigma_{cr} = \frac{\lambda\!\!\!^{-}_u}{\gamma}(\frac{\gamma J_A}{J})^{1/4}. \tag{7}$$

As exposed above, this parameter separates two different characteristic situations of SASE FEL – so-called cases of thin and wide beams.

BEAM TRANSPORT AND PHASING

An excitation caused by an ion at input will be transported together with electron beam developing exponentially independent of the ion; at the output from electron beam the ion acquire the momentum correlated with its input velocity. A firm correlation is possible unless the excitation reaches the nonlinear regime, i.e. the density modulation within the required scale of distances remains relatively small. It is, of course, necessary to provide the optimum output phase relations in the position, and velocity of an ion with respect to electron "avalanche" produced by the ion. Such a task is facilitated by the motion of ions and electrons in the fields given are absolutely different. In particular, after interaction at the "input" the beams can be separated and then can be made interacting again at the "output".

Compensation for Electron Delay

The gain process of CEC requires introduction of an alternating transverse magnetic field along the amplification section. This causes a decrease of electron translation velocity compared to the velocity of ion beam, hence, may lead to an ion run far away off the developed cloud of electron polarization initiated by the ion.. The picture is simple in case of an electrostatic instability used for the amplification, since in such a case the initiated polarization cloud does not propagate through the electron beam at equal absolute velocities of electron and ion beam ($\gamma_e=\gamma_h$), the related coherent delay of electrons can be compensated by divorcing two beams, and then introducing (or using) bend of the hadron beam, according to the condition

$$\int[\cos\alpha_e(s) - \cos\alpha_h(s)]ds = 0,$$

or

$$< \alpha_e^2 > \approx < \alpha_h^2 >$$

where $\alpha_e(s)$, $\alpha_h e(s)$ are the electron and hadron orbit angle deviation from a straight line connecting the start (end of modulator) and finish (start of kicker) points of the electron bend. Other approach to compensation for a delay may consist of an increase of electron energy while avoiding bend of the hadron beam along straight section with continuous (helical) undulator (which covers all the CEC section), according to equation

$$\gamma_e^{-2} + \alpha_e^2 = \gamma_h^{-2}$$

$$\gamma_e = \gamma_h / \sqrt{1 - \gamma_h^2 \alpha_e^2}$$

For example, $\gamma_e=\gamma_h\sqrt{2}$ at $\theta_u = 1/(\gamma_h\sqrt{2})$. It should be noted that at a condition $\lambda\!\!\!^{-}_u \theta_u < \sigma_\perp$ the effective interaction force of ions with electrons in the modulator and kicker section will not decrease.

At use of SASE process for amplification, one has to take into account that the peak of electron polarization overtakes the translation motion of electrons in an undulator [17], that eases the compensation for electron delay.

An estimate of tolerances on static errors of the compensating field $b(s)$ leads to criterion as follow:

$$\delta s \cong \frac{\delta b}{b} < \alpha^2 > \sqrt{L l_{corr}} < \lambda\!\!\!^{-} \approx \frac{\lambda\!\!\!^{-}_u}{\gamma^2},$$

where L is effective length of section with bending dipoles (including the undulator section), and l_{corr} is the

correlation length of the errors. In case of static errors $\delta s >> \lambdabar$, the residual mismatch can be compensated and controlled by a specific additional low dipole field.

Optimizing the Longitudinal Dispersion of Hadrons

After merging with electron beam in kicker section, an ion with momentum deviation δp from reference particle will have longitudinal displacement determined by the slip-factor α_s:

$$\Delta s \equiv |\alpha_s| L(\Delta p / p) \cong (\sigma_\perp / \gamma)$$

with $\alpha_s=\gamma^{-2}-<KD>$, where K and D are curvature and dispersion along reference orbit of ions.

An Optimal Focusing in Modulator and Kicker

At use of FEL mechanism for amplification of electron response to ions, which is adequate to high energy beams, the effective longitudinal length of polarization signal, $\sigma_\perp / \gamma$, produced by a single ion in the electron beam should not exceed the wave length of the FEL radiation:

$$\lambdabar_u \geq \gamma\sigma_\perp \tag{8}$$

From comparison between this condition and formula (7) for critical beam size associated with SASE's diffraction phenomenon we conclude that conditioning (8) can be realized only in case of "thin beam", when the diffraction size of FEL radiation exceeds the beam transverse size. Such optimization may require design of a low-beta focusing of ions in the modulator and kicker sections

Organizing the Transverse Cooling

Due to that possible gain mechanisms of CEC are naturally associated with the longitudinal interaction forces in electron beam, the excited polarization of electron space charge and related forces are in most longitudinal, as well. This circumstance would make transverse cooling ineffective compared to the longitudinal one, unless one implements a redistribution of cooling decrements. Similarly to re-distribution of the decrements of synchrotron radiation or electron cooling [12], it is possible to re-distribute decrements of CEC within the boundaries of the invariant sum of decrement. An effective method of re-distribution inherent to nature of CEC is proposed in work [10].

LIMITATIONS ON GAIN AND COOLING RATES OF CEC

Gain Limitation Due to Shot-noise of the Electron Beam

Apart from friction the particles will experience the scattering on the electron density fluctuations developing from the initial level at the input. Evaluations show that in the case of an unsuppressed Schottky-noise effect in the input (saturation regime of electron gun current), in this case the gain should not exceed the mass relation, in contrary the diffusion dominates over the friction [9]:

$$G < G_1 \equiv \frac{m_h}{m_e} \tag{9}$$

There are possibilities for suppressing the Schottky-noise [9].

A. It is well known that Schottky-noise is sharply decreased by collective interaction when operation the gun in the so-called "3/2 run". When accelerating electrons up to higher energies the beam (after leaving the "3/2" area) should be accelerated adiabatically in order to reach the further decreasing in the noise level.

B. Principle possibilities for decreasing the Schottky-noise effect exist also at operation of electron gun in saturation run. The idea consists in producing at the gain section input (where starts an exponential development of fluctuations) such phase relations in the noise in order to avoid amplification in the "over-heat" noise level (the heat oscillations cannot have the phase correlations). This appears feasible because of the boundary condition on the cathode for the Schottky-noise is the absence of the group fluctuations for electron velocities. This possibility is limited by the wave dispersion of plasma oscillation and inhomogeneity of the e-beam.

C. Finally, the longitudinal thermalization of plasma oscillation can be used for the suppression of Schottky-noise. In view of effective freezing of transverse electron motion by strong accompanying magnetic field, one can consider the electron beam as plasma with temperature equal to longitudinal temperature of the electron beam, which can be very low [13]. In such a situation the longitudinal plasma oscillations relax to thermodynamic level (corresponding to this temperature), which is a minimum among other shot-noise levels. Maintenance of that low shot-noise level along beam acceleration and transport before cooling section is an issue for study.

At suppression of shot-noise field by a factor Γ the admissible gain is increased by this factor:

$$G < G_\Gamma \equiv (m_h / m_e)\Gamma^2 \tag{10}$$

On the whole, the possibilities visible now for suppressing the Schottky-noise require their detail studies in the physical and technical aspects.

Gain Limits Due to Saturation of a Microwave Instability

Let us consider briefly the main limitations of an achievable increase for the response, due to non-linear saturation of instability. The most principal limitation is

$$G_{\max} < (n_e\sigma^3 / \gamma) \approx N_e(\sigma_\perp / \gamma\sigma_z).$$

due to a finite number of electrons participating effectively in the response.

The meaning of this limitation is self-evident: under this increase the deformation of an electron cloud of a size becomes (on the order of magnitude) unitary i.e. instability enters the nonlinear regime and an exponential evolution is ceased.

By taking into account the shot-noise of the electron beam, one has to reduce the achievable gain by the following one:

$$G < G_2 \equiv \Gamma(n_e \sigma_\perp^3 / \gamma)^{1/2}$$

By comparing this criterion with the previous one, we may conclude that maximum useful shot-noise suppression factor can be estimated as

$$\Gamma_{\max} \sim (n_e \sigma_\perp^3 / \gamma)^{1/2}$$

An additional limitation on gain is connected with "Schottky-noise" caused by the particles of the beam under cooling: since in the interaction region there are about $n_i \sigma_\perp^3 / \gamma$ ions, then

$$G < G_3 \equiv (n_e \sigma^3 / \gamma) / (n_i \sigma^3 / \gamma)^{1/2}$$

By reviewing the three estimated limitations, we can write a combined limitation on achievable gain:

$$G \le \min(G_2, G_3, \Gamma^2 \frac{m_p}{m_e})$$

The Shield Effect in CEC

There is a limitation on cooling time in method of *stochastic cooling* due to the shielding interaction of ions via the amplifier [17]:

$$\tau_c \ge \frac{(J_p / e)}{(\Delta\omega)^2} \frac{f_0}{\Delta f_0}$$

Where J_p is the current of a (coasted) beam under cooling, Δf_0 is the spread of particle revolution frequency f_0,

$$\Delta\omega = 2\pi\Delta f \le (c / l_\perp) \qquad (11)$$

is the penetration frequency bandwidth of an amplifier, and $l_\perp$ is an effective aperture of the pickup-kicker electrodes. When considering a correspondent limitation on cooling time of CEC, we have to substitute the frequency bandwidth in (11) as

$$\Delta\omega = \frac{\gamma\beta c}{\sigma_\perp}.$$

One can see that the shield limitation of CEC to be substantially weaker than in ordinary stochastic cooling. The difference is especially big in ultra relativistic region. This limitation seems to be insignificant even when cooling very short bunches in colliders. When cooling at low energies, it is important that this limitation does not increase but decrease with the cooling process. In particular, when stacking, the cooling of a new portion of particles is not essentially decelerated by the presence of an already stored intense beam that is different from the case of stochastic cooling. In this aspect the method suggested here maintains in practice the properties of an ordinary electron cooling method.

To finish our general observation of the method, note the shielding effect is related to the question of collective stability beam under cooling which also has to be studied as a possible limiting factor.

CONCLUSIONS AND OUTLOOK

The method considered above combines principles of electron and stochastic cooling and microwave amplification using an electron beam. Such unification promises to frequently increase the cooling rate compared to both the electron cooling and conventional stochastic cooling. It might find important applications to projects based on cooling and stacking of high-temperature, intense heavy particle beams in a wide energy range.

Some tentative schematics and estimations of cooling rates of CEC that could be used for luminosity increase in colliders with hadron beams are presented in work [10]. The preliminary results are encouraging. Certainly, for the whole understanding of new possibilities thorough theoretical study is required of all principle properties and other factors of the method.

ACKNOWLEDGMENTS

I am truly grateful to V. Litvinenko for numerous stimulating discussions in process if this work. I am also very happy about an opportunity to collaborate with him in efforts on developing an FEL based scheme of CEC as described in paper [10].

REFERENCES

[1] A. Fedotov, in Proc. of Cool 07
[2] V.Ptitsyn et al, http://www.bnl.gov/cad/erhic/Documents/AD_Position_Paper_2007.pdf
[3] V.N. Litvinenko et al., in Proc. PAC 2005.
[4] Ya. Derbenev et al., in Proc. of PAC 07.
I.Meshkov, Phys. Part. Nucl., 25, 6 (1994) 631
S.Nagaitsev et al., Phys. Rev. Lett. **96**, 044801 (2006).
[7] A.V. Fedotov et al, New J. of Physics **8** (2006) 283.
[8] Ya. Derbenev, in Proc. of Cool 07.
[9] Ya. Derbenev, Proc. of 7th All-Union Conference on Charged Particle Accelerators, 14-16 October 1980, Dubna, USSR, p. 269 (in Russian); Ya. Derbenev, AIP Conf. Proc. No. 253, p.103 (1992).
[10] V. Litvinenko and Ya. Derbenev, in Proceedings of FEL 2007.
[11] G. Budker, At. En. (Sov.) 33, 346 (1967).
[12] G. Budker and A.N. Skrinsky, Sov. Phys. Usp. 124 N. 4, 561 (1978).
[13] Ya. Derbenev and A.N. Skrinsky, Sov.Phys.Rev. 1, 165 (1981).
[14] A.V. Burov, Ya. Derbenev, Preprint IYaF AN SSSR No. 81-33 (1981).
[15] A. Kondratenko, E. Saldin, Part. Acc.**10** (1980) 207.
[16] E.L. Saldin, E.A. Schneidmiller, M.V. Yurkov, The Physics of Free Electron Lasers, Springer, 1999.
[17] S. van der Meer, CERN/ISR-RF/72-46 (1972).

ELECTRON BEAMS AS STOCHASTIC 3D KICKERS

V.V. Parkhomchuk, V.B. Reva, A.V. Ivanov
BINP, Novosibirsk, Russia

Abstract

This article describes an idea combining electron and stochastic cooling in one device. The amplified signal of displacements of the ion from the pick-up electrode is applied to the control electrode of an electron gun. Thus, a wave of space charge in the electron beam is induced. This wave propagates with the electron beam to the cooling section. The space charge of the electron beam acts on the ion beam producing a kick. The effectiveness of the amplification can be improved with using a structure similar to a traveling-wave tube.

INTRODUCTION

Stochastic cooling is a typical feedback systems used in accelerators [1]. A displacement of a particle induces a signal on a pickup electrode. This signal from the pickup is amplified and applied to the kicker device acting on the particle. With a proper choice of the feedback parameters the oscillations of the target particle are damped. Other particles of the beam cause a parasitic noise and limit the maximum cooling rate. A typical kicker device is an electrodynamics structure like a strip line or slow-wave array. The bandwidth of the system is about 1 GHz with a power of few kW.

Experiments [2-4] with electron beams show that the space-charge field can be an effective tool for impacting on an ion. The space charge of the electron beam can be used as the kicker in stochastic cooling systems. A sketch of such a device is shown in Figure 1. The signal from the pick-up or array of pick-ups is applied to the amplifier system. The signal from the amplifier is applied to the control system of the electron gun which produces a fluctuation of the electron current of required form. After that the electron beam is accelerated and the space charge fluctuation proceeds to the cooling section. Here the fluctuation moving together with an ion acts via the electrical field of the space charge.

The effective kicker device should satisfy many requirements. The rate of cooling depends on the system bandwidth. The bandwidth is limited by its highest frequency. Aside from technological issues, there is a limit of the typical aperture of the kicker. Problems appear when the kicker aperture becomes comparable to the wavelength at high frequencies when the particle with $\beta<1$ does not have time to fly through the kicker during the impulse. Most of the problems are easily solved in high-energy accelerators but for low and medium energy range new criteria may be useful. The physical size of the electron kicker is small. The size may be easily changed in proportion to the size of the ion beam, thus the kicker parameters will be optimal. The size of the electron kicker does not depend on the aperture of the vacuum pipe. It is not necessarily a plunging device.

From the physical point of view the electron cooler device as kicker enables one to obtain 40 GHz ranges of frequencies. One of the imiting factors is the size of the electron beam. A wave with wave-length about thr transverse size of the beam is difficult to inject by usual RF methods and may have strong dispersion and damping.

The electron kicker is effective for the velocity matching of kick impulse and ion. Adjusting the energy of the electron beam the phase velocity of the space-charge wave may be equalized to the ion velocities with high accuracy. This result may be obtained at large variation of the ion velocities $0<\beta<1$.

The space charge of the electron beam enables one to obtain the 3D distribution of the electric field at the same time. So, if the control structure of the electron gun can modulate the electron gun axial-asymmetrically then all 3D kick types (vertical, horizontal and momentum) are available in one single device.

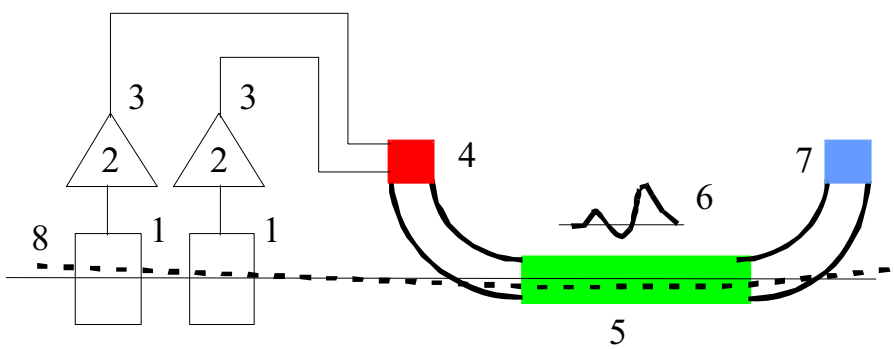

Figure 1: Scheme of stochastic cooling with electron cooler as 3D kicker. 1 – pick-up system, 2 – hybrid and amplifier, 3 – cable system, 4 – electron gun with the current modulation, 5 – cooling section, 6 – modulation of the space-charge density in the cooling section, 7 – collector of the electron beam, 8 – ion trajectory.

This idea is a variant of Derbenev's idea [5] about the use of instability for the amplification of the cooling force.

STRENGTH OF THE ELECTRON KICKER

The performance of some stochastic cooling systems may be limited not only by the system bandwidth but also by the strength of the kick. The maximum value of the electron current fluctuation is limited. In order that the electron kicker works in the linear regime the condition $\sqrt{(\Delta I)^2} = \Delta i_{\max} << I_0$ is desirable. Here $\Delta i_{\max}$ is the r.m.s. value of the possible fluctuation of the electron current, I_0 is the total current of the electron beam.

The electric fields of the space charge fluctuation can be written as

$$E_\perp = \frac{2}{\gamma\beta c}\frac{\xi}{a^2} i\,, \qquad E_{\mathrm{II}} = \frac{1}{\gamma\beta c}\left(2\ln\left(\frac{b}{a}\right)+1\right)\frac{\partial i}{\partial z}\,,$$

where $E_\perp$ and E_{II} are the transverse and longitudinal electric fields the in co-moving reference system, i is the electron current, b and a are the radii of the vacuum pipe and electron beam, respectively, ξ is the "pseudo"-displacement of the center of space charge describing the amplitude of the dipole fluctuation, and z is the longitudinal coordinate.

If the transverse and longitudinal momenta of the single particle before and after a kick can be described by the equation

$$A_c = A - \lambda A\,,$$

then the minimal stochastic cooling time τ_{cool} of a single particle is

$$\tau_{cool}^{-1} = 2\lambda f_0\,.$$

Here we do not take into account effects related to the role of the rest particle in the interaction region, "bad" and "good" mixing and so on. The maximum strength of the kicker is limited to

$$\lambda_{\max} A = \delta A_{\max}\,.$$

The signal from the pickup is formed by the all other passing particles within the time $1/\Gamma$, where Γ is the bandwidth of the system. Thus, the useful part of the kick is only $1/\sqrt{N_s}$ part of total value. The term $N_s = N \cdot f_0/\Gamma$ is the conventional value for the particle numbers per sample at revolution frequency f_0 and the particles in the beam N. The resulting equations for the kicker strength of the electron beam are

$$\lambda_{\mathrm{II}}^{\max}\frac{\Delta p_{\mathrm{II}}}{p} = \frac{1}{\gamma^2\beta^4} r_q \frac{\Gamma\, l_{cool}}{q\cdot c^2}\frac{\Delta i_{\max}}{\sqrt{N_s}}\left(2\ln\left(\frac{b}{a}\right)+1\right)$$

and

$$\lambda_{\perp}^{\max}\frac{\Delta p_\perp}{p} = \frac{2}{\gamma^3\beta^3} r_q \frac{l_{cool}}{qca}\frac{\Delta i'_{\max}}{\sqrt{N_s}}\,.$$

Here $\lambda_{\mathrm{II}}^{\max}$ and $\lambda_{\perp}^{\max}$ are the maximum rates of transverse and momentum cooling of the particle, l_{cool} is the length of the cooling section, $\Delta p_\perp/p$ and $\Delta p_{\mathrm{II}}/p$ are the initial spreads of the transverse and longitudinal momenta of the particle, $\Delta i'_{\max} = I_0\,\xi/a$ is the amplitude of dipole fluctuations of the electron beam, and r_q is the classical charge radius.

Table 1

Parameter	Value
modulation of electron current $\Delta i'_{\max}$ and $\Delta i_{\max}$	50 mA
cooler length	4 m
bandwidth of the amplifier	2 GHz
radius of electron beam	0.5 cm
radius of vacuum pipe	5 cm
β-function in cooling section	15 m
revolution frequency	1 MHz
initial normalized emittance (1σ value)	10 π·mm·mrad
initial momentum spread (1σ value)	$5\ 10^{-3}$

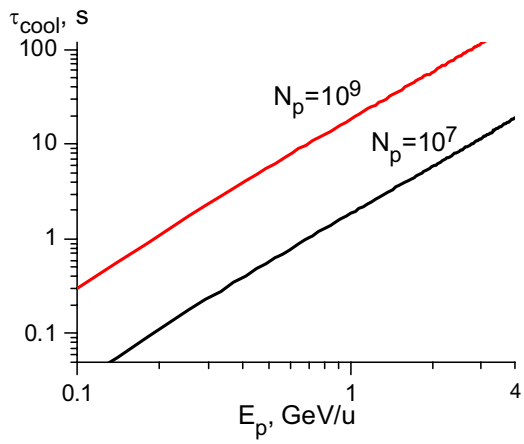

Figure 2: Maximal value of the longitudinal cooling rate versus energy of the cooled particle.

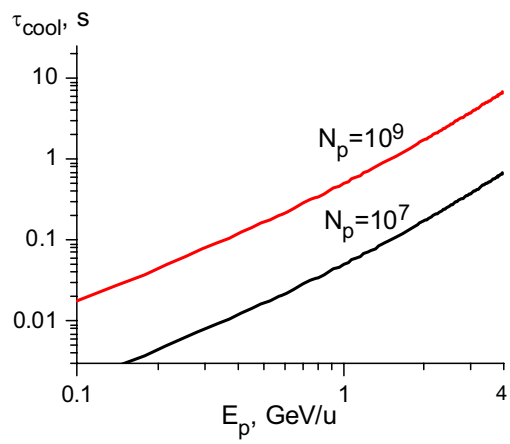

Figure 3: Maximal value of the transverse cooling rate versus energy of the cooled particle.

The figures 2 and 3 show the cooling rate versus the energy of the cooled particles. The other parameters of the estimation are listed in Table 1. One can see that a reasonable cooling rate is obtainable in the energy region 0.1 – 1 GeV/u or less. The corresponding energy of the electron beam is 50 – 500 keV.

DISPERSION AND ROTATION OF THE KICKER PULS IN ELECTRON BEAMS

One of the characteristic problems related to this type of kick is a distortion of the kick impulse induced by wave dynamic. The dispersion equations of the space-charge fluctuation propagating in the electron flow are

$$\omega_l = kv_e \mp k\frac{\omega_{pe}a}{\sqrt{2}}\sqrt{\ln\left(\frac{b}{a}\right)+\frac{1}{2}},$$

$$\omega_t = kv_e \mp \frac{\omega_{pe}}{\sqrt{2}}\frac{a^2}{b}k$$

for longitudinal and transverse fluctuations. A perturbation propagates with the group velocity v_e and diverges because of the action of space charge. If no particular care is taken against excitations only one oscillation mode exists with velocities $v_e \pm u$. The widening δl of the initial impulse with length l_0 is about

$$\frac{\delta l}{l_0} = \frac{u\Gamma\, l_{cool}}{(\gamma\beta c)^2}.$$

Figure 4 shows numerical estimates of the impulse splitter for typical parameters of the electron beam. One can see this effect may be essential for the longitudinal wave at low energy that limits the maximum electron current at such condition. This effect is negligible for propagaton of the transverse kick pulse.

This problem can be resolved if the modulation system excites fluctuations only in one mode. For example, the modulation system contains the slow-wave electromagnetic structure. So, the traveling wave of the input impulse interacts with an oscillation mode of the electron beam. A theory of such interactions has been developed in detail for the description of a traveling tube device [6]. An example of such a device is the Kompfner splitter [6] that transfers energy from the structure to the beam without amplification.

In this case, the problem of pulse dispersion remains in any case but moves to the term $\propto k^2$ in the dispersion equation. An expansion of the dispersion equation to higher powers of k for the longitudinal wave can be found in [7],

$$\omega = kv_e \mp k\frac{\omega_{pe}a}{\sqrt{2}}\sqrt{\ln\left(\frac{b}{a}\right)}\cdot\left(1-\frac{k^2b^2}{4\ln\left(\frac{b}{a}\right)}\right).$$

The widening of the initial impulse described by the set of equations

$$D = \frac{1}{2}\frac{\partial^2\omega}{\partial k^2}, \qquad l_0 + \delta l = l_0\sqrt{1+\frac{4D^2t^2}{\sigma^4}},$$

$$t = \frac{l_{cool}}{\gamma\beta c}, \quad \sigma = \frac{\gamma\beta c}{\Gamma}, \qquad k \approx \frac{\pi}{\sigma}$$

is shown in Figure 5. So, it enables to use larger values of the electron current for the kick with minimal pulse widening. In the range of small energies a decrease of the bandwidth of the electron current is possible.

The rotation of the kick at the combined action of crossed electrical and magnetic fields is nonessential. The radial electric field of the electron beam,

$$E_r = \frac{2}{\gamma\beta c}\frac{r}{a^2}J_e,$$

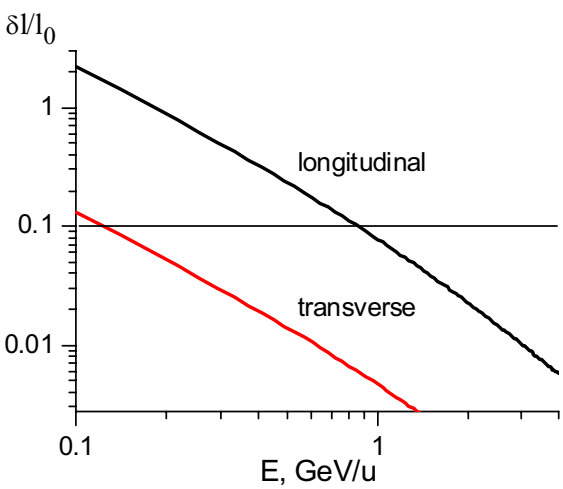

Figure 4: Widening of the kick pulse induced by diverging of two waves. Electron current is I_0=0.5 A, radius of electron beam is a=0.5 cm, frequency bandwidth is Γ=2 GHz.

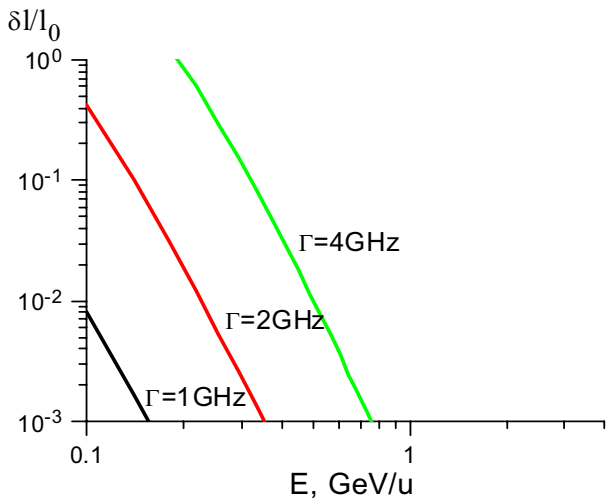

Figure 5: Widening of the kick pulse induced by dispersion of the longitudinal wave. Electron current I_0=0.5 A, radius of electron beam a=0.5 cm, frequency bandwidth Γ=1, 2 and 4 GHz.

leads to a rotation of the kick in the longitudinal magnetic field on the angle

$$\Delta\theta_M = c\frac{E_r}{B_{cool}}\frac{\tau_{flight}}{r}.$$

At electron energy 50 keV and ion energy 0.1 GeV/u the rotation angle is $\Delta\theta_M = 0.6$. The remaining parameters are taken from Table 1. At the highest energy this effect is negligible.

ESTIMATION OF COOLING RATE FOR A REAL ELECTRON GUN

In order to estimate the usefulness of such kicker device the authors tested the electron gun of the EC-35, EC-300, EC-40 coolers from this point of view. Fig. 6 shows the modulation capability of the electron gun versus frequency. The simulations were performed by RF modification of the UltraSAM code [8]. Obviously, this existing construction is not a high frequency device (curve 1) but the situation may be improved slightly by decreasing the geometrical size of the gun by a factor of tow (curve 2). The response of the control grid is 1-1.5 mA per V, the typical frequency is about 1 GHz., the maximal input RF power applied to the gun may be about 50 W at the maximal fluctuation current 50 mA.

Figure 7 shows estimates of the cooling time for fixed total amplifier coefficients. One can see that the not well matched electron gun can produce a kick sufficient for obtaining a reasonable cooling time of about 1 s or less in the medium energy range. So, it may be expected, that a special RF gun may be more successful.

SUMMARY

The use of an electron cooler as kicker in the medium range of the energy (0.1 – 1 GeV/u for heavy charged particles) may have the following advantages: one device

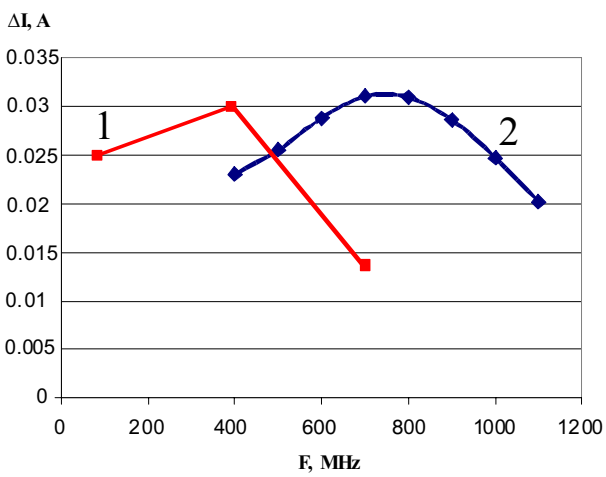

Figure 6: Modulation current versus frequency at 20 V modulation voltage. The curve 1 corresponds to usual BINP electron gun used in EC-35 (CSRm), EC-300 (CSRe), EC-40 (LEIR), curve 2 is variant 1 decreases in scale 2.

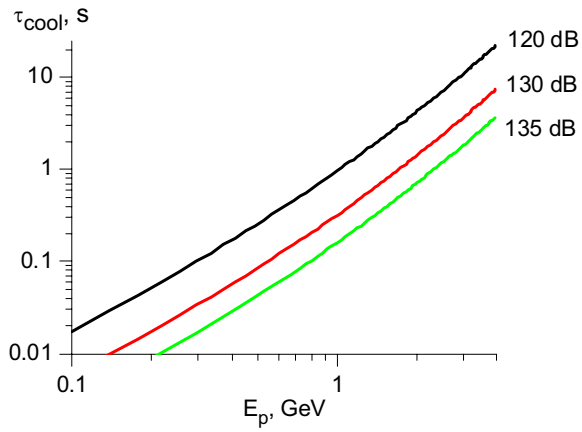

Figure 7: Transverse cooling time versus energy at the different values total amplifier gain. The rest parameters of the estimation are $N_p=10^9$, Γ=1 GHz, f_0=1 MHz, ρ=50 Ohm, T_{ampl}=60 K, L_{cool}=4 m, βcool=15 m, Z_{gun}^{-1}=1 mA/V.

providing a 3D kick at the same time; velocity matching of kicking pulse with ion in the wide range of charges; free aperture; using existing devices (certainly, if electron cooler exists yet); frequency bandwidth may be very high; such type of the kicker does not restriction on frequency bandwidth at low ion velocities when the time-of-flight factor becomes essential.

Further improvement of the gun construction may follow the way of the traveling wave tube (TWT) device. An electron cooler contains all main components of TWT device: cathode, control electrode, longitudinal magnetic field and collector. It is necessary to provide an electron flow by the special slow-wave structure at intermediate energies of a few kV only. Amplification of the RF signal and modulation of the electron current can be obtained in such type of control system. The RF power of the electrostatic fluctuation with the electron beam is delivered straight on to the ion beam. The electrostatic fields of the space charge induce the required kick on an ion during the time of the joint flight of electron and ion beams in the cooling section. The parameters of a TWT tubes are comfortable for an electron cooler. For example, the kinetic energy of the electron beam is typically 3-10 keV and beam currents in the range 200-500 mA are produced from the TWTs by useing the antiproton source of FERMILAB. The output parameters of a compact Industrial TWT are sufficient. The amplifier gain is up to 30-50 dB, the bandwidth is up to 20 GHz and the power is up to 50 W in the continuous regime. If one supposes a 30 dB RF signal amplification directly in the modulation system, then the requirement on the amplifier of the pick-up signal becomes very low. The noise loading of the amplifier can be 0.1 W or less at the effective amplifier temperature 60 K.

Thus, the use of an electron cooler as a 3D kicker may be very perspective in the medium energy region. It is possible to construct a very low power device which is able to cool ions in about one second or less.

REFERENCES

[1] Marriner J. Nucl.Instrum.Meth. A532 (2004) 11-18
[2] V.V.Parkhomchuk, V.B.Reva, V.D.Shil'tsev. Technical Physics, Vol. 48, N8, 2003, pp.1042-1046.
[3] S.G.Konstantinov, V.V.Parkhomchuk, V.B.Reva. Space Charge Oscillation in Electron Cooling Devices. Technical Physics, Vol. 48, N1, 2003, pp.85-89.
[4] V.V.Parkhomchukю. Nucl. Instr. Meth. Vol. A 441, 2000, pp.9-17.
[5] Y. Derbenev, Proceedings of the 7th National Accelerator Conference, V. 1, p. 269, (Dubna, Oct. 1980)
[6] W. Lousisell, Coupled mode and parametric electronics, John Wiley, New York, 1960.
[7] A. Burov, V. Kudelainen et al, "Experimental investigation of the compensated state of an electron beam", Preprint BINP 89-116, 1989.
[8] A.V. Ivanov, M.A. Tiunov, "ULTRASAM - 2D Code for Simulation of Electron Guns with Ultra High Precision", EPAC'02, Paris, June 2002, p. 1634.

ELECTRON COOLING SIMULATION FOR ARBITRARY DISTRIBUTION OF ELECTRONS

A. Sidorin#, A. Smirnov, JINR, Dubna, Russia
A. Fedotov, I. Ben-Zvi, D. Kayran, BNL, USA

Abstract

Typically, several approximations are being used in simulation of electron cooling process, for example, density distribution of electrons is calculated using an analytical expression and distribution in the velocity space is assumed to be Maxwellian in all degrees of freedom. However, in many applications, accurate description of the cooling process based on realistic distribution of electrons is very useful. This is especially true for a high-energy electron cooling system which requires bunched electron beam produced by an Energy Recovery Linac (ERL). Such systems are proposed, for instance, for RHIC and electron – ion collider. To address unique features of the RHIC-II cooler, new algorithms were introduced in BETACOOL code which allow us to take into account local properties of electron distribution as well as calculate friction force for an arbitrary velocity distribution. Here, we describe these new numerical models. Results based on these numerical models are compared with typical approximations using electron distribution produced by simulations of electron bunch through ERL of RHIC-II cooler.

INTRODUCTION

A traditional electron cooling system employed at low-energy coolers is based on a uniform electron beam immersed in a longitudinal magnetic field of a solenoid. In this case the action of electron cooling on the ion dynamics inside a storage ring can be described using a few standard simplifications:

1. Angular deviation of the longitudinal magnetic field line is sufficiently less than the ion beam angular spread.
2. Ion transverse displacement inside the cooling section is small compared to the electron beam radius.
3. Ion beam temperature is substantially larger than electron one and ion diffusion in the electron beam can be neglected.
4. Electron beam has a cross-section with a round shape and uniform density distribution in the radial direction.

Under these assumptions and using analytic asymptotic representation of the friction force, the formulae for characteristic times of emittance and momentum spread decrease for electron cooling were obtained (see, for example, Ref. [1]). This model was used in several programs dedicated to electron cooling simulation, for example, in the first version of the BETACOOL [2]. An uncertainty in predictions of the cooling rate based on such an estimate is typically a factor of two or three, which is acceptable for most designs of a traditional cooling system. However, this model can not cover all possible versions of the electron cooling system design, and its accuracy is insufficient for a design of high energy electron coolers.

Recently, modifications of the usual configuration of the low energy electron cooling system were proposed. To avoid instability of the ion beam related to an extremely large density of the cooled beam it was proposed to use so called “hollow” electron beam – the beam with small density in the central part. The “hollow” electron beam is efficient for ion beam storage using cooling-stacking procedure. The low electron density in the stack region avoids overcooling of the stack and decreases (for heavy ions) recombination in the cooling section. Therefore, a few electron cooling systems with hollow electron beam were recently constructed.

Extension of the electron cooling method to the region of electron energy of a few MeV, which was successfully realized at Recycler in Fermilab and proposed for HESR (GSI, Darmstadt) and COSY (FZJ, Juelich), led to some changes of the electron beam properties. Accurate matching of an intensive electron beam with transport line in the cooling section is a complicated task in this energy range. The electron beam mismatch leads to fast decrease of the electron beam quality in the radial direction from the central part to the beam edge that can significantly affect the ion distribution under cooling.

Further increase of the electron energy is related with an RF acceleration of the electrons. In this case one can have Gaussian distribution of the electrons in radial plane and, if the electron bunch is shorter than the ion one, in longitudinal direction also. Simulation of the cooling process in this case requires modification both of the electron beam and the physical model.

Successful operation of the Recycler electron cooling system demonstrated good cooling efficiency in the case when the longitudinal magnetic field is used for electron beam transport only and does not influence the friction force significantly. This indicates that a strong magnetic field is unavoidable only in the case when a deep cooling of the ion beam is necessary (as, for example, for HESR in high resolution mode of operation). When the electron cooling is used for compensation of heating effects and stabilization of the ion beam phase volume at relatively large value, the non-magnetized cooling can be competitive as well. For example, although extensive studies of the magnetized cooling approach for RHIC showed that it is feasible [3] and would provide required luminosities for the RHIC-II, the baseline of the project was recently changed to the non-magnetized one. Application of electron cooling using the non-magnetized electron beam significantly simplifies the RHIC-II cooler

sidorin@jinr.ru

design. Generation and acceleration of the electron bunch without longitudinal magnetic field allows low values of the emittance for the electron beam in the cooling section. Therefore, the cooling efficiency is comparable with the case of strong magnetic field application.

Other peculiarity of high-energy cooling system is a big length of the cooling section – up to about 20 - 100 m. To obtain very high accuracy of the magnetic field is difficult technical task, and cost of the cooling system utilizing the magnetized cooling will strongly depend on the required level of the accuracy. Therefore, before designing of the cooling section solenoid, one needs to investigate influence of the magnetic field line curvature on the cooling process.

Most of the effects can be taken into account by numerical solution of the ion motion equations inside the cooling section. For such simulations, an electron beam model should calculate the friction force components as a function of the ion velocity and the ion position inside the electron beam. The required local parameters of the electron beam can be calculated using some analytical model describing electron density and velocity spread as functions of co-ordinates, or, in a general case, from electron distribution imported from output file of a program dedicated to the electron dynamics simulations. In this report, we describe a few analytical models of the electron beam realized in the BETACOOL program and the algorithm of the friction force calculation from an electron array calculated with PARMELA code [4] for RHIC electron cooling system.

FRICTION FORCE MODELS

In the particle rest frame (PRF) the friction force acting on the ion with a charge number Z passing through an electron beam of density n_e can be evaluated in the absence of magnetic field by numerical integration of the following formula [5]:

$$\vec{F} = -\frac{4\pi m_e e^4 Z^2}{m}\int \ln\left(\frac{\rho_{\max}}{\rho_{\min}}\right)\frac{\vec{V}-\vec{v}_e}{\left|\vec{V}-\vec{v}_e\right|^3} f(v_e)d^3v_e \qquad (1)$$

where e and m are the electron charge and mass, V and v_e are the ion and electron velocities, respectively. The Coulomb logarithm is kept under the integral because the minimal impact parameter depends on electron velocity:

$$\rho_{\min} = \frac{Ze^2}{m}\frac{1}{\left|\vec{V}-\vec{v}_e\right|^2}.$$

At a given value of the ion velocity the maximum impact parameter $\rho_{\max}$ is constant and determined by either the dynamic shielding radius or by the time of flight of an ion through the cooling section. Inside the ion vicinity of radius equals to the maximum impact parameter the electrons are distributed over velocities in accordance with the function $f(v_e)$. In a practical case, the maximum impact parameter is sufficiently less than the electron beam radius and all the friction force formulae presume that the electron density inside the vicinity of the ion is uniform.

The formula (1) is valid also in the case when a magnetic field of a small value is used for the electron beam focusing in the cooling section. The magnetic field does not affect the force value when a radius of the electron gyration $\rho_\perp$ is larger than the maximum impact parameter. However, even in this case the magnetic field modifies the electron distribution over velocities due to coupling between transverse planes. For a standard assumption that the thermal velocity distribution is Gaussian, the distribution function can be presented as

$$f(v_e) = \left(\frac{1}{2\pi}\right)^{3/2}\frac{1}{\Delta_\perp^2\Delta_\parallel}\exp\left(-\frac{v_\perp^2}{2\Delta_\perp^2}-\frac{v_\parallel^2}{2\Delta_\parallel^2}\right), \qquad (2)$$

where $\Delta_\perp$ and $\Delta_\parallel$ are the electron rms velocity spreads in the transverse and longitudinal direction correspondingly. Therefore, the friction force can be presented as a sum of radial and longitudinal components. In the absence of longitudinal magnetic field in the cooling section the electron motion in transverse planes is uncoupled. The electron beam can have different thermal velocity in the horizontal and vertical planes. In this case the force is a vector with all three different components.

For large magnetic field (when $\rho_\perp << \rho_{\max}$) the integrand in Eq. (1) is modified. In the framework of binary collision model the transverse and longitudinal components of the friction force for strong magnetization can be approximated by the formulae [6]:

$$F_\parallel = -\frac{4\pi Z^2 e^4 n_e L_M}{m}\int \frac{V_\perp^2\left(V_\parallel - v_e\right)}{\left(V_\perp^2+\left(V_\parallel-v_e\right)^2\right)^{5/2}} f\left(v_\parallel\right)dv_\parallel$$

$$F_\perp = -\frac{2\pi Z^2 e^4 n_e L_M}{m}\int \frac{V_\perp\left(V_\perp^2-2\left(V_\parallel-v_e\right)^2\right)}{\left(V_\perp^2+\left(V_\parallel-v_e\right)^2\right)^{5/2}} f\left(v_\parallel\right)dv_\parallel \qquad (3)$$

where the Coulomb logarithm is equal to $L_M = \ln\left(\frac{\rho_{\max}}{\rho_\perp}\right)$.

In these formulae it is assumed that the transverse electron motion is completely suppressed by the magnetic field. The binary collision model for finite value of the magnetic field was developed by Erlangen University group [7]. The obtained formulae contain dependence on both the longitudinal and transverse electron velocities.

To calculate the friction force components using analytical formulae, the electron beam model have to calculate the following local (in a given ion position inside electron beam) parameters:

- electron density,
- electron longitudinal velocity spread $\Delta_\parallel$,
- electron transverse velocity spread $\Delta_\perp$ to calculate the force in presence of a magnetic field,
- electron horizontal and vertical velocity spreads in absence of the magnetic field.

When the electron beam is presented as an array of particles, the distribution function over velocities is given as a series of δ- functions:

$$f(v) = \frac{1}{N_{loc}}\sum_{j=1}^{N_{loc}}\delta\left(\vec{v}-\vec{v}_j\right), \qquad (4)$$

where N_{loc} - number of the electrons in small vicinity of the ion position.

ANALYTICAL MODELS OF ELECTRON BEAM

A few analytical models for electron beam representation are now available in BETACOOL: uniform cylinder, Gaussian cylinder, Gaussian bunch, "hollow" beam and electron beam with parabolic density distribution. The cooler model takes into account variation of the electron beam position and angular deviation along the cooling section (it can be caused, for example, by magnetic field errors in the cooling section). For this purpose, the co-ordinates of the electron beam trajectory inside the cooling section can be read from an additional external file, and the ion motion equations are solved numerically inside the cooler. The friction force can be calculated in accordance with one of the analytical models or using results of numerical calculations imported from an external file.

As an illustration of the principle, we briefly describe the electron beam model for the parabolic density shape developed for simulation of antiproton cooling at the Recyler. Input parameters of the model are the beam radius a and the beam current I_e. The electron density n as a function of radial coordinate r is calculated in accordance with

$$n(r) = n_0\left(1-\left(\frac{r}{a}\right)^2\right), \tag{5}$$

when $r < a$ and equal to zero in opposite case. The central density n_0 is calculated from the beam current as

$$n_0 = \frac{3I_e}{\pi a^2 v e}, \tag{6}$$

where v is the electron velocity.

The effect of the beam mismatch in the cooling section is taken into account as a linear increase of the electron transverse velocity spread with the radial position

$$\Delta_\perp = \Delta_{\perp,0} + \frac{d\Delta_\perp}{dr} r, \tag{7}$$

where $\Delta_{\perp,0}$ – is the velocity spread at the beam axis, and the velocity gradient $d\Delta_\perp / dr$ is an input parameter. The longitudinal velocity spread is assumed to be independent on the radial co-ordinate.

ELECTRON ARRAY

The distribution of electrons can be generated with an external code. For example, in the case of RHIC-II simulations such electron distribution is an output of PARMELA code [6], which is used to simulate electron beam transport to the cooling section. The distribution of electrons is then read into BETACOOL and is referred to as "electron array".

For the friction force calculation, the local model uses local parameters within electron array calculated as a function of the ion coordinates. The program first finds local number of electrons N_{loc} which have minimum distance to the ion position (the value of N_{loc} is an input parameter). For N_{loc} found, the program calculates mean and root mean square parameters for all the coordinates and velocity components, which are used to calculate the local density of the electrons.

The local density and rms parameters found can be used in calculation of the friction force with analytic formulas and assumption of Gaussian velocity distribution. Such a model is called here "local-Gaussian". In most cases, this approach is sufficient. It allows to compare cooling process based on local characteristics of electron distribution with the one expected based on the friction force calculation using projected global rms parameters of the whole distribution.

In another local model, an assumption that local velocity distribution is Gaussian is not used. The velocity components are calculated directly which allows us to study friction force for an arbitrary velocity distribution. Here, we refer to this model as "local-arbitrary". The distribution function of the local electrons is given by formula (4). For non-magnetized cooling it leads to the following expression for the friction force components

$$F_\alpha = \frac{4\pi m_e Z^2 e^4}{m} \times \frac{1}{N_{loc}} \sum_{j=1}^{N_{loc}} \frac{\left(V_\alpha - v_{j,\alpha}\right) L_{C,j}}{\left(\sqrt{\left(V_x - v_{j,x}\right)^2 + \left(V_y - v_{j,y}\right)^2 + \left(V_z - v_{j,z}\right)^2}\right)^3} \tag{8}$$

where V_α are the components of ion velocity in the particle rest frame, $v_{j,\alpha}$ – the velocity components of j-th electron ($\alpha = x, y, z$). The minimum impact parameter in the Coulomb logarithm $L_{C,j}$ is calculated via velocity of j-th electron.

EXAMPLE OF RHIC-II SIMULATION

The high-energy electron cooling system for RHIC-II requires bunched electron beam. Electron bunches are produced by an Energy Recovery Linac (ERL), and cooling is planned without longitudinal magnetic field.

Simulations of electron beam dynamics were performed including compensation of space-charge defocusing in the cooling section. Electron distributions used in these studies were obtained by starting with the uniform cylinder (beer-can) at the cathode and tracking it through the ERL.

In general, electron beam dynamics simulations are aimed at minimization of global projected rms emittance and momentum spread while local rms velocity spread could have smaller values which would enhance cooling.

Another feature of electron distribution resulting from RF acceleration is that longitudinal rms velocity spread of electrons is not Gaussian, as shown in Fig. 1.

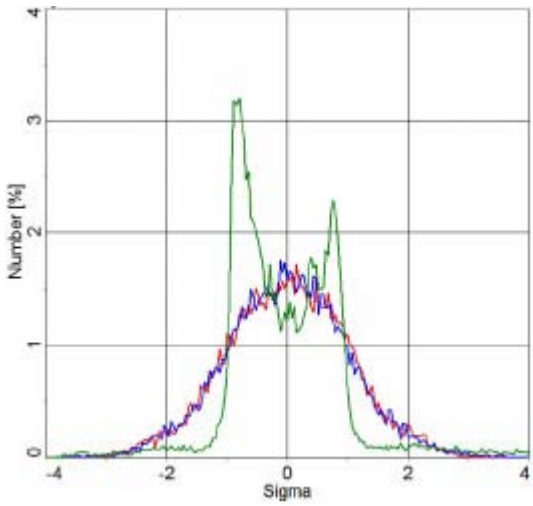

Figure 1: Histogram of velocity distribution of electrons at the start of the cooling section. Red and blue – horizontal and vertical; green – longitudinal.

As a result, different cooling dynamics can be observed in simulations when assumption of Gaussian velocity distribution is used instead of calculation using Eq. (8). This is shown in Figs. 2 and 3, where only electron cooling was included in simulations, with all other effects turned off.

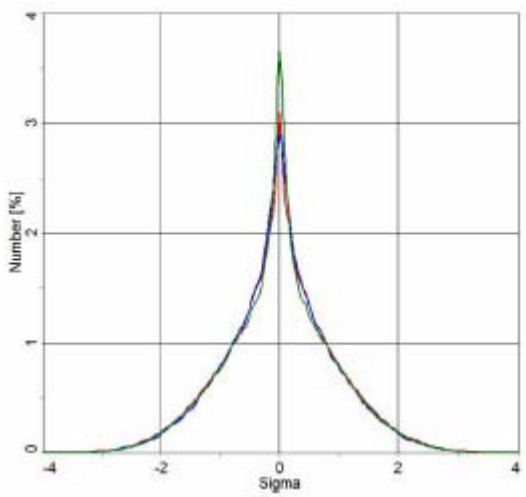

Figure 2: Horizontal (red), vertical (blue) and longitudinal (green) ion beam profiles based on assumption of Gaussian velocity distribution in all three planes.

During simulations electron beam was kept in a fixed position with respect to the center of the ion bunch. In Fig. 3, one can see that the hollow longitudinal velocity distribution (Fig. 1) prevents collapse of the distribution core which happens for Gaussian velocity distribution in Fig. 2, otherwise.

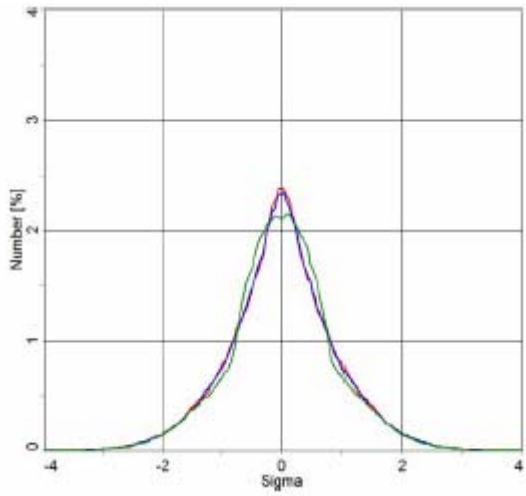

Figure 3: Horizontal (red), vertical (blue) and longitudinal (green) ion beam profiles after 5 minutes of cooling based on velocity distribution shown in Fig. 1.

The effect of hollow velocity distribution is less pronounced when intrabeam scattering is included in simulations, which prevents core collapse as well. However, the local model shows more effective cooling since most of the electrons in the core of the distribution have small angular spread [8].

REFERENCES

[1] I. Meshkov, Electron cooling: Status and Perspectives, Phys. Part. Nucl., 25, (6), 1994, 631.
[2] A. Lavrentev, I. Meshkov "The computation of electron cooling process in a storage ring", preprint JINR E9-96-347, 1996.
[3] RHIC Electron cooling, http://www.bnl.gov/cad/ecooling.
[4] L. M. Young, J. H. Billen, "Parmela documentation", LA-UR-96-1835.
[5] Description of various friction force formulas can be found, for example, in Ref. "BETACOOL Physics Guide", BNL Tech Note C-A/AP/#262 (Nov. 2006).
[6] V.V. Parkhomchuk, Physics of fast electron cooling, doctoral thesis, Novosibirsk, 1984.
[7] B. Mollers et al, Drag force on ions in magnetized electron plasmas, NIM B 207 (2003) 462-481
[8] A.V. Fedotov, I. Ben-Zvi, D. Kayran, E. Pozdeyev A. Sidorin, A. Smirnov, High-Energy Electron Cooling Based on Realistic Six Dimensional Distribution of Electrons, Proceedings of PAC07, Albuquerque, New Mexico, USA.

IMPLEMENTATION OF SYNCHROTRON MOTION IN BARRIER BUCKETS IN THE BETACOOL PROGRAM*

A. Sidorin, A. Smirnov, G. Trubnikov#, JINR, Dubna, Russia
O. Boine-Frankenheim, GSI, Germany

Abstract

The model of ion synchrotron motion in a stationary square wave barrier bucket was implemented into both main algorithms of the Betacool program: rms dynamics and Model Beam algorithm. In the frame of rms dynamics the calculation of the cooling and heating rates was modified in accordance with analytic expression for the ion phase trajectory in the longitudinal phase plane. In the Model Beam algorithm the generation of matched stationary particle array and simulation of the synchrotron motion were developed.

INTRODUCTION

Moving barrier RF bucket is an effective ion beam accumulation method used, for instance, in Fermilab's Recycler and proposed for NESR at FAIR project. A possible application of a stationary RF bucket is to compensate ionization energy loss in experiment with internal target. The ionization energy loss is the main physical effect limiting the experiment duration. The barrier bucket application permits to sufficiently decrease of required power of a cooling system when a high resolution in experiment is necessary. It is essentially true for dense internal target, for instance a pellet target. So an application of stationary RF bucket for WASA at COSY experiment can allow sufficiently decrease requirements for maximum electron current in proposed high voltage electron cooling system [1].

The mean energy loss can be compensated by usual sinusoidal RF system at relatively small voltage amplitude; however this leads to sufficient increase of intrabeam scattering (IBS) growth rates. Even at long length of the bunch the particle density in its central part increases significantly in comparison with a coasting beam. At a barrier RF bucket application the particle density inside the bucket is almost uniform. Therefore the IBS growth rates increase by a factor equal to ratio of the ring circumference to the bucket length only. This advantage of the barrier bucket is of great importance when the experiment requires high momentum resolution and, correspondingly, the ion beam momentum spread has to be as small as possible.

Recently a new program was developed for barrier RF bucket simulation for FAIR rings [2]. To compare predictions of different models and to estimate efficiency of the barrier bucket application in internal target experiments the new algorithms were implemented into Betacool program [3] also.

* This is work is supported by grant of president of Russian Federation for young scientists - candidates of science program 2007-2008.
# trubnikov@jinr.ru

The general goal of the BETACOOL program is to simulate long term processes (in comparison with the ion revolution period) leading to the variation of the ion distribution function in six dimensional phase space. Therefore the Betacool is not a tracking code, and simulation of transverse and longitudinal ion motion is based on analytical expressions for the phase trajectories.

Evolution of the second order momenta of the ion distribution function is realized in so called "rms dynamics" algorithm based on assumption of Gaussian shape of the distribution. Here all the heating and cooling effects are characterized by rates of emittance variation or particle loss.

The investigation of the beam dynamics at arbitrary shape of the distribution is performed using multi particle simulation in the frame of the Model Beam algorithm. In this algorithm the ion beam is represented by an array of model particles. The heating and cooling processes involved into the simulations lead to a change of the particle momentum components and particle number.

Therefore implementation of the new model required corrections in algorithms for heating and cooling rate calculation, development of algorithms for generation of the model particle array matched with RF system and simulation of the model particle synchrotron motion. New tools for the data post processing and visualization of the results were developed also.

General behaviours of the synchrotron motion are determined by integrated RF pulse strength, and essential physics is independent on the exact shape of the barrier RF wave. Simplest analytical solution for the phase trajectory can be obtained at square wave barrier bucket; therefore this model was implemented into the program at the first step. In future we plan to develop the algorithms for synchrotron motion simulation at arbitrary RF shape and moving barrier bucket.

SINCHROTRON MOTION IN SQUARE WAVE BARRIER BUCKET

The RF voltage time dependence at square wave barrier bucket can be written as

$$V(t)=\begin{cases} sign(\eta)V_0 & if \quad -(T_2+T_1)/2 \le t \le -(T_2-T_1)/2 \\ -sign(\eta)V_0 & if \quad (T_2-T_1)/2 \le t \le (T_2+T_1)/2 \\ 0 & otherwise \end{cases},$$

where V_0 is the voltage height, T_1 is the pulse width, T_2 is the gap duration, η is the ring off-momentum factor.

The equations of the synchrotron motion of the ion at charge eZ written in the variables (s-s_0, $\delta = \Delta p / p$) are

$$\begin{cases} \dfrac{d(s-s_0)}{dt} = |\eta|\beta c\delta_A \\ \dfrac{d\delta}{dt} = 0 \end{cases}$$

inside the gap of the RF voltage, and

$$\begin{cases} \dfrac{d(s-s_0)}{dt} = |\eta|\beta c\delta \\ \dfrac{d\delta}{dt} = -\dfrac{ZeV_0}{Cp_0} \end{cases}$$

when the particle crosses the cavity during the voltage pulse. Here δ_A is the amplitude of the momentum deviation; C is the ring circumference, p_0 – synchronous momentum.

From solution of the motion equations one can obtain main parameters of the bucket. The maximum momentum deviation (the barrier height) can be calculated from the following equation

$$\delta^2_{A,\max} = \frac{2T_1}{T_0}\frac{ZeV_0}{\beta c p_0|\eta|}, \quad (1)$$

where T_0 is the revolution period. Inside the bucket the period of the synchrotron oscillations is equal to

$$T_s = \frac{2T_2}{|\eta|\delta_A} + \frac{4Cp_0\delta_A}{ZeV_0}, \quad (2)$$

and the trajectory length is given by

$$S_b = T_2\beta c + \frac{|\eta|\beta c C p_0 \delta_A^2}{ZeV_0}. \quad (3)$$

Rms momentum deviation σ_δ relates to the amplitude as follows

$$\sigma_\delta^2 = \frac{(2/3)|\eta|Cp_0\delta_A^4 + ZeV_0T_2\delta_A^2}{2|\eta|Cp_0\delta_A^2 + ZeV_0T_2}. \quad (4)$$

RATE CALCULATION

Modifications in the rms dynamics algorithm are related mainly to calculation of IBS heating and electron cooling rates. At simulation of an interaction with an internal target the mean energy loss is ignored and characteristic growth time of the momentum spread is calculated using expression for the energy loss fluctuations.

The IBS process in the first approximation can be simulated using formulae for coasting beam at substitution of the bucket length instead the ring circumference. The bucket length is calculated in the following steps. For given rms momentum spread the amplitude of the rms particle oscillations is to be found from the equation (4). Introducing

$$\xi^2 = \frac{ZeV_0T_2}{2|\eta|Cp_0} \quad (5)$$

one can obtain

$$\delta_A^2 = \frac{\sqrt{9\left(\xi^2-\sigma_\delta^2\right)^2 + 12\xi^2\sigma_\delta^2} - 3\left(\xi^2-\sigma_\delta^2\right)}{2}. \quad (6)$$

For this amplitude the bucket length is calculated in accordance with (3).

The cooling rate calculation is based on averaging of the friction force acting on the "rms ion" in the cooling section over phases of betatron and synchrotron oscillations [4]. To realize this procedure one needs to recalculate the ion co-ordinates (s-s_0,δ), obtained at the exit of the cooling section, into its rms momentum deviation. For the particle at given longitudinal co-ordinates (s-s_0,δ) the amplitude of oscillations is calculated in accordance with the phase trajectory equation. The result is obvious, when (s-s_0) lies in the gap between RF waves: $\delta_A = \delta$. Inside the wave the amplitude is equal to

$$\delta_A^2 = \delta^2 + \frac{2ZeV_0}{|\eta|\beta c C p_0}(s-s_0), \quad (6)$$

where (s-s_0) is measured from the beginning of the wave. The corresponding rms momentum deviation is given by:

$$\left\langle\delta^2\right\rangle = \frac{\delta_A^4 + 3\xi^2\delta_A^2}{3\left(\delta_A^2+\xi^2\right)}, \quad (7)$$

where ξ is determined by (5).

GENERATION OF MATCHED MODEL PARTICLE ARRAY

The beam dynamics simulation in the Model Beam algorithm is started with a model particle array with Gaussian distribution in all degrees of freedom.

Generation of initial ion distribution in the longitudinal phase plane, generation of new model particle at losses are based on procedures for generation of individual ion co-ordinates and matching of the ion with the ring lattice in the generation position. Generation of the ion longitudinal co-ordinates in the case of barrier bucket application is realized in the following steps.

1. Initially the momentum deviation is generated in accordance with Gaussian law at standard deviation equal to the rms momentum spread.
2. For the given momentum deviation the maximum momentum deviation is calculated in accordance with the formula (1).
3. The period of the ion synchrotron oscillations is calculated in accordance with (2).
4. At given maximum deviation the values of the momentum deviation and longitudinal co-ordinate are calculated using equations of the phase-space trajectory at the moment of time uniformly distributed from 0 to T_s.

Repetition of this procedure is resulted in a stationary particle array (without oscillations of the particle density during synchrotron motion) with Gaussian distribution over the momentum deviation.

SIMULATION OF LONGITUDINAL MOTION

The Model Beam algorithm realizes Monte-Carlo method for solution of Langevin equation based on an assumption, that the integration step over time is sufficiently longer than the decoherence period (a few millions of revolutions). In this case the phase advance of betatron and synchrotron oscillations during the integration step is an arbitrary number. In the transverse phase space the betatron motion is simulated using linear transformation maps.

In the case of a barrier bucket application the period of synchrotron oscillation is determined by the particle momentum deviation. At low momentum spread it can be of the order of a few seconds (see, for example, Table 1 below). Correspondingly, the decoherence time can be compared or even longer than the step of the integration over time. To take into account this peculiarity of the synchrotron motion two algorithms were developed: at random and regular phase advance during the integration step.

At the random phase advance the amplitude of the particle momentum deviation is calculated from its actual momentum and longitudinal co-ordinate using formulae (6) and (7). Thereafter the phase of synchrotron oscillations is generated uniformly between 0 and 2π and new co-ordinate and momentum are calculated as functions of the phase.

At regular phase advance the phase of the synchrotron oscillations of the particle is calculated from its co-ordinate and momentum deviation. The phase advance for each particle is calculated from the period of its synchrotron oscillations as $\Delta\varphi = 2\pi \cdot \Delta t / T_s$, where Δt is the integration step. New particle coordinates are obtained from the phase trajectory equation.

EXAMPLE OF HESR SIMULATION

Possibilities of the new algorithms can be illustrated by example of the antiproton cooling simulation in High Energy Storage Ring of FAIR project (GSI).

One of the main goals of electron cooling application at the HESR is to reach equilibrium relative momentum spread at the level of 10^{-5} in the energy range from 2 to 8 GeV. Challenge of the project is to compensate a beam heating due to interaction with an internal hydrogen pellet target at the thickness of about $4\cdot10^{15}$ atoms/cm^2, which is required to obtain the design luminosity. The electron cooling system was designed in TSL for the cooling section length of 20 m and electron current up to 1 A. In [5] it is shown that this system permits to obtain equilibrium 90% relative momentum spread of the antiproton beam at the level of $4\cdot10^{-5}$.

An additional benefit in the beam quality can be provided by compensation of mean ionization energy loss in the target using a barrier bucket system. To prove this fact the 8.9 GeV/c antiproton beam dynamics was simulated at barrier bucket parameters listed in the Table 1. Number of the antiprotons was equal to 10^{10} and the cooling process was simulated with account of IBS.

Table 1: Parameters of barrier RF bucket used in the simulations.

Pulse width, T_1/T_0		0.1
Gap duration, T_2/T_0		0.7
Voltage amplitude	V	20
The barrier height, $\delta_{A,max}$		$1.14\cdot10^{-4}$
Rms bucket length at $\delta = 2\cdot10^{-5}$	m	405.4
Synchrotron period at $\delta = 2\cdot10^{-5}$	s	3.93

The transverse beam emittance was stabilized at the level of $5\cdot10^{-8}$ π·m·rad by the electron beam tilt in respect to the antiproton orbit. At 8 m of the beta-function in the target position it provides good overlap with the pellet target. Ionization energy loss in the target was simulated in accordance with Urban model [6] taking into account a probability of large fluctuations. The transverse particle momentum variation was calculated in accordance with plural scattering model.

Initial value of the rms relative momentum spread was chosen to $2\cdot10^{-5}$. First 20 seconds of cooling the momentum spread decreases to equilibrium and thereafter stays a constant during long period of time (Fig. 1). (The "sigma" at horizontal axis in the Figures 1, 2 corresponds to relative momentum deviation of $2\cdot10^{-5}$.)

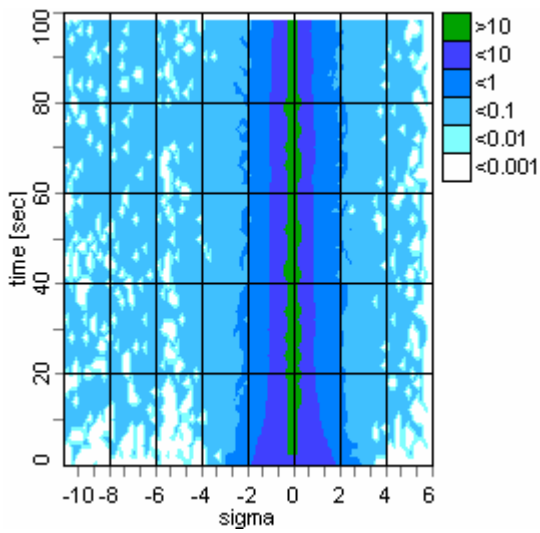

Figure 1: Beam momentum spread evolution during first 100 seconds of the electron cooling. The different colors indicate the relative particle number in logarithmic scale.

Inside the bucket the particle distribution over the momentum deviation (Fig. 2) is close to Gaussian at the rms width of about 10^{-5}. Long low energy tail (below momentum deviation of $-5\sigma_0$, which corresponds to the bucket height) is formed by the particles lost from the bucket. Intensity of the tail is below 10^{-3} and, in principle, it can be suppressed by increase of the voltage height.

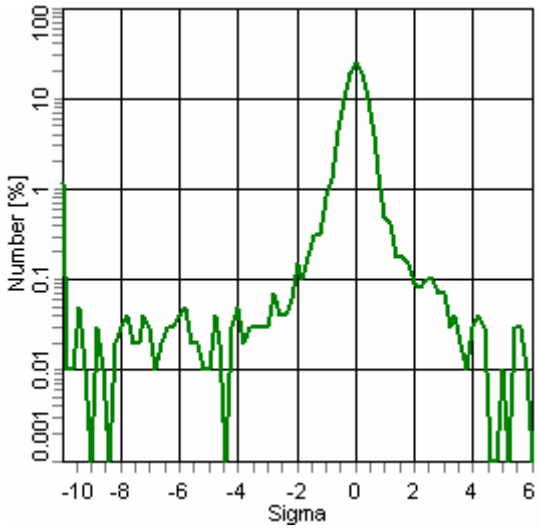

Figure 2: Ion distribution over the momentum deviation after 100 seconds of cooling.

From the particle distribution in the longitudinal phase plane presented in the Fig. 3 one can see that the particle density is practically uniform along the bucket.

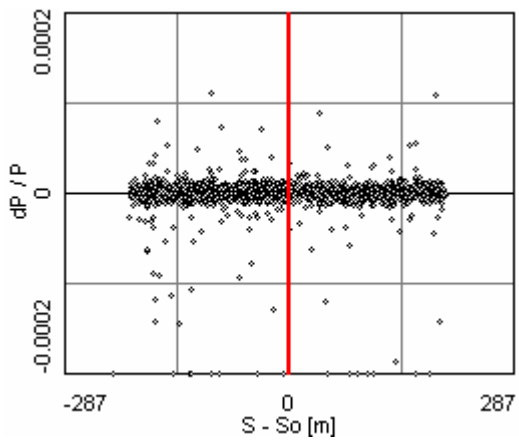

Figure 3: Particle distribution in the longitudinal phase plane after 100 seconds of cooling.

Comparison between cooling in the case of the coasting beam and the barrier bucket application shows that the barrier bucket system permits to reach the same value of the momentum spread at electron current value less by about 1.5 times. The burrier bucket system increases the bunching factor insufficiently, and permits to provide acceptable peak to mean luminosity ratio.

REFERENCES

[1] I. Meshkov et. al., "Study of High Energy Electron Cooling (2 MeV) and Stochastic Cooling with Different Internal Targets", final report, Dubna, 2007.

[2] T. Katayama et. al., "Simulation Study of Ion beam Accumulation with Moving Barrier Bucket assisted with Electron Cooling", these Proceedings.

[3] I. Meshkov et. al., NIM A 558 (2006), 325-328.

[4] "BETACOOL Physics Guide", BNL Tech Note C-A/AP/#262 (Nov. 2006).

[5] D.Reistad et. al., "Calculations on high-energy electron cooling in the HESR", these Proceedings.

[6] Application Software Group, Computing and Networks Division, GEANT Detector description and Simulation Tool, CERN Program Library Long Writeup W5013.

OPTIMIZATION OF THE MAGNET SYSTEM FOR LOW ENERGY COOLERS

A. Bubley, V. Panasyuk, V. Parkhomchuk ,V. Reva, Budker INP, Novosibirsk, 630090, Russia

Abstract

Aspects of magnet design and field measurements are discussed in the view of low energy coolers construction. The paper describes some engineering solutions for the magnetic field improvement which provides appropriate conditions for the cooling process as well as electron and ion beams motion.

INTRODUCTION

In installations of electron cooling, the electron beam passes from the cathode of an electron gun then through bending section to cooling solenoid and then up to absorbing collector in a continuous longitudinal magnetic field. Requirements of quality of a magnetic field are various for various parts of installation. Most they are high for cooling section - the central solenoid. Efficiency of the cooling process strongly depends on quality of the guiding magnetic field produced by the solenoid. Acceptable of cooling rate can be achieved, if non-parallelism of the field force lines, in relation to an axis of the solenoid $B_{\perp}/B_{\parallel}$ in a vicinity of ion trajectories does not exceed size of angular spread of the ion beam. The aspiration to achieve extreme high cooling rate produces rigid requirements to straightforwardness of the field force lines - from 10^{-4} for low energy electrons up to 10^{-5} and even less - for high energy. For achievement of these high requirements the special designs of the central solenoid, as well as a technique of correction of heterogeneity of a magnetic field and precision system of its measurement were developed.

CORRECTION OF THE MAGNETIC FIELD AT COOLING SECTION

Asymmetry of the magnetic system leads to inhomogeneous magnetic field rise at the cooling section. This effect can be eliminated by the inclination of the solenoid coils. As a step of a commissioning such a procedure was performed for EC-300 cooler (IMP China) at 0.75 kG longitudinal field. Also small-scale disturbances of the transverse field were minimized those originated from imperfectness of the coils alignment. Data obtained is shown in fig.1 – curve 1,[1].

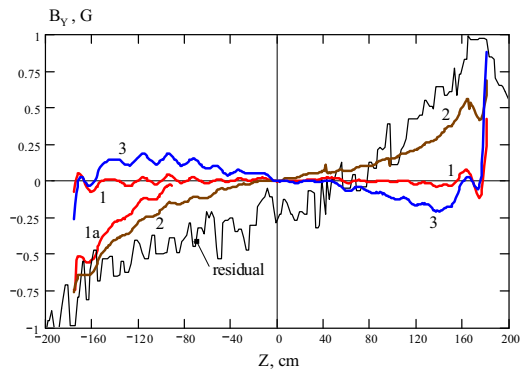

Figure 1: Vertical fields at cooling section of EX-300 measured at longitudinal field: curve 1: 0.75 kG, curve 2: 0.5 kG, curve 3: 1 kG. Curve 1a: 1-st switching on after return to a field of 0.75 kG. "Residual" – result of Hall probe measurements of the residual field.

However non-uniform vertical fields appeared to show up again at a change of the longitudinal field. Plots of the vertical field distribution are shown in Fig.1 (curves 1,2,3). It can be easily estimated that these fields have linear and cubic components. It is visible, that small-scale disturbances are proportional to a field. On the other hand horizontal component kept stably small independent on longitudinal field.

It appears, that (curve 1) at return from *1kG* to *0.75kG* the achieved field slickness is restored only after several turning on and off of the magnet system (normalization cycle). After 1-st turning on the vertical component is restored only in the central part of the solenoid (curve 1a). After normalization cycle in the solenoid it is formed rather steady and about a linear vertical residual field (curve 'residual' in Fig.1). Apparently, a course of curves 2 and 3, is determined by this residual field especially in the central part of the solenoid namely, inclination of the coils overcompensate the residual field at *1kG* an under compensate at *0.5kG*.

So, the technique of alignment of the field by coils inclination [2], [3] suits only for a fixed longitudinal field. Therefore special correctors of a linear and cubic field should be used for operative reaction to a change of a longitudinal field.

Measures to Enlarge Good Field Region

According to design requirements, effective length of cooling section has to be as close as possible to the mechanical length of the solenoid. Therefore effort should be made to enlarge good field region.

EC-40 (LEIR, CERN) was designed as a cooler with changeable longitudinal field, so its magnet system contains various corrections installed on the cooling solenoid [4].

Curve 1 in Fig.2 shows result of Hall-probe measurements performed at cooling solenoid after rough alignment of the coils [3]. Then couple of coils on both ends of the solenoid was inclined outwards by higher angles in comparison with regular part (curve 2). This distribution has expressed linear component which can be compensated with linear field corrector. Result of the improvement is shown in Fig.2 (curve 3).

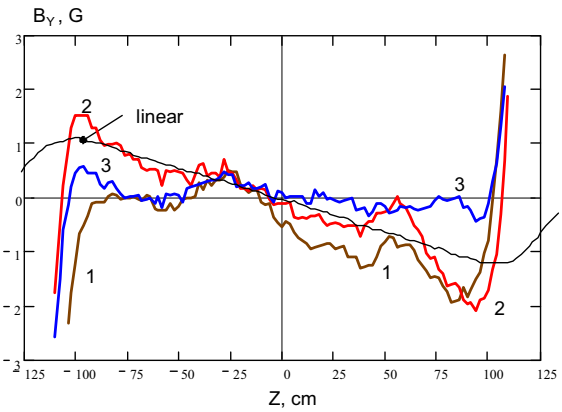

Figure 2: Vertical field before inclination of margin coils - 1, and after - 2, compensation with linear corrector; linear - a field of the linear corrector with an opposite current.

The results of Hall probe measurements are important from the point of view of further field adjustment because compass-based measurement system [5] has rather narrow dynamic range. Obtained amplitude of ±0.8G of transverse field components is sufficient for operation of the compass system in automatic mode. The laser beam of the measurement system was aligned on a geometrical axis of the solenoid. Some regular errors could arise due to misalignment between the beam and a magnetic axis, as well as the beam and a magnetic moment of the compass. Those errors can be eliminated with the help of vertical and horizontal steering coils with homogeneous field. With the help of techniques described transverse field components were reduced down to *±0.05G* at longitudinal field of *1kG* [4].

As a result the effective length of cooling section increased on *15-20 см*.

Magnetic Diaphragms

One of the methods to increase area of a good field inside the central solenoid is use of the magnetic diaphragms on joints of the solenoid and toroids. Figure 3 shows vertical components of a field on one of edges of the solenoid for two cases: 1 -with magnetic diaphragm and 2 - without it.

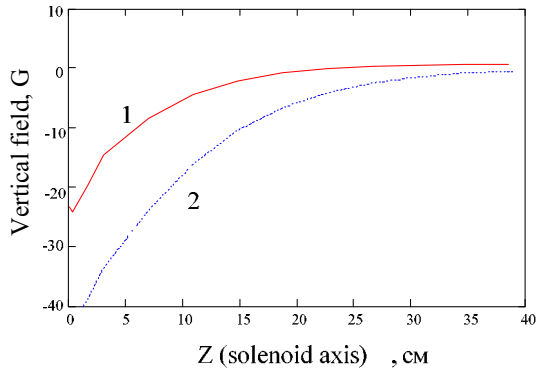

Figure 3: Vertical field distribution at solenoid and toroid junction: 1 - with magnetic diaphragm, 2 - without it.

Although diaphragms (so-called “magnetic mirrors”) provide significant improvement of uniformity of the field at the solenoid their use is complicated for several reasons. First, practically there is no enough room for their installation due to space required for installation of the vacuum chamber, heating jackets and thermal screen. On the other hand presence of the magnetic diaphragms increases influence of a residual field, which is strongly dependent on the sequence of switching on different sections of the magnet system.

ELECTRON TRAJECTORY CORRECTION AT BENDING SECTION

As well as the central solenoid, bending magnets (toroids) and solenoids of the gun and collector are constructed from flat, connected in series, coils. Mmagnetic yoke, serving as a mechanical skeleton for all units of magnetic system, weakly influences on the conducting field, closes a return magnetic flux. Magnetic diaphragms also are used on the transitions between the gun (or collector) solenoids and bending toroids. In this case is possible to correct a trajectory of movement of the electronic beam in ben.

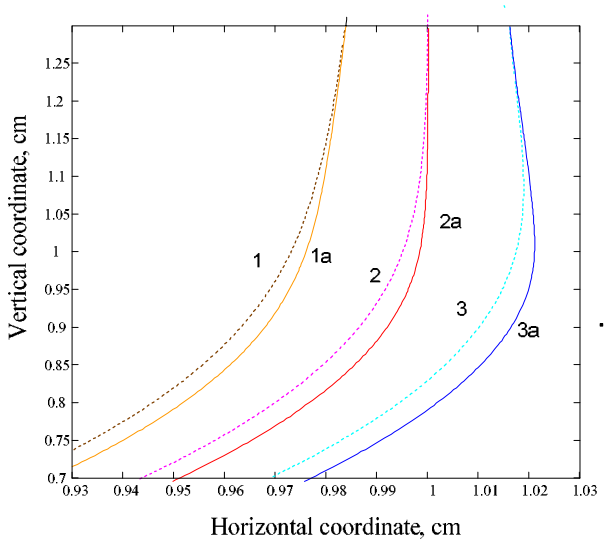

Figure: 4 Results of simulations of electron beam trajectory. 1,2,3 - without diaphragm 1a, 2a, 3a with diaphragm.

The matter is that the solenoid of a gun has small length, in comparison with diameter, and radial component of the field in the toroid displaces a beam practically right after its exit from the gun. As a result the electrons appreciably deviate from an axis of a bending toroid. Magnetic diaphragms significantly (Fig.4), correct the electrons orbit, reducing current load on correctors those area are rather weak because of remoteness from the axis.

However, when we deal with optimization of magnetic structure for installations on medium or high energy, it is important to take into account possible negative effects. Sharp change of curvature of the longitudinal magnetic field inevitably resulted from use of diaphragms, can result in increase of electrons transverse velocity, that is inadmissible from the point of view of cooling.

CORRECTION OF THE ION BEAM ORBIT

Passing through the magnetic system of electron cooler, an ion beam experiences impact due to strong vertical components of a magnetic field in bending toroids. Special dipoles are used for ion orbit correction. Magnets are designed under classical scheme; however their arrangement is a little bit unusual. Magnet yoke is introduced into bending toroid as shown in Fig.5.

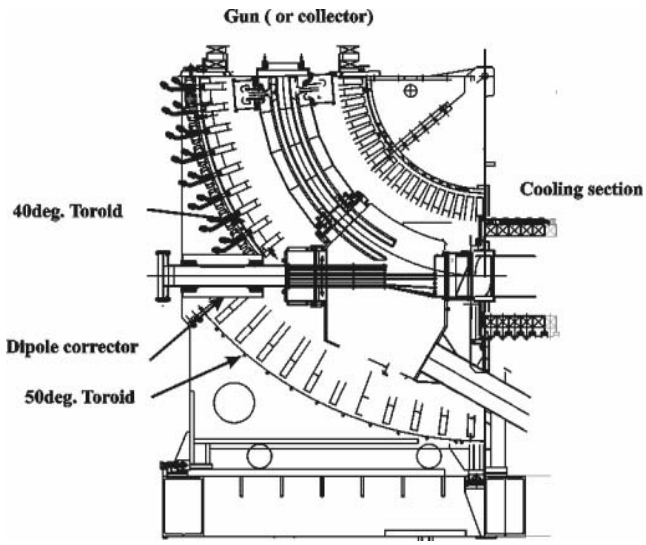

Figure 5: Dipole corrector inserted into 50 deg. bending section.

It allows reducing the cross-section of the vacuum chamber as well as mechanical length of the magnet system

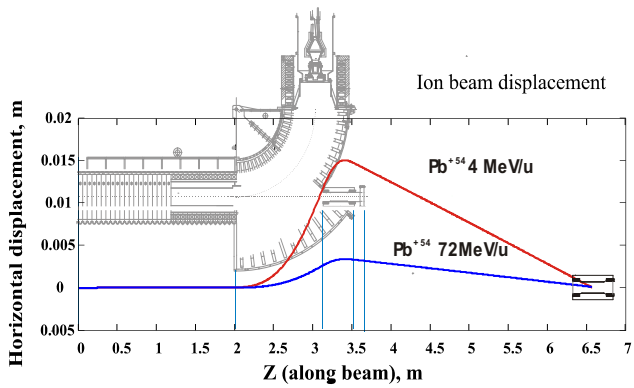

Figure 6: Scheme of correction of ion beam orbit.

The scheme of ion orbit correction of EC-40 cooler is shown in Fig.6. Plots represent horizontal displacement of ions at passage of magnet system of installation for energy of injection 4.2 MeV/nucleon (upper curve) and extraction 72 MeV/nucleon (lower curve). Having received displacement, the ion gets in dipole magnet where it is displaced in an opposite direction. The field of the dipole corrector is chosen so that particles have a small angle (10^{-3} rad.) on an exit from installation to return them into a stationary orbit by means of the additional correction established on a ring (it is schematically represented in the right part of figure 6).

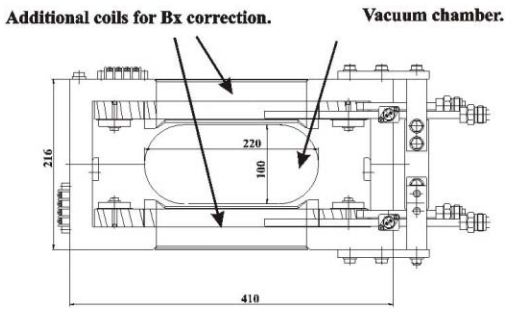

Figure 7: Design of the dipole corrector.

Passing the bending toroids, the ion beam experiences action of rather strong longitudinal and vertical field. It results in occurrence not only horizontal, but also vertical displacement. Actually, for a considered case it quite small (only 2 mm on energy of injection) so that can be compensated with the help of additional low-current coils wound over the of poles of the dipole corrector, as shown in Fig.7.

REFERENCES

[1] E. Behtenev et al., "Commissioning of Electron Cooler EC-300 for HIRFL-CSR", AIP 0-7354-0314-7/06/, p334.
[2] A.V. Bublei et al., "New Technology for Production of Precision Solenoid for Electron Cooling System", Proceedings of MEEC-98, Dubna, 1998, Russia.
[3] V. Bocharov et al., "Precise Measurements of a Magnetic field at the Solenoids for Low Energy Coolers", AIP 0-7354-0314-7/06/, p360.
[4] V. Bocharov et al., "First Tests of LEIR-Cooler at BINP", AIP 0-7354-0314-7/06/, p355.
[5] V.N. Bocharov et al., "The precise magnetic field sensor for solenoid for coolin section", Proceedings of the XVII Workshop on Particle Accelerators, Protvino, Russia, October 17-20, 2000.

COOLING IN A COMPOUND BUCKET

A. Shemyakin#, C. Bhat, D. Broemmelsiek, A. Burov, M. Hu
FNAL*, Batavia, IL 60510, USA

Abstract

Electron cooling in the Fermilab Recycler ring is found to create correlation between longitudinal and transverse tails of the antiproton distribution. By separating the core of the beam from the tail and cooling the tail using "gated" stochastic cooling while applying electron cooling on the entire beam, one may be able to significantly increase the over all cooling rate. In this paper, we describe the procedure and first experimental results.

INTRODUCTION

Presently, antiprotons in the Fermilab Recycler ring [1] are stored between rectangular RF barriers and are cooled both by a stochastic cooling system in the full duty-cycle mode (primarily in the transverse planes) and by a DC electron beam (primarily in the longitudinal phase-space). As the number of antiprotons, N_p, in the Recycler increases, the rate of stochastic cooling decreases according to $1/N_p$ [2]. In the case of electron cooling, the cooling strength does not depend on N_p, but it is significantly stronger on the core particles as compared to that in the tail region of the 6D-phase-space [3]. These properties combined result in a formation of a dense core but long tails and a poor beam life time. In this paper, we propose a technique of separating core and tail particles to combine advantages of both cooling techniques in the Recycler.

COMPONENTS OF THE SCHEME

Tail Correlation

Measurements in the Recycler have shown [4] that the longitudinal cooling force quickly drops at a radial offset inside the electron beam of ≤1 mm. Typical rms radius of newly arrived antiprotons from the Accumulator ring is about 2 mm. Consequently, particles with large transverse actions are only weakly affected by the electron cooling. Eventually, the tail of the momentum distribution is populated primarily with particles of large transverse action (see Fig.3 in Ref. [4]). Note that this feature is not observed in an antiproton beam cooled by stochastic cooling alone.

Compound bucket

The effect of tail correlation can be used for longitudinal separation of the core and tails by application of a so-called compound bucket. The scheme of the compound bucket is illustrated in Fig.1. Normally, the beam is stored between two rectangular barriers, labeled as #6 and #7 in Fig.1 in accordance with the internal Recycler system. In the compound bucket, two lower-width "mini-barriers"#3 and #4 create an additional step in the effective RF potential, so that only particles with a large energy offset travel between barriers #4 and #7. Below we refer to this area as to the tail region.

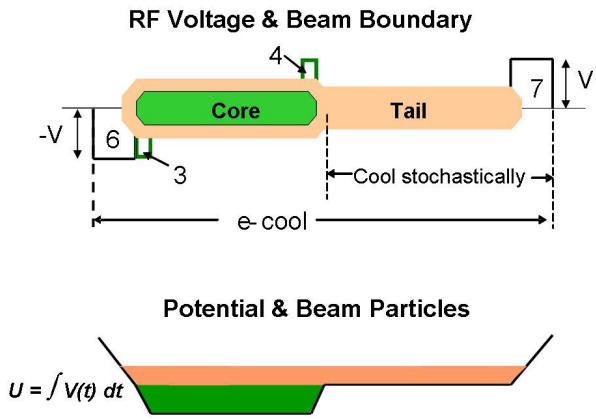

Figure 1: Scheme of the compound bucket. Horizontal axis shows the longitudinal phase (usually expressed as a time delay from the arrival of the bunch head) and corresponds to one revolution period. The top plot shows positions of RF barriers and tlongitudinal phase space of antiprotons (with vertical axis representing energy deviation). The bottom plot pictures corresponding effective RF potential.

Momentum Coating

The concept of the compound bucket was first introduced in Ref. [5] for the momentum coating injection scheme.

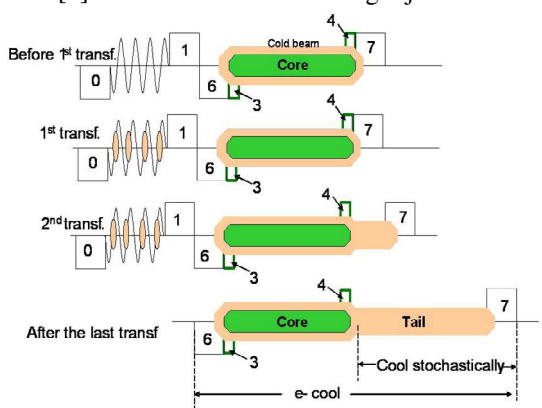

Figure 2: Injection with the compound bucket. RF forms and momentum distributions are shown for the case of two transfers.

In this scheme (Fig.2), the cold beam in the Recycler ring is kept between mini-barriers #3 and #4 while the new particles arriving from the Accumulator are injected in

* FNAL is operated by Fermi Research Alliance, LLC under Contract No. DE-AC02-07CH11359 with the United States Department of Energy.
#shemyakin@fnal.gov

between barriers #0 and #1 at the energy corresponding to the potential between main barriers #6 and #7 so that they "coat" the cold beam in the energy-phase space.

Gated Stochastic Cooling

In addition to operation in the full duty-cycle mode, the Recycler stochastic cooling system can be turned on for a part of the revolution period so that cooling is applied only for a portion of the circulating beam [6]. Below we will refer to such timing as "gating". In the described scheme, the transverse stochastic cooling system is gated only on the region between barriers #4 and #7. The height of the mini-barriers is chosen so that the density of antiprotons in the tail is noticeably lower than that in the core region. Hence, the stochastic cooling can be applied with a high gain that significantly speeds up transverse cooling where it is needed the most, i.e. for the newly injected antiprotons with large transverse emittances.

COOLING IN THE COMPOUND BUCKET

Figure 3 shows schematically the idea of cooling in the compound bucket. The goal is to put all antiprotons into the phase-space core (area A) as fast as possible. Electron cooling effectively drags particles with low transverse action from area D. Antiprotons in area C are subject to the gated stochastic cooling that squeezes them into area D. Intra-beam scattering, scattering on the residual gas, and other mechanisms present at regular operation continuously heat the core particles (we refer to this as natural heating). Transverse natural heating pushes them to area B, while longitudinal heating in the area between barriers #3 and #4 moves these antiprotons from area B to C. The latter move needs to be fast enough to avoid losing antiprotons from area B due to the transverse diffusion of all sorts. Because the natural heating rate was found to be too low, an external longitudinal heating is applied, so that eventually all particles spend most of their time in area A by completing the cycle shown in Fig. 3.

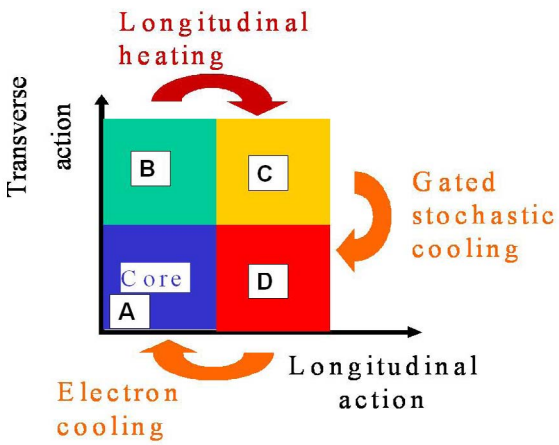

Figure 3: Illustration of cooling in compound buckets.

DIAGNOSTICS

Several types of diagnostics are used to analyze characteristics of the antiproton beam in the Recycler.

1. Flying wire (FW) is used to measure transverse emittances of the beam. Monitor signals originated from the interaction of the beam particles with carbon filaments are gated to a certain longitudinal region of the beam. The beam profiles from these signals are first fit to a Gaussian distribution (plus a linear function) to reduce the effect of noise on the measurements, and the rms width of the fitted curve is used to estimate the emittance. Such measurements were made for both horizontal and vertical planes. However, horizontal and vertical emittances in the Recycler usually are close to one another, and here. we report only the average emittance at different stages of cooling. When the FWs are gated to the core region (see Fig. 1), the data emphasize properties of the beam core; in this case the effect of the tail particles is small. Gating on the tail region gives data describing properties of the newly arrived antiprotons and high momentum particles escaped from the core.
2. Transverse and longitudinal Schottky pickups provide information about transverse emittances and the longitudinal momentum spread, either for the entire beam or for a specific region if gated. The un-gated emittances are measured to accuracy of ~ 10%. The ratio between 95% emittances measured with the Schottky detector and FW varied widely. For a stochastically–cooled beam, when the distribution is close to Gaussian, the ratio was 1.5, and we have not found a good explanation for this difference. The deeper is the effect of electron cooling, the higher the ratio, increasing up to a factor of 3. In the gated mode, an uncertainty in the beam intensity normalization added ~10% error to transverse emittance of the core and even a larger number for the tail.
3. A resistive wall current monitor (RWM) is used to measure the current density distribution along the bunch. An online application program (written by P. Derwent) calculates the portion of the antiproton beam populating the region between barriers #4 and #7, which gives a good representation of the longitudinal tail intensity. Combined analysis of RWM and RF signals allows restoration of the antiproton momentum distribution over the longitudinal action by so-called longitudinal phase-space tomography [7].
4. The main diagnostics for the number of antiprotons in the Recycler, the Direct Current Transformer (DCCT), was not functional in the period when the measurements were made. The available alternatives, a toroid and RWM, are AC coupled and sensitive to the beam temporal structure. As a result, no reliable data for the beam life time were available unless the beam loss rate was large.

HEATING PROCEDURES

Successful implementation of the scheme is dependent upon a viable method of additional longitudinal heating of the high transverse amplitude particles in the spatial core to move them into the spatial tail (transition from B to C in Fig. 3). A suitable technique has to provide an optimal balance first, between heating of core particles versus possible degradation of the life time caused by heating of particles in the tail, and second, between applied heating and available strength of electron cooling. Several heating techniques have been tested.

One of the methods was to turn the longitudinal stochastic system into a heating mode by removing the notch filter and gating the system to the core region. The test, however, showed a significant degradation of the beam life time.

Another heating technique was shaking the mini-barrier #4. By this method some growth of particle number in the tail region was observed without degradation of the life time. However, it was found to be quite inefficient. Synchrotron frequency of a particle in a barrier RF bucket is proportional to its momentum offset. Consequently, the synchrotron motion of the antiprotons with the momentum close to nominal is slow so that the particles experience infrequent collisions with the moving barrier and are weakly affected by such shaking. At the same time, hot particles can be heated even more that limits the speed and amplitude of shaking. So we abandoned this technique.

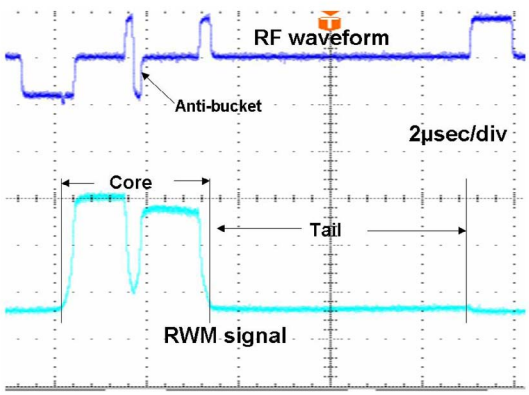

Figure 4: Heating with an anti-bucket. One revolution is shown.

So far, the most promising procedure is beam heating by an anti-bucket [8]. Two narrow barriers with opposite polarities are grown back-to-back in the middle of the core region (Fig. 4), creating a local maximum ("anti-bucket") of the effective potential. The anti-bucket was moved with a random delay in a random direction by 0.6 μs with the speed of 0.8 μs/s. When the anti-bucket is at rest, its provides reflection of antiprotons with 7 MeV/c momentum offset, while the corresponding "height" of the main barriers #6 and #7 is 16 MeV/c. Typically, the time of transition through the anti-bucket is much smaller than the total time of the anti-bucket motion. Hence, the high- offset particles fly through it without changing the momentum, while the low-offset antiprotons can pick up an additional momentum to be eventually transferred to the tail region.

MEASUREMENTS

Several sets of preliminary measurements, gradually approaching realization of the scheme described above, have been made. First, we cooled the antiprotons in the compound bucket with electron beam only with stochastic cooling turned off. In this case we found that the portion of particles in the tail area decreased rapidly until reaching equilibrium. This clearly indicated a move of antiprotons from area D to A as shown in Fig. 3. The transverse FW emittance of the particles remaining in the tail region decreased at the much slower rate than that of the core. This feature is consistent with the concept of the tail correlation in electron-cooled beam.

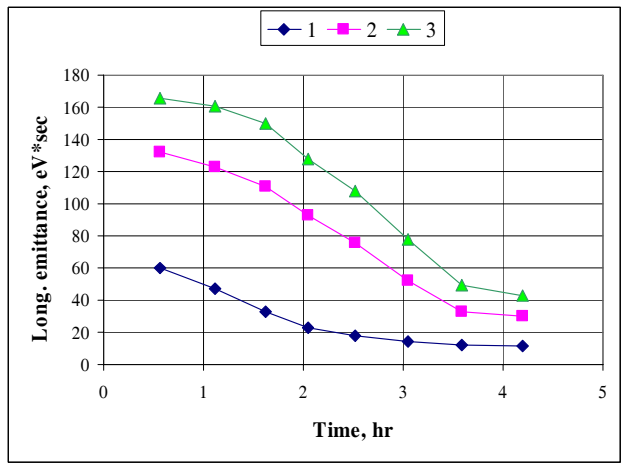

Figure 5: Evolution of the longitudinal emittance in the time of cooling in the compound bucket, restored with longitudinal tomography. The curves 1, 2, and 3 show emittance for 60%, 90%, and 95% of particles, correspondingly. N_p= 250·10^{10}. A 0.1 A, DC electron beam was on axis for the entire time of the experiment. The gated stochastic cooling was on during hours from 1.5 to 3.5.

In the next measurement, a gated transverse stochastic cooling was applied to the tail region. This resulted in a further decrease of the tail portion of antiprotons as well as in a decrease of the transverse emittance of particles there. In other words, longitudinal cooling rate of electron cooling was significantly enhanced by the gated stochastic cooling (Fig. 5). The portion of tail area particles was decreased to the level of ~5% of the total beam. However, no noticeable change in the Schottky emittance of the core was observed, even though FW showed observable decrease in core emittance. Therefore, we concluded that the naturally occurring longitudinal diffusion for the particles in area B is too weak to overcome the diffusion from A to B.

Further, the injection with momentum coating was adopted. FW emittance of the tail area was larger than that for the core even before applying electron cooling. This is

in agreement with higher emittances of newly injected antiprotons.

Finally, all manipulations were made in accordance with the complete scheme presented in Fig. 3. The total amount of antiprotons in the Recycler used for this experiment was about $230 \cdot 10^{10}$ after beam injections. Out of that, the newly injected beam in three transfers was about $30 \cdot 10^{10}$. Gated stochastic cooling was turned on soon after the injection had been done, and at the same time the electron beam was moved on axis (normally at this number of antiprotons the electron beam is kept at the vertical offset of 2 mm to avoid overcooling and preserve the life time [9]). After half an hour, the anti-barrier was grown, and core region was heated for an hour. At the end of the process, the portion of the hot area particles was found to increase and slowly went up from 5% to ~10%.

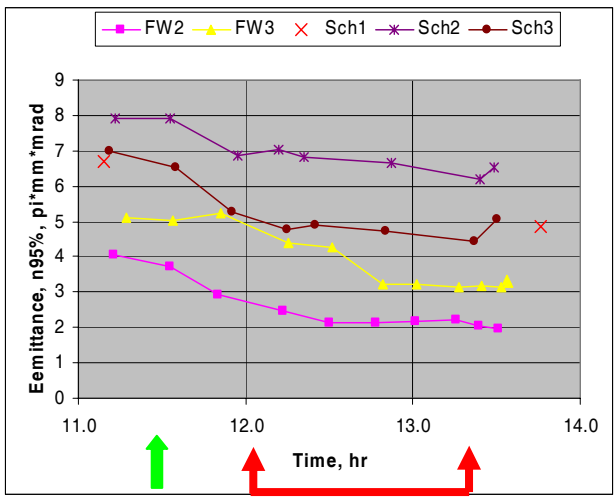

Figure 6: Evolution of emittances during cooling in the compound bucket. FW and Sch indicate average emittance measured with flying wires and Schottky detectors, respectively. Indexes 1, 2, and 3 refer to the entire beam, core region, and tail region, respectively. The single arrow indicates time of turning on the gated stochastic cooling and moving the electron beam on axis. The double-arrow shows time of applying heating by moving anti-bucket.

Evolution of measured FW and Schottky emittances during the final experiment is shown in Fig. 6. For the first time, we observed a significant, ~20%, decrease in the core Schottky emittance as well as all qualitative features of cooling cycle shown in Fig. 3. We hope that eventually it should result in an improvement of the beam life time while providing fast cooling. We plan to repeat the measurements with a new DCCT which is being currently installed in the Recycler.

CONCLUSION

Antiproton beam cooling in the compound bucket appears to be a promising way of using both electron and stochastic cooling systems in the Recycler to their maximum strengths. All components of the scheme have been tested successfully. The final judgment about usefulness of the scheme will be made when the measurement are repeated with a good diagnostics for the beam life-time.

ACKNOWLEDGMENTS

The authors are grateful to P. Derwent for providing with the online application program to measure amount of beam in the tail region using RWM signal and to C. Gattuso for his help with operational issues. Our special thanks are due to V. Lebedev for many useful discussions. Run coordination team's cooperation is acknowledged and appreciated.

REFERENCES

[1] G. Jackson, Fermilab-TM-1991, November, 1996; P.Derwent et al., Status of the Recycler Ring, this conference.
[2] D. Moehl, Stochastic cooling, CERN-95-06, 587.
[3] L. Prost and A.Shemyakin, PAC2007 (2007), p 1715.
[4] A.Shemyakin et al., Electron cooling at the Recycler Cooler, this conference
[5] C. M. Bhat, Proc. of RPIA2006, KEK Proceedings 2006-12, January 2007, p 45.
[6] D.R. Broemmelsiek et.al, EPAC2004 (2004) p 794.
[7] A. Burov, Beams Doc. 2866-v1 (2007) (unpublished); http://beamdocs.fnal.gov/AD-public/DocDB/ShowDocument?docid=2866
[8] C. M. Bhat, Beams Doc. 2355-v1 (2002) (unpublished); http://beamdocs.fnal.gov/DocDB/0023/002355/ 001/RR-a-controlled-ecool-v2a.pdf.
[9] L. Prost et.al, Electron cooling status and characterization at Fermilab's Recycler, this conference

ELECTRON COOLING IN THE RECYCLER COOLER

A. Shemyakin #, L.R. Prost, FNAL*, Batavia, IL 60510, U.S.A.
A. Fedotov, BNL, Upton, NY 11973, USA
A. Sidorin, JINR, Dubna 141980, Russia

Abstract

A 0.1-0.5 A, 4.3 MeV DC electron beam provides cooling of 8 GeV antiprotons in Fermilab's Recycler storage ring. The most detailed information about the cooling properties of the electron beam comes from drag rate measurements. We find that the measured drag rate can significantly differ from the cooling force experienced by a single antiproton because the area of effective cooling is significantly smaller than the physical size of the electron beam and is comparable with the size of the antiproton beam used as a probe. Modeling by the BETACOOL code supports the conclusion about a large radial gradient of transverse velocities in the presently used electron beam.

INTRODUCTION

Since the first demonstration of relativistic electron cooling in the Recycler Electron Cooler (REC) [1], cooling measurements of various types have been performed. In some, the cooling force was derived from the longitudinal distribution of the antiproton beam being in equilibrium with either IBS [1] or an external wide band noise source [2]. The most relevant figures of merit for operation, the cooling rates, were measured as changes of the time derivative of the longitudinal momentum spread and transverse emittances, when the electron beam is turned on [3]. In this paper, we concentrate primarily on drag rate measurements. First, we analyze the conditions, for which the measured drag rate correctly represents the cooling force experienced by a single antiproton, then present the results of the measurements, and compare them with simulations.

DRAG RATE AND COOLING FORCE

In a drag rate measurement, the electron energy is changed by a jump, and the time derivative of the average antiproton momentum, $\dot{\bar{p}}$, is recorded [4]. For a pencil-like antiproton beam with a small enough momentum spread, this derivative is equal to the cooling force applied to an antiproton with momentum offset $\delta p = \bar{p} - p_0$, where p_0 is the equilibrium momentum. Generally speaking, for the beam with finite emittances, the drag rate is given by integration over the 6D antiproton and electron distributions. For typical REC parameters, several simplified assumptions are valid:

- in the time of a drag rate measurement, the transverse antiproton distribution does not change, so that transverse diffusion and cooling can be neglected for the longitudinal dynamics;
- the antiproton beam is axially symmetrical in the cooling section;
- direct effect of the transverse antiproton velocities is negligible, because the transverse electron velocities are much larger. Therefore, the cooling force depends on the radial position of an antiproton with respect to the electron beam center r but not on the antiproton transverse velocity.

In this case, the drag rate can be written as an integral of the non-magnetized cooling force over the radial and momentum antiproton distribution as follows:

$$\dot{\bar{p}} = \int\int F(\delta W, \alpha_e, j_e, \Delta p) \cdot f(p,r)\, 2\pi \cdot r\, dr\, dp\,, \qquad (1)$$

where the cooling force is shown dependent on the electron energy spread δW, angle α_e, and current density j_e averaged over the length of the cooling section, as well as on the antiproton momentum offset $\Delta p = p - p_0$. Similarly, changes of the r.m.s. momentum spread $\sigma_p^2 = \int\int (p-\bar{p})^2 \cdot f(p,r)\, 2\pi \cdot r\, dr\, dp$ are given by

$$\frac{d}{dt}\sigma_p^2 = D + 2\int\int F(\delta W, \alpha_e, j_e, \Delta p) \cdot f(p,r) \cdot 2\pi \cdot r\, dr\, dp\,, \qquad (2)$$

where D is the longitudinal diffusion coefficient.

Dependence of the cooling force on the radius comes from the radial distributions of the current density and angles, while the electron energy spread is determined primarily by the terminal voltage fluctuations. If the electron beam is cold, its current density distribution in the cooling section follows the one on the cathode $j_{cath}(r_{cath})$:

$$j_e(r) = j_{cath}\left(r \cdot \sqrt{\frac{B_{cs}}{B_{cath}}} \right) \cdot \frac{B_{cs}}{B_{cath}}\,, \qquad (3)$$

where B_{cs} and B_{cath} are the magnetic field magnitudes in the cooling section and at the cathode, respectively.

Gun simulations and Eq.(3) give for j_e a distribution close to parabolic in the main portion of the beam

$$j_e(r) \approx j_0 \cdot \left(1 - \frac{r^2}{a^2}\right), \qquad (4)$$

with $j_0 = 0.96$ A/cm^2 and $a = 2.9$ mm.

Angles are composed of a component α_0 constant across the beam (associated with thermal velocities and dipole perturbations in the cooling section magnetic field) and a component linear with radius (caused by envelope scalloping), added in quadratures,

* FNAL is operated by Fermi Research Alliance, LLC under Contract No. DE-AC02-07CH11359 with the United States Department of Energy.
# shemyakin@fnal.gov

$$\alpha_e^2 = \alpha_0^2 \cdot \left[1+\left(\frac{\alpha_b r}{\alpha_o r_b}\right)^2\right] \equiv \alpha_0^2 \cdot \left[1+\left(\frac{r}{b}\right)^2\right]. \qquad (5)$$

Taking into account that the first derivative of both above distributions is zero on axis, the first terms of the Tailor expansion of the cooling force over radius and momentum give

$$\dot{\bar{p}} \approx F(\delta p,0) + \frac{\partial^2 F(\delta p,0)}{\partial p^2}\cdot\frac{\sigma_p^2}{2} + \frac{\partial^2 F(\delta p,0)}{\partial r^2}\cdot\frac{\sigma_r^2}{2} \qquad (6)$$

$$\sigma_r^2 = \int\int r^2 \cdot f(p,r)\, 2\pi \cdot r\, dr\, dp$$

The drag rate is close to the cooling force experienced by an on-axis antiproton,

$$\dot{\bar{p}} \approx F(\delta p,0), \qquad (7)$$

when the terms with second derivatives are small. With the assumption that Eq.(7) was valid, the drag rate data $\dot{\bar{p}}(\delta p)$ presented in Ref.[4] (reproduced as data Set 1 in Fig.2 below) were fitted to the non-magnetized formula with a constant Coulomb logarithm L_c outside of the integral [5], and the second derivatives were calculated. For typical parameters (δp = 1-20 MeV/c, $\sigma_r \sim$ 0.5 mm), the contribution of the second derivative terms in Eq.(6) is below 10% if $\sigma_p < 0.4$ MeV/c and the coefficient b from Eq.(5) is >2 mm. While the first restriction is comparatively easy to fulfill for the typical number of antiprotons in these measurements ($N_p \sim 4\cdot10^{10}$), we were not able to extract the correct value of b from direct measurements of the electron beam properties. However, this value can be roughly estimated from the radial dependence of the drag rate.

DRAG RATE MEASUREMENTS

The drag rates measured as a function of the parallel offset between the electron and antiproton beams are shown in Fig.1. ε_{Sch} and ε_{FW} indicate emittances measured with Schottky detectors and flying wires, correspondingly, in π mm·mrad, normalized, 95%, averaged for vertical and horizontal. The beta-function in the cooling section is 30 m. The solid curve in Fig.1 is $\propto\left[1-(r/a)^2\right]/\left[1+(r/c)^2\right]$ with a= 2.9 mm, c= 1.15 mm and is shown for visual representation. The values of σ_r are estimated from ε_{FW} assuming a Gaussian distribution (unless noted otherwise).

The width of the measured distributions is significantly lower than 2 mm required for Eq. (7) to be valid. Indeed, for nearly identical electron beam parameters and, therefore, the same cooling force, the drag rate changes significantly with a decrease of the antiproton beam size. Most likely, the frequently observed effect of a decrease of the drag rate within a set of measurements (see sets 1 and 2 in Fig.1) is related to the creation of long low-intensity transverse tails that affect the drag rates, and which are measured with the Schottky detectors but not in ε_{FW}, which is extracted from the high-background flying wire signals. Because the width of the curves of Fig.1 is comparable with the antiproton beam size, the radial dependence of the cooling force should be even sharper, so that at least $b \le 1$ mm.

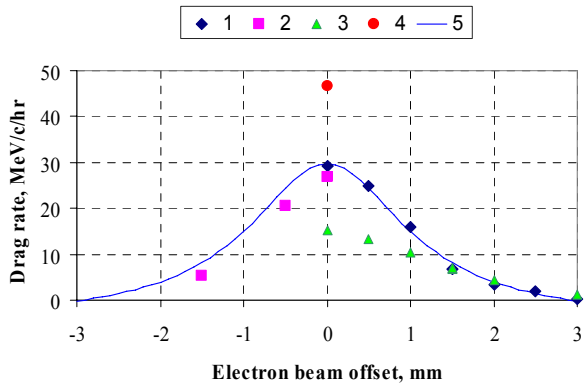

Figure 1: Drag rate as a function of the electron beam offset. Voltage jump was 2 kV, I_e = 0.1 A, $N_p = 4\cdot10^{10}$. Set 1: the antiproton beam was scraped to the radius in the cooling section of 1.1 mm, 25 min prior to the measurement. Set 2: negative offsets measured the same day 2 hours after the scrape. During both measurements, ε_{FW} = 0.3-0.7 ($\sigma_r \sim$ 0.5 mm). Set 3: data of Feb. 2006, taken several hours after scraping. ε_{Sch} = 1.5-3. Point 4: drag measurement immediately after scraping to 1.1 mm. $\varepsilon_{FW} \sim$ 0.1-0.2 ($\sigma_r \sim$ 0.3 mm).

Data showing the dependence of the drag rate on the value of the voltage jump (re-calculated to δp in Fig.2) exhibit the same trend of an increasing drag rate for lower antiproton emittances. The data can still be fitted to the simple non-magnetized model (Table 1).

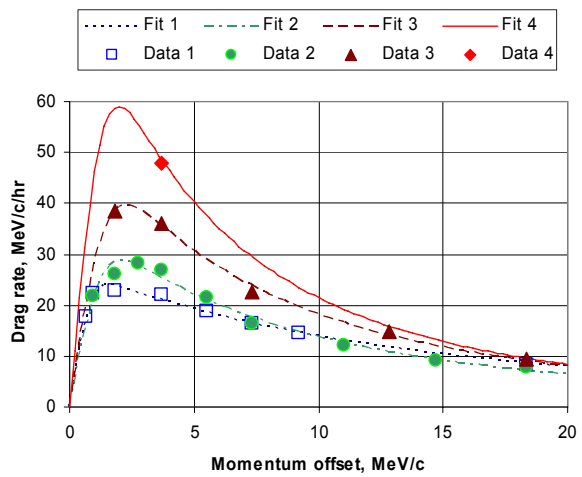

Figure 2: Longitudinal cooling force (negated) as a function of the antiproton momentum deviation. In all measurements, I_e=100 mA, on-axis. In sets 2÷4, transverse stochastic cooling was applied all time.

Table 1: Fitting parameters for the data shown in Fig.2 using the non-magnetized formula with a constant $L_c = 12$ outside of the integral.

Set	Date	Fitting parameters			Comments
		δW, eV	j_e, A/cm^2	α_e, mrad	
1	6-Feb-2006	370	1.1	0.20	No scraping. ε_{Sch} =1-2
2	3-Jul-2007	550	0.60	0.12	4 hrs after scraping. ε_{FW}= 0.3-0.7
3	24-Jul-2007	620	0.71	0.11	Scraping for each point. ε_{FW}< 0.5
4	3-Jul-2007	550	0.64	0.09	After scraping to 1.1 mm

One of the consequences of the unevenness of the electron beam properties is an ineffective cooling of antiprotons with large transverse actions. Over time, this effect creates a strong correlation between the longitudinal and transverse tails of the antiproton distribution. Direct evidence is presented in Figure 3, showing a significant decrease of the momentum distribution width in the time of vertical scraping. Note that dispersion in the location of the scraper is small (~10 cm), and this effect was not observed while scraping a stochastically-cooled beam. This fact has operational consequences for the Recycler (see Ref. [6] and [7]).

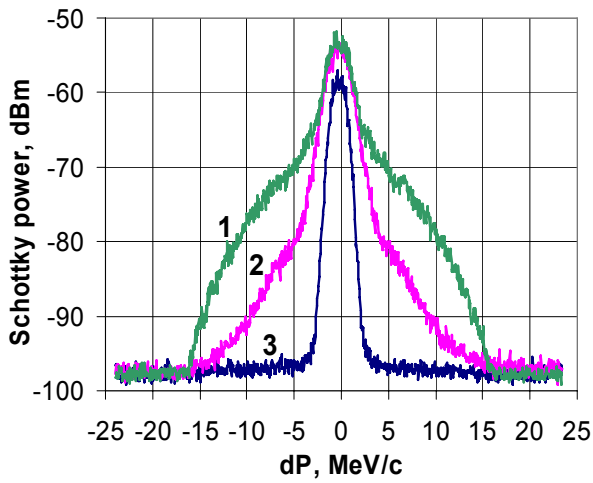

Figure 3: Evolution of the longitudinal 1.75 GHz Schottky profile of a deeply electron-cooled antiproton beam in the time of vertical scraping. For the curves 1, 2, and 3, the number of antiprotons, in units of 10^{10}, is 26, 20, and 4, and the offset of the vertical scraper re-calculated into a cooling section-equivalent position is 5.9, 2.1, and 1.7 mm, correspondingly. Before the scrape, antiprotons were cooled with a 0.1 A electron beam for ~ 40 min. $\varepsilon_{FW} = 0.7$ π·mm·mrad (95%, n) at the start of the scrape.

COMPARISON WITH BETACOOL

The measured cooling rates of an operational-intensity antiproton beam reported in Ref. [3] were compared with BETACOOL [8] simulations (Figure 4). For these simulations, the measured drag rate (Set 1 in Fig.2) was interpreted as a cooling force and fitted to the non-magnetized formula with the Coulomb logarithm inside the integral. The fitted parameters were found to be $\delta W = 300$ eV, $\alpha_e = 0.11$ mrad, and the beam size a in Eq.(4), 3.5 mm for a 100 mA beam. These parameters were used to predict the cooling rates where the diffusion coefficients were adjusted to fit the slopes obtained before electron cooling was applied and the gradient of the angular spread was tuned to match the longitudinal rate (which gives $b = 2.1$ mm). The transverse cooling rate measured with flying wires was higher than the simulated one by a factor of two. The agreement was considered reasonably good because the transverse rate measured at the same time with Schottky monitors was almost 3 times lower than the FW's, and we do not have a complete explanation for this.

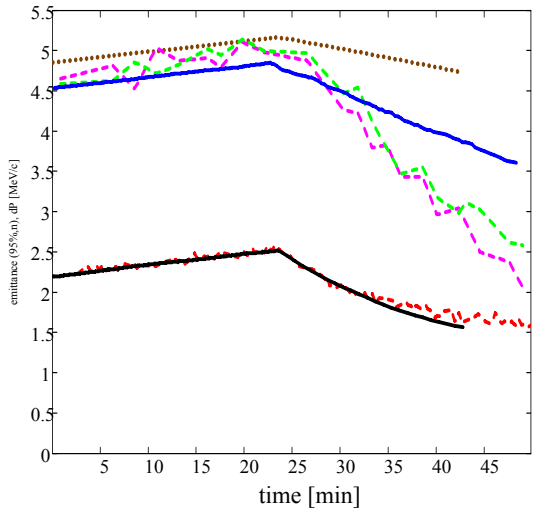

Figure 4: Comparison of measured cooling rates with simulation by the BETACOOL code. Set 1 (lower curves): momentum spread - solid black line (simulations); dash red line (measurements). Set 2 (upper curves): emittance - dashed pink and green lines (FW horizontal and vertical measurements), solid blue line (simulations with Gaussian fit); dotted brown line (simulation with rms of full distribution with non-Gaussian tails). Electron beam was turned on at 23 min.

The evolution of the longitudinal profiles in a set of drag rate measurements at various electron beam currents was simulated as well. Fitting the data within measurement errors for both $\dot{\bar{p}}$ and $\dot{\sigma}_p$ required $\alpha_0 = 0.09$ mrad and $b = 0.35$ mm. While these differ significantly from our previous estimations of the electron beam properties (for example, [4]), these numbers are in agreement with the data presented in the previous chapter and with recently found indications of large envelope

oscillations in the cooling section [7]. If correct, this interpretation means that the cooling force of an antiproton on axis can be noticeably higher than the measured drag rates and that a decrease of the angle gradient by careful adjustment of the envelope oscillations can increase the effective cooling rate in operation significantly.

CONCLUSION

1. The drag rate is equal to the cooling force experienced by a single antiproton when the electron beam properties are nearly constant across the antiproton beam. Analysis of the drag rate measurements show that this condition is not fulfilled in the Recycler cooler.
2. Most likely, the portion of the electron beam where electron cooling is effective is significantly decreased because of a large radial gradient of the electron transverse velocities.
3. Careful adjustment of envelope oscillations may eliminate that gradient and increase the cooling rates by several times.

ACKNOWLEDGMENTS

We are grateful to the entire Recycler department for the help with measurements and many discussions.

REFERENCES

[1] S. Nagaitsev *et al.*, Phys. Rev. Lett. **96**, 044801 (2006)
[2] D.R. Broemmelsiek and S. Nagaitsev, Proc. of EPAC'06, Edinburgh, UK, June 26-30, 2006, p.1241
[3] L.R. Prost and A.Shemyakin, Proc. of PAC'07, Albuquerque, U.S.A., June 2007, p. 1715.
[4] L. Prost *et al.*, in Proc. of HB2006, Tsukuba, Japan, May 29-June 2, 2006, WEAY02, p 182
[5] Ya.S. Derbenev and A.N. Skrinsky, Particle Accelerators **8** (1977) 1
[6] L.R. Prost *et al.*, this conference
[7] A. Shemyakin *et al.*, this conference
[8] I.N. Meshkov *et al.*, Physics guide of BETACOOL code, v.1.1, BNL note C-A/AP#262

BEAM-BASED FIELD ALIGNMENT OF THE COOLING SOLENOIDS FOR FERMILAB'S ELECTRON COOLER*

L.R. Prost#, A. Shemyakin, FNAL, Batavia, IL 60510, U.S.A.

Abstract

The cooling section of FNAL's electron cooler (4.3 MeV, 0.1 A DC) [1] is composed of ten (10) 2 m-long, 105 G solenoids. When it was first installed at the Recycler ring, the magnetic field of the cooling solenoids was carefully measured and compensated to attain the field quality necessary for effective cooling [2]. However, the tunnel ground motion deteriorates the field quality perceived by the beam over time. We have developed a technique which uses the cooling strength as an indication of the relative field quality and allowing us to re-align the longitudinal magnetic field in the successive solenoids of the cooling section assuming that the transverse component distribution of the field within each solenoid has not changed.

INTRODUCTION

For electron cooling purposes, a cold (i.e. with low transverse velocities, or angles in the lab frame) electron beam must be generated, transported to the cooling section (CS), where electrons interact with the particles that need cooling, and must remain cold until the beam exits the CS. While there are many sources contributing to the total rms angle in the beam [4], having a magnetic field in the CS with a large transverse component would prevent any efficient cooling. Assuming that all solenoids were perfectly aligned, we estimated that the field quality achieved for the compensated magnetic field lead to a total rms angle of 50 μrad for the electron beam [2]. However, we observed its deterioration over time, which needed to be corrected.

In this paper, we present our observations of the field degradation, and described the procedure we developed to correct it (different in nature than the one proposed in Ref. [3]), using the cooling strength as a diagnostic for the 'straightness' of the field. Results of this method are discussed.

OBSERVATIONS

Once the compensation of the magnetic field has been optimized and set, the electron beam trajectories in the cooling section should remain the same for fixed initial conditions of the centroid. However, over several months, we find that the trajectories get perturbed. This is illustrated in Figure 1, which shows the difference of trajectories taken a few months apart, and where one set of trajectories was obtained after the field had been re-aligned for the first time using the procedure we will describe. Beam position monitors (BPM) are located between each solenoid, with the first BPM being at the entrance of the first solenoid. On Figure 1, '0 cm' is a reference point outside of the first solenoid.

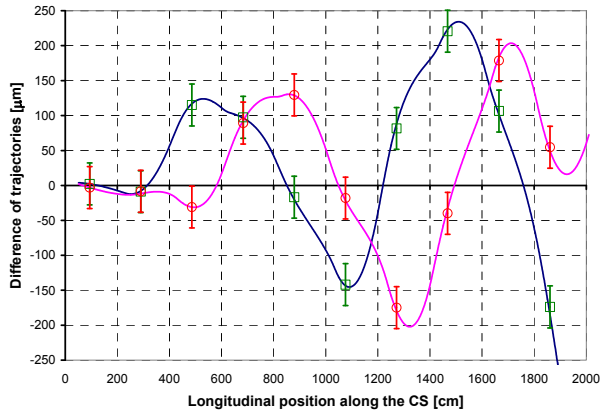

Figure 1: Difference of trajectories taken 3 months apart. Green squares: Horizontal; Red circles: Vertical. I_b = 100 mA, on-axis. The solid lines are fitted trajectories using the measured magnetic fields and solenoid-to-solenoid magnetic offsets as fitting parameters.

Note that the trajectories are taken for the same beam current (100 mA) and initial conditions where the beam is so-called 'on-axis', meaning that, ideally, trajectories coincide with the antiprotons central orbit. Moreover, the beam position monitors (BPM) are calibrated such that the antiprotons central orbit corresponds to zero position after the calibration procedure. The BPMs typically move, randomly from BPM to BPM, by 50 μm rms for all BPMs (100 μm in the worst BPM) over one year [5]. On the other hand, the electronic drift is <3 μm rms for all the BPMs (± 10 μm peak-to-peak in the worst BPM) over several weeks [5]. Both sources of error are about 5 times (or more) smaller than the effect shown on Figure 1.

PRINCIPLE OF THE METHOD AND PROCEDURE

The reason for the beam trajectories to change with time is likely because of ground motion in the tunnel, which moves the solenoids independently to one another, so that they appear inclined to a beam going through (Figure 2). Because each solenoid behaves like a rigid object [6], we can assume that the transverse component distribution of the magnetic field within each solenoid does not change. Hence, as illustrated in Figure **2**, the beam experiences a transverse magnetic field, $B_\perp$, when it travels from one solenoid to the next and oscillates in a fashion consistent with the trajectories shown in Figure 1.

Changing currents in all correctors in a solenoid by the same amount creates a nearly constant dipole field

* Operated by Fermi Research Alliance, LLC under Contract No. DE-AC02-07CH11359 with the United States Department of Energy
# lprost@fnal.gov

offset $\Delta B_\perp$, equivalent to tilting the solenoid. Hence, the goal of the procedure is to find and apply the proper $\Delta B_\perp$'s that will cancel out $B_\perp$'s. The first and most challenging step of the procedure is to align the field in the first solenoid, i.e. to make sure that the beam enters and exits on-axis with a zero angle with respect to the longitudinal magnetic field, B_{z0}. Then, merely zeroing the position in the remaining BPM's of the CS one by one by adjusting $\Delta B_\perp$ ensures that the accompanying field is straight.

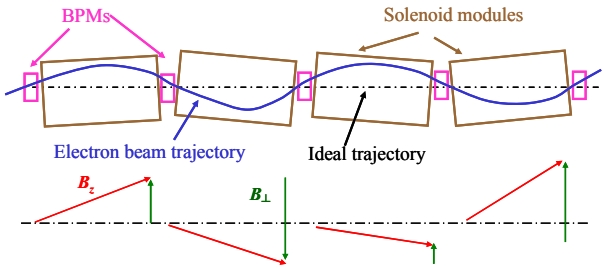

Figure 2: Illustration of the CS with inclined solenoids and corresponding 'transverse dipole offsets'.

To align the field in the first solenoid, we rely on the sensitivity of the cooling force to the electron angle. To first order, the cooling force is proportional to $1/\alpha^2$, where α is the total rms angle of the electron beam. We then assume

$$\alpha^2(z) = \alpha_T^2 + \alpha_D^2(z) \qquad (1)$$

where α_T is the non-coherent, temperature-like component of the angle and α_D, the component resulting from the solenoid tilts. If the positions at the entrance and the exit of the solenoid are fixed to zero (by a dedicated control program using upstream correctors), the trajectory within the solenoid is close to parabolic and, in this approximation, we can analytically calculate the average cooling force, $<F>$, and express the ratio

$$\frac{<F>}{F_{Max}} = \frac{\arctan(\alpha_0/\alpha_T)}{\alpha_0/\alpha_T} \qquad (2)$$

where α_0 is the initial angle of the beam w.r.t. B_{z0} and F_{Max} is the maximum cooling force (when the initial angle is zero). Using Eq. (2), if we estimate that α_T = 100 μrad and that changes of the cooling force of the order of 10% can be resolved, we can expect to reduce α_0 to 50-60 μrad. This is of the same order as our best estimate for perfectly aligned solenoids [2], which would imply that the total angle resulting from field imperfections would be of the order of 70 μrad (angles added in quadrature).

We can use two types of measurements to evaluate the cooling force while varying α_0 (i.e. varying $\Delta B_\perp$): cooling rate measurements [7] or drag rate measurements by the voltage jump method [4]. But, since the goal of these measurements is to maximize the cooling force in the first solenoid only, a preliminary step is to adjust the beam trajectory such that the solenoids downstream of the first one do not contribute to cooling. This is achieved by using the first few correctors of the second solenoid to kick the electron beam away from the axis by 3-4 mm. Then, evaluation of the cooling force is carried out for one direction at a time (i.e. first vary the dipole correctors in the horizontal direction, find the optimum, then repeat in the vertical direction). We typically go through two iterations, the second one with smaller steps for the dipole setting offsets.

SAMPLE MEASUREMENTS

With the Cooling Rate Method

For the cooling rate method [7], the momentum spread as a function of time is measured for various dipole corrector settings. The slope of a linear fit to the data is what defines the cooling/heating rate. Figure 3 shows the longitudinal cooling/heating rate measured as a function of the dipole correctors offset in the vertical direction. The momentum spread is measured using a 1.75 GHz Schottky detector, and each slope is determined after staying 15 minutes at a fixed corrector set point.

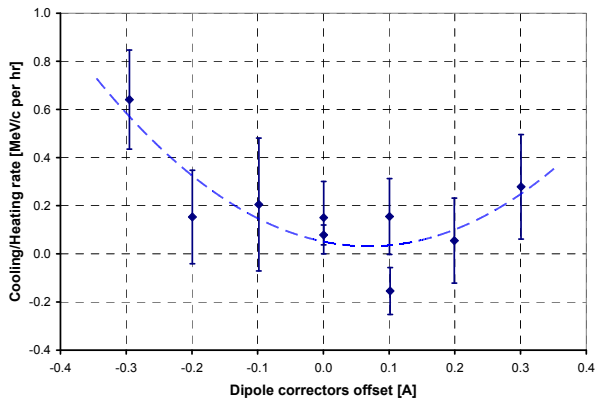

Figure 3: Cooling/heating rate as a function of the dipole correctors offset for the first solenoid (vertical, i.e. horizontal field). I_b = 200 mA, on-axis. N_p = 44×10^{10}, 6.1 μs bunch. Error bars are the statistical errors of the fit (1σ) when extracting the slope from the raw data. The dashed line is an arbitrary polynomial fit (2nd order).

This method proved to have several drawbacks. First, the results are very noisy and the determination of the cooling/heating rate (i.e. the slope) has large uncertainties. In addition, since the cooling rate in a single solenoid is quite weak, this measurement is very sensitive to diffusion, which depends on several factors such as emittances and details of the momentum distribution, just to name a couple, all of which may vary over the length of the measurement. Then, at a minimum of 15 minutes per step, the whole procedure takes a lot of time to complete.

With the Drag Rate Method

The procedure for drag rate measurements is the same as described in Ref. [4]. Starting from an equilibrium, $\Delta B_\perp$ is changed before each measurement and the corresponding drag rate recorded. Figure 4 shows

the drag rate as a function of dipole correctors offset in the vertical direction.

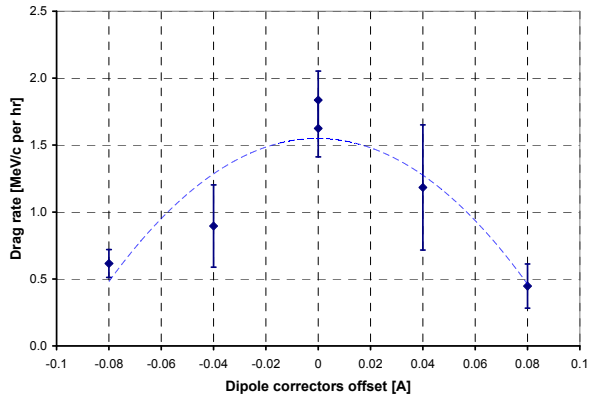

Figure 4: Drag rate as a function of the dipole correctors offset for the first solenoid (vertical i.e. horizontal field). I_b = 100 mA, on- axis. Voltage jump is 2 kV. Error bars are the statistical errors of the fit (1σ) when extracting the drag rate from the raw data. The dotted line is an arbitrary polynomial fit (2nd order).

The drag rate method has several advantages over the cooling rate method. First, the signal-to-noise ratio is more favorable which allows for speeding up the data acquisition. Each measurement (one corrector setting step) takes only 3-5 minutes. In addition, after each step, the antiproton beam is returned to its original conditions (i.e. an equilibrium), which makes the measurements more consistent over time. Moreover, for the low rate measured with a single solenoid, the drag rate measurements are less sensitive to the momentum distribution details and the momentum spread of the antiproton beam. We also have automated the data taking sequence, which helps both with the speed of the procedure and maintaining fixed initial conditions. On the other hand, this method is sensitive to the electron beam energy variations which could be non-negligible in respect with the energy offset from the voltage jump itself and to the transverse emittance of the antiproton beam [8].

RESULTS AND DISCUSSION

Although the uncertainties are quite large for both methods, one can extract an optimum value for the corrector dipole settings. For the measurements carried out in March 2007, using the drag rate method, we found that the corrector settings in the horizontal direction should be changed by -35 mA (i.e 28 mG) and remain unchanged in the vertical direction. This corresponded to a 0.13 mrad angle correction for the electron beam in the first cooling solenoid and presumably to a vertical tilt correction of 0.25 mrad of the 2-m solenoid.

After the rest of the cooling section magnetic field was aligned standard cooling rate measurements were performed accordingly to the procedure detailed in Ref. [7]. We find that the longitudinal cooling rate increased by 12%, while the transverse cooling rate increased by 35%.

A couple of reasons can be brought forward to explain the large uncertainties of the measurements presented in Figure 3 and Figure 4. First, we have recently found that the drag rate and cooling rate depend greatly on the transverse emittance of the antiprotons [8]. In neither case was the transverse emittance controlled to the level needed to ensure that even without changing dipole corrector settings, the cooling or drag rates were stable. Also, one of the assumptions for this method is that the rms angle of the electron beam is incoherent except for the dipole component resulting from the tilt of the solenoid. If the rms angle of the electron beam is dominated by envelope scalloping then the distribution of angles is such that there is overall a region of good cooling (where the angles are low) and a region of bad cooling (where the angles are high). By adding a transverse magnetic field dipole, one merely shifts this distribution of angles [1], so that, the change in the cooling rate can not necessarily be linked to an improvement of the straightness of the field. The shape of the electron beam recently observed on a scintillator screen at the exit of the CS certainly points toward high coherent angles [8].

CONCLUSION

The straightness of the magnetic field in the cooling section degrades with time. We presented a procedure that uses measurements of the cooling force using only the first solenoid to re-align the magnetic field.

Although the data obtained for both methods shown (cooling rate and drag rate methods) have large uncertainties, they have been successful and resulted in an immediate improvement of the cooling efficiency.

ACKNOWLEDGMENTS

We would like to acknowledge the entire Recycler Department personnel for their assistance with various parts of the measurements.

REFERENCES

[1] A. Shemyakin *et al.*, AIP Conf. Proc. **821** (2006) 280.
[2] V. Tupikov *et al.*, AIP Conf. Proc. **821** (2006) 375.
[3] S.M. Seletskiy and V. Tupikov, AIP Conf. Proc. **821** (2006) 386.
[4] L. Prost *et al.*, in Proc. of HB2006, Tsukuba, Japan, May 29-June 2, 2006, WEAY02, p 182.
[5] L. Prost and A. Shemyakin, Internal note FNAL Beams-doc-2861-v5. http://beamdocs.fnal.gov/AD-public/DocDB/ShowDocument?docid=2861
[6] A.C. Crawford *et al.*, in Proc. of PAC'01, Chicago, Illinois, June 18-22, 2001, p 195.
[7] L. Prost and A. Shemyakin, in Proc. of PAC'07, Albuquerque, New Mexico, June 25-29, 2007, TUPAS030, p 1715.
[8] L. Prost *et al.*, Electron Cooling Status and Characterization at Fermilab's Recycler, *these proceedings*.

STATUS OF DESIGN WORK TOWARDS AN ELECTRON COOLER FOR HESR*

Björn Gålnander#, Torsten Bergmark, Olle Byström, Stefan Johnson, Tomas Johnson, Tor Lofnes, Gunnar Norman, Tord Peterson, Karin Rathsman, Dag Reistad
The Svedberg Laboratory, Uppsala University, Sweden
Håkan Danared
Manne Siegbahn Laboratory, Stockholm University, Sweden

Abstract

The HESR-ring of the future FAIR-facility at GSI will include both electron cooling and stochastic cooling in order to achieve the demanding beam parameters required by the PANDA experiment. The high-energy electron cooler will cool antiprotons in the energy range 0.8 GeV to 8 GeV. The design is based on an electrostatic accelerator and shall not exclude a further upgrade to the full energy of HESR, 14.1 GeV. The beam is transported in a longitudinal magnetic field of 0.2 T and the requirement on the straightness of the magnetic field is as demanding as 10^{-5} radians rms at the interaction section. Furthermore, care must be taken in order to achieve an electron beam with sufficiently small coherent cyclotron motion and envelope scalloping. This puts demanding requirements on the electron beam diagnostics as well as the magnetic field measuring equipment. Prototype tests of certain components for these tasks are being performed. The paper will discuss these tests and recent development in the design including the high-voltage tank, electron gun and collector, magnet system, electron beam diagnostics and the magnetic field measurement system.

INTRODUCTION

The High Energy Storage Ring (HESR) is a part of the future FAIR facility [1] and will be dedicated to Strong interaction studies with antiprotons in the momentum range of 1.5 to 15 GeV/c. In order to meet the demanding requirements of the experiments both stochastic cooling [2] and electron cooling will be employed. Electron cooling is needed, in particular, to reach the low momentum spread requirements for the high-resolution mode of PANDA.

The design work of HESR is carried out in a consortium formed between FZ Jülich, GSI and Uppsala University. Earlier studies of the electron cooling system for HESR were carried out by the Budker Institute of Nuclear Physics (BINP) and GSI [3].

The design of the high-energy electron cooler is based on an electrostatic accelerator and will be used to cool antiprotons in the energy range 0.8 GeV to 8 GeV. However, the design should not exclude a future upgrade to the full energy of HESR, 14.1 GeV. This was one reason to base the design on a Pelletron which is modular and is possible to extend in energy. [4]. A similar electron cooling system is in operation at Fermilab [5].

The PANDA experiment will use an internal target, most probably a hydrogen pellet target. The cooler will have to compensate for the effects of this target on the antiproton beam. For this to take place efficiently, magnetised cooling is required. The details of the interaction between the target effects and electron cooling in HESR are further discussed in Ref. [6]

Technical Challenges

One challenge for the electron cooler design is beam alignment between electrons and anti-protons. The deviation of the electron beam relative to the anti- proton beam should be smaller than 10^{-5} radians rms to fulfil the beam quality and lifetime demands of the anti-protons. This requires very accurate procedures for beam diagnostics and alignment along the 24-meter interaction section.

Another difficult requirement on the solenoid is that the magnetic field must be continuous enough, that the straightness of the magnetic field, measured within 5 mm distance from the nominal path of the electron beam must be within 10^{-5} radians rms.

The field must also be continuous enough or shaped so than an electron beam with diameter 10 mm and energy anywhere in the range from 0.45 to 8 MeV must not be "heated" by any variation of the magnetic field. The dipole and envelope oscillations created by the total effect of all such transitions in the system should be smaller than a corresponding Larmor radius of 0.1 mm.

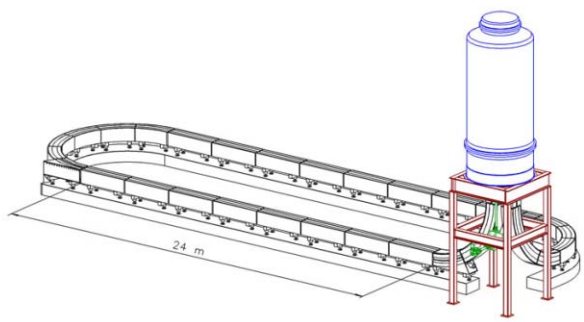

Figure 1: Layout of the HESR electron cooler showing the Pelletron tank and the beam line system of solenoid magnets. The length of the interaction section is 24 m.

MAGNET SYSTEM

The Layout of the HESR Electron Cooler is shown in Fig. 1. The electrons are produced by the gun in the high voltage tank and circulate the beam transport system before being captured by the collector. The beam transport system is 94 meter in total and has been divided into several sections listed in Table 1.

Table 1: Overview of the different sections in the magnetic field system.

Section	field strenght [T]	length [m]	angle [degree]	number of pancakes
Acceleation column	0.07	4		15
Transition	0.07- 0.2	3		22
Entrance bend	0.2	6	90	48
Interaction straight	0.2	24		184
Exit bend	0.2	13	180	96
Return straight	0.2	25		192
Horizontal return bend	0.2	6	90	48
Vertical return bend	0.2	6	90	48
Transition	0.2 - 0.07	3		22
Deceleration column	0.07	4		15
Total		**94**	**450**	**690**

The Solenoid Field

The magnetic field strength outside of the high voltage tank is 0.2 T and has been chosen according to the following criteria:

- The electron beam size at interaction straight should be of the same size as the antiproton beam which is of the size 5×5 mm (including 50% of particles). This puts an upper limit of the solenoid field to 0.2 T because in the acceleration column, there is an aperture limit of one inch. With 0.2 T and some safety margins this corresponds to an electron beam diameter of 10 mm at the interaction section.
- A strong solenoid field enhances the cooling force. To get fully magnetised electrons in HESR, more than 0.2 T is required. Recent force calculations show however that magnetised cooling appears at lower field strength.
- One technical challenge associated with electron beam transport is generation of Larmor oscillations, especially at high energy and low solenoid field. Therefore, all the bending should take place at highest possible field strength.

The field transition between 0.07 T and 0.2 T takes place semi-adiabatically over two meter long sections which reside half inside and half outside of the high voltage tank. The excess magnetic flux is returned without need of long return bridges.

On high voltage there are limitations in both generating and cooling away of power in the tank column. The solenoid field in the acceleration and deceleration columns is therefore limited to 0.07 T.

The over all bending radius is chosen to be 4 meters to reduce generation of Larmor oscillations. This choice also allows for electrostatic centrifugal drift compensation in the case the collector efficiency will be lower than expected. Secondary electrons can then travel back and forth between the gun and collector until its energy is restored to the average electron energy.

Modules

The electron beam transport system outside of the high voltage tank is divided into a number of manageable modules, see Fig. 2. These modules are about three meters at the straight sections and two meters in the arcs, corresponding to a bending angle of 30 degrees. The modules consist of short pancake solenoids mounted in a rigid iron stand. The pancake solenoids can be adjusted individually to a high precision [7].

The modules are designed to be mechanically rigid so that floor instabilities or other mechanical shifts should not deform the modules. Corrector windings of the same length as the modules will be used to correct the direction of the magnetic field.

During build-up or after repair the modules will be brought into the beam-line fully equipped with the solenoids pre-aligned to give the required field straightness. Thereafter the modules will be aligned mechanically relative to each other and to the HESR ring.

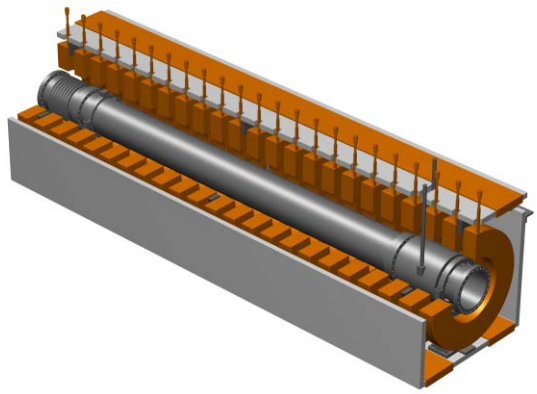

Figure 2: Each straight module on the interaction straight includes: 23 pancake solenoids, four corrector windings, a vacuum chamber with diagnostic unit and bellows.

Pancake Solenoids

The design parameters of the pancake solenoids are summarized in Table 2 and have been chosen to meet the following requirements:

- Generate a homogenous field. The magnetic field along the interaction straight must be continuous enough, that the straightness of the magnetic field, measured within 5 mm distance from the nominal path of the electron beam must be within 10^{-5} rad. rms. This is to ensure that accurate field measurements can be carried out.
- Make room for diagnostics and bakeout equipment.
- Allow assembly, especially to fasten 24 bolts on the Conflat flanges between adjacent modules.
- Minimize cost (copper and power consumption)

Table 2: Parameters for pancake solenoids

Pancake Solenoid Parameters		
Inner radius	R	170 mm
Period	L	130 mm
Wire dimension	δ	13 mm
Width	D	80 mm
Height	H	145 mm
Number of turns	N	63
Conductor		
Copper cross section	A_{CU}	116 mm^2
Cooling water hole	D	∅ 6 mm
Length	λ	96.5 m
Weight	M	100 Kg
Power consumption		
Current	J	328 A
Power consumption	P	1.8 kW
Voltage	U	5.5 V

ELECTRON COOLING OPTIMIZATION

Straightness of the Longitudinal Magnetic Field

The straightness of the longitudinal magnetic field at the interaction straight section is an important parameter in order to reach the necessary cooling force. As already mentioned the straightness has to be adjusted to 10^{-5} rad. rms. It should be possible to verify the magnetic field straightness without opening the vacuum system.

A prototype straightness measurement system, which is UHV-compatible, has been designed and manufactured. The system is based on a compass needle sensor and consists of a carriage with wheels that can be moved along the interaction straight under vacuum. The vacuum tube at the interaction section is made of aluminium and has integrated rails which the wheels rest on. The sensor should be kept in a position closer than 5 mm from the symmetry axis.

Similar devices have been used for verification of the straightness of the magnetic field lines in much shorter electron cooling systems. [8] Also, previous devices have not been designed to be ultra-high vacuum compatible.

The magnetic field sensor has been designed and manufactured by BINP [9, 10]. The design goal is to measure the field direction with a resolution of 2×10^{-6}. The sensor mounted in its dedicated holder is shown in Fig. 3. The entire magnetic field measurement system is presently being tested at TSL.

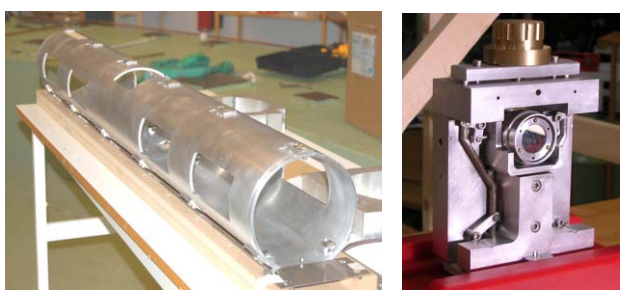

Figure 3: Carriage used for magnetic field measurements (left). Compass based sensor mounted in dedicated holder mechanism (right).

Alignment Between Electrons and Antiprotons

The antiproton beam needs to be made parallel or accurately tilted with respect to the direction of the straight magnetic field within 2×10^{-6} radians (50 μm over 24 m).

To minimise deviations of the electrons relative to the antiprotons, beam-based alignment will be applied. The offset of the electron beam relative to the antiproton beam will be measured and corrected for using the corrector windings. This requires pick-up electrodes in each module with a resolution of 10 μm.

Suppression of Dipole Oscillations

Coherent dipole oscillation will be kept to a minimum by applying beam matching of high accuracy. The corrector windings in arcs will be used to generate the bending field. The angles of the pancake solenoids are adjusted so that the solenoid field matches a reference path determined by the bending field. Simulations using TOSCA have been carried out showing that the matching can be made so that beam dipole oscillations are reduced to the required Larmor radius of 0.1 mm. Electron beam diagnostics (see next Section) and correction systems will be used to detect and quench remaining oscillations.

Suppression of Beam Envelope Oscillations

The solenoid of merging modules is made out of ordinary and racetrack shaped pancakes. To make the solenoid field uniform along the electron reference path extra current will be added to the ordinary power supply.

Electron beam diagnostics (see next Section) and correction systems will be used to detect and quench remaining oscillations.

ELECTRON BEAM DIAGNOSTICS

First of all, it will be necessary to commission the electron beam diagnostics to establish a recirculating electron beam. A pulsed electron beam is used to start with, and it will be necessary to measure its position along the beam transport system. Once recirculation is established, it will be necessary to measure the alignment of the electron beam to the antiproton beam most accurately in order to achieve the required alignment angle of 10^{-5} rad. rms. An even more challenging task will be to measure the envelope oscillation of the electron beam. The following list of different types of electron beam diagnostics elements is anticipated:

- Integrated beam position monitor and scraper unit. 9 units.
- Beam position monitors. 6 units.
- Beam loss monitors. 18 units.
- Beam profile monitors: OTR (Optical Transition Radiation) devices. 3 units.

Integrated Pick-up and Scraper

In the interaction straight section of the electron cooler there will be 9 pairs of beam position monitors, horizontal and vertical. Due to space limitations, the position monitors have to be integrated with scrapers. A prototype

of such a device has been designed and manufactured and will be tested at TSL, see Fig. 4. This unit has been named SPUC, Scraper and Pick-Up Combined.

The position monitor consists of 4 electrodes that together form a cylinder. The radius of the electrode cylinder is 100 mm. The radius of the cylinder behind the electrodes in the position monitors is 125 mm. This cylinder is kept at ground potential. The length of the monitor is 200 mm. The radius of the vacuum chamber at the position monitor is 134 mm. The radius elsewhere of the vacuum chamber is 100 mm.

Between the electrodes there are four plates, which are at ground potential. Two of these plates are used as scrapers, the two plates positioned to the right and to the left of the vacuum chamber centre. These two plates are possible to fold in towards the centre of the vacuum chamber. At the end of each of these plates there is an orifice with a diameter of 10 mm. The electron beam will pass through this orifice.

When the scraper plates are folded in to the beam centre the unit acts as a scraper, and when the scraper plates are in their parking position, the unit acts as a position monitor. The scraper will mainly be used to measure the envelope oscillation of the beam.

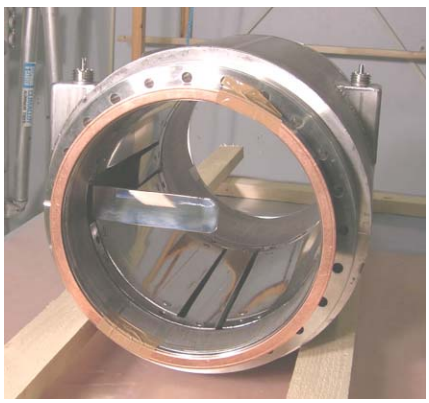

Figure 4: SPUC prototype. (Before the orifice is drilled in the scraper.)

GUN AND COLLECTOR

Electron Gun

The electron gun has a similar design as the one at the Fermilab cooler [11]. The main difference is that the cathode diameter is increased from 7.6 mm to 10 mm and that the magnetic field at the cathode is increased from 0.02 T to 0.2 T.

The parameters of the electron gun are

Anode voltage	26	kV
Beam current (max)	1	A
Cathode diameter	10	mm
Cathode field	0.2	T

The gun has a negatively biased control electrode which can be used for production of a pulsed beam and for fast closing of the gun. Simulation of the electron optics in the gun has been carried out using the UltraSAM [12] code.

Electron Collector

The design of the collector is also based on the Fermilab collector [11, 13] and assumes that the collector size is large enough and the collector perveance is low enough to suppress the secondary electrons by applying a transverse magnetic field to the collector cavity. The transverse component of the magnetic field in the cavity is created by permanent magnets and two iron plates outside the chamber. An electrode near the collector entrance, the collector control electrode, can be used for fine tuning of the primary beam envelope. Its operational potential is close to the one of the collector.

The collector cavity consists of a stainless steel bottle, inside of which a cylinder of OFHC copper is brazed. The copper cylinder has water channels for cooling. The power deposited by the beam is 5 kW (at a beam current of 1 A and a collector voltage of 5 kV) and the beam spot diameter is about 60 mm.

Simulations of electron optics in the collector have been carried out using the UltraSAM [12] code (2D with space charge) and with Mag3D and TOSCA (3D without space charge).

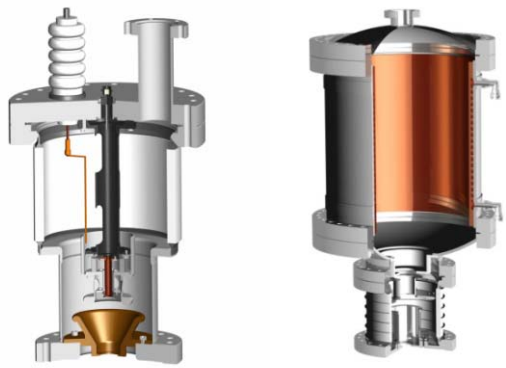

Figure 5: CAD drawings of electron gun (left) and collector (right). The components generating the magnetic field are not shown.

HIGH-VOLTAGE SOLENOID

The high-voltage solenoids are used to create a longitudinal magnetic field in the accelerating tubes of the Pelletron. The solenoids are mounted on the separation boxes in the high voltage column. The separation boxes with attached solenoids are cooled by convective heat transfer to the surrounding SF6 gas.

The coil consists of 690 turns of enamelled copper wire with a cross section of 3 x 7 mm. The coil consists of two concentric windings separated by an aluminium ring. The coil is surrounded by an aluminium cover. The distance between the solenoids in the accelerating column is 0.305 m centre to centre. A current of 25 A generates the desired average field of 0.07 T in the accelerating column.

A prototype solenoid has been designed and manufactured. To test the principle of cooling it has been

mounted on an aluminium box with geometry similar to a real separation box. The cross section is shown in Fig. 6.

Test Set-up and Measurements

The solenoid was mounted on a test "separation box". The surface flatness of the separation box was < 0.1 mm. The separation box was cooled by a tangential fan blowing air (16° C, 20 liters/s) between the two aluminium plates. The distrubution of temperatures at steady-state (24 h) applying 25 A are shown in Fig. 6.

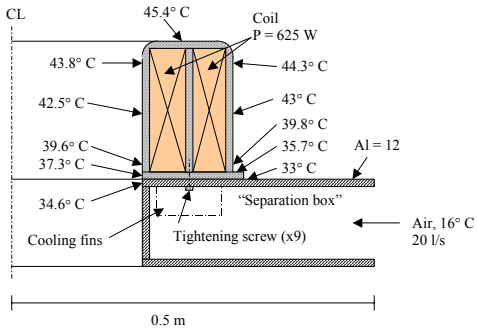

Figure 6: Cross section of the solenoid mounted on the test separation box and the measured steady-state temperatures (after 24 hours) on the surface.

The average coil temperature rise was calculated from the resistance variation assuming that the temperature coefficient of copper $\alpha = 0.00393$, see Fig. 7.

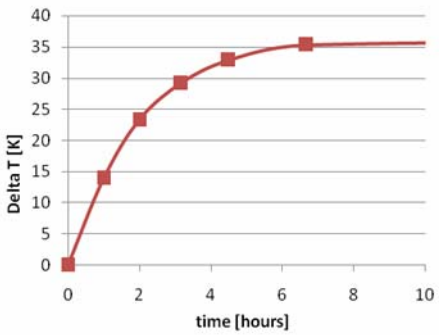

Figure 7: Average coil temperature rise with current 25 A (P=625 W after 8 hours).

Simulations

Simulation of heat transfer in the solenoid has been done with COMSOL Multiphysics, see Fig. 8. Uncertain parameters in the simulations are heat transfer coefficients between solenoid and separation box and between the conductors in the coil. Comparisons between measurements and simulations will be used to determine the heat transfer coefficients.

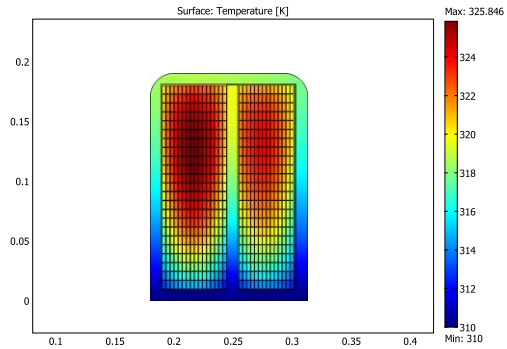

Figure 8: Simulation of temperature distribution in a cross-section of the coil. The temperature of the bottom surface is fixed at 310 K (=37° C). The other surfaces are isolated.

Conclusions

The maximum temperature inside the coil must be kept below 70° C to avoid epoxi softening.

The tests show that this can be achieved by:

- Cooling the SF6 gas to 20 ° C.
- Forced circulation of SF6 inside separation box.
- Good thermal contact between solenoid and separation box.

ACKNOWLEDGEMENTS

The authors would like acknowledge the help and support from Alexander Shemyakin, Vladimir Reva and Michail Tiunov, who have contributed to the project in different aspects. Important discussions with Mark Sundqvist at NEC are also acknowledged.

REFERENCES

[1] FAIR Baseline Technical Report, Volume 2, Darmstadt 2006. http://www.gsi.de/fair/reports/btr.htm
[2] H. Stockhorst, these proceedings.
[3] O. Bazhenov et al., Electron Cooling for HESR, Final Report, Novosibirsk 2003, unpublished. M. Steck, K. Beckert et al., EPAC 2004, 1969. http://cern.ch/AccelConf/e04/PAPERS/WEPLT056.PDF
[4] T. Bergmark, O Byström et al., EPAC 2006, 1648. http://cern.ch/AccelConf/e06/PAPERS/TUPLS067.PDF
[5] L.R.Prost et al., these proceedings.
[6] D. Reistad et al., these proceedings.
[7] E. Behtenev, V. Bocharov et al. RuPAC 2004, 506. http://cern.ch/AccelConf/e04/PAPERS/TUPLT120.PDF
[8] V. Prieto, R. Sautier et al. EPAC 2006 1651. http://cern.ch/AccelConf/e06/PAPERS/TUPLS068.PDF
[9] V.N.Bocharov, A.V.Bublei et al., Instruments and Experimental Techniques, **48** (2005) 78.
[10] V. Bocharov, A. Bubley et al. Proc. COOL05, 360.
[11] A Sharapa, A. Shemyakin and S. Nagaitsev, NIMA **417** (1998) 177.
[12] A.V. Ivanov and M.A. Tiunov, EPAC 2002, 1634. http://cern.ch/AccelConf/e02/PAPERS/WEPRI050.pdf
[13] L.R Prost and A. Shemyakin, PAC 2005, 2387. http://cern.ch/AccelConf/p05/PAPERS/TPPE035.PDF

ELECTRON COOLING FOR A HIGH LUMINOSITY ELECTRON–ION COLLIDER*

Ya. Derbenev, J. Musson and Y. Zhang
Thomas Jefferson National Accelerator Facility, Virginia, USA

Abstract

A conceptual design of a polarized ring-ring electron-ion collider (ELIC) based on CEBAF with luminosity up to 10^{35} $cm^{-2}s^{-1}$ has been developed at Jefferson Lab. A vital component of this collider is high energy electron cooling (EC) of ion beams. This cooling facility consists of a 30 mA, 125 MeV energy recovery linac (ERL) and a 3 A circulator-cooler ring (CCR) operating at 15 and 1500 MHz bunch repetition rate respectively. Fast kickers of frequency bandwidth above 2 GHz have been designed for switching bunches between the ERL and CCR. Design parameters of this cooling facility, preliminary studies of electron beam transport, stability and emittance maintenance in the ERL and CCR, and the scenario of forming and cooling of ion beams will be presented.

INTRODUCTION

At Jefferson Lab, a polarized high luminosity electron-ion collider (ELIC) based on the CEBAF facility, as shown in Figure 1, was proposed as a future facility for nuclear science quest [1,2]. The ultra high luminosity of ELIC calls for a green-field design of its ion complex and a new approach to organization of the interaction region. For the ELIC electron complex, selection of a storage ring over an energy recovery linac (ERL) relaxes the high average current requirement on the polarized source while still preserving high luminosity. The 12 GeV CEBAF accelerator will be utilized as a full-energy injector of electron bunches into a ring of a 2.5 A stored current [3]. The ELIC ion complex, consisting of a SRF linac, a pre-booster, a large booster and a collider ring, will generate and store up to a 1 A polarized (p, d, ^{3}He and Li) or non-polarized (up to A=208) ion beam with energy up to 225 GeV for protons or 100 GeV/n for ions [1]. The figure 8 topology of the ELIC booster and collider rings provides preservation and easy manipulation of spins for all species. There are four interaction points arranged symmetrically on the two crossing straights for high science productivity. Table 1 summarizes ELIC's main design parameters.

The luminosity concept of ELIC has been established on careful consideration of multi beam physics effects including beam cooling, space charge, beam-beam interactions and intra-beam scattering (IBS) [3,4]. In this paper we present a scheme of forming of high intensity ion beams and cooling of these beams to meet requirements of ultra high luminosity. To assist ion beam stacking and accumulation, stochastic cooling will be utilitized in the pre-booster and the collider ring [1]. Electron cooling (EC) will provide initial longitudinal cooling and a continuous 6D cooling of the ion beam in collisions mode. In cooperation with a strong bunching SRF field of high frequency in the collider ring, EC delivers very short (5 mm or less) ion bunches with desired small emittances, thus enables *super-strong focusing* at collision points and *crab crossing colliding beams* required for a high bunch collision rate (1.5 GHz) [5].

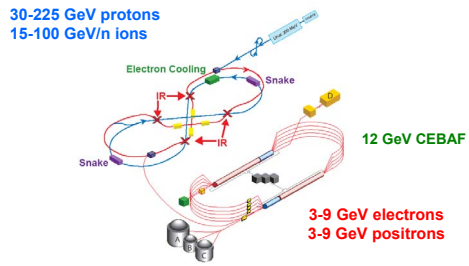

Figure 1: A schematic drawing of ELIC ring-ring design.

Table 1: Basic parameters for ELIC.

Beam energy	GeV	225/9	150/7	30/3
Collision rate	GHz	1.5		
Particles/bunch	10^{10}	.42/.77	.42/1	.13/1.7
Beam current	A	1/1.85	1/2.5	.3/4.1
Ener. spread, rms	10^{-4}	3		
Bunch length, rms	mm	5		
Beta-star	mm	5		
Hori. emit. norm.	μm	1.2/90	1.06/90	.21/37.5
Vert. emit., norm.	μm	.05/3.6	.04/3.6	.21/37.5
Beam-beam tune shift (vert.) per IP		.006/ .086	.01/ .086	.01/ .007
Space charge tune shift in p-beam			.015	.06
Lumi. per IP, 10^{34}	$cm^{-2}s^{-1}$	5.7	6	0.6
Lumi. lifetime	hours	24	24	>24

ION STACKING AND COOLING SCENARIO

Forming and Pre-cooling of Ion Beams by Stochastic Cooling

An ion beam from a 285 MV SRF linac will be stacked in a 3 GeV pre-booster with stochastic cooling. Our estimates show accumulation of a 1 A ion beam of space charge limited emittances of 10-15 μm within several minutes. Accumulated beam, after bunching and accelerating to 3 GeV, will be injected into the large booster which has common arcs with the electron ring. About 10 to 15 injections are needed to fill the whole orbit of the large booster ring. The beam will then be accelerated to 30 GeV for protons or up to 15 GeV/n for ions and injected into the ion collider ring. Here

* Authored by Jefferson Science Associates, LLC under U.S. DOE Contract No. DE-AC05-06OR23177. The U.S. Government retains a non-exclusive, paid-up, irrevocable, world-wide license to publish or reproduce this manuscript for U.S. Government purposes.

stochastic cooling will be put to work again for reduction of normalized emittance to a level below 1 μm in about 30 min. Table 2 summarizes design parameters for stochastic cooling in the pre-booster and collider ring.

Table 2: Stochastic cooling in pre-booster/collider ring.

Beam energy	GeV	0.2/30
Momentum spread	%	1/0.5
Pulse current from linac	mA	2
Cooling time	s	4/1200
Accumulated current	A	0.7/1
Stacking cycle duration (pre-booster)	min	2
Equilibrium emittance, norm.	mm	12/0.1
Laslett tune shift		0.03

ERL-based Electron Cooling with Circulator Ring

At this stage, electron cooling starts to work effectively for further reduction of energy spread and for reaching and then maintaining ion beam quality required for the ELIC high luminosity. To achieve the goal, the ELIC electron cooling facility should be capable of delivering a 3 A beam up to 125 MeV energy. Currently, an R&D program is in progress at BNL for design and test of a 54 MeV, 100 mA ERL-based facility for cooling heavy ion beams in RHIC [6]. The ELIC electron cooling facility design is based on a multi-turn ERL with a circulator-cooler ring as shown in Figure 2 [1]. Electron bunches from the ERL circulate one hundred turns inside the CCR while cooling ion bunches before being ejected and sent back to the ERL for energy recovery. Therefore, by employing a CCR, the required average current from the ERL is reduced to a modest value of 20-30 mA. Our estimates showed that high quality of the electron beam survives at least a few hundred revolutions in the CCR before the cooling rate decays noticeably due to degradation of beam energy spread and emittance caused by the inter-beam and intra-beam scattering [4].

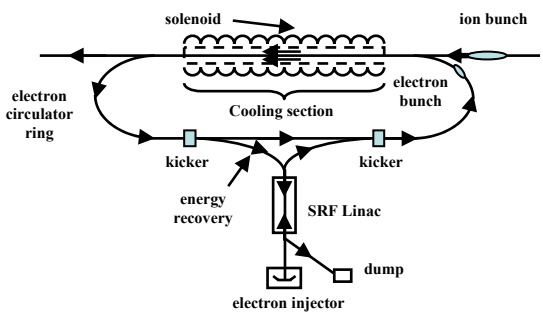

Figure 2: Layout of electron cooler for ELIC.

CONDITIONED ELECTRON COOLING

Several schemes/techniques may be implemented in the ELIC electron cooling design in order to minimize cooling time and equilibrium emittances.

Staged Cooling

Since electron cooling time drops when ion beam energy and emittance decrease, it is advantageous to start electron cooling as early as possible, which is at injector energy of the collider ring, then to continue cooling after acceleration of the ion beam to high energy with already reduced emittance [5].

Sweep Cooling

After transverse stochastic cooling at injection energy in the collider ring, ion beams will have quite a small transverse temperature but a large longitudinal one. In order to reduce the time required for initial longitudinal electron cooling, one can use *sweep cooling* [7,8] illustrated in Figure 3, in this way gaining a factor of $(\Delta\gamma_i/\Delta\gamma_e)^2$ in cooling time.

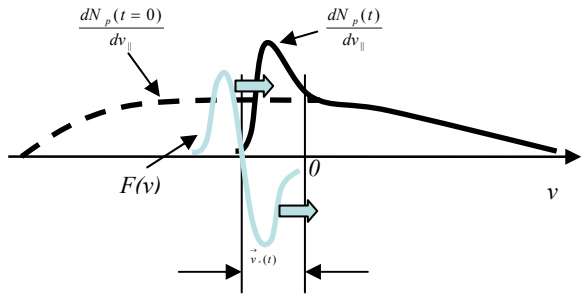

.Figure 3: The longitudinal sweep cooling method.

Dispersive Electron Cooling [8]

This method can be used to compensate low transverse cooling rate at high energies due to large transverse velocity spread compared to the longitudinal one (in rest frame) caused by IBS. The transverse temperature of relativistic beams is usually large with respect to the longitudinal one ($\gamma\theta >> \Delta\gamma/\gamma$, where θ is the angular spread, γ is the Lorentz factor and $\Delta\gamma$ is spread of γ). This results in a correspondent ratio between cooling times: $(\tau_\perp / \tau_\parallel) \approx (\gamma^2\theta / \Delta\gamma)$. The transverse extension of beams is usually considered as a method to raise the transverse cooling rate; however, this requires a very large beam defocusing in the cooling section, which makes beam alignment difficult. Instead, one can redistribute the cooling decrements according to the *dispersive cooling* method. The arrangement may consist of introducing dispersion for both the hadron and electron beam in the cooling section.

Flat Beam Cooling [4]

This method is based on flattening ion beam by reduction of coupling around the ring, while maintaining beam area. Here, the IBS impact on the 6D emittance becomes reduced compared to the cooling rate. The minimum coupling leads to a flat equilibrium, minimum ε_6 and maximum cooling rate. Since the luminosity is determined by the product of two transverse emittances, reduction of transverse coupling to a minimum while conserving the beam area would benefit one with a decrease of energy scattering, and hence, a decrease of the whole IBS impact on luminosity. Electron cooling then leads to a flat equilibrium with a large aspect ratio. In order to achieve an optimum cooling effect at equilibrium, the electron beam area in the solenoid should also be

transformed to an elliptical one of a similar aspect ratio, applying adapting optics [16].

BEAM TRANSPORT AND CCR DESIGN

Use of an electron circulator ring as a complement to the accelerator line was suggested earlier as an option for beam transport for medium energy relativistic electron cooling [7]. The optical scheme of a circulator ring matched with a magnetized electron gun through an RF accelerator line has been developed in conceptual studies of electron cooling of a proton beam in PETRA for HERA [9]. A circulator-cooler ring can work in conjunction with ERL as well; the only considerable addition to a CW single loop scheme would be fast kickers for switching the electron bunches between the ERL and the circulator [1].

EC AND BEAM PARAMETERS

Tables 3 and 4 illustrate design parameters of the electron cooler for the ELIC [5].

Table 3: Initial electron cooling (p/e).

Energy	GeV/MeV	20/10
Cooling length/ circumference	%	1
Particles/bunch	10^{10}	0.2/1
Energy spread*	10^{-4}	3/1
Bunch length*	cm	20/3
Proton emittance, norm*	μm	4
Cooling time	min	10
Equilibrium emittance, **	μm	1
Equilibrium bunch length**	cm	2
Laslett tune shift		0.1

* max.amplitude

** norm.,rms

Table 4: ERL-based EC with circulator ring.

Max/min energy of e-beam	MeV	75/10
Electrons/bunch	10^{10}	1
Number of bunch revolutions in CR	100	1
Current in CR/current in ERL	A	2.5/0.025
Bunch rep. rate in CR	GHz	1.5
CR circumference	M	60
Cooling section length	M	15
Circulation duration	μs	20
Bunch length	Cm	1
Energy spread	10^{-4}	3-5
Solenoid field in cooling section	T	2
Beam radius in solenoid	Mm	1
Cyclotron beta-function	M	0.6
Thermal cyclotron radius	μm	2
Beam radius at cathode	Mm	3
Solenoid field at cathode	kG	2
Laslett tune shift in CR at 10 MeV		0.03
Time of longitudinal inter/intra beam heating	μs	200

ELECTRON INJECTOR

An electron injector capable of delivering 30 mA average current up to 125 MeV energy, with appropriate bunch length, transverse emittance and energy spread for an optimal cooling effectiveness, is required to fill electron bunches in the CCR. This injector operates at a 15 MHz bunch repetition rate, taking into account 100 circulations of a bunch in the CCR, which leads to 1 nC charge per bunch. In designing such an injector, two challenging requirements must be met first. The first one is the source life time. The electron photo-injector of the ELIC cooling facility draws about 2.6 kC charge per day from the source, a considerably challenging R&D requirement from the current 0.2 kC/day state-of-art [10]. More beam studies, especially computer simulations, will help to exploit the higher number of circulations of electron bunches in the CCR, thus further reducing the average current from the injector. The second one is 3.75 MW average beam power from the RF cavities. This challenge can be solved readily through energy recovery.

The high average current electron beam is one of the key R&D issues for many ERL based light sources; therefore high current injectors for these light source applications are under active R&D worldwide. Two outstanding programs, among others, are the JLab 10 kW and 100 kW FEL facility [11] and the Cornell ERL based light source [12], both employing DC photo-injectors. Though there may be different requirements for beam properties, much R&D done for injectors of light source applications can be readily applied to the ELIC cooling application. As an initial conceptual design of the driving injector for the ELIC circulator cooler, we will adopt the existing baseline of the JLab FEL photo-injector. Future design iteration and optimization will be carried out as the ELIC design continually evolves.

The injector design for the ELIC cooling facility consists of the following key elements: a 350 to 500 keV photo-cathode DC gun, a single cell normal or superconducting RF bunching cavity, two high gradient SRF modules for energy boost, and several solenoids and quadrupoles for beam focusing and emittance compensation. Magnetization of electron bunches is realized by adding a solenoid at the photo-cathode. In addition, a fast kicker will be attached to the injector for kicking bunches into the CCR. One previous study showed that, after optimization, the injector beam with 0.8 to 0.9 nC bunch charge up to 15 MeV can reach a 1 mm or shorter bunch length while the longitudinal emittance is less than 50 mm-keV, and transverse emittence is less than 0.8 mm-mrad [12].

DEVELOPMENT OF AN ULTRA-FAST KICKER

Requirements to the ERL-CCR Kicker

Operation of the multi-turn CCR requires that a single electron bunch be extracted after 100 turns and replaced by a fresh bunch from the injector. To achieve such extraction, a kicker must be able to interact temporally with a single bunch while leaving neighboring bunches unaffected. Therefore, a pulse having an envelope of 0.5 ns in duration and a peak power of 10-20 kW is required to achieve the necessary integrated transverse field to kick the electron bunch.

Since the ultra fast kicker (UFK) is one of the key components in the electron cooling system, it is imperative to realize electronics which can produce the required pulses. Estimated parameters for a UFK system and electronics appear in Table 5.

Table 5: Estimated parameters for the kicker.

Beam energy	MeV	125
Kick angle	10^{-4}	3
Integrated BdL	GM	1.25
Frequency BW	GHz	2
Kicker aperture	Cm	2
Peak kicker field	G	3
Kicker repetition rate	MHz	15
Peak power/cell	kW	10
Average power/cell	W	15
Number of cells		20

Pulse-compression Technique

Present research involving *pulse compression techniques* is providing several potential options for producing short, medium-power RF pulses with the required 10 to 15 MHz repetition rate. Pulse compression employs a swept RF source in conjunction with a dispersive element, resulting in multiple wave-fronts piling up at the output to produce a very short, high peak power pulse [14]. Recent experiments using a helically corrugated waveguide as the dispersive element have achieved compression and power enhancement ratios of 12 or better, creating 2 ns pulses at a 12 MHz repetition rate, and having a peak power of 11 kW [15]. In these tests, a swept RF source provides a gated "chirp" signal, which is then amplified by a gated traveling-wave tube amplifier (TWTA), which is coupled to the load via the dispersive helically corrugated waveguide. Figure 4 illustrates the technique, along with associated frequency spectra.

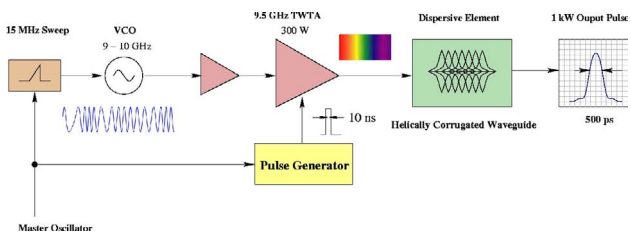

Figure 4: Schematic of pulse compression technique using helically corrugated waveguide. Output pulse envelope is the result of "chirping" the RF input, and letting all wave-fronts pile up at the output.

Although experiments have shown that it is possible to nearly realize the required pulse parameters with a single stage, it is likely that more stages (10-20) having reduced power, will provide the required BdL (1.25 G m), and also possibly satisfy space limitations. This is especially attractive, since the required output power from each individual amplifier decreases quadratically with the total number of stages. Also, since the primary goal of the experimenters was high peak power, specifically for plasma physics and radar applications, it can be expected that a reduction in peak power will further reduce pulse width. Conceptually, the power electronics would reside above-ground to facilitate accessibility and repair. Due to its manageable size, the dispersive element can be located either with the electronics, or at the beamline.

An optimum frequency range will have to be selected, based on pulse-beam interaction requirements, and also on availability and cost of components. Given some freedom, it would be possible to benefit from previous research efforts, RADAR, satellite transponder or ISM band component availability.

Pulse compression appears to possess many of the virtues required by the kicker electronics. Therefore, it is expected that this is the clearest path to achieving the required pulse requirements. A test stand is proposed which would verify the operational parameters of pulse compression techniques, as well as the ability to optimize pulse widths vs. peak output power and repetition rates. In addition to pulse compression, other options and techniques will continue to be explored, in an effort to find the most efficient conceptual and technical solution.

CONCLUSIONS

The ERL-based high energy electron cooling seems quite promising in approaching a very high luminosity in colliders with hadron beams. The low longitudinal emittance of the electron beam and possibility of staged cooling are the important advantages of the ERL approach. To operate at a modest average beam current, the ERL accelerator should be complemented with an electron circulator-cooler ring. Also, certain improvements in forming and transporting the hadron beams before injecting to collider ring might be required in order to reduce time of initial electron cooling in the ring [9]. A comprehensive analysis, simulation and experimental studies should precede development of recommendations for practical design of electron cooling and high luminosity colliding beams.

REFERENCES

[1] A. Bogacz et al., Proc. of PAC 2007[1].
[2] V. Ptitsyn, Proc. of PAC 2007.
[3] Ya. Derbenev et al., Proc. of RuPAC 2006.
[4] Ya. Derbenevet al., Proc. of EPAC 2004.
[5] Ya. Derbenev et al., Proc. of PAC 2005.
[6] I. Ben-Zvi, Proc. of this Workshop.
[7] G. Budker and A. Skrinsky, Sov. Phys. Usp. 21 (1978) 277.
[8] Ya. Derbenev and A. Skrinsky, Sov. Phys. Rev., 1 (1981) 165.
[9] Yu. Martirosyan et al., Proc. EPAC 2000.
[10] J. Grames, *private communications.*
[11] C. Hernandez-Garcia, etc., Proc. PAC 2005.
[12] I. Bazarov and C. Sinclair, PRST 8, 034202 (2005).
[13] R. Hajima and R. Nagai, NIM A 557 (2006) 103.
[14] Y. Iwashiti, Proc. of LINAC 2002, Gyeongju, Korea.
[15] K. Ronald, et al., EPS Conf. on Plasma Physics, June 2006, Rome, ECA Vol. 30I, P-5.175.
[16] A.Burov et al., Phys. Rev. E 66:016503, 2002.

RECENT DEVELOPMENTS FOR THE HESR STOCHASTIC COOLING SYSTEM

R. Stassen, P. Brittner, R. Greven, H. Singer, H. Stockhorst, Forschungszentrum Juelich, Germany,
L. Thorndahl, CERN

Abstract

Two cooling systems will be installed in the High-Energy Storage Ring (HESR) of the future international Facility for Antiproton and Ion Research (FAIR) [1] at the GSI in Darmstadt: an electron cooler (1.5-8 GeV/c) and a stochastic cooling system from 3.8 GeV/c up to the highest momentum of the HESR (15 GeV/c). Both coolers are mandatory for the operation of the HESR with the PANDA pellet target. The relative low aperture (89mm) of the HESR suggests fixed structures without a plunging system. An octagonal layout was chosen to increase the sensitivity of the electrodes. Two different types of electrodes were built and tested. We will report on the comparison of printed lambda/4 loops and new broadband slot couplers.

HESR STOCHASTIC COOLING

The modified (2-4GHz) AC CERN [2] loop pairs with a distance of 20mm [3] are basis for the simulations of the HESR stochastic cooling system. For practical reasons and costs reduction aspects we prefer fixed pickup loops without plunging system. One loop pair with a distance of the HESR aperture will give a poor response. The loss of particle image current is not tolerable. The coupling impedance can be increased by combining several rows of electrodes arranged in an octagonal array.

Printed loop Coupler

Printed loops [5] are a cost saving alternative to the mechanical complex structures like the CERN AC structures [2] or the COSY pickups [4]. The first design of the HESR stochastic cooling pickups uses 50-Ohm printed loop couplers containing rectangular electrodes with rounded corners. Each loop ends at a 50-Ohm SMD resistor. These loops are combined via several impedance transforming networks and are located at the combiner side, whereas the coupling is done through the dielectric material of low permittivity (ε_r=3.27). Only simple through-holes are needed to connect the terminating resistors at the electrodes. Loops and combining network are located on the same board. This simplified the whole structure and minimized the fabrication costs. New structures can be easily exchanged. The relatively high bandwidth of 2-4 GHz requires at least two-stage transforming networks. Compared to Wilkinson couplers these combiners are a little bit more space consuming but have lower losses. The printed loop boards have been constructed as a part of a universal modular octagonal structure (fig. 1). Different modes of signal combinations outside the vacuum envelopes will allow to pick up different transversal beam positions as a part e.g. of a core or a halo cooling system.

We compared the transversal sensitivity of the new printed loops to that of the COSY-loop structure of 1.8 to 3 GHz [6] simulating the beam by an air microstrip line.

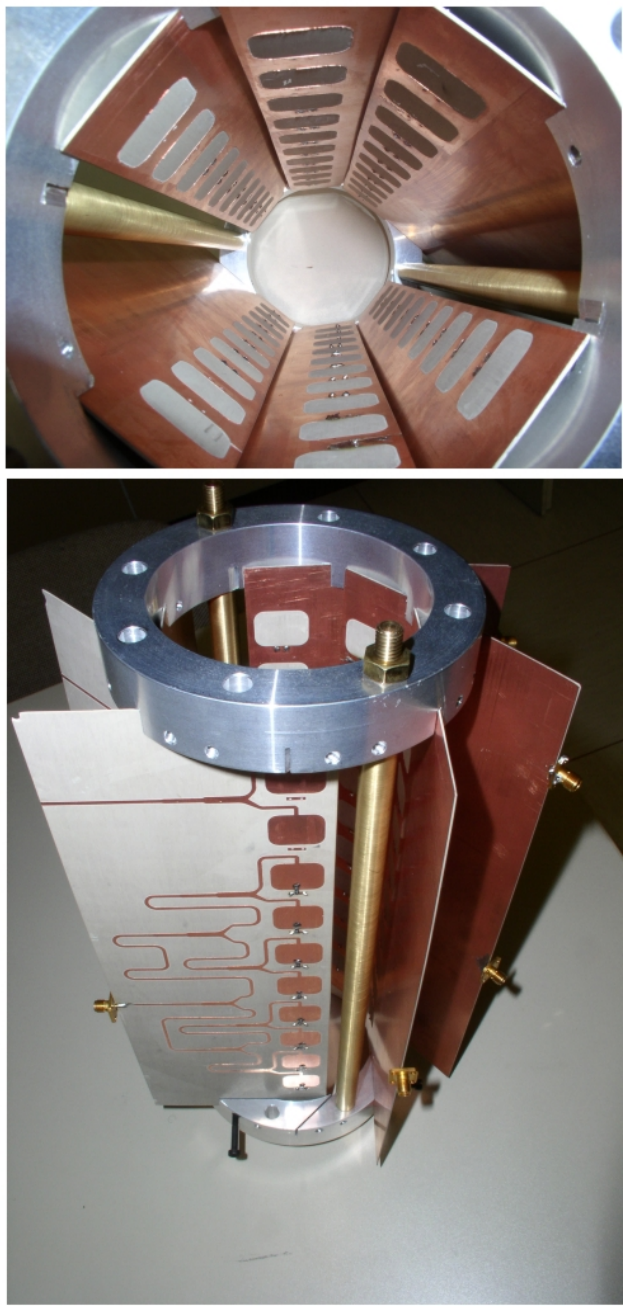

Figure 1: Octagonal pickup structure, equipped with 6 λ/4-electrode rows.

The width of the COSY loops, which were adapted

from the CERN AC structures, is the same as in the first layout of the printed loops. Even the number of combined loops are the same, thus a direct comparison is possible. The results of the measurements are presented in fig. 2. The printed loops show the same transversal sensitivity as the COSY-loops and can be used even at frequencies below 2GHz. Thus, a 1-2GHz precooling system seems possible with the same coupler loops.

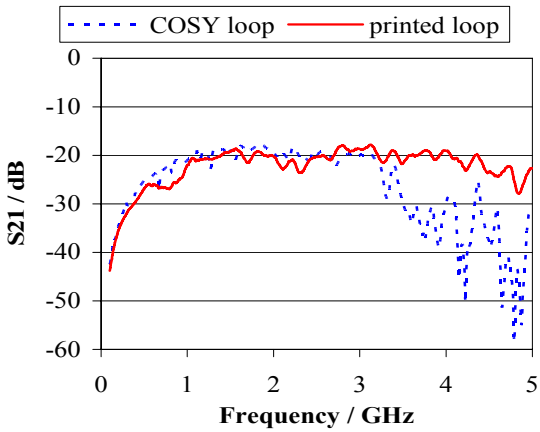

Figure 2: Comparison of COSY-loop and printed loop structures.

A new support structure closes the gaps between the electrode boards (fig. 3) and integrates high power water cooled resistors for kicker operation. Through-holes are no longer needed.

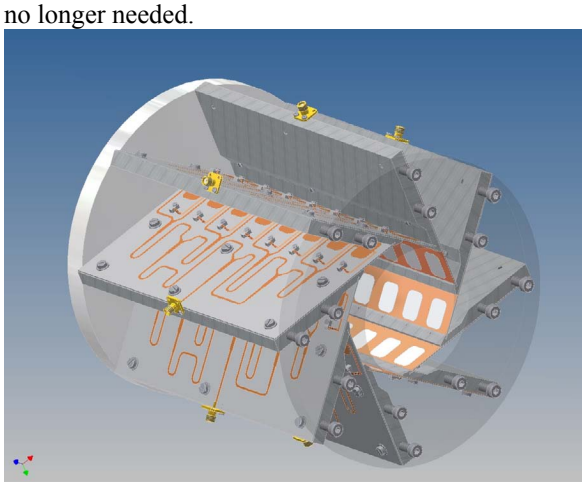

Figure 3: modified support with high power resistors to operate the structure as pickup and as kicker.

The sensitivity of the octagonal structure is sufficient for a transversal stochastic cooling system both as pickup and as kicker structure, but first HFSS [10] simulations [7] show that the sensitivity of the printed loops for longitudinal signals is nearly a factor of four lower than the AC loops.

Ring Slot Coupler

Starting with slot couplers like [9] we found that a ring structure with octagonal arrangement of shorted electrodes will give significant higher longitudinal impedance than any lambda/4 structure [7]. We analysed a slot coupler with the same HESR aperture of 89mm. The structure consists of AlMg4,5Mn rings with 8 shorted electrodes (Fig. 4). The total image current passes the surrounding uninterrupted gap formed by two adjacent rings. The round cell is somewhat like a classical iris-loaded linac cell which is heavily loaded with the eight 50 Ohm coaxial lines to obtain the octave bandwidth. HFSS gives more than two times higher longitudinal coupling impedance per unit length than comparable lambda/4 structures. A TM10 mode enhancement has been found. The field uniformity is good. This round structure offers the most compact solution. With about 2m total active length it satisfies the initial specification of the HESR longitudinal cooling. Different ring slot coupler designs have been analysed including the producibility.

The modular design of this structure allows an easy increase of the number of rings. Two following octagonal rings are centred together by circumferential steps of 3mm length and fits of the diameter within 0.05mm; pivots provide the angular fits.

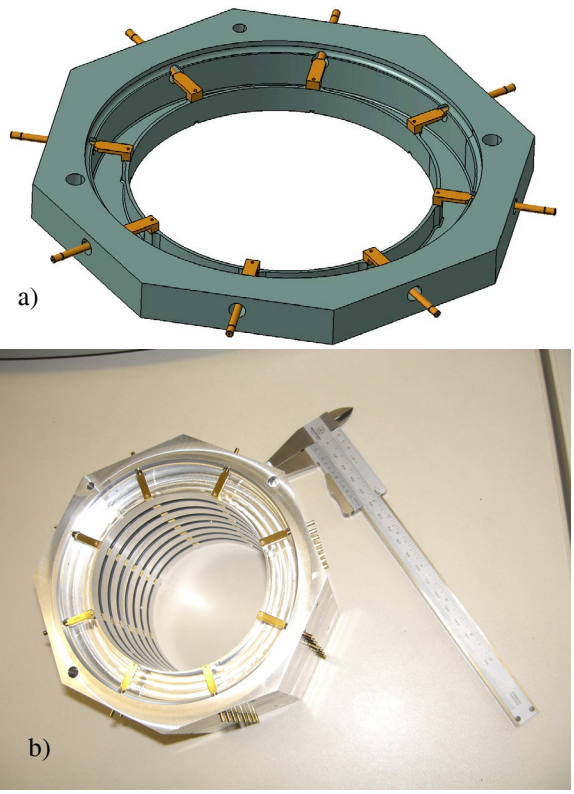

Figure 4: a) single ring with 8 50Ohm electrodes, b) Photo of stack with 8 rings.

A similar combiner board as the simple transforming network used for the lambda/4 coupler cannot be used in this case because of great influence of neighbouring low-impedance electrodes. A good decoupling has been reached by using Wilkinson couplers instead of impedance transforming networks. The 33mm inner conductor of a 31/8" RF transmission line has been used to measure the longitudinal sensitivity of both structures. Together with 90mm inner diameter of the structures we

get a 60 Ohm coaxial system. Both ends of this system are completed by commercial 31/8" to N-norm transitions. Using one transition to excite the TEM measurement mode the other transition will be terminated. 60 Ohms are close enough to the 50 Ohm of the network-analyzer impedance that reflections will not influence the TEM field very much.

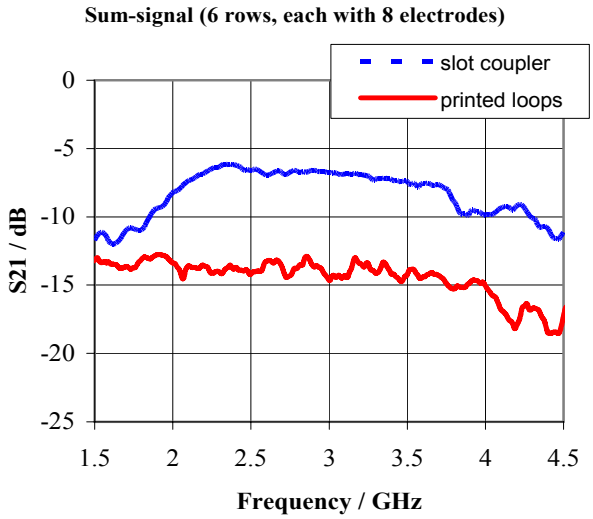

Figure 5: Transmission form 60 Ohm coaxial beam simulation to combined electrodes output.

The slot coupler is not as wide-banded as the printed loops, but shows much higher coupling impedance than the printed loops, although the length in beam direction is only halved. The measurements are comparable to the simulations taking into account the small losses of the combiner boards.

SC TEST-TANK

A cooling tank has been designed to test the different structures with real beam (fig. 6). This tank is already under construction and will be installed in the COSY ring end of this year. In advance, modified gaskets were installed at the chosen place to check whether the aperture reduction to the HESR size (89mm) will influence the number of injected protons.

Two cold heads cool down the structures to about 20K. The whole inner part including the structures can be moved in vertical and horizontal direction to centre the structures according to the beam. The signals of each electrode row are feed through the vacuum system. Thus any combination of signal combining can be tested.

OUTLOOK

The beta functions at different energies are well known in COSY. So the output signals of the new structures can be very easily compared to the existing cooling system in sum-mode as well as in difference mode. First results are expected in 2008 during the first proton beam time.

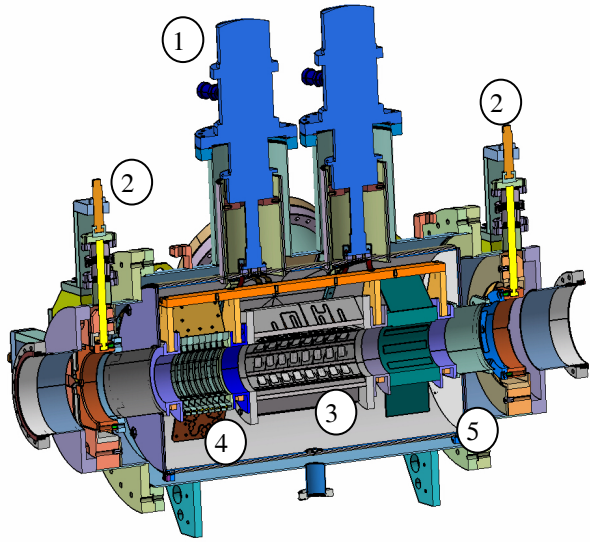

Figure 6: Cooling structures test-tank: (1) cold heads, (2) x-y support, (3) printed loops, (4) ring slot coupler, (5) thermal shield, tank length: 1.15m flange to flange.

ACKNOWLEDGEMENT

We acknowledge the support of the European Community RESEARCH INFRASTRUCTURES ACTION under the FP6 programme: Structuring the European Research Area Specific - DESIGN STUDY (contract 515873 - DIRACsecondary-Beams).

REFERENCES

[1] W.F. Henning, An International Accelerator Facility for Research with Ions and Antiprotons, proceedings of EPAC04, Lucerne, Switzerland

[2] B. Autin, G. Carron, F. Caspers, S. Milner, L. Thorndahl, S. van der Meer, ACOL stochastic cooling systems, proceedings of PAC87, Washington, USA, 1987

[3] H. Stockhorst, B. Lorentz, R. Maier, D. Prasuhn, T. Katayama, Stochastic cooling for the HESR at the GSI-FAIR complex, EPAC2006, Edinburgh, UK

[4] P. Brittner, H.U. Hacker, R. Maier, U. Pfister, D. Prasuhn, H. Singer, W. Spiess, R. Stassen, H. Stockhorst, A. Zumloh, The stochastic cooling system for COSY, proceedings of EPAC92, Berlin

[5] J. Petter, et al, Novel stochastic cooling Pickups/ Kickers, proceedings of PAC89, Chicago, USA

[6] R. Stassen, Pickup structures for HESR stochastic cooling system, EPAC2006, Edinburgh, U

[7] L. Thorndahl, Fixed 90mm Full-Aperture Structures with TM10-Mode propagation for Stochastic Cooling in HESR, 2006

[8] HighFrequencyStructureSimulator, Ansoft Corporation, USA, http://www.ansoft.com

[9] C. Peschke, F. Nolden, M. Balk, Planar pick-up electrodes for stochastic cooling, Nuclear Inst. & Methods, A 532, p. 459-464, 2004

PICK-UP ELECTRODE SYSTEM FOR THE CR STOCHASTIC COOLING SYSTEM*

C. Peschke, F. Nolden, GSI, Darmstadt, Germany

Abstract

The collector ring (CR) of the FAIR project will include a fast stochastic cooling system for rare isotope beams ($\beta = 0.83$) and antiprotons ($\beta = 0.97$). To reach a good signal to noise ratio of the pick-up even with a low number of particles, a cryogenic movable pick-up electrode system based on slotlines is under development. The sensitivity and noise properties of an electrode array has been calculated using field-simulation and equivalent circuits. For three-dimensional field measurements, an electric near-field probe moved by a computer controlled mapper has been used.

SLOTLINE PICK-UPS FOR THE CR

The pick-ups must have a large bandwidth, a high S/N ratio and a large aperture. A new planar electrode is developed [1] to meet these requirements. The electrodes consist of a slotline perpendicular to the beam and a microstrip circuit on the rear side of a planar Al_2O_3 substrate (Fig. 1, top, left). The mirror currents induce traveling waves in both directions of the slotline. At approx. $\lambda/4$ from the end of the slotline, the signal is coupled out to the microstrip line. The $\lambda/4$-section at the beginning of the microstrip is a virtual short to one of the two conductors of the slotline. The exact length of these sections has been used to optimize the frequency response. The two signals are coupled out to 110 Ω microstrip lines and are combined in a 100 Ω to 50 Ω Wilkinson combiner. The position of the 110 Ω to 100 Ω transition has also been optimized.

The figure 1 (top, left) shows the layout of an eight slot pick-up board on a scale of 1:3. A pick-up tank will consist of two times eight modules. The modules will be cooled down to 30 K using cold heads and will be movable. The two figures below show a simplified design of a module. The right figure shows a cut across the first module prototype. Beside the PU board, the module also contains vertical connection boards. On these Al_2O_3 boards, a cryogenic low noise amplifier is foreseen. A small antenna can be used to test all connections and amplifiers of the module

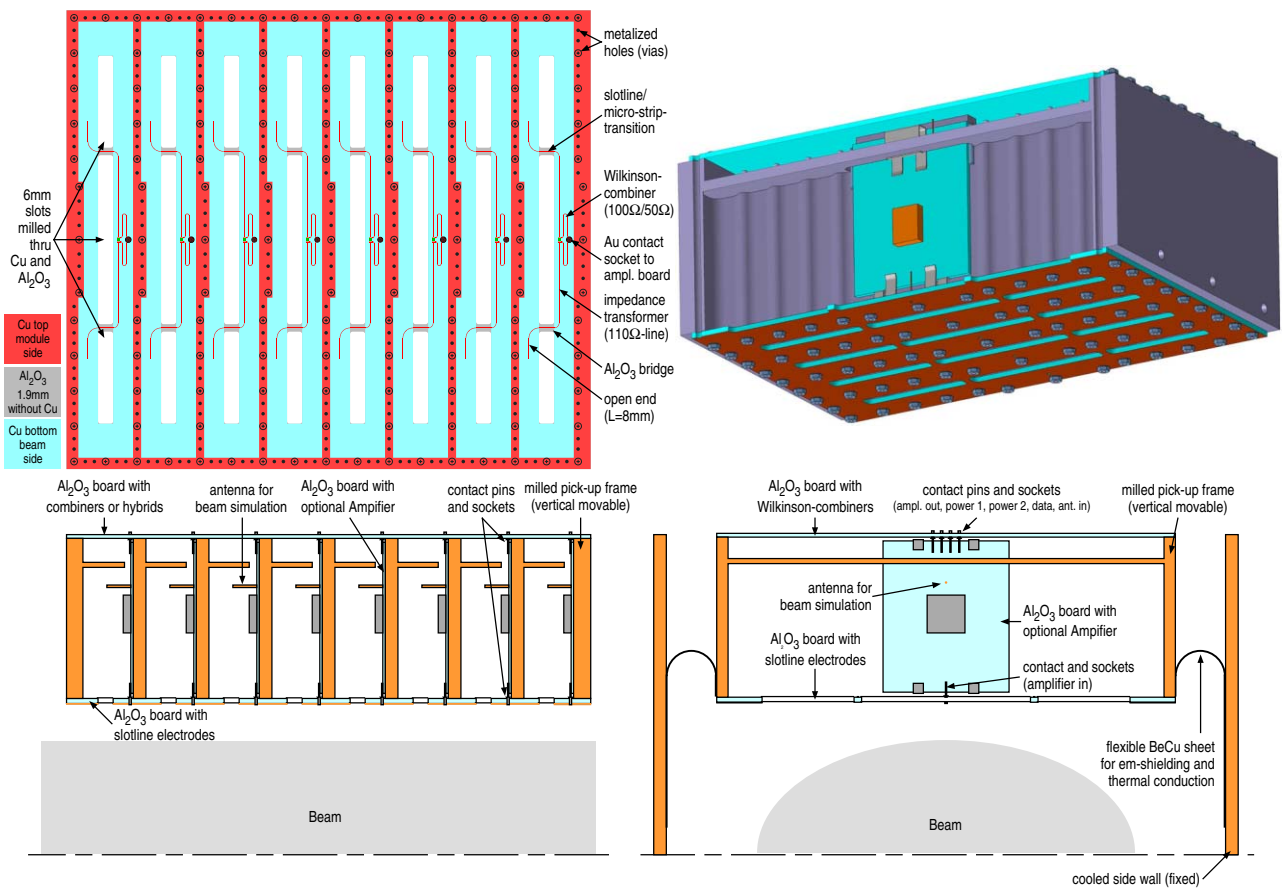

Figure 1: Layout of eight slot pick-up module prototype on a scale of 1:3.

* Work supported by EU design study (contract 515873 -DIRACsecondary-Beams)

without beam. The board on top of the module contains the phase-correct signal combination for $\beta = 0.97$. The signals of the eight modules will be combined outside the tank with switchable delays for $\beta = 0.83$ and $\beta = 0.97$.

The layout of the pick-up board is the result of numerical field calculations and an equivalent circuit based optimization. Compared to the unoptimized precursor, the position of the Al_2O_3 bridges over the slots and the dimensions of the microstrip lines have been modified. The equivalent circuit, including the first combiner and an additional 110 Ω line has been optimized with respect to maximum voltage and flatness. The diagram in figure 2 is a result of the optimization. It shows the magnitude and phase of the voltage over the center of the slotline versus the frequency.

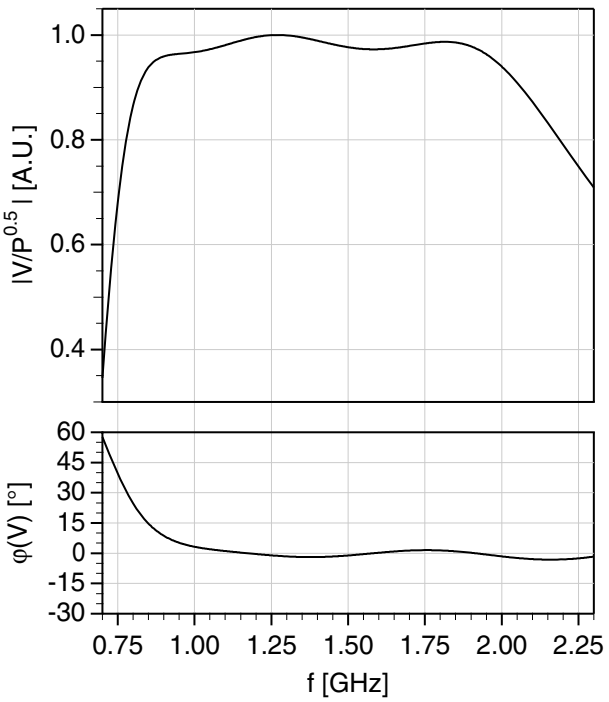

Figure 2: Voltage and phase over one slotline of Fig. 1 (simulated with equivalent circuit).

A prototype of a module with this layout is under construction in order to compare the equivalent circuit with measurement results.

FIELD MEASUREMENTS

To perform four-dimensional (x,y,z,f) field measurements, a computer controlled E-Field mapper has been built. A small dipole (8 mm) is used as a near field probe. Figure 3 shows from left to right the controlling PC, the network analyzer, the CNC-machine which has been abused to move the probe over the test object, and the stepper controller. The detail shows the dipole at the end of the probe with small terminators. The feed line consists of two 1.2 mm semi-rigid cables.

Figure 3: Computer controlled E-field mapper with near field probe (detail).

Figure 4 shows a two-dimensional example of a field measurement. The single slot test pick-up for the equivalent circuit based optimization with 0.2 mm bridge and 10 mm open end has been fed with a 1.5 GHz signal at both ports. The diagram shows the magnitude of the E-field in z-direction, 5 mm above the surface. The sensitivity is relatively flat in the x-direction. The bridges with the microstrip tansitions are at ±30 mm and the slot ends at ±75 mm. In z-direction, the field decreases very fast. The next slots in a pick-up module would be at z=±25 mm.

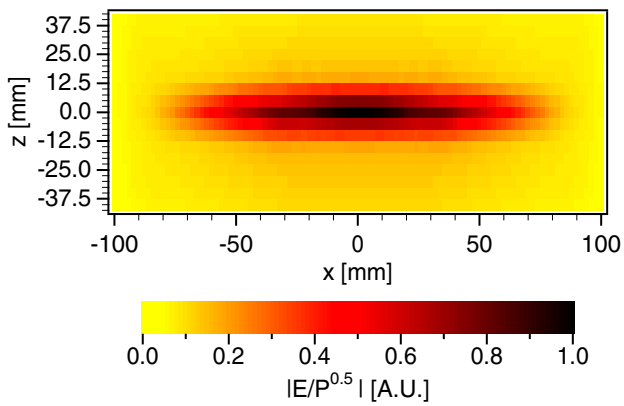

Figure 4: $|E_z|$-field 5 mm above the test structure.

Suitable integration with β=0.97 over z gives the voltage over the particle trajectory. The diagram in figure 5 shows measured voltages at x = 0 in dependence of the frequency for different lengths of the open end. The peak at 1.1 GHz is an unwanted resonance of the measurement setup and will be avoided in the next measurements. The results of this measurements have been used for the optimization.

EQUIVALENT CIRCUIT BASED OPTIMIZATION

To optimize the frequency response of the pick-up in detail, an equivalent circuit based approach has been chosen. To come close to a realistic behavior of the equivalent

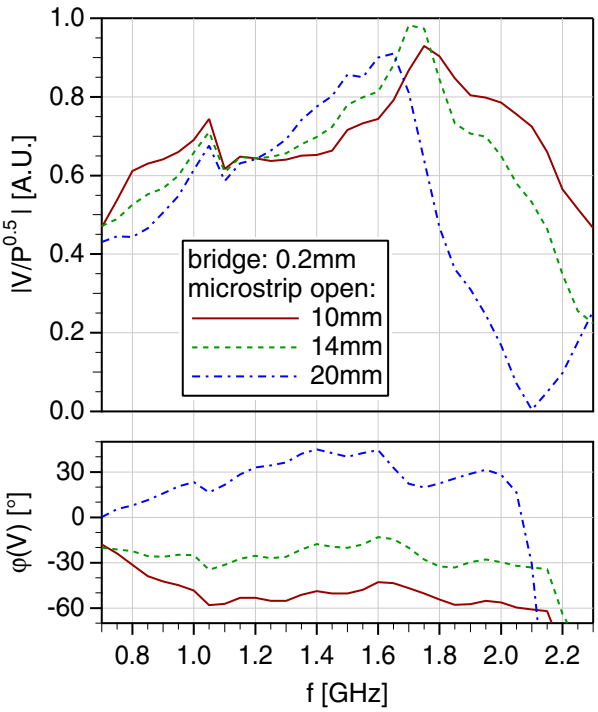

Figure 5: Voltage 5 mm above the slot of the test pick-up structure with three different lengths of the microstrip open end.

circuit, a simple test structure (Fig. 6) has been built and measured with the field mapper. The voltage, 5 mm above the slot, and the S-parameters between the two ports have been measured with six different lengths from 10 mm to 20 mm of the micro-strip open end and with two different widths of 0.2 mm and 2 mm of the microstrip lines on the Al_2O_3-bridges.

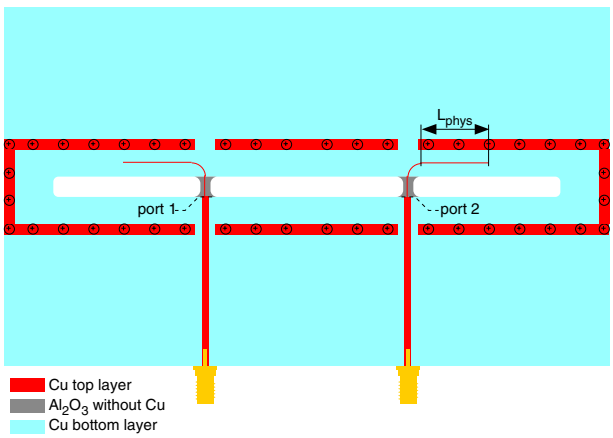

Figure 6: Layout of the test pick-up structure.

The circuit diagram (Fig. 7) shows the equivalent circuit of the test structure. The circuit has been simulated using Microwave Office [3]. The green underlined values are the fit parameters. The slotlines have been modeled by transmission lines with a frequency dependent impedance Z_{slot} and relative dielectric constant ε_{slot}. The losses of the slotlines have been modeled by the two attenuators with a voltage damping of D_{slot}. The main contribution to the losses comes from electromagnetic radiation. The resistive and dielectric losses are much lower. The parameters for the slotline have been derived from a numerical field calculation [2] of the slotline in the module using Microwave Studio [4]. The microstrip lines have been modeled by a Microwave Office model. The transition between slotline and microstrip line have been modeled by an ideal transformer and two suspended ground microstrip line, H_2 above the groundplane. The fit parameters for these components have been derived from the 12 field and S-parameter measurements.

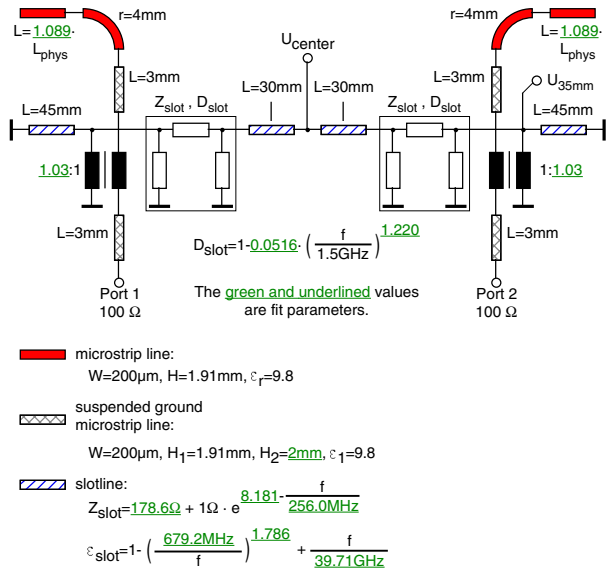

Figure 7: Equivalent circuit of the test pick-up structure in Fig. 6.

The diagrams in figure 8, 9 and 10 show a comparison of the final equivalent circuit results with the measured data. All the measurement equipment has an impedance of 50 Ω, whereas the pick-up is a 100 Ω device. The interfaces are at the dashed lines (port 1 and 2) in figure 6. The influence of this reflection, all cables and connectors as well as the frequency response of the near-field probe, has been eliminated from the measurement data in the diagrams. Figure 8 shows the transmission and figure 9 the reflection on port 1. Figure 10 shows the voltage above the center of the slot. The diagrams show a good agreement between the equivalent circuit and the measurements.

After the “calibration” of the equivalent circuit, it has been used to optimize the pick-up by varying the lengths of the slots and microstrips and the widths of the microstrips. The first result is the pick-up layout in figure 1 with the frequency response in figure 2.

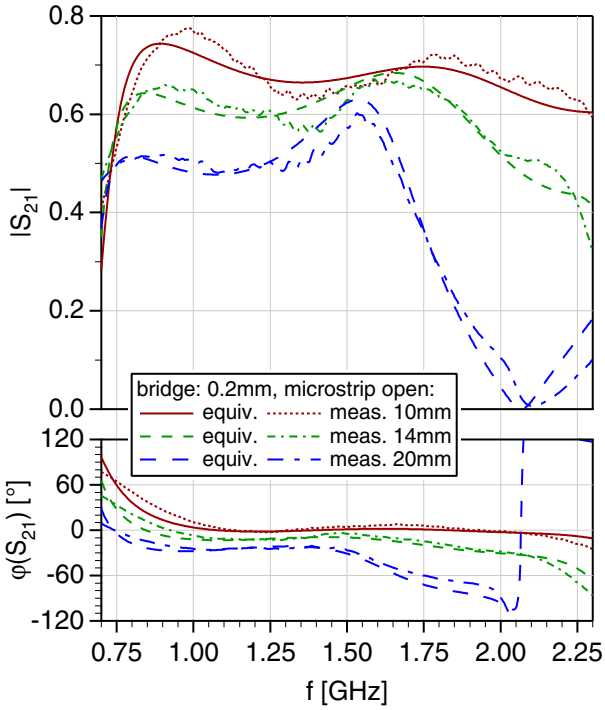

Figure 8: S_{21} of equivalent circuit and test structure.

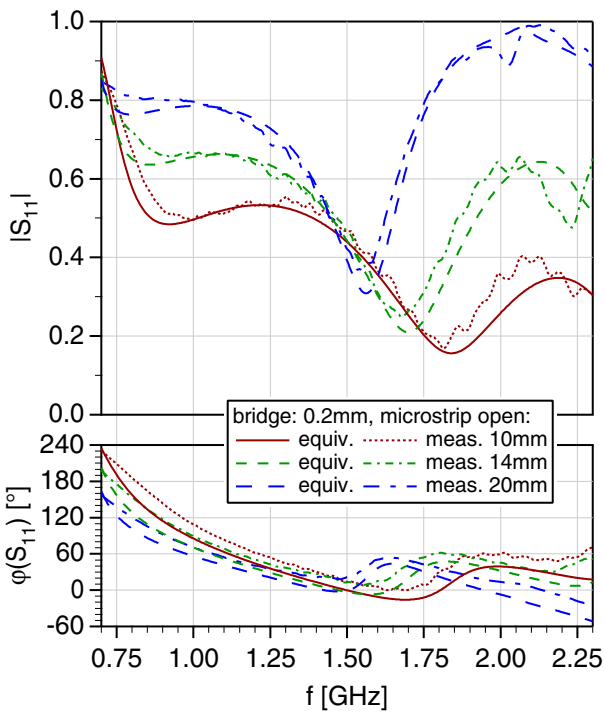

Figure 9: S_{11} of equivalent circuit and test structure.

SUMMARY AND OUTLOOK

The developed planar pick-up electrode has a large bandwidth and is suitable for a large aperture. The field measurement shows, that even the test structure (Fig. 6) has a relatively flat amplitude and very flat phase versus the frequency over one octave. The field measurements of the test structure together with S-parameter measurements provides data to construct an adequate equivalent circuit. This circuit has been used to optimize the layout. The result of the simulation (Fig. 2) in promising.

The next step will be a field measurement of a complete module using the field mapper and the middle wire method.

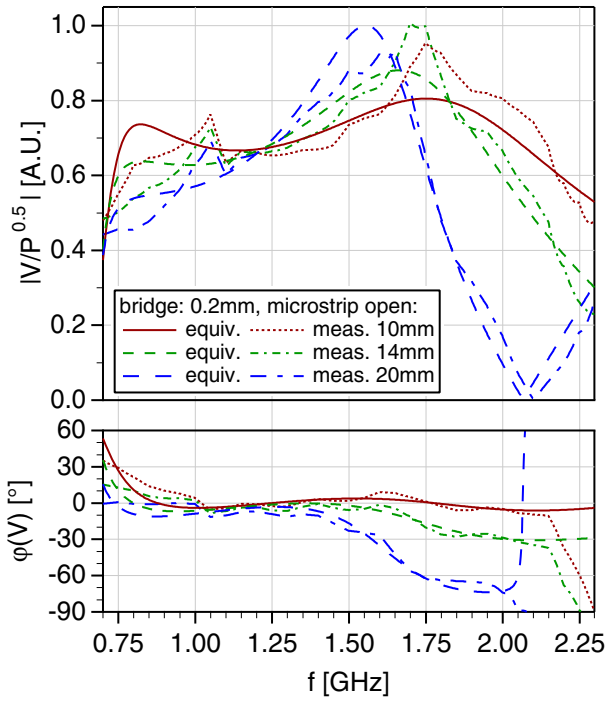

Figure 10: Voltage over the slot of equivalent circuit and test structure.

REFERENCES

[1] C. Peschke, F. Nolden, M. Balk: “Planar Pick-Up Electrodes for Stochastic Cooling”; Nuclear Instruments and Methods A 532 (2004), pages 459–464

[2] C. Peschke, F. Nolden, L. Thorndahl: “Pick-Up and Kicker Electrodes for the CR”; COOL 05, AIP Conference Proceedings 821, pages 221-225

[3] Program “Microwave Office”, Applied Wave Research Inc., 1960 E. Grand Avenue, Suite 430, El Segundo, CA 90245, http://www.appwave.com

[4] Program “Microwave Studio”, CST GmbH, Bad Nauheimer Straße 19, D-64289 Darmstadt, Germany, http://www.cst.de

BEAM BASED MEASUREMENTS FOR STOCHASTIC COOLING SYSTEMS AT FERMILAB *

Ralph J. Pasquinelli, Valeri Lebedev, Steven J. Werkema, Fermilab, Batavia, Illinois, USA

Abstract

Improvement of antiproton stacking rates has been pursued for the last twenty years at Fermilab. The last twelve months have been dedicated to improving the computer model of the Stacktail system.[1] The production of antiprotons encompasses the use of the entire accelerator chain with the exception of the Tevatron. In the Antiproton Source two storage rings, the Debuncher and Accumulator are responsible for the accumulation of antiprotons in quantities that can exceed $2x10^{12}$, but more routinely, stacks of $5x10^{11}$ antiprotons are accumulated before being transferred to the Recycler ring. Since the beginning of this recent enterprise, peak accumulation rates have increased from $2x10^{11}$ to greater than $2.3x10^{11}$ antiprotons per hour. A goal of $3x10^{11}$ per hour has been established. Improvements to the stochastic cooling systems are but a part of this current effort. This paper will discuss Stacktail system measurements and experienced system limitations.

STACKTAIL DESCRIPTION

The Stacktail[2] system (Figure 2) is the largest and most complicated of the nine stochastic cooling systems in the Accumulator. This one system is responsible for taking freshly injected antiprotons and decelerating them to the core while increasing the longitudinal density. Accordingly, the Stacktail system requires a dynamic range in excess of 40 dB as 2×10^8 injected antiprotons per pulse every 2.2 seconds yields a core exceeding 5×10^{11} in a few hours. (Figure 1) The front-end pickups have three distinct energy positions which, along with the pre-amplifiers, are cooled to liquid nitrogen temperatures to maximize signal to noise ratio. Three notch filters provide gain shaping and "protection" for the core. The high level consists of eight kicker tanks powered by 32 200-Watt Traveling Wave Tubes (TWT).

TRANSFER FUNCTION MEASUREMENTS

Transfer function measurements with a network analyzer are made by placing a narrow momentum bite of antiprotons at various revolution frequencies corresponding to the different beam positions of the pickups, (which are located in a high dispersion section of the Accumulator). Of the three pickup legs, the leg at the deposition orbit (leg 1) has the largest number of antennas. The nonlinear beam density profile in Figure 1 is a consequence of the exponential gain profile (Figure3) of the Stacktail cooling system. This results in very large gain at all revolution frequencies corresponding to the deposition energy. For this reason, transfer function measurements must be performed with a comparatively small beam current depending on the beam energy to avoid saturation of the front-end preamplifiers. Finding this linear beam current limit took several iterations of transfer function measurements before the maximum beam current for each beam position was determined. In addition to limiting the beam current, the momentum width must also be controlled with the use of longitudinal scrapers or in the case of core and near core measurements, with the 4-8 GHz core momentum cooling. With a large gain slope, a wide momentum profile would provide a different transfer function than a narrow distribution with the same beam current.

To verify the linearity of the results, two sets of measurements were taken. The first set of transfer functions is obtained with the network analyzer in frequency list mode set to harmonics of the revolution frequency (between 1.5-4.5 GHz) of the beam distribution centroid. The network analyzer excites a coherent mode on the beam motion resulting in a response in all three legs (Figure 4). If the excitation and/or beam current are too large, the resulting response may saturate the preamplifiers.

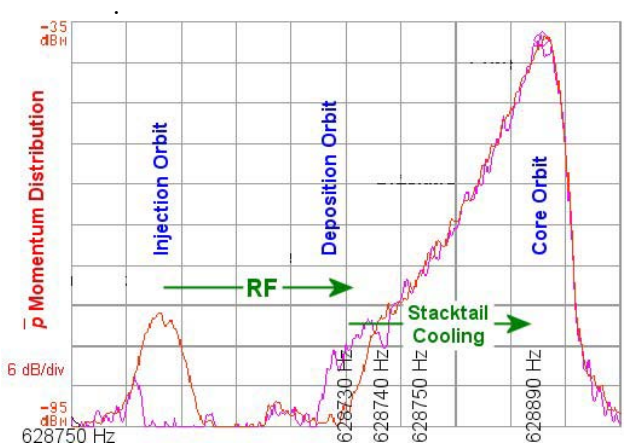

Figure 1: Stacktail Schottky profile vs. revolution frequency. Red trace with freshly injected antiprotons on the injection orbit, purple trace shows remnant antiprotons not picked up by the RF system and the resultant momentum displacement due to the Stacktail cooling.

*Work supported by Fermi Research Alliance under contract to the US Department of Energy.

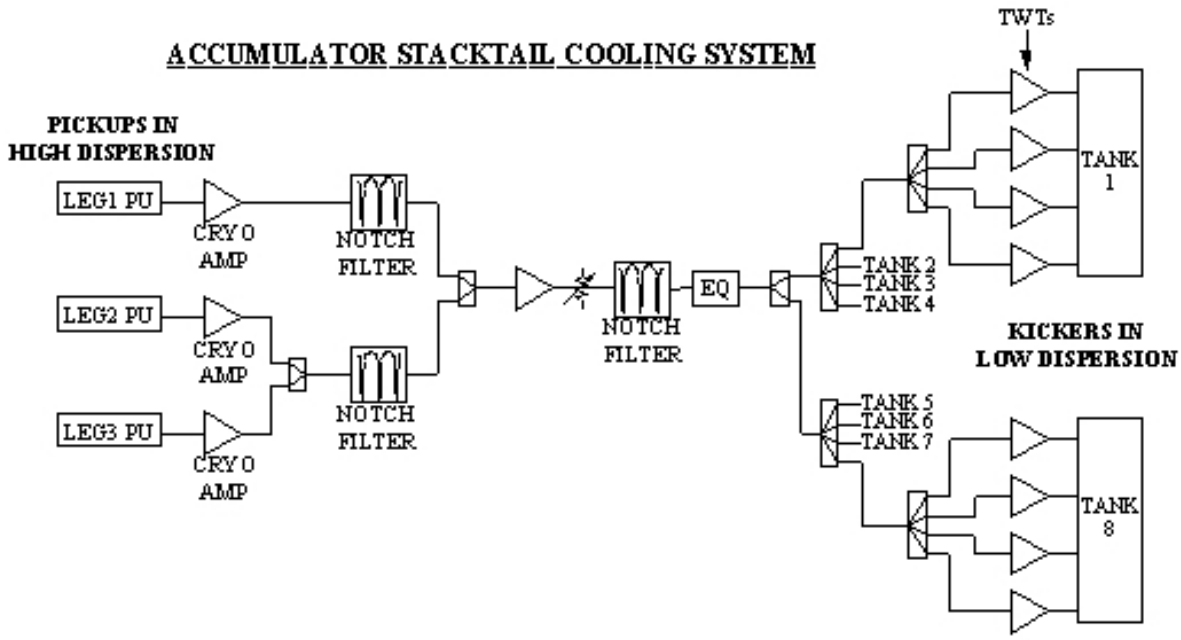

Figure 2: Block diagram of Stacktail cooling system.

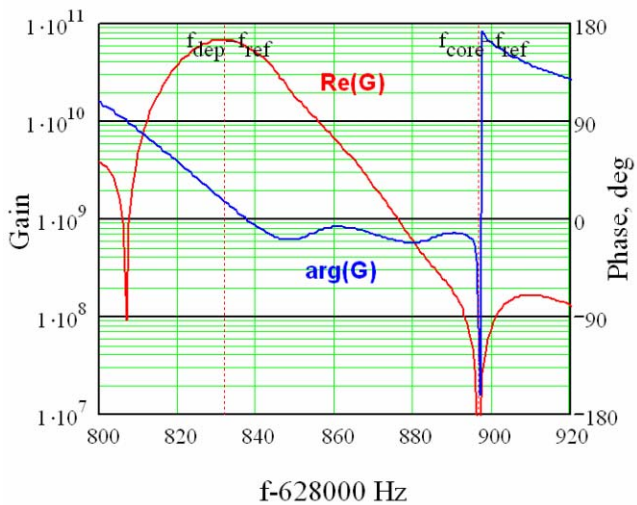

Figure 3: Gain profile of the Stacktail with real part of the gain function and phase as a function of revolution frequency.

A second set of measurements is taken slightly off the central frequency harmonics. For this second measurement, the coherent response of the beam is reduced by some 10-20 dB and shifted in phase by 180 degrees, but remains above the system noise floor. Beam currents were reduced until the ratio of on-resonant and off-resonant measurements were proportional guaranteeing amplifier linearity. All subsequent

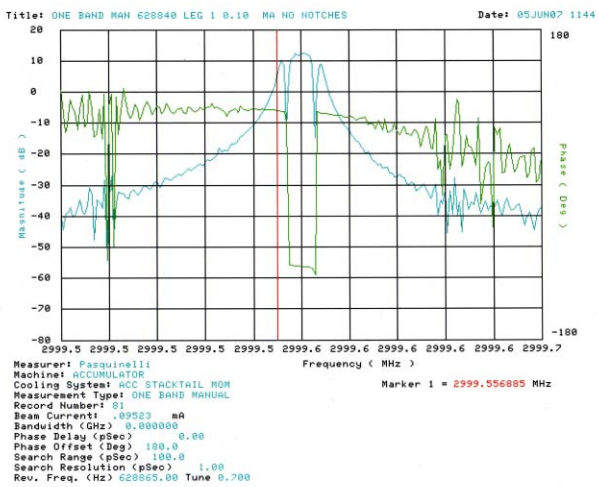

Figure 4: Single Schottky band transfer function measurement. Center frequency is at the beam revolution harmonic, red line marker off resonance frequency. Note 180-degree phase shift along with reduced amplitude response.

measurements are made with this determined beam current and momentum distribution. (Figure 5) An additional cross check with narrow band measurements at different revolution frequencies has also proven beneficial.

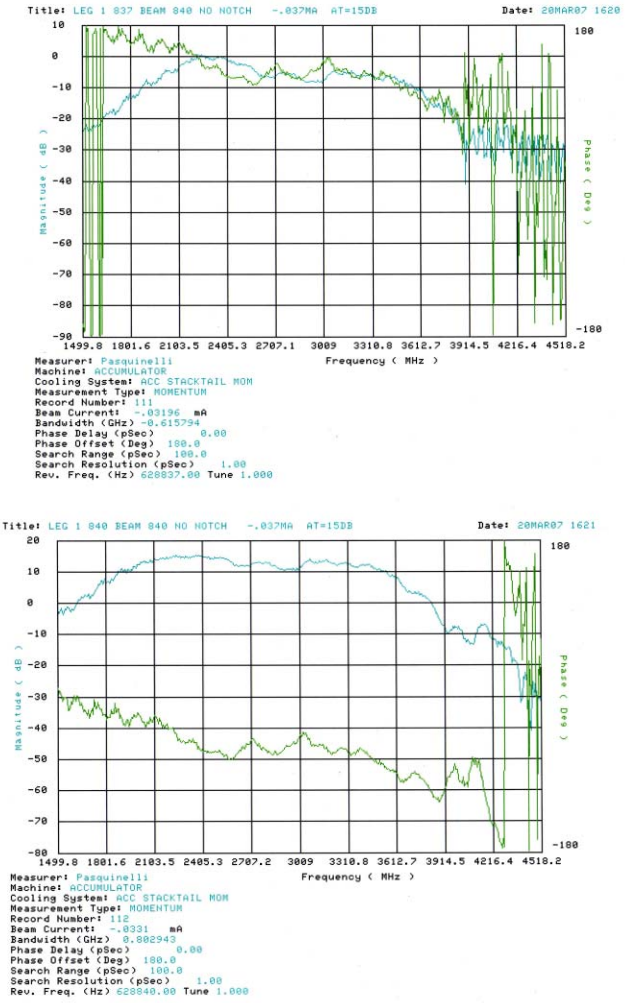

Figure 5: Top transfer function off resonance, bottom transfer function on resonance. Note significant gain and 180-degree phase shift, but there is a proportional relationship between the two indicating no amplifier saturation on resonance.

Notch filters provide rapid gain and phase variations with frequency, which complicates analysis of the measurements. To exclude these complications all measurements were taken with notch filters off (long leg of correlator filters terminated). Notch filters were measured separately and their effect was taken into account in the simulations and system optimization.

To build a Stacktail model, in addition to the measurements of transfer functions, one needs to know dependence of pickup sensitivity as a function of beam energy within each pickup array. It was obtained by measuring Schottky noise in a narrow band (usually a single revolution frequency band at 2.4 GHz) for each pickup array and comparing it to a signal of a 79 MHz Schottky monitor which is located at zero dispersion and therefore does not have direct dependence of the signal on the beam energy. Relating all signals to the first harmonic of revolution frequency and making a square root of

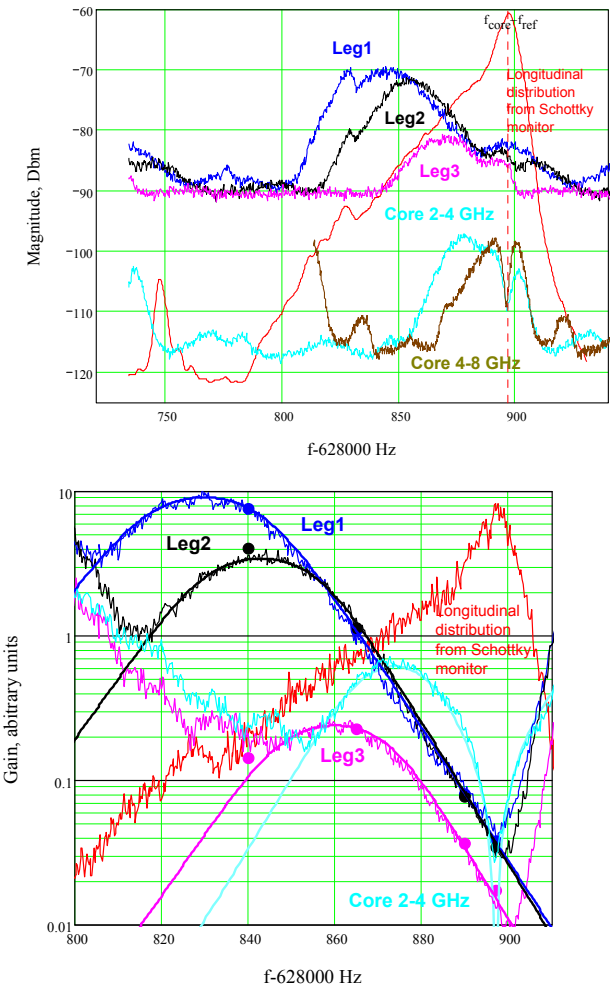

Figure 6: Top shows the Schottky signals from all longitudinal cooling systems in the Accumulator while stacking. Leg 1,2,3 refers to the Schottky signal from each individual pickup of the Stacktail system. Also included is the Stacktail longitudinal profile. Bottom shows the Schottky signals normalized to the distribution profile. The dots are the network analyzer transfer function measurements at various revolution frequencies. The close agreement indicates the transfer functions are truly representative of the system gain, which is most important for the computer model.

signal ratios from a Stacktail pickup and Schottky monitor, one obtains a dependence of corresponding pickup sensitivity on the horizontal particle position within pickup (see Figure 6). To acquire this data all longitudinal cooling systems including the Stacktail have to be stopped to avoid changes of the distribution during measurements. This was verified by acquiring longitudinal Schottky monitor signals at the beginning and at the end of measurements. Automation of the measurements allowed us to reduce time of data acquisition to about 10 minutes. The final transfer function measurements for three different revolution

frequencies as a function of 2-4 GHz system bandwidth is shown in Figure 7.

SYSTEM LIMITATIONS

Once the transfer functions were understood and faithfully reproducible, these measurements were used to design an equalizer[3] to maximize system performance. The equalizer took two iterations to perfect and did provide improved system bandwidth and phase linearity. The intention was that the equalizer would allow for increasing system gain, hence pushing beam away from the deposition orbit before the next batch arrives.

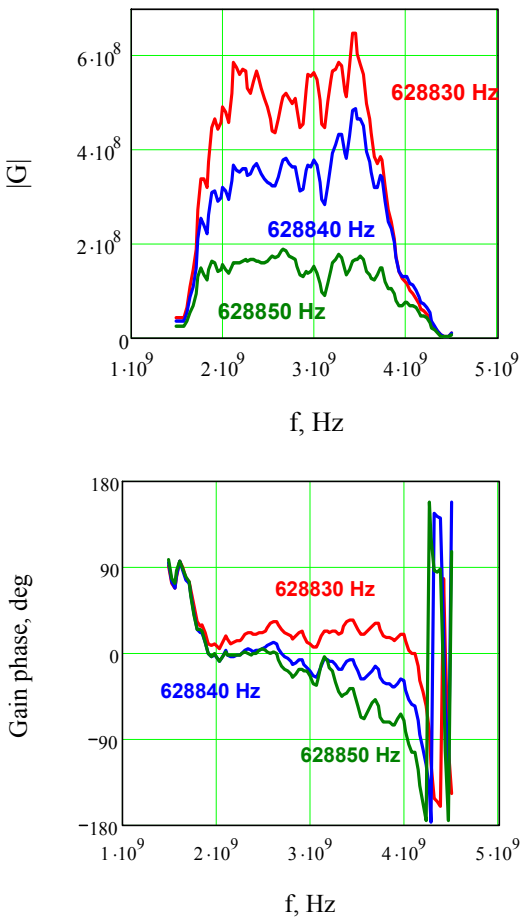

Figure 7: Transfer functions as a function of beam revolution frequency in the 2-4 GHz system bandwidth.

Operational power is 1-2 kilowatts from the 32 installed TWTs with 200-Watts capacity each. This power level is well below the available saturated power, but the TWTs exhibit significant intermodulation distortion as saturated power is approached.[4] These intermods cause the notches to fill in with uncorrelated noise power that tends to heat the core.

Experimenting with system gain showed that the beam could now be moved from the deposition orbit more quickly but only at the expense of longitudinal core blow up. A new core 4-8 GHz momentum equalizer has been installed to improve that system's effectiveness.

Transverse core heating was also observed with increased Stacktail power levels. This problem was addressed by a lattice redesign[5] that significantly lowered detrimental transverse heating from the Stacktail.

The Stacktail system has a multidimensional tuning space with knobs controlling gain, phase intercept, delay, and notch filter frequencies. This coupled with the fact that the tuning procedure distorts the stack profile makes for a challenging optimization that has been in progress for over two decades.

REFERENCES

[1] Valeri Lebedev, Antiproton Production and Accumulation, Proceedings of this Workshop.

[2] Ralph J. Pasquinelli, Dave McGinnis, Performance of the Upgraded Stacktail Momentum Cooling System in the Fermilab Antiproton Source, Proceedings of the 1993 Particle Accelerator Conference, pages 2361-2363

[3] Ding Sun, Development and Design of Equalizers for Stochastic Cooling at Fermilab, Proceedings of this Workshop.

[4] Ralph J. Pasquinelli, Signal to Noise and Dynamic Range Issues in System Design, Proceedings of the 1993 Beam Instrumentation Workshop Santa Fe, New Mexico, AIP Conference Proceedings #319, pages 58-71

[5] Vladimir P. Nagaslaev, Lattice Optimization for the Stochastic Cooling in the Accumulator Ring at Fermilab, Proceedings of this Workshop.

NEW EQUALIZERS FOR ANTIPROTON STOCHASTIC COOLING AT FERMILAB *

Ding Sun, Valeri Lebedev, Ralph J. Pasquinelli, Fermilab, Batavia, Illinois, USA

Abstract

In the continuous effort to improve antiproton stacking rate, a new type of equalizers has been developed and installed in antiproton accumulator. The R&D of these new equalizers is described in this paper.

INTRODUCTION

Equalizers are used in Fermilab antiproton stochastic cooling to compensate frequency response of the cooling system. Usually both amplitude and phase compensations are needed. However in most cases it is difficult to achieve a satisfactory compensation for both because of their interdependence. To make it more difficult is that in some cases large compensations (10 to 20 db of amplitude compensation or more than 100 degree of phase compensation) are needed near the low or high ends of a frequency band. Recently a new compensation scheme of equalizers is proposed for Fermilab antiproton accumulator. This scheme originated from the requirement to maximize the system performance resulting in a request for the phase of the cooling system transfer function to be extremely flat. For this kind of phase correction, a new type of equalizers has been developed.

NEW EQUALIZERS

The feature of this new type of equalizer is that it consists of two separate parts: the phase equalizer and the amplitude equalizer. Each part is made and tuned separately. The function of the phase equalizer is to correct only the phase. Then the amplitude equalizer corrects the amplitude (including the distortion caused by the phase equalizer part) to a desired shape. This approach not only makes the equalizer perform as required but also increases the adjustability of the equalizer. Each equalizer part can be categorized as a transversal or analog FIR (Finite Impulse Response) filter, though the FIR filter design algorithm was not followed during design of these filters. Shown in Fig. 1 is a schematic of one of these new equalizers.

The phase equalizer part of the new equalizer consists of power splitters, two or more two-port low-Q resonant circuit components, attenuators and delay lines. Shown between point A and B in Fig. 1 is a schematic of a phase equalizer part consisting of three resonant components. The input signal is first split into several signals.

*Work supported by Fermi Research Alliance under contract to the US Department of Energy.

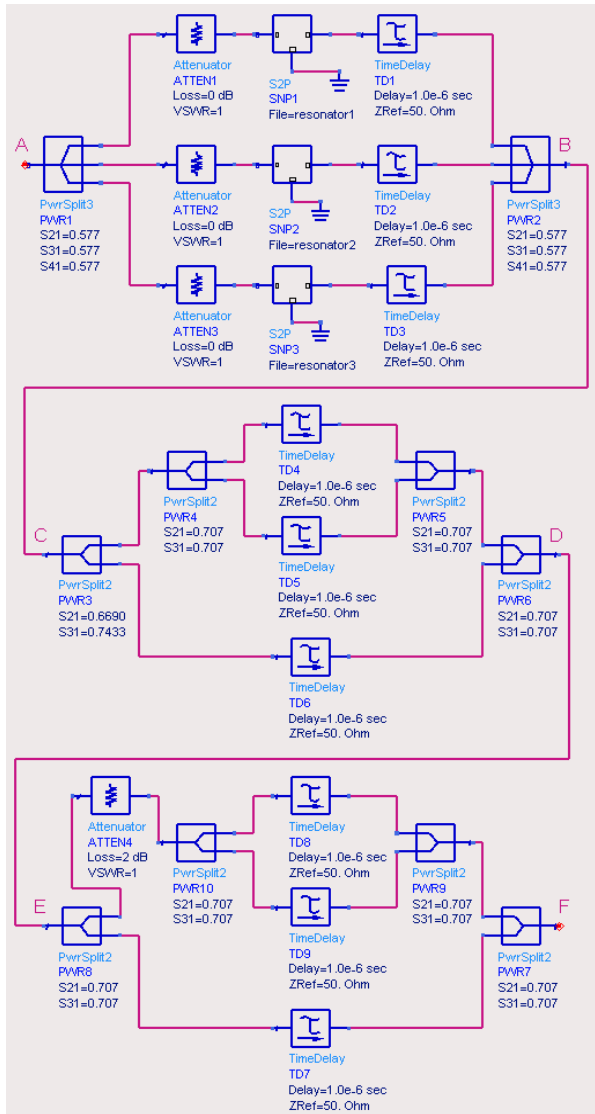

Figure 1: Schematic of a new equalizer.

Then the split signals are attenuated to various levels and fed into resonant components. After the resonant components, the split signals are recombined with various delay time for each sub-signal. Parameters of each individual circuit component such as resonant frequency, Q, attenuation, and delay time are used to control the location and slop of the phase change. Resonant components in Fig. 1 are implemented with parallel coupled microstrip (or stripline) lines. Shown in Fig. 2 is one of such resonant components. Other structures can also be used as long as they can generate desired phase change. To shorten R&D time, commercial power

splitters (combiners) with equal split ratio and attenuators are used as shown in Fig. 1. However, they can be replaced with a splitter of unequal split ratio to make the phase equalizer part more compact (as long as the split ratio is not too large to be implemented). Shown in Fig. 3 and 4 are the measured phase and amplitude of a phase equalizer part. This phase equalizer part has five resonant components (five boxes shown in Fig. 7). The more resonant components are used, the finer phase correction can be achieved.

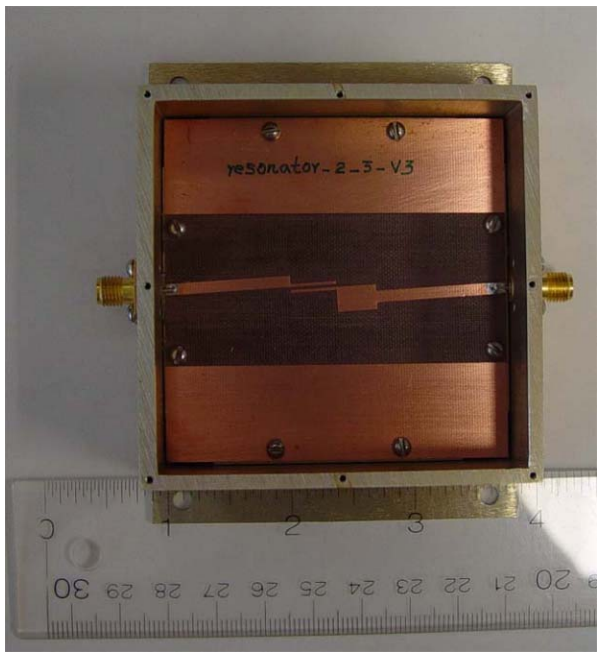

Figure 2: A resonant component.

The amplitude equalizer part is essentially one or more low-Q notch filters which "corrects" (compensates) amplitude of original transfer function plus the amplitude distortion caused by the phase equalizer part to a desired shape while keeping phase unchanged. Each notch filter consists of four splitters/combiners, attenuators and delay lines of various lengths. Shown between point C and F in Fig.1 is the amplitude equalizer part which has two units: between C and D and between E and F. In the unit between C and D, the input signal is first split unequally. One of the split signals is split again and recombined with different delay times. Then the two signals are combined again with different delay times. The first split ratio controls the depth of the notch and the difference between delay times control the location of the notch and flatness of the phase. The unit between E and F is similar to the one between C and D. The only difference is that the unequal splitter is replaced with an equal splitter and an attenuator. The more of these units are used, the finer amplitude correction can be achieved. Shown in Fig. 5 and 6 are measured amplitude and phase of an amplitude equalizer part (single unit). This amplitude equalizer part is shown in Fig. 7 alongside the phase equalizer part (five boxes).

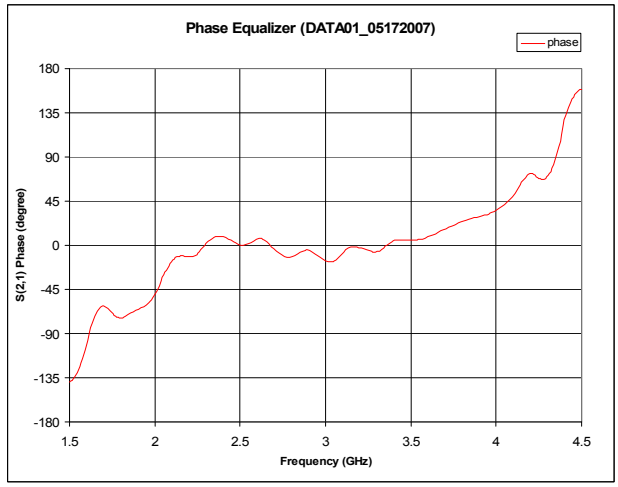

Figure 3: Phase of a phase equalizer part.

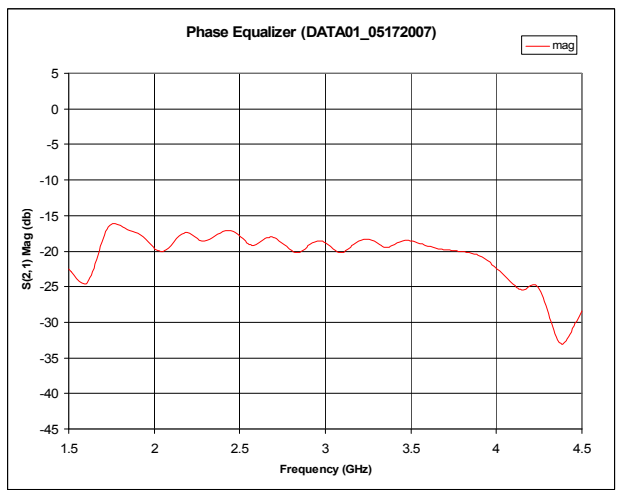

Figure 4: Amplitude of a phase equalizer part.

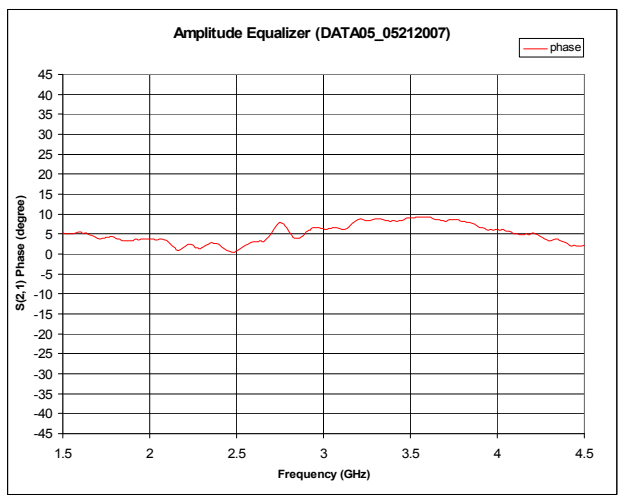

Figure 5: Phase of an amplitude equalizer part.

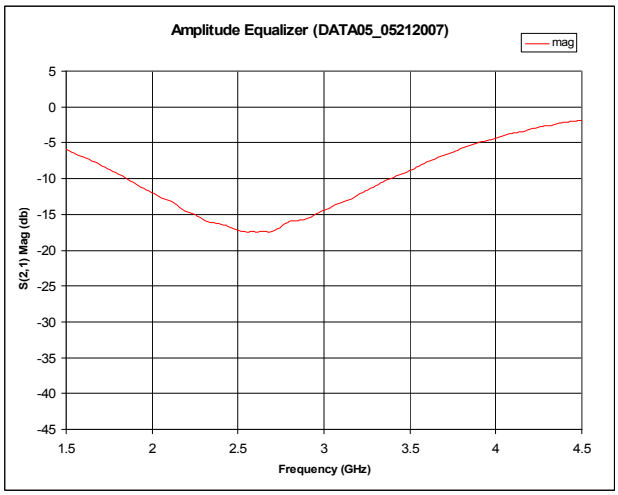

Figure 6: Amplitude of an amplitude equalizer part.

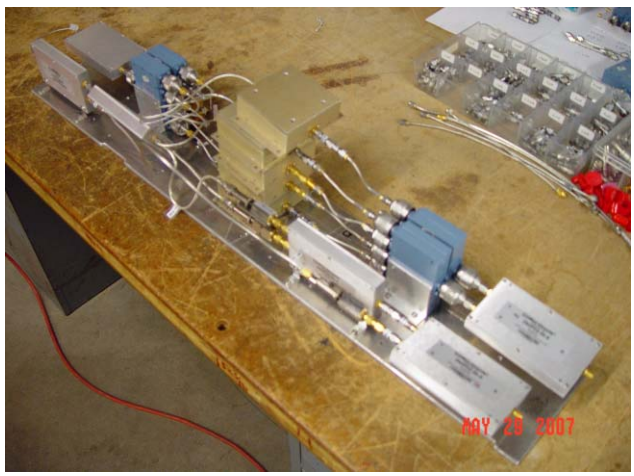

Figure 7: Assembly of a new equalizer.

Shown in Fig. 7 is an assembly of a new equalizer with the phase equalizer part (five resonant components) and amplitude equalizer part (single unit) described in the previous sections. The measured phase and amplitude of system transfer function with this equalizer versus the one without this equalizer are shown in Fig. 8 and 9. The goal is to flatten the phase between 1.75 GHz and 4.25 GHz. (Note: the amplitude part does not need to be flat up to 4.25 GHz due to heating problem generated by noise in that frequency region). This equalizer has been put in use in stacktail system and cooling rate has been improved by 5-10% [1]. Shown in Fig. 10 and 11 are the gain of the stacktail system before and after the installation of a new equalizer. A similar equalizer has been built and installed in core 4 – 8 GHz momentum system (Fig. 12).

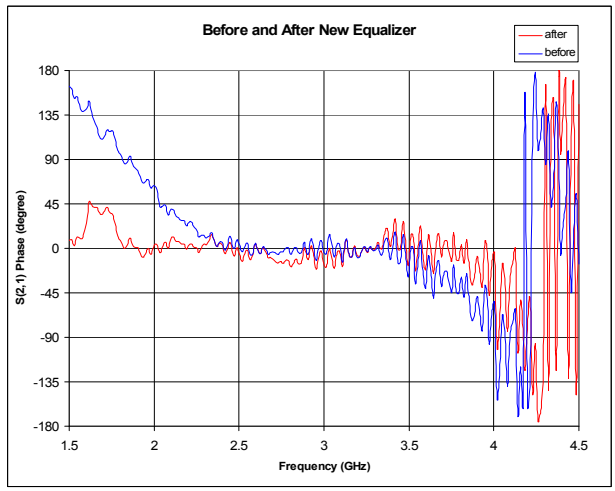

Figure 8: Phase of transfer function before and after installation of an equalizer.

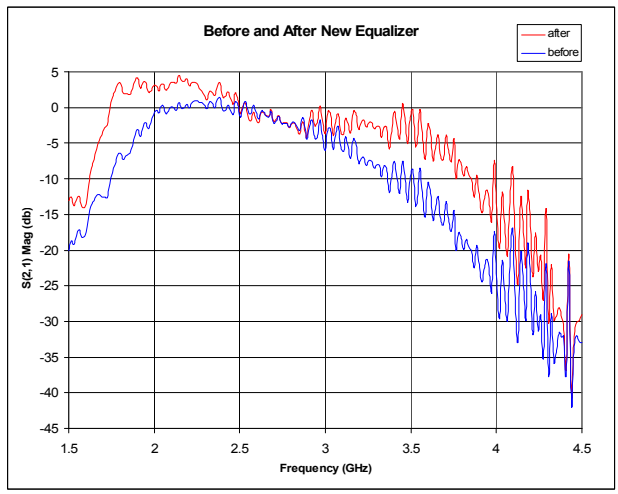

Figure 9: Amplitude of transfer function before and after installation of an equalizer.

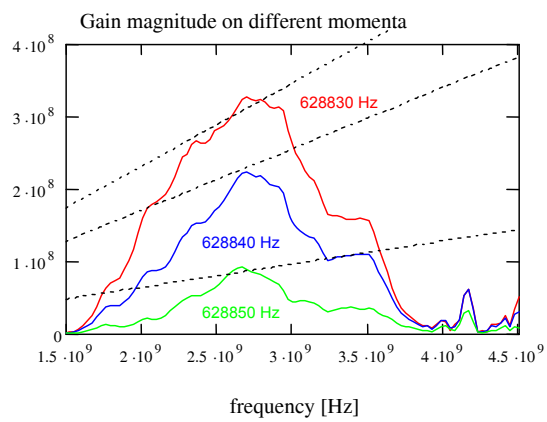

Figure 10: Stacktail gain before installation of an equalizer.

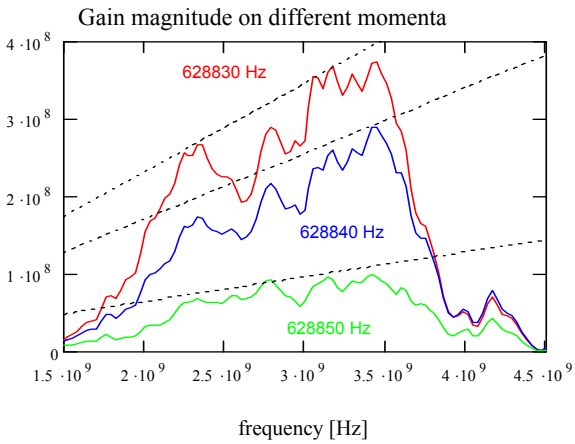

Figure 11: Stacktail gain after installation of an equalizer.

Figure 12: A new equalizer installed in core 4-8 GHz momentum system.

REFERENCES

[1] Valeri Lebedev, "Antiproton Production and Accumulation", Proceedings of this Workshop.

INFLUENCES OF SPACE CHARGE EFFECT DURING ION ACCUMULATION USING MOVING BARRIER BUCKET COOPERATED WITH BEAM COOLING*

T. Kikuchi†, S. Kawata, Utsunomiya Univ., Utsunomiya 321-8585, Japan
T. Katayama, GSI, Darmstadt, Germany

Abstract

A longitudinal ion storage method by using a moving barrier bucket with a beam cooling can accumulate the ions in a storage ring, effectively. After the multicycle injections of the beam bunch by the method, the space charge effect due to the stored particles can interfere the next accumulation of the ions, because the space charge potential can cancel the effective barrier voltage. Using numerical simulations, we employ the longitudinal particle tracking, which takes into account the barrier bucket voltage, the beam cooling and the space charge effect, for the study of the beam dynamics during the accumulation operations. As a result, it is found that the space charge effect limits the accumulation of the ions in the longitudinal storage method.

INTRODUCTION

Longitudinal beam stacking by using a moving barrier bucket system with a stochastic momentum cooling has been proposed [1]. In the proposal, not only the stochastic cooling was applied, but also the electron cooling can be a candidate for the operation [2]. The ion storage experiment by using a barrier bucket with the electron cooling has been carried out, and the experimental results are succeeded for the ion beam stacking [3].

During the ion beam stacking, the beam current will be increased with the injection numbers. The high current beam can create the strong space charge potential. The electric field induced by the space charge may interferer the large number of the bunch injections and the higher stacking ratio.

In this study, we developed the longitudinal particle tracking code with the space charge effect, and the beam dynamics is numerically investigated by using the developed code. The numerical simulation results indicate the limitation of the ion accumulation derived from the self electric field in the stacking method. Also the space charge effect can be predicted by the simple ellipsoid shape model, and it is useful to estimate the stacking limit.

* Work supported by Japan Society for the Promotion of Science (KAKENHI No.17740361).

† tkikuchi@cc.utsunomiya-u.ac.jp

OPERATION OF ION ACCUMULATION BY MOVING BARRIER BUCKET WITH ELECTRON COOLING

The longitudinal ion accumulation by using the moving barrier bucket with the electron cooling can be operated as follows [2, 4]. First, the bunch is injected into the region between two barrier voltages. The energy spread of the beam is decreased by the electron cooling. After the cooling, the beam with the small energy spread is separated by the moving barrier bucket operation for the partitioning. To repeat the above procedure, the ions are accumulated with the new injections.

LONGITUDINAL PARTICLE TRACKING OPERATED BY MOVING BARRIER BUCKET WITH SPACE CHARGE EFFECT

Basic Equations of Motion in Phase Space

The energy difference $\Delta E = E - E_s$ [eV/n] from the synchronous energy E_s in the barrier bucket is calculated by

$$\frac{d\Delta E}{dt} = \frac{q}{m}\frac{V_{bb}}{T_0} - E_{cool} - \frac{q}{m}\frac{g}{4\pi\epsilon_0\gamma^2}\frac{d\lambda}{d\tau}. \qquad (1)$$

where q is the charge state of the beam ion, m is the atomic mass number, $V_{bb} \equiv V_{bb}(t,\tau)$ is the voltage of the moving barrier bucket, T_0 is the revolution period, E_{cool} is the beam cooling term, g is the geometry factor, ϵ_0 is the permittivity of free space, and λ is the line charge density.

The time τ in the moving frame depends on time t in the laboratory frame is calculated by

$$\frac{d\tau}{dt} = \frac{\eta}{\beta^2}\frac{\Delta E}{E_0},$$

where β is the velocity divided by light speed c, $\eta = 1/\gamma^2 - 1/\gamma_{tr}^2$ is the phase slip factor with the transition gamma γ_{tr}. Here $E_0 = E_k + m_0c^2$ is the synchronous energy per nucleon, where E_k is the kinetic energy per nucleon and $m_0c^2 = 931.481$ MeV is the rest energy of the atomic mass unit based on ^{12}C.

Barrier Bucket Voltage

Figure 1 shows the barrier bucket voltage waveform at each injection time. The barrier bucket shape is a sinusoidal waveform, and the pulse duration T_1 is 200 ns. The duration between the left and right barrier pulses $T_2 \equiv T_2(t)$

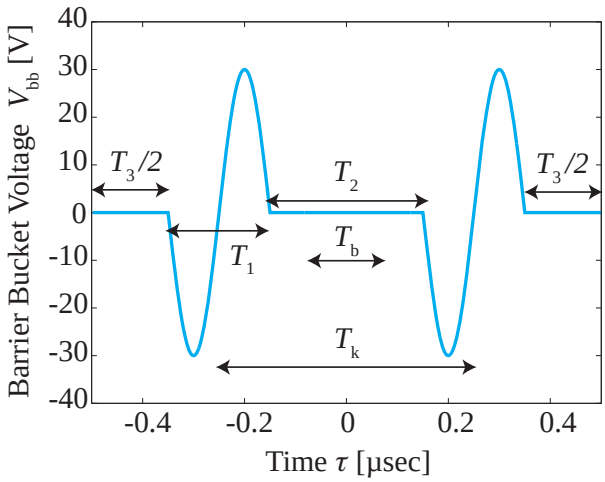

Figure 1: Barrier bucket voltage waveform at each injection time.

is changed as $-T_1/2 \sim 300$ ns. The duration of the storage region $T_3 \equiv T_3(t)$ is > 300 ns. The flat-top region of the magnetic kicker pulse T_k is 500 ns. The injection of new batch is carried out in the duration $T_b = 150$ ns. The maximum amplitude of the barrier bucket voltage is 30 V in this paper. According to the above voltage waveform, the kinetic energies of the ions are changed as the first term of the right hand side in Eq. (1).

Electron Cooling

The electron cooling term (second term of the right hand side in Eq. (1)) is solved by

$$E_{cool} = -\Delta E\, k_c G,$$

for the longitudinal direction, and $d\,\varepsilon_t/dt = -2k_c\,\varepsilon_t\,G$, for the transverse emittance ε_t. Here

$$G = \left[\frac{\beta^2\gamma^2\varepsilon_t}{\beta_c} + \left(\frac{\Delta E}{\beta E_s}\right)^2 + \frac{2\,T_{eff}}{m_e c^2}\right]^{-3/2},$$

and the coefficient is

$$k_c = \frac{4 r_e r_n c\, n_e \eta_c L_p}{\gamma^2}\frac{q^2}{m},$$

where β_c is the beta function at the cooler section, T_{eff} is the effective temperature of the electron beam, m_e is the electron mass, r_e and r_n are the classical electron and proton radii, n_e is the number density of the electron beam, and L_p is the Coulomb logarithm. Here $\eta_c = L_{ec}/C$, where L_{ec} is the cooler length and C is the circumference of the ring.

Space Charge Effect

The calculation for the space charge effect is based on a particle-in-cell (PIC) method [5]. The particles give the charge to the grid points, and the line charge density can be calculated at each grid. According to the third term of the right hand side in Eq. (1), the space charge effect can be included in the longitudinal particle dynamics.

ESTIMATION OF SPACE CHARGE POTENTIAL BY SIMPLE BUNCH MODEL

When a beam bunch has the uniform density with the ellipsoid shape, the space charge potential can be calculated by an analytical formula. The maximum potential of the ellipsoidal bunch in free space is given as [6]

$$|\phi_{fs}| = \frac{\rho_0}{2\epsilon_0} M_E {z_b}^2, \qquad (2)$$

where ρ_0 is the uniform charge density and the factor M_E is derived by

$$M_E = \frac{1-\xi^2}{\xi^2}\left(\frac{1}{2\xi}\log\frac{1+\xi}{1-\xi} - 1\right).$$

Here $\xi = \sqrt{1 - r_b^2/z_b^2}$, where r_b is the beam radius and z_b is the bunch half length in the longitudinal direction. The charge density is calculated by

$$\rho_0 = \frac{qeN_b(N_{inj}-1)}{V_b},$$

where e is the elementary charge, N_b is the number of ions per batch, N_{inj} is the injection number, and the volume of the ellipsoid is written by $V_b = 4\pi {r_b}^2 z_b/3$. The bunch half length is estimated by $z_b = T_3 C/2T_0$.

From Eq. (2), the potential is calculated by $|\phi_{fs}| = 31.4$ V ($> V_{bb}$) after 16 injections, and the space charge potential overcomes the barrier bucket voltage. The parameters for the estimate are as follows:

Table 1: Bunch parameters

Ring circumference C	108.36 m
Revolution time T_0	1000 ns
Beam radius r_b	0.1 mm
Charge state q	18
Number of Ions per batch N_b	7×10^7

NUMERICAL SIMULATION RESULTS

We numerically simulate the beam dynamics in the moving barrier bucket with a momentum cooling process by using the procedures described in the previous section. The example calculation is performed by using data of the last ESR experiment [3]. The condition is summarized as Table 2.

The injected ions per batch are represented by 500 particles in a manner as PIC method, and the ions have a Gaussian distribution as the energy spread and a uniform distribution in the time at the injection time. The longitudinal

Table 2: Parameters for numerical simulations

Beam	
Ion species	$^{40}Ar^{18+}$
Kinetic energy	65.3 MeV
Particle number per batch	7×10^{7}
Energy spread (1σ) of injection batch	0.3 MeV
Ring	
Circumference C	108.36 m
Energy acceptance	+/- 0.6 MeV
Phase slip factor η	-0.6959
Electron cooler	
Electron beam current	0.3 A
Effective temperature T_{eff}	10^{-3} eV
Cooler length L_{ec}	1.8 m
Beam diameter	50 mm
Beta function β_c	16 m

phase space is discretized by 50 grids for the space charge calculation. A new injection bunch is added in the particle tracking calculation at each injection time, and the particles in the region of the kicker magnet operation become the lost particles before the injection procedure. The geometry factor is assumed to be $g = 2$, and the Coulomb logarithm is $L_p = 2$. The initial transverse emittance at each injected ion ε_t is set by 1.36 mm mrad.

Figure 2 shows the typical particle distributions, the barrier bucket voltage waveforms and the space charge potentials. The stacked ions are separated by the moving barrier bucket voltage, and the ions are accumulated into T_3 region. The stacked ions generate the space charge potential.

The longitudinal emittance during the operation is shown in Fig. 3. The longitudinal emittance ε_z is given by

$$\varepsilon_z = \left[\left\langle (\Delta E - \Delta E_0)^2 \right\rangle \left\langle (\tau - \tau_0)^2 \right\rangle - \left\langle (\Delta E - \Delta E_0)(\tau - \tau_0) \right\rangle^2\right]^{1/2},$$

where ΔE_0 and τ_0 are the average values. After the beam injection into the storage ring, the longitudinal emittance decreases rapidly, because the energy spread can be decreased by the electron cooling. The cooled beam is separated by the barrier bucket to the accumulation region T_3, and the longitudinal emittance is slightly increased by the operation. The emittance increases due to the new beam bunch injected with the large energy spread. Since the stacked ions can be continued cooling by the electron cooler, the fluctuations of the longitudinal emittance become comfortable into some level.

The accumulated ion number normalized by the number of ions per batch is shown in Fig. 4, and Figure 5 shows the ratio of the stacked ions in the ring to the number of injected ions. Although the number of the accumulated ions increases with the new bunch injections, the particle number is saturated as shown in Fig. 4. As shown in Fig. 5, the stacking efficiency is rapidly decreased after 150 sec.

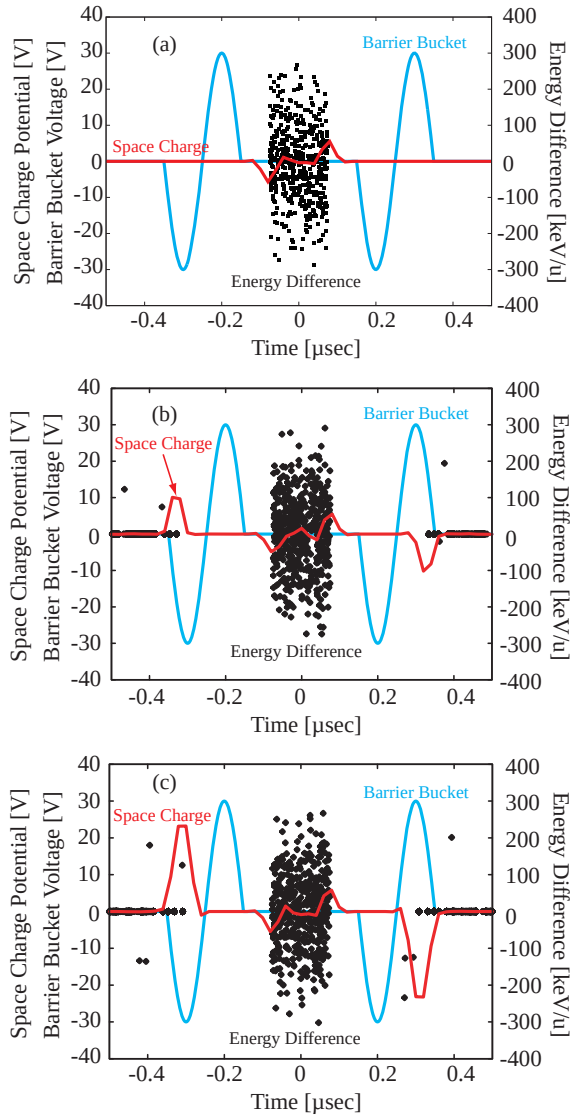

Figure 2: Particle distribution (black dot) in $\Delta E - \tau$ phase space and barrier bucket voltage (cyan line) and space charge potential (red line), (a) for initial condition (1st injection), (b) for 6th injection, and (c) for 21th injection.

The space charge potential generated by the accumulated ions at each injection number is shown in Fig. 6. Figure 7 shows the amplitude of the barrier bucket voltage and the maximum values of the space charge potential created by the stacked ions at each stacking number $N_{inj} - 1$. The maximum value of the space charge potential is indicated as the numerical simulation results in Fig. 6. The solid curve in Fig. 7 is estimated by the ellipsoid bunch shape model in Eq. (2).

The space charge potential can cancel the barrier voltage, and the effective voltage of the barrier bucket decreases. For this reason, the stacked ions penetrate the barrier bucket region as shown in Fig. 2, and the barrier bucket cannot effectively control the ions due to the space charge effect. The ions penetrated inside the barrier bucket are kicked out

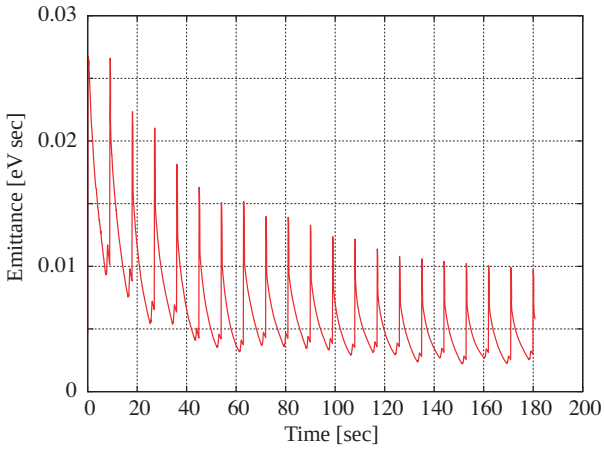

Figure 3: Longitudinal emittance history.

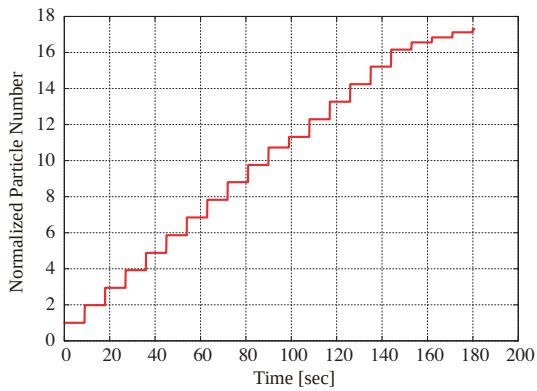

Figure 4: Stacked particle number normalized by the ions per injection batch.

from the ring at the next magnetic kicker operation.

CONCLUSIONS

Space charge effect during the ion accumulation using the moving barrier bucket cooperated with the electron cooling was numerically investigated by using the longitudinal particle tracking. It was found that the ion accumulation can be interfered due to the space charge potential created by the stacked ions. Space charge effect is one of important roles for stacking antiprotons and ions in an accumulation ring. The space charge effect can be predicted by the simple ellipsoid shape model, and it may be useful to design the barrier voltage.

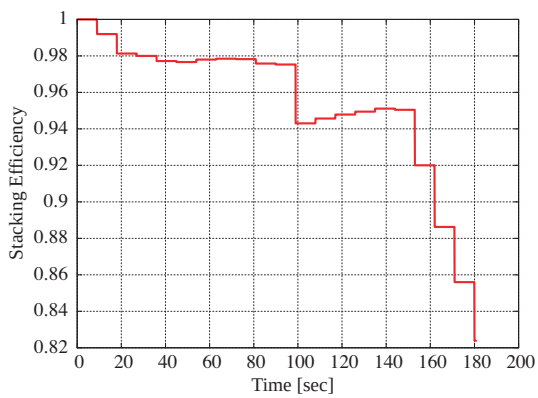

Figure 5: Stacking efficiency (= particle number in the ring / injected particle number).

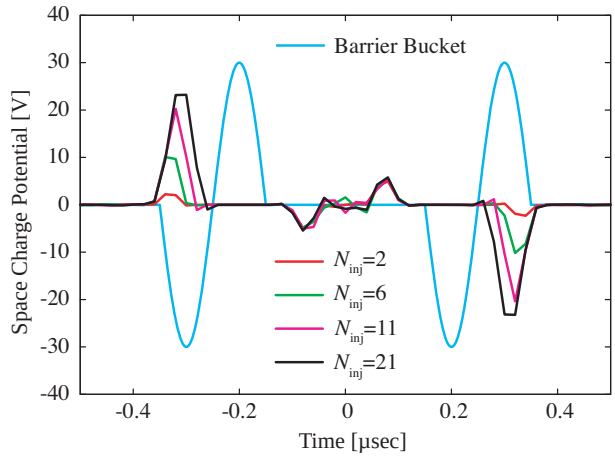

Figure 6: Barrier bucket voltage and space charge potential during the ion storage.

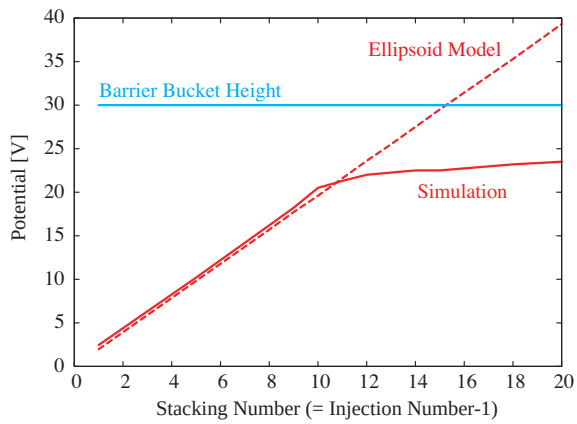

Figure 7: Space charge potential of the analytical estimation and the simulation result.

REFERENCES

[1] T. Katayama, et al., Proc. of International Workshop on Beam Cooling and Related Topics (COOL05), Illinois, 18-23 September 2005, AIP Conf. Proc. Vol.821, pp.196-205.

[2] C. Dimopoulou, et al., Phys. Rev. ST-AB **10**, 020101 (2007).

[3] C. Dimopoulou, et al., *in this proceedings*.

[4] T. Katayama, et al., *in this proceedings*.

[5] R.W. Hockney and J.W. Eastwood, *Computer Simulation Using Particles*, McGraw-Hill, New York, (1981).

[6] M. Reiser, *Theory and Design of Charged Particle Beams*, Wiley, New York, (1994).

INTERNAL TARGET EFFECTS IN THE ESR STORAGE RING WITH COOLING

V. Gostishchev#, C. Dimopoulou, A. Dolinskii, F. Nolden, M. Steck, GSI, Darmstadt, Germany

Abstract

The accurate description of internal target effects is important for the prediction of operation conditions which are required for future experiments in the storage rings of the FAIR facility at GSI. A number of codes such as PTARGET, MOCAC, PETAG01 and BETACOOL have been developed to evaluate the beam dynamics in the storage ring, where an internal target in combination with an electron cooling is applied. The systematic benchmarking experiments were carried out at the ESR storage ring at GSI. The 'zero' dispersion mode (dispersion at target position is only 0.09 m) was applied to evaluate the influence of the dispersion function on the small beam parameters when the internal target is on. The influence of the internal target on the beam parameters is demonstrated. Comparison of the experimental results with the Bethe-Bloch formula describing the energy loss of the beam particles in the target as well as with simulations with the BETACOOL code will be given.

INTRODUCTION

Nuclear physics and fundamental interaction studies in collisions of rare isotope or antiproton beams with internal targets, play an important role in the NESR and HESR storage rings of the future FAIR facility [1]. High luminosities of up to 2×10^{32} $cm^{-2}s^{-1}$ are required for experiments with a hydrogen pellet target in the HESR. Therefore, an understanding of the process of beam-target interaction is crucial for prediction of the target effects which effect on the parameters of the stored beam. Investigations of the interplay between electron cooling, intrabeam scattering (IBS) and target effect is essential for the prediction of equilibrium beam parameters. Some experiments with gas targets in light ion storage rings have been reported before [2,3]. Recently the first systematic investigation of internal target effects in a storage ring for highly charged ions was performed at GSI [4]. The blow-up measurement was performed in 'zero' dispersion mode (the dispersion function at the target position was about 0.09 m) in the recent experiment. This experiment was performed in the Experimental Storage Ring (ESR) [5], which is equipped with an electron cooler [6] and an internal gas-jet target at GSI [7].

EXPERIMENTAL PROCEDURE

The experiment was carried out with a stored coasting beam of bare nickel ions (Ni^{28+}) with an intensity of a few times 10^7 particles and a kinetic energy of 400 MeV/u. The electron cooler was used to increase the phase space density of the injected beam and provide a high quality, dense stored beam for experiment and to compensate heating by the target. Two target gases (Ar and Kr) were used in the gas-jet, with thickness of about 6×10^{12} atoms/cm^2 for both gases (gas-jet diameter ≈ 5 mm).

The momentum spread was determined by Schottky noise analysis from the frequency spread Δf/f according to $\Delta p/p = \eta^{-1}\,\Delta f/f$, where η is the frequency slip factor $\eta = \gamma^{-2} - \gamma_{tr}^{-2}$, with γ_{tr} =2.78. The horizontal emittance ε_x was non-destructively measured with the residual gas beam profile monitor (BPM). The beam size measured with the BPM was cross-checked by beam scraping, taking into account the ratio of the beta function values at the locations of the diagnostic devices (see [6]). Transverse Schottky noise power spectra from a stochastic cooling pickup (measured at the central frequency 1.3 GHz of the system) were used to measure the transverse beam emittances $\varepsilon_{x,y}$ due to the fact that the area under a sideband is proportional to the $\varepsilon_{x,y}$ [8]. The transverse emittance $\varepsilon_{x,y}$ values obtained in this way were calibrated against measurements with scrapers both in the horizontal and in the vertical plane and cross-checked with the BPM in the horizontal plane. The $\varepsilon_{x,y}$ values are estimated to be accurate within 30%. This accuracy is essentially given by the precision of the BPM and scrapers. Obviously, for relative effects such as the time evolution of beam parameters, the accuracy is much higher and benchmarking of simulations is possible.

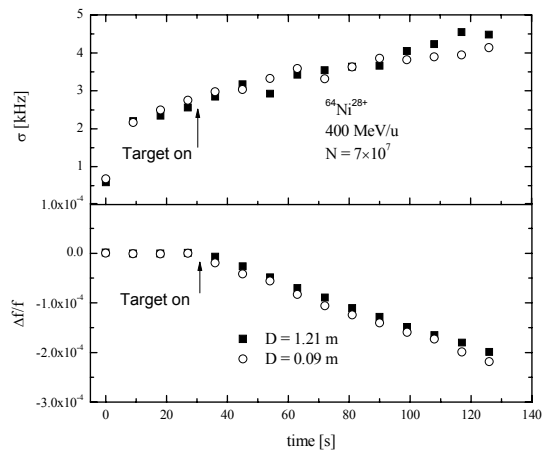

Figure 1: Relative change of the mean frequency Δf/f caused by the energy loss due to the internal target (Kr-target 6×10^{12} atoms/cm^2). The change of the width of distribution σ with the time.

There are two main procedures in our study. Firstly, the blow-up measurements were performed to investigate 'pure' target effects. A possible influence of dispersion function, particularly, at the pick-up position, on the horizontal emittance decrease was investigated (see [4]). The blow-up measurements were performed at the 'zero'

#V.Gostishchev@gsi.de

dispersion mode ($D_T \approx 0.09$ m) obtained by ion optical tuning of the ESR storage ring. Similar measurements were performed when the dispersion function at the target position D_T was 1.21 m. The measurements were performed over 2 min which corresponds to previous measurements. The beam was cooled down to the equilibrium state and at t=0 the electron cooler was switched off. Then, after about 30 seconds delay to allow for the relaxation of the beam phase space due to IBS, the gas-jet target was switched on (t=30 s: target ON). Secondly, at fixed ion beam intensity, the beam parameters at equilibrium between electron cooling, IBS and target effects were measured for electron currents in the cooler in the range 20 − 800 mA. In order to identify target effects the corresponding measurements without target were performed, thus enabling a direct comparison.

RESULTS AND DISCUSSION

Energy Loss Due to the Internal Target

The relative change of the mean frequency due to energy loss in the Kr target (6×10^{12} atoms/cm^2) and the growth of the distribution width σ due to energy straggling are shown in Fig. 1. After switching off the electron current in the cooler (t=0), Δf/f remains constant up to the moment when the target is switched on. After the target is switched on ($t \geq 30$ s), the position of the peak shifts to lower frequencies i.e. to lower energy due to energy loss and the width of the distribution increases due to energy straggling. Both target effects are clearly demonstrated in these graphs. Because of the non-zero dispersion at the target ($D_T \approx 1.21$ m), the beam is horizontally displaced from the closed orbit as Δp/p increases. The situation similar to the previous experiments is observed. As can be seen from Fig.1, there is no great difference between measurements when the dispersion function at the target position is different ($D_T \approx 1.21$ m and $D_T \approx 0.09$m).

Table 1: Dispersion dependence of the energy loss

Target gas atoms/cm^2	**Kr** 6×10^{12}	**Kr** 6×10^{12}
D_T	1.21 m	0.09 m
ξ_0	0.06 eV	0.06 eV
calc. $\langle E_{turn}\rangle$	1.2 eV/turn	1.2 eV/turn
calc. $\langle E_{turn}\rangle$ for 66% overlap	0.9 eV/turn	0.9 eV/turn
meas. E_{loss}	0.16 eV/turn	0.15 eV/turn

From the observed linear shift of the center of gravity with time the corresponding energy loss rate was obtained and found to be very similar for two dispersion values D_T at the target position, namely ~1.2 eV/turn (revolution period = 506 ns). The results are given in Table 1 in comparison with the mean energy loss per turn $\langle E_{turn}\rangle$ calculated by the analytical formula in [9,10]. The measured values are almost the same for two cases ($D_T \approx 1.21$ m and $D_T \approx 0.09$m). The calculated values are larger than the measured ones by factor of 6. The target dependence enters into $\langle E_{turn}\rangle$ through the parameter $\xi_0 \propto$ (mass number × density in g cm^{-2}/atomic number) in accordance with the Bethe-Bloch formula. The ion beam size at the target (beta function: $\beta_T = 15.7$ m) calculated from the measured r.m.s $\varepsilon_x \approx 0.1$ mm mrad (see the lower part of Fig. 2 below) was less than the jet diameter. Thus, the overlap factor between the beam (assumed to have a Gaussian distribution) and the gas-jet (assumed to have a uniform distribution) is estimated to be about 66%. Taking this simplified overlap model into account, the agreement between experiment and calculation is reasonably good within the experimental accuracy.

Beam Blow-up Induced by the Target

The experimental results for the time evolution of Δp/p and $\varepsilon_{x,y}$ without target and with Kr target ($d=6\times10^{12}$ atoms/cm^2) are shown in Fig. 2 in comparison with a BETACOOL [11] simulation made under similar conditions as in the experiment. In the simulation, the Martini model is used for the IBS [12], the Parkhomchuk formula [13] for the cooling force and the gas-jet diameter was fixed to 5 mm whereas the target density $d_{sim} = 4.36\times10^{12}$ atoms/cm^2 was chosen as a fitting parameter. For the relative blow-up of Δp/p the agreement is very good. The optimum d_{sim} is ≈ 66% of d and this is just the geometrical beam-jet overlap factor discussed above. This means the beam is immersed into the target completely but there is no complete overlap. Hence the target thickness should be reduced in the BETACOOL simulations due to geometrical factors.

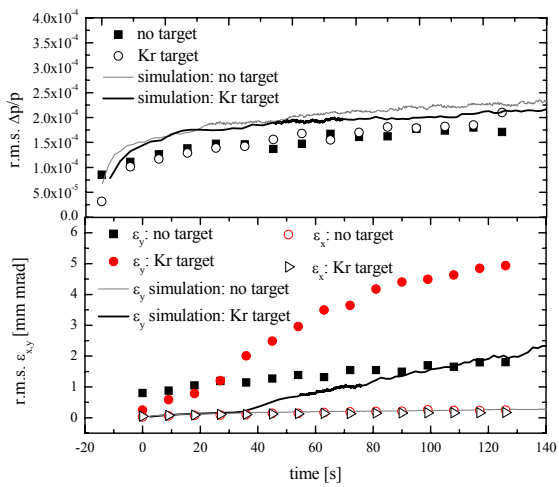

Figure 2: Evolution of Δp/p and $\varepsilon_{x,y}$ for Kr target (6×10^{12} atoms/cm^2) compared with BETACOOL result for an ′effective' density of 4.36×10^{12}atoms/cm^2.

The evolution of $\varepsilon_{x,y}$, which were obtained from the transverse Schottky noise analysis, is also plotted in Fig. 2 for the 'zero' dispersion mode. For ε_y, the BETACOOL result, which for simplicity is not shown in

Fig. 2, was in qualitative agreement with the experiment. A decrease of ε_x (noise power signal) was measured in previous experiments in the ESR storage ring (see e.g. [4]). It was suggested that a possible reason for ε_x decrease is the shift of the beam from the sensitive volume of the pick-up due to the dispersion function at the target position. This fact causes the reduction of the noise power signal which was measured. In the recent experiments the value of the dispersion function at the target position was reduced from 1.2 m to 0.09 m. A rather small growth of ε_x is observed instead of an ε_x decrease in the recent blow-up measurements. Therefore, the suggestion about an influence of the dispersion function is assumed to be valid. Obviously, it is difficult to estimate an increase of $\Delta p/p$ due to the target heating in Fig. 2. The relatively large growth of ε_y is also observed in the experiment. Considering now the absolute magnitudes in Fig. 2 for $t < 30$ s i.e. when only the IBS acts on the pre-cooled beam, the simulation predicts systematically larger values of $\Delta p/p$ and lower values of ε_x than the experiment shows. The simulations for ε_x were excluded from the Fig.2 for simplicity. The measurements show a great target effect in the vertical plane as shown in Fig. 2. In fact, the results obtained from simulations with BETACOOL code are similar to the measured ones but they have smaller magnitudes in comparison with measured values in the vertical plane. Calibration by means of beam scraping was not performed for the mode with $D_T \approx 0.09$ m. The measurements of ε_y can not be cross-checked with beam profile measurements. Probably, because of this fact, the values of vertical emittance, which were obtained from transverse Schottky spectra analysis, are too large in comparison with horizontal ones. The calibration of ε_x measurements was performed by means of cross-checking values obtained from transverse Schottky spectra and measured by the BPM. The discrepancy in magnitudes between simulations and measurements is not very surprising since the equilibrium states are quite sensitive to the choice of the cooling force model.

Beam Parameters at Equilibrium between Cooling, IBS and Target

The measured values of the equilibrium ε_x (from the BPM) and $\Delta p/p$ of the 400 MeV/u Ni^{28+} beam are shown in Fig. 3 as a function of the electron current (I_e) in the cooler, without target, with Kr (6×10^{12} atoms/cm^2). The dependence of beam parameters on I_e is a result of the equilibrium between electron cooling and IBS when the target is off and electron cooling, IBS and target effects when the target is on, respectively.

Beam dynamics simulations with a gas-jet target were made with the BETACOOL code for the operation parameters of the ESR cooler (electron beam diameter = 5 cm, magnetic field strength = 0.1 T) and for two cooling force models, namely, the non-magnetised (NM) force model and the Parkhomchuk formula (with $V_{eff,e}=1.5\times10^4$ m/s corresponding to magnetic field errors of $\sim5\times10^{-5}$). In some cases, in simulations for very low I_e the heating effect of the target could not be compensated by cooling, leading to beam blow-up and, therefore, no data points are given in Fig. 3. As it can be seen in Fig. 3, the NM model is in better overall agreement with the experiment: it qualitatively reproduces the dependence of ε_x and $\Delta p/p$ on I_e for the case without target. However, it fails to reproduce the target-induced blow-up of $\Delta p/p$ observed in the experiment.

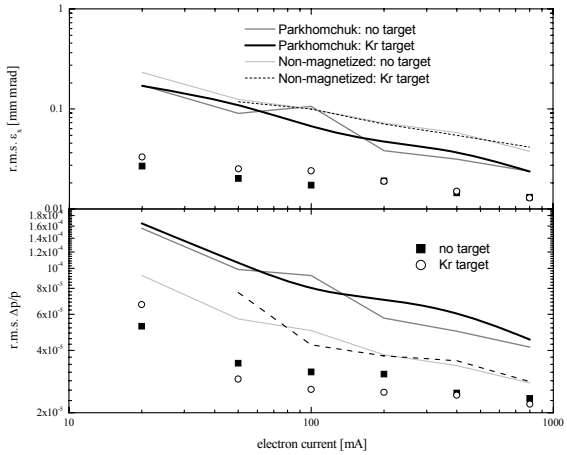

Figure 3: Equilibrium beam parameters compared with BETACOOL simulations using the non-magnetised and Parkhomchuk electron cooling model.

REFERENCES

[1] An International Accelerator Facility for Beams of Ions and Antiprotons, Conceptual Design Report, GSI, 2001.

[2] F. Sperisen et al., IUCF Scientific and Technical Rep. (1989/90) 117.

[3] C. Ekström, NIM A 362 (1995) 1.

[4] V. Gostishchev et al., Proceeding of EPAC 06, Edinburgh.

[5] B. Franzke, NIM B 24/25 (1987) 18.

[6] M. Steck et al., NIM A 532 (2004) 357.

[7] H. Reich et al., Nucl. Phys. A 626 (1997) 417c.

[8] D. Boussard, CAS, 5th Advanced Accelerator Physics Course Proceedings, CERN 95-06 (1995) 391.

[9] F. Hinterberger, D. Prasuhn, NIM A 279 (1989) 413.

[10] O. Boine-Frankenheim et al., NIM A 560 (2006) 245.

[11] A.O. Sidorin et al., NIM A 558 (2006) 325.

[12] M.Martini, CERN PS-84-9, 1984.

[13] V.V. Parkhomchuk, NIM A 441 (2000) 9.

LONGITUDINAL SCHOTTKY SIGNALS OF COLD SYSTEMS WITH LOW NUMBER OF PARTICLES

Rainer W. Hasse, GSI Darmstadt, Darmstadt, Germany

Abstract

Very cold systems of ions with sufficiently low number of particles arrange in an ordered string-like fashion. The determination of the longitudinal momentum spread and of the transverse temperature then is no longer possible by normal Schottky diagnosis. In this paper we simulate such systems in an infinitely long beam pipe with periodic boundary conditions under the influence of all long-range Coulomb interactions by Ewald summation. Then we derive the behaviour of the longitudinal Schottky signals for cold string-like systems as well as for the transition to warmer systems when the strings break, up to hot gas-like systems. Here effects from the finite number of particles, of higher harmonics and of temperature agree with those derived analytically in the limits of very low and very high temperatures.

INTRODUCTION

Schottky analysis has been an efficient tool for the determination of the momentum spread of a heavy ion beam. After the construction of the electron cooler [1] in the ESR ring, see [2], at GSI in 1990 a pickup was installed and connected to a Schottky device. From the width of the signal the momentum spread $\delta p/p$ can be deduced, see e.g. Fig. 1.

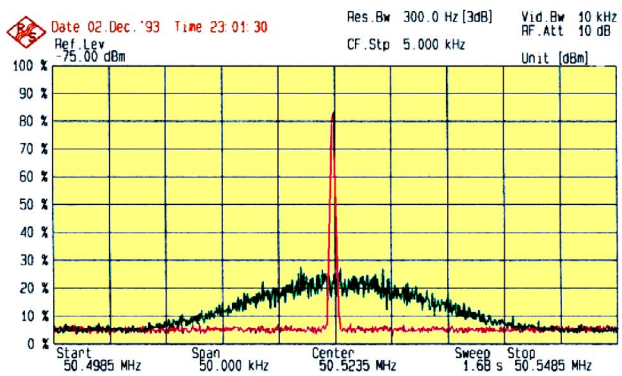

Figure 1: Early (1993) Schottky spectra from the ESR before (green) and after (red with $\delta p/p = 2 \times 10^{-5}$) electron cooling.

At high intensities of cooled systems momentum spreads below 10^{-5} could be reached. For very low densities, on the other hand, and if cooled properly, $\delta p/p$ decreases until intrabeam scattering breaks down [3]. Then the momentum spread levels off at a very low level of the order of 10^{-6} only due to ripples of the power supplies etc, see Fig. 2. These two regions are well separated by a a well defined jump in $\delta p/p$.

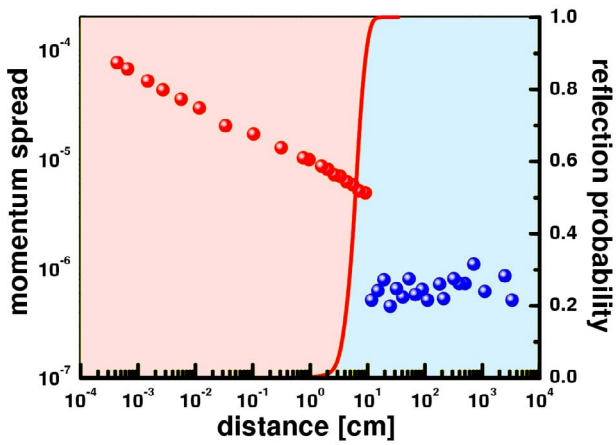

Figure 2: Momentum spreads of an U^{92+} beam at 360 MeV/u. The red line is the calculated reflection probability, see below. After Steck [3] and Hasse [4].

This effect has been detected in the ESR for various ions from protons and carbon up to uranium. Afterwards it was also confirmed in different storage rings like SIS18 at GSI [5], Cryring at Stockholm [6], and, recently, at the S-LSR at ICR, Kyoto University [7].

These results posed a challenge to theory and were soon explained in ref. [4]: If the interparticle distance becomes as small as 10 cm and if the ions are sufficiently cold in the transverse direction then the ions arrange in a string-like fashion and they repel each other rather than passing. Lateron in ref. [8] simple general criteria were derived for the existence of such Coulomb strings which turned to be out to be valid for all storage rings.

SCHOTTKY SIGNALS

A particle passing by at the Schottky pickup induces a signal called the Schottky noise. The theory of Schottky noise has first been applied to stochastic cooling at CERN. It can be found in various CERN accelerator school lectures e.g. by Chattopadhyay [10] or Boussard [11]. For an ideal (hot) gas at high density the signal is proportional to the longitudinal kinetic energy (or temperature),

$$|P_{\rm gas}|^2 \propto T_{||} \,, \qquad (1)$$

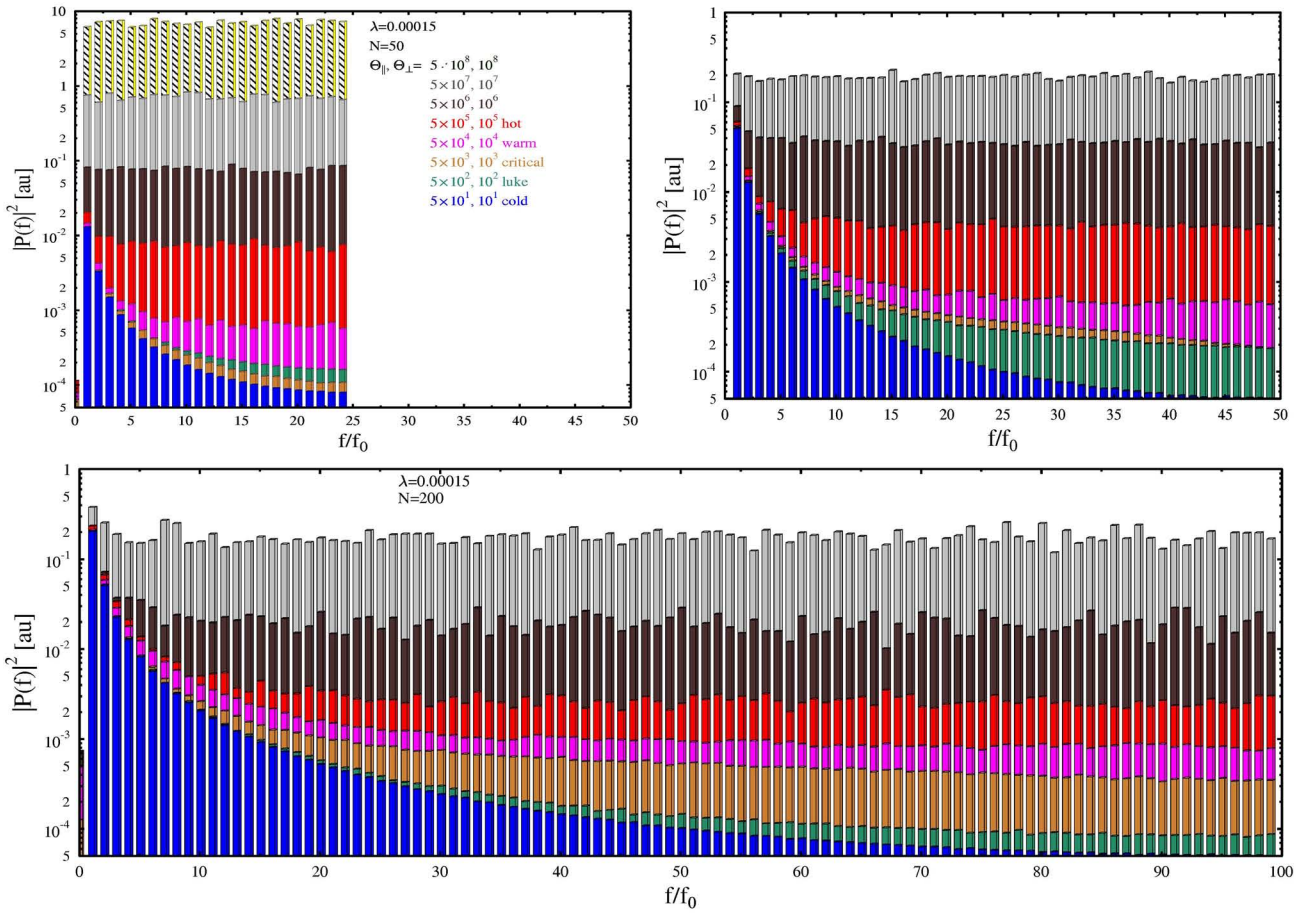

Figure 3: Calculated integrated Schottky spectra for the linar density $\lambda = 0.00015$ at various longitudinal and transverse temperatures and various number of particles N=50 (a: top left), N=100 (b: top right) and N=200 (c: bottom).

which, in turn converts to momentum spread by the relation $T_{||} = M(c\beta\delta p/p)^2/(8\log 2)$, where M is the mass and βc is the ion velocity. Note that it is independent of the measuring frequency (or harmonic number $n = f/f_0$), where f_0 is the revolution frequency and, certainly, independent of the number of ions N, see ref. [3].

On the other hand, if the ions are very cold and are ordered along a string, then

$$|P_{\rm string}|^2 \propto \frac{N^2}{n^2}\ , \qquad (2)$$

which is, certainly, independent of temperature. For N ions there exist N/2 different harmonic Fourier transforms which are continued in a mirrored fashion so that $|f_{\rm string}|^2(n = 2N) = |f_{\rm string}|^2(n = N)$ which gives additional effects in the Schottky spectra from low particle numbers not contained in eq. (2). For intermediate temperatures no analytical results are available.

In the following we study this important transition region by particle simulations of intermediate temperatures and reasonably low number of particles.

SIMULATIONS

For that purpose we use the code *RODS* (*R*eorganization *O*f *D*ynamical *S*ystems)[2] which was developed in the context of (1D or 3D) Coulomb crystals [12] and was successfully applied to derive the necessary conditions for the existence of Coulomb strings [4, 8] and to studies of the exchange of energy from transverse to longitudinal degrees of freedom [9] in an ion beam.

Since Coulomb systems scale nicely, the density can just be characterized by the dimensionless quantity $\lambda = a_{\rm WS}/d$, where d is the average linear distance in the string region and $1.8a_{\rm WS}$ would be the average 3D distance in an ion gas and $a_{\rm WS} = (3q^2/2M\omega_\beta^2)^{1/3}$ being the Wigner-Seitz radius (q is the charge, M the mass and ω_β the betatron frequency). $\lambda = 0.00015$ is a typical value in the string region, see [4]. Longitudinal, $\Theta_{||}$, and transverse, $\Theta_\perp$, relative temperatures are the respective kinetic energies measured in units of $\epsilon_0 = q^2/d$.

The program places at random a number N of ions with linear density λ at transverse temperature $\Theta_\perp$and longitudinal temperature, in general $5\Theta_{||}$, in a cylinder of length

[2]The Windows® program can be downloaded from the website *http://www.gsi.de/~hasse*.

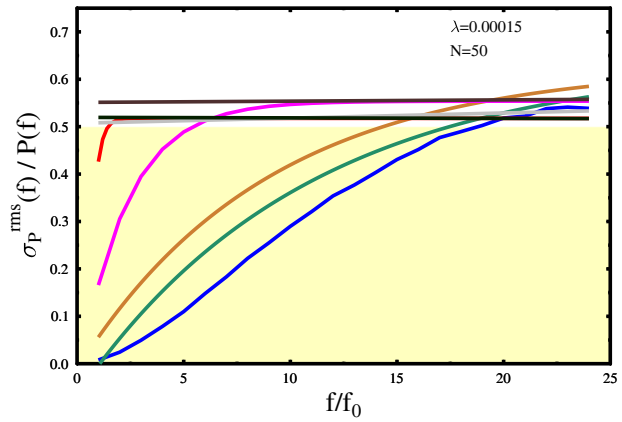

Figure 4: Rms width over average value of the integrated Schottky spectra of Fig. 3a for various temperatures (same color code).

Nd with periodic boundary conditions. Then the equations of motion are solved by molecular daynamics, hereby summing up all long-range Coulomb interactions by Ewald summation, see ref. [12]. After sufficient time when equilibrium has been reached the process is repeated a few hundred times in order to yield good statistics.

With this procedure was recorded whether or not the particles were repelled when approaching each other and the reflection probability as function of density was calculated. As shown in [4] exactly at a number of particles corresponding to the gap between the experimental red (hot) and cold (blue) points of Fig. 2 this calculated reflection probability jumps from zero to 100%.

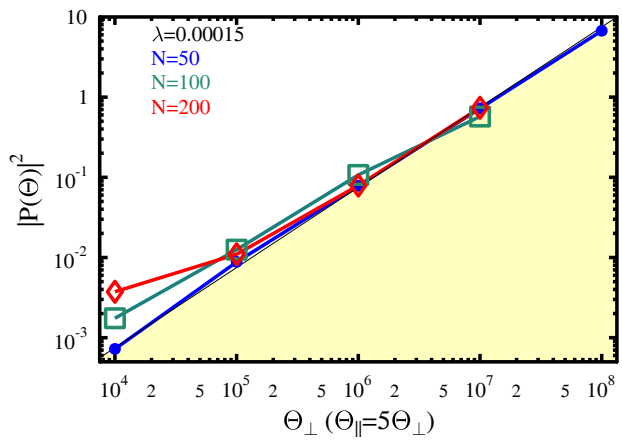

Figure 5: Temperature dependence of hot integrated Schottky signals for various particle numbers.

RESULTS

This procedure is now extended to also record the Schottky signals. They are Fourier transformed and integrated over one harmonic to yield the Schottky frequency spectra $|P(f)|$ of Fig. 3. Fig. 4, in addition, also shows the ratio of rms width to average value of the integrated spectra of Fig. 3 vs. harmonic number.

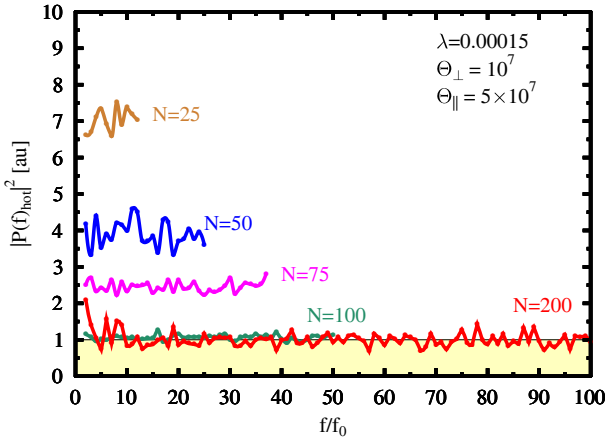

Figure 6: Particle number dependence of hot integrated Schottky signals vs. harmonic normalized to unity for $N \to \infty$.

In Fig. 3 one observes the transition from cold (ordered) over critical to warm (random) systems which manifests itself in such a way that the $1/n^2$ behaviour of eq. (2) gradually goes over into a flat distribution of eq. (1) which is independent of frequency and particle number. The critical temperatures where this transition occurs correspond roughly to the critical temperatures derived in ref. [8]. The widths of Fig. 4 reflect the same behaviour: For hot systems they level off to a value around 0.5 independent of temperature as is the case for thermal equilibrium. For the cold string-like systems the width is almost zero for low temperatures, thus also indicating very small momentum spreads.

PARTICLE NUMBER DEPENDENCE

The linear temperature dependence for hot systems is extracted from Fig. 3 and presented in Fig. 5. The proportionality to temperature of eq. (1) (averaged over the plateau harmonics) is reproduced over the three hot decades in temperature. Only for cold systems a slight dependence on par-

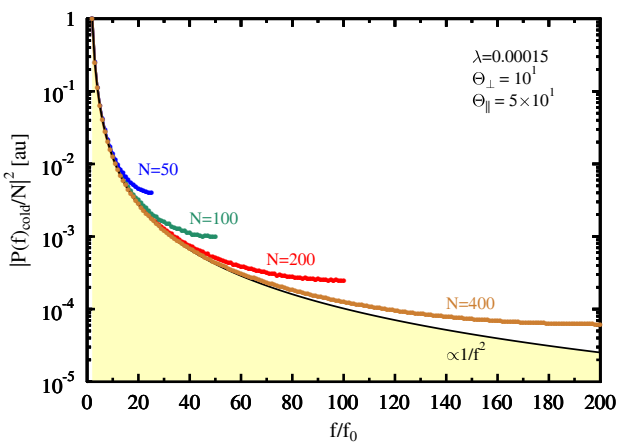

Figure 7: Particle number dependence of cold integrated Schottky signals (divided by N^2)vs. harmonic.

ticle number is found. Different behaviours are found for the frequency dependence of the hot and cold systems of of Figs. 6,7, respectively. Here for systems with only a few particles as is the case in the ultracold region, the Schottky signals depend strikingly on N. Most strikingly, only for more than 100 particles the trend with N^2 is reproduced for the hot systems. This might be used for the determination of the actual particle numbers in the rings.

REFERENCES

[1] N. Angert, W. Bourgeois, H. Emig, B. Franzke, B. Langenbeck, K.D. Leible, H. Schulte, P. Spädtke, B.H. Wolf, *Proc. EPAC Rome*, 1988, p.1436.

[2] F. Nolden, S. Baumann, K. Beckert, H. Eickhoff, B. Franczak, B. Franzke, O. Klepper, W. König, U. Schaaf, H. Schulte, P. Spädtke, M. Steck, J. Struckmeier, *Proc. PAC San Francisco*, 1991, IEEE, New York, 1991, p.2880.

[3] M. Steck, K. Beckert, H. Eickhoff, B. Franzke, F. Nolden, H. Reich, B. Schlitt, and T. Winkler, Phys. Rev. Lett. 77, 3803 (1996); M. Steck, K. Beckert, H. Eickhoff, B. Franzke, F. Nolden, H. Reich, P. Spädtke, and T. Winkler, Hyperfine Interact. **99** (1996) 245;
M. Steck, Nucl. Phys. **A626** (1997) 473c.

[4] R.W. Hasse, Phys. Rev. Lett. **83** (1999) 3430.

[5] R.W. Hasse, M. Steck, *Proc. EPAC Vienna*, 2000, p. 274 (JACoW TUBF201).

[6] H. Danared *et al.*, Phys. Rev. Lett. **88** (2002) 174801-1.

[7] A. Noda, M. Ikegami, T. Shirai, New J. Phys. **8** (2006) 288; T. Shirai *et al.*, Phys. Rev. Lrtt. **98** (2007) 204801;
and this conference.

[8] R.W. Hasse, Phys. Rev. Lett. **90** (2003) 204801-1.

[9] R.W. Hasse, Phys. Rev. **A46** (1992) 5189.

[10] S. Chattopadhyay, *Some Fundamental Aspects of Fluctuations and Coherence in Charged-particle Beams in Storage Rings*, Proc. CERN Accel. School, 1984, CERN Report 84-11 (1984).

[11] D. Boussard, *Schottky Noise and Beam Transfer Function Diagnostics*, Proc. CERN Accel. School, 5*th* Advanced Course, p. 749, CERN Report 95-06 (1995).

[12] R.W. Hasse, J.P. Schiffer, Ann. Phys. (NY) **203** (1990) 419.

LIMITATIONS TO THE OBSERVATION OF BEAM ORDERING

M. Steck, K. Beckert, P. Beller, C. Dimopoulou, F. Nolden, GSI Darmstadt, Germany

Abstract

The observation of beam ordering for low intensity cooled ion beams depends on various parameters. Experimental observations concerning the influence of fluctuations of beam energy and magnetic field on the lowest measured momentum spread detected by Schottky noise analysis are reported. Further measurements illustrate the limits due to the sensitivity of the Schottky noise detection system and the resolution of transverse beam size measurements.

INTRODUCTION

Experiments with electron cooled heavy ion beams have evidenced a linear ordering of the ions at low beam intensity. The main criterion was a discontinuous reduction of the momentum spread of the ion beam when the particle number was reduced to a few thousand [1], [2], [3]. Later, a similar reduction of the transverse emittance for these low intensity beams measured by destructive beam scraping confirmed the transition from a gaseous to a liquid-like state with longitudinal ordering [4]. The beam quality in the high intensity gaseous state is determined by an equilibrium between intrabeam scattering and cooling. For the low intensity ordered beam intrabeam scattering is suppressed and the beam temperature is dependent on the ability to provide most powerful cooling in order to achieve lowest beam temperature. The detection of this low beam temperature requires highest stability of all technical systems and diagnostics systems with exceptional resolution for the beam parameters, longitudinal momentum spread and transverse emittance. Therefore the observation of the transition to the ordered state depends on various technical parameters which influence the lowest achievable and detectable beam temperature. In addition a significant increase of beam temperature in the intrabeam scattering dominated regime, which means a large heating rate, is required to distinguish the two regimes. As a consequence, the strongest reduction of the beam temperature was observed for highly charged ions, as for these the intrabeam scattering rate is highest.

INFLUENCE OF INTRABEAM SCATTERING

The transition from the gaseous to the ordered beam state is most pronounced, if the intrabeam scattering rate and therefore also the beam temperature is high. The highest intrabeam scattering rate is achieved, if the ion beam is cooled in full six-dimensional phase space under optimum cooling conditions. An intentional reduction of the cooling rate of the electron cooling system can be easily achieved by a misalignment between the ion and the electron beam in the cooling section. Normally the ion and electron beam are aligned parallel to each other with an angular error of less than 0.1 mrad. The increase of the transverse ion beam emittance caused by the misalignment results in a reduced intrabeam scattering rate. Consequently, the longitudinal momentum spread can be reduced, if the reduction of the longitudinal heating rate outbalances the reduction of the cooling rate due to the misalignment.

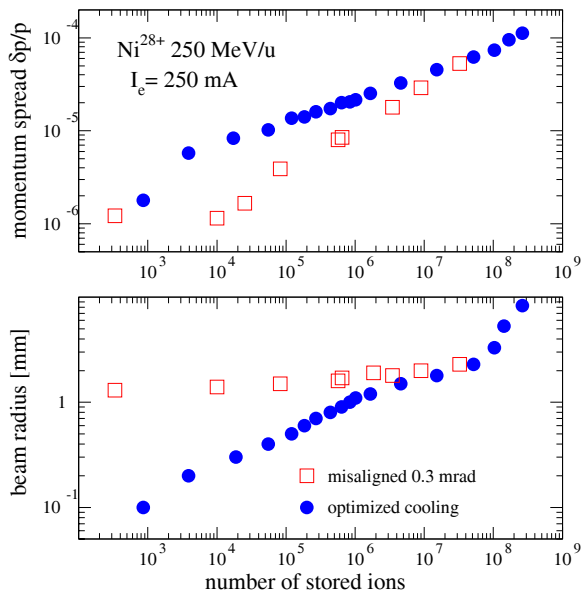

Figure 1: Measurement of the momentum spread and the beam radius of an ion beam ($^{58}Ni^{28+}$ 250 MeV/u) with perfect alignment of ion and electron beam and with an intentional misalignment of the electron beam by 0.3 mrad. At low intensity the ion beam radius is determined by the misalignment angle, whereas an even smaller momentum spread can be achieved with the misaligned electron beam.

The method of intentional misalignment can also be useful if a reduced longitudinal momentum spread at the expense of an increased transverse emittance is beneficial for the experiment. Therefore, with misaligned beams, already at higher ion beam intensity the momentum spread can be as small as the one in the low intensity ordered state (Fig. 1). Even if there is a transition to the ordered state, it cannot be observed in the usual way as a reduction of the

momentum spread. In the transverse degree of freedom the ion beam emittance is limited by the misalignment angle to a minimum value.

The introduction of a misalignment is one way to increase the transverse emittance intentionally and reduce the momentum spread. The dependence of the momentum spread on the number of stored ions can be modified, if there is additional transverse heating of the ion beam. The heating can originate from external source like rf noise or the use of an internal target. Strong transverse heating occurs, if the ion beam is cooled to the transverse space charge limit, which is particularly relevant for low energy beams [5].

STABILITY OF THE REVOLUTION FREQUENCY

The measurement of the momentum spread by detection of longitudinal Schottky noise requires highest stability of the revolution frequency, as the longitudinal momentum spread is proportional to the width of the frequency distribution. Any variation of the revolution frequency during the time interval of the frequency analysis will broaden the Schottky signal and therefore limit the measurement of smallest frequency spreads. The main frequency uncertainties come from current variations of the dipole power converter. Any change of the current δI_p causes a change of the bending field strength δB_{dip} and consequently a change of the revolution frequency $\delta f_{rev} = \frac{1}{\gamma_t^2}\frac{\delta B_{dip}}{B_{dip}} f_{rev}$. Already for the very first observations of the momentum spread reduction this was identified as the limiting parameter for the determination of the lowest longitudinal beam temperature. The longitudinal beam temperature is proportional to the square of the measured frequency spread and to the ion mass $kT_{\|} = m_i c^2 \beta^2 (\frac{\delta p}{p})^2_{rms}$ and $\delta p/p = \eta^{-1}\delta f/f$ with the frequency slip factor η. For a frequency spread which is determined by the dipole power converter stability the lowest temperatures occur for the lightest ions. Therefore conclusions about limiting temperatures due the electron beam must be determined with light ions.

Current variations of power converters depend on the current level. The best relative stability will usually be achieved at high output current, but the relative stability of the output current depends on the electronic circuits and cannot necessarily be described by a simple analytic dependence on the output current. Generally lower output current will have less relative stability. The corresponding frequency uncertainty can be larger than the smallest frequency spread of the beam in the intrabeam scattering dominated regime. In this case the observation of the discontinuous momentum spread reduction is complicated or even ruled out.

The momentum spread of bare krypton ions at different energies as a function of the number of stored ions is shown in Fig. 2 for similar electron density ($n_e \simeq 6 \times 10^6$ cm^{-3}), i.e. similar cooling rate. The variation of the momentum spread in the intrabeam scattering dominate regime is weak, but the minimum momentum spread at lowest particle numbers varies almost linearly with beam momentum and the corresponding bending field strength of the storage ring dipole magnets. Other magnetic elements of the ring can also effect the orbit length, but their influence is much weaker. According to their influence on the orbit length relative to the dipole magnet field, the specification of the power converters for other ring magnets must be defined.

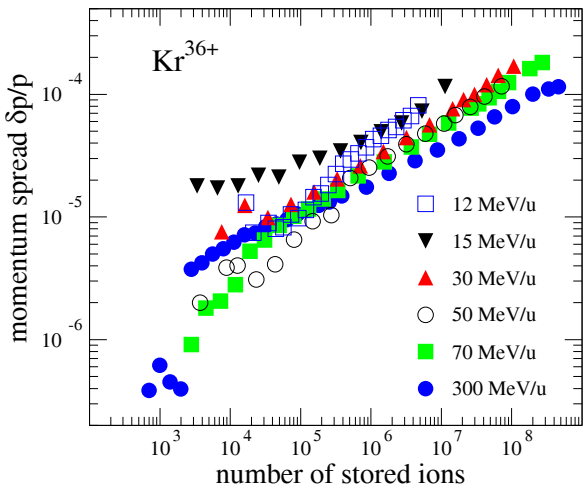

Figure 2: Momentum spread of a beam of bare krypton ions at various energies for an electron density $n_e = 6 \times 10^6$ cm^{-3}. The stability of the magnetic field of the ring dipole magnets determines the minimum momentum spread at low intensity.

STABILITY OF ELECTRON BEAM ENERGY

The revolution frequency of the ion beam is proportional to the ion velocity. At non-relativistic beam energies any variation of the beam velocity will cause proportional frequency variations. The electron beam drags the ion beam to the electron velocity. The drag force and consequently the response of the ion beam to any change of the electron velocity depends on the cooling force, which is a function of the relative velocity between ions and electrons. Any temporal variations of the electron velocity will result in ion velocity variations. The coupling of the ion beam to the electron beam, to first order, is proportional to the electron density in the beam frame. Electron energy variations are mainly caused by variations of accelerating voltage of the electron beam. Another source of velocity variations can be changes of the space charge compensation, which has to be controlled precisely in experiments with very cold beams.

For variations of the accelerating voltage of the electron beam the situation is similar as for the power converters of the ring bending magnets. The difference is that the coupling to the ion beam is not directly proportional, but depends on the cooling force. The influence of electron energy variations is most pronounced for the lowest beam en-

ergies, when energy changes result in proportional velocity changes and when space charge effects are largest.

An example of the influence of the stability of the electron beam energy is shown in Fig. 3. A bare gold beam at 75 MeV/u was cooled by electron currents in the range from 50 to 300 mA. The momentum spread as a function of the number of stored ions shows the usual dependency with $\delta p/p \propto N^{0.3}$ in the intrabeam scattering dominated regime above 10^4 stored ions. There is only a weak indication that for higher electron current smaller momentum spreads can be achieved. In the low intensity regime the behavior is more obvious. Smaller electron currents result in smaller momentum spreads. The variations of the electron beam accelerating voltage couple most strongly to the ion beam when the electron current is highest. The momentum spread at low intensity is about proportional to the electron current. For the linear regime of the cooling force this behavior is expected. The typical variations of the accelerating voltage of the ESR electron cooler of $\delta V/V \leq 2\times10^{-5}$ agree with the assumption of a cooling force which is proportional to the relative velocity caused by voltage fluctuations.

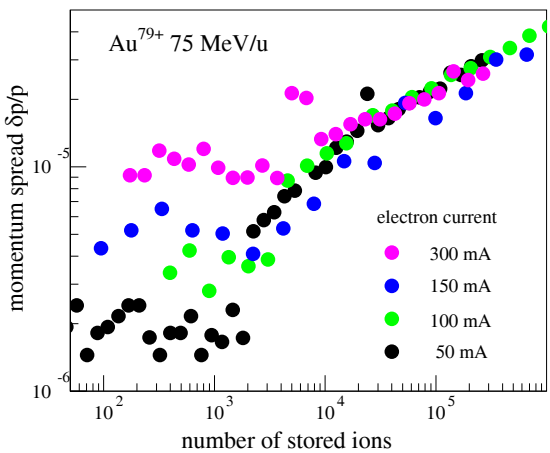

Figure 3: Momentum spread of a bare gold beam at 75 MeV/u cooled with different electron currents. At low intensity the momentum spread depends on the electron current due to the stability of the electron energy.

The main aspect with respect to the observation of ordering is the fact the the momentum spread reduction is only evidenced for small electron currents (50 and 100 mA). At higher electron currents the energy variations caused by fluctuations of the accelerating voltage of the electron beam smear out the momentum spread reduction. Therefore, in the situation of an insufficient stability of the accelerating voltage it can be beneficial to cool with reduced electron current in order to achieve minimum variations of the revolution frequency and consequently smallest frequency spread in the Schottky signal.

If the electron energy is stable enough, it has been observed that higher electron currents result in an increase of the transition particle number [1], [3]. Consequently, it depends on the energy stability of the electron beam, whether higher electron current, i.e. higher cooling rate, improves or decreases the possibility of the observation of ordering.

Temporal variations of the revolution frequency can be overcome if the sampling time of the frequency analysis system is shorter than the time constant of the fluctuations. Schottky analysis at higher frequencies gives higher frequency resolution or allows a reduction of the sampling time.

DETECTION LIMIT OF THE SCHOTTKY NOISE

The reduction of the momentum spread which evidences the linear ordering occurs at low intensity, for the ESR storage ring typically around one thousand stored ions. No significant dependence of the transition particle number on the ion species has been observed [1]. This is attributed to the charge dependence of the cooling force in the linear cooling force regime, which is relevant for well cooled beams with small emittance and momentum spread. The q^2-dependence of the Schottky noise power provides high sensitivity and good signal to noise ratio for highly charged ions. For cooled beams with a momentum spread below 10^{-6} single ions are routinely detected with the standard ESR Schottky noise detection system, which was designed for versatile use rather than for a specific application or certain beam parameters [6]. Bare uranium ions (charge 92) induce a Schottky signal which corresponds to nearly 10^4 singly charged ions of the same frequency spread. With increased frequency spread the signal to noise ratio drops inversely proportionally to the frequency width of the Schottky signal. Therefore it is quite obvious, that a measurement of the Schottky noise signal of protons at low intensity is limited to more than 10^4 stored protons. By connecting the Schottky pick-up to a resonant circuit the signal to noise ratio at the resonant frequency can be increased by an order of magnitude, thus lowering the detection limit to some 10^3 protons.

The measurement shown in Fig. 4 evidences that the lowest momentum spread (2σ) achieved in these experiments is 2×10^{-6}. Although the protons have an energy of 400 MeV like the heavy ions which showed an ordering effect, their magnetic rigidity is more than a factor of two lower. At the lower magnetic field level the stability of the bending field is reduced. The rigidity of the proton beam is the same as for bare gold beam at the energy of 75 MeV/u shown in Fig. 2. In both cases the frequency spread ($\delta f/f \simeq 1 \times 10^{-6}$) is a mark of the bending field stability, which for a bending field of 0.50 T in the ESR is about $\delta B/B = \gamma_t^{-2}\delta f/f = 6 \times 10^{-6}$. The rms momentum spread of 1×10^{-6} corresponds for protons to a longitudinal proton temperature of 0.5 meV. An improvement of the field stability will allow to test the temperature of the electron beam, for which a lowest value of about 0.2 meV was determined in experiments with bare carbon ions at two times higher magnetic field strength [4].

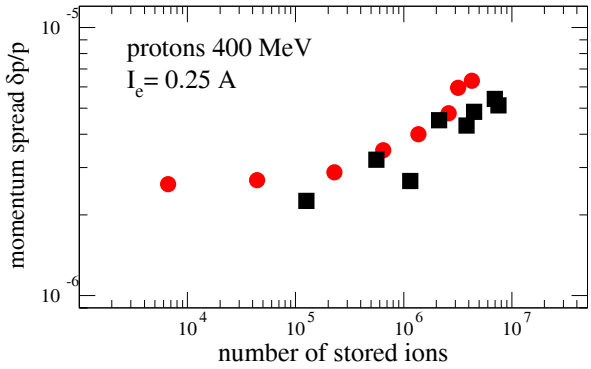

Figure 4: Momentum spread of protons at 400 MeV cooled with an electron current of 0.25 A. The black data points were measured with the standard set-up of the Schottky pick-up at 59.3 MHz, for the red data points the Schottky pick-up was connected to a resonant circuit (29.7 MHz) to increase the signal to noise ratio.

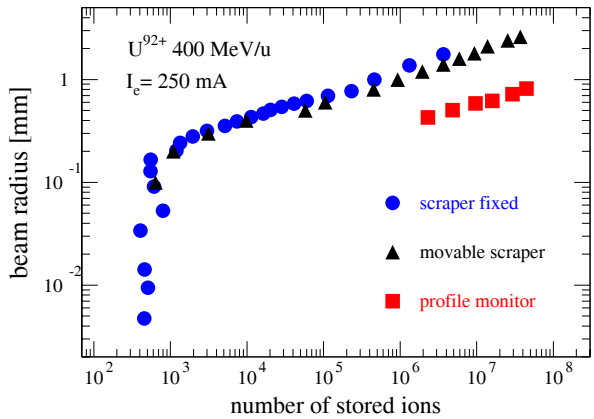

Figure 5: Beam radius measurement of a cooled beam (U^{92+}, 400 MeV/u) with a residual gas ionization profile monitor (1σ-value), a movable scraper and the method of shifting the ion beam towards the scraper by energy variation of the electron beam.

DISCONTINUOUS REDUCTION OF THE TRANSVERSE BEAM SIZE

For ordered beams with low transverse temperatures, typically in the range of meV, a beam radius of the order of μm is expected. Non-destructive transverse diagnostics with suitable resolution and sufficient sensitivity to detect the low intensity ordered beam parameters are not available. The only method which was useful so far for quantitative measurements of the transverse emittance of low intensity ordered beams is destructive beam scraping. Such scrapers have to be calibrated against non-destructive detection systems at higher intensity in order to allow quantitative measurements of the transverse width of the distribution. Positioning scrapers with μm precision is a difficult task. An alternative method for horizontal beam radius measurements has been developed. The ion beam center is shifted relative to a scraper which has a fixed inner end position and which is only moved into the beam for about a second and moved out afterwards [7]. The scraper is located in a section with small dispersion ($D \leq 1$ m) and the beam momentum is changed with changes of the energy of the cooling electron beam. Thus the resolution does not depend on the positioning accuracy of the scraper and with tiny changes of the electron energy the ion beam position can be changed in the μm range. A small value of the dispersion at the scraper is favorable, as it increases the resolution for the beam size determination and minimizes the influence of the momentum spread on the measurement of the horizontal beam size. The ion optical β-function at the scraper location should be large to achieve good resolution.

The detection of a reduction of the transverse beam size is strongly dependent on the resolution as shown in Fig. 5. The standard profile monitor which is based on ionization of the residual gas has a resolution limit of about 0.5 mm (1σ) which does not allow a profile measurement below 10^6 stored ions. By comparison of the beam size measurement with profile monitor and scraper, it can be concluded that the scraper cuts the beam at about 3σ of the distribution. With a movable scraper a resolution of about 100 μm (3σ) is achieved routinely, with high precision positioning it can be reduced to about 20 μm. With the scraper method based on small energy changes a resolution better than 5 μm (3σ) has been achieved, which clearly evidenced the discontinuous beam radius reduction when the beam transits to the ordered state. With optimized parameters a resolution down to 1 μm is feasible.

Such scraper measurement which extend over several minutes require an extraordinary stability of the beam orbit and of the beam center at the scraper, particularly. Nevertheless, at the ESR it has been found that these measurements can be well reproduced at the μm level [4].

REFERENCES

[1] M. Steck, K. Beckert, H. Eickhoff, B. Franzke, F. Nolden, H. Reich, B. Schlitt, Phys. Rev. Lett. 77 (1996) 3803.

[2] R.W. Hasse, M. Steck, Proc. of the 7^{th} Europ. Part. Acc. Conf., Vienna, (2000) 274-277.

[3] H. Danared, A. Källberg, K.-G. Rensfelt, A. Simonsson, Phys. Rev. Lett. 88 (2002) 174801-1.

[4] M. Steck, K. Beckert, P. Beller, B. Franzke, F. Nolden, Nucl. Instr. Meth. in Phys. Res. A 532 (2004) 357.

[5] M. Steck, L. Groening, K. Blasche, H. Eickhoff, B. Franczak, B. Franzke, T. Winkler, V.V. Parkhomchuk, Proc. of the 1999 Part. Acc. Conf., New York, (1999) 1704-1706.

[6] K. Beckert, S. Cocher, B. Franzke, U. Schaaf, Proc. of the 2^{nd} Europ. Part. Acc. Conf., Nice, (1990) 777-779.

[7] M. Steck, K. Beckert, P. Beller, B. Franczak, B. Franzke, F. Nolden, Proc. of the 9^{th} Europ. Part. Acc. Conf., Lucerne, (2004) 1963-1965.

PRESENT STATUS AND RECENT ACTIVITY ON LASER COOLING AT S-LSR *

A. Noda, M. Ikegami, T. Ishikawa, M. Nakao, T. Shirai, H. Souda, M. Tanabe, H. Tongu,
ICR, Kyoto University, Uji, Kyoto, 611-0011, Japan
I. Meshkov, A.V. Smirnov, JINR, Dubna, Moscow Region, 141980, Russia
M. Grieser, MPI für Kernphysik, D-69029, Heidelberg, Postfach 103980, Germany
K. Noda, NIRS, Inage-ku, Chiba-city, Chiba, 263-8555, Japan

Abstract

Laser cooling of an 40 keV 10^8 - $^{24}Mg^+$ ion beam combined with induction deceleration reduced the momentum spread to 2.9×10^{-4} which was limited by intra-beam scattering. An optical observation system for laser cooling applicable for smaller number of ions has been developed and just installed into S-LSR. With the special feature of the S-LSR lattice allowing for reduction of the shear force and with the newly developed optical measurement system, further approaches towards the realization of a multi-dimensional crystalline ion beam are to be started from now on.

INTRODUCTION

At ICR of Kyoto University, an ion storage and cooler ring, S-LSR was constructed between 2001 and 2005 by collaboration with NIRS. Beam commissioning started in October, 2005. Up to now electron cooling of a hot ion beam [1] was studied. At very low proton numbers of 2000, a one dimensional ordered state of a 7 MeV proton beam could be achieved [2]. The onset of transverse coherent instabilities in the vertical direction, induced by electron cooling stacking, could be suppressed by a feedback system [3]. Furthermore the formation of very short bunches could be successfully realized by the application of the bunch rotation method and electron cooling [4]. In addition, the S-LSR is optimized to realize a multi-dimensional crystalline beam with laser cooling [5]. In the present paper, the special feature of the S-LSR in connection with the above motivation is described briefly and then recent experimental results by the laser cooling applied to 40 keV $^{24}Mg^+$ ions are presented together with an overview of the future development.

SPECIAL FEATURE OF S-LSR

Basic Structure

According to the theoretical studies using MD simulations to achieve a crystalline ion beam, the ring has to satisfy the following conditions

$$\gamma \leq \gamma_t , \qquad (1)$$

$$N_{sp} \geq 2\sqrt{{\nu_H}^2 + {\nu_H}^2} , \qquad (2)$$

where γ_t, $\nu_{H,V}$ and N_{sp} are the transition γ of the ring, the betatron tunes in horizontal, vertical directions and the superperiodicity, respectively. Eqs. (1) and (2) represent the so-called formation and maintenance conditions for a crystalline beam, respectively [6,7]. The ring S-LSR is designed with 6-fold symmetry in order to enlarge the region of operation points satisfying the above maintenance condition. A further condition to avoid the

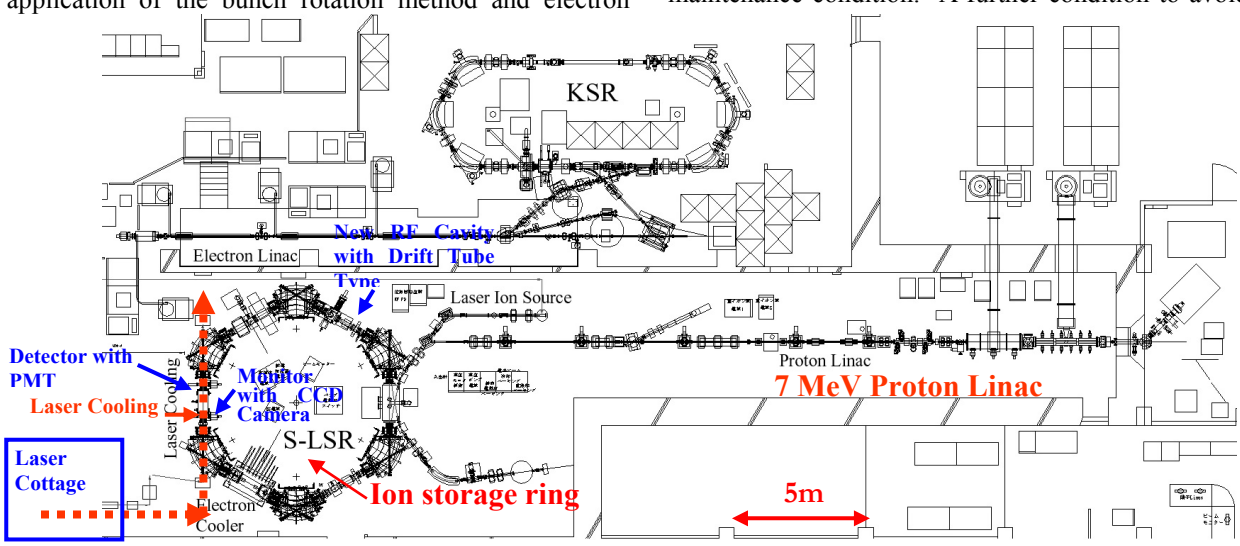

Figure 1: Layout of the radiation controlled experimental room where S-LSR is installed. As the injection beam for S-LSR, 7 MeV proton from the linac and 40 keV $^{24}Mg^+$ ion beam has been utilized up to now.

* Work supported by Advanced Compact Accelerator Development Project by MEXT of Japanese Government and 21COE of Kyoto University-Center for Diversity and Universality in Physics
# noda@kyticr.kuicr.kyoto-u.ac.jp

Table 1: Main parameters of S-LSR

Circumference	22.557 m
Average Radius	3.59 m
Superperiodicity	6
Ion Species	Proton :7 MeV $^{24}Mg^{+}$:40 keV $^{12}C^{6+}$:2 MeV/u
Operation Point	(1.65, 1.21) :Electron Cooling (1.45, 1.44), (2.07, 1.07), (2.07, 2.07) : Laser Cooling
Radius of Curvature	1.05 m

effect of linear resonances in the cases of high beam line densities, the S-LSR lattice has to fulfil also the requirement [8]

$$N_{sp} \geq 4\nu_{H(V)}. \qquad (3)$$

The superperiod of S-LSR consists of a dipole magnet and two quadrupole magnets at its both sides (Fig. 1).

Dispersion-Free Mode to Suppress Shear Heating

Laser cooling applied up to now for ion beams circulating in storage rings has been applied in the longitudinal direction. By dynamical coupling of the horizontal betatron motion and longitudinal synchrotron motion, laser cooling is extended to all three directions [9]. If a strong laser cooling force can be achieved for the three degrees of freedom, it is expected to create a multi-dimensional crystalline beam. The beam crystal, however, will be unstable caused by so called "Shear Heating" due to the increase of the beam line density [10, 11].

To avoid such "Shear Heating", a dispersion suppressed lattice with dispersion free bends consisting of crossed electric and magnetic fields was first proposed by Pollock [12]. For that purpose we have re-investigated this capability [13], developed electrodes, and installed them in all 6 dipole magnet chambers. All electrodes can be moved out from the beam aperture of the normal mode by a special driving mechanism without breaking the vacuum [14]. Only with the help of a coupling cavity [15], however, synchro-betatron coupling can be realized with the dispersion free lattice. Tapered laser cooling, an alternative to this scheme, is proposed, where the laser cooling force is applied only inside a Wien Filter, installed in a long straight section for laser cooling [16]. This idea, however, requires further fabrication of the needed hardware.

Operation Points

Table 2: Beam life of $^{24}Mg^{+}$ for various operation points

ν_x	ν_y	Beam Life
2.069	1.075	5.3 s
2.115	0.724	14.2 s
1.53	1.34	14.1 s
1.642	1.198	13.5 s

Up to now, several operation points of the working point are studied as listed up in table 2 [17]. The measured beam life time at the operating point of (2.07, 1.07), utilized for synchro-betatron coupling is shorter compared with the other operating points. The reason of this behaviour has to be investigated from now on.

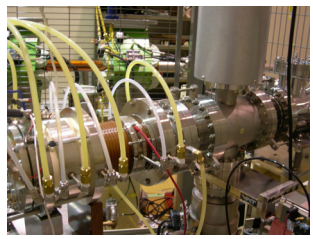

Figure 2 (a): Ion source of $^{24}Mg^{+}$ extracted by 40 kV.

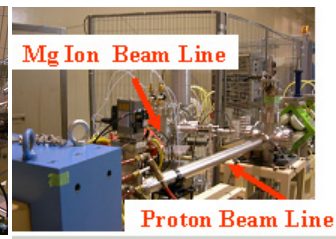

Figure 2 (b): $^{24}Mg^{+}$ ion beam merged with proton beam.

LASER COOLING SYSTEM

Ion Beam Orbit of $^{24}Mg^{+}$

The Mg ions produced from a CHORDIS ion source (Fig. 2 (a)) and extracted with a high voltage of 40 kV has been directly transported to the S-LSR merging with the transport line of 7 MeV proton (Fig. 2 (b)). The kinetic energy of the laser cooled Mg ion has been increased to 40 keV from the initial design of 35 keV due to the stable operation condition in the frequency region of the present laser system. The merged $^{24}Mg^{+}$ ion beam is transported through an injection septum magnet and then single-turn injected by an electric kicker with the duration covering over one revolution (~40 μs) with short turn-off time (a few tenth μs). As the duration of the injection kicker, usually 100 μs is utilized, while 10 μs duration is adopted for the purpose of beam observation with the use of an electrostatic pick up.

The closed orbit of the $^{24}Mg^{+}$ ion is adjusted to the central orbit. The correction is based on the measurement of the closed orbit by the electrostatic pick-ups. The closed orbit distortion after correction is smaller than ± 0.5 mm. In order to guarantee overlapping of the ion beam with the laser for cooling, the ion beam orbit in the straight section for laser cooling is defined by two apertures. The aperture size can be chosen from 2, 3, 6 and 10 mmϕ and the closed orbit is adjusted to realize a beam life of about 1 s using two apertures of 6 mm ϕ at positions illustrated in Fig. 3 [17].

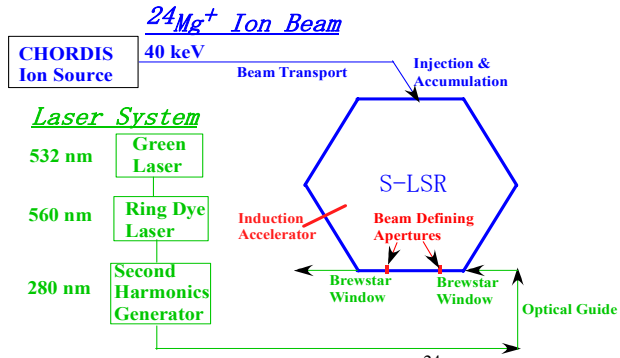

Figure 3: Laser cooling scheme for $^{24}Mg^{+}$ ion beam.

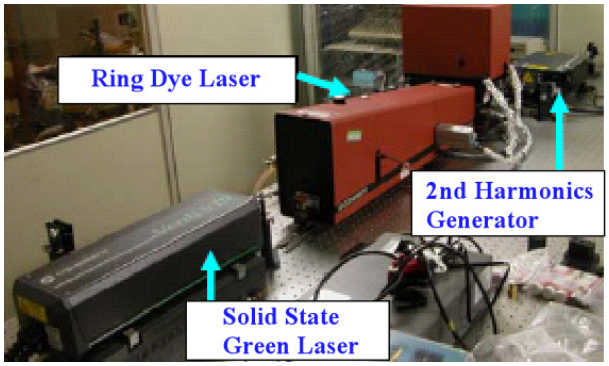

(a) Overall View of laser cooling

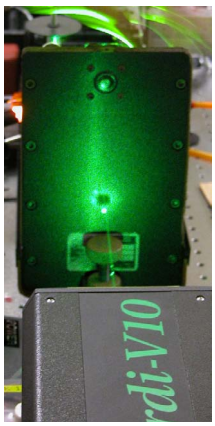

(b) Green Laser

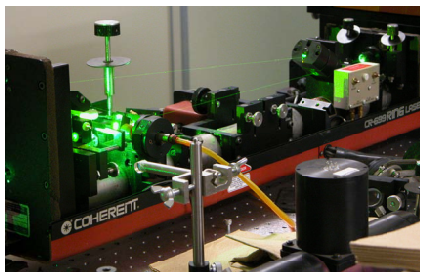

(c) Ring Dye Laser

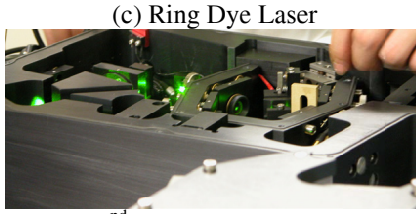

(d) 2nd Harmonics Generator

Figure 4: (a) An overall view of the laser system for beam cooling of Mg ions, consisting of (b) a solid state green laser (VERDI) with the wavelength 532 nm, (c) a ring dye-laser with the wave length ~560 nm pumped by the green laser and (c) a second harmonics generator for generation of the wave length of ~280 nm.

Laser System

In Fig. 3, the block diagram of our laser cooling system is shown. The laser system is set on a stage avoiding vibration, installed in a temperature and humidity controlled cottage, shown in Fig. 4 (a). A ring dye-laser (Fig. 4 (c)) pumped with a solid state green laser (COHERENT VERDI) with wavelength 532 nm and a peak power of 10 W (Fig. 4 (b)) is frequency doubled by a second harmonic generator (COHERENT MBD-200) (Fig. 4 (d)) to the wavelength ~280 nm, which is finally adjusted taking the small Doppler shift effect (0.19 %) into account [18].

The output of the 2nd harmonics generator with a power of about 40 mW is guided through the optical system composed of focusing lenses and reflection mirrors and injected into a long straight section of the S-LSR through a Brewster window. The laser path is defined by the two apertures defining the beam size. Final adjustment of the laser path is done with apertures of 2 mm ϕ chosen from several sizes of apertures by the linear driving mechanisms. The laser used for cooling is also monitored, taking out from S-LSR through a Brewster window at the down stream end of the laser cooling section.

LASER COOLING EXPERIMENTS

Up to now, laser cooling experiments have been performed with the normal lattice of finite dispersion by normal bends composed of pure dipole magnetic fields. A single laser which co-propagates with $^{24}Mg^{+}$ ion beam in the same direction has been utilized, because only one laser system of the wavelength ~280 nm is available at the moment. The sensitive momentum spread region for laser cooling is estimated to be ~2×10^{-5}. Two laser cooling schemes have been applied. In the first method, the ion beam is decelerated by a velocity independent induction voltage keeping the laser frequency fixed and in the second one, the laser frequency was swept so as to survey the total momentum region of the accumulated ions. The main parameters of laser cooling at S-LSR are listed up in Table 3.

Laser Cooling by Simultaneous Application of Induction Voltage with Fixed Laser Frequency

The Schottky signals observed before and after laser cooling are shown in Fig. 5 for an $^{24}Mg^{+}$ ion beam with an initial intensity of about 10^{8} and a momentum spread of 1.7×10^{-3} (1σ). The operation point of (2.1, 0.8) was utilized for this measurement. In this case, the laser frequency was fixed and deceleration with an induction voltage of about 6 mV was simultaneously applied. The relatively large momentum spread after cooling (2.9×10^{-4}) is considered to be due to momentum transfer from the transverse degree of freedom to the longitudinal one due to intra-beam scattering. The longitudinal temperature of the $^{24}Mg^{+}$ ion after laser cooling is estimated to be several tens Kelvin, which could be reduced to a few Kelvin by

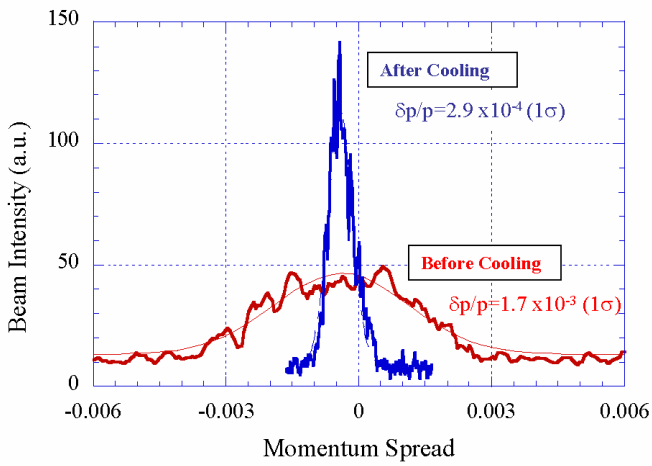

Figure 5: Effect of laser cooling on momentum spread of $^{24}Mg^{+}$ ions. Laser cooling keeping its frequency fixed was applied to $^{24}Mg^{+}$ ions with the intensity of ~10^{8} together with an induction deceleration voltage of ~6 mV, which reduced the fractional momentum spread from 1.7 x 10^{-3} to 2.9 x 10^{-4}. The spectrum after cooling was measured 5 second after the start of laser cooling.

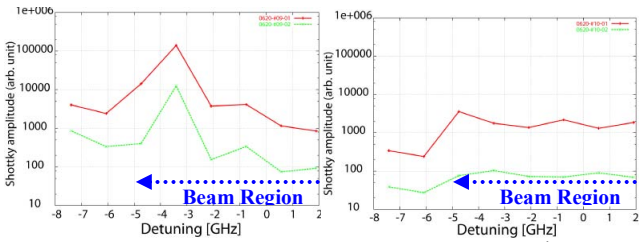

Figure 6: Dependence of the peak values of the 9th (a) and 10th (b) harmonics of the revolution frequency on the detuning frequency of the laser.

reducing the Mg ion number to 10^6. Achievement of much lower temperature requires further reduction of ion numbers, which has not yet been realized because it is difficult to observe the Schottky signal of a low intensity beam, which is expected to be solved by the recent development of the optical observation system (a photomultiplier or a CCD camera), using the emitted light, coming from the transition from upper to lower states, described in the next section.

Laser Cooling with Laser Frequency Shift

The positive frequency sweep of the single laser was applied to the $^{24}Mg^+$ ion beam in order to investigate the beam response to the longitudinal laser cooling force, although there was no equilibrium point for this case. In Fig. 6, the peak heights of the Schottky signal observed by an electrostatic beam pick up for various laser frequency detuning are shown for the 9th (a) and 10th (b) harmonics. The experiment was performed at an operation point of (1.53, 1.34). Strong coherent enhancement of the Schottky signal more than one order of magnitude is observed for odd harmonics just after the detuned frequency of the laser begins to overlap with ion beam region, while such an effect is not as strong for even harmonics as shown in Fig. 6, the explanation of which is a subject of our further investigation.

Table 3: Parameters of Laser Cooling at S-LSR

Cooled Ion	$^{24}Mg^+$
Kinetic Energy	40 keV
Transition	Lower State :$3s^2S_{1/2}$ Upper State:$3p^2P_{3/2}$
Laser Wavelength	280 nm
Beam Current	~2 μA
Revolution Frequency	25.2 KHz
Beam Life	>10 s (except for operation point of (2.07, 1.07))

FUTURE PROSPECT OF LASER COOLING AT S-LSR

Optical Beam Observation System

Because beam observation with the use of Schottky signals is rather difficult for beam intensities less than 10^6, which is required to suppress the effect of intra-beam scattering, an optical beam measurement system has been

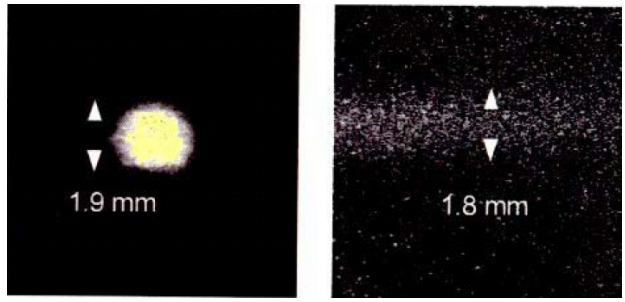

(a) Laser spot size (b) Vertical beam size

Figure 7: Laser spot size observed by a fluorescent screen (a) and vertical size of Mg ion beam by observation of the spontaneous emission light with the use of a CCD camera (b).

developed [19]. As indicated in Fig. 1, detectors of spontaneous emission light with a photo-multiplier (PMT) and a CCD camera are utilized. Up to now, the vertical size of the Mg ion beam is monitored by observation of spontaneous emission light, which is consistent with the laser spot size (1.9 mmϕ) observed by a fluorescent screen as shown in Fig.7. This observation, however, largely depended on the optical alignment of the laser. In many cases, the observation system suffered with heavy background, due to scattered laser light. Photon counting of the spontaneous emission with a photo-multiplier tube (PMT) was not possible because of severe background of the same origin. In order to improve this situation, an aperture shown in Fig. 8 (a) was installed just after the Brewster window for laser injection during the vacuum system break down at the end of August, 2007. We hope that the tail of the laser will be cut off with this aperture and the scattered laser light and, hence, the background photons will be largely reduced.

In parallel, PAT (Post Acceleration Tube) as shown in Fig. 8 (b) is also installed into the straight section for laser cooling in this summer. By counting the spontaneous emission coming through the side hole of the PAT with a PMT, sweeping an electrostatic potential applied to the PAT with a fixed laser-frequency, the velocity distribution of $^{24}Mg^+$ ion beam can be obtained. Such a

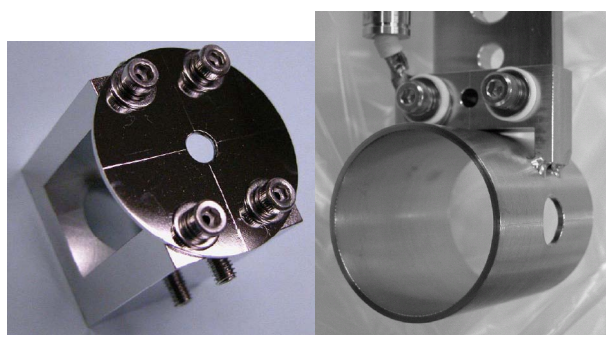

(a) (b)

Figure 8: Newly installed aperture, which is to reduce the scattered light of the laser to improve the optical beam measurement just after the Brewster window for introducing the laser into the vacuum system of the S-LSR (a) and newly installed PAT (Post Acceleration Tube) for observation of energy distribution of $^{24}Mg^+$ ion (b).

measurement is to be performed this fall. We have just finished the baking procedure after vacuum break down.

Bunched Beam Laser Cooling

The ferrite loaded un-tuned RF cavity used for 7 MeV protons has a gap (G) and an inner diameter (D) with sizes of 20 mm and 158.4 mm, respectively, the effective length of the RF electric field becomes 119.5 mm because of the poor aspect ratio (D/G) of ~8. The passing time of an 40 keV $^{24}Mg^{+}$ ion through this distance, ~210 ns, is almost comparable with the half period of the applied RF (2.52 MHz) with a harmonic number of 100. Such a situation results in the worse transit time factor of ~0.5 for the case of 40 keV $^{24}Mg^{+}$ ions compared with the value higher than 0.99995 for 7 MeV protons with harmonic number of 1. In order to improve such a situation, a new RF system with a drift tube has been fabricated [17] (Fig.9). The effective length of the drift tube is about 27 mm and and the inner diameter is 35 mm, resulting in a better aspect ratio of ~1.3. The new RF drift tube was installed into S-LSR in this summer. It will play an important role for the investigation of the bunched beam laser cooling in this fall.

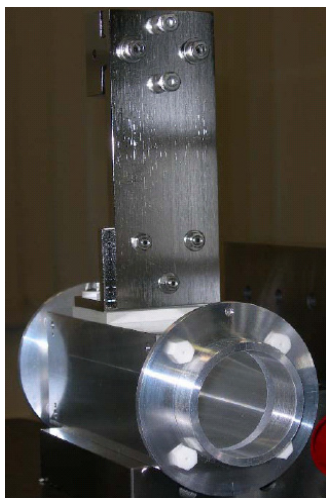

Figure 9: New RF cavity with better aspect ratio (~1.3) recently installed into S-LSR.

SUMMARY

Laser cooling has been applied at the S-LSR for a $^{24}Mg^{+}$ ion beam with kinetic energy of 40 keV. With the use of a single laser co-propagating with the ion beam together with an induction deceleration voltage of 6mV, the momentum spread (1σ) of 10^8 ions is reduced from 1.7×10^{-3} to 2.9×10^{-4} resulting in a longitudinal beam temperature of several tens Kelvin, which was reduced to a few Kelvin by reducing the number of stored ions to 10^6. For the achievement of much lower temperatures, further reduction of the ion number to suppress intra-beam scattering and transverse cooling is needed. Improvement of the optical measurement system has just been applied to enable cooling experiments with a lower intensity beam together with precise energy-spectrum measurement, which will be started this autumn.

REFERENCES

[1] H. Fadil et al., "Electron Beam Cooling Experiments at S-LSR", NIRS Report, HIMAC-111 (2006).

[2] T. Shirai, M. Ikegami, S. Fujimoto, H. Souda, M. Tanabe, H. Tongu, A. Noda, K. Noda, T. Fujimoto, S. Iwata, S. Shibuya, A. Smirnov, I. Meshkov, H. Fadil, and M. Grieser. "One-Dimensional Beam Ordering of Protons in a Storage Ring", Phys. Rev. Lett. 98, 204801 (2007) and the talk by T. Shirai at this workshop.

[3] S. Fujimoto, T. Shirai, A. Noda, M. Ikegami, H. Tongu and K. Noda, "Feedback Damping of a Coherent Instability at Small-Laser Equipped Storage Ring, S-LSR", Jpn. J. Appl. Phys., Vol. 45, No. 49 (2006), pp. L1307–L1310,

[4] T. Fujimoto et al., "Fast extraction of the short-bunched proton beam for investigation of free-radicals behaviour", to be submitted to Jpn. J. Appl. Phys.

[5] A. Noda, M. Ikegami and T. Shirai, "Approach to ordered structure of the beam at S-LSR", New Journal of Physics, **8** (2006) 288-307.

[6] J. Wei, X-P. Li and A.M. Sessler, "Low-Energy States of Circulating Stored Ion Beams: Crystalline Beams", Phys. Rev. Lett., **73** (1994), 3089-.3092

[7] X-P. Li et al., "Phonon spectrum and the maintenance condition of crystalline beams", Phys. Rev. ST-AB, **9** (2006), 034201

[8] K. Okabe and H. Okamoto, "Emmittance Limitation in Cooled Hadron Beams", Jpn. J. Appl. Phys. **42** (2003), 4584-4592.

[9] H. Okamoto, "Transverse laser cooling induced through dispersion at an rf cavity", Phys. Rev. **E50** (1994), 4982-4996.

[10] Y. Yuri and H. Okamoto, "Generating Ultralow-Emittance Ion Beams in a Storage Ring", Phys. Rev. Lett. **93** (2004), 204801.

[11] Y. Yuri and H. Okamoto, "Feasibility of beam crystallization in a cooler storage ring", Phys. Rev. ST-AB, **8** (2005), 114201.

[12] R.E. Pollock, Z. Phys. A: Hadrons and Nuclei, **341** (1991) 95.

[13] M. Ikegami et al., "Heavy ion storage ring without linear dispersion ", Phys. Rev. ST-AB, **7** (2004) 120101.

[14] A. Noda et al., "Laser Cooling for 3-D Crystalline State at S-LSR", Proc. of International Workshop on Beam Cooling and Related Topics-COOL05, Galena, Illinois, USA, 18-23, September (2005), 491-500.

[15] M. Kihara et al., "Three-dimensional laser cooling method based on resonant linear coupling", Phys. Rev. **E59** (1999), 3594-3604.

[16] A. Noda, M. Ikegami, S. Sakabe and T. Aruga, "Possible Tapered Laser Cooling Keeping Superperiodicity", Beam Science and Technology, **10** (2006), 39-40.

[17] H. Souda et al., "Beam Optimization for laser Cooling at S-LSR", Proceedings of the 4th Annual Meeting of Particle Accelerator Society of Japan and the 32nd Linear Accelerator Meeting in Japan, 2007, Wako-city, Saitama, Japan, in print (in Japanese).

[18] M. Tanabe et al., "Laser Cooling of Mg+ Beam at S-LSR", ibid.

[19] T. Ishikawa et al., "Optical beam monitors in S-LSR", ibid.

SCHOTTKY NOISE SIGNAL AND MOMENTUM SPREAD FOR LASER-COOLED BEAMS AT RELATIVISTIC ENERGIES

M. Bussmann, D. Habs, Ludwig-Maximilians-University, Munich, Germany
U. Schramm, FZD, Dresden, Germany
K. Beckert, P. Beller, B. Franzke, C. Kozhuharov, T. Kühl,
W. Nörtershäuser, F. Nolden, M. Steck, GSI, Darmstadt, Germany
S. Karpuk, C. Geppert, C. Novotny, Johannes-Gutenberg-University, Mainz, Germany,
G. Saathoff, MPQ, Munich, Germany
S. Reinhardt, MPI-K, Heidelberg, Germany

Abstract

We present results on laser-cooling of relativistic bunched $C3^+$ ion beams at the the Experimental Storage Ring at GSI, Darmstadt. With moderate bunching at a few volts, beams of triply charged carbon ions with a beam energy of 122 MeV per nucleon have been laser-cooled to relative longitudinal momentum spreads of about 2×10^{-6} and below at beam currents of the order of several μA. By detuning the bunching frequency relative to the laser frequency, the acceptance range of the laser force can be increased to match the beam momentum spread. Subsequently decreasing the detuning reduces the momentum spread to values below the resolution of the Schottky noise spectrograph. The reduction of the beam momentum spread is accompanied by a drop in the Schottky noise power by seven to eight orders of magnitude until the signal vanishes completely.

INTRODUCTION

The Experimental Storage Ring (ESR) (see Fig.1) establishes an ideal testbed for laser-cooling experiments at relativistic energies using standard laser equipment (see Tab. 1 for experimental parameters). Exploiting the relativistic Doppler-shift of the laser frequency from the laboratory frame to the rest frame of the ions, a variety of ions can be directly laser-cooled using a single laser system and choosing the appropriate beam energy [1]. The results presented in the following serve as a valuable input for laser-cooling experiments at the future FAIR facility [1, 2].

Different to typical laser-cooling setups in traps, for laser cooling of ion beams at relativistic energies, moderately bunching the beam is necessary to provide for a counteracting force to the laser force [3] (see Tab. 1 for a listing of all experimental parameters). The combined force of the bucket and the laser results in a momentum-dependent force with a controllable, stable cooling point in momentum space. For the data sets discussed here, bunching of a few volts was applied at the 20th harmonic of the revolution frequency f_{rev}, while the mixing frequency at which the Schottky signal was observed was set to the 47th harmonic.

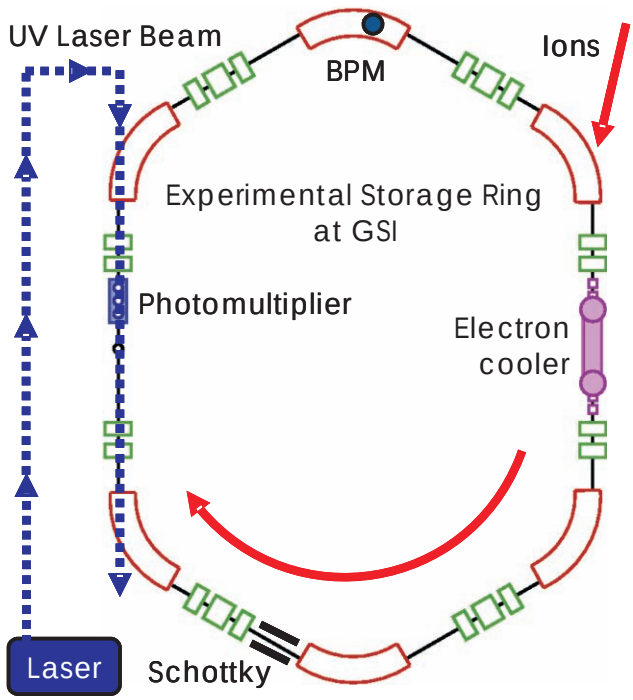

Figure 1: View of the ESR at GSI, Darmstadt. Laser beam and ion beam are brought in overlap in a straight section of the ring. The focus of the laser beam is adjusted to the position of the photomultiplier where the fluorescence signal of the ion beam is recorded. Also marked are the position of the electron cooler, the beam profile monitor (BPM) and the pickup electrode (Schottky). The ions revolve clockwise in the ring, the laser beam is counterpropagating to the ion beam.

A combination of two laser systems, namely two frequency-doubled argon ion lasers, has been used for laser cooling. While the first of the two laser beams is frequency-stabilized by measuring the absorption signal of the beam passing through an iodine vapor cell, the frequency of the

Table 1: Experimental parameters for the storage ring, ion beam and laser system.

ESR	
circumference	108 m
betatron tune	2.3
slip factor	0.6
Beam	
ion species	C^{3+}
beam energy	1.47 GeV
revolution frequency	1.295 MHz
relativistic β,γ	0.47, 1.13
beam lifetime	300 s to 450 s
Laser	
laser source	Ar^{+} ion laser
operational mode	cw, single mode
wave length	257.34 nm (SHG)
power	40-100 mW
Cooling Transitions	
$2S_{1/2} \rightarrow 2P_{1/2}$	155.07 nm
$2S_{1/2} \rightarrow 2P_{3/2}$	155.81 nm

second beam is scanned relatively to the frequency of the first. The frequency offset Δf_{beat} between the two laser beams is determined by overlapping the beams and measuring the beat signal. Both beams are brought in overlap with the ion beam in a straight section of the ring. (see Fig. 2). The fixed-frequency laser beam is used to cool the ions to their ultimate small momentum spread, while the other laser-beam is applied to increase the momentum acceptance of the laser force, especially addressing those ions which escape the momentum acceptance of the first laser beam due to intra-beam scattering.

The initial momentum spread of the bunched beam is about three orders of magnitude bigger than the momentum acceptance of the force of the fixed-frequency laser beam. Although the scanning laser system increases this acceptance range by almost one order of magnitude [4] (the maximum detuning of both lasers is about 400 MHz in the UV for all data sets presented here), the momentum mismatch is still to large to cool all ions confined in the bucket. To directly cool all ions, the bunching frequency is detuned relatively to the fixed laser frequency, thus subsequently bringing different velocity classes of ions in overlap with the laser force. A reduction of the detuning reduces the total longitudinal momentum spread until the laser frequency is close to the cooling transition frequency for those ions resting in the bucket center as shown in Fig. 3.

Finally, additional moderate electron cooling at a few mA electron current is used to increase the coupling of the transverse to the longitudinal degree of freedom of the ion motion in the bucket. In all cases, electron cooling is switched on for only a few seconds until the coupling has been increased to the desired degree. With a combination of these two cooling techniques, three-dimensional cold beams can be attained [5].

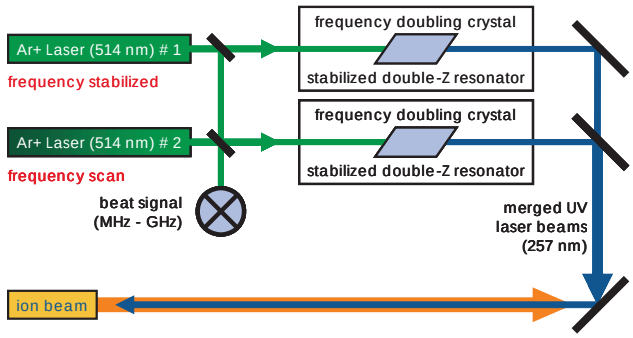

Figure 2: Laser system used for laser-cooling. The frequency of one laser beam is scanned relatively to the fixed frequency of another laser system. The scanning is controlled by measuring the beat signal of the two laser beams. Both laser beams are frequency-doubled separately using beta-barium borate crystals placed in a double-Z resonator geometry. After frequency-doubling, both beams are merged to one and brought in overlap with the ion beam.

SCHOTTKY NOISE SPECTRA

At the ESR, Schottky noise spectra provide a relative longitudinal momentum resolution for a single bunched beam to about 2×10^{-6}. A further increase in resolution is possible using optical detection of the fluorescence signal of the laser-cooled beam [6]. Here, we concentrate on the dynamics of ions confined in the bucket which can be deduced from the Schottky noise signal.

The spectrum of the Schottky noise signal of a bunched laser-cooled ion beam shows sharp, pronounced peaks at a spacing determined by the synchrotron oscillation frequency of the ions in the bucket pseudo-potential. The center peak marks the center of the bunch in frequency space. The spread Δf_{b} of the satellite peaks, which are symmetrically distributed around the center peak, determines the longitudinal momentum spread of the ions. The momentum spread is then given by the frequency spread as [5]

$$\frac{\Delta p_{\mathrm{long}}}{p_{\mathrm{long}}} = \frac{1}{\eta} \frac{\Delta f_{\mathrm{b}}}{f_{\mathrm{b}}}. \qquad (1)$$

The limitation of the momentum spread measurement stems from the fact that the determination of the frequency spread requires the existence of at least one sideband on each side of the carrier peak. Momentum spreads smaller than the resolution limit determined by these two first order sidebands of the spectrum thus cannot be resolved.

Recently, the dynamics of laser-cooled bunched beams have been discussed in detail [4], showing qualitatively new features at the transition from the intra-beam scattering dominated regime to the space-charge dominated regime [5]. At this transition, the momentum spread of the beam reaches the resolution of the Schottky measurement.

As in the case of the momentum spread, the Schottky signal intensity is derived from the Schottky spectrum by first subtracting the constant signal background before

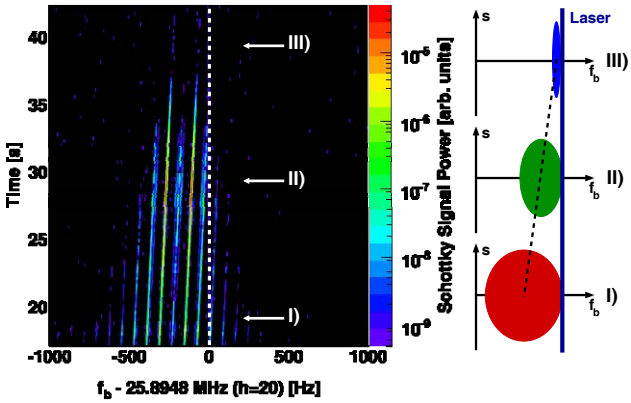

Figure 3: Schematic view of the cooling scheme. The bunching frequency f_b is detuned continuously relative to the laser frequency marked by the dashed white line in the middle of the color-coded Schottky noise spectrum. The Schottky noise signal strength is plotted logarithmically, the X-axis showing the detuning of the bunching frequency, the Y-axis showing the time in which the detuning is reduced. Three steps indicated by the numbers I, II and III are marked in the spectrum. On the right side of the figure, the phase space volume of the ion distribution in the bucket at each of these steps is illustrated by three ellipses. When the detuning is reduced, the momentum spread decreases with the position of the laser beam marking the maximum momentum spread.

summing up the intensity of all individual peaks. At low Schottky signal intensities, a longer signal integration time is used to clearly distinguish the signal from the background. All the intensities were weighed by this integration time.

SCHOTTKY NOISE INTENSITY AND MOMENTUM SPREAD

Previous experiments using electron-cooled coasting beams [7, 8, 9] have shown a drop in the Schottky intensity by several orders of magnitude at low ion beam currents, meaning low ion densities. This drop has been attributed to an onset of beam ordering [8].
While in these experiments the ion current has to be varied in order to determine the ion density at which the drop of the Schottky signal intensity is observed, in laser-cooling experiments, the momentum spread is simply controlled varying the detuning Δf_b of the bunching frequency relatively to the fixed laser frequency. This offers additional experimental control over the longitudinal momentum spread, which in turn becomes almost independent of the ion current.

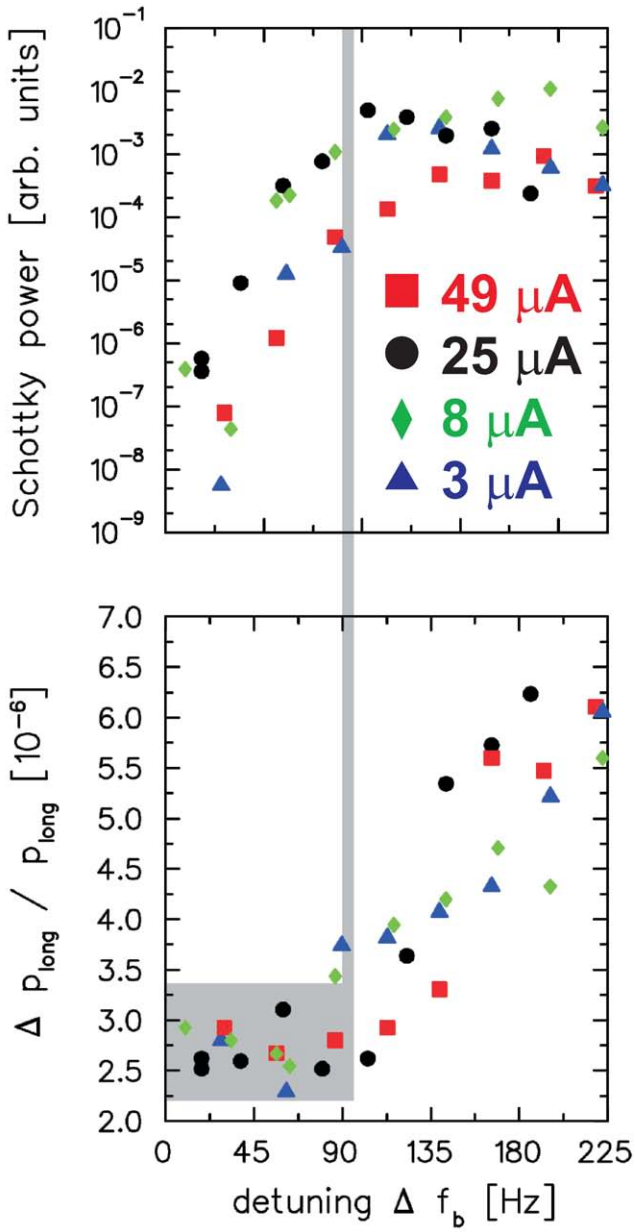

Figure 4: **Upper Part:** Integrated Schottky signal power versus detuning of the bunching frequency. The power of the Schottky signal is extracted from the Schottky spectrum, removing the constant background noise value and summing the signal for all peaks. For each detuning value a short time integration (usually 0.1 s) of the Schottky signal has been used to extract the corresponding power signal. The total signal power has been normalized to this integration time.
Lower Part: Corresponding momentum spread. The resolution limit of the Schottky measurement is indicated by the gray bar. At this point, the ion beam typically enters the space-charge dominated regime. The position marking the onset of the drop in Schottky power is indicated by the gray line.

The upper part of Fig. 4 shows a plot of the Schottky signal intensity extracted from the spectrum as described in the previous section. The intensity is plotted versus the de-

tuning Δf_b. The various markers indicate various beam currents. All data points follow the same trend. At large detuning the intensity of the Schottky signal decreases only weakly with decreasing detuning. At a detuning of about 90 Hz, as indicated by the gray line in Fig. 4, the signal intensity drops rapidly until the level of the background noise is reached. The relative reduction of the signal strength is about seven to eight orders of magnitude. It has to be pointed out that the reduction is not caused by ion loss, instead the ions reside in the bucket center and the beam current remains almost constant during the scanning of the bunching frequency.

Interestingly, the drop occurs at the same detuning value at which the measured momentum spread of the ion beam, as shown in the lower part of Fig. 4, becomes limited by the resolution of the Schottky measurement. The reduction of the momentum spread below the limit of the Schottky measurement has been previously found to mark the transition of the bunched beam to the space-charge dominated regime [4, 5, 6].

The decrease in Schottky signal power sets a severe limitation to the observation of ultra-cold beams. It shows, that as soon as coherent movement of the ions due to an increase in coupling between the ions in the bucket could be observed, the Schottky signal is reduced by several orders of magnitude, thus limiting the amount of information on the dynamics of ultra-cold bunched beams which can be extracted from the Schottky signal.

Fortunately, with laser-cooling, the fluorescence intensity of the laser-cooled ions, which depends on the Doppler-shift of the cooling transition frequency relative to the laser frequency, can serve as a high-resolution diagnostic tool complementary to the Schottky noise signal. Unfortunately, with the current experimental setup, the observed fluorescence rate was in most cases too low for high precision measurements of the momentum spread.

Nevertheless, recent measurements of the fluorescence signal of a laser-cooled bunched beam [6] indicate that the longitudinal momentum spread could be at least one order of magnitude smaller than the value measured using the resolution-limited Schottky signal.

CONCLUSION AND OUTLOOK

We have shown that laser-cooling of relativistic ion beams is possible in a typical storage ring using a standard laser system and moderate bunching. Our main focus in this paper was on the information which can be extracted from the Schottky noise spectrum at low momentum spread. In the space-charge dominated regime, the information on the ion dynamics which can be deduced from the Schottky noise spectrum is sparse. Yet, all data indicate that collective ion motion due to increased inter-ion coupling dominates the ion dynamics in the bucket.

A clear fluorescence signal from the laser-cooled ions can provide a much higher resolution for determining the longitudinal beam momentum spread. Thus, for future experiments, a new experimental setup including at least two photomultipliers placed inside the beam tube in vacuum, near to the ion beam, is proposed.

In addition to extending the resolution of the beam diagnostics, it is foreseen to complement the single-frequency laser system by a pulsed laser system with high repetition rate and a pulse length comparable to the ion bunch length. The energy spread of the pulsed laser beam will then match the acceptance of the laser force to the initial ion momentum spread without the need for detuning the bunching frequency, while the high repetition rate increases the integrated cooling strength of the laser force.

REFERENCES

[1] Schramm, U., Bussmann, M. and Habs, D., Nuclear Instruments and Methods in Physics Research Section A 532(1-2) (2004) 348.

[2] Backe, H., Hyperfine Interactions 171(1) (2006) 93.

[3] Hangst, J. S., Nielsen, J. S., Poulsen, O., Shi, P. and Schiffer, J. P., Physical Review Letters 74(22) (1995) 4432.

[4] Bussmann, M. et al, Journal of Physics: Conference Series, Proceedings ICPEAC07, Freiburg, July 2007 (accepted for publication)

[5] Schramm, U. et al, AIP Conference Proceedings 821(1) (2006) 501.

[6] Schramm, U. et al, Hyperfine Interactions 162(1) (2005) 181

[7] Steck, M. et al, Physical Review Letters 77(18) (1996) 3803.

[8] Danared, H., Källberg, A., Rensfelt, K.-G. and Simonsson, A., Physical Review Letters 88(17) (2002) 174801.

[9] Noda, A., Ikegami, M. and Shirai, T., New Journal of Physics 8(11) (2006) 288

ELECTRON COOLING WITH PHOTOCATHODE ELECTRON BEAMS APPLIED TO SLOW IONS AT TSR AND CSR

D. A. Orlov#, H. Fadil, M. Grieser, C. Krantz, J. Hoffmann, O. Novotny, S. Novotny, A. Wolf
Max-Planck-Institut für Kernphysik, 69117, Heidelberg, Germany

Abstract

We report electron cooling experiments using a cold electron beam of 53 eV produced by a cryogenic GaAs photocathode. With this device a beam of CF^+ (mass 31) of only 97 keV/u (3 MeV) was cooled down to a very small equilibrium beam size of about 0.04×0.2 mm^2. A transverse cooling time below 2 seconds was obtained.

INTRODUCTION

Cold electron beams at low energies are currently a subject of high interest in view of next-generation electrostatic storage rings where electron cooling of very slow ions as well as high-resolution electron-ion merged beam experiments are planned to be performed. The use of electrostatic rings (instead of magnetic ones normally used for lighter high energy beams) is the only possibility to store heavy molecules, clusters and biomolecules. The energies of stored ions in electrostatic rings are about 20-300 keV (per charge state), limited by the maximum voltage applied to the ring optics. Thus velocities of stored heavy molecules are very low.

An electrostatic Cryogenic Storage Ring (CSR) for ion beams, including protons, highly charged ions, and polyatomic molecules, is under construction at MPI-K [1]. Electron cooling at electron beam energies from 165 eV for 300 keV protons down to a few eV for polyatomic singly charged ions will be applied. The quality of an electron beam with respect of density and longitudinal temperature degrades at low energies. Thus electron beams of low emission energy spreads are needed. For the CSR cooler, the cryogenic photocathode source developed for the Heidelberg TSR target [2] will be used to generate electron beams with emission energy spreads of about 10 meV [2,3], that is at least by a factor of 10 better compared to conventional thermocathode sources. At high energies the main drawback of photocathode coolers is the limited extraction current (at the TSR target a maximum current of 1 mA is presently obtained from GaAs source). At low voltages, however, this disadvantage vanishes as the current becomes limited by gun perveance anyway to about 1-2 mA at 100 V.

Electron cooling experiments of slow CF^+ molecules were performed at the Heidelberg TSR target using an ultracold electron beam of 53 eV, produced by a cryogenic GaAs photocathode. A transverse cooling time below 2 seconds to a very small equilibrium beam size was observed with an electron current of 0.3 mA (corresponding to an electron density of about $3\cdot10^6$ cm^{-3})

#orlov@mpi-hd.mpg.de

LOW-ENERGY ELECTRON BEAMS

The key parameters of electron beams used for ion cooling and merged beam experiments in storage rings are density as well as transverse and longitudinal temperatures. The transverse temperature of the electrons is not affected by electron acceleration and it can be reduced by an adiabatic magnetic expansion α down to $kT_\perp = kT_c/\alpha$ [4], where T_c is the cathode temperature. The use of a cryogenic photocathode source makes it possible to obtain transverse temperatures below 1 meV [2]. The longitudinal temperature and density of the electron beams, however, degrade strongly at low energies. Indeed, the electron current I and density n_e are limited by gun perveance P (with typical values of about 1-2 μPerv):

$$n_e = \frac{4PU}{\pi D^2 e\sqrt{2\eta}} \approx 6\times10^6\ cm^{-3}\left(\frac{P}{1\,\mu Perv}\frac{U}{100V}\right)\left(\frac{15mm}{D}\right)^2$$

$$I = PU^{3/2} = 1mA\left(\frac{P}{1\,\mu Perv}\right)\left(\frac{U}{100\ V}\right)^{3/2}, \qquad (1)$$

where D is the diameter of the electron beam in the interaction section.

The longitudinal electron temperature $kT_{||}$ of the electron beam is described by the following expression:

$$kT_{||} \approx \frac{(kT_C)^2}{W} + C\frac{e^2 n_e^{1/3}}{4\pi\varepsilon_0}, \qquad (2)$$

where $W=e\cdot U$ is the electron energy and C is the acceleration constant. The first term is due to kinematic transformation of the electron temperature from the laboratory to the co-moving system. It is also taking into consideration that the part of the transverse energy is transferred to the longitudinal temperature during adiabatic magnetic expansion increasing the first term by a factor of about 2 [5]. The second, density term, is connected to a relaxation of the potential energy of the accelerated beam [6]. The acceleration constant C for high acceleration voltages was found to be of about 1.9 [6]. Our studies (work in progress) show, however, that a value of about 0.9 appears to be more appropriate for the C constant. Moreover, for low energies with the first term being dominant the description of the longitudinal temperature for different acceleration energies with a fixed value of C is found to be inaccurate. Figure 1 shows the longitudinal temperatures of electron beams as a function of the kinetic energy calculated for thermocathode (kT_c=100 meV) and photocathode (kT_c=10 meV) electron sources. For the calculations we assumed a gun perveance of 2 μPerv and a beam diameter of 13.5 mm. We see that for the thermocathode the longitudinal

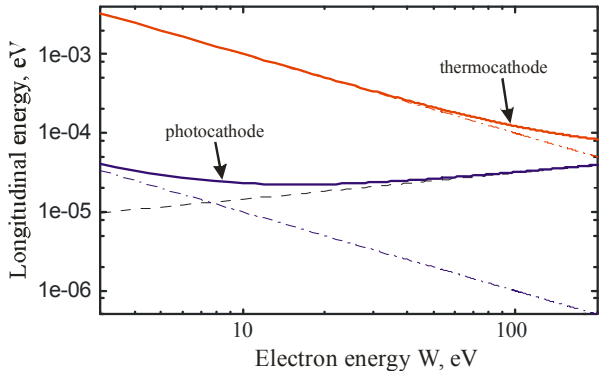

Figure 1: Longitudinal temperature vs electron energy for th ermocathode and photocathode electron beams. The kinematic (dashed-dotted lines) and density (dashed line) terms of the Eq. 2 are also shown.

temperature is dominated by the kinematic contribution over the entire considered range as a consequence of the high cathode temperature. For the cryogenic photocathode, with its small emission energy spread, the kinematic term is smaller by a factor of 100, which yields a much colder electron beam at low energies.

Low transverse and longitudinal temperatures of the electron beam are required for high resolution merged beam experiments. The high cooling force due to low longitudinal temperature also allows to strongly suppress the ion beam scattering and to obtain a small equilibrium size of the ion beam.

The cooling time of the stored ions strongly depends on both the transverse and the longitudinal temperatures of the electron beam as well as on the charge Ze and mass M_{ion} of the ions. The longitudinal momentum spread of the ions as well as the transverse emittance of the ion source is also important to calculate cooling times. However, a first approximation can be done in the model of a non-magnetized electron beam [7] with an electron temperature kT_e identical to the transverse temperature:

$$\tau = \frac{3mc^3(4\pi\varepsilon_0)^2}{8\sqrt{2\pi}e^4}\,\frac{M_{ion}}{n_e\cdot Z^2\cdot L_C}\cdot\left(\frac{k_B T_e}{m c^2}\right)^{3/2}, \qquad (3)$$

where L_c is the Coulomb logarithm. For cold ion beams, injected to the ring with a momentum spread lower than the electron momentum spread, the cooling time can be reduced by a magnetized electron beam with small longitudinal temperatures [8]. Typically, the cross-section of the injected ion beam is few cm which is about the diameter of the electron beam. Ions in the centre or at the edge of the electron beam will see electrons of different velocities, as the space-charge varies across the electron beam. The space-charge induced momentum spread for high perveance electron guns is typically much larger than the longitudinal momentum spread of the electrons. The situation changes at very low energies (≤10 eV) as temperature-induced momentum spread of the electrons approaches the space-charge momentum spread. Thus, the impact of longitudinal electron temperature on the cooling time will be even more important at extremely low energies. The possibility to use electron guns with higher perveance at very low energies also has to be considered.

PHOTOCATHODE ELECTRON SOURCE

An atomically clean surface of p^+-GaAs with a thin layer of cesium and oxygen produces a state with effective Negative Electron Affinity (NEA), where the vacuum energy level lies below the conduction band in the bulk [9] (Fig.2). Electrons photoexcited from the valence band to the conduction band rapidly thermalize to the bottom of the conduction band and reach the surface with energy spreads defined by the temperature of the bulk, of around 100 K in our case. Due to the NEA, a large fraction of these electrons can escape into the vacuum. During the escape process, however, electrons undergo strong energy and momentum relaxation [3]. As a result, the transverse and longitudinal energy spreads of photoemitted electrons are enlarged to about the value of the NEA (typically about 150-250 meV). However, it was found that electrons emitted with a longitudinal energy above E_C (with a potential barrier produced by a space charge) have transverse and longitudinal momentum spreads of about the bulk temperature [3,10]. For these electrons energy spreads of about 7 meV have been measured at 90 K [3].

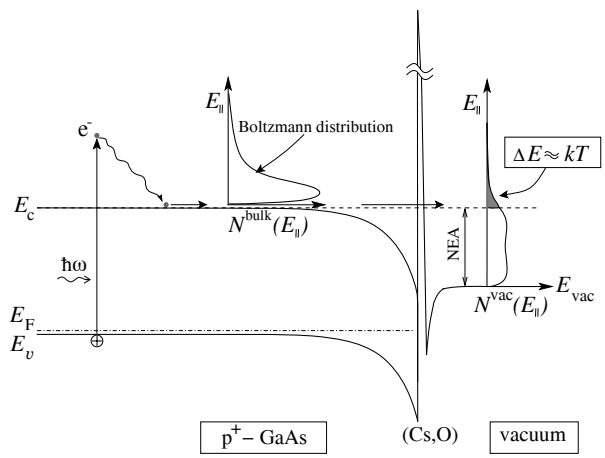

Figure 2: Band diagram of NEA GaAs schematically illustrating the photoemission process.

The vacuum photocathode setup of the TSR target includes a loading (with an attached atomic hydrogen chamber), a preparation and a gun chamber, separated by all-metal gate valves, with base pressures of 10^{-10}, $5\cdot10^{-12}$ and 10^{-11} mbar respectively [12]. Inside the vacuum the samples are transferred by magnetically coupled manipulators. In the preparation chamber the samples are fixed on a carousel capable of keeping four cathodes. The carousel can be rotated into different positions for thermal cleaning and activation of the photocathodes with cesium and oxygen. The effective quantum yield for the cold electrons at 90 K is found to be 1-2%, while the total quantum yield (QY) is about 20-30 % [11]. In the electron gun the sapphire substrate of the cathode is pressed to a copper cold head by a spring force of 100 N in order to obtain a good thermocontact [12]. The photocathode is

illuminated in transmission mode by a 800 nm diode laser with a power of about 1 W. By flooding the cold head with liquid nitrogen an operating temperature of about 100 K is reached. When the QY of the cathode drops down, the degraded cathode can be changed to another one stored in the preparation chamber. It takes about 30 min to change the sample and to cool it down. The samples are usually re-used 3-5 times by radiative heating and re-activation in the preparation chamber before they loose their performance. Then atomic hydrogen cleaning is used to recover the surface properties of the degraded cathode by removing contaminations [13]. Details of photocathode setup and surface preparation techniques can be found elsewhere [12,14].

Using the cryogenic photocathode source ultra cold electron beams were obtained, with transverse and longitudinal temperatures of about 0.5 meV and 0.03 meV respectively [2]. Recently the performance and reliability of the photocathode source have been strongly improved. This was achieved by controlling different degradation effects like cryosorption, back stream of ionised rest gas, pressure raise due to electron induced gas desorption from the chamber walls. Presently, the photocathode can deliver electron currents of up to 1 mA at photocathode lifetimes above 24 hours.

CF^+ COOLING BY 53 EV ELECTRONS

Electron cooling experiments at low energies were performed at the TSR target on a CF^+ beam of energy 3 MeV (about 97 keV/u). The corresponding electron energy was about 53 eV and the electron current was 0.3 mA.

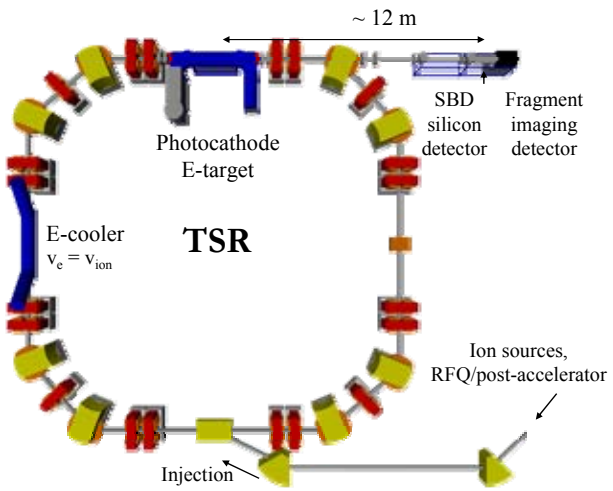

Figure 3: Layout of the Heidelberg Test Storage Ring.

The Heidelberg TSR is a magnetic storage ring with a maximum magnetic rigidity of 1.5 Tm. It is equipped with an electron cooler and an electron target (Fig.3). Typically the electron cooler is used for phase space cooling of the stored ion beams and the photocathode target provides cold electron beams for high-resolution merged beam experiments. However, in the case of the slow CF^+ ion beam the electron target was found to be by far stronger in cooling force providing much shorter cooling times. So, these experiments were performed mainly with the photocathode target serving as both cooler and target. The diameter of the magnetically expanded electron beam was 13 mm (α=20), the electron current was limited by gun perveance to about 0.34 mA (electron density $3x10^6$ cm^{-3}). A magnetic guiding field of 0.04 T was used. The CF^+ current in the storage ring after injection was estimated to be few 100 pA and the lifetime of the ion beam was about 4 s.

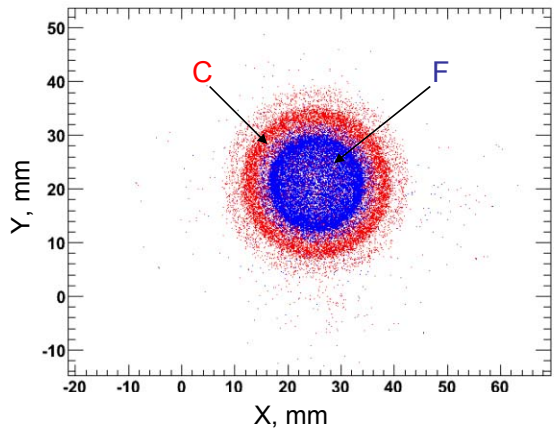

Figure 4: Image of C and F neutral fragments of the cooled ion beam after 12 s.

Imaging detectors 12 m downstream of the electron target are used to measure neutral recombination fragments and to analyze the dissociation dynamics. The transverse momentum of the dissociation fragments is recorded event by event using a spatially resolving multi-hit detector (two-dimensional fragment imaging) [15]. Figure 4 shows a pattern of C and F neutral fragments from dissociative recombination of the stored CF^+ molecular ions in the electron target at zero (cooling) energy, as observed on the imaging detector. Due to the kinetic energy release the neutrals are deflected from the centre. The maximum deflection distance comes from the molecules dissociated transversely to the ion beam propagation with the lighter fragment (C, red) forming the outermost rings on the image and with F atoms (blue) corresponding to inner rings. For CF^+ two different final levels of the C atoms cause two rings each for C and F, respectively, with a smaller branching ratio for the *high* kinetic energy release.

For atomic ion beams the spatial profile of neutral atoms produced by recombination in the electron target directly reflects the angular divergence of the ion beams [16]. For molecules the imaging profile can not be used directly to monitor transverse ion beam properties during the phase space cooling due to the significant kinetic energy release in the dissociation process. However, this can be achieved by monitoring the centre-of-mass of all fragment hit positions for a given recombination event, which reflects the direction of the molecular ion before it captured an electron in the target [17].

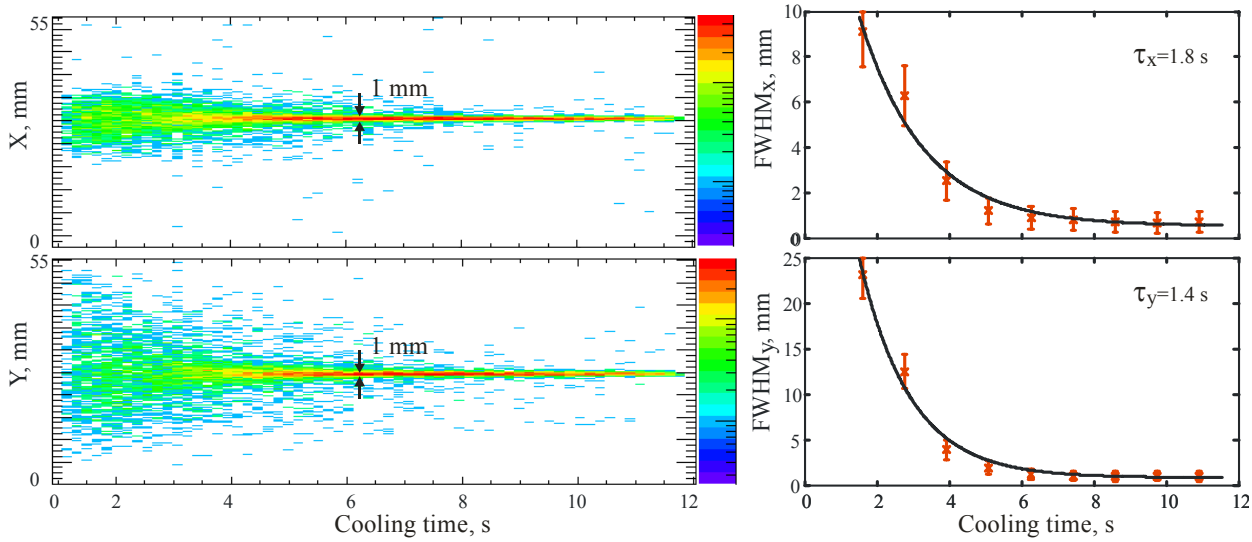

Figure 5: Transverse electron cooling of 97 keV/u CF^+. Centre-of-mass positions of the C and F neutral fragments vs time, recorded 12 m downstream of the electron target by the imaging detector and indicating rms divergence angles of about $3 \cdot 10^{-5}$.

Figure 5 (left) shows positions of the centre-of-mass as a function of the cooling time derived from correlated two-hit events for both transverse directions. The FWHM of the centre-of-mass distribution vs time is also shown in Fig.5 (right). A transverse cooling time below 2 s was achieved, demonstrating a high cooling efficiency of the photocathode beam. An estimation of the cooling time from Eq.3, assuming an isotropic electron beam with 1 meV temperature, L_c=3.3 and the length of the target to be about 2.2% of the ring circumference, gives a value of about 1.5 s for the cold ion beam and 6 s for the hot ion beam (with a diameter of the injected ion beam about 2 times larger than that of the electron beam). After 6 s a FWHM of the centre-of-mass distribution of 1 mm (horizontally) and 0.7 mm (vertically) was measured by the imaging detector 12 m downstream of the target. Assuming a longitudinal ion spread ΔP/P of about $5 \cdot 10^{-5}$ and using the horizontal TSR dispersion of 2 m and the β functions of 3.9 m (horizontal) and 1.5 m (vertical) at the target section, the divergence and size of the ion beam can be derived. The divergence was found to be of about $3 \cdot 10^{-5}$ in both transverse directions and the 1σ size was about 0.04 mm (vertically) and 0.2 mm (horizontally). The larger size of the ion beam in the horizontal direction arises from the ring dispersion and from stability of the power supplies for dipole magnets and cathode voltage.

CONCLUSIONS

Electron cooling of low-energy heavy molecular beams (CF^+, 31 amu) was performed by a cold electron beam of 53 eV delivering by cryogenic photocathodes. An electron current of about 0.3 mA was used. Short cooling times (below 2 s) and a very small equilibrium beam size (0.04×0.2 mm^2) obtained in these experiments demonstrate the high potential of cryogenic photocathode electron beams for electron cooling of slow ions.

REFERENCES

[1] D. Zajfman et al., J.Phys.: Conf. Ser. 4 (2005) 296; A. Wolf et al., in: "Beam cooling and relating topics", COOL05, AIP 821, September 2005, p. 473.
[2] D.A. Orlov et al., J.Phys.: Conf. Ser. 4 (2005) 290.
[3] D.A. Orlov et al., Appl. Phys. Letters 78 (2001) 2721.
[4] S. Pastuszka et al., NIM A 369 (1996) 11.
[5] D.A. Orlov et al., in: "Non-neutral plasma physocs VI", NNP06, June 2006, AIP 862, p. 274.
[6] N.S. Dikansky et al., "Ultimate possibilities of electron cooling", Preprint 88-61, Institute of Nuclear Physics, Novosibirsk, 1988.
[7] L. Spitzer, "Physics of fully ionized gases", Interscience, New York, 1956.
[8] Ya.S. Derbenev, A.N. Skrinskii, Sov. Phys. Rev. 1 (1981) 165.
[9] J.J. Scheer and J. van Laar, Solid State Commun. 3 (1965) 189.
[10] S. Pastuszka et al., Appl. Phys. 88 (2000). 6788.
[11] D.A. Orlov et al., in: "Polarized sources and targets", PST02, October 2002, World Scientific, New Jersey, p.151.
[12] U. Weigel et al., NIM A 536 (2005) 323.
[13] D.A. Orlov et al., in: "Proc. SPIN2004", World Scientific Publishing, October 2004, Singapore, p. 943.
[14] D.A. Orlov et al., NIM A 532 (2004) 418.
[15] Z. Amitay, Phys. Rev. A 54 (1996) 4032.
[16] G.I. Budker et al., Part. Accel. 7 (1976) 197.
[17] A. Wolf et al., NIM A 532 (2004) 69.

STUDIES OF COOLING AND DECELERATION AT CRYRING FOR FLAIR

H. Danared, A. Källberg and A. Simonsson
Manne Siegbahn Laboratory
Frescativägen 28, S-104 05 Stockholm, Sweden

Abstract

FLAIR will be a facility for low-energy ions and antiprotons at FAIR, the proposed centre for nuclear and hadron physics in Darmstadt, Germany. As a preparation for a possible transfer of CRYRING from the Manne Siegbahn Laboratory to FLAIR, where it would serve to decelerate antiprotons and ions, machine studies have been performed at CRYRING to ensure that that it meets the requirements at FLAIR. In these experiments, the space-charge limit for protons at 300 keV, cooling times for H^- ions and deceleration of protons from 30 MeV to 300 keV have been investigated. It is found that CRYRING as it is configured already today can decelerate more than 3×10^8 protons from 30 MeV to 300 keV.

FLAIR

At FAIR [1], the proposed new centre for nuclear and hadron physics in Darmstadt, Germany, antiprotons will be produced at rates at least as high as at CERN during the time of operation of the proton–antiproton collider, and much higher than today's rates at the antiproton decelerator AD. Also, beams of radioactive ions will be available at intensities far superior to those at RIB facilities like GSI today. While much of the physics at FAIR will use these beams of antiprotons and ions at high energies, FLAIR, the Facility for Low-energy Antiproton and Ion Research [2], will give the possibility to make experiments with antiprotons and ions at very low energy, or even at rest.

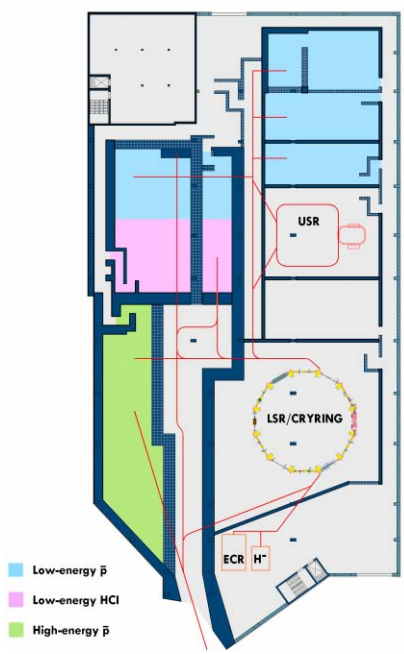

Figure 1: Layout of the FLAIR hall.

FLAIR was not part of the original conceptual design report for FAIR that was submitted to the German government in 2003. Since then, however, a thorough review has been made of the experimental programme at FAIR, and the FLAIR proposal has been part of this process. As a result of the very positive review of the physics programme with low-energy antiprotons, and also of the atomic-physics programme within the SPARC [3] collaboration, FLAIR is now part of the proposed core experimental programme at FAIR.

FLAIR will receive beams from a chain of synchrotrons and storage rings at FAIR ending with the NESR ring. These beams can supply FLAIR experiments, including HITRAP, directly, or they can be directed to the first deceleration ring in the FLAIR hall, the LSR (Low Energy Storage ring). Antiprotons will be transferred to LSR at a fixed energy of 30 MeV, and ions will be transported at the same rigidity as 30 MeV antiprotons, independently of their charge-to-mass ratio.

LSR will bring the antiprotons from 30 MeV down to a minimum energy of 300 keV, and ions will be decelerated through the same range of magnetic rigidities. This matches the energy range of CRYRING, which is approximately 200 keV to 96 MeV for (anti-)protons. CRYRING also has the electron cooling required to keep the beam emittance small at deceleration, good vacuum (better than 1×10^{-11} torr N_2-equivalent pressure which is necessary for storing highly charged ions), operational deceleration, easy and frequent shifting between positive and negative particles, etc., and it is therefore proposed that CRYRING will be transferred from the Manne Siegbahn Laboratory to FLAIR for use as the LSR ring.

LSR will provide beams of antiprotons to HITRAP, the electrostatic USR ring or directly to experiments, and the same possibilities will exist for ions. The USR ring will decelerate antiprotons from 300 keV to 20 keV and cool them, and from 20 keV, antiprotons can be brought to rest for capture in traps just by using a small voltage gap. Compared to today's Antiproton Decelerator, AD, at CERN, antiprotons at FLAIR will thus be cooled at much lower energies, providing phase-space densities of very-low-energy antiprotons which are orders of magnitudes higher than at the AD.

Several experiments have been made at CRYRING in order to evaluate its performance relating to deceleration of antiprotons at FLAIR. The throughput of antiprotons

will be determined by the maximum number of particles that can be decelerated in each machine cycle and by the length of the cycle. The maximum particle number is set by the space-charge limit, and the length of the machine cycle may be limited by the time required for electron cooling. Both the space-charge limit and cooling times have been investigated, and tests of deceleration of protons from 30 MeV to 300 keV have been performed in order to verify that existing control and diagnostics systems are adequate for the deceleration of such a beam with acceptable particle losses.

SPACE-CHARGE LIMIT

For a storage ring like CRYRING, the maximum beam current is determined by the space charge of the beam which induces an incoherent tune shift ΔQ according to the simple expression

$$\Delta Q = -\frac{N r_0}{4\varepsilon\beta^2\gamma^3},$$

where N is the total number of particles stored in the ring, r_0 is the classical particle radius, ε is the un-normalized beam emittance and β and γ are the usual relativistic factors. We assume a round beam with unit charge and mass, with a Gaussian density profile, and we use the 1σ emittance. Protons or antiprotons at 30 MeV or below have γ close to 1, so plotting N as a function of particle energy, for a fixed ΔQ, gives straight lines as shown in Fig. 2.

The lines in Fig. 2 are drawn for a coasting beam and a conservative value of the maximum permissible tune shift equal to –0.02. For a bunched beam, which is relevant for deceleration, the maximum particle number must be multiplied by the bunching factor which has a value around 0.3.

In order to verify that CRYRING can store particles up to this space-charge limit, protons were injected into the

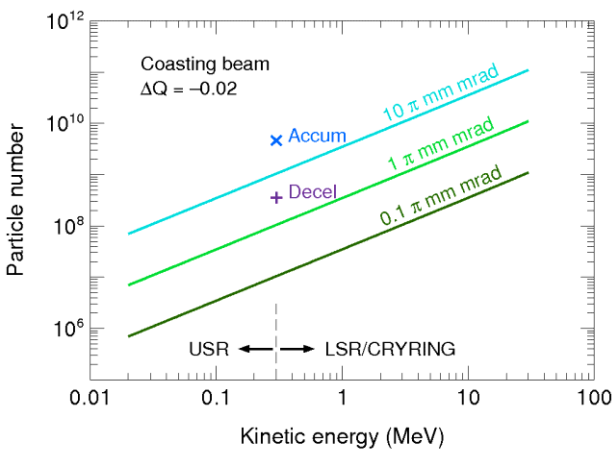

Figure 2: Space charge limit in LSR/CRYRING and USR for a coasting beam with ΔQ = –0.02. The crosses represent the maximum number of protons that could be accumulated in CRYRING and the maximum number that has been decelerated.

ring in batches every 0.5 s at 300 keV while the electron cooling was on, moving the particles away from the injection orbit and continuously increasing the beam current and the phase-space density of the beam. The highest particle number observed, after several minutes of accumulation, was 4.7×10^9 as indicated by a cross in Fig. 2. The emittance could be estimated, using residual-gas beam-profile monitors [4] in both planes, to 15π mm mrad horizontally and 5π mm mrad vertically, indicating a ΔQ of approximately –0.1.

This beam was, however, quite unstable. Taking into account also the bunching factor, one can conclude that an upper intensity limit for decelerated antiprotons in LSR/CRYRING is in the order of 1×10^9 particles at an emittance of 10π mm mrad.

Also indicated in fig. 2 is the maximum number of particles that has actually been decelerated from 30 MeV to 300 keV according to the experiments on deceleration described below. This number is 3.6×10^8, and it should thus be possible to increase it somewhat through better adjustment of magnet ramps and more cooling.

ELECTRON COOLING OF H^- IONS

Electron cooling is in the first approximation based on the Coulomb interaction between the electrons in the cooler and the stored ions, and cooling rates should thus be sensitive only to the ion charge squared. However, the magnetic field in the cooler makes the ion–electron interaction more complicated and can make cooling rates depend on the sign of the ion charge. Such effects were seen in measurements of drag forces on protons and H^- ions in Novosibirsk [5], where a stronger drag force was observed for the negatively charged particles.

The first measurements at CRYRING concerned transverse cooling times for H^- ions at 3 MeV. It is anticipated that cooling at a similar energy is desirable for the deceleration of antiprotons from 30 MeV to 300 keV, and transverse cooling times are expected to dominate over longitudinal ones.

Fig. 3 shows a set of vertical beam profiles, measured with a residual-gas-ionization beam-profile monitor [4]. The initial beam emittance was approx. 5π mm mrad, which is more than expected for antiprotons at 3 MeV if they are injected with an estimated 0.25π mm mrad 1σ emittance at 30 MeV. The beam was cooled using an electron current of only 18 mA, giving an electron density of 3.8×10^{12} m^{-3}.

The resulting cooling time can be compared to previous measurements of transverse cooling times for singly and multiply charged ions in CRYRING [6]. In those measurements, hollow ion beams were produced by misaligning the electron beam with respect to the ion beam, such that all ions performed betatron oscillations with the same amplitude, and cooling rates could thus be determined as a function of betatron amplitude. Such hollow beams were not used in the present studies of H^- ions. Instead markers were put manually in an attempt to get a representative beam width, as indicated in fig. 3.

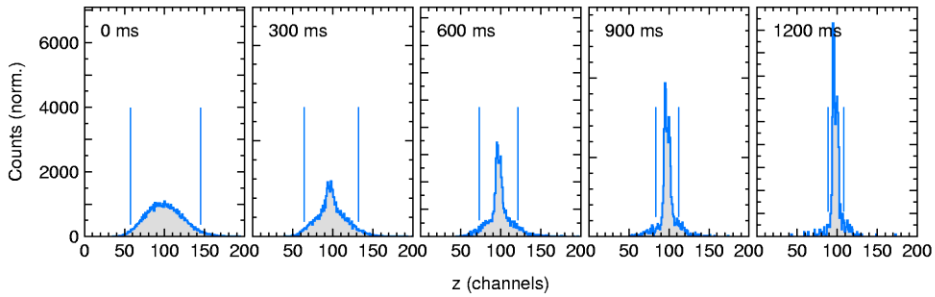

Figure 3: Transverse beam profiles during electron cooling of H^- ions. The full horizontal scale of 200 channels corresponds to 40 mm, and the time interval between the profiles is 300 ms.

The resulting comparison between H^- ions and positive ions is shown in fig. 4. Although there is a small uncertainty due to the difference in the definition of the beam width, no significant difference in cooling times between negative and positive ions is seen. The beam reached a cold equilibrium state in about 1.5 s, which is sufficiently short so that electron cooling in the LSR will not be a limiting factor for the throughput of antiprotons. Note that the cooling time plotted in fig. 4 is shorter than 1.5 s since it is normalized to a higher electron density.

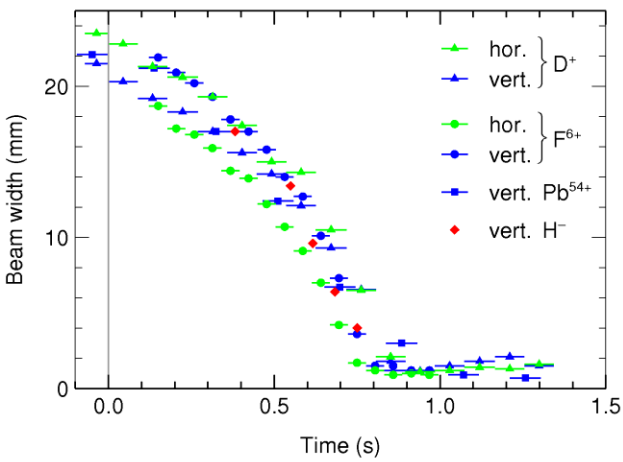

Figure 4: Transverse cooling times of positive ions with different charge states [5] and of H^- ions. The new H^- data are normalized to the same electron density of 1.7×10^{13} cm^{-3} as used for the positive ions, and these were in addition scaled with $q^{1.7}/A$. The new H^- data points were also shifted horizontally so that the beam reaches a cold equilibrium at approximately 0.7 s, as was the case for the positive ions.

DECELERATION OF PROTONS

CRYRING has been used for deceleration in a few cases where users have requested light ions at energies lower than the injection energy of 300 keV per nucleon, as given by the RFQ. For the present investigation of CRYRING properties relevant to FLAIR, however, deceleration throughout the entire range planned for the LSR ring at FLAIR, from 30 MeV to 300 keV, should be performed. Since the injection energy for protons at CRYRING is fixed at 300 keV, these tests must be made by first accelerating the particles from 300 keV to 30 MeV. This does not imply, however, that deceleration can be performed just by reversing the magnet and rf ramps used for acceleration. Remanence and hysteresis effects in the magnets make the deceleration process independent of the acceleration.

Fig. 5 shows an example of beam current and corresponding particle number during an acceleration–deceleration cycle. The beam current was measured using a DC current transformer, and to get a sufficiently good reading of the current, many injection pulses were accumulated at 300 keV, as in the study of the space-charge limit. The resulting stepwise increase of the particle number can be hinted in the figure. Acceleration starts at time zero when the current has reached 4.9 μA, corresponding to 2.1×10^8 stored particles. (The curves are averages from many machine cycles.)

The beam was accelerated first from 300 keV to 3 MeV, and at that energy it was cooled again during 1.5 s while staying bunched before it was accelerated up to 30 MeV. The intermediate cooling was necessary in order to minimize the losses during the deceleration. During acceleration, the current increases with the beam velocity, whereas the particle number should stay constant if there are no losses. It is seen from the figure that there was a small loss of particles at the start of the acceleration, but that the rest of the acceleration and the cooling were made without losses.

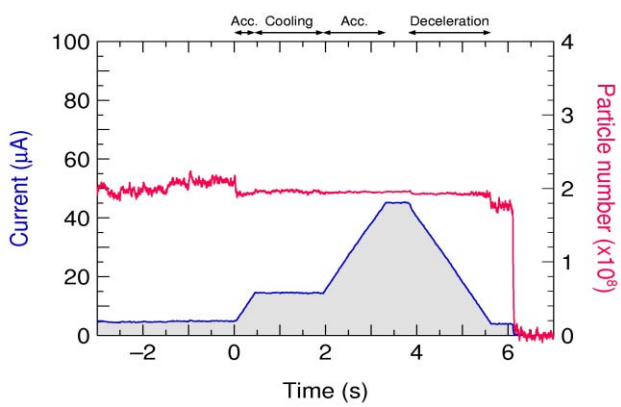

Figure 5: Proton beam current and particle number as functions of time during acceleration and deceleration.

The beam was stored for 0.5 s at 30 MeV, still bunched, and then decelerated back to 300 keV in 1.8 s without further cooling. At 6.1 s, the beam was dumped, and a new cycle started. A very small loss occurred at the start of the deceleration, and somewhat more particles were lost when the deceleration ramp met the flat bottom level. The result was that 1.8×10^8 protons remained when the beam was back at 300 keV. For FLAIR it is the efficiency in deceleration from 30 MeV to 300 keV that is important, and it is thus shown that this deceleration can be made with at least 90% efficiency given the beam properties at 30 MeV of this experiment.

Fig. 6 shows a similar acceleration–deceleration cycle but with an initial beam current almost twice as high. Here the losses were somewhat larger, in particular when the deceleration ramp meets the flat bottom. Still, 2.8×10^8 particles were brought back to 300 keV. With still somewhat higher losses, up to 3.6×10^8 protons have been decelerated down to 300 keV as mentioned above and indicated in fig. 1.

In order to understand why it seems necessary to cool at 3 MeV, the bunch length at 30 MeV has been studied as a function of the amount of cooling at 3 MeV at the same time as deceleration losses were measured. Without cooling at 3 MeV, the space-charge forces were seen to be strong enough for particles to completely fill the rf bucket at 30 MeV even though the beam was cooled at the injection energy. At 3 MeV, the cooling is stronger than at 300 keV since a higher electron current can be used, resulting in bunches that are considerably shorter also at 30 MeV. The result was that a clear correlation between bunch length and deceleration losses was found. At the same time, moderate transverse displacements of the ion beam before deceleration did not cause any losses.

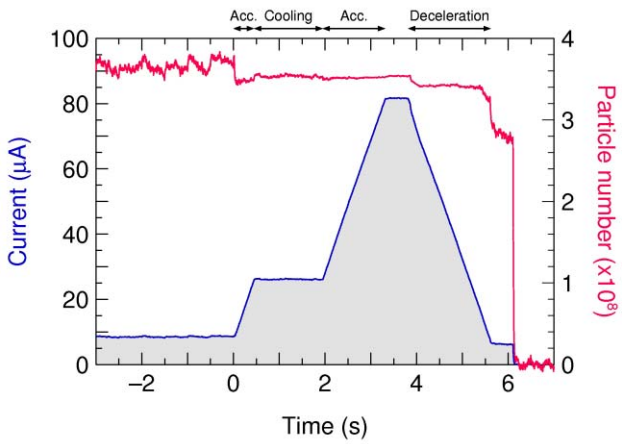

Figure 6: Proton beam current and particle number as in fig. 5 but at higher beam intensity.

It should be added that cooling at 30 MeV was not attempted. The CRYRING cooler in its present configuration uses a 100 times beam expansion and has a quite small electron gun with only 4 mm cathode diameter. This small gun has not been tested to voltages higher than about 10 kV, while electron cooling at 30 MeV would require 16 kV cathode voltage.

CONCLUSION

The deceleration tests presented here prove that CRYRING, as it is set up and operated already today, is able to decelerate protons with high efficiency over the entire energy range required at FLAIR. According to the present planning for FAIR, the end of the commissioning period and the start of operations at FLAIR is defined to occur when 1×10^8 antiprotons have been decelerated to 300 keV. This limit has exceeded by more than a factor three, showing that CRYRING should be able to perform very well as an antiproton and ion deceleration ring at FLAIR.

REFERENCES

[1] FAIR Baseline Technical Report, Eds. H. H. Gutbrod *et al.*, GSI 2006
[2] C.P. Welsch and H. Danared, Proc. EPAC 2006, Edinburg, p. 220 (2006).
[3] Th. Stöhlker *et al.*, Nucl. Instr. Meth B 235, 494 (2005).
[4] A. Paál *et al.*, Proc. EPAC 2004, Lucerne, p. 2748 (2004).
[5] N.S. Dikansky *et al.*, Preprint 88-61, INP Novosibirsk (1988).
[6] H. Danared *et al.*, Proc. EPAC 2000, Vienna, p. 301 (2000).

SIMULATION STUDY OF BEAM ACCUMULATION WITH MOVING BARRIER BUCKETS AND ELECTRON COOLING

T. Katayama, C. Dimopoulou, B. Franzke, M. Steck, GSI, Darmstadt, Germany

D. Moehl, CERN, Geneva, Switzerland

T. Kikuchi, Utsunomiya University, Utsunomiya, Japan

Abstract

An effective ion beam accumulation method for the NESR of the FAIR project, is investigated numerically. The principle of the proposed accumulation method is as follows. The ion beam bunch from the Collector Ring is injected in the longitudinal gap prepared by two moving barrier pulses. The injected beam becomes coasting after switching off the barrier voltages and merges with the previously stacked beam. After the momentum spread is well cooled by electron cooling, the barrier voltages are switched on and moved away from each other to prepare the empty space for the next beam injection. This process is repeated to attain the required intensity. We have investigated this stacking process numerically, including Intra Beam Scattering which limits the momentum spread of the stacked beam and hence the stacked particle number in the ring. Calculated results are compared with experimental data from the ESR where a proof of principle experiment of the proposed method was performed. This experiment is described in a companion paper at the present workshop.

INTRODUCTION

The Barrier Bucket (BB) method is a new way of beam manipulation in longitudinal phase space in synchrotrons and storage rings. One important application of the BB method is a beam injection and accumulation into a storage ring with simultaneous use of beam cooling. As an example, we reported a feasibility study of 3 GeV antiproton beam accumulation in a storage ring with use of BB operation and stochastic cooling in the last workshop [1].

In the present paper, we study a scheme of BB operation for the injection and accumulation of rare isotope beams, typically $^{132}Sn^{50+}$ ions, into the storage ring, NESR (New Experimental Storage Ring), which is conceived as a key experimental ring for the FAIR project at GSI [2].

In the scenario of FAIR, a beam of radioactive nuclei is produced through the nuclear reaction of projectile fragmentation of a high energy heavy ion beam with a target nucleus. Among the many kinds of unstable nuclei produced, the required nuclei beam is selected in the fragment separator and is injected into the Collector Ring (CR). In the CR, momentum spread and transverse emittances of the rare isotope beam are cooled down with stochastic cooling. The cooling time in the CR is a key limitation of repetition time for the injection into the NESR. For the $^{132}Sn^{50+}$ beam with 10^8 ions, and an initial relative momentum spread of 10^{-3} (2σ), the e-folding cooling time is estimated at around 2 sec. The pre-cooled rare isotope beam in the CR is re-bunched with RF field of harmonic number h=1, and is fast extracted. If necessary the beam will be decelerated to 100 MeV/u in another storage ring RESR before injection into the NESR.

The accumulated rare isotope beam in NESR will be used for experiments with an internal target or for head on collision experiments with an electron beam or antiproton beam. To achieve high intensity of the rare isotope beam in the NESR in order to realize a sufficient luminosity, a short cycle time and a highly efficient beam accumulation method is required.

In the present paper, a BB method assisted by electron cooling for stacking of the rare isotope beam is investigated from the point of view of beam dynamics and simulation results are presented. The calculated results are compared with experimental data from the ESR where a proof of principle experiment was performed to verify the accumulation method of the present scenario [3].

OPERATION OF BEAM STACKING

Typical beam parameters of the $^{132}Sn^{50+}$ beam from the Collector Ring are tabulated in Table 1.

Table 1: Beam parameters of $^{132}Sn^{50+}$

Beam energy	740 MeV/u
Number of ions	10^8/batch
Momentum spread at coasting (2σ)	0.05%
Beam duration	400 nsec
Energy spread	±0.6 MeV/u
Transverse emittance (H&V)	0.5π·mm·mrad

Several operation schemes of BB stacking are conceivable, e.g. use of a fixed barrier pulse instead of moving barriers, or use of half wavelength barrier pulses instead of full wave length ones. However we believe that the scheme studied here is the most appropriate option. The operation of the barrier pulses during the first Injection

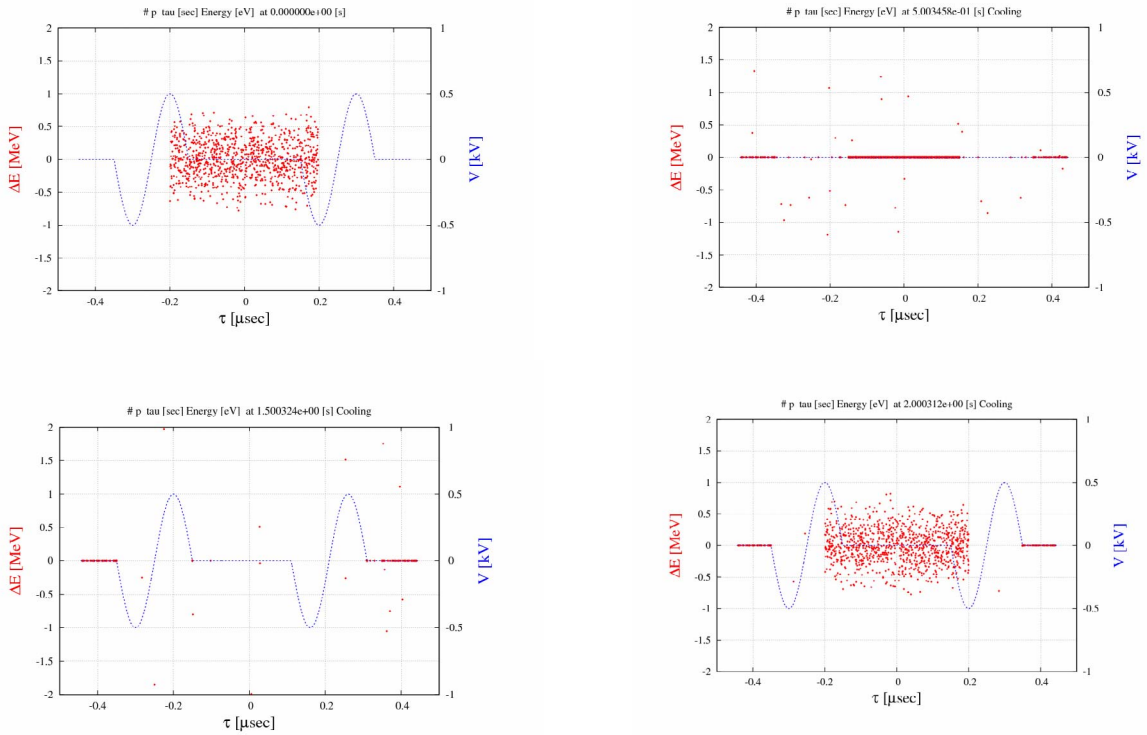

Figure 1: Barrier pulses (blue color) and particle mapping (red points) in the longitudinal phase space. From top left to bottom right, t=0 sec (1st Injection), t=0.5 sec (Cooling), t=1.5 sec (Compression) and t=2.0 sec (2nd injection).

cycle is illustrated in Fig 1. At t=0.0 sec, beam is injected into the 400 nsec gap between the two barriers (Injection). The barrier voltages are gradually decreased and switched off so that the beam becomes coasting (Debunching). At t=1.6 sec the beam is well cooled (Cooling). Then the two BB pulses are switched on next to each other, and moved apart to open the gap for the next beam injection. The previously injected beam is compressed and cooled in the stacked area (Compression). In this example the RF voltage is 500 Volt. At t=2.0 sec, the new batch is injected.

ALGORITHM AND EQUATIONS FOR SIMULATION

Phase Equations

Equations of motion in the longitudinal phase space governed by the barrier bucket voltages are given by

$$\frac{d\tau}{dt} = -\frac{\eta \Delta E}{\beta^2 E_0}, \quad \frac{d(\Delta E)}{dt} = \frac{\varepsilon e V(\tau)}{T_0} \qquad (1)$$

where η is the slip factor of the ring, β the relativistic factor, E_0 the total energy per nucleon of synchronous particle, ΔE the energy deviation from synchronous energy, V the BB pulse voltage. $\varepsilon = Q/A$ is the charge to mass ratio of the ion and T_0 the revolution period in the ring.

Here the canonical variables are τ and ΔE. Note that in the present paper all the values related with energy or momentum are given as the value per nucleon. Separatrix height, namely the maximum deviation of energy in the stable region, is given as

$$\Delta E_b = \left(\frac{2\beta^2 E_0 \varepsilon e V_0 T_1}{\pi |\eta| T_0} \right)^{1/2} \qquad (2)$$

where a barrier voltage of *sin* shape with one full wave length and an amplitude V_0 is assumed. T_1 is the duration of the barrier pulse. It is clear from this formula that the small momentum spread obtained by electron cooling will have a benefit of needing only a low barrier voltage to confine a cooled beam in the stable phase area.

Drag Force of Electron Cooling

Strong electron cooling is a key factor of this scenario. To calculate the cooling drag force, among several formulae, we employ the Parkhomchuk empirical formula [4] which is represented in the laboratory frame as follows. Here ΔE is a energy difference and ε the transverse emittance.

$$\frac{d(\Delta E)}{dt} = -\Delta E \cdot k \cdot G, \quad \frac{d\varepsilon}{dt} = -\varepsilon \cdot 2k \cdot G$$

$$G = \frac{1}{\left[\beta^2\gamma^2\varepsilon/\beta_c + (\Delta E/\beta E_s)^2 + 2T_{e,eff}/m_e c^2\right]^{3/2}}$$

$$k = \frac{4 r_e r_n c n_e \eta_c L_p}{\gamma^2} \cdot \frac{Z^2}{A} \qquad (3)$$

where β and γ are relativistic factors, β_c the betafunction at the cooler section, $T_{e,eff}$ the effective energy spread of electron beam, r_e and r_n are classical electron and nucleon radius, respectively, η_c the ratio of length of electron cooler and ring circumference. The effective electron temperature reflects the quality of the electron cooler and the recent electron cooler has a number of around 10^{-4} eV. The Coulomb logarithm is given as 2.0 for the NESR electron cooler.

Intra Beam Scattering Effects

When one accumulates a large number of ions of low energy and high charge state in the storage ring, the cooled momentum spread and transverse emittances are limited by Intra Beam Scattering. In the present study we calculated the IBS heating rates with use of Martini analytical formula [5] where particle distribution functions are assumed as Gaussian and IBS rates are calculated with use of rms values of momentum spread and transverse emittances. In the present particle tracking, sigma values of Δp/p and transverse emittances are derived from 6D phase points of injected and accumulated particles. IBS heating rates are functions of Twiss parameters of the ring and then they are calculated at each element of the ring and are averaged along the ring circumference.

With use of the calculated IBS heating rates, in the present simulation study, each particle receives a random kick proportional to the heating rate at each computing cycle.

COMPARISON OF CALCULATED AND EXPERIMENTAL RESULTS AT ESR

In order to check the validity of the present stacking scheme we have performed a stacking experiment at ESR [3]. In the following experimental parameters related to the BB operation are compiled.

The circumference of ESR is 108.36 m and the revolution time of the 65 MeV/u $^{40}Ar^{18+}$ ion beam is close to 1.0 μsec. The measured relative momentum spread of the injected beam from SIS-18 is 10^{-3}, defined as 2σ with the Gaussian distribution. The bunch length of injected beam is about 200 nsec, containing $7{\cdot}10^7$ ions.

Table 2: ESR experimental parameters

Beam energy	65.3 MeV/u
Number of ions	$7{\cdot}10^7$/batch
Relative momentum spread at coasting beam(2σ)	0.1%
Bunch duration at injection	200 nsec
Transverse emittance	0.5 π·mm·mrad
Effective cooler length	1.8 m
Beta functions at cooler H/V(Dispersion=0)	16 m/6.88 m
Electron beam current	100–500 mA
Electron beam diameter	5 cm
Magnetic field	0.04 T
Effective electron energy spread $T_{eff,e}$	10^{-3} eV
Maxmal BB Pulse voltage	±170 V
BB Pulse width (*sin* shape)	200 ns (5 MHz)
Adiabatic switch ON of BB	0.5 sec
BB pulse movement speed	0.5 sec
BB voltage decreasing time	10^{-6} sec

Evolution of Electron Cooling and Equilibrium Values

A typical example of the calculated evolution of momentum spread and transverse emittances is illustrated in Fig. 2. The full cooling time down to equilibrium is around 7 sec, and the equilibrium values are determined by the balance of IBS heating and electron cooling.

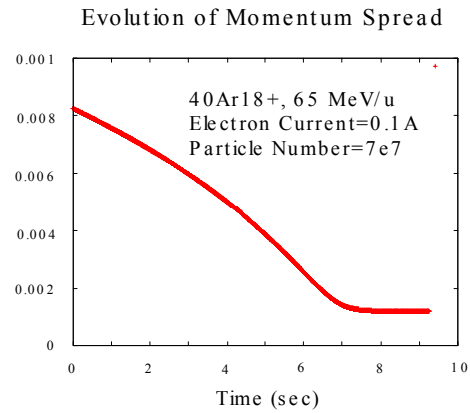

Figure 2 (a): Calculated evolution of momentum spread of the 65 MeV/u $^{40}Ar^{18+}$ beam at ESR. Electron current is 0.1 A and particle number is $7{\cdot}10^7$.

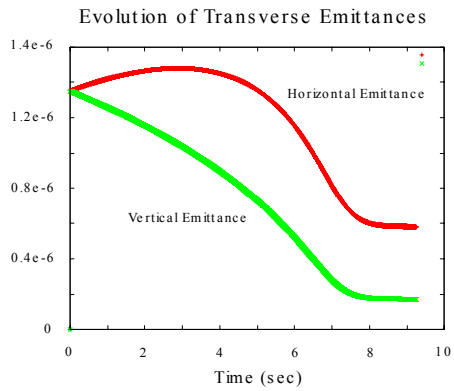

Figure 2 (b): Calculated evolution of transverse emittances. Electron current is 0.1 A and particle number is $7 \cdot 10^7$.

The calculated and measured equilibrium values are given in Fig. 3 as a function of the number of ions. In the figure blue squares show the calculated results and red circles the measured ones. For the horizontal emittance both are quite well in agreement while for the momentum spread the calculated ones are around a factor of 2 larger than the experimental results.

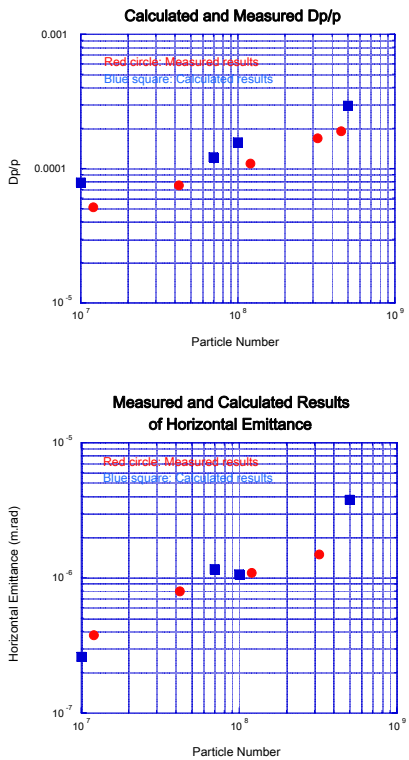

Figure 3: Equilibrium values of momentum spread (top) and horizontal emittance (bottom). Electron current is 0.1 A. Blue squares represent the calculated results and red circle the measured ones.

Stacking Simulation & Experiments

We calculated the stacking process for the ESR parameters and compared them with the experimental results. Typical results of stacking simulations are given in Fig. 4 where accumulated particle number and stacking efficiency are given as a function of time. The cycle time is set as 5 second. The stacking efficiency is around 60 % which has to be compared with the measured results of around 70 %.

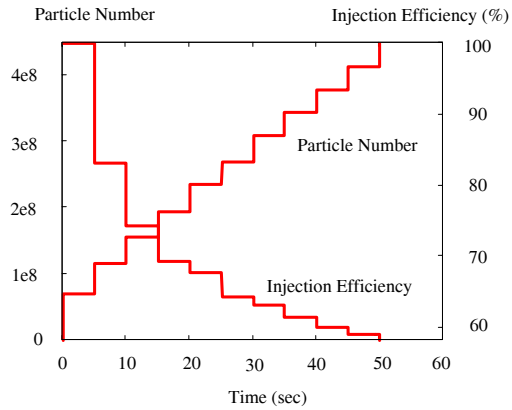

Figure 4: Calculated particle number and stacking efficiency as a function of time. Cycle time is 5 sec, electron current is 0.1 A and the barrier voltage is 120 Volt.

In the experiment the electron current were set at 0.1 A and 0.2 A, and the barrier voltage was 120 Volt. The stacking efficiency gradually decreased during 8 times injection, and the stacking efficiency was around 70 % after the 8th injection. A visible difference of stacking efficiency was not observed for the two electron currents. The primary reason of particle loss is as follows. Accumulated particles that fall into the pulsing time of the injection kicker will be aborted. This happens to particles which are not sufficiently fast moved into the stacking area or if the kicker pulse is misfired or too long. The second reason for losses is that the momentum spread of particles becomes larger than the ring acceptance during the operation of the barrier pulse. In the simulation, these particles are labelled as “LOST PARTICLE”.

SIMULATION RESULTS OF NESR CASE

As described in the preceding sections, the simulation code with moving barrier pulses, electron cooling and IBS, gives results well in agreement with ESR experiment. Therefore we can proceed with confidence to investigate the NESR case with this code.

Parameters of the simulation for the NESR are given in Table 3. Barrier voltages are assumed as ±2kV which will be available with the present RF technology and are sufficient to compress the cooled beam. The time for moving the barrier pulse around half of the NESR circumference is selected as 0. 5 sec which is found to be slow enough to compress the cooled beam into the

stacking area. Then the cycle time of barrier bucket operation is 2 sec.

Table 3: Parameters for simulation of the NESR case

Ion	$^{132}Sn^{50+}$, 740 MeV/u
Transverse emittance (1σ)	0.5π·mm·mrad
Ring revolution time	0.8922 μsec
Injected beam pulse width	0.4 μsec
Fractional momentum spread (1σ)	$2.5 \cdot 10^{-4}$
Ring slipping factor	-0.280
BB Voltage (*sin* wave)	±2kV
BB pulse width (1 λ)	200 nsec
Cycle time	2 sec
Cooler length	5 m
Electron current	1A
Beta function at cooler section (H/V)	22/10 m
Electron diameter	1 cm
Effective electron energy spread	10^{-4} eV

The electron current of the cooler, 1 Ampere is assumed as uniform in the cross sectional area of circle with diameter 1 cm. This diameter matches the ion beam at the cooler section with a beta function of 20m. The electron cooling is continuously applied to the ion beam during the whole process.

The evolution of momentum spread during electron cooling is given in Fig. 5 where we find that the time for cooling to equilibrium is around 0.15 sec. This cooling time is short enough to perform the whole accumulation cycle within 2 sec.

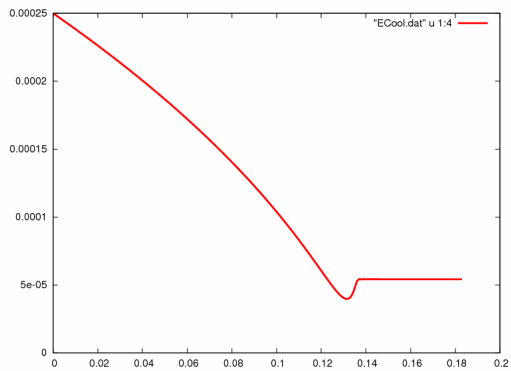

Figure 5: Evolution of momentum spread as a function of time in the NESR.

In Fig. 6 the calculated result of the stacked particle num-ber and the stacking efficiency are illustrated. After 10^{th} injection, the stacking efficiency is 92 % and the number of stacked ions reaches to $9.2 \cdot 10^{8}$.

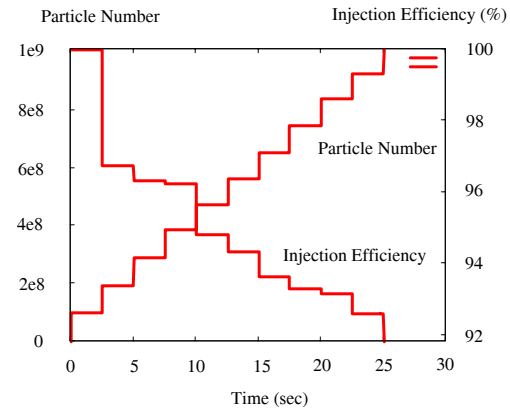

Figure 6: Calculated particle number and stacking efficiency at NESR.

CONCLUSION

We have studied numerically the process of ion beam stacking with moving barrier pulses assisted by electron cooling for the parameters of ESR and NESR. Results for the ESR are compared with the experimental data obtained for a 65 MeV/u Ar beam. The evolution of electron cooling and equilibrium values for momentum spread and transverse emittances are fairly well in agreement with the simulation results. Also the measured stacking efficiency is well reproduced by the simulation code. Therefore it can be reliably expected that a stacking efficiency of more than 90 % will be available with 2kV barrier voltages in the NESR. Another important subject related with the present accumulation method is the space charge repulsion force due the stacked high intensity beam, which reduces the effective barrier voltages and may result in the reduction of the stacked particle number in the accumulated area [6].

REFERENCES

[1] T. Katayama et al., Proc. of the International Workshop on Beam Cooling and Related Topics (COOL05), Illinois, 18-23, September 2005. AIPConf Proc. Vol. 821, p. 196.
[2] C. Dimopoulou et al., Phys. Rev. ST-AB **10**, (2007) 020101
[3] C. Dimopoulou et al., *in this Proceedings*.
[4] V. V. Parkhomchuk, NIM A441 (2000) 9.
[5] M. Martini, CERN PS/84-9 (AA) (1984)
[6] T. Kikuchi et al., *in this Proceedings.*

ELECTRON COOLING SIMULATIONS FOR LOW-ENERGY RHIC OPERATION*

A.V. Fedotov#, I. Ben-Zvi, X. Chang, D. Kayran, T. Satogata, BNL, Upton, NY 11973

Abstract

Recently, a strong interest emerged in running the Relativistic Heavy Ion Collider (RHIC) at low beam total energies of 2.5-25 GeV/nucleon, substantially lower than the nominal beam total energy of 100 GeV/nucleon. Collisions in this low energy range are motivated by one of the key questions of quantum chromodynamics (QCD) about the existence and location of critical point on the QCD phase diagram. Applying electron cooling directly at these low energies in RHIC would result in significant luminosity increase and long beam stores for physics. Without direct cooling in RHIC at these low energies, beam lifetime and store times are very short, limited by strong transverse and longitudinal intrabeam scattering (IBS). In addition, for the lowest energies of the proposed energy scan, the longitudinal emittance of ions injected from the AGS into RHIC may be too big to fit into the RHIC RF bucket. An improvement in the longitudinal emittance of the ion beam can be provided by an electron cooling system at the AGS injection energy. Simulations of electron cooling both for direct cooling at low energies in RHIC and for injection energy cooling in the AGS were performed and are summarized in this report.

INTRODUCTION

RHIC has completed seven successful physics runs since commissioning in 1999. RHIC was built to study the interactions of quarks and gluons and test QCD, the theory describing these interactions. At RHIC, nuclear matter at energy densities only seen in the very early universe is created with relativistic heavy-ion collisions. It was found that at these very large energy densities the matter equilibrates very rapidly, flows as a nearly perfect liquid (small viscosity), has large color fields, collective excitations, and final hadron distributions that reflect the underlying quark structure.

Exploration of the fundamental questions of QCD at RHIC requires large integrated luminosities, as well as high polarization of proton beams. Equally important is the ability to collide various ion species at the full range of available energies. The planned RHIC upgrades are summarized in Ref. [1]. The major upgrade of RHIC calls for 10-fold increase in the luminosity of Au ions at the top energy of 100 GeV/nucleon (termed RHIC-II). Such a boost in luminosity for RHIC-II is achievable with implementation of high-energy electron cooling which is summarized in a separate report [2].

In addition to RHIC-II program at high energies there is a significant interest in low-energy RHIC collisions in the range of 2.5-25 GeV/nucleon total energy of a single beam, motivated by a search for the QCD phase transition critical point [3, 4]. RHIC data will complement existing fixed-target data from AGS and SPS. In this energy range an energy scan will be conducted over about 7 different energies. Although required integrated luminosities needed in this scan are relatively low (5M events minimum per energy), there are several challenges to operate RHIC at such low energies. To evaluate the severity of these challenges and make projections for low-energy operation there have been two one-day test runs during RHIC operations in 2006 and 2007. Results of these test runs are summarized in Ref. [5].

In this report, we present some results of simulations which were performed to evaluate limitations caused by intrabeam scattering (IBS) at these energies, as well as various schemes of electron cooling systems that could be used to counteract IBS growth. All simulations presented in this report were done using the BETACOOL code [6].

PERFORMANCE AND LUMINOSITY LIMITATIONS

For heavy ions at 2.5 GeV/nucleon (total beam energy) the beam size is larger than the nominal injection energy beam size by over a factor of two. As a result, simply fitting low-energy beam into RHIC aperture is challenging. Luminosity lifetime is limited by IBS. An example of emittance growth due to IBS is shown in Fig. 1 for this lowest energy, corresponding to a beam kinetic energy of E_k=1.57 GeV/nucleon. Simulation parameters are given in Table 1, and the corresponding intensity loss due to IBS is shown in Fig. 2. In these simulations it was assumed that the initial longitudinal emittance of the ion bunch is small enough to fit into the bucket acceptance of 0.08 eV-s. To obtain such small emittance, pre-cooling in AGS before injecting into RHIC may be needed; this is discussed later in this paper.

Table 1: Parameters of Au beam for lowest energy scan.

Parameter	Value
Beam total energy E, GeV/nucleon	2.5
Kinetic energy E_k, GeV/nucleon	1.57
Relativistic γ	2.68
Bunch intensity, 10^9	1.0
Rms momentum spread	4×10^{-4}
Rms bunch length, cm	155
Rms emittance (unnormalized), μm	1.04
RF harmonic	387
RF voltage, kV	300

*Work supported by the U.S. Department of Energy
Author email: fedotov@bnl.gov

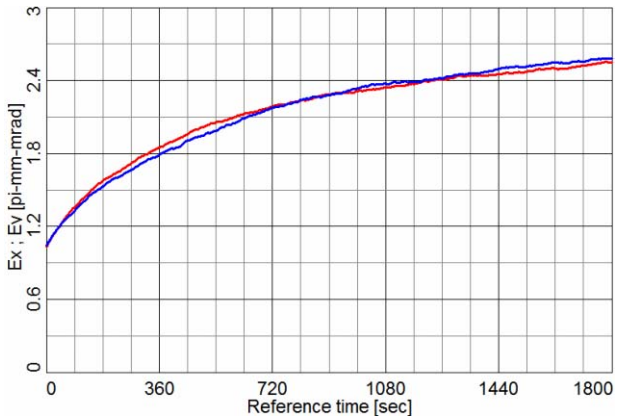

Figure 1: Growth of rms unnormalized emittances (horizontal and vertical) of Au ions in RHIC at kinetic energy of 1.57 GeV/nucleon for parameters of ion bunch given in Table 1.

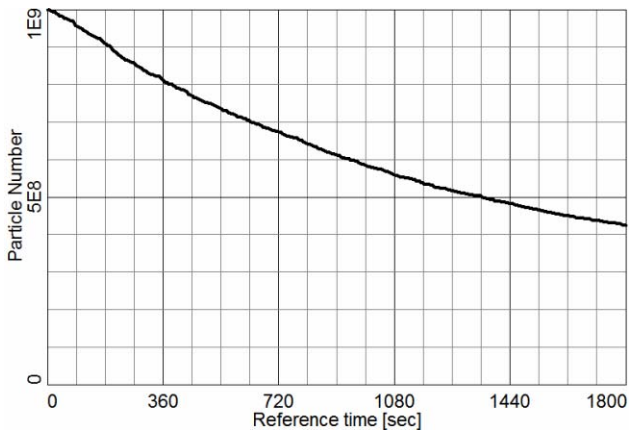

Figure 2: Bunch intensity loss due to IBS at kinetic energy of 1.57 GeV/nucleon for parameters of ion bunch given in Table 1.

For parameters in Table 1 the initial IBS growth times are 250 and 100 sec for transverse and longitudinal emittance, respectively. In IBS simulations shown in Figs. 1-2 no loss on transverse acceptance was assumed. All loss in simulations was purely due to longitudinal IBS resulting in escape of particles from the RF bucket. Slow intensity loss rates of several minutes were observed in the June 2007 test run at E_k=3.66 GeV/nucleon, consistent with predicted transverse IBS growth at that energy [5].

ELECTRON COOLING AT LOW ENERGIES IN RHIC

In Ref. [3] the proposed list of collision energies for the QCD critical point search corresponds to ion beam kinetic energies of E_k=1.6, 2.2, 2.9, 3.45, 5.2, 8.1 and 13.1 GeV/nucleon. An electron beam with a kinetic energy range of 0.87-7.1 MeV is required to cool ions in this energy range. However, for beam energies at and above the present injection energy in RHIC (E_k=10.8 GeV/nucleon), requested luminosities can be easily delivered with only 1-2 days of operations per energy point. As a result, improvements based on electron cooling are not essential for the largest energy points (above E_k=8 GeV/nucleon) in the proposed energy scan. Conversely, the lowest energy points benefit the most from electron cooling; these correspond to electron beam E_k=0.9-2.8 MeV, and are the energies explored here.

Use of electron cooling at low energies in RHIC would counteract IBS and result in small beam emittance and long physics stores. Studies reported in Ref. [7] were based on an electron cooling system developed for RHIC-II [8] which assumed 5nC electron bunches delivered by an Energy Recovery Linac (ERL) and a cooling section up to 80 meters in length. Less demanding cooling scenarios are presented in this paper.

For the lowest energy point, expected peak luminosities are about 5×10^{22} $cm^{-2}s^{-1}$ without electron cooling in RHIC. However, due to a rapid debunching and strong transverse emittance growth, the store length will be just a few minutes with an average luminosity per store about 1×10^{22} $cm^{-2}s^{-1}$. Applying electron cooling directly in RHIC (with parameters of the cooler discussed in this section) will increase average integrated luminosity by at least a factor of 10, and will provide long stores for physics.

ERL based cooler

For proposed high-energy cooling for RHIC-II, the electron beam is delivered by a superconducting ERL with a maximum electron beam energy of 54.3 MeV [9]. To test the hardware and to explore various beam dynamics questions a prototype ERL is presently under construction at BNL with commissioning being planned in early 2009 [10]. This ERL is based on ½ cell superconducting RF gun and a 5-cell superconducting accelerating cavity. It can deliver electron bunches up to energy of 20 MeV. Note that only the gun is needed for electron E_k=0.9-2.8 MeV of interest, and the cooling system can consist of a simple gun to dump setup. In these studies we assume an electron beam charge of 1nC and we limit simulations to the lowest energy of interest. Parameters of electron cooler used in simulations in Figs. 3-4 are given in Table 2. Parameters of the ion beam are given in Table 1. No losses were included in cooling simulations shown, only IBS and electron cooling.

Table 2: Parameters of superconducting gun based electron cooler for low-energy RHIC operation.

Parameter	Value
Kinetic energy, MeV	0.87
Charge per bunch, nC	1
Cooling length L, m	20
Normalized rms emittance, μm	2
Rms momentum spread	3×10^{-4}
Rms beam radius, mm	5
Rms bunch length, mm	8

Figure 3 shows emittance evolution (rms, unnormalized) due to IBS without application of electron cooling (upper black curve) and with electron cooling (lower blue curve). Figure 4 shows evolution of rms

bunch length without electron cooling (upper black curve) and with electron cooling (lower blue curve). One can see that ERL-based cooler at this energy could easily counteract transverse and longitudinal IBS, enabling very long physics store and resulting in a significant luminosity increase.

Note that one gets cooling performance shown in Figs. 3-4 if rms normalized emittance of electron beam with charge of 1 nC is about 2 μm. When emittance of 1 nC bunch is increased up to 4 μm, IBS growth is just compensated (no cooling but no growth due transverse and longitudinal IBS either), which could be sufficient.

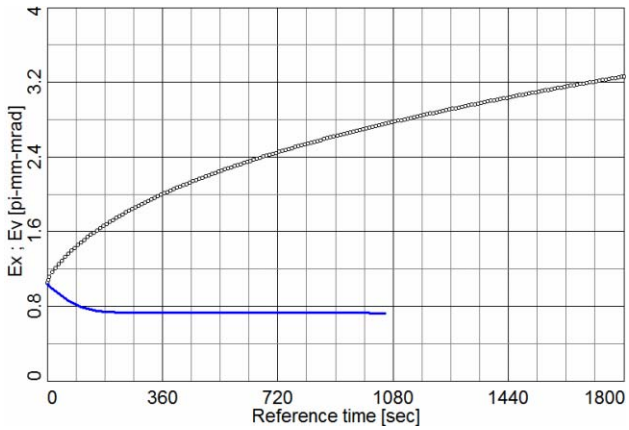

Figure 3: Evolution of transverse emittance (rms, unnormalized) without electron cooling (black upper curve) and with ERL based electron cooling with parameters in Table 2 (blue lower curve).

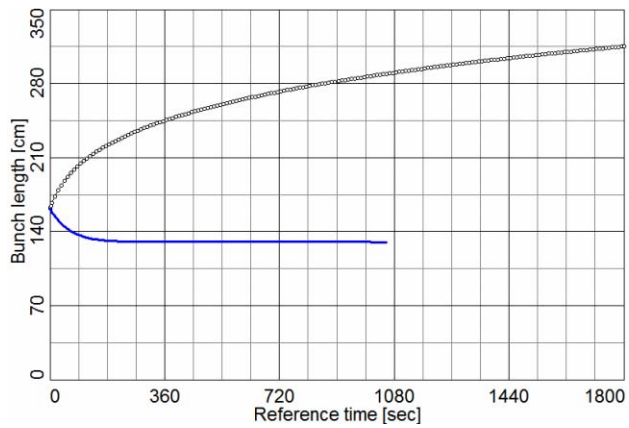

Figure 4: Evolution of rms bunch length without electron cooling (black upper curve) and with ERL based electron cooling with parameters in Table 2 (blue lower curve).

DC Electron Beam Cooler

For completeness, we note that electron cooling with electron beam E_k=0.9-3 MeV can be performed using a DC electron beam, such as from the Recycler cooler at Fermilab [11]. RHIC cooling times would be much smaller than those measured at the Recycler since we need to cool Au ions compared to antiprotons in Recycler. The cooling time is thus reduced by a factor of Z^2/A, where A and Z are the atomic mass and charge of Au ions, respectively.

Figures 5 and 6 show electron cooling simulation for ion beam parameter in Table 1. For simulation based on Recycler cooler, standard parameters of DC electron beam with 0.2A electron beam current were used [12]. One can see comparable performance with both systems. The ERL-based cooling cools at higher energies as well while Recycler cooler is limited to cooling of ions below 9 GeV/nucleon total beam energy.

It should be noted that the present cooling simulations are not optimized, as no specific design of low energy cooling for RHIC exists. However these simulations are promising, and indicate that low energy cooling at RHIC is feasible with realistic electron beam parameters.

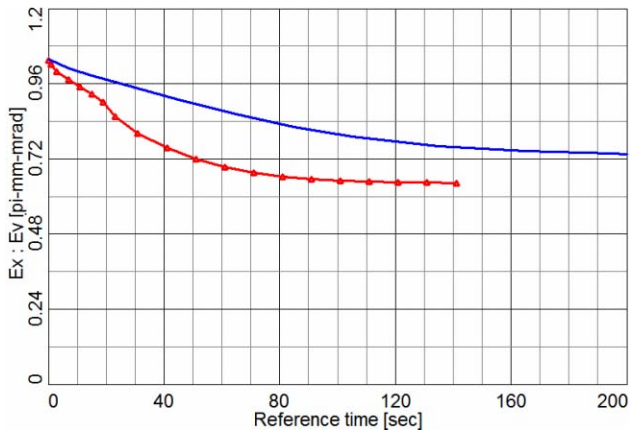

Figure 5: Evolution of transverse emittance (rms, unnormalized) with Recycler-based electron cooling (red lower curve with triangles) and with ERL based electron cooling with parameters in Table 2 (blue upper curve).

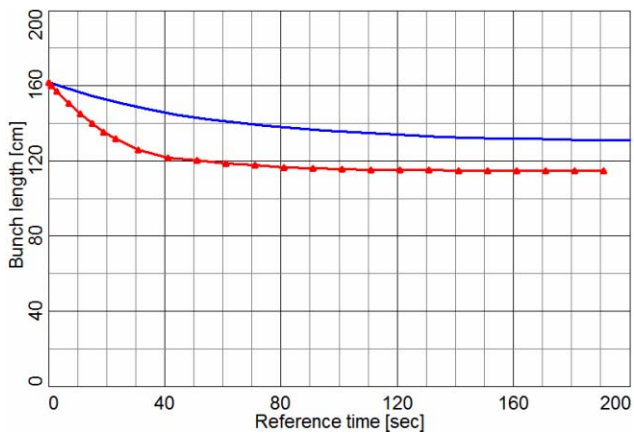

Figure 6: Evolution of rms bunch length with Recycler-based electron cooling (red lower curve with triangles) and with ERL based electron cooling with parameters in Table 2 (blue upper curve).

AGS PRE-COOLING

Although RHIC low-energy electron cooling would provide a significant luminosity increase, very high integrated luminosity is not fully motivated. For the proposed energy scan run, the modest requested luminosities can be delivered without electron cooling in RHIC. 90% longitudinal injection efficiency was achieved

during the test run in June 2007 with an ion beam kinetic energy of 3.66 GeV/nucleon [5]. However, for the remaining 3 lowest energy points the present longitudinal emittance of ion beam may be too big to fit into the RHIC RF acceptance. To improve injection efficiency into RHIC pre-cooling of longitudinal emittance of ion beam at AGS injection energy was considered.

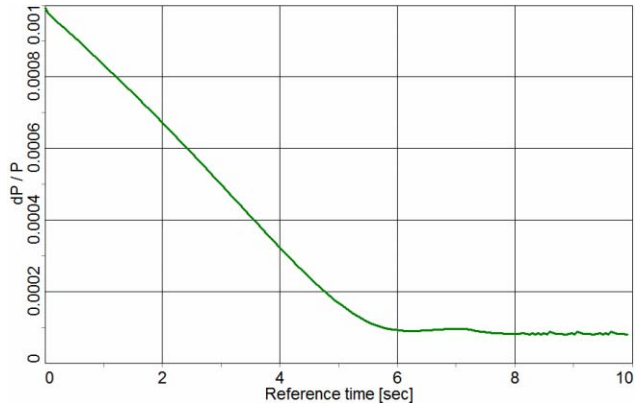

Figure 7: Cooling of rms momentum spread of coasting beam of Au ions at injection energy of AGS.

Table 3: Parameters of AGS cooler and Au ion beam used in simulations of Fig. 7.

Parameter	Value
Electron kinetic energy, keV	53
Relativistic γ	1.1
Relativistic β	0.42
Effective cooling length, m	1.0
Solenoidal magnetic field, T	0.1
Electron beam current, A	1.0
Ion rms momentum spread	1×10^{-3}
Ion rms emittance, unnormalized, μm	3.6
Number of ions	1×10^{9}

The ion beam is injected into AGS with kinetic energy of 97 MeV/nucleon, accelerated and then injected into RHIC. To cool ions at 97 MeV/nucleon one would need standard low-energy DC electron cooler with 53 keV energy. However, in AGS case, one is physically constrained that the full length of the cooler, including toroids, should not exceed 2.6m to fit into the free space available between the magnets, which limits the length of the cooling section increasing the cooling time. On the other hand, cooling time should be fast enough not to impact RHIC injection cycle significantly. In AGS 24 bunches are merged into 4 bunches which are then accelerated and injected into RHIC. To accumulate 100 bunches in a single RHIC ring one then needs 25 AGS cycles (3 seconds each). These constraints were taken into account in simulation studies of electron cooling in AGS. It was found that needed parameters for required cooling are achievable with standard technology. Example of such AGS cooling simulations are shown in Fig. 7. Parameters of AGS cooler used in simulations are given in Table 3.

Simulations in Fig. 7 were done for 1A of electron beam without taken into account well known reduction in cooling rate for high current due to space charge (see for example [13]). A design of the cooler should be carefully done to maximize effective cooling length and to insure good operation at high current to keep cooling times close to the constraints of AGS cycle of about 3 seconds.

FUTURE PLANS

A 14 week low-energy run which should scan 6-7 energies has been proposed for RHIC run 2009-2010. On such a time scale, implementation of electron cooling directly in RHIC is presently not being considered. Commissioning of the ERL is presently scheduled for Spring 2009 [10], and the ERL electron gun may be available in 2010. Feasibility of pre-cooling in AGS is presently under investigation [14]. A test of gold collisions at 1.6 GeV/nucleon kinetic beam energy has been proposed for 2007-2008 RHIC run to determine luminosity lifetime, and to evaluate requirements for potential AGS cooling.

ACKNOWLEDGMENTS

We would like to thank M. Blaskiewicz, M. Brennan, V. Litvinenko, E. Pozdeyev, T. Roser and A. Sidorin for useful discussions.

REFERENCES

[1] A.V. Fedotov, "RHIC plans towards high luminosity", Proc. of PAC07 (Albuquerque, NM, 2007), p. 709.
[2] A.V. Fedotov, "Progress of high-energy cooling for RHIC", these proceedings.
[3] Proceedings of Workshop "Can we discover QCD critical point at RHIC?" (BNL, March 2006), RIKEN BNL Research Center Report No. BNL-75692-2006; http://www..bnl.gov/riken/QCDRhic.
[4] A. Cho, Science, V. 312, April 12, 2006, p 190.
[5] T. Satogata et al., "RHIC challenges for low energy operation", Proceed. of PA C07 (Albuquerque, NM, 2007), p. 1877.
[6] BETACOOL code: http://lepta.jinr.ru; A. Sidorin et al., NIM A 558, p. 325 (2006).
[7] A.V. Fedotov, presentation in Ref. [3].
[8] Electron cooling for RHIC: http://www.bnl.gov/cad/ecooling.
[9] I. Ben-Zvi, Proc. of EPAC06 (Edinburgh), p. 940.
[10] V. N. Litvinenko et al., "Status of R&D ERL at BNL", Proc. of PAC07 (Albuquerque, NM), p. 1347.
[11] S. Nagaitsev et al., PRL. 96, 044801 (2006).
[12] L. Prost, "Electron cooling status at FNAL Recycler", these proceedings.
[13] A.V. Fedotov, B. Galnander, V.N. Litvinenko, T. Lofnes, A. Sidorin, A. Smirnov, V. Ziemann, Phys. Rev. E 73, 066503 (2006).
[14] E. Pozdeyev et al. Detailed assessment of the need of AGS cooling is presently under way.

List of Authors

Italic papercodes indicate primary authors

Institutes List

AEC
Chiba
- Fujimoto, T.
- Iwata, S.I.
- Shibuya, S.

BINP SB RAS
Novosibirsk
- Bubley, A.V.
- Ivanov, A.V.
- Panasyuk, V.M.
- Parkhomchuk, V.V.
- Reva, V.B.

BNL
Upton, Long Island, New York
- Bai, M.
- Ben-Zvi, I.
- Berg, J.S.
- Blaskiewicz, M.
- Brennan, J.M.
- Chang, X.
- Fedotov, A.V.
- Fernow, R.C.
- Fischer, W.
- Gallardo, J.C.
- Kayran, D.
- Kirk, H.G.
- Litvinenko, V.
- Palmer, R. B.
- Podobedov, B.
- Satogata, T.
- Wei, J.
- Yakimenko, V.

CERN
Geneva
- Belochitskii, P.
- Carli, C.
- Möhl, D.
- Thorndahl, L.
- Tranquille, G.

CNS
Saitama
- Katayama, T.

DPNC
Genève
- Blondel, A.P.
- Graulich, J.S.

FZD
Dresden
- Schramm, U.

FZJ
Jülich
- Brittner, P.B.
- Dietrich, J.
- Greven, R.
- Maier, R.
- Prasuhn, D.
- Senichev, Y.
- Singer, H.
- Stassen, R.
- Stockhorst, H.

Fermilab
Batavia, Illinois
- Alexahin, Y.
- Bhat, C.M.
- Broemmelsiek, D.R.
- Burov, A.V.
- Carlson, K.
- Derwent, P.
- Hu, M.
- Kamerdzhiev, V.
- Kuznetsov, G.F.
- Lebedev, V.A.
- Nagaslaev, V.P.
- Neuffer, D.V.
- Pasquinelli, R.J.
- Prost, L.R.
- Shemyakin, A.V.
- Shiltsev, V.D.
- Sun, D.
- Sutherland, M.
- Warner, A.
- Werkema, S.J.
- Zhang, X.

GSI
Darmstadt
- Beckert, K.
- Beller, P.
- Boine-Frankenheim, O.
- Bosch, F.G.
- Dimopoulou, C.
- Dolinskii, A.
- Franchetti, G.
- Franzke, B.
- Gostishchev, V.
- Hasse, R.W.
- Herfurth, F.
- Katayama, T.
- Kester, O.K.
- Kluge, H.J.
- Koszudowski, S.
- Kozhuharov, C.
- Krämer, D.
- Kuehl, T.
- Maero, G.

- Noertershaeuser, W.
- Nolden, F.
- Peschke, C.
- Quint, W.
- Schreiber, G.
- Sorge, S.
- Steck, M.

HU/AdSM
Higashi-Hiroshima
- Kaneta, K.
- Sugimoto, H.
- Yuri, Y.

Hiroshima University
Higashi-Hiroshima
- Okamoto, H.

IHEP Beijing
Beijing
- Wang, S.

IMP
Lanzhou
- Gao, D.Q.
- He, Y.
- Li, G.H.
- Li, J.
- Liu, Y.
- Mao, L.J.
- Mao, R.S.
- Song, M.T.
- Xia, J.W.
- Xiao, G.Q.
- Yang, J.C.
- Yang, X.D.
- Yang, X.T.
- Yuan, Y.J.
- Zhan, W.-L.
- Zhang, W.
- Zhao, H.W.
- Zhao, T.C.
- Zheng, J.H.
- Zhou, Z.Z.

IUCF
Bloomington, Indiana
- Lee, S.-Y.

JINR
Dubna, Moscow Region
- Ahmanova, E.V.
- Bykovsky, V.
- Kobets, A.G.
- Korotaev, I.I.
- Lokhmatov, V.I.
- Malakhov, V.N.
- Meshkov, I.N.
- Pavlov, V.
- Pivin, R.
- Rudakov, A.Yu.
- Sidorin, A.O.
- Smirnov, A.V.
- Syresin, E.
- Trubnikov, G.V.
- Yakovenko, S.

Jefferson Lab
Newport News, Virginia
- Derbenev, Y.S.

Johannes Gutenberg University Mainz
Mainz
- Geppert, Ch.
- Karpuk, S.

Johannes Gutenberg University Mainz, Institut für Physik
Mainz
- Novotny, C.

Kyoto ICR
Uji, Kyoto
- Fujimoto, S.
- Ikegami, M.
- Ishikawa, T.
- Nakao, M.
- Noda, A.
- Shirai, T.
- Souda, H.
- Tanabe, M.
- Tongu, H.

LBNL
Berkeley, California
- Barletta, W.A.
- Sessler, A.
- Zholents, A.
- Zolotorev, M.S.

LMU
München
- Bussmann, M.H.
- Habs, D.

MIT
Cambridge, Massachusetts
- Hays-Wehle, J.P.
- Kaertner, F.X.
- Redwine, R.P.
- Siddiqui, A.M.
- Dow, K.A.
- Franklin, W.A.
- Milner, R.
- Tschalaer, C.
- Tsentalovich, E.

- Wang, D.
- Wang, F.
- van der Laan, J.

MPI-K
Heidelberg
- Fadil, H.
- Grieser, M.
- Hoffmann, J.
- Krantz, C.
- Novotny, O.
- Novotny, S.
- Orlov, D.
- Reinhardt, S.
- Wolf, A.

MPQ
Garching, Munich
- Saathoff, G.

MSL
Stockholm
- Danared, H.
- Källberg, A.
- Simonsson, A.

Muons, Inc
Batavia
- Johnson, R.P.
- Kahn, S.A.

NIRS
Chiba-shi
- Noda, K.

NSCL
East Lansing, Michigan
- Schwarz, S.

TSL
Uppsala
- Bergmark, T.
- Byström, O.
- Gålnander, B.
- Johnson, S.
- Johnson, T.
- Lofnes, T.
- Norman, G.
- Peterson, T.
- Rathsman, K.
- Reistad, D.

Tech-X
Boulder, Colorado
- Bell, G.I.
- Bruhwiler, D.L.
- Sobol, A.V.

UMiss
University, Mississippi
- Summers, D.J.

Utsunomiya University
Utsunomiya
- Kawata, S.
- Kikuchi, T.

Participants List

— A —

Brigitte **Azzara**
GSI
D-64291 Darmstadt
Germany

— B —

Pavel **Belochitskii**
CERN, AB
CH-1211 Geneva 23
Switzerland

Ilan **Ben-Zvi**
Brookhaven National Laboratory
11973 Upton, NY
USA

Michael **Blaskiewicz**
Brookhaven National Laboratory
11973 Upton, NY
USA

Fritz **Bosch**
GSI
D-64291 Darmstadt
Germany

Mike **Brennan**
Brookhaven National Laboratory
11973 Upton, NY
USA

David **Bruhwiler**
Tech-X-Corporation
80303 Boulder, CO
USA

Alexander **Bubley**
Budker Institute of Nuclear Physics
630090 Novosibirsk, Sibirea
Russia

Michael **Bussmann**
LMU München
D-85748 Garching
Germany

— C —

Christian **Carli**
CERN, AB
CH-1211 Geneva 23
Switzerland

— D —

Håkan **Danared**
Manne Siegbahn Laboratory
S-10405 Stockholm
Sweden

Yaroslav S **Derbenev**
Thomas Jefferson
National Accelerator Facility
23606 Newport News, VA
USA

Paul F **Derwent**
Fermi National Accelerator Laboratory
60510 Batavia, IL
USA

Jürgen **Dietrich**
FZ Jülich
D-52425 Jülich
Germany

Christina **Dimopoulou**
GSI
D-64291 Darmstadt
Germany

Erika C. **Ditter**
GSI
D-64291 Darmstadt
Germany

Alexeii **Dolinskii**
GSI
D-64291 Darmstadt
Germany

— F —

Alexei **Fedotov**
Brookhaven National Laboratory
11973 Upton, NY
USA

Wilbur **Franklin**
Bates Linear Accelerator Center, M.I.T.
01949 Middleton, MA
USA

Bernhard **Franzke**
GSI
D-64291 Darmstadt
Germany

— G —

Björn **Gålnander**
TSL Uppsala Univ.
S-75121 Uppsala
Sweden

Oleksii **Gorda**
GSI
D-64291 Darmstadt
Germany

Vitaliy **Gostishchev**
GSI
D-64291 Darmstadt
Germany

Jean-Sebastien **Graulich**
DPNC, Universite de Geneve
CH-1211 Geneva 23
Switzerland

Manfred **Grieser**
DPNC, Universite dè Geneve
D-69120 Heidelberg
Germany

— H —

Rainer W. **Hasse**
GSI
D-64291 Darmstadt
Germany

— J —

Rolland P. **Johnson**
Muons, Inc.
23606 Newport News, VA
USA

— K —

Vsevolod **Kamerdzhiev**
FNAL
60510 Batavia, IL
USA

Paola **Karampougiouki**
GSI
D-64291 Darmstadt
Germany

Takeshi **Katayama**
GSI
188-0004 Nishi, Tokyo
Japan

Takashi **Kikuchi**
Utsunomiya University
3218585 Utsunomiya, Tochigi
Japan

Andriy G **Kobets**
Joint Institute for Nuclear Research
141980 Dubna
Russia

Claude **Krantz**
MPI Heidelberg
D-69120 Heidelberg
Germany

Dieter **Krämer**
GSI
D-64291 Darmstadt
Germany

— L —

Valeri A **Lebedev**
Accelerator Division
Fermi National Accelerator Laboratory
60510 Batavia, IL
USA

— M —

Giancarlo **Maero**
GSI
D-64291 Darmstadt
Germany

Michaela **Marx**
DESY
D-22607 Hamburg
Germany

Igor N. **Meshkov**
JINR
141980 Dubna
Russia

Dieter **Möhl**
CERN
CH-1211 Geneva 23
Switzerland

— N —

Vladimir P **Nagaslaev**
Fermi National Accelerator Laboratory
60510 Batavia, IL
USA

Akira **Noda**
Institute for Chemical Research,
Kyoto University
611-0011 UJi-city, Kyoto
Japan

Fritz **Nolden**
GSI
D-64291 Darmstadt
Germany

Gunnar **Norman**
TSL, Uppsala University
S-75121 Uppsala
Sweden

— O —

Hiromi **Okamoto**
Hiroshima University
Higashi-Hiroshima
Japan

Dmitry **Orlov**
MPI für Kernphysik
D-69120 Heidelberg
Germany

— P —

Vasily V. **Parkhomchuk**
Budker Institute of Nuclear Physics
630090 Novosibirsk, Sibirea
Russia

Ralph J **Pasquinelli**
AD/RF Department
Fermi National Accelerator Laboratory
60510 Batavia, IL
USA

Claudius **Peschke**
GSI
D-64291 Darmstadt
Germany

Eduard G. **Pozdeyev**
Brookhaven National Laboratory
11973 Upton, NY
USA

Lionel R **Prost**
Fermi National Accelerator Laboratory
60510 Batavia, IL
USA

— R —

Dag **Reistad**
TSL Uppsala University
S-75121 Uppsala
Sweden

Vladimir B. **Reva**
Budker Institute of Nuclear Physics
630090 Novosibirsk, Sibirea
Russia

— S —

Volker RW **Schaa**
GSI
D-64291 Darmstadt
Germany

Yury **Senichev**
FZ Jülich
D-52425 Jülich
Germany

Andrew M. **Sessler**
Lawrence Berkeley National Laboratory
94720 Berkeley, CA
USA

Alexander V. **Shemyakin**
AD/Recycler
Fermi National Accelerator Laboratory
60134 Batavia, IL
USA

Toshiyuki **Shirai**
Institute for Chemical Research,
Kyoto University
6110011 Uji, Kyoto
Japan

Anatoly O. **Sidorin**
Joint Institute for Nuclear Research
141980 Dubna
Russia

Alexander **Skrinsky**
Budker Institute of Nuclear Physics
630090 Novosibirsk, Sibirea
Russia

Alexander V **Smirnov**
Joint Institute for Nuclear Research
141980 Dubna
Russia

Stefan **Sorge**
GSI
D-64291 Darmstadt
Germany

Rolf **Stassen**
FZ Jülich
D-52425 Jülich
Germany

Markus **Steck**
GSI
D-64291 Darmstadt
Germany

Hans **Stockhorst**
FZ Jülich
D-52425 Jülich
Germany

Evgeny M **Syresin**
Joint Institute for Nuclear Research
141980 Dubna
Russia

— T —

Lars **Thorndahl**
CERN
CH-1211 Geneva 23
Switzerland

Gerard **Tranquille**
CERN, AB
CH-1211 Geneva 23
Switzerland

Chris **Tschalaer**
MIT-Bates
Rockport, MA
USA

— W —

Jie **Wei**
Brookhaven National Laboratory
11973 Upton, NY
USA

Andreas **Wolf**
Max-Planck-Institut für Kernphysik
D-69117 Heidelberg
Germany

— Y —

Xiaodong **Yang**
Institute of Modern Physics
Chinese Academy of Sciences
730000 Lanzhou, Gansu
P.R. China

— Z —

Max S **Zolotorev**
Lawrence Berkeley National Laboratory
94720 Berkeley, CA
USA